



**FRIEDRICH-SCHILLER-  
UNIVERSITÄT  
JENA**

# **Synthesis and Investigation of [FeFe] Hydrogenase Mimics**

## **Dissertation**

**(kumulativ)**

zur Erlangung des akademischen Grades doctor rerum naturalium

(Dr. rer. nat.)

vorgelegt dem Rat der Chemisch-Geowissenschaftlichen Fakultät

der Friedrich-Schiller-Universität Jena

von M.Sc. Stefan Benndorf

geboren am 19.07.1990 in Chemnitz

Gutachter:

1. Prof. Dr. Wolfgang Weigand, Friedrich-Schiller-Universität Jena, Chemisch-Geowissenschaftliche Fakultät, Institut für Anorganische und Analytische Chemie, 07743 Jena, Deutschland
2. Prof. Dr. Bernd Schöllhorn, Université Paris Cité, CNRS, Laboratoire d'Electrochimie Moléculaire, F-75013 Paris, Frankreich

Tag der öffentlichen Verteidigung: 23.02.2024

“There is nothing more exciting than science. You get all the fun of sitting still, being quiet, writing down numbers, paying attention... Science has it all.”

- Principal Skinner -

# Table of contents

<b>ABBREVIATIONS</b> .....	<b>I</b>
<b>1. LIST OF PUBLICATIONS</b> .....	<b>IV</b>
1.1 ADDITIONAL PUBLICATIONS.....	VI
1.2 ADDITIONAL PRESENTATIONS .....	VI
<b>2. DECLARATION</b> .....	<b>VIII</b>
2.1 DOCUMENTATION OF AUTHORSHIP .....	IX
<b>3. MOTIVATION AND STATE-OF-THE-ART</b> .....	<b>1</b>
3.1 H <sub>2</sub> – SUSTAINABLE ENERGY CARRIER OF THE FUTURE.....	4
3.1.1 Utilization and Storage of H <sub>2</sub> .....	4
3.1.2 “Colors” of H <sub>2</sub> .....	6
3.1.3 The Hydrogen Square Model.....	6
3.1.4 H <sub>2</sub> Generation.....	7
3.1.4.1 Electrolysis.....	7
3.1.4.2 Photolysis .....	8
3.1.4.3 Biomass .....	9
3.2 HYDROGENASE ENZYMES .....	12
3.2.1 Hydrogenase Classification .....	14
3.2.1.1 [Fe] Hydrogenases .....	14
3.2.1.2 [NiFe] Hydrogenases .....	15
3.2.1.3 [FeFe] Hydrogenases .....	16
3.2.2 [FeFe] Hydrogenase Maturation .....	18
3.2.3 [FeFe] Hydrogenase Modification .....	19
3.2.4. Catalytic cycle of the biological hydrogen evolution reaction.....	20
3.3 MIMICKING [FeFe] HYDROGENASE ENZYMES.....	23
3.3.1 Synthesis of [FeFe] Hydrogenase Mimics .....	24
3.3.2 Electrocatalytic active [FeFe] Hydrogenase Mimics .....	28
3.3.2.1 Electrocatalytic hydrogen evolution reaction mechanism .....	29
3.3.2.2 Enhanced electrocatalytic hydrogen evolution .....	32
3.3.3 Photocatalytic active [FeFe] H <sub>2</sub> ase Mimics.....	32
<b>4. DISCUSSION</b> .....	<b>35</b>
4.1 SB-1 UNRAVELLING THE MYSTERY: ENLIGHTENMENT OF THE UNCOMMON ELECTROCHEMISTRY OF NAPHTHALENE MONOIMIDE [FeFe] HYDROGENASE MIMICS .....	36
4.2 SB-2 COVALENT FUNCTIONALIZATION OF CdSe QUANTUM DOT FILMS WITH MOLECULAR [FeFe] HYDROGENASE MIMICS FOR LIGHT-DRIVEN HYDROGEN EVOLUTION .....	41

4.3 SB-3 SYNTHESIS OF [FeFe] HYDROGENASE MIMICS WITH LIPOIC ACID AND ITS SELENIUM ANALOGUE AS ANCHOR GROUPS.....	47
4.4 SB-4 NMP MAKES THE DIFFERENCE – FACILITATED SYNTHESIS OF [FeFe] HYDROGENASE MIMICS.....	52
<b>5. SUMMARY .....</b>	<b>58</b>
<b>6. ZUSAMMENFASSUNG .....</b>	<b>63</b>
<b>7. PUBLICATIONS .....</b>	<b>68</b>
7.1 [SB-1] .....	68
7.2 [SB-2] .....	108
7.3 [SB-3] .....	135
7.4 [SB-4] .....	169
7.5 [SB-5] .....	199
<b>8. ACKNOWLEDGMENTS .....</b>	<b>212</b>
<b>9. DECLARATION OF AUTHORSHIP / SELBSTSTÄNDIGKEITSERKLÄRUNG .....</b>	<b>214</b>
<b>10. REFERENCES.....</b>	<b>215</b>

## Abbreviations

AcOH	acetic acid
C	chemical process (CV)
CCS	Carbon Capture and Storage
CdSe	cadmium selenide
<i>C.E.</i>	catalytic efficiency
CTPs'	climate tipping points
CV	cyclic voltammetry
DC	direct current
DCC	<i>N, N'</i> -dicyclohexylcarbodiimide
DMAP	4-dimethylaminopyridine
E	electrochemical process (CV)
e.g.	<i>exempli gratia</i>
EPR	electron paramagnetic resonance
equiv.	equivalents
ET	electron transfer
GC-TCD	gas chromatography - thermal conductivity detector
GHG	greenhouse gases
H <sub>2</sub> ase	hydrogenase
HBF <sub>4</sub>	tetrafluoroboric acid
HClO <sub>4</sub>	perchloric acid
HER	hydrogen evolution reaction
HM-AA	[FeFe] H <sub>2</sub> ase mimic based on 2-carboxy-1,3-propanedithiol

HM-LA	[FeFe] hydrogenase mimic based on 6,8-dithiooctanoic acid
HOTf	triflic acid
HydS	Hydrogen Square
ICP-OES	inductively coupled plasma optical emission spectrometry
IR	infrared spectral region
L	ligand
MPA	mercaptopropionic acid
MS	mass spectrometry
NHE	normal hydrogen electrode
nm	nanometer
NMP	<i>N</i> -methyl-2-pyrrolidone
NMR	nuclear magnetic resonance
PCET	proton-coupled electron transfer
PS	photosensitizer
PSI	photosynthesis system I
PSII	photosynthesis system II
PV	photovoltaics
QD	quantum dot
RT	room temperature
SAMs	self-assembled monolayers
SEC	spectroelectrochemical
SED	sacrificial electron donor
TFA	trifluoroacetic acid

THF	tetrahydrofuran
TOF	turnover frequency
TON	turnover number
TOPO	trioctylphosphine oxide
UV-Vis	ultraviolet and visible spectral region
XPS	X-ray photoelectron spectroscopy
$\mu$ XRF	micro-X-ray fluorescence spectrometry



## 1. List of Publications

**[SB-1]** Unravelling the Mystery: Enlightenment of the Uncommon Electrochemistry of Naphthalene Monoimide [FeFe] Hydrogenase Mimics

Stefan Benndorf, Elisabeth Hofmeister, Maria Wächtler, Helmar Görls, Phil Liebing, Kalina Peneva, Stefanie Gräfe, Stephan Kupfer, Benjamin Dietzek-Ivanšić and Wolfgang Weigand

*Eur. J. Inorg. Chem.* **2022**, 3, e202100959.

**[SB-2]** Covalent Functionalization of CdSe Quantum Dot Films with Molecular [FeFe] Hydrogenase Mimics for Light-Driven Hydrogen Evolution

Stefan Benndorf,<sup>‡</sup> Alexander Schleusener,<sup>‡</sup> Riccarda Müller, Mathias Micheel, Raktim Baruah, Jan Dellith, Andreas Undisz, Christof Neumann, Andrey Turchanin, Kerstin Leopold, Wolfgang Weigand and Maria Wächtler

*ACS Appl. Mater. Interfaces* **2023**, 15, 18889–18897.

<sup>‡</sup> These authors contributed equally.

**[SB-3]** Synthesis of [FeFe] Hydrogenase Mimics with Lipoic acid and its Selenium Analogue as Anchor Groups

Stefan Benndorf, Sihem Groni, Leanne M. Stafast, Helmar Görls, Claire Fave, Bernd Schöllhorn and Wolfgang Weigand

*Eur. J. Inorg. Chem.* **2023**, 26, e202200684.

**[SB-4]** NMP makes the Difference – Facilitated Synthesis of [FeFe] Hydrogenase Mimics

Stefan Benndorf, Philipp Buday, Benedikt Callies, Helmar Görls, Stephan Kupfer and Wolfgang Weigand

*Dalton trans.* **2023**, 52, 7421.

**[SB-5]** Neue Synthesemethode zur Herstellung zweikerniger Eisenhexacarbonylkomplexe mit schwefel-, selen- oder tellurhaltigen Liganden

Stefan Benndorf and Wolfgang Weigand

Offenlegungsschrift, *DE 10 2021 001 823 A1*, 06.10.2022.

## 1.1 Additional publications

**[1]** Ultrafast Electron Transfer from CdSe Quantum Dots to an [FeFe]-Hydrogenase Mimic

Alexander Schleusener, Mathias Micheel, Stefan Benndorf, Markus Rettenmayr, Wolfgang Weigand and Maria Wächtler

*J. Phys. Chem. Lett.* **2021**, *12*, 4385–4391.

## 1.2 Additional presentations

**[1]** Synthesis of Cellulose-based [FeFe]-Hydrogenase Model Complexes

Stefan Benndorf, Martin Gericke, Kalina Peneva, Thomas Heinze und Wolfgang Weigand

*15. Mitteldeutsches Anorganiker Nachwuchssymposium, Leipzig, 2017.*

**[2]** Synthesis of Photoactive [FeFe] Hydrogenase Model Systems (poster)

Stefan Benndorf, Alexander Schleusener, Maria Wächtler, Martin Gericke, Thomas Heinze, Kalina Peneva and Wolfgang Weigand

*28<sup>th</sup> International Symposium on Organic Chemistry of Sulfur, ISOCS, Tokyo, 2018.*

**[3]** Synthesis of Photoactive [FeFe] Hydrogenase Mimics

Stefan Benndorf and Wolfgang Weigand

*Presentation at Rikkyo University, Tokyo, 2018.*

**[4] Synthesis of Photoactive [FeFe] Hydrogenase Mimics**

Stefan Benndorf and Wolfgang Weigand

*Iwate-Rikkyo Research Seminar, Rikuzentakata, 2018.*

**[5] Synthesis of Photoactive [FeFe] Hydrogenase Mimics**

Stefan Benndorf, Alexander Schleusener, Maria Wächtler, Martin Gericke, Thomas Heinze, Kalina Peneva and Wolfgang Weigand

*Koordinationschemiker-Treffen, KCT20, Freiburg, 2020.*



## 2.1 Documentation of Authorship

### “Unravelling the Mystery: Enlightenment of the Uncommon Electrochemistry of Naphthalene Monoimide [FeFe] Hydrogenase Mimics”

Stefan Benndorf,<sup>1</sup> Elisabeth Hofmeister,<sup>2</sup> Maria Wächtler,<sup>3</sup> Helmar Görls,<sup>4</sup> Phil Liebing,<sup>5</sup>  
**SB-1** Kalina Peneva,<sup>6</sup> Stefanie Gräfe,<sup>7</sup> Stephan Kupfer,<sup>8</sup> Benjamin Dietzek-Ivanšić,<sup>9</sup> and  
 Wolfgang Weigand<sup>10</sup>

*Eur. J. Inorg. Chem.* **2022**, 3, e202100959.

Author	1	2	3	4	5	6	7	8	9	10
Conceptual development	X		X							X
Synthesis	X									
Cyclic voltammetry	X									
Spectroelectro chemistry	X	X								
Crystal structures				X	X					
DFT calculations								X		
EPR measurements		X								
Other analytical measurements	X									
Preparation of manuscript	X	X						X		
Correction of manuscript	X	X	X	X	X	X	X	X	X	X
Preparation of cover graphic	X									
Proposed publication equivalent	1.0									

### “Covalent Functionalization of CdSe Quantum Dot Films with Molecular [FeFe] Hydrogenase Mimics for Light-Driven Hydrogen Evolution”

Stefan Benndorf,<sup>1‡</sup> Alexander Schleusener,<sup>2‡</sup> Riccarda Müller,<sup>3</sup> Mathias Micheel,<sup>4</sup> Raktim  
**SB-2** Baruah,<sup>5</sup> Jan Dellith,<sup>6</sup> Andreas Undisz,<sup>7</sup> Christof Neumann,<sup>8</sup> Andrey Turchanin,<sup>9</sup> Kerstin  
 Leopold,<sup>10</sup> Wolfgang Weigand<sup>11</sup> and Maria Wächtler<sup>12</sup>

*ACS Appl. Mater. Interfaces* **2023**, 15, 18889–18897.

Author	1	2	3	4	5	6	7	8	9	10	11	12
Conceptual development	X	X									X	X
Synthesis	X	X										
Sample preparation	X	X			X							
HER experiments	X											
XPS measurements								X				
μXRF measurements			X									
Other analytical measurements	X	X			X	X	X					
Preparation of manuscript		X		X				X				
Correction of manuscript	X	X	X	X	X			X	X	X	X	X
Investigation	X	X	X		X	X	X	X				
Preparation of cover graphic		X										
Proposed publication equivalent	1.0											

‡ Shared first authorship

**“Synthesis of [FeFe] Hydrogenase Mimics with Lipoic acid and its Selenium Analogue as Anchor Groups”**

**SB-3** Stefan Benndorf,<sup>1</sup> Sihem Groni,<sup>2</sup> Leanne M. Stafast,<sup>3</sup> Helmar Görls,<sup>4</sup> Claire Fave,<sup>5</sup>  
Bernd Schöllhorn<sup>6</sup> and Wolfgang Weigand<sup>7</sup>

*Eur. J. Inorg. Chem.* **2023**, 26, e202200684.

<b>Author</b>	1	2	3	4	5	6	7
Conceptual development	X					X	X
Synthesis	X		X				
Cyclic voltammetry	X	X			X		
Spectroelectro chemistry	X						
Crystal structures				X			
Electrode modification		X			X		
Other analytical measurements	X		X				
Preparation of manuscript	X				X	X	
Correction of manuscript	X	X	X	X	X	X	X
Preparation of cover graphic	X						X
Proposed publication equivalent	1.0						

**“NMP makes the Difference – Facilitated Synthesis of [FeFe] Hydrogenase Mimics”**

**SB-4** Stefan Benndorf,<sup>1</sup> Philipp Buday,<sup>2</sup> Benedikt Callies,<sup>3</sup> Helmar Görls,<sup>4</sup> Stephan Kupfer<sup>5</sup>  
and Wolfgang Weigand<sup>6</sup>

*Dalton Trans.* **2023**, 52, 7421.

<b>Author</b>	1	2	3	4	5	6
Conceptual development	X					X
Synthesis	X	X	X			
Kinetic studies	X					
Crystal structures				X		
DFT calculations					X	
Other analytical measurements	X	X	X			
Preparation of manuscript	X		X		X	
Correction of manuscript	X	X	X	X	X	X
Preparation of cover graphic	X					
Proposed publication equivalent	1.0					

**“Neue Synthesemethode zur Herstellung zweikerniger Eisenhexacarbonylkomplexe  
mit schwefel-, selen- oder tellurhaltigen Liganden”**

**SB-5**

Stefan Benndorf<sup>1</sup> and Wolfgang Weigand<sup>2</sup>

*Offenlegungsschrift, DE 10 2021 001 823 A1, 06.10.2022.*

<b>Author</b>	<b>1</b>	<b>2</b>
Conceptual development	X	X
Synthesis	X	
Other analytical measurements	X	
Preparation of manuscript	X	
Correction of manuscript	X	X
Proposed publication equivalent	0.0	



### 3. Motivation and State-of-the-art

To this date, there is a need for change regarding the current energy and climate crises, which have been propounded to be the most critical worldwide threats.<sup>[1-5]</sup> Increasing population and their desire to improve their living standard result in a rising demand for energy and pollution of the environment that appear interminable.<sup>[3-12]</sup> Consequently, national and international conflicts in the past and future were based on the scarcity of natural resources, like fossil fuels such as mineral oil, natural gas, charcoal, transition metals, or even water, that are indispensable to obtain the needed energy.<sup>[12,13]</sup> Still, most significant global economies count on fossil fuels, even though natural gas and petroleum availability are decreasing apace, estimated within this century.<sup>[12,14]</sup> Additionally, the combustion of unsustainable carbon-based energy carriers is a primary reason for the ongoing climate change caused by the emission of greenhouse gases (GHG) such as carbon dioxide CO<sub>2</sub>, methane CH<sub>4</sub>, nitrous oxides NO<sub>x</sub>, hydrofluorocarbons, perfluorocarbons, and sulfur hexafluoride SF<sub>6</sub>. Almost any branch of the economy worldwide is infected by this development.<sup>[6,15]</sup>

Nowadays, fossil fuels provide approximately 80% of all consumed energy globally.<sup>[12]</sup> The search for alternative sustainable, long-term available, low-cost, environmentally friendly, safe, and versatile applicable energy sources and mitigating CO<sub>2</sub> gas emissions became essential concerning environmental, health-wise, and economic survival.<sup>[2,12,16-18]</sup> Reaching 1.5 °C global average temperature above pre-industrial levels could trigger so-called climate tipping points (CTPs) that involve significant impacts on the Earth system functioning, including notable sea level rise from melting ice sheets, carbon release from unfreezing permafrost or extinction of biodiverse biomes like the Amazon rainforest or coral reefs.<sup>[2]</sup> Recent studies observed severe changes in the West Antarctic ice sheet that might have reached its CTP already. Continuing with the current policies could trigger multiple CTPs caused by human activities within this century.<sup>[2,19]</sup>

Mitigating climate change by limiting the increase of the global average temperature below 1.5 to 2 °C above pre-industrial levels, protecting the environment, reducing the release of GHG, and securing the energy supply were

keystones of the Paris Agreement in 2015, which was enacted by 195 countries at the 21<sup>st</sup> Conference of Parties (COP21) during the United Nations Framework Convention on Climate Change.<sup>[20,21]</sup> To reach this long-term goal, it is necessary to decline the global net anthropogenic CO<sub>2</sub> emissions by nearly 25% until 2030 and net zero until 2075.<sup>[21]</sup> The predecessor approach of COP21, the Kyoto Protocol, was declared in 1997 as the first global commitment to stop climate change, containing legally binding emission targets for industrialized countries to be fulfilled by 2012.<sup>[22]</sup> It was accounted to be a breakthrough in international climate policy, even though not every participating government ratified it, and the emission goals, e.g., stabilizing the atmospheric CO<sub>2</sub> concentration to 450 ppm or reducing global emissions by 1 to 3% per year, were being left open for interpretation.<sup>[22,23]</sup> However, scientists in academia, governments, and commercial organizations worldwide have increased their ambitions to invest and collaborate in renewable energy sources (RES) research over the last decades to realize these ambitions.<sup>[17,20]</sup>

The usage of clean energy sources offers a multitude of advantages, such as the development of new fields of employment in new industrial and technological branches of the economy, the export of environmentally sustainable inventions, energy self-sufficiency with local energy generation to reduce supplier dependencies, improvement of urban air quality, and the reduction of GHG emissions.<sup>[12,17,24–27]</sup> However, the progress of renewable power depends on significant factors, among them economics, technological development, environmental requirements, social acceptance, regulations, infrastructure, and political interests.<sup>[18,27–31]</sup>

Renewable energy can compete with conventional energy sources regarding cheap and stable energy supply due to the pioneering research that needed considerable investments to improve inefficient energy production.<sup>[18,20]</sup> While the state-subsidized cost of fossil fuels like coal, oil, and gas remain very similar compared to what they were 140 years ago, prices of solar photovoltaics (PV) and batteries have dropped almost exponentially by approximately 10% per year since

the first commercial use of solar PV in 1958.<sup>[18]</sup> In contrast, the cost of nuclear power has increased since the start of its commercial utilization.<sup>[18]</sup>

However, PV or wind power only applies when wind or sun radiation is abundant among the abovementioned factors.<sup>[20,28-31]</sup> Most recent renewable energy technologies are still in the initial phase and have not been commercialized due to their high cost during the design and development.<sup>[24,32,33]</sup> An underestimated inhibiting influence is climate change itself. Raising temperatures and extreme weather events like aridity impact the reliability and performance of energy systems, not only renewable sources.<sup>[26,34]</sup> RESs offer several advantages for a sustainable and secure future. They should displace fossil-based energy sources from their sole lead position in the ongoing energy revolution as soon as possible.

### 3.1 H<sub>2</sub> – Sustainable Energy Carrier of the Future

Additionally, it is necessary to find a safe, cheap, and sustainable energy carrier that can act as a temporary energy carrier of renewable energy due to its inconsistent supply concerning fluctuating weather patterns.<sup>[35]</sup> Refined fossil fuels like natural gas or mineral oil do not meet these requirements. Batteries are not entirely suitable at this juncture due to their massive demand for metals like lithium, cobalt, or manganese, the unsustainable mining of their resources, and safety issues due to their high sensitivity against exposure to oxygen or nitrogen in case of an accident, associated to the high reactivity of native alkali metals.<sup>[36-40]</sup>

Dihydrogen (H<sub>2</sub>) could be the key solution as an energy carrier of the future, fulfilling the demands to be green if it is generated from renewable and environmentally friendly energy sources such as hydro, solar, wind, wave, biomass, and geothermal energy; by bioreactors and catalysts made of earth-abundant sustainable materials.<sup>[12,41,42]</sup>

#### 3.1.1 Utilization and Storage of H<sub>2</sub>

Hydrogen has excellent availability as the most abundant element in the universe, being contained in fossil fuels, biomass, and water.<sup>[43]</sup> While H<sub>2</sub> has the highest energy content per kilogram of any fuel among the known representatives, its only by-product, during its combustion, is water without releasing any GHGs (Table 1).<sup>[12,44]</sup> Its versatile application area offers numerous possibilities to replace carbon-based energy sources. In case it is not possible to forgo fossil fuels in processes, combining H<sub>2</sub> with carbon-based fuels provides new options to reduce the release of GHGs, e.g., blending H<sub>2</sub> with CO<sub>2</sub> enables the generation of methane as “synthetic natural gas” or mixing H<sub>2</sub> with diesel fuel in engines.<sup>[45-49]</sup>

Furthermore, H<sub>2</sub> is already integrated into many industry segments, such as ammonia synthesis via the Haber-Bosch process that consumes nearly half of all hydrogen produced globally; Fischer-Tropsch process; food processing such as fat hardening; semiconductor production; petrochemical and metal refining, amongst others.<sup>[35,50,51]</sup> It can potentially be used as an energy carrier just as natural gas, in fuel cells to generate electricity on demand in vehicles, as transportation fuel, or as a long-term storage medium.<sup>[45,51-54]</sup>

**Table 1. Different types of fuel sources and energy content<sup>[55]</sup>**

<b>Fuel type</b>	<b>Energy content [MJ kg<sup>-1</sup>]</b>
Hydrogen	120
Propane	49.6
Ethanol	29.6
Methanol	19.7
Aviation gasoline	46.8
Automotive gasoline	46.4
Automotive diesel	45.6
Natural gas	54.4
Wood	16.2
Coke	28.4
Bagasse	9.6

However, another current field of research that gets much interest is the storage of H<sub>2</sub> as a gas, which remains a technical issue due to its extremely low density at standard conditions, room temperature (RT), and atmospheric pressure.<sup>[12,56,57]</sup> There is a need to overcome this concern to achieve a hydrogen-oriented economy. Therefore, new storage applications were developed to accumulate H<sub>2</sub> physically or chemically in solid-state materials, such as metal hydrides, that achieve high gravimetric capacity in an efficient, compact, and replicable performance. Unfortunately, they lack rapid kinetics and manageable temperature control during the ab- and desorption.<sup>[44,58]</sup> Further concepts to store H<sub>2</sub> are the physical absorption to activated carbon, zeolites, carbon nitrides, or metal-organic frameworks (MOFs); compression, liquefaction, or the combination of both techniques; complex hydrides such as NaAlH<sub>4</sub> and the formation of chemical hydrides like ammonia, methanol or formic acid, amongst others.<sup>[41,50,56,57,59–62]</sup>

### 3.1.2 “Colors” of H<sub>2</sub>

To this date, produced H<sub>2</sub> is labeled by a color code: grey, blue, purple, and green, depending on the type of energy source or technology used for its production. While grey and blue H<sub>2</sub> is based on steam-reforming or pyrolysis of hydrocarbons originating from fossil fuels, blue H<sub>2</sub> includes at least a Carbon Capture and Storage (CCS) process. Purple H<sub>2</sub> is generated from nuclear energy. In contrast, green H<sub>2</sub> must be generated from 100% renewable energies.<sup>[63]</sup> However, this color code cannot determine the number of GHGs emitted during the process.

### 3.1.3 The Hydrogen Square Model

*Dawood et al.* proposed a four-corner-shaped model, Hydrogen Square (HydS), to assess hydrogen production methods regarding H<sub>2</sub> storage, safety, production, and utilization.<sup>[64]</sup> The model depicts the interdependence between those four criteria to identify the purity standard of the overall system. More precisely, to confirm a zero-carbon emission production of H<sub>2</sub>, it is necessary to ensure that all system stages are carbon-free (Figure 1).<sup>[64]</sup>

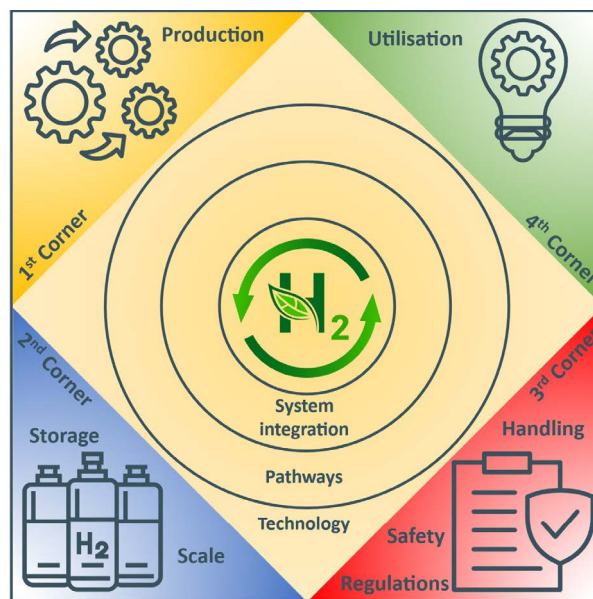


**Figure 1. Hydrogen Square model of green hydrogen production requirements. Adapted from *Dawood et al.*<sup>[64]</sup> Pictograms were obtained from Adobe Stock.**

### 3.1.4 H<sub>2</sub> Generation

At the moment, around 95% of the global hydrogen demand is met by using fossil fuels as the primary source in natural gas reforming, methane partial oxidation, and coal gasification processes, caused by the high efficiency (up to 80%), low cost, and technically matured methods.<sup>[63,65,66]</sup> Therefore, it is imperative to investigate new sustainable ways of H<sub>2</sub> production, such as electrolysis, solar, or biomass-based H<sub>2</sub> production, to be ready for the market (Figure 2).<sup>[67]</sup>

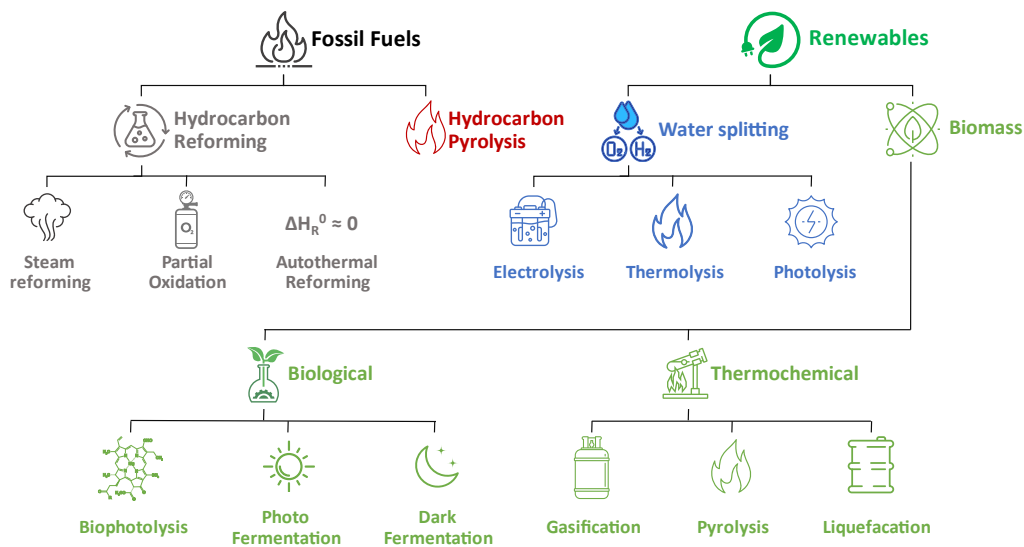


**Figure 2. Overview of H<sub>2</sub> generation from fossil fuels and renewables. Adapted from Nikolaidis et al.<sup>[68]</sup>** Pictograms were obtained from Adobe Stock.

#### 3.1.4.1 Electrolysis

Generation of H<sub>2</sub> via water electrolysis techniques appears to be an elementary process that only produces oxygen as a by-product. A direct current (DC) power source is applied to an aqueous solution by two electrodes made of inert metals like platinum, iridium, or stainless steel and separated by a thin ion-conducting layer to split water into H<sub>2</sub> (cathode) and O<sub>2</sub> (anode) gas via two differing electrochemical processes.<sup>[35]</sup> Separating both electrodes with a gas-impermeable is necessary to inhibit the recombination of the evolved gases.<sup>[51]</sup>

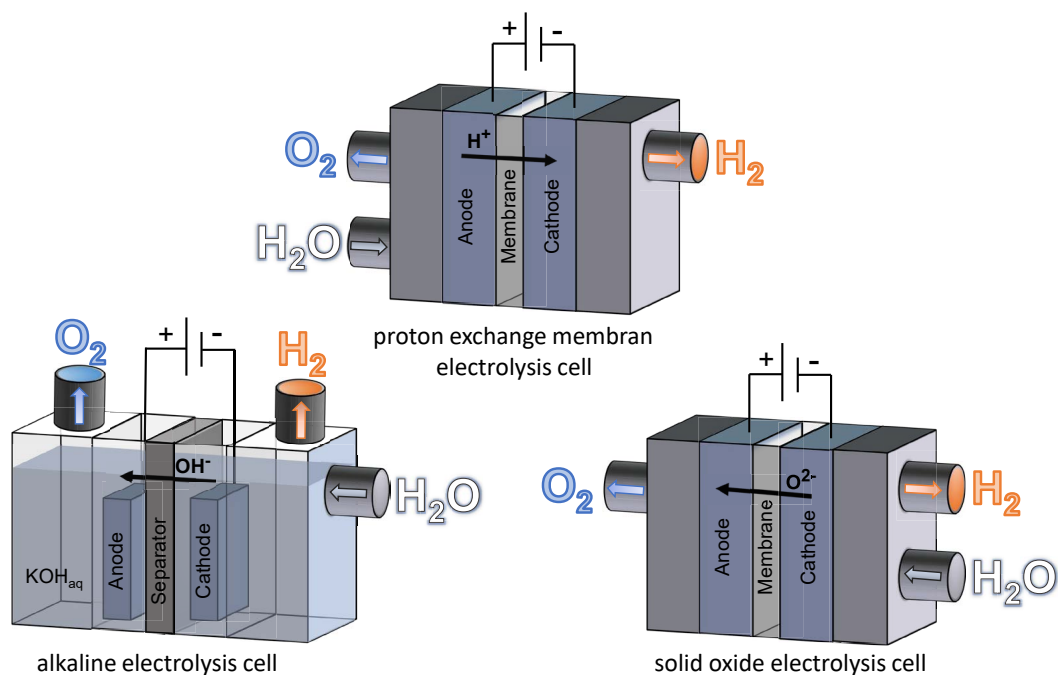


**Figure 3. Schematic designs of different electrolysis cell types. Adapted from Schmidt et al.<sup>[69]</sup>**

The main technologies of electrolyzers are alkaline, proton exchange membrane (PEM), and solid oxide electrolysis cells (SOEC), varying in their reaction mechanisms, electrolyte, composition, working temperature, separator, and efficiency, amongst others (Figure 3).<sup>[51,70–72]</sup> Sustainable H<sub>2</sub> generation with high efficiency and high purity could be achieved via coupling of water electrolysis and renewable energy sources like PV, wind, hydro, tidal, ocean thermal, biomass, or geothermal energy if its cost becomes capable of competing established technologies by further research efforts.<sup>[63,69,73–76]</sup>

#### 3.1.4.2 Photolysis

The direct utilization of solar energy via photo-splitting of water in a single process could be the future technology that is needed instead of the two-step way: generating electricity in PV modules and transferring it to electrolyzer cells.<sup>[77]</sup> Absorption of photons to a semiconductor material like TiO<sub>2</sub> generates electron-hole pairs without the entire conversion to heat. As first described by *Fujishima* and *Honda* in 1972, the electron hole in the TiO<sub>2</sub> anode acted as an oxidizing agent to generate O<sub>2</sub> from water, while the electrons were transferred to a platinum cathode to reduce protons to H<sub>2</sub> (Figure 4).<sup>[77,78]</sup> The photoelectrode material in photo-electrochemical cells (PEC) can vary to be n-type (cathode) or p-type



(anode) semiconductors with small band gaps that determine the needed energy for the transition from the valence band to the conduction band.<sup>[77]</sup> There is a necessity for a conduction band minimum that is higher than the reduction potential for H<sub>2</sub>/H<sub>2</sub>O. In contrast, for an efficient photo-splitting process, the valence band maximum has to be lower than the oxidation potential of O<sub>2</sub>/H<sub>2</sub>O.<sup>[77,79]</sup> Additionally, the photoelectrodes should be stable under irradiation conditions, inexpensive, and can absorb a wide range of the solar spectrum.<sup>[79]</sup> During the last decades, efforts to improve the performance of PECs were made by modifying the TiO<sub>2</sub> microstructure, integrating organic dyes in so-called Grätzel cells, or choosing other stable, non-oxide semiconductor materials like GaAs, WSe<sub>2</sub>, MoSe<sub>2</sub>, CdSe, amongst others.<sup>[79,80]</sup> For instance, CdS and CdSe meet the requirements for suitable band gaps and are utilized in quantum dot and quantum rod assemblies to generate H<sub>2</sub>.<sup>[77,81–91]</sup> However, no commercial application of this technology is ready for the market due to chemical stability problems caused by high-level UV radiation and its high costs.<sup>[70,77]</sup>

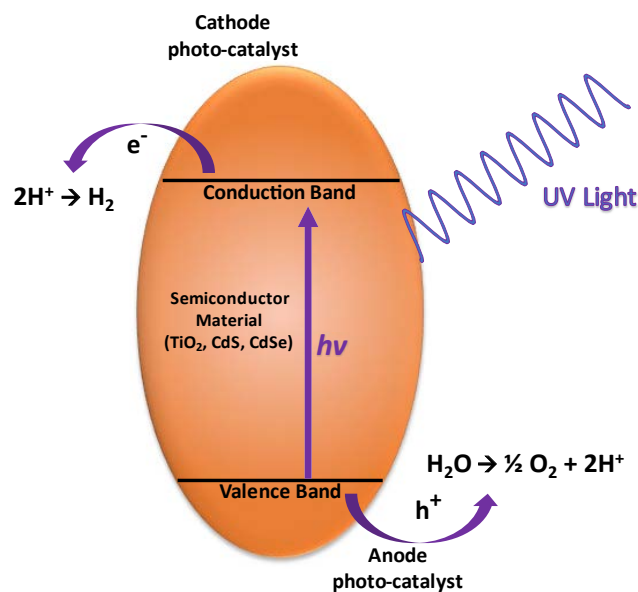


Figure 4. Schematic design of a semiconductor photolysis cell. Adapted from Scott.<sup>[77]</sup>

### 3.1.4.3 Biomass

Biomass represents the all-natural plant, animal, or microorganism origin materials abundantly available as a sustainable feedstock from the agricultural industry, fishery, animal dung, or municipal waste.<sup>[65,66]</sup> One of the leading

biomass-to-hydrogen technologies is steam gasification, which converts biomass into combustible gases like H<sub>2</sub>, CO, CO<sub>2</sub>, CH<sub>4</sub>, and hydrocarbons, utilizing catalysts, absorbents, and water vapor at high temperatures.<sup>[65–67,92]</sup> While this method is applicable for the large-scale production of high-quality syngas, the purification of the gas products, cost-effective catalysts, generated tar, and its high energetic costs remain issues. If research efforts optimize the conditions and prices, H<sub>2</sub> production could be a future technology.<sup>[65,66]</sup>

Nevertheless, producing H<sub>2</sub> directly from biomass via biological processes would be more efficient. Therefore, it is possible to avoid additional reforming and purification steps.<sup>[77]</sup> There are versatile approaches for the biological production of H<sub>2</sub>, including direct and indirect biophotolysis, biological water–gas shift (WGS) reaction, and photo- and dark fermentations, that require low energy input and generate a low environmental impact.<sup>[43,55,77,93–95]</sup> Direct biophotolysis implies the light-driven generation of H<sub>2</sub> in the presence of micro-algae or cyanobacteria via photosynthesis systems I (PSI) and II (PSII) along with a hydrogenase (H<sub>2</sub>ase) enzyme.<sup>[43,55,95]</sup> If there is no H<sub>2</sub>ase present, as in green plants, PSI reduces CO<sub>2</sub> instead.<sup>[95]</sup> The indirect process consists of multiple steps, including forming carbohydrates and O<sub>2</sub> via PSI and PSII and the aerobic dark fermentation of the carbohydrates to H<sub>2</sub> via the H<sub>2</sub>ase entity.<sup>[43,50,95,96]</sup> Some photoheterotrophic bacteria can apply biological WGS reactions to survive in the dark, utilizing CO as the primary carbon source, producing CO<sub>2</sub> and H<sub>2</sub>.<sup>[95,97,98]</sup> While this method is still in an early stage of development, it is promising due to its low costs compared to thermochemical WGS processes.<sup>[50,95]</sup>

The photo-fermentation process utilizes biomass or organic acids, solar energy, and light-harvesting pigments like chlorophylls to split water molecules into protons, electrons, and O<sub>2</sub>.<sup>[50]</sup> Purple non-sulfur bacteria can perform this technique.<sup>[55]</sup> Using this method for H<sub>2</sub> evolution requires cost-intensive and complex reactor designs with high-performance light penetration control.<sup>[35,99]</sup> In contrast, dark fermentation employs mesophile or thermophile anaerobic bacteria or micro-algae on carbohydrates in the absence of O<sub>2</sub> and light, enabling a simple, energy-saving technique with higher efficiency.<sup>[55]</sup> One drawback of this

process is the formation of other gases, such as CO<sub>2</sub>, H<sub>2</sub>S, or CH<sub>4</sub>, and by-products like butyric, lactic, and acetic acids.<sup>[43,50,100]</sup> There are new approaches to combine both fermentation processes to maximize the conversion of substrate to H<sub>2</sub> to include additives such as metals (e.g., Fe, Mo, Ni, Zn), metal oxides (e.g., TiO<sub>2</sub>, ZnO), amino acids, or vitamins; as well as investigation of the influence of pre-treatment of the raw biomass.<sup>[101–103]</sup> To this date, none of these processes can be used commercially due to low H<sub>2</sub> conversion efficiency, unstable hydrogen production, high cost, and its early stage of development.<sup>[35,43,77,94]</sup>

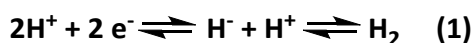
In summary, green H<sub>2</sub> production is about to play a vital role in a successful energy transition, even though a large part of these technologies is still in its infancy but on its way to being ready for the market. Nowadays, H<sub>2</sub> generation by water electrolysis from RES like sun, wind, hydro, tidal, ocean thermal, biomass, or geothermal energy might be the most promising technique for a sustainable and clean H<sub>2</sub> economy.<sup>[35,64]</sup> Nevertheless, upcoming technologies are worth investigating, improving, and optimizing to get ahead of established electrolysis.

## 3.2 Hydrogenase Enzymes

H<sub>2</sub> production by utilizing organisms such as bacteria, archaea, and eukarya that exploit H<sub>2</sub> as an energy carrier, a compensator of the redox potential of a cell, and storage for billions of years, could be a bionic approach, as described in the previous chapter.<sup>[43,104]</sup>

It is assumed that the origin of H<sub>2</sub>ase enzymes occurred during the early stages of life on Earth and the first primitive life forms relied on H<sub>2</sub> as the primary energy source.<sup>[105]</sup> This hypothesis is supported by the high oxygen sensitivity towards inhibiting several H<sub>2</sub>ase representatives that probably could not evolve within the current atmospheric composition.<sup>[106–108]</sup>

The search for their mechanics and mode of functioning revealed a particular type of metalloenzymes, called H<sub>2</sub>ase, that consists of highly complex and ingenious bioinorganic structures that catalyze the conversion of para- to ortho-H<sub>2</sub> as well as the two-electron reduction of protons to H<sub>2</sub> and vice versa via the formation of a hydride species (Equation 1).<sup>[43,109]</sup> The term “hydrogenase” was first described by *Stephenson* and *Stickland* in 1931, who discovered a bacterial enzyme in prokaryotes of type *Escherichia coli* that catalyzed the reversible oxidation of H<sub>2</sub>.<sup>[110,111]</sup> H<sub>2</sub>ases manage elementary redox reactions in a highly efficient manner, e.g., the [FeFe] H<sub>2</sub>ase enzyme detected and isolated from *Desulfovibrio desulfuricans* can produce up to 9000 molecules H<sub>2</sub> per second at neutral pH and low overpotential (-0.1 to -0.5 V vs. normal hydrogen electrode (NHE)).<sup>[112]</sup>



Photosynthetic H<sub>2</sub> evolution was first described for green algae *Chlamydomonas reinhardtii*, which utilizes H<sub>2</sub> metabolism for controlling excess reduction equivalents under physiological conditions.<sup>[113]</sup> There are two possible proposed sources for the necessary electrons. The transfer of electrons can be realized via PSII and PSI to the chloroplast ferredoxin after the photo-initiated oxidation of H<sub>2</sub>O. The ferredoxin is connected to the H<sub>2</sub>ase and provides the electrons to its catalytic site, leading to the generation of H<sub>2</sub>.<sup>[113]</sup> Unfortunately, O<sub>2</sub> generated from the photosynthetic PSII process acts as an inhibitor of the enzymatic reaction

and limits this mechanism to a short time interval (30-90 s).<sup>[108]</sup> Alternatively, the electrons are delivered from endogenous substrate catabolism into the thylakoid membrane by dark fermentation processes, including the discharge of CO<sub>2</sub> to the medium.<sup>[93]</sup> Subsequent illumination in the presence of 3-(3',4'-dichlorophenyl)-1,1-dimethylurea (DCMU), which inhibits PSII, initiates high rates for H<sub>2</sub> evolution.<sup>[114]</sup> This mechanism evolves H<sub>2</sub> and CO<sub>2</sub> in 2:1 stoichiometric amounts, it decelerates, however, quickly due to the lack of sustainability of the cells during the high rates of electron transfer (ET) reactions.<sup>[113]</sup>

### 3.2.1 Hydrogenase Classification

There are four subtypes of H<sub>2</sub>ase enzymes: [Fe], [NiFe], [NiFeSe], and [FeFe] H<sub>2</sub>ases, which vary in their structure, metal content, occurrence, and preferential function (Table 2).<sup>[109,115]</sup> They are located in the periplasm or cytoplasm in a soluble or membrane-bound form that determines if the primary function is H<sub>2</sub> evolution or uptake.<sup>[109,116]</sup> Additionally, H<sub>2</sub>ases can operate bidirectional, depending on the physiological environment in the cell.<sup>[109]</sup>

**Table 2. Classification of H<sub>2</sub>ases<sup>[115]</sup>**

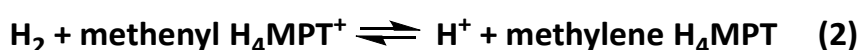
Classification	Structure	Occurrence	Localization	Function
[Fe]	monomeric	methanogens	cytoplasmic	uptake of dihydrogen
[NiFe]	heterodimeric, multimeric	anaerobic, photosynthetic bacteria, cyanobacteria	cytoplasmic, membrane- bound, periplasmic	uptake of dihydrogen
[NiFeSe]	oligomeric	methanogens	cytoplasmic, membrane- bound	oxidation of dihydrogen
[FeFe]	monomeric, heteromeric	photosynthetic bacteria, anaerobic fermentative bacteria cyanobacteria, green algae, protozoan	cytoplasmic, membrane- bound, periplasmic, chloroplasts, hydrogenosomes	formation of dihydrogen

#### 3.2.1.1 [Fe] Hydrogenases

In contrast to the already mentioned types of H<sub>2</sub>ase enzymes, [Fe] H<sub>2</sub>ases are cluster-free. Nevertheless, they feature the so-called Fe-guanylylpyridinol (FeGP) co-factor containing a low-spin Fe(II) core with octahedral coordination geometry that consists of two *cis*-arranged CO ligands, a cysteine, an exchangeable water molecule and a 2-pyridone moiety (Figure 5).<sup>[117]</sup> The crystal structures of [Fe]-only

H<sub>2</sub>ases from *Methanocaldococcus jannaschii* and *Methanopyrus kandleri* were solved by *Shima et al.* in 2006.<sup>[118]</sup>

While [FeFe] and [NiFe] H<sub>2</sub>ases are characterized as redox enzymes, [Fe]-only H<sub>2</sub>ases, the also called H<sub>2</sub>-forming methylenetetrahydromethanopterin dehydrogenases (Hmd), cleave H<sub>2</sub> heterolytic and transfer H<sup>-</sup> to the organic substrate methenyltetrahydromethanopterin (methenyl-H<sub>4</sub>MPT<sup>+</sup>) to generate methylene-H<sub>4</sub>MPT and H<sup>+</sup> to the solvent and vice versa (Equation 2).<sup>[119]</sup> This reaction is involved in the methanogenesis of many methanogenic archaea.<sup>[117]</sup>



Furthermore, it can perform an H<sup>+</sup>/H<sub>2</sub> exchange reaction, but only in the presence of the substrate.<sup>[120]</sup>

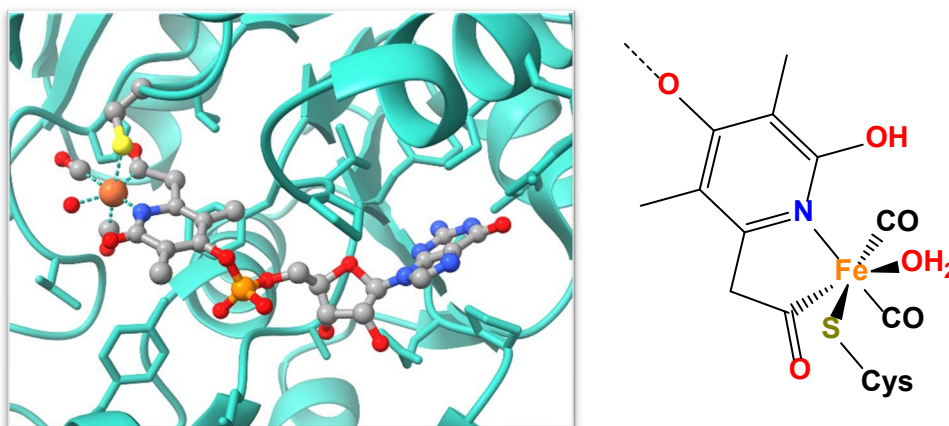


Figure 5. Crystal structure of the FeGP cofactor binding site in holo-Hmd from *Methanocaldococcus jannaschii* and the molecular structure of its active center (PDB ID code 4YT4). Adapted from *Shima et al.* by using UCSF ChimeraX software.<sup>[121,122]</sup>

### 3.2.1.2 [NiFe] Hydrogenases

This variety of H<sub>2</sub>ase enzymes contains several subtypes based on their molecular phylogeny, such as membrane-bound H<sub>2</sub> uptake H<sub>2</sub>ases, sensory H<sub>2</sub>ases; F<sub>420</sub>-reducing, NAD(P)-reducing, methyl-viologen-reducing, and bidirectional NAD(P)-reducing H<sub>2</sub>ases; and energy-converting H<sub>2</sub>ases, amongst others.<sup>[109,123]</sup>

The first crystal structure of an [NiFe] H<sub>2</sub>ase enzyme from *Desulfovibrio gigas*, including the bimetallic [NiFe]center, was presented by *Fontecilla-Camps et al.* in 1995.<sup>[124]</sup> Four coordinating cysteine residues integrate the active site into a large protein subunit (Figure 6). Two cysteinato ligands coordinate to the Ni ion, and

two are bridging ligands between Ni and Fe. The kind of third bridging ligand is proposed to be  $\text{H}^-$ ,  $\text{SO}$ ,  $\text{H}_2\text{O}$ ,  $\text{OH}^-$  or  $\text{O}^{2-}$ , depending on the redox state (Figure 6, X).<sup>[123]</sup> As revealed by infrared (IR) spectroscopy, the low spin Fe(II) ion is surrounded by one CO and two  $\text{CN}^-$  or  $\text{SO}$ ,  $\text{CO}$ , and  $\text{CN}^-$  ligands (Figure 6).<sup>[123]</sup> The highlighted Fe-S clusters are well-arranged to provide an electron shuttle to the active site.<sup>[125]</sup>

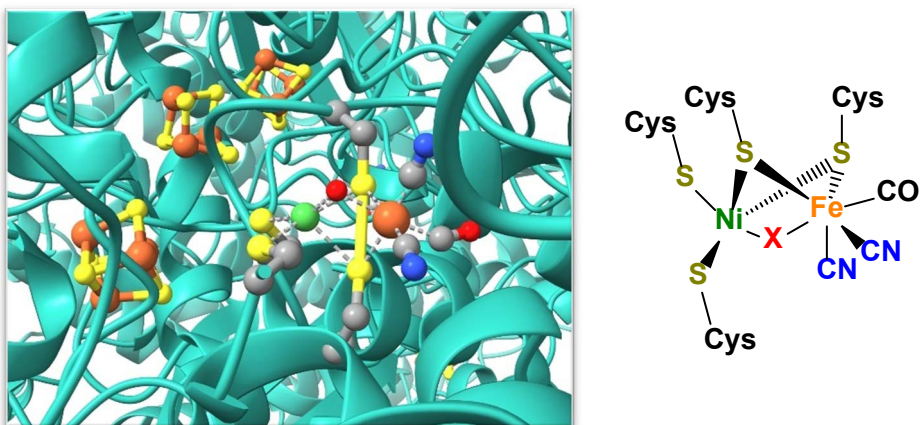


**Figure 6.** Crystal structure of the [NiFe]  $\text{H}_2$ ase enzyme from *Desulfovibrio gigas* and the molecular structure of its active site (PDB ID code 2FRV). X =  $\text{H}^-$ ,  $\text{SO}$ ,  $\text{H}_2\text{O}$ ,  $\text{OH}^-$  or  $\text{O}^{2-}$ . Adapted from *Fontecilla-Camps et al.* by using UCSF ChimeraX software.<sup>[122,126]</sup>

There are [NiFe]  $\text{H}_2$ ases from aerobic organisms that developed  $\text{O}_2$  tolerance by an additional unique FeS cluster that differs from anaerobic types.<sup>[127]</sup> Another subtype, the so-called [NiFeSe]  $\text{H}_2$ ase, contains one selenocysteine instead of cysteine at the Ni atom of the active center. They exhibit high efficiency towards  $\text{H}_2$  generation, while [NiFe]  $\text{H}_2$ ases are frequently involved in  $\text{H}_2$  oxidation rather than production.<sup>[125,128]</sup>

### 3.2.1.3 [FeFe] Hydrogenases

Due to their sensitivity to  $\text{O}_2$ , these representatives of  $\text{H}_2$ ase enzymes are found in anaerobic organisms and were first crystallized from *Clostridium pasteurianum* (Cpl) by *Peters et al.* in 1998 and *Desulfovibrio desulfuricans* (DdHase) by *Nicolet et al.* in 1999.<sup>[129,130]</sup> The catalytic active site, the so-called H-cluster, is connected to the peptide matrix, containing a [4Fe4S] cluster and a [2Fe2S] cluster bridged via a cysteine moiety. The H-cluster is considered essential for the enzyme's function since there are [FeFe]  $\text{H}_2$ ases from green algae that do not contain any additional Fe-S cluster.<sup>[109]</sup> The iron atoms of the [2Fe2S] cluster are termed proximal Fe ( $\text{Fe}_p$ ) and distal Fe ( $\text{Fe}_d$ ), where  $\text{Fe}_p$  is



adjoining the [4Fe4S] cluster. The bimetallic center is bridged by an azadithiolate (adt) moiety and one  $\mu$ -CO ligand. The type of the bridgehead atom was long-time unidentified to be CH<sub>2</sub>, NH, or O. Nevertheless, *Lubitz et al.* proved the presence of an aza-group by experimental evidence. Additionally, each Fe atom is coordinated by a terminal CO and a CN<sup>-</sup> ligand. Whereas Fe<sub>p</sub> is coordinatively saturated, binding to the bridging cysteine moiety, Fe<sub>d</sub> possesses a vacant coordination site to interact with hydrogenic species such as H<sup>+</sup>, H<sub>2</sub>, H<sub>2</sub>O, or H<sup>-</sup> (Figure 7).<sup>[131]</sup> The coordination of an additional CO at the vacant position inhibits the activity of the H-cluster.<sup>[132]</sup> While the [4Fe4S] and other Fe-S clusters manage to switch between oxidized and reduced states to serve as an electron reservoir and relay, the [2Fe2S] acts as the active catalytic center of H<sub>2</sub> formation or splitting.<sup>[131]</sup> Various [FeFe] H<sub>2</sub>ases can be cataloged into three groups, depending on their primary function as prototypical and electron-bifurcating, ancestral, or sensory enzymes. The first group has been most intensely characterized and can be divided into several subtypes based on their development of Fe-S clusters.<sup>[133,134]</sup> The other types are less well-studied and need more detailed investigation.

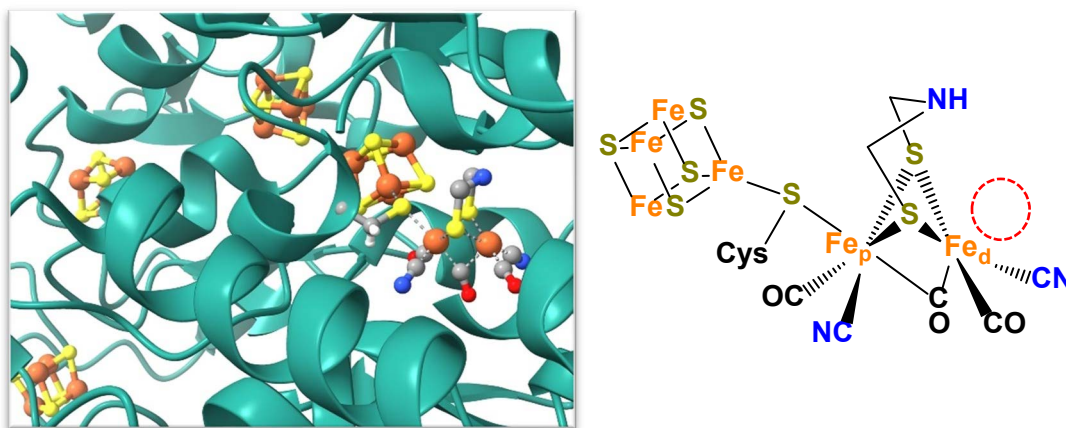


**Figure 7.** Crystal structure of the [FeFe] H<sub>2</sub>ase enzyme from *Clostridium pasteurianum* and the molecular structure of its active site (PDB ID code 6YF4). The vacant site of the distal Fe atom is highlighted. Adapted from *Happe et al.* by using UCSF ChimeraX software.<sup>[122,135]</sup>

The H-cluster is harbored deep inside a hydrophobic protein framework that is involved in the coordination of the active site by non-covalent synergies like hydrogen bonding or electrostatic interactions. The amino acid residues such as proline, serine, glutamine, lysine, methionine, or cysteine influence the arrangement of the [4Fe4S] cluster, the adt bridge, and the CO and CN<sup>-</sup> ligands.<sup>[136]</sup>

In addition, the protein framework manages the gas access channels, ET chains, and proton transfer pathways for efficient catalysis.<sup>[109,136]</sup> This thesis will focus on synthesizing and investigating [FeFe] H<sub>2</sub>ase mimics.

### 3.2.2 [FeFe] Hydrogenase Maturation

Maturation mechanisms of [NiFe] and [Fe]-only H<sub>2</sub>ase enzymes are discussed in the literature.<sup>[109,137,138]</sup>

The maturation of the [2Fe2S] subsite of the H-cluster involves multi-enzymatic biosynthetic processes that are still not investigated comprehensively. Still, some key steps have been resolved based on structural analysis and *in vitro* experiments of isolated proteins.<sup>[109]</sup>

It is known that the assembly requires the performance of three accessory proteins, HydE, HydF, and HydG, as far as known.<sup>[139,140]</sup> HydE and HydG are assigned to the radical S-adenosylmethionine family of proteins that contain a [4Fe4S] cluster to bind the S-adenosylmethionine cofactor and C-terminal binding motives to fix an additional Fe-S cluster.<sup>[141]</sup> These enzymes catalyze several radical reactions, and HydG is supposed to convert tyrosine to dihydroglycerine and, in a further step, to CO and CN<sup>-</sup> ligands.<sup>[142,143]</sup>

The precursor generation of the H-cluster is also expected from HydG via multiple steps, including a Fe-chelating non-proteinic cysteine moiety, the substitution of coordinating ligands water and histidine to CO and CN<sup>-</sup> along with the release of [(Cys)Fe(CO)<sub>2</sub>CN]<sup>-</sup>, a complex that serves as a synthon for the [2Fe2S] cluster.<sup>[143–146]</sup> The role of HydE and the final formation of the [2Fe2S] cluster have not been solved yet, but HydE is assumed to be involved in the biosynthesis of the adt ligand by enabling serine.<sup>[147]</sup> Serine is proved to be incorporated in the adt assembly by isotopic labeling of <sup>13</sup>C and <sup>15</sup>N in combination with advanced electron paramagnetic resonance (EPR) techniques.<sup>[143,148]</sup> In addition, HydE might manage the dimerization of the synthon to a [Fe<sup>I</sup><sub>2</sub>S<sub>2</sub>(CO)<sub>4</sub>(CN)<sub>2</sub>] precursor complex.<sup>[144]</sup>

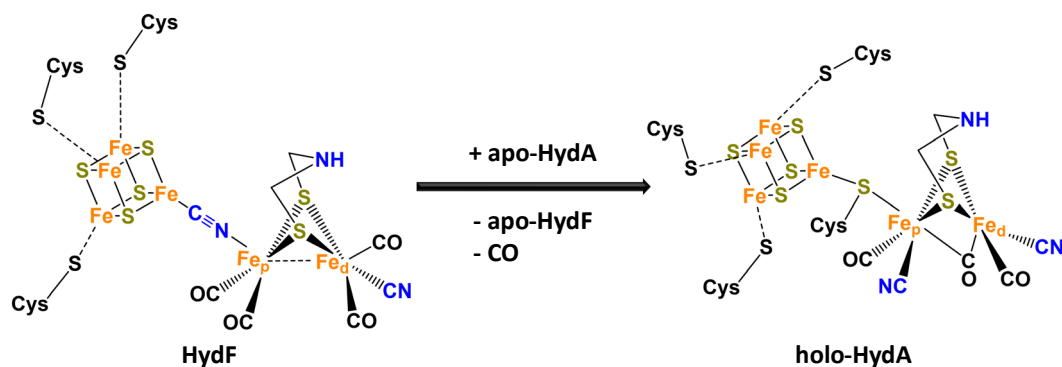


Figure 8. The final step of the proposed HydA assembly mechanism.<sup>[143]</sup>

The preformed [2Fe2S] subsite is assembled to a maturation enzyme, HydF, that contains one [4Fe4S] cluster and delivers the subsite to the apo-hydrogenase (apo-HydA) for its activation (Figure 8).<sup>[139,143,149]</sup>

### 3.2.3 [FeFe] Hydrogenase Modification

To understand the complex mechanisms of [FeFe] H<sub>2</sub>ase maturation, experiments of isolated proteins and synthesized mimics of the [2Fe2S] cluster were performed, generating semisynthetic [FeFe] H<sub>2</sub>ase enzymes.<sup>[150–152]</sup>

There are various ways to modify the H-cluster, including a variation of sulfur atoms to selenium or tellurium at the [2Fe2S] or [4Fe4S] cluster, changing the amine group in the bridgehead to methylene or chalcogens, substitution of CO or CN<sup>-</sup> to phosphor-based ligands (PR<sub>3</sub>); exchange of the iron atoms to Ni, Mo, Co or Ru; or increasing the bulkiness of the bridging moiety (Figure 9).<sup>[151–154]</sup>

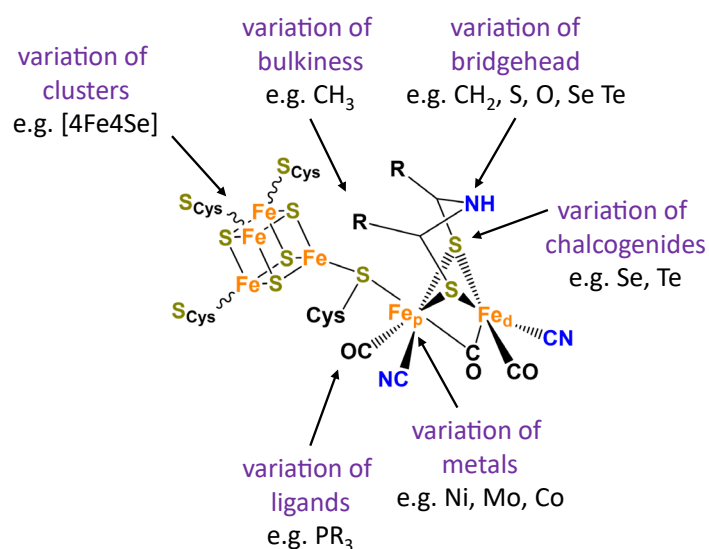


Figure 9. Possible modifications on the H-cluster. Adapted from Wittkamp *et al.*<sup>[150,151]</sup>

The cooperative work of *Fontecave*, *Lubitz*, and *Happe* enabled the assembly of a semisynthetic and fully functional [FeFe] H<sub>2</sub>ase enzyme by binding the artificial cofactor to HydF, which was able to transfer the mimic to an apo-HydA.<sup>[152]</sup> Further approaches accomplished an active enzyme without HydF by self-assembling the synthetic cofactor to the inactive apo-HydA.<sup>[155,156]</sup> However, most modified cofactors lack catalytic activity, while the nature archetype contains the best composition for an efficient hydrogen evolution reaction (HER).<sup>[154]</sup> The modification of the bridgehead amine moiety resulted in an intense drop in activity, indicating the importance of this critical structural element for the catalytic cycle.<sup>[154]</sup> There are more than 300 synthetic mimics of the [2Fe2S] cluster, and only a minor amount is tested to this day, leaving a chance to overcome the nature genuine.<sup>[131,157–159]</sup>

#### 3.2.4. Catalytic cycle of the biological hydrogen evolution reaction

Revealing the mechanism of biological hydrogen evolution has challenged researchers for decades, generating possible catalytic cycles that have gained more complexity and substantiated over time.<sup>[160–165]</sup> These investigations benefit from advanced spectroscopic methods and modifications of the active cofactor of [FeFe] H<sub>2</sub>ase enzymes by showing which structural moieties are essential for the processes and revealing new insights into the influence on the HER activity. However, the discussion of the actual catalytic cycle of [FeFe] H<sub>2</sub>ases endures. Therefore, it is still necessary to investigate the different states of catalysis due to the many assumptions and approximations made to interpret complex experimental data.

Two feasible proposed cycles are developed in the [FeFe] H<sub>2</sub>ase community, the models of *Lubitz* and *Stripp*, labeled as cycles **1** and **2**, respectively (Figure 10).<sup>[134,150,151,160,166]</sup> Cycle **2** has two segments that follow different routes from the **H'**<sub>red</sub> to the **H**<sub>hyd</sub> state in a fast (orange) and slow cycle (yellow), marked as **2A** and **2B**, respectively. Both models agree in the same starting species **H**<sub>ox</sub>, the [4Fe4S]<sup>2+</sup>-[Fe<sub>p</sub><sup>2+</sup>Fe<sub>d</sub><sup>1+</sup>] state, which is characterized by versatile techniques such as X-ray diffraction, density-functional theory (DFT) calculations, IR, Mössbauer, and advanced EPR spectroscopy methods.<sup>[133]</sup>

The first Cycle **1** starts with an ET to the [4Fe4S] cluster to give  $H_{red}$ . The protonation of the bridgehead amine group leads to an ET from the reduced [4Fe4S] cluster to the proximal iron atom afterward to form  $H_{red}H^+$ . This process is assigned as an electronic rearrangement, not a proton-coupled electron transfer (PCET) reaction.<sup>[160]</sup> Follow-up reduction of the [4Fe4S] subcluster affords the so-called super-reduced state  $H_{sred}H^+$ .<sup>[133]</sup> Combining the two accumulated electrons with the proton of the adt bridge forms a terminal hydride at the distal iron. It oxidizes both iron atoms, resulting in the isomer  $H_{hyd}$  species.<sup>[167]</sup> Further protonation at the amine leads to a proton-hydride pair ( $H_{hyd}H^+$ ) that could be observed recently.<sup>[168]</sup> This metastable intermediate immediately reacts to the  $H_2$ -containing state  $H_{ox}H_2$ , which releases  $H_2$  to close cycle **1**, regenerating  $H_{ox}$ .<sup>[131,133,168]</sup>

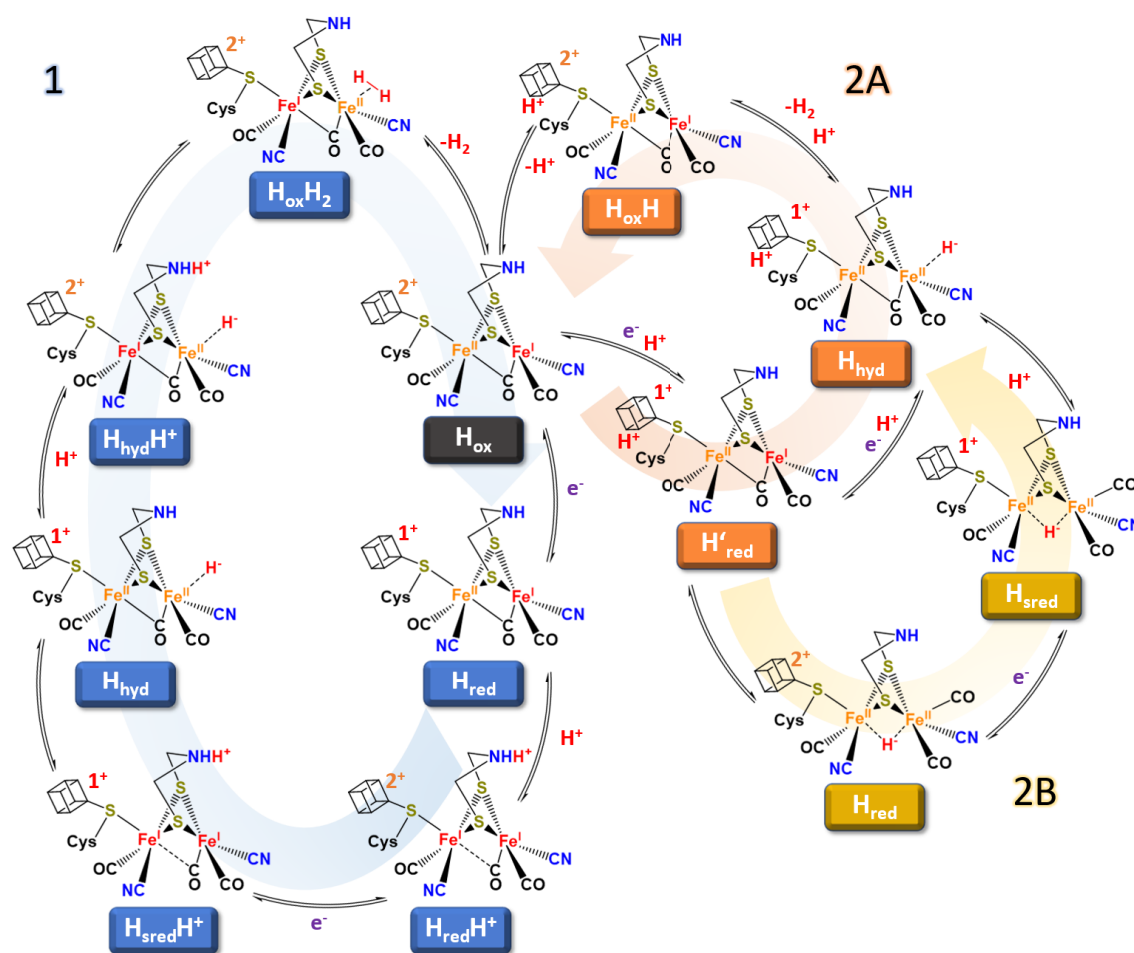


Figure 10. Schematic catalytic cycles of the two proposed models for catalytic hydrogen conversion in [FeFe]  $H_2$ ase enzymes. 1) Model of *Lubitz et al.* (blue); 2A) fast model from *Stripp et al.* (orange); 2B) additional slow steps of the model from *Stripp et al.* (yellow). Both cycles start at  $H_{ox}$ . Adapted from *Birrell et al.*<sup>[133,169]</sup>

In contrast, cycle **2** follows a PCET mechanism to reduce and protonate the [4Fe4S] cluster in a concerted reaction to generate  $\mathbf{H}'_{\text{red}}$  (Figure 10).<sup>[133]</sup> PCETs are very suitable for nature reduction processes to balance the charge of the reduced species, especially in short-range transfer reactions. Otherwise, separate steps are necessary.<sup>[170]</sup>

There are two possible ways for the next step. The fast cycle **2A** continues with an additional PCET mechanism to the  $\mathbf{H}_{\text{hyd}}$  state, similar to the  $\mathbf{H}_{\text{hyd}}$  of cycle **1**, besides the protonated [4Fe4S] cluster.<sup>[133,151]</sup> Further protonation enables the formation and release of  $\text{H}_2$ , leaving the H-cluster in state  $\mathbf{H}_{\text{oxH}}$ , which is still protonated at the [4Fe4S] cluster. Elimination of the proton closes the “fast” cycle **2A**.<sup>[151]</sup> Figure 10 shows an alternative pathway after the  $\mathbf{H}'_{\text{red}}$  state by structural rearrangement and forming a bridging hydride between both iron centers ( $\mathbf{H}_{\text{red}}$ ). Subsequent reduction and protonation lead to the formation of  $\mathbf{H}_{\text{hyd}}$  via  $\mathbf{H}_{\text{sred}}$  and close the additional “slow” cycle **2B**.<sup>[133,151,171]</sup> Bridging hydrides react slowly with protons due to increased thermodynamic stability.<sup>[172]</sup> However, the formation of a bridging hydride species is highly controversially discussed.<sup>[169]</sup>

Until now, no evidence exists of which model matches best with the nature archetype, but future investigations might lead us closer to the truth of these complex redox systems.<sup>[133]</sup>

### 3.3 Mimicking [FeFe] Hydrogenase Enzymes

In the late 1920s, *Reihlen et al.* described the synthesis of iron complexes that exhibited similar structures as the active center [2Fe2S] subsite of the H-cluster. Unfortunately, they could not assume that because its composition was not discovered till the end of the 20th century.<sup>[129,130,173,174]</sup> Numerous follow-up works of *Hieber, Huttner, Seyferth,* and *King* presented systematic studies of low valent [2Fe2S] complexes with the first verified X-ray structure analysis by *Dahl et al.* This research area was seemingly completed in all topics of interest regarding this complex and gradually lost attention.<sup>[157,175–180]</sup>

After resolving the first molecular structure of the [FeFe] H<sub>2</sub>ase protein, including the H-cluster by X-ray diffraction methods in 1998, the renaissance of [2Fe2S] complexes began as great improvements were made by mimicking the natural enzymes [FeFe] H<sub>2</sub>ase during the last decades, driven by the exceptional work of *Rauchfuss, Darensbourg,* and *Pickett.*<sup>[111,129,130,136,181–187]</sup> Inspired by the nature archetypes, numerous model complexes from small carbonyl clusters to artificial protein replications were created, sharing the dimetallic dichalcogenide core of the active site and varying at the bridging ligands, metal-bond chalcogenides, and coordinating ligands, *e.g.*, CO, CN<sup>-</sup>, PR<sub>3</sub>, P(OR)<sub>3</sub>, chelates, NO, or *N*-heterocyclic carbenes (Figure 11).<sup>[131,153,154,158,188,189]</sup> Various studies investigated different fields of knowledge, such as the biological structure of the natural [FeFe] H<sub>2</sub>ases, electrocatalysis, photocatalysis, immobilization of [FeFe] H<sub>2</sub>ases and its mimics on electrode surfaces or polymers, H-cluster modification as semiartificial enzymes, abiological ligands, and artificial hydride formation, amongst others.<sup>[131,158,182]</sup>

The formed diiron complexes are relatively unreactive and tolerate a bunch of other substituent targeting reaction types such as thioamide formation from amides with Lawesson's reagent,<sup>[190]</sup> esterification,<sup>[191,192]</sup> azide alkin click reactions,<sup>[193,194]</sup> cross-couplings,<sup>[195–197]</sup> polymerizations,<sup>[197–199]</sup> reductions with NaBH<sub>4</sub>,<sup>[198]</sup> oxidation with mild oxidation agents,<sup>[191,201]</sup> chemisorption<sup>[199,200]</sup> and complexation,<sup>[196,197,201]</sup> amongst others.<sup>[157]</sup>

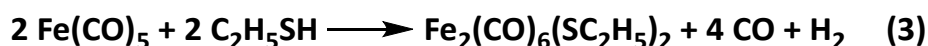
Many of the designed [FeFe] H<sub>2</sub>ase mimic assemblies demonstrated decent activities in terms of catalytic dihydrogen formation in electro and photochemical

experiments since the pioneering report by *Rauchfuss et al.*<sup>[188,202]</sup> However, previous attempts lack consistency and high activity during the catalytic process, compared to the natural ideal with high catalytic efficiency, up to  $10^4 \text{ s}^{-1}$  per active site.<sup>[116,123,181,203–205]</sup>

Multiple reaction routes can obtain the synthesis of the hexacarbonyl moiety. The primary synthetic methods are discussed in the following chapter.

### 3.3.1 Synthesis of [FeFe] Hydrogenase Mimics

*Reihlen et al.* presented a bis-mercaptoethyl hexacarbonyl diiron complex that was generated from iron pentacarbonyl and mercaptoethane at 60 °C with additional irradiation of a mercury vapor lamp for almost 10 h of reaction time. The postulated mechanism involved the formation of diiron nonacarbonyl from iron pentacarbonyl by irradiation and the evolution of four equivalents of CO and one equivalent of H<sub>2</sub> gas (Equation 3).<sup>[173]</sup>



This example was the first of many reactions of an iron(0) reagent with thiols, the most common and versatile synthesis route for diiron dithiolate hexacarbonyl complexes (Figure 11).<sup>[157]</sup> *Hieber et al.* were the first to use triiron dodecacarbonyl Fe<sub>3</sub>(CO)<sub>12</sub> to react with thiophenol or naphthalene-1-thiol to form the corresponding hexacarbonyl complexes.<sup>[175,206]</sup>

The reactivity of the three iron(0) precursors, iron pentacarbonyl Fe(CO)<sub>5</sub>, diiron nonacarbonyl Fe<sub>2</sub>(CO)<sub>9</sub> and Fe<sub>3</sub>(CO)<sub>12</sub> increases with the amount of potential “Fe(CO)<sub>4</sub>” units, however, the proposed mechanism of Fe<sub>3</sub>(CO)<sub>12</sub> differs regarding the formation of hexacarbonyl complexes.<sup>[157,207]</sup>



Fe(CO)<sub>5</sub> and Fe<sub>2</sub>(CO)<sub>9</sub> are suggested to generate Fe(HSR)(CO)<sub>4</sub> during the reaction with thiols that dimerize to their appropriate diiron complexes, accompanied by the release of CO and H<sub>2</sub>.<sup>[208,209]</sup> In contrast, Fe<sub>3</sub>(CO)<sub>12</sub> is proposed to form Fe<sub>3</sub>(μ-SR)(μ-H)(CO)<sub>9</sub> or [Fe<sub>3</sub>(μ-SR)(CO)<sub>9</sub>]<sup>-</sup> intermediates that react with an additional thiol to Fe<sub>3</sub>(μ-SR)<sub>2</sub>(CO)<sub>9</sub> and the final diiron product upon heating.<sup>[210–</sup>



212] While these precursors are very reactive towards SH moieties, various functional groups are tolerated, opening this reaction to various multifunctional thiols (Figure 11).<sup>[207,213–222]</sup>

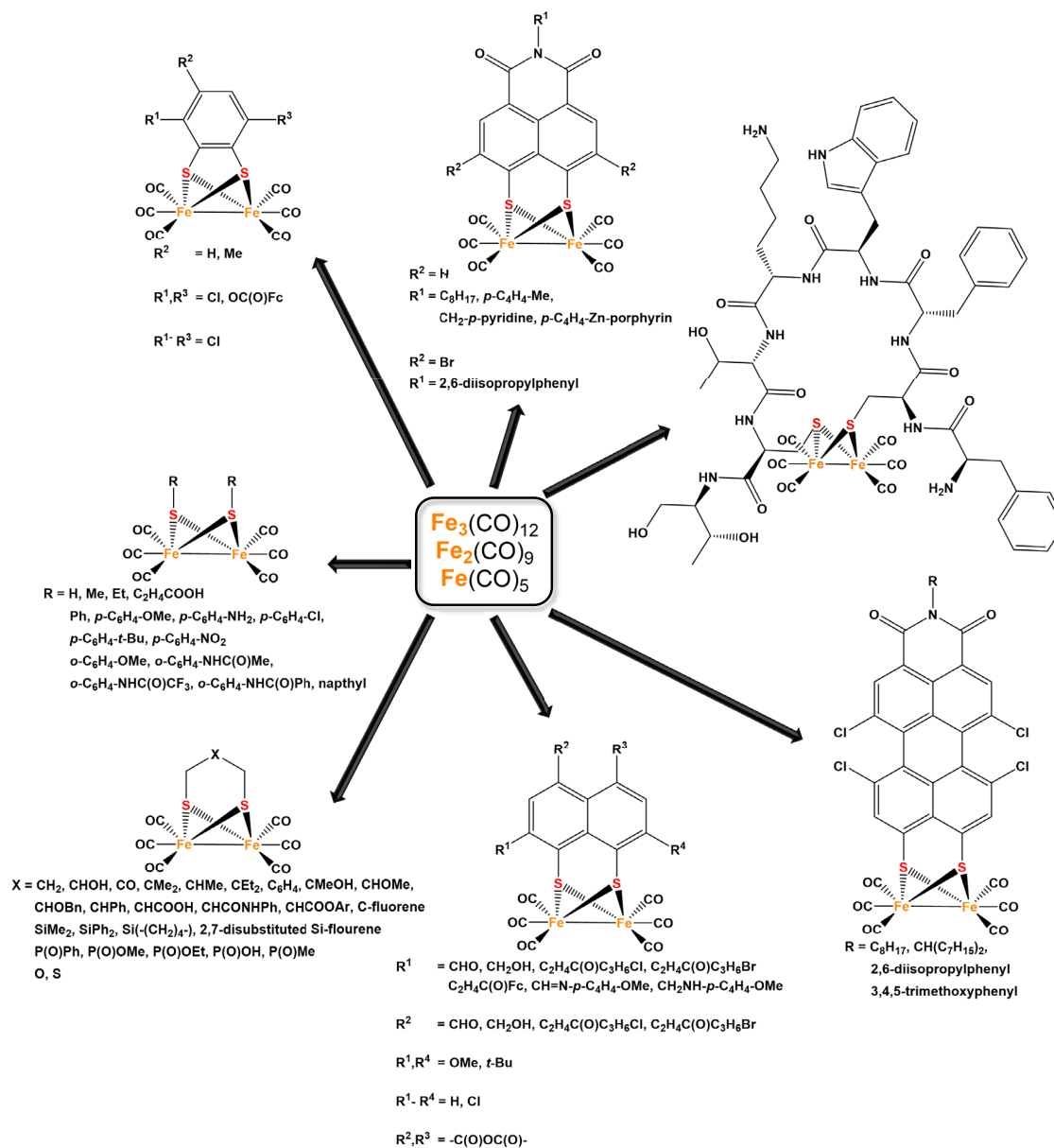


**Figure 11. Versatile examples for forming dithiolato [FeFe] H<sub>2</sub>ase mimics using iron(0) precursors. Residues that are not described in detail are defined as hydrogen atoms.**<sup>[131,157,182,223–227]</sup>

Another class of starting materials represents disulfides (RSSR) that are oxidatively added to iron(0) precursors, as first described by *Hieber et al.*<sup>[228]</sup> Disulfides are less reactive than thiols. However, they open new possible complexes with differing thiolate residues or more complex structures such as natural materials, peri-naphthalene or peri-perylene derivatives, and perthioesters (Figure 11).<sup>[214,223,229–236]</sup>

In addition, disulfides are convenient to handle due to higher boiling points, e.g., MeSH vs. Me<sub>2</sub>S<sub>2</sub>, less intense odor, and low volatility.<sup>[157,237]</sup> In contrast, there are only a few examples of the conversion of thioethers or polysulfides, which appear to react very slowly, generating complexes in low yields that can be obtained more efficiently using thiols.<sup>[238–240]</sup> The conversion of thioketones and thioalcones leads to many products recently investigated by the *Weigand* group.<sup>[241–245]</sup>

To simplify the complicated synthesis routes of interesting thiols or disulfides, utilizing organic thio-, seleno-, or tellurocyanates that can be comfortably obtained from precursor halides can unlock another promising path to [FeFe] H<sub>2</sub>ase models.<sup>[246–248]</sup> Furthermore, it is a convenient way to introduce selenium or tellurium to generate mixed dichalcogenides that offer new variables for the electrochemical tuning of the mimics.<sup>[246,249–253]</sup>

Some desired complexes are very hard to accomplish due to, e.g., unstable thiol ligands, insufficient reactivity, formation of bis(diiron(I)) species,<sup>[254,255]</sup> that an alternative route can be achieved by applying iron(I) precursors such as Li<sub>2</sub>[Fe<sub>2</sub>(μ-S)<sub>2</sub>(CO)<sub>6</sub>] or [Fe<sub>2</sub>(μ-SH)<sub>2</sub>(CO)<sub>6</sub>], that were first described by *Seyferth et al.*<sup>[178,256]</sup> The synthesis of this kind of precursor is carried out by the reduction of Fe<sub>2</sub>(μ-S)<sub>2</sub>(CO)<sub>6</sub> with two equivalents of the so-called “super hydride” LiHBEt<sub>3</sub> at -78 °C, whose first equivalent cleaves the S-S bond and the second one removes the proton to form H<sub>2</sub> (Figure 12).<sup>[256]</sup> Subsequent acidification with trifluoroacetic acid leads to H<sub>2</sub>[Fe<sub>2</sub>(μ-S)<sub>2</sub>(CO)<sub>6</sub>].<sup>[256,257]</sup> These strong nucleophiles efficiently react with alkyl halides or tosylates, whereas aryl halides are not electrophile enough in most cases.<sup>[157]</sup>

Special attention has been received on this method for the synthesis of azadithiolate (adt) analogs Fe<sub>2</sub>[(μ-SCH<sub>2</sub>)<sub>2</sub>NR](CO)<sub>6</sub>, which gives the desired complexes from (ClCH<sub>2</sub>)<sub>2</sub>NR precursors in moderate yields.<sup>[190,196,197,201,258,259]</sup> Furthermore, recent studies exchanged the bridgehead NR moiety to phosphine oxides P(O)R;<sup>[260,261]</sup> and substituted tetrels such as CR<sub>2</sub>,<sup>[262,263]</sup> SiR<sub>2</sub>,<sup>[225,262–265]</sup> GeR<sub>2</sub><sup>[266,267]</sup> or SnR<sub>2</sub><sup>[251,266]</sup> (Figure 12). Michael reaction-related addition of unsaturated organic electrophiles such as dicarbonyls, aldehydes, ketones,

alkenes, or alkynes to  $[\text{Fe}_2(\mu\text{-SH})_2(\text{CO})_6]$  leads to new  $\{\text{FeFe}\}$  H<sub>2</sub>ase mimicking complexes.<sup>[190,268]</sup>

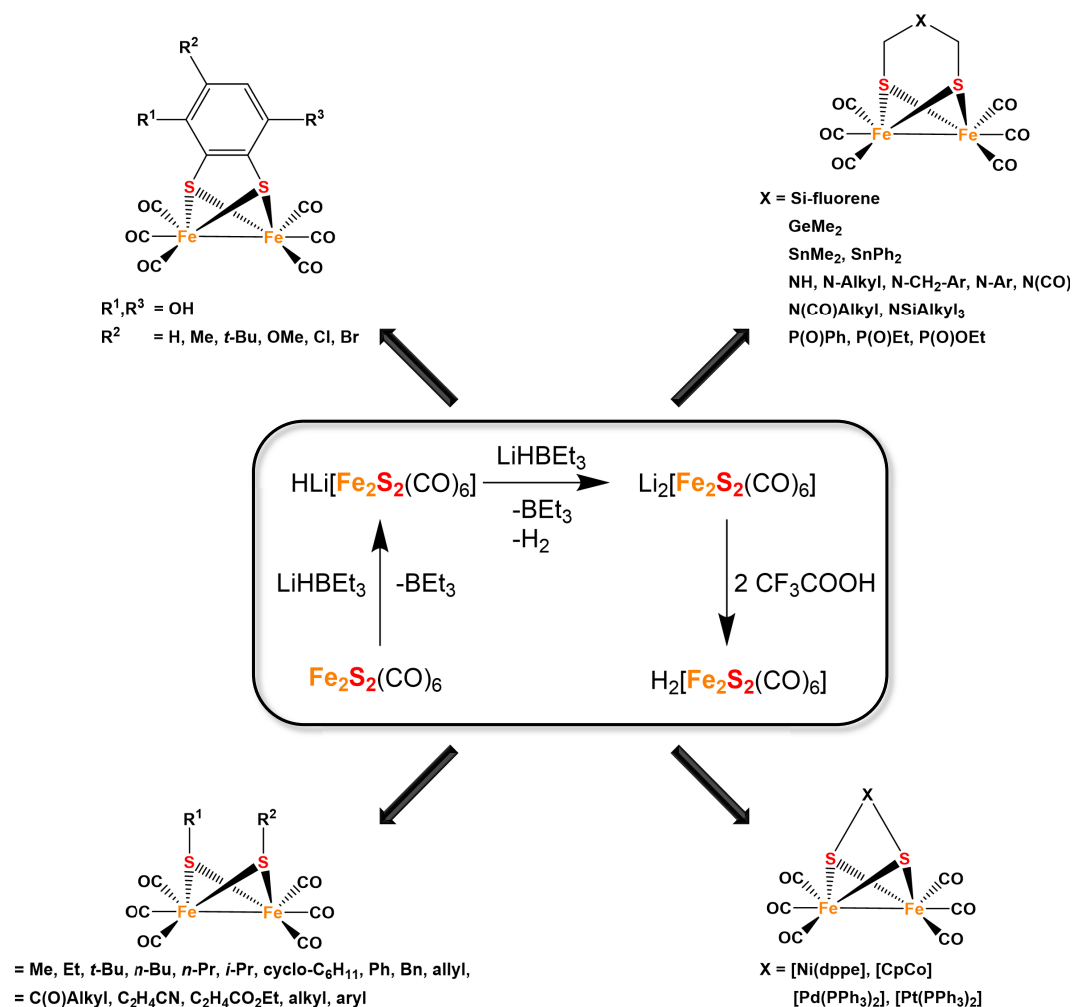


**Figure 12.** Versatile examples for forming dithiolato  $[\text{FeFe}]$  H<sub>2</sub>ase mimics using iron(I) precursors.<sup>[131,157,182,223,260]</sup>

The selenium and tellurium analogs  $\text{Fe}_2(\mu\text{-Se})_2(\text{CO})_6$  and  $\text{Fe}_2(\mu\text{-Te})_2(\text{CO})_6$  are also able to perform these reactions, but the number of described examples is relatively small.<sup>[258,269]</sup>

Another underestimated method is utilizing  $\text{Fe}_2(\mu\text{-S})_2(\text{CO})_6$  without any pre-treatment, which can access unsymmetric complexes by adding unsaturated organic electrophiles, occasionally under photochemical conditions.<sup>[190,268,270–273]</sup> Hydroquinone analogs were realized by photoaddition of quinone derivatives to  $\text{Fe}_2(\mu\text{-S})_2(\text{CO})_6$  or by addition of quinone derivatives to  $\text{Fe}_2(\mu\text{-SH})_2(\text{CO})_6$  in the presence of piperidine.<sup>[274]</sup> Furthermore, this precursor can react with carbanionic compounds like organolithium or Grignard reagents to generate mono-alkylated reactive intermediates,  $\text{Fe}_2(\mu\text{-SR})(\mu\text{-SM})(\text{CO})_6$  ( $\text{M} = \text{Li, MgX}$ ), that react with

electrophiles such as carboxylic chlorides, alkyl halides, alkenes, epoxides to unsymmetric diiron complexes (Figure 12).<sup>[157,275–278]</sup>

The addition of low-valent transition metal precursors such as  $\text{Pt}(\text{PPh}_3)_4$ ,  $\text{Pd}(\text{PPh}_3)_3\text{CO}$ ,  $\text{CoCp}(\text{CO})_2$ , or  $\text{Ni}(\text{dppe})(\text{CO})_2$  leads to the insertion of the additional metal centers into the S-S bond of the iron(I) precursor.<sup>[279]</sup>

### 3.3.2 Electrocatalytic active [FeFe] Hydrogenase Mimics

One key feature of interest of [FeFe]  $\text{H}_2$ ase mimics is the redox behavior in the absence and presence of diverse acids such as acetic acid (AcOH), trifluoroacetic acid (TFA), triflic acid (HOTf), fluoroboric acid diethyl ether adduct ( $\text{HBF}_4 \cdot \text{Et}_2\text{O}$ ) or perchloric acid ( $\text{HClO}_4$ ), amongst others. For this purpose, powerful electrochemical measurements like cyclic voltammetry (CV) or polarography were performed to detect the redox and catalytic activities of the complexes.<sup>[280]</sup>

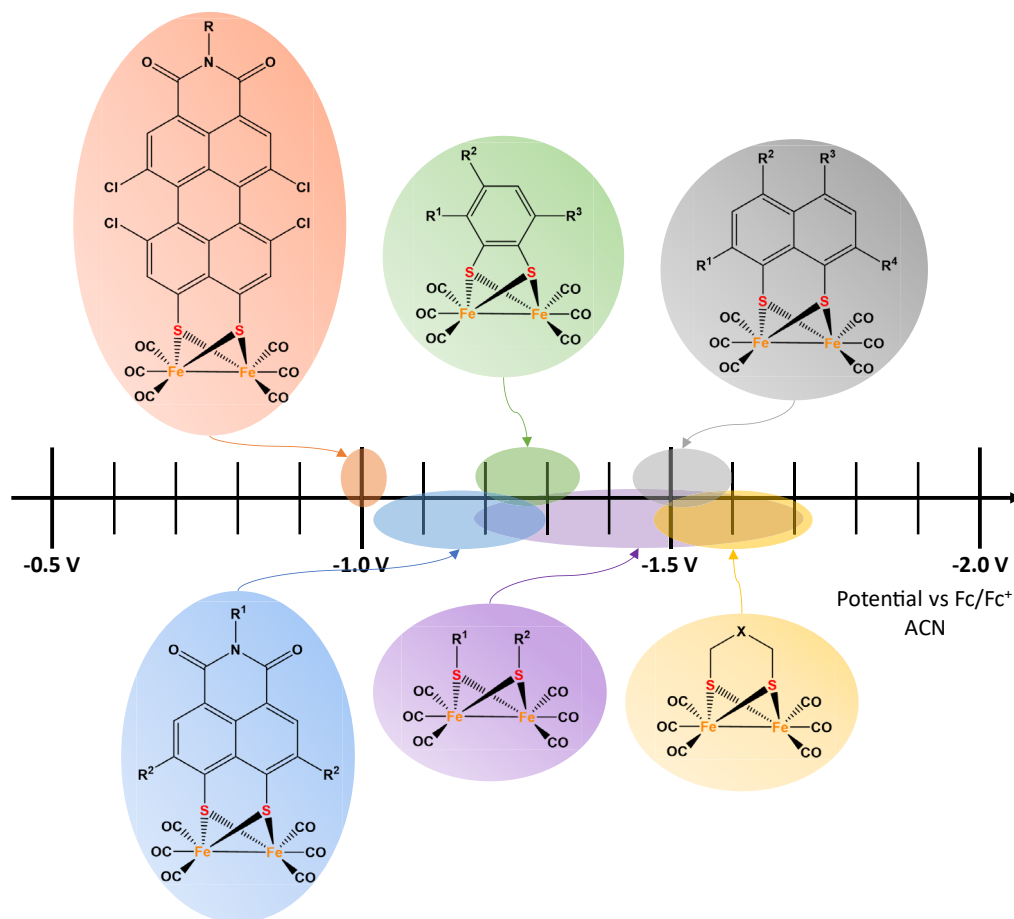


**Figure 13.** Electrochemical reduction potential ranges in the absence of acid for various [FeFe]  $\text{H}_2$ ase mimics. Residues R are specified in Figures 11 and 12. Adapted from *Gao et al.*<sup>[182,188]</sup>

Conveniently, CV can be enabled in organic or aqueous solutions to analyze almost any soluble compound. Hence, it has great popularity in the [FeFe] H<sub>2</sub>ase community. In addition, a broad electroactive window to perform electrochemical reactions is present, depending on solvent, electrolyte, and electrode material.<sup>[280]</sup> Adding an internal standard reference such as ferrocene (Fc) and referencing to the Fc/Fc<sup>+</sup> couple at 0 V enhances the comparability between different mimics due to varying electrochemical setups and conditions in each laboratory (Figure 13).<sup>[280]</sup>

Detailed CV investigations of [FeFe] H<sub>2</sub>ases reveal their suitability to perform efficient HER, information about catalytic mechanisms, and influences of structural moieties towards electrochemical behavior, e.g., shift of the reduction potential by replacing one CO ligand at the iron center with electron donating or withdrawing ligands, or exchange of sulfur atoms to selenium or tellurium.<sup>[131,157,182,251]</sup> Deeper insights are generated by combination with spectroscopical techniques such as UV-Vis, EPR, or IR spectroscopy and theoretical calculations.<sup>[225,233,281–293]</sup> These findings might help develop an “optimized” artificial [FeFe] H<sub>2</sub>ase.

### *3.3.2.1 Electrocatalytic hydrogen evolution reaction mechanism*

Depending on the structure of the [FeFe] H<sub>2</sub>ase mimic and added proton source, multiple catalytic cycles are discussed in the literature.<sup>[131,182,188,250]</sup> Most hexacarbonyl complexes initiate their catalytic process from an inactive Fe<sup>I</sup>Fe<sup>I</sup> state, while native [FeFe] H<sub>2</sub>ases start from their H<sub>ox</sub> state (Fe<sup>II</sup>Fe<sup>I</sup>). Usually, the first step of the HER of propanedithiolato (pdt) analog mimic is a one-electron uptake (E = electrochemical process) at the iron center, followed by a protonation (C = chemical process) or another reduction step, depending on the strength of the acid and the basicity of the mimic.

The protonation with a strong acid like HOTf (pK<sub>a</sub>(acetonitrile (ACN)) ≈ 8)<sup>[294]</sup> involves the generation of a hydride species that can be reduced and protonated in further steps to release H<sub>2</sub>, closing the “slow” catalytic cycle to start again from the Fe<sup>I</sup>Fe<sup>I</sup> state (ECEC mechanism, Figure 14 blue cycle). In addition, the reduction of the double-reduced and deprotonated at more negative potential and follow-

up release of H<sub>2</sub> closes the “fast” cycle to the mono-reduced species ((E)CECE) mechanism, Figure 14 red cycle).<sup>[283,295,296]</sup> Naphthalene bridged mimics are also proposed to follow this mechanism.<sup>[182,297]</sup>

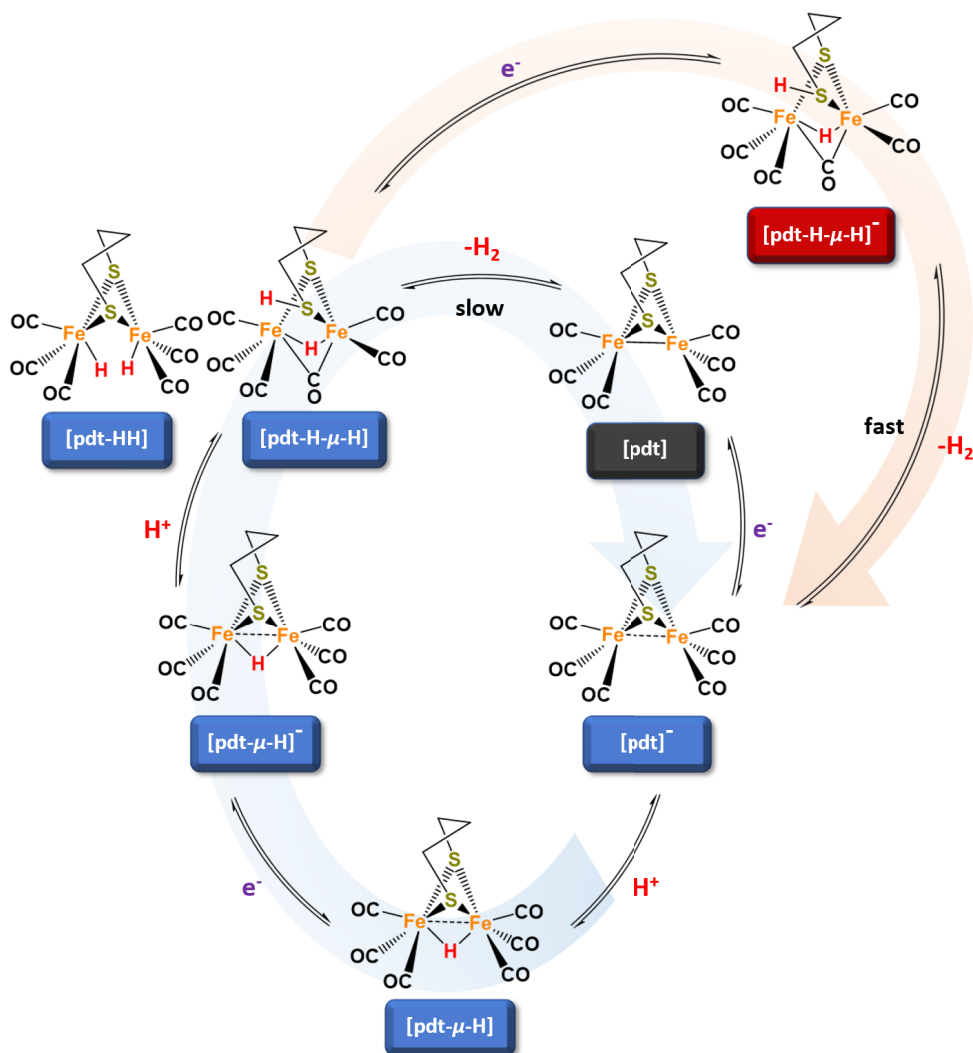


**Figure 14.** Proposed catalytic cycle of pdt analog [FeFe] H<sub>2</sub>ase mimics in the presence of HOTf.<sup>[131,283,295,296]</sup>

In some cases, the substitution of CO by more potent electron-donating ligands such as phosphanes, carbenes, or cyanides leads to an increase in electron density at the iron center that can enable a direct protonation of the unreduced complex if the resulting basicity is strong enough.<sup>[202,251,298–301]</sup> Also, it is possible to protonate a basic bridging moiety, e.g., tertiary amines.<sup>[298,300]</sup>

While pdt analogs typically follow ECEC or (E)CECE mechanisms (Figure 14), a disubstitution at the CH<sub>2</sub> bridgehead can lead to an EECC process in the presence of HOTf due to steric interactions between the CO ligands and the substituents at the bridgehead carbon atom.<sup>[250]</sup> This mechanism is well described for benzodithiolato (bdt) [FeFe] H<sub>2</sub>ase mimics, including the so-called potential inversion that describes a reduced reduction potential for the second ET after the first one due to structural rearrangements after the first ET (Figure 15).<sup>[250,302]</sup> The double-reduced bdt mimic is basic enough to be protonated by acids, even by weak acids like AcOH (pK<sub>a</sub>(ACN) ≈ 23).<sup>[182,303]</sup>

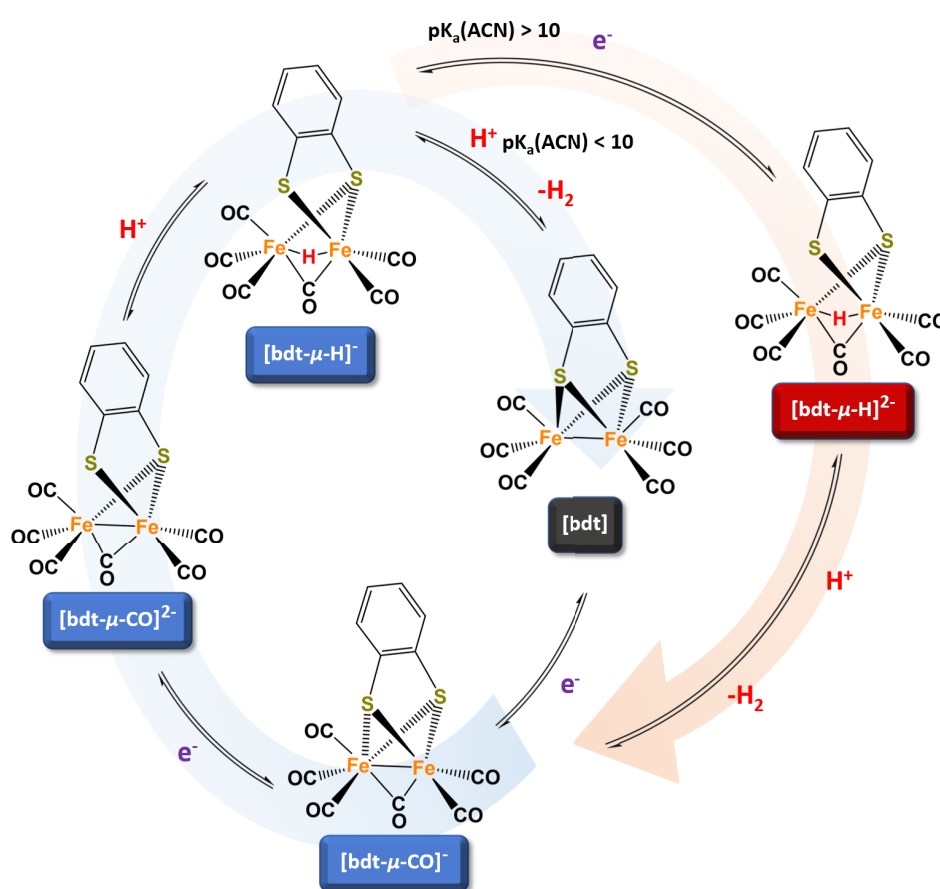


Figure 15. The proposed catalytic cycle of bdt analog [FeFe] H<sub>2</sub>ase mimics in the presence of weak (AcOH, red cycle) and strong (HOTf, blue cycle) acids.<sup>[182,303–305]</sup>

In this process, computational calculations predict a bridging hydride ( $\mu$ -H) species instead of a terminal hydride or a protonation at the sulfur atom. However, this state is only basic enough to be protonated by strong acids (pK<sub>a</sub>(ACN) < 10) to release H<sub>2</sub> (EECC mechanism, Figure 15 blue cycle). In the case of weak acids, the complex must undergo another reduction step before further protonation

appears to close the catalytic cycle ((E)ECEC) mechanism, Figure 15 red cycle).<sup>[182,303,304]</sup>

### 3.3.2.2 Enhanced electrocatalytic hydrogen evolution

Transporting electrons from the electrode surface to the active species is necessary for efficient catalysis.<sup>[306,307]</sup> This process is diffusion-limited. Therefore, immobilizing catalysts to the electrode surface to reduce the electron transfer pathway is promising to overcome this issue. Different approaches utilizing chemically modified electrodes were investigated, including electrostatic adsorption,<sup>[308]</sup> embedding in redox-active hydrogels or polymers,<sup>[194,309–316]</sup> reduction of diazonium salt spacers on carbon electrodes,<sup>[317–319]</sup> carboxylic acid group on nickel oxide or fluorine-doped tin oxide (FTO) electrodes,<sup>[320,321]</sup> and thiol spacer groups on gold electrodes, amongst others.<sup>[307,322–333]</sup> Unfortunately, attached [FeFe] H<sub>2</sub>ase mimics lack consistency and activity for HER due to their oxygen sensitivity, irreversible electrocatalytic behavior, and instability of the linker groups.<sup>[317,320,334–336]</sup> However, they benefit from their independence of the solvent for HER due to the low solubility of most [FeFe] H<sub>2</sub>ase mimics in water.

### 3.3.3 Photocatalytic active [FeFe] H<sub>2</sub>ase Mimics

Another promising approach is the HER under photocatalytic conditions, potentially utilizing solar power for hydrogen generation (Figure 16).

The group of photoactive [FeFe] H<sub>2</sub>ase mimics can be divided into two subtypes: systems with intermolecular and intramolecular photosensitizers (PS). Their catalytic activity is usually evaluated by the turnover number (TON), which represents the number of moles of substrate that a mole of catalyst can convert during the catalysis or turnover frequency (TOF), which implies the ratio of TON to a specific duration.<sup>[183,263]</sup>

While intermolecular [FeFe] H<sub>2</sub>ase mimics rely on external electron transfer mechanisms, intramolecular mimics can absorb light by themselves, minimizing electron transfer pathways from the PS to the catalytic [FeFe] center.<sup>[337]</sup> However, intermolecular catalyst systems feature great accessibility and a broad spectrum of absorption wavelengths and redox potentials. Unfortunately, their catalytic



rates are tremendously limited by the diffusion of the reaction components.<sup>[337]</sup> To overcome this issue, recent approaches benefit from non-covalent interactions, such as ionic or supramolecular assemblies.<sup>[183]</sup>

Known examples of mimics with integrated PS and great catalytic activity are rare due to the difficulties in the synthesis routes that are needed to include a photoactive moiety, unfavorable redox-potentials between catalyst ( $\text{Fe}_2\text{S}_2$ ), electron donor (ED) and PS, and limited absorption ranges.<sup>[183,225]</sup> Hence, a big part of these dyads (PS- $\text{Fe}_2\text{S}_2$ ) or triads (ED-PS- $\text{Fe}_2\text{S}_2$ ) lack catalytic activity with TONs below 30.<sup>[233,264,338–343]</sup> One major issue is the degradation of the complexes during irradiation in the UV region due to the loss of CO ligands.<sup>[344,345]</sup> Another drawback of several mimics is their reliance on precious transition metals such as ruthenium, iridium, or rhenium.<sup>[196,197,340,341,346–350]</sup>

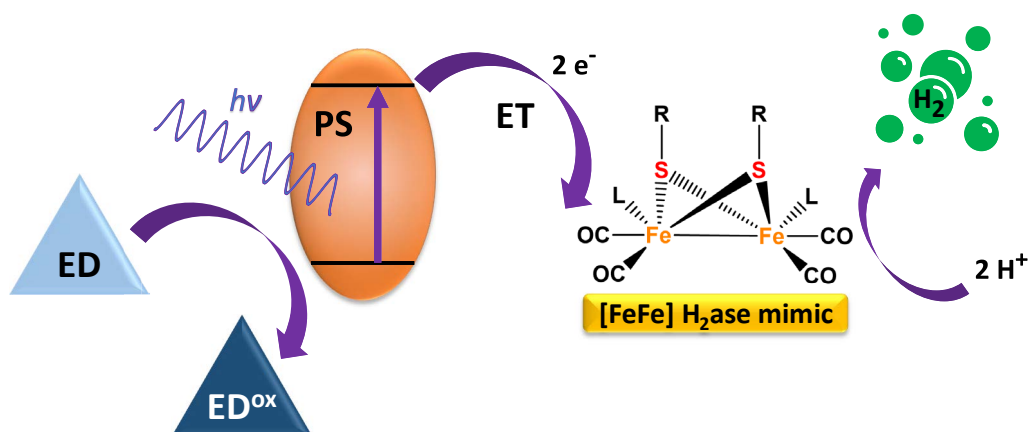


**Figure 16.** Possible mechanism of the light-driven hydrogen evolution reaction. R and L represent various modifications of the diiron subunit of [FeFe]  $\text{H}_2$ ase mimics. Adapted from *Amaro-Gahete et al.*<sup>[183]</sup>

Recently, *Weigand and co-workers* developed a new precious metal-free dyad system consisting of a silafluorene-based bridging dithiolate moiety with an oligothiophene extended chromophore that can perform the HER with an unmatched TON value up to 210 under visible light irradiation.<sup>[225]</sup> Preceding studies of his group investigated (sila)fluorene-based [FeFe]  $\text{H}_2$ ase mimics that revealed outstanding performance with TONs up to 540 under UV light.<sup>[263]</sup>

However, these TON values of intramolecular PS [FeFe]  $\text{H}_2$ ase mimics cannot compete with intermolecular PS systems that were investigated in the last

decade.<sup>[183]</sup> Especially, photocatalysts based on CdSe or CdTe quantum dots (QDs) PSs perform exceptionally well HER under visible light irradiation in aqueous solutions with TONs up to 83,600.<sup>[351–356]</sup>

However, due to a multitude of factors such as versatile sources of electrons and protons, pH value, temperature, reagent concentrations and ratios, reactor type, solvents, irradiation wavelength, and intensity, amongst others, it is a big challenge to compare these systems regarding their performance of light-driven catalysis.<sup>[183,184,357]</sup> Recently, *Ziegenbalg et al.* suggested a dataset for objectively comparing light-driven experiments, including chemical parameters, reactor setup, operation conditions, light sources, and performance indicators.<sup>[357]</sup>

To overcome the issues of photocatalytic hydrogen evolution, researchers of different areas of expertise will need to collaborate and investigate new systems that might be able to perform a sustainable, stable, and economic HER someday.

## 4. Discussion

The following chapter describes the four published papers that were prepared in advance of this thesis (Figure 17). Each of them focuses on a different facet of [FeFe] H<sub>2</sub>ase mimic chemistry, including deep insights into the electrochemical behavior of non-innocent bridging ligands connected to the hexacarbonyl diiron moiety (SB-1), photocatalytic performance of assembled PS - [FeFe] H<sub>2</sub>ase mimic systems (SB-2), electrochemistry of self-assembled monolayers of [FeFe] H<sub>2</sub>ase mimics with lipoic acid moieties as anchor groups (SB-3), and a facilitated procedure for the preparation of [FeFe] H<sub>2</sub>ase mimics via the addition of *N*-methylpyrrolidone (NMP) as a co-solvent (SB-4). SB-5 is a patent application correlated to the findings of SB-4 that was registered in advance.

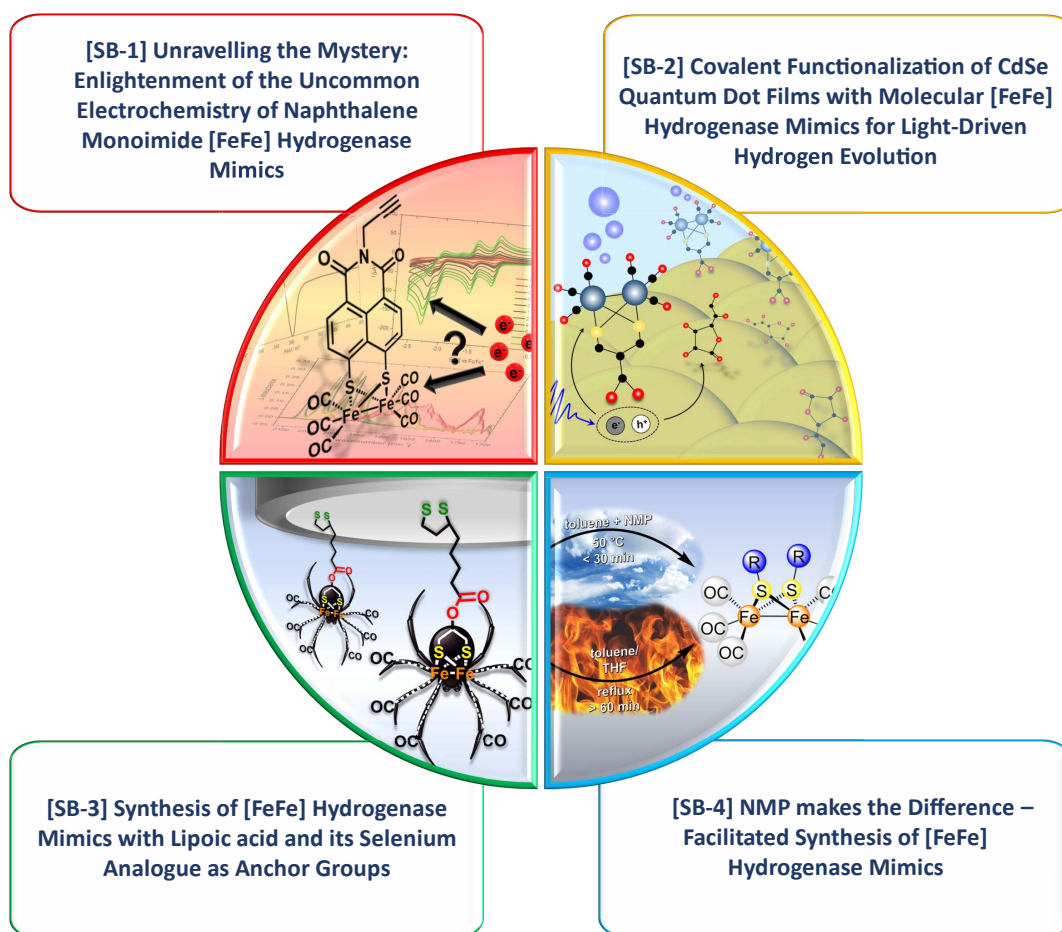


Figure 17. Overview of published papers during this Ph.D. thesis.

## 4.1 SB-1 Unravelling the Mystery: Enlightenment of the Uncommon Electrochemistry of Naphthalene Monoimide [FeFe] Hydrogenase Mimics

*Eur. J. Inorg. Chem.* **2022**, *3*, e202100959.

This work describes the synthesis; electrochemical, spectroelectrochemical (SEC), and EPR investigation; crystal structure analysis; and quantum chemical simulations of a new example of naphthalene monoimide (NMI) based [FeFe] H<sub>2</sub>ase mimics featuring an alkyne group at the imide functionality (compound **4**). Therefore, an adapted procedure was established, utilizing NMP as a co-solvent to increase the solubility of its disulfide precursor 4,5-Dithio-1,8-naphthalenedicarboxylic *N*-propargyl-monoimide **3**, that was synthesized via a three-step synthesis route (SB-1, Scheme 1). A more detailed analysis of the facilitated procedure of synthesizing [FeFe] H<sub>2</sub>ase mimics will be discussed in Chapter 4.4.

The structure of **4** was confirmed by X-ray diffraction analysis, revealing the characteristic butterfly conformation of the [2Fe<sub>2</sub>S] cluster with an almost orthogonal arrangement (91.87°) of the Fe-Fe axis to the naphthalene plane similar to the previously reported mimics.<sup>[226,227,358,359]</sup>

This project aimed to examine the electrochemical behavior of [FeFe] H<sub>2</sub>ase mimics with bridging NMI dithiolate ligands. Due to the possibility of delocalizing electron density to the conjugated aromatic bridging ligands during the reduction of [FeFe] H<sub>2</sub>ase model complexes, the stability of the reduced species is enhanced. While the one-electron reduction of the pdt analog occurs irreversible, the bdt-based [FeFe] H<sub>2</sub>ase mimic performs a fully reversible two-electron reduction at a less negative potential (Figure 13). Enlargement of the aromatic moiety supports the stabilizing effect. However, the bridging ligands without electron-withdrawing groups tend to increase the electron density at the iron cores and shift their reduction potentials to more negative values (Figure 13, e.g., naphthalene moiety). While the reductions of these examples were described as iron-centered, introducing non-innocent ligands made this assumption controvertible, as those

could also perform electrochemical reactions.<sup>[360]</sup> Especially, 1,8-naphthalic anhydride, naphthalene, and perylene monoimide-based [FeFe] H<sub>2</sub>ase mimics revealed comparatively low reduction potentials (Figure 13).<sup>[226,227,286,359]</sup> The group of *Reek et al.* was the first to investigate whether the ligand or the iron core is reduced during the first reduction step by utilizing EPR measurements and IR SEC - revealing the first reduction taking place at the NMI moiety.<sup>[286]</sup> While they focused exclusively on the first reduction step, further reduction steps were explored with various (electro)spectroscopic and EPR methods supported by DFT calculations.

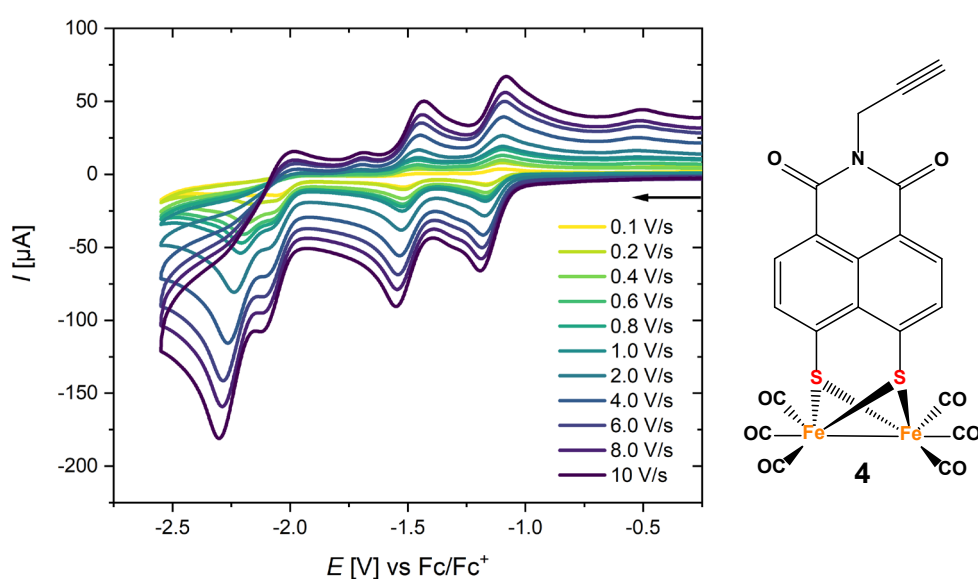


**Figure 18.** CV with different scan rates of compound **4** ( $c = 1 \text{ mmol/L}$ ) in N<sub>2</sub>-purged ACN/[NBu<sub>4</sub>][BF<sub>4</sub>] (0.1 mol/L) at RT. The arrow indicates the scan direction. The potential  $E$  is given in V and referenced to the Fc/Fc<sup>+</sup> couple. Adapted from SB-1.<sup>[361]</sup>

The CV of NMI-based [FeFe] H<sub>2</sub>ase mimic **4** exhibits two quasi-reversible reduction steps at  $E_1 = -1.16 \text{ V}$  and  $E_2 = -1.52 \text{ V}$  and two irreversible reduction processes at  $E_3 = -2.05 \text{ V}$  and  $E_4 = -2.16 \text{ V}$ , where the latter two became more distinguished at higher scan rates (Figure 18). All of them represent a one-electron transfer, as suggested by the scan rate dependence of the current function (SB-1, Figure S2). Furthermore, we compared these findings with the previously reported compound **4a**, which features a 4-toluene moiety at the imide group. No significant differences could be observed, only a minor shift to a more positive reduction potential by 30 mV (SB-1, Figure S1A).

While DFT calculations supported the exhibited performance of [FeFe] H<sub>2</sub>ase mimics **4** and **4a** in the case of the first reduction event, the formation of two possible species, a doubly reduced singlet or a doubly reduced triplet, was feasible for the second reduction. IR, UV-Vis SEC, and EPR measurements were performed to clarify this uncertainty.

An optically transparent thin-layer electrochemical (OTTLE) cell enabled the IR SEC measurement during the CV experiment with slow scan rates of 2 mV/s (Figure 19). Especially the  $\tilde{\nu}(\text{CO})$  bands of metal carbonyls show high sensitivity towards the complex's geometry and charge state.<sup>[281,283]</sup> Due to the change of electron density at the iron cores, caused by the electron uptake or release, the back donation to the anti-bonding  $\pi^*$  orbital of the carbonyl ligands gets stronger, and the C $\equiv$ O triple bond gets weakened or vice versa. Therefore, all carbonyl bands in the IR spectra were bathochromic shifted during the reduction of the complexes.

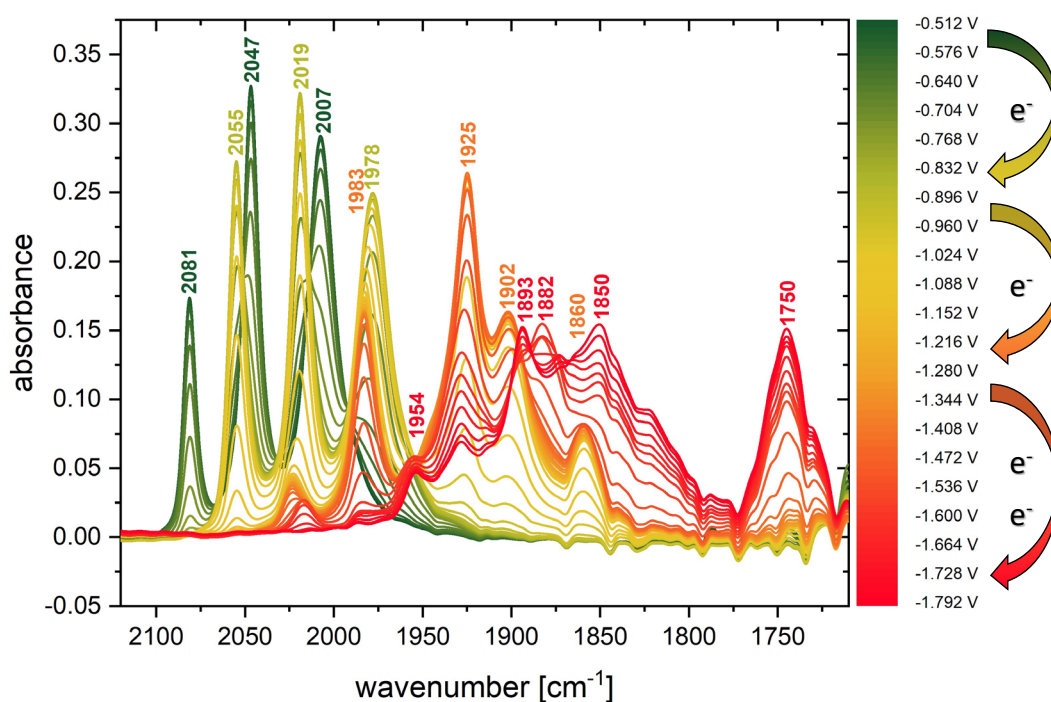


Figure 19. IR SEC spectra of compound **4** (ACN,  $c = 2$  mmol/L) at different cathodic potentials (- 0.512 V to - 1.792 V) were recorded within an OTTLE cell. IR region of the  $\tilde{\nu}(\text{CO})$  bands. Remember that there is a difference in cathodic shifts between the CV and the IR SEC experiments due to using different electrodes (for further details, see SI of SB-1). Adapted from SB-1.<sup>[361]</sup>

Figure 19 demonstrates the different reduction steps of compound **4**. The pattern of the carbonyl bands remained intact after the first reduction (green to yellow).

However, the shift of the first reduction was significantly smaller ( $\Delta\tilde{\nu}(\text{CO}) \approx 22 \text{ cm}^{-1}$ ) than comparable examples from the literature ( $\Delta\tilde{\nu}(\text{CO}) \approx 60\text{-}79 \text{ cm}^{-1}$ ), indicating the reduction of the NMI moiety that partially transferred electron density to the carbonyls.<sup>[283,286]</sup> This finding was supported by UV-Vis SEC, EPR measurements of chemical-reduced complex **4** by  $\text{Cp}^*_2\text{Co}$ , and DFT calculations.

The second electron uptake (yellow to orange) led to structural rearrangements indicated by a change of shape of the absorption bands and significant bathochromic shifts ( $\Delta\tilde{\nu}(\text{CO}) \approx 80 \text{ cm}^{-1}$ ), as expected for a one-electron reduction of the iron cores.<sup>[362]</sup> DFT simulations predicted no structural changes for the singlet state. Hence, the double reduced species was concluded to be in a triplet state with one electron at the NMI and the iron core, respectively. Furthermore, the group of *Ott et al.* assumed a dimerization of such kind of iron-centered one-electron reduced species that formed a bridging CO band at  $\tilde{\nu}(\mu\text{-CO}) = 1727 \text{ cm}^{-1}$ , similar to the minor absorption band at  $\tilde{\nu}(\mu\text{-CO}) = 1738 \text{ cm}^{-1}$  of complex **4** after the second reduction.<sup>[363]</sup> Unfortunately, due to its unstable nature, no sample of this state could be isolated for further analysis.

The further irreversible reduction steps led to the degradation of the complex (orange to red), revealed by the appearance of a new distinguished band at  $\tilde{\nu} = 1750 \text{ cm}^{-1}$ , which is attributed to the formation of  $[\text{Fe}(\text{CO})_4]^{2-}$ , a degradation product of iron carbonyl complexes.<sup>[289,364]</sup>

Electrochemical experiments in the presence of acids (AcOH or TFA) were conducted to study whether complex **4** could perform the HER under electrocatalytic conditions (Figure 20). The CV experiments confirmed catalytic processes whose currents increased with increasing acid concentration. However, reducing the NMI moiety was still the first step, while the catalytic performance was possible subsequently.

In addition, the photocatalytic performance was investigated in the presence of CdSe as PS and ascorbic acid as electron and proton source. Unfortunately, there was no catalytic activity detectable. Probably, the complex needed a higher reduction potential than the PS could provide. Additional DFT calculations clarified

that the complex could not perform the HER under photocatalytic conditions due to the electron-harvesting properties of the NMI moiety. Previously, before these findings, this kind of complex was intended to be included in a polysaccharide network via azide-alkyne click chemistry to mimic an enzyme backbone that was supposed to support and protect the [FeFe] H<sub>2</sub>ase mimic. Even though the functionalization could be realized, no photocatalytic HER was observable.

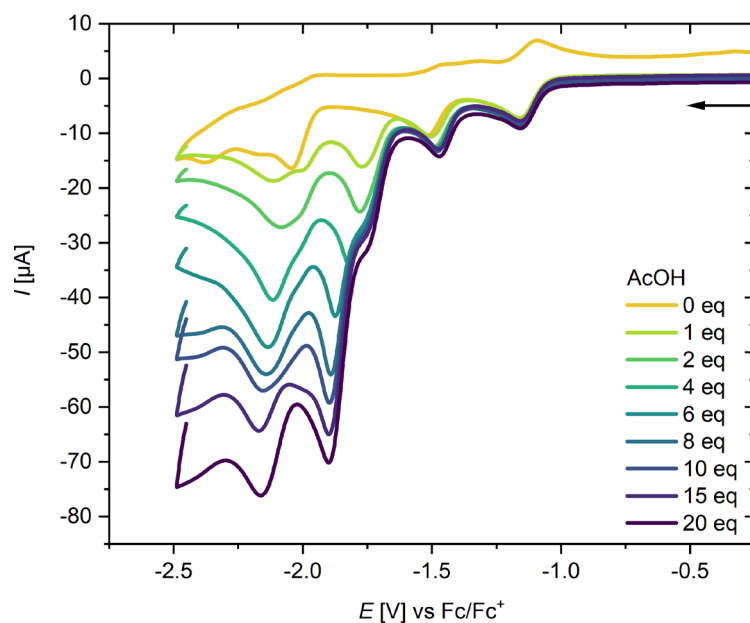


**Figure 20.** Cyclic voltammograms ( $v = 0.2$  V/s) of compound 4 ( $c = 1$  mmol/L) with various amounts of acetic acid in N<sub>2</sub>-purged ACN/[NBu<sub>4</sub>][BF<sub>4</sub>] (0.1 mol/L) at RT. The arrow indicates the scan direction. The potential *E* is given in V and referenced to the Fc/Fc<sup>+</sup> couple (SB-1, Figure 7).<sup>[361]</sup>



## 4.2 SB-2 Covalent Functionalization of CdSe Quantum Dot Films with Molecular [FeFe] Hydrogenase Mimics for Light-Driven Hydrogen Evolution

*ACS Appl. Mater. Interfaces* **2023**, *15*, 18889–18897.

Another approach for photocatalytic HER was carried out during the experiments for paper SB-2. This work aimed to form PS-CAT systems containing colloidal semiconductor nanoparticles, such as CdSe QDs, that connected with [FeFe] H<sub>2</sub>ase mimics to keep the electron pathways as short as possible. Several research groups have confirmed that such PS-CAT systems show good to excellent catalytic performances.<sup>[183,365–368]</sup>

Photoinduced catalytic reactions undergo three steps as follows: (i) absorption of photons initiates the generation of electron-hole pairs, so-called excitons;<sup>[85]</sup> (ii) the excited electron is transferred to the catalyst or a substrate while the hole is quenched by a sacrificial electron donor such as ascorbic acid (AA) or triethylamine (TEA), to avoid recombination; (iii) the chemical reaction at the catalyst.<sup>[365]</sup> The redox potentials of PS and CAT should be matched very well to facilitate the charge transfer. In addition, the distance between them should be as small as possible via chemical bonds or intermolecular interactions to ensure an efficient transfer and avoid electron/hole recombination.<sup>[365]</sup>

CdSe QDs show high absorption coefficients in the UV-Vis region, while their local absorption maxima vary by the size and shape of the particles.<sup>[369]</sup> Moreover, their surface can be modified by an exchange of surrounding ligands to enable them to generate a stable colloid solution in polar (e.g., mercaptopropionic acid - MPA) or nonpolar media (e.g., trioctylphosphine oxide - TOPO).<sup>[370]</sup>

Although their combination with noble metal catalysts such as platinum, palladium, or rhodium exhibits excellent catalytic performances, they are unsuitable for large-scale applications due to their high cost and limited abundance of the metals.<sup>[365,371]</sup> Therefore, synthetic molecular catalysts with earth-abundant elements like iron or nickel inspired by nature appear more promising, even though they are less stable.<sup>[365]</sup>

To combine bioinspired molecular catalysts and efficient energy transfer from semiconducting PSs, two previously reported carboxylic group bearing [FeFe] H<sub>2</sub>ase mimics with varying spacer lengths (**HM-LA**, [FeFe] H<sub>2</sub>ase mimic based on 6,8-dithiooctanoic acid; **HM-AA**, [FeFe] H<sub>2</sub>ase mimic based on 2-carboxy-1,3-propanedithiol; Figure 21A) were selected and synthesized using the facilitated procedure, that will be discussed in Chapter 4.4.<sup>[221,372,373]</sup>

Our approach was to utilize TOPO surface-functionalized CdSe QDs as thin films and attach HER catalysts via carboxylic groups to circumvent two significant drawbacks water-dispersible QDs and [FeFe] H<sub>2</sub>ase mimics suffer from. While the catalytic activity of [FeFe] H<sub>2</sub>ase mimics benefits from slightly acidic pH values (pH ≈ 4),<sup>[183]</sup> water-dispersible CdSe QDs lose their colloidal stability due to the protonation of their surface-functionalized mercaptocarboxylic acids that are required in a deprotonated state in aqueous dispersions. Additionally, these ligands bind to the surface with their thiol moiety, whose lone pairs can act as hole traps, impeding photocatalysis.<sup>[374,375]</sup> The close arrangement of PS-CAT is also advantageous for transferring the two indispensable electrons for HER.

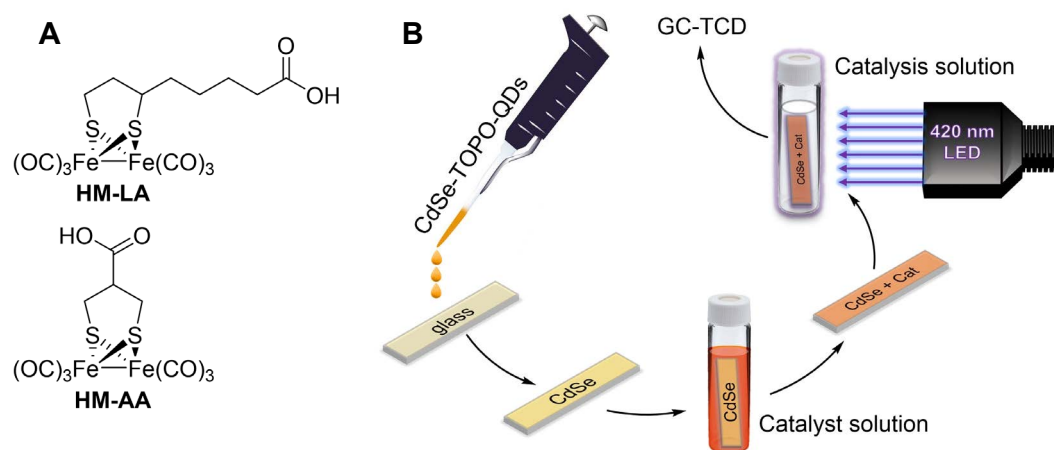


**Figure 21. A) Synthesized and investigated [FeFe] H<sub>2</sub>ase mimics; B) Schematic overview of the functionalization procedure, the photocatalytic HER experiment, and the H<sub>2</sub> determination via GC-TCD (SB-2, Figure 1).<sup>[376]</sup>**

Commonly, well-performing PS-CAT systems with semiconducting PSs follow indirect binding approaches via electrostatic interactions or grafting onto hydrophilic polymers. At the same time, the direct linkage remains challenging due

to the colloidal stability of the nanoparticles upon functionalization.<sup>[351-353,355,377,378]</sup>

Utilizing thin films circumvents the need for colloidal stability in solution and enables water-insoluble catalysts for their use in aqueous media. The functionalization of the glass substrates was carried out by the drop-casting technique to obtain homogeneous thin films on an average of four QD layers.<sup>[379]</sup> These films were treated with methanolic solutions ( $c \approx 2$  mmol/L) of the respective [FeFe] H<sub>2</sub>ase mimics **HM-LA** and **HM-AA** for 22 h. After rinsing with methanol, the substrates were transferred to the catalysis solution containing ascorbic acid as a sacrificial electron donor (SED) in a pH-adjusted (pH = 4.4) water/methanol mixture.

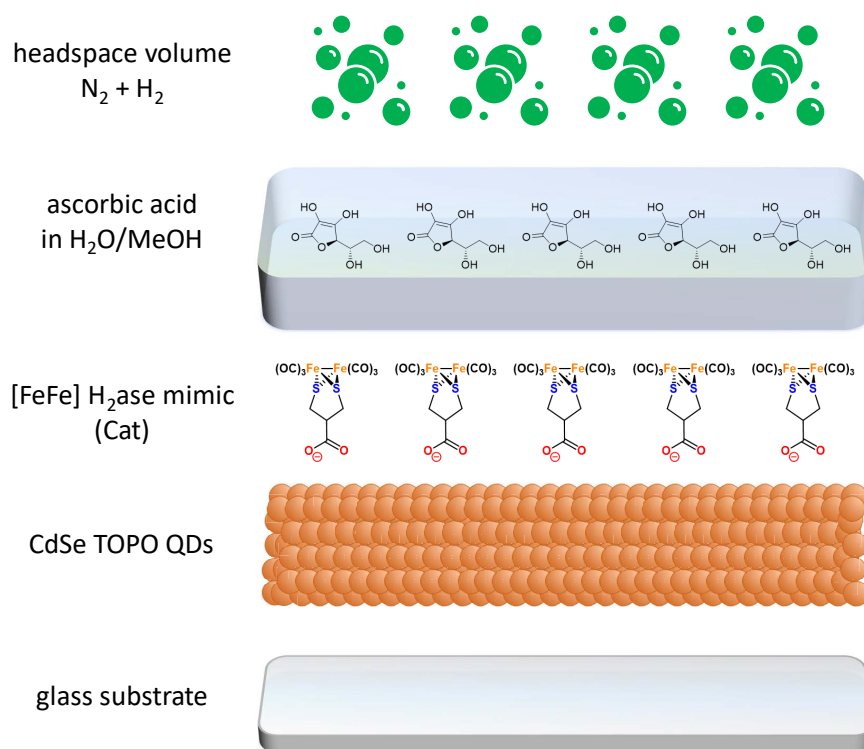


**Figure 22. Layered view of the experimental setup for catalytic HER of CdSe QDs with attached [FeFe] H<sub>2</sub>ase mimics.**

These vials were irradiated with a 420 nm LED ( $P = 8.5$  mW cm<sup>-2</sup>) for 21 h before the hydrogen content of an aliquot of the headspace volume was determined via gas chromatography with a thermal conductivity detector (GC-TCD) (Figure 21B). Figure 22 illustrates the different layers of the experimental setup for photocatalytic HER. The successful functionalization was monitored by IR, UV/Vis,

photoluminescence, and X-ray photoelectron spectroscopy (XPS) experiments. The performances of these PS-CAT systems differed firmly (0.6  $\mu\text{mol}$  for **HM-LA** and 2.8  $\mu\text{mol}$  for **HM-AA**) from the unfunctionalized QD films that already exhibited low photocatalytic activity under the same conditions (42 nmol  $\text{H}_2$ ) (Figure 23). While other homogenous systems show higher activities, it should be noted that these systems could not perform HER at all due to their hydrophobic and accumulating nature in aqueous solutions.<sup>[183]</sup>

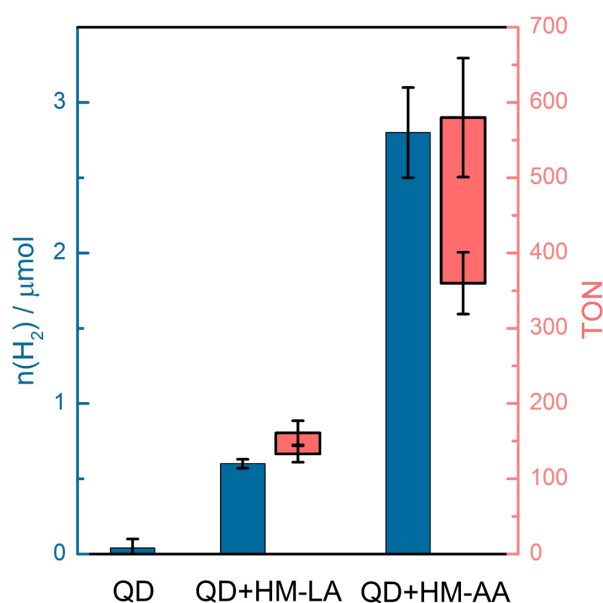


**Figure 23.** Measured amounts of evolved  $\text{H}_2$  and calculated TON values during the photocatalysis of the investigated PS-CAT systems and CdSe QDs films without [FeFe]  $\text{H}_2\text{ase}$  mimics (SB-2, Figure 1).<sup>[376]</sup>

To estimate the TON values of the HER experiments, micro-X-ray fluorescence spectrometry ( $\mu\text{XRF}$ ) was applied to determine the amounts of [FeFe]  $\text{H}_2\text{ase}$  complex functionalized on the films. These analyses revealed differing loadings in the ranges of 3.0–3.6  $\text{nmol cm}^{-2}$  for **HM-LA** and 3.8–6.1  $\text{nmol cm}^{-2}$  for **HM-AA**, suggesting that **HM-AA** was a higher affinity for substitution of TOPO ligands due to its more compact nature in opposite to **HM-LA** with its long alkyl chain that might interact with the surface ligands. In addition, **HM-AA** was predicted to contain a more acidic carboxylic group, resulting in a higher number of deprotonated species. Afterward, the TON numbers could be calculated to TON (**HM-LA**) = 133–161 and TON (**HM-AA**) = 361–579, revealing additional effects to the catalytic activity than the overall loading of [FeFe]  $\text{H}_2\text{ase}$  mimics. A short time

ago, the group of *Dukovic et al.* examined the influence of spacer length between CdS nanorods and an [FeFe] H<sub>2</sub>ase enzyme, showing a decrease of catalytic efficiency by 80% when the spacer was extended by 0.4 nm.<sup>[306]</sup> These findings were comparable to **HM-AA** and **HM-LA**, exhibiting a similar reduction of approximately 60%, suggesting that the longer alkyl chain interfered with the charge transfer rates and the charge separation for both consecutive electron-transfer steps essential for hydrogen generation.

To approximate the number of [FeFe] H<sub>2</sub>ase mimics connected to the surface of one CdSe QD, inductively coupled plasma optical emission spectrometry measurements (ICP-OES) were applied to estimate the CdSe film coverage to 0.2-0.3 nmol cm<sup>-2</sup>, resulting in a CAT/QD ratio of 20 for **HM-LA**/QD and 40 for **HM-AA**/QD. Assuming only the top QD layers were functionalized, their ratio might be higher, resulting in an almost complete surface ligand exchange (Figure 24).

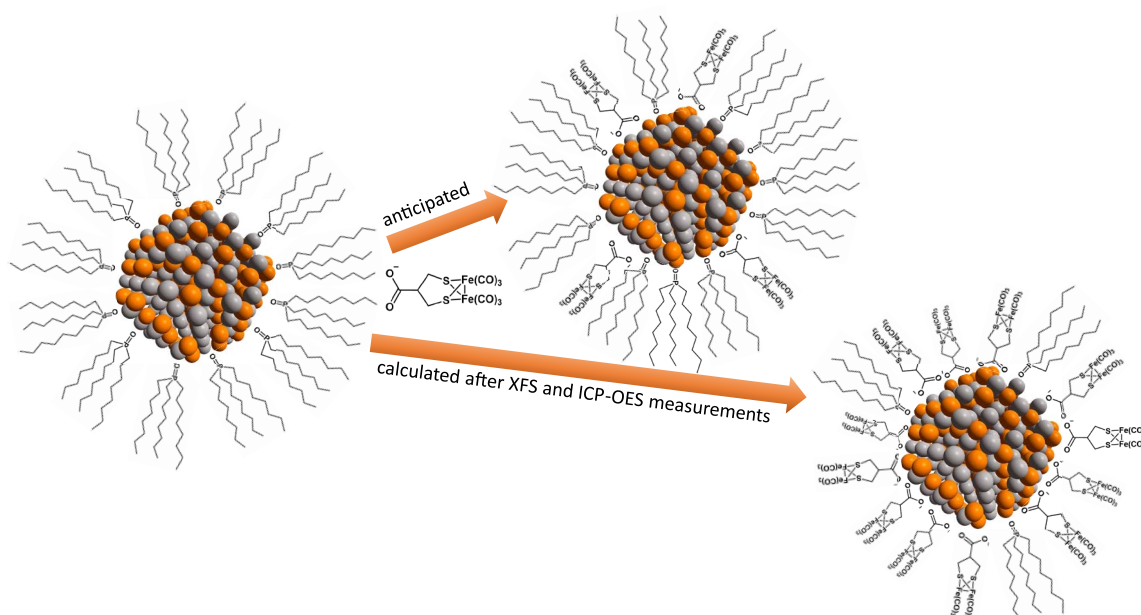


**Figure 24. Schematic representation of the anticipated vs. estimated CAT/QD ratios. The presentation of CdSe was adapted from *Xu et al.* using MERCURY software.<sup>[380]</sup>**

Due to this observation, the overall TON values were relatively low compared to other PS-CAT assemblies based on CdSe and [FeFe] H<sub>2</sub>ase mimics.<sup>[183]</sup> While the larger amount of catalysts reduced the TON during the calculation, the excessive loading of the catalyst adversely affected the HER by increasing losses from the recombination processes of separated charges.<sup>[90]</sup> Furthermore, the degradation

of the catalyst could be monitored by recording IR spectra after the photocatalysis (SB-2, Figure S12).

In summary, this proof-of-concept study demonstrated heterogeneous photocatalysis of immobilized CdSe QDs functionalized with two different [FeFe] H<sub>2</sub>ase mimics in an aqueous solution, showing decent activity comparable to similar previously reported examples in dispersion. Additionally, this approach can potentially recycle the toxic CdSe QDs after photocatalysis.

Nevertheless, follow-up experiments could optimize the conditions, e.g., reducing the CAT/QD ratio by diluting the [FeFe] H<sub>2</sub>ase mimic solutions during the functionalization step or the addition of a second similar strong carboxylic acid such as acetic acid or propionic acid that are also able to perform a ligand exchange reaction competing against the [FeFe] H<sub>2</sub>ase mimic to get a mix of ligands. Furthermore, parameters such as light source, irradiation wavelength, irradiation time, QD diameter, and surface functionalization could be examined.

### 4.3 SB-3 Synthesis of [FeFe] Hydrogenase Mimics with Lipoic acid and its Selenium Analogue as Anchor Groups

*Eur. J. Inorg. Chem.* **2023**, *26*, e202200684.

This approach utilized lipoic acid ester derivatives of [FeFe] H<sub>2</sub>ase mimics whose dithiolane or diselenolane anchoring groups showed great affinity to gold and platinum surfaces. Electrochemical conditions enabled the formation of stable self-assembled monolayers (SAMs), as previously reported by *Schöllhorn et al.*<sup>[381–384]</sup> Using this kind of chemically modified electrodes is beneficial to keep the electron pathways between the catalyst and the electron source as short as possible (see Chapter 3.3.2.2). Furthermore, the influence of sulfur exchange to selenium and substituting one carbonyl to triphenylphosphine (PPh<sub>3</sub>) to the redox behavior was investigated.

Therefore, four complexes varying in the distribution of sulfur and selenium at the iron cluster along with the lipoic acid anchor group were synthesized by Steglich esterification of 2-hydroxy-1,3-propanedithiolate and 2-hydroxy-1,3-propandicyanoselenolate [FeFe] H<sub>2</sub>ase mimics with lipoic or selenolipoic acid in the presence of *N,N'*-dicyclohexylcarbodiimide (DCC) and 4-dimethylaminopyridine (DMAP).<sup>[385]</sup> In addition, derivative **7** was obtained from complex **2** by ligand exchange reaction of one carbonyl to PPh<sub>3</sub> ligand in the presence of trimethylamine *N*-oxide dihydrate (Figure 25).<sup>[361]</sup>

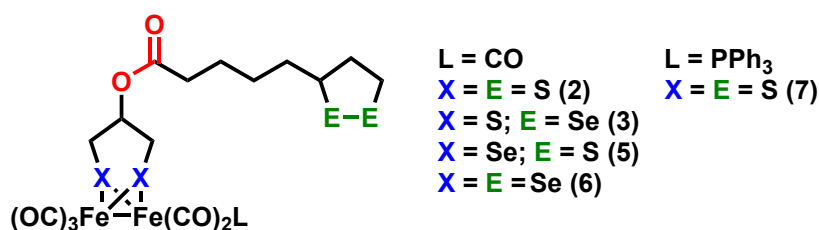


**Figure 25.** Synthesized derivatives of [FeFe] H<sub>2</sub>ase mimics containing lipoic or selenolipoic acid esters. Adapted from SB-3.<sup>[386]</sup>

First, CV experiments were carried out on complexes **2**, **3**, **5**, and **6** to determine the redox potentials (Figure 26). As expected, the reduction potentials for the first one-electron-reduction step differed only in a minor way between  $E_{pc}^1 = -1.57$  (**2**) and  $E_{pc}^1 = -1.51$  (**5**). Due to its weaker electron-donating nature, a small shift to

less negative potentials ( $\Delta E \approx 30\text{-}50\text{ mV}$ ) was gained by introducing selenium to the diiron hexacarbonyl cluster (complexes **5** and **6**).<sup>[246,250,251]</sup>

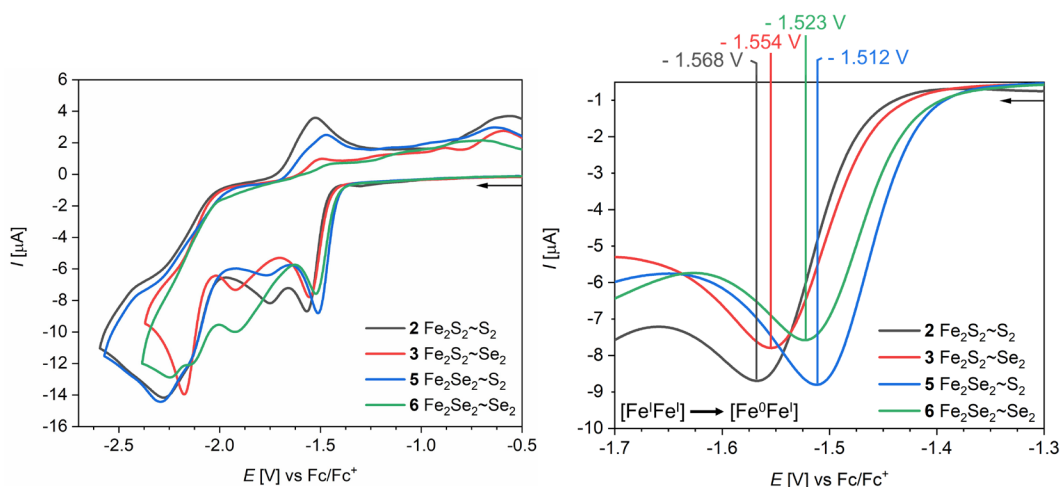


**Figure 26.** CV of compounds **2**, **3**, **5**, and **6** ( $c = 1\text{ mmol/L}$ ) in  $\text{N}_2$ -purged  $\text{ACN}/[\text{NBu}_4][\text{BF}_4]$  ( $0.1\text{ mol/L}$ ) at RT and the zoomed area of the first reduction event. The arrow indicates the scan direction. The potential  $E$  is given in V and referenced to the  $\text{Fc}/\text{Fc}^+$  couple (SB-3, Figures 2 and 3).<sup>[386]</sup>

Further reduction steps of the derivatives varied, as demonstrated in Table 3. While the lipoic acid analogs exhibited their second electron uptake around  $E_{\text{pc}}^2 = -1.75\text{ V}$ , the selenolipoic acid counterparts were reduced at  $E_{\text{pc}}^2 = -1.92\text{ V}$ . Additional reduction events occurred between  $E_{\text{pc}}^3 = -2.13\text{ V}$  and  $E_{\text{pc}}^4 = -2.29\text{ V}$ . However, assigning these to the iron centers or the (seleno)lipoic acid moieties that are also electrochemical active was not possible.<sup>[381,387]</sup> CV studies of the pure acids and precursor of  $[\text{FeFe}] \text{H}_2\text{ase}$  complexes involved clarity. The first reduction event of **2**, **3**, **5**, and **6** referred to the reduction of the iron centers ( $[\text{Fe}^{\text{I}}\text{Fe}^{\text{I}}]$  to  $[\text{Fe}^{\text{0}}\text{Fe}^{\text{I}}]$ ), while the second events were related to the (seleno)lipoic acid moieties (SB-3, Figure S5 and S6). Due to the overlap of the second reduction at the iron cores and the reduction of lipoic acid, the third reduction events of **2** and **5** were not attributable. In contrast, the third reduction of complexes **3** and **6** could be assigned to the reduction of the iron centers, as previously reported for their precursor of  $[\text{FeFe}] \text{H}_2\text{ase}$  complexes.<sup>[254,388]</sup>

Additional IR SEC experiments (see Chapter 4.1) were performed in an OTTLE cell (Supporting information (SI) SB-1 or SI SB-3) to confirm these findings.



**Table 3. Summary of the reduction potentials of complexes 2, 3, 5, 6, and 7. Potentials  $E$  are given in V, referenced to the  $\text{Fc}/\text{Fc}^+$  couple. Adapted from SB-3.<sup>[386]</sup>**

complex	$E_{\text{pc}}^1$ [V]	$E_{\text{pc}}^2$ [V]	$E_{\text{pc}}^3$ [V]	$E_{\text{pc}}^4$ [V]
<b>2</b> $\text{Fe}_2\text{S}_2\sim\text{S}_2$	-1.57	-1.75	-2.13 <sup>a</sup>	-2.28
<b>3</b> $\text{Fe}_2\text{S}_2\sim\text{Se}_2$	-1.55	-1.92	-2.18	
<b>5</b> $\text{Fe}_2\text{Se}_2\sim\text{S}_2$	-1.51	-1.77	-2.13 <sup>a</sup>	-2.29
<b>6</b> $\text{Fe}_2\text{Se}_2\sim\text{Se}_2$	-1.52	-1.92	-2.13	-2.25
<b>7</b> $\text{Fe}_2\text{S}_2\text{PPh}_3\sim\text{S}_2$	-1.75	-2.13 <sup>a</sup>	-2.30	

<sup>a</sup>This reduction event appeared as a weak shoulder.

The IR SEC of complex **2** exhibited observable bathochromic shifts of the terminal carbonyl signals by  $\Delta\tilde{\nu}(\text{CO}) \approx 55\text{-}103\text{ cm}^{-1}$  (Figure 27, left side, green to yellow), in good agreement with one-electron-reduction step at the iron center. However, the shape and ratio of the absorption bands changed, indicating follow-up structural rearrangements.<sup>[289,293,362,389]</sup> In contrast, the precursor complex did not show this behavior under the same conditions. Its IR SEC spectra were close to those observed for  $[\text{FeFe}] \text{H}_2\text{ase pdt}$  (SB-3, Figure S9).<sup>[283,361]</sup>

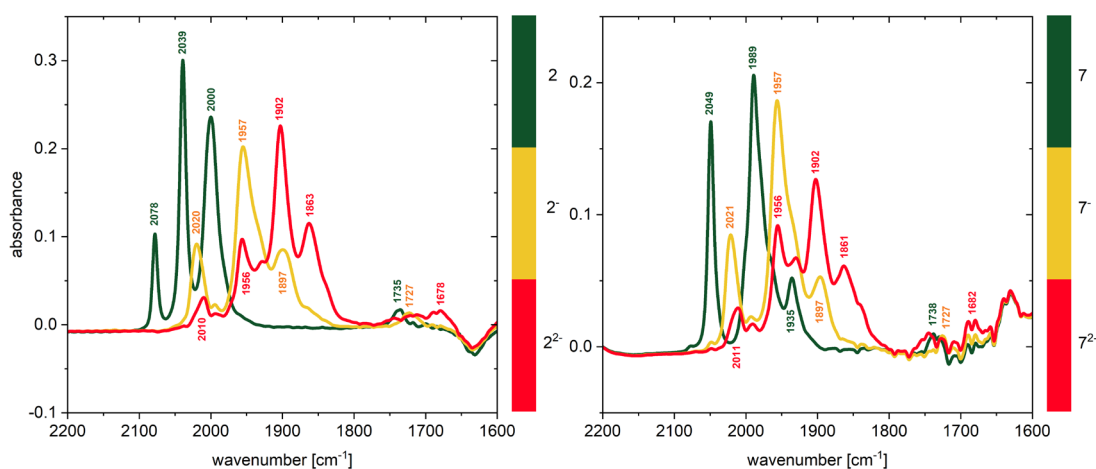


**Figure 27. IR SEC spectra of compounds 2 (left) and 7 (right) (ACN,  $c = 2\text{ mmol/L}$ ) at different oxidation states, recorded within an OTTLE cell (S-3, Figure S17).<sup>[386]</sup>**

A further shift of  $\Delta\tilde{\nu}(\text{CO}) \approx 33\text{-}66\text{ cm}^{-1}$  (Figure 27, left side, yellow to red) was observable for the second reduction event, which is assigned to the reduction of the iron center to form a double reduced state. Additional electron uptake led to the degradation of the compound. However, no further reduction event was detected between the first and second reduction events of the iron center during the IR SEC experiment, compared to the previous observation of the CV (SB-3,

Figure S8), indicating that the second reduction event  $E_{pc}^2$  might proceed during the first reduction of the SEC experiment due to its two magnitude slower scan rate.

Furthermore, the CV and IR SEC of compound **7** were investigated to get a closer look at the influence of the substituted  $PPh_3$  ligand known to increase the electron density at the iron center and impede electron uptake.<sup>[390–392]</sup> Therefore, the first reduction step of **7** was shifted to more negative potentials by  $\Delta E_{pc}^1 = 180$  mV in comparison to the first reduction of complex **2**, and the second reduction event, as shown for complex **2**, was not observable or overlapped by the first one (SB-3, Figure S7). The CV of complex **7** exhibited a second and third reduction step at similar potentials as complex **2**, its third and fourth one, which was uncommon for mono-substituted  $[FeFe]$  H<sub>2</sub>ase mimics.<sup>[392]</sup>

A closer look at the IR SEC spectra of complex **7** after the first reduction step revealed an almost identical pattern of the IR spectra compared to compound **2** after the first reduction, indicating similar electron density and complex geometry at the iron center (Figure 27). Additionally, the spectra after the second reduction assigned to the iron center were comparable. One explanation would be the elimination of  $PPh_3$  or CO, leading to the same mono-reduced species. Furthermore, weak coordination of the lipoic acid moiety via the lone pair of the disulfide group to the vacant site of the diiron pentacarbonyl cluster could explain the IR pattern that showed significant similarity with previously reported  $[FeFe]$  H<sub>2</sub>ase mimics containing a coordinating thioether moiety (Figure 28).<sup>[220,285,393]</sup> The varying oxidation states could explain the difference in wave number values.

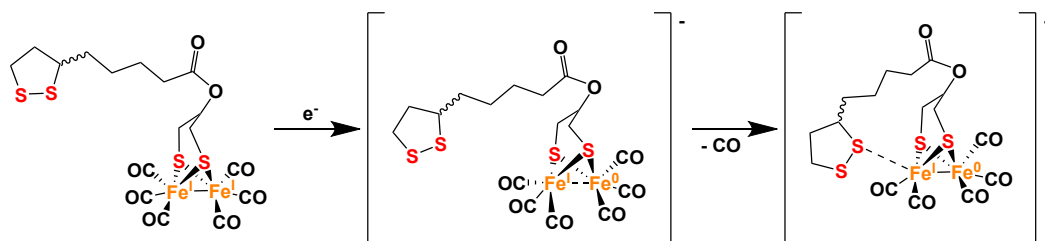


**Figure 28.** Possible mechanism of the first reduction of complex **2** and a feasible follow-up reaction.

Afterward, the formation and electrochemical behavior of SAMs of complexes **2** and **6** on gold and platinum electrodes were investigated. While both complexes could form SAMs on both surfaces, the platinum was suitable to create the more stable ones, confirmed by CV experiments. Unfortunately, going to more negative potential than  $E = -1.8$  V (vs. SCE) led to the SAMs' desorption, so they could not be tested for HER under similar conditions.

Nevertheless, complexes **2**, **3**, **5**, and **6** exhibited catalytic activity, as confirmed by CV experiments in the presence of various amounts of AcOH. The catalytic efficiency (*C.E.*) was determined by the definition of *Felton et al.* to be 0.47 (**5**), 0.58 (**3**), and 0.66 (**2** and **6**) and declared as medium scope of efficiency (0.25-0.75).<sup>[188]</sup>

#### 4.4 SB-4 NMP makes the Difference – Facilitated Synthesis of [FeFe] Hydrogenase Mimics

*Dalton Trans.* **2023**, *52*, 7421.

Chapter 3.3.1 describes versatile, well-established ways to synthesize [FeFe] H<sub>2</sub>ase model complexes with various functional moieties. This chapter indicates an update of a well-known procedure of using thiol or disulfide precursors to react with Fe<sub>3</sub>(CO)<sub>12</sub> in the presence of aprotic polar co-solvents such as NMP, dimethylacetamide (DMA), tetramethylurea (TMU), or  $\gamma$ -butyrolactone (GBL)(Figure 29). These co-solvents are supposed to stabilize charged intermediates during the formation of [FeFe] H<sub>2</sub>ase mimics.<sup>[157,210–212]</sup>

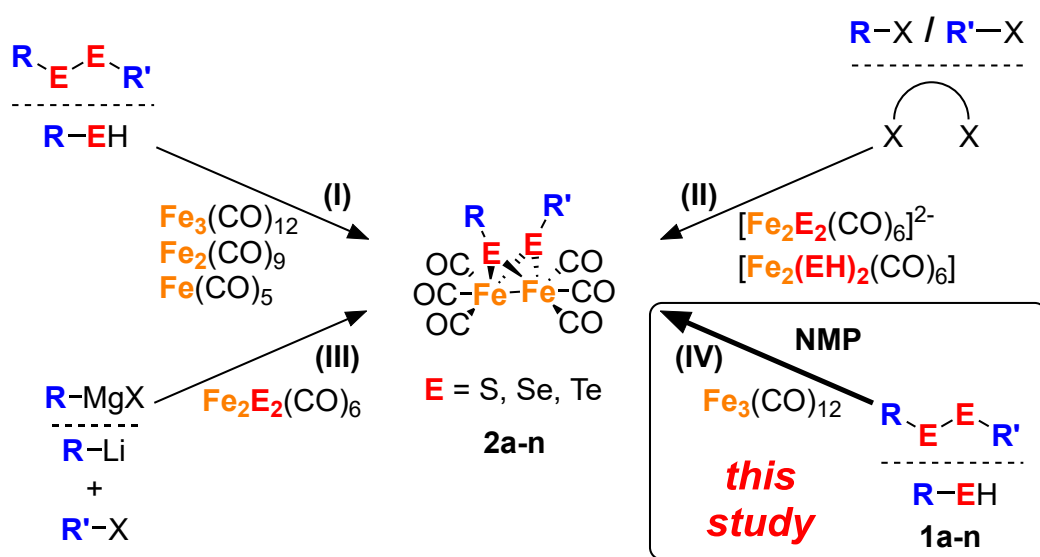
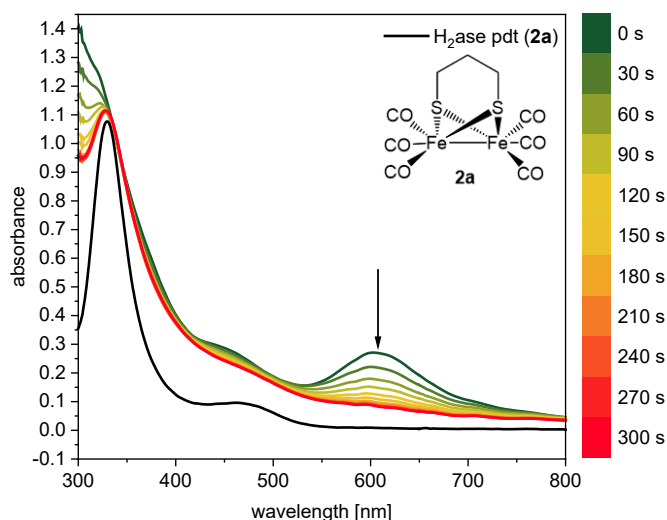


Figure 29. Well-established reaction pathways towards [FeFe] H<sub>2</sub>ase mimics (I-III) and the new approach (IV).<sup>[372]</sup>

The addition of this kind of co-solvent led to a decrease in both the reaction temperature and time, as demonstrated by versatile examples. At the same time, the yield of some products increased compared to the previously published results (SB-4, Table 1).

In this modified procedure, the precursor was dissolved in a toluene/NMP (10:1) mixture heated to 50 °C before adding Fe<sub>3</sub>(CO)<sub>12</sub> in one portion. The reaction proceeded until the dark green solution turned red, and the crude product was purified by column chromatography, yielding the target complex as red solids.



**Figure 30.** Time-resolved UV-Vis spectra during the reaction of **1a** with equimolar amounts of  $\text{Fe}_3(\text{CO})_{12}$  (toluene/NMP (10:1),  $c = 2.2 \times 10^{-4} \text{ M}$ ) at  $50.9^\circ \text{C}$ .<sup>[372]</sup>

To investigate the influence of NMP on the reaction kinetics (Table 4), UV-Vis monitoring was applied at various temperatures and NMP concentrations for the reaction of the precursor pdt (**1a**, SB-4, Table 1) and  $\text{Fe}_3(\text{CO})_{12}$  in a tempered glass cuvette. The absorption band at  $\lambda = 606 \text{ nm}$ , attributed to the ligand-field excitation of  $\text{Fe}_3(\text{CO})_{12}$ , was selected for monitoring since it is traceable and distinctive.<sup>[394]</sup>

As illustrated in Figure 30, the selected absorption band of  $\text{Fe}_3(\text{CO})_{12}$  declined within 300 seconds at  $50.9^\circ \text{C}$ . The calculation of the differential spectra showed the changes during the reaction (SB-4, Figure S6). However, due to the product's (**2a**) lack of distinctive absorption bands, its formation could not be monitored.

Therefore, another chromophore containing ligand (**1n**,  $\lambda_{\text{max}} = 463 \text{ nm}$ , SB-4, Table 1) was chosen for further experiments. The respective [FeFe]  $\text{H}_2\text{ase}$  mimic **2n** ( $\lambda_{\text{max}} = 375 \text{ nm}$ ) exhibited absorption bands in the visible spectral region with only minor interferences with the other species in such a way that it was possible to follow the formation of the product bands in the differential spectra (Figure 31).

Table 4. Rate constants in toluene for the decline of  $\text{Fe}_3(\text{CO})_{12}$  (606 nm,  $c = 2.2 \times 10^{-4}$  M) during the reaction with ligand **1n** ( $\text{Fe}_3(\text{CO})_{12}/\mathbf{1n}$  (1:10)), and NMP ( $\text{Fe}_3(\text{CO})_{12}/\text{NMP}$  (1:4300)) without any ligand at varying temperatures. Adapted from SB-4.<sup>[372]</sup>

Ligand	$T$ [°C]	$T_{\text{abs}}$ [K]	$k_{\text{obs}}$ ( $\text{Fe}_3(\text{CO})_{12}$ ) [ $\text{s}^{-1}$ ]
<b>1n</b>	49.0	322.2	$1.2 \times 10^{-3}$
<b>1n</b>	57.0	330.2	$2.8 \times 10^{-3}$
<b>1n</b>	64.0	337.1	$5.4 \times 10^{-3}$
<b>1n</b>	72.0	345.1	$1.1 \times 10^{-2}$
<b>1n<sup>a</sup></b>	49.0	322.2	$1.6 \times 10^{-4}$
<b>1n<sup>a</sup></b>	57.0	330.2	$3.2 \times 10^{-4}$
<b>1n<sup>a</sup></b>	64.0	337.1	$7.5 \times 10^{-4}$
<b>1n<sup>a</sup></b>	72.0	345.1	$1.8 \times 10^{-3}$
<b>NMP<sup>b</sup></b>	45.0	318.15	$4.7 \times 10^{-3}$
<b>NMP<sup>b</sup></b>	53.2	326.35	$9.0 \times 10^{-3}$
<b>NMP<sup>b</sup></b>	60.4	333.55	$9.3 \times 10^{-3}$
<b>NMP<sup>b</sup></b>	68.9	342.05	$2.1 \times 10^{-2}$
$\text{Fe}_3(\text{CO})_{12}^{\text{a,b}}$	43.2	316.35	$3.7 \times 10^{-5}$
$\text{Fe}_3(\text{CO})_{12}^{\text{a,b}}$	53.2	326.35	$1.1 \times 10^{-4}$
$\text{Fe}_3(\text{CO})_{12}^{\text{a,b}}$	62.6	335.75	$1.1 \times 10^{-4}$
$\text{Fe}_3(\text{CO})_{12}^{\text{a,b}}$	71.1	344.25	$2.6 \times 10^{-4}$
$\text{Fe}_3(\text{CO})_{12}^{\text{a,b}}$	75.1	348.25	$3.2 \times 10^{-4}$

<sup>a</sup>without NMP, <sup>b</sup> without any ligand

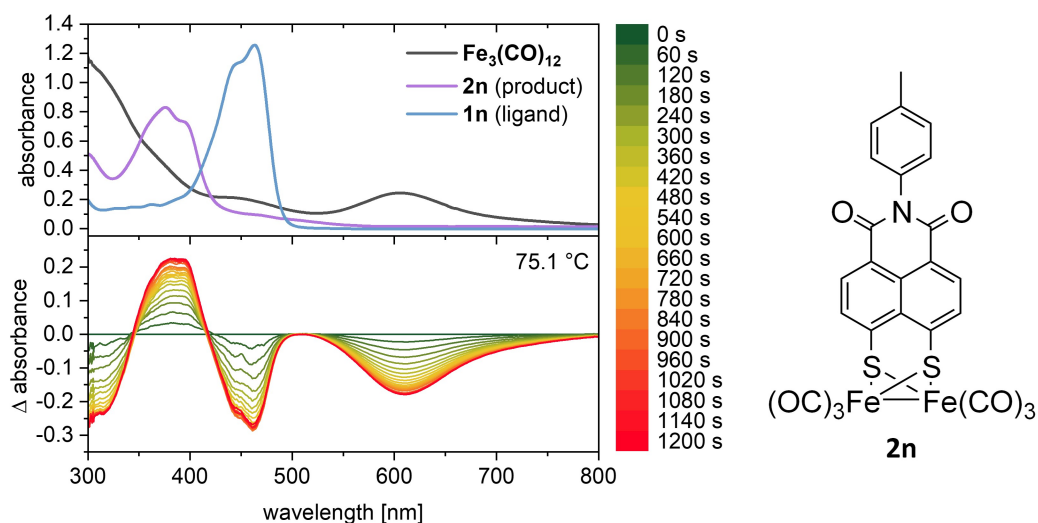


Figure 31. UV-Vis spectra of the starting materials and the desired product (top); time-resolved differential UV-Vis spectra during the reaction of **1n** with equimolar amounts of  $\text{Fe}_3(\text{CO})_{12}$  (toluene/NMP (10:1),  $c = 2.2 \times 10^{-4}$  M) at 75.1 °C (bottom). The  $\Delta$  absorbance spectra were calculated by subtracting the initial spectrum ( $t = 0$  s). Adapted from SB-4.<sup>[372]</sup>

To measure time- and temperature-dependent kinetics under pseudo-first-order conditions, all experiments were carried out with a ten-fold excess of precursor **1n** and NMP in a vast excess ( $\approx 5000$  equivalents) and without NMP. The resulting data agreed well with pseudo-first-order reaction kinetics (SB-4, Figure S8). They revealed an increase in the reaction rate by approximately one magnitude when NMP was added to the reaction mixture (Table 4). However, the plotted decrease of **1n** and the formation of **2n** occurred in non-linear shapes, revealing a higher-order reaction kinetics (SB-4, Figure S9). Additionally, Arrhenius plots were utilized to calculate the activation energies for both circumstances to  $E_a = 91.4 \text{ kJ mol}^{-1}$  and  $E_a = 99.5 \text{ kJ mol}^{-1}$  in the presence and absence of NMP, respectively.

Analysis of the concentration-dependence of NMP towards the reaction rate of **1a** and equimolar amounts of  $\text{Fe}_3(\text{CO})_{12}$  was performed with various toluene/NMP ratios at  $50.9 \text{ }^\circ\text{C}$ , revealing a strong influence on the rate constant (SB-4, Figure S11). Since adding up to a thousand equivalents of NMP had only a minor impact, a catalytic effect of the NMP was excluded. It was plausible that the increase in the polarity of the solvent mixture stabilized the formation of charged intermediates.<sup>[157]</sup>

IR spectroscopic experiments were conducted to check if it was possible to observe the intermediates of the reaction. Therefore, the reaction of **1a** and  $\text{Fe}_3(\text{CO})_{12}$  in the presence of NMP was monitored in an OTTLE cell over 4500 seconds at RT (Figure 32). The slow transformation of  $\text{Fe}_3(\text{CO})_{12}$  ( $\tilde{\nu} = 2047 \text{ cm}^{-1}$ , and  $2023 \text{ cm}^{-1}$ ) to complex **2a**, identifiable from the three main bands at  $\tilde{\nu} = 2072 \text{ cm}^{-1}$ ,  $2032 \text{ cm}^{-1}$ , and  $1994 \text{ cm}^{-1}$  was followed, while the appearance of another unidentified species was observable. This observation revealed whether NMP could react with  $\text{Fe}_3(\text{CO})_{12}$  without any precursor molecule.

Therefore, this reaction was first conducted in a Schlenk flask under inert conditions, resulting in the fast formation of a purple, oxygen-sensitive product (SB-4, Figure S12) that was analyzed by mass spectrometry (MS), IR, UV-Vis, and nuclear magnetic resonance spectroscopy (NMR) to be a derivative of  $\text{Fe}_3(\text{CO})_{12}$ , namely  $\text{Fe}_3(\text{CO})_{11}\text{NMP}$ . A comparison of the IR spectra confirmed its formation during the experiment in the presence of **1a** (Figure 32).

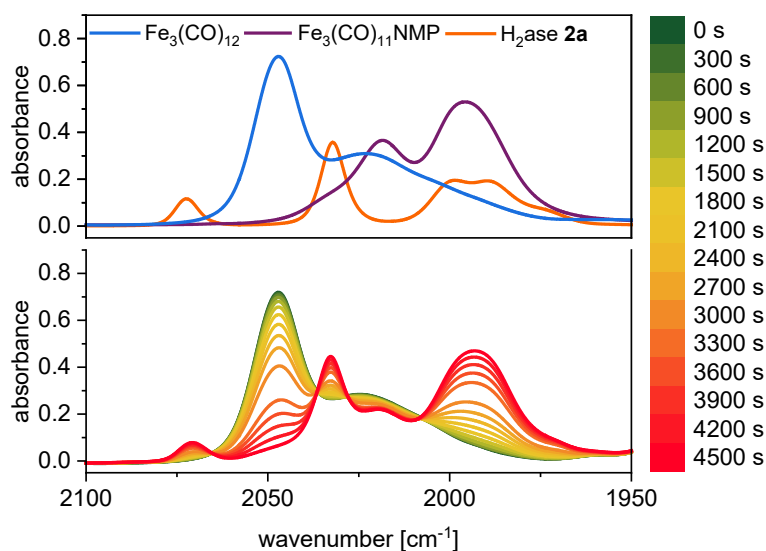


**Figure 32.** IR spectra of  $\text{Fe}_3(\text{CO})_{12}$ ,  $\text{Fe}_3(\text{CO})_{11}\text{NMP}$  and **2a** (top); time-resolved IR spectra during the reaction of **1a** with equimolar amounts of  $\text{Fe}_3(\text{CO})_{12}$  (toluene/NMP (10:1),  $c = 2.2 \times 10^{-3}$  M) at  $24.3^\circ\text{C}$  (bottom).<sup>[372]</sup>

Follow-up quantum chemical studies were performed to investigate three different binding modes of NMP to the iron carbonyl cluster, proposing structure **B** as the most probable isomer.

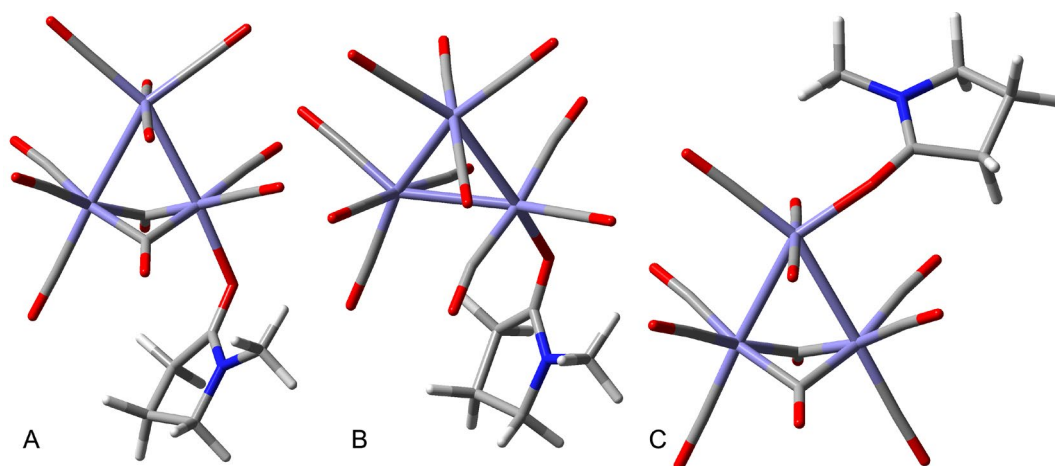


**Figure 33.** Simulated isomeric structures of  $\text{Fe}_3(\text{CO})_{11}\text{NMP}$ .

This assumption was supported by the IR spectra of  $\text{Fe}_3(\text{CO})_{12}$  and  $\text{Fe}_3(\text{CO})_{11}\text{NMP}$  in a solid state, which indicated the absence of bridging carbonyl bands between  $\tilde{\nu}(\mu\text{-CO}) = 1800\text{ cm}^{-1}$  and  $1900\text{ cm}^{-1}$  (SB-4, Figure S13). This loss of a significant structural feature might cause a high sensitivity toward oxygen, which led to its decomposition. Furthermore, reactivity towards thiol compounds such as **1a** was not observed. This finding excluded  $\text{Fe}_3(\text{CO})_{11}\text{NMP}$  to be an intermediate.



Additional UV-Vis kinetic studies revealed a higher rate constant for forming  $\text{Fe}_3(\text{CO})_{11}\text{NMP}$  in the absence of a thiol precursor than the reaction in its presence (Table 4), leading to the question: Why was the formation of **2a** favored?

A possible explanation would be that the formation of a potentially charged intermediate of  $\text{Fe}_3(\text{CO})_{12}$  and the thiol or disulfide might be faster ( $k_{a1}$ ) than the reaction with NMP ( $k_{b1}$ ). However, the follow-up step(s) for finalizing the [FeFe] H<sub>2</sub>ase mimic might be rate-limiting ( $k_{a2}$ ) so that the overall reaction is slower than the reaction of  $\text{Fe}_3(\text{CO})_{12}$  and NMP as observed by the UV-Vis kinetic studies (Figure 34). Follow-up studies might be able to resolve this problem.

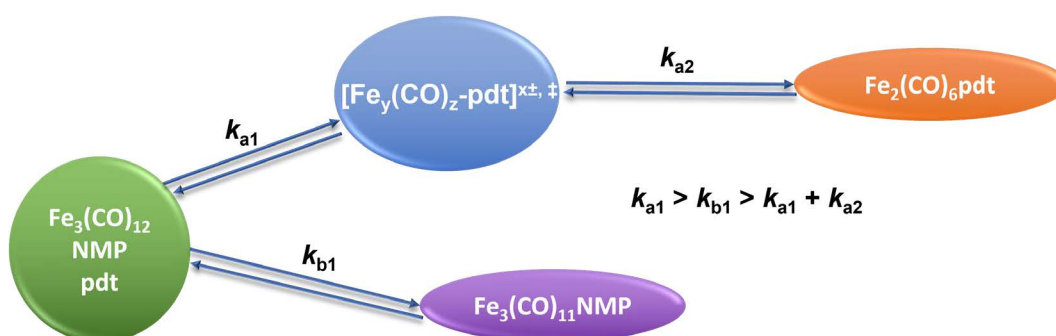


**Figure 34. A possible mechanism for the favored formation of [FeFe] H<sub>2</sub>ase mimics.**

Finally, another aprotic polar co-solvent, such as TMU, GBL, and DMA, was probed to see if they behave in the same way as NMP. As expected, they act the same since they facilitated the formation of [FeFe] H<sub>2</sub>ase mimics from precursor thiols or disulfides with  $\text{Fe}_3(\text{CO})_{12}$  at comparable rates. Furthermore, they react with  $\text{Fe}_3(\text{CO})_{12}$  to form oxygen-sensitive purple complexes exhibiting similar IR spectra to  $\text{Fe}_3(\text{CO})_{11}\text{NMP}$ .

This modified procedure of the synthesis of diiron hexacarbonyl complexes mediated by sulfur, selenium, or tellurium- ligands, considered [FeFe]-hydrogenase mimics, was submitted to the German patent office (Munich) and proved to be new and worth publishing as a patent application (SB-5).

## 5. Summary

This thesis sheds light on new insights and developments in the promising research field of [FeFe] H<sub>2</sub>ase mimics, in which each subtopic focuses on a different aspect. After synthesizing and characterizing diiron complexes that mimic the H-cluster of natural [FeFe] H<sub>2</sub>ase enzymes, follow-up functionalization was conducted or intended to show the versatile strategies of hydrogen evolution with its prospects, chances, and current limitations. One of the drawbacks of these synthetic approaches was the lack of stability and sensitivity towards side reactions during the HER under electrocatalytic and photocatalytic conditions.

In the first described publication [SB-1], a new derivative of NMI-based [FeFe] H<sub>2</sub>ase mimics featuring a propargyl group at the imide functionality was synthesized utilizing the enhanced procedure of [SB-4] and characterized by versatile techniques such as crystal structure analysis, CV, IR and UV-Vis SEC, EPR spectroscopy and quantum chemical simulations (Figure 35).

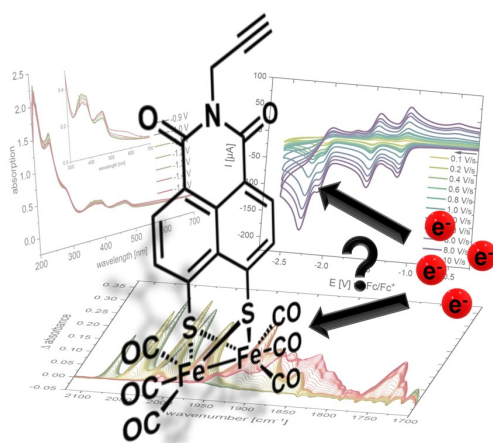


**Figure 35.** Table of content (TOC) artwork of [SB-1]. It illustrates the central issue of the paper regarding the nature of electrochemical reduction of the NMI-based [FeFe] H<sub>2</sub>ase mimic **4**.<sup>[361]</sup>

The most significant result of this publication confirmed that the findings postulated by *Reek et al.* regarding the first reduction step of such complexes belong to the NMI moiety and not to the iron cores.<sup>[286]</sup> The second reduction step has not been analyzed so far. Therefore, further spectroscopical analysis and DFT simulations were performed to clarify where the subsequent electron uptake was localized and whether a doubly reduced singlet or a doubly reduced triplet was the more feasible species.

Due to the behavior of **4** in the IR SEC, structural rearrangements were indicated by a change of shape of the absorption bands and a significant bathochromic shift of the absorption bands that implied an electron uptake at the iron center. With the support of DFT calculations, the second reduction step was supposed to lead to a doubly reduced triplet state with one electron at the NMI and iron core, respectively. Further reduction steps implied the degradation of the complex.

After these findings, it was confirmed that this kind of [FeFe] H<sub>2</sub>ase mimic could still perform HER under electrocatalytic conditions in the presence of acids such as AcOH or TFA. However, DFT calculations clarified that the complex is not catalytically active toward HER under photocatalytic conditions due to the electron-harvesting properties of the NMI moiety.

**[SB-2].** In this article, two already known [FeFe] H<sub>2</sub>ase mimics bearing carboxylic acid moieties with varying linker lengths were synthesized and utilized as catalysts in a PS-CAT ensemble with CdSe QDs as the PS to generate hydrogen in a photocatalytic manner (Figure 36). Therefore, the CdSe QDs were coated on a glass substrate and treated with a methanol solution of the respective complexes (**HM-LA**, [FeFe] H<sub>2</sub>ase mimic based on 6,8-dithiooctanoic acid; **HM-AA**, [FeFe] H<sub>2</sub>ase mimic based on 2-carboxy-1,3-propanedithiol; Figure 36C) to form surface-functionalized PS-CAT films, that were irradiated by a 420 nm LED in a pH-adjusted aqueous solution in a gas-tight vial in the presence of ascorbic acid as SED and proton source. The successful functionalization was monitored by IR, UV/Vis, photoluminescence, and XPS experiments.

Finally, the hydrogen content of the headspace volume was measured by GC-TCD, and the TON values were calculated by using the iron content of the films determined by  $\mu$ XRF and determining the amounts of [FeFe] H<sub>2</sub>ase mimics (Figure 36B and 36D). While the most extended spacer group of **HM-LA** generated TON values between 133-161, the short spacer (**HM-AA**) yielded higher TONs in the range of 361-579. These results agreed well with previous findings of *Dukovic et al.*, who examined the influence of spacer length between CdS nanorods and an [FeFe] H<sub>2</sub>ase enzymes, showing a decrease of catalytic efficiency with increasing spacer length.<sup>[306]</sup>

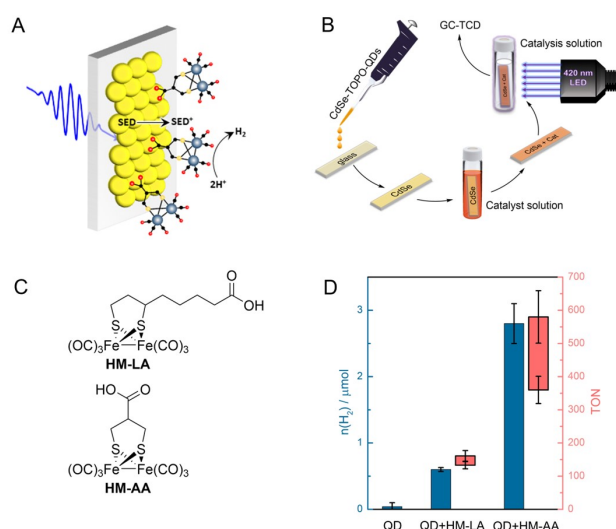


**Figure 36.** (A) Schematic illustration of QDs immobilized in a thin-film architecture on a substrate with covalently linked [FeFe] hydrogenase mimics. (B) Schematic overview of the functionalization procedure. (C) Molecular structures of the two [FeFe] hydrogenase mimics with varying linker lengths were under investigation. (D) HER performance of pristine and functionalized CdSe films. Error bars indicate a standard deviation of at least five separate measurements.<sup>[376]</sup>

Since these absolute numbers were relatively low compared to other PS-CAT assemblies based on CdSe and [FeFe] H<sub>2</sub>ase mimics, the high CAT/QD ratio (20 for **HM-LA**/QD and 40 for **HM-AA**/QD) and the instability of the complexes during the irradiation are considered as an explanation.<sup>[183]</sup>

**[SB-3].** This work investigated the influences of an additional dithiolane moiety in the form of a functionalized liponic acid substituent to [FeFe] H<sub>2</sub>ase mimics, related to the prototype complex H<sub>2</sub>ase pdt, regarding electrochemistry and their ability to form SAMs on gold or platinum electrode surfaces. Applying the formation of SAMs was aimed at reducing electron pathways from the electrode to the catalyst. To demonstrate the impacts on their electrochemical behaviors, the sulfur atoms were partially or entirely substituted by selenium, giving four derivatives with different constitutions and one derivative with a PPh<sub>3</sub> coordinating ligand.

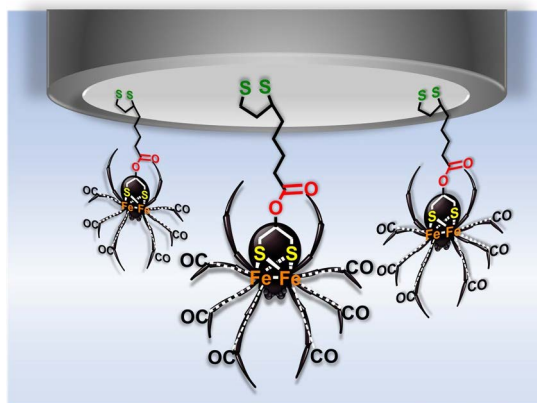


**Figure 37. TOC artwork of [SB-3]. It illustrates the central issue of the paper regarding the formation of SAMs with lipoic acid ester derivatives and their electrochemical properties.<sup>[386]</sup>**

Therefore, the four diiron hexacarbonyl complexes were synthesized by Steglich esterification of 2-hydroxy-1,3-propanedithiolate and 2-hydroxy-1,3-propanediselenolate [FeFe] H<sub>2</sub>ase mimics with lipoic or selenolipoic acid and the PPh<sub>3</sub> derivative by ligand exchange reaction (Figure 25). Afterward, they were characterized with NMR, MS, elemental analysis, and CV in the presence and absence of AcOH and IR SEC, revealing varying electrochemical behavior. While the selenolipoic acid ester complexes provided expected CV data that exhibited spectra like a combination of their precursor molecules, the lipoic acid ester compounds showed interactions between the lipoic acid moiety and the diiron cluster.

Further IR SEC investigations revealed the formation of the same species of **2** and **7** after the first reduction step, including eliminating a CO or PPh<sub>3</sub> ligand, respectively. A possible mechanism was conceived after the paper's release and was not confirmed by DFT calculations or additional experiments (Figure 28).

Afterward, the ability of complexes **2** and **6** to form SAMs on gold and platinum electrodes was investigated, leading to stable SAMs of **2** on a platinum surface. However, they could not perform HER due to the desorption of the SAMs under the catalysis conditions.

The fourth paper [SB-4] included in this thesis introduced an enhancement of a well-known synthesis route for diiron hexacarbonyl complexes related to the active center of [FeFe] H<sub>2</sub>ase enzymes by adding an aprotic polar co-solvent such

as NMP, DMA, TMU, or GBL to the reaction mixture of  $\text{Fe}_3(\text{CO})_{12}$  and a thiol or disulfide precursor. This modification led to a reduction of the reaction temperature and time and an enhancement of the yield of some products, as demonstrated by versatile examples. (Figure 38).

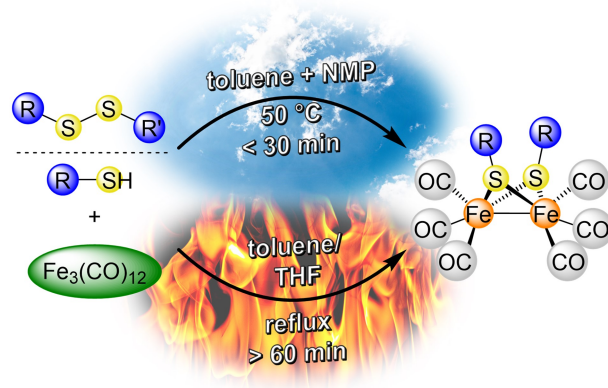


**Figure 38.** TOC artwork of [SB-4]. It illustrates the central issue of the paper regarding the facilitated formation of [FeFe] H<sub>2</sub>ase mimics.<sup>[372]</sup>

The influence on the kinetic of the reaction in the presence of these co-solvents was investigated by UV-Vis spectroscopy with ligand **1n** and NMP, revealing an increase of the reaction rate by approximately one magnitude compared to the same reaction without NMP. In addition, the concentration-dependence of NMP towards the reaction rate of **1a** and equimolar amounts of  $\text{Fe}_3(\text{CO})_{12}$  showed that NMP was not acting like a catalyst. It was supposed that NMP can stabilize charged intermediates during the formation of [FeFe] H<sub>2</sub>ase mimics.<sup>[157]</sup> Furthermore, IR monitored reactions of **1a** with  $\text{Fe}_3(\text{CO})_{12}$  in the presence of NMP, exposing the formation of a side product assigned to be  $\text{Fe}_3(\text{CO})_{11}\text{NMP}$ . Follow-up reactions of this compound with excess amounts of **1a** were not observed. This finding indicates that  $\text{Fe}_3(\text{CO})_{11}\text{NMP}$  is not considered as an intermediate. Furthermore, the use of TMU, DMA, and GBL as aprotic polar co-solvents results in similar findings to that of NMP.

## 6. Zusammenfassung

Diese Arbeit liefert neue Erkenntnisse auf dem aktuellen Forschungsgebiet der [FeFe] H<sub>2</sub>ase Modellkomplexe, wobei jeder Artikel seinen eigenen Schwerpunkt hat. Nach der Synthese und Charakterisierung der Dieisen-Komplexe, die den H-Cluster natürlicher [FeFe] H<sub>2</sub>ase-Enzyme nachahmen, wurde eine Funktionalisierung durchgeführt oder zumindest beabsichtigt, um vielseitige Möglichkeiten der Wasserstoffentwicklung zu realisieren und deren Chancen, aber auch Grenzen zu zeigen. Eines der größten Probleme bei dieser Art von Komplexen war deren mangelnde Stabilität während der Wasserstofferzeugung unter elektrokatalytischen bzw. photokatalytischen Bedingungen.

**[SB-1]** In der ersten Veröffentlichung wurde ein neues Derivat von NMI-basierten [FeFe] H<sub>2</sub>ase Modellkomplexen mit einer Propargyl-Gruppe an der Imid-Funktionalität synthetisiert und durch vielseitige Analyseverfahren wie Kristallstrukturanalyse, CV, IR- und UV-Vis-SEC und EPR-Spektroskopie charakterisiert. (Abb. 1).

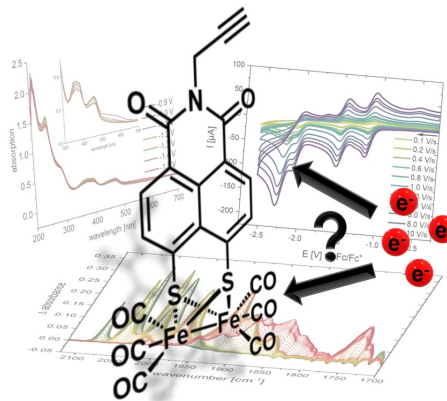


**Abbildung 1.** TOC-Grafik von [SB-1] zur Illustration des Hauptthemas der ersten Veröffentlichung über das elektrochemische Verhalten von NMI-basierten [FeFe] H<sub>2</sub>ase Modellkomplexen.<sup>[361]</sup>

Zunächst wurden die Erkenntnisse von *Reek et al.* bezüglich des ersten Reduktionsschritts an der NMI-Einheit bei dieser Art von Komplexen bestätigt.<sup>[286]</sup> Der zweite Reduktionsschritt wurde bisher nicht charakterisiert, daher wurden weitere spektroskopische Untersuchungen sowie DFT-Simulationen durchgeführt, um herauszufinden, wo dieser lokalisiert war und ob ein doppelt reduziertes

Singulett oder ein doppelt reduziertes Triplett die wahrscheinlichere gebildete Spezies war.

Die Ergebnisse der IR-SEC Messungen an Komplex **4** weisen auf Umorganisierung in der Komplexstruktur hin. Zudem deutete die Größe der bathochromen Verschiebung der Absorptionsbänder auf eine Reduktion am Eisenzentrum hin. Mit Hilfe von DFT-Berechnungen wurde angenommen, dass der zweite Reduktionsschritt zu einem doppelt reduzierten Triplettzustand führte, bei dem sich jeweils ein Elektron am NMI-Liganden und eines am Eisen aufhalten. Weitere Reduktionsschritte führten zum Abbau des Komplexes.

Zudem wurde gezeigt, dass diese Art von [FeFe] H<sub>2</sub>ase Modellkomplexen immer noch in der Lage war, die HER unter elektrokatalytischen Bedingungen in Gegenwart von Säuren wie AcOH oder TFA zu katalysieren. Unter photokatalytischen Bedingungen war dies nicht möglich, wie DFT-Berechnungen zeigten.

**[SB-2]** In diesem Artikel wurden zwei [FeFe] H<sub>2</sub>ase Modellkomplexe mit Carboxylato-Liganden mit unterschiedlicher Kettenlänge synthetisiert und als Katalysatoren in einem PS-CAT-Ensemble mit CdSe-QDs als PS zur photokatalytischen Wasserstofferzeugung eingesetzt (Abb.2). Dafür wurden die CdSe-QDs auf ein Glassubstrat beschichtet und mit einer Methanollösung der jeweiligen Komplexe (**HM-LA**, [FeFe] H<sub>2</sub>ase-Mimik basierend auf Liponsäure; **HM-AA**, [FeFe] H<sub>2</sub>ase-Mimik basierend auf Asparaginsäure; Abb. 2C) behandelt, um oberflächenfunktionalisierte PS-CAT-Filme zu bilden. Diese wurden in einem gasdichten Probegefäß in einer pH-gepufferten wässrigen Lösung unter Bestrahlung mit einer 420 nm LED in Anwesenheit von Ascorbinsäure belichtet. Die erfolgreiche Funktionalisierung wurde mittels IR-, UV/Vis-, Photolumineszenz- und XPS-Experimenten überwacht. Anschließend wurde der Wasserstoffgehalt der Gasphase mittels GC-TCD gemessen und die TON-Werte unter Verwendung des Eisengehalts der Filme, der durch  $\mu$ XRF bestimmt wurde, und der daraus resultierenden Menge an [FeFe] H<sub>2</sub>ase Modellkomplexen berechnet (Abb. 2B und 2D)."



Während die längere Spacer-Gruppe von **HM-LA** TON-Werte zwischen 133-161 erzeugte, erreichte der kurze Spacer (**HM-AA**) höhere TONs im Bereich von 361-579. Diese Ergebnisse bestätigen die früheren Erkenntnisse von *Dukovic et al.*, die den Einfluss der Spacer-Länge zwischen CdS-Nanostäbchen und [FeFe] H<sub>2</sub>ase-Enzymen untersuchten und eine Abnahme der katalytischen Effizienz mit zunehmender Spacer-Länge beobachteten.<sup>[306]</sup>

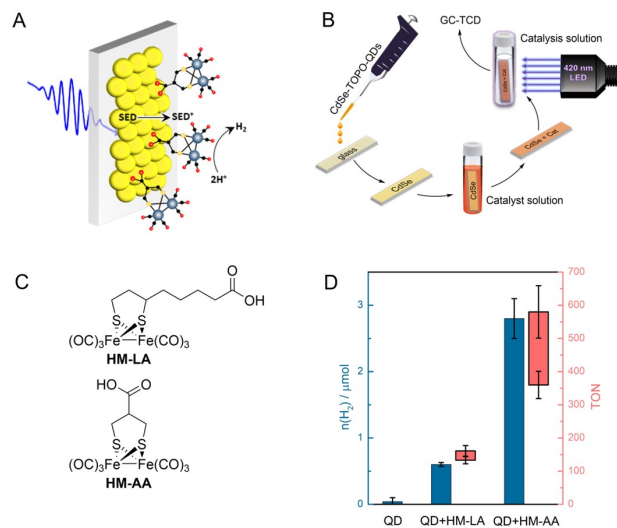


**Abbildung 2.** (A) Grafik der als dünner Film immobilisierten QDs auf einem Glassubstrat mit kovalent gebundenen [FeFe] H<sub>2</sub>ase Modellkomplexen. (B) Übersicht der Funktionalisierungsschritte und der photokatalytischen HER. (C) Strukturen der Modellkomplexe HM-LA und HM-AA. (D) Übersicht der erzeugten Mengen an Wasserstoff und der berechneten TONs.<sup>[376]</sup>

Da diese absoluten Zahlen im Vergleich zu anderen PS-CAT-Systemen auf CdSe und [FeFe] H<sub>2</sub>ase Modellen relativ niedrig waren, wurde das hohe CAT/QD-Verhältnis (20 für **HM-LA**/QD und 40 für **HM-AA**/QD) und die Instabilität der Komplexe während der Bestrahlung als Erklärung in Betracht gezogen.<sup>[183]</sup>

**[SB-3]** In dieser Arbeit wurde der Einfluss einer Dithiolan-Modifikation auf [FeFe] H<sub>2</sub>ase Modellkomplexe untersucht, die einem der ersten Modellkomplexe H<sub>2</sub>ase pdt ähnlich sind. Dabei wurde die Elektrochemie und ihre Fähigkeit zur Bildung von SAMs auf Gold- oder Platin-Elektrodenoberflächen analysiert. Diese sollten die Elektronentransferwege von der Elektrode zum Katalysator reduzieren. Zusätzlich führte das partielle oder vollständige Austauschen der Schwefelatome durch Selen zu vier Derivaten mit unterschiedlichen Zusammensetzungen. Diese wurden durch Steglich-Veresterung von 2-Hydroxy-1,3-propandithiolat bzw. 2-

Hydroxy-1,3-propandiselenolat-basierten [FeFe] H<sub>2</sub>ase Modellkomplexen mit Liponsäure oder Selenoliponsäure synthetisiert. Zudem wurde ein Derivat mit einem PPh<sub>3</sub> Liganden durch Ligandenaustauschreaktion hergestellt (Figure 25).

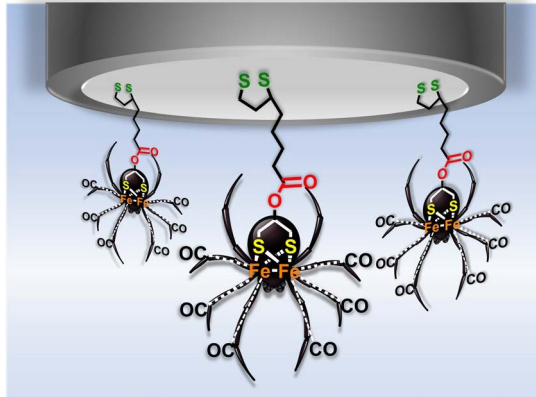


**Abbildung 3.** TOC-Grafik von [SB-3] zur Illustration des Hauptthemas dieser Veröffentlichung über die Bildung von SAMs von [FeFe] H<sub>2</sub>ase Komplexen mit funktionalisierten Liponsäureestern und deren elektrochemischen Eigenschaften.<sup>[386]</sup>

Anschließend wurden diese mit CV in Anwesenheit und Abwesenheit von AcOH und IR-SEC charakterisiert, wobei unterschiedliche elektrochemische Verhalten festgestellt wurden. Die Selenoliponsäureester-Komplexe zeigten die erwarteten CV-Daten, die aus einer Kombination ihrer Vorläufermoleküle bestanden. Dahingegen schienen die Liponsäureester-Verbindungen Wechselwirkungen zwischen der Liponsäure-Einheit und dem Dieisen-Cluster aufzuweisen.

Weitere IR-SEC Experimente zeigten die Bildung derselben Spezies nach dem ersten Reduktionsschritt der Komplexe **2** und **7**. Dies implizierte die Eliminierung eines CO- bzw. PPh<sub>3</sub>-Liganden. Ein möglicher Mechanismus wurde nach Veröffentlichung des Artikels entwickelt, jedoch bisher nicht durch DFT-Berechnungen oder zusätzliche Experimente bestätigt (Figure 28). Anschließend wurde die Fähigkeit der Komplexe **2** und **6** zur Bildung von SAMs auf Gold- und Platin-Elektroden untersucht, wobei stabile SAMs von **2** auf einer Platin-Oberfläche erzeugt werden konnten. Diese waren jedoch nicht in der Lage, die HER durchzuführen, da die SAMs unter den elektrokatalytischen Bedingungen desorbierten.

**[SB-4]** beschreibt die Verbesserung eines etablierten Synthesewegs für Dieisen-Hexacarbonyl-Komplexe, indem ein aprotisches polares Kosolvent wie

NMP, DMA, TMU oder GBL zur Reaktionsmischung hinzugefügt wurde. Dies führte zu einer Verminderung sowohl der Reaktionstemperaturen als auch der Reaktionszeiten, während die Ausbeuten in einigen Fällen sogar gesteigert werden konnten (Abb. 4).

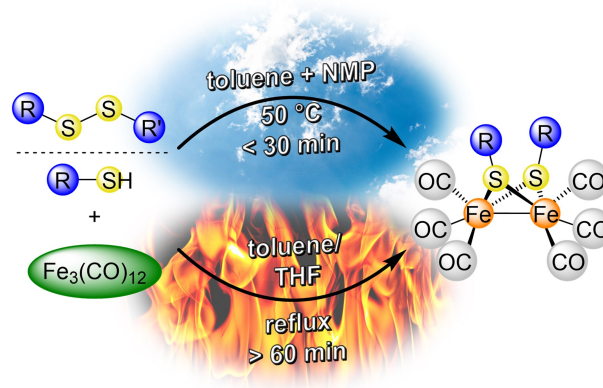


**Abbildung 4. TOC-Grafik von [SB-4] zur Illustration des Hauptthemas dieser Veröffentlichung über die verbesserte Synthese von [FeFe] H<sub>2</sub>ase Modellkomplexen.<sup>[372]</sup>**

Der Einfluss auf die Reaktionskinetik in Gegenwart dieser Co-Lösungsmittel wurde durch UV-Vis-Spektroskopie mit dem Liganden **1n** und NMP untersucht, wobei eine Erhöhung der Reaktionsgeschwindigkeit um etwa eine Größenordnung im Vergleich zur gleichen Reaktion ohne NMP festgestellt wurde. Darüber hinaus zeigte die konzentrationsabhängige Reaktion von NMP auf die Reaktionsgeschwindigkeit von **1a** und äquimolaren Mengen von Fe<sub>3</sub>(CO)<sub>12</sub>, dass NMP nicht wie ein Katalysator wirkte. Daher wurde vermutet, dass NMP in der Lage ist, geladene Zwischenprodukte der Synthese zu stabilisieren.<sup>[157]</sup>

Des Weiteren wurde die Reaktionen von **1a** mit Fe<sub>3</sub>(CO)<sub>12</sub> in Gegenwart von NMP per IR-Spektroskopie verfolgt. Dabei konnte die Bildung eines Nebenprodukts, das als Fe<sub>3</sub>(CO)<sub>11</sub>NMP identifiziert wurde, beobachtet werden. Dessen Reaktion mit **1a** wurden nicht beobachtet, was ausschließt, dass Fe<sub>3</sub>(CO)<sub>11</sub>NMP als Zwischenprodukt infrage kommt. Darüber hinaus wurden TMU, DMA und GBL getestet. Diese zeigten ein ähnliches Verhalten wie NMP.

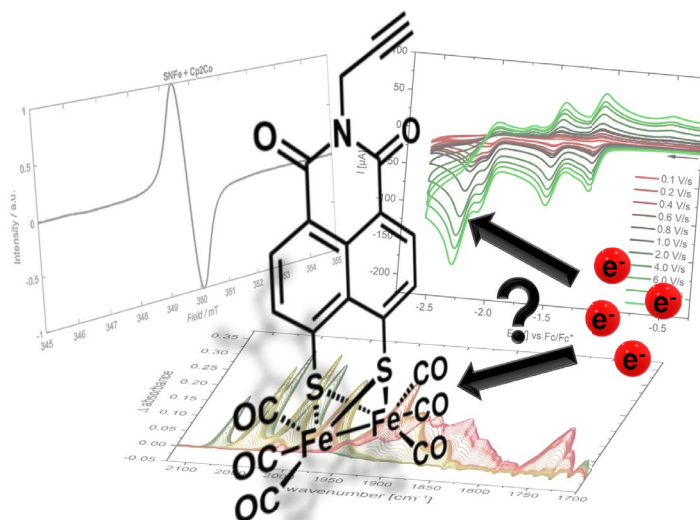
## 7. Publications

### 7.1 [SB-1]

#### [SB-1] Unravelling the Mystery: Enlightenment of the Uncommon Electrochemistry of Naphthalene Monoimide [FeFe] Hydrogenase Mimics

Stefan Benndorf, Elisabeth Hofmeister, Maria Wächtler, Helmar Görls, Phil Liebing, Kalina Peneva, Stefanie Gräfe, Stephan Kupfer, Benjamin Dietzek-Ivanšić and Wolfgang Weigand

*Eur. J. Inorg. Chem.* **2022**, 3, e202100959.



© 2021 The Authors. European Journal of Inorganic Chemistry published by Wiley-VCH GmbH

This is an open-access article under the terms of the Creative Commons Attribution License, which permits use, distribution, and reproduction in any medium, provided the original work is properly cited.

<https://chemistry-europe.onlinelibrary.wiley.com/doi/full/10.1002/ejic.202100959>

# Unravelling the Mystery: Enlightenment of the Uncommon Electrochemistry of Naphthalene Monoimide [FeFe] Hydrogenase Mimics

Stefan Benndorf,<sup>[a]</sup> Elisabeth Hofmeister,<sup>[b]</sup> Maria Wächtler,<sup>[b, c, e]</sup> Helmar Görls,<sup>[a]</sup> Phil Liebing,<sup>[a]</sup> Kalina Peneva,<sup>[d, f]</sup> Stefanie Gräfe,<sup>[c, e]</sup> Stephan Kupfer,<sup>\*,[c]</sup> Benjamin Dietzek-Ivanšić,<sup>\*,[b, c, e, f]</sup> and Wolfgang Weigand<sup>\*,[a, f]</sup>

[FeFe] hydrogenase mimicking complexes containing *N*-substituted naphthalene monoimide (NMI) of peri-substituted dichalcogenides as bridging ligands have been prepared and characterized using different spectroscopic as well as by X-ray diffraction methods. The redox behaviour has been investigated by cyclic voltammetry, IR and UV-Vis spectroelectrochemistry (IR and UV-Vis SEC), electron paramagnetic resonance (EPR) spectroscopy and quantum chemical simulations. IR SEC and EPR experiments combined with DFT calculations revealed the

non-innocent character of the NMI bridging ligands. EPR spectroscopy was applied to study the singly and doubly reduced state. Chemical reduction with one equivalent of Cp\*<sub>2</sub>Co revealed the formation of an organic radical with a *g*-value of 2.0028 at room temperature. When two equivalents of Cp\*<sub>2</sub>Co were used to carry out the second reduction, no EPR signal could be detected anymore. IR SEC measurements indicate the formation of an EPR-silent dimeric structure after the second reduction.

## Introduction

Hydrogen as a promising fuel of the future is already known as an energy carrier in bacteria like *Desulfovibrio desulfuricans* or algae.<sup>[1]</sup> For this purpose, special metalloenzymes called hydrogenases have evolved. Especially, [FeFe] hydrogenases can catalyse the reversible reduction of protons to dihydrogen with

high turnover frequencies up to 9000 s<sup>-1</sup> per active site.<sup>[1,2]</sup> After resolving the molecular structure of the protein by *Peters et al.*, including the active site, the so-called H cluster, by X-ray diffraction methods, many attempts were made to mimic this active centre.<sup>[1,2,3]</sup> However, none of the synthetic approaches reached the enzymatic activity of the natural archetype.<sup>[2a,3b,4]</sup>

Nevertheless, [FeFe] hydrogenase mimicking complexes are used as electrocatalysts for hydrogen evolution reaction (HER). The reduction potentials and the reversibility of the catalytic reactions strongly depend on the nature of the coordinating ligands.<sup>[5]</sup>

During the past few decades model complexes with bridging aliphatic and aromatic dithiolato ligands were synthesized to unravel the mechanism of HER in detail,<sup>[5,6]</sup> revealing diverse reduction behaviours. E.g. the propane-1,3-dithiolate (pdt) bridged analogue which shows an irreversible one-electron reduction.<sup>[7]</sup> By changing the bridging ligand to an aromatic moiety like benzene-1,2-dithiolate (bdt) a reversible two-electron reduction appears, indicating a partial shift of electron density to the aromatic ligand and a structural rearrangement of the carbonyl ligands during the reduction event.<sup>[8]</sup>

The expansion to a naphthalene-1,8-dithiolate (naphth) bridging moiety leads to an enhanced stability of the reduced species due to an increased delocalization of the electron density at the aromatic system. Nevertheless, the reduction events are described to be iron-centred.<sup>[9]</sup> Further modification of the aromatic moiety to electron poor or electron-deficient conjugated ligands shifts the reduction potential to less negative values.<sup>[5,10]</sup>

Things are not so simple regarding the electrochemical behaviour of 1,8-naphthalic anhydride and naphthalene as well as perylene monoimides as bridging moieties, as publications

[a] S. Benndorf, Dr. H. Görls, Dr. P. Liebing, Prof. Dr. W. Weigand  
Institute of Inorganic and Analytical Chemistry,  
Friedrich Schiller University Jena,  
Humboldtstrasse 8, 07743 Jena, Germany  
E-mail: wolfgang.weigand@uni-jena.de

[b] E. Hofmeister, Dr. M. Wächtler, Prof. Dr. B. Dietzek-Ivanšić  
Department Functional Interfaces,  
Leibniz Institute of Photonic Technology Jena (Leibniz-IPHT),  
Albert-Einstein-Straße 9, 07745 Jena, Germany  
E-mail: benjamin.dietzek@uni-jena.de

[c] Dr. M. Wächtler, Prof. Dr. S. Gräfe, Dr. S. Kupfer, Prof. Dr. B. Dietzek-Ivanšić  
Institute of Physical Chemistry, Friedrich Schiller University Jena,  
Helmholtzweg 4, 07743 Jena, Germany  
E-mail: stephan.kupfer@uni-jena.de

[d] Prof. Dr. K. Peneva  
Institute of Organic Chemistry and Macromolecular Chemistry,  
Friedrich Schiller University Jena,  
Lessingstraße 8, 07743 Jena, Germany

[e] Dr. M. Wächtler, Prof. Dr. S. Gräfe, Prof. Dr. B. Dietzek-Ivanšić  
Abbe Center of Photonics (ACP),  
Friedrich Schiller University Jena,  
Albert-Einstein-Straße 6, 07745 Jena, Germany

[f] Prof. Dr. K. Peneva, Prof. Dr. B. Dietzek-Ivanšić, Prof. Dr. W. Weigand  
Center for Energy and Environmental Chemistry Jena (CEEC Jena),  
Jena Center of Soft Matter, Friedrich Schiller University Jena,  
Philosophenweg 7a, 07743 Jena, Germany

Supporting information for this article is available on the WWW under  
<https://doi.org/10.1002/ejic.202100959>

© 2021 The Authors. European Journal of Inorganic Chemistry published by Wiley-VCH GmbH. This is an open access article under the terms of the Creative Commons Attribution License, which permits use, distribution and reproduction in any medium, provided the original work is properly cited.

of the past few years clearly demonstrated.<sup>[9,11]</sup> It is indispensable to study the redox behaviour of [FeFe] hydrogenase mimics containing conjugated aromatic ligands, to address the mechanistic key question whether the first electron uptake is reducing the iron cores or the aromatic ligand system. Pioneering experiments were carried out by the group of Reek who started to investigate the electrochemistry of naphthalene monoimide-based (NMI) complexes with spectroscopic methods, putting their focus exclusively on the first reduction event.<sup>[9]</sup> In their study they revealed the non-innocent character of the NMI ligand during the first reduction step by using IR spectroelectrochemistry and EPR (electron paramagnetic resonance) measurements.<sup>[9]</sup>

In the present contribution, we investigated the properties and (photo)reactivity of propargyl-modified NMI-based [FeFe] hydrogenase mimics combining various methods such as X-ray diffraction methods, cyclic voltammetry, IR and UV-Vis spectroelectrochemistry, protonation studies using weak ( $\text{CH}_3\text{CO}_2\text{H}$ ) and moderately strong ( $\text{CF}_3\text{CO}_2\text{H}$ ) acids, EPR measurements and quantum chemical calculations to obtain a deeper insight in the first, second and higher reduction steps.

## Results and Discussion

### Synthesis of naphthalene monoimide complexes 4, 4a and 5

The synthetic procedures and characterizations of the precursor compounds 1–3 are described in the Supporting Information. The syntheses of complexes 4 and 4a<sup>[11b]</sup> were carried out by use of a novel synthetic pathway developed recently in our group, to generate [FeFe] hydrogenase model complexes more efficiently, by using NMP (*N*-Methyl-2-pyrrolidone) as a solvent.

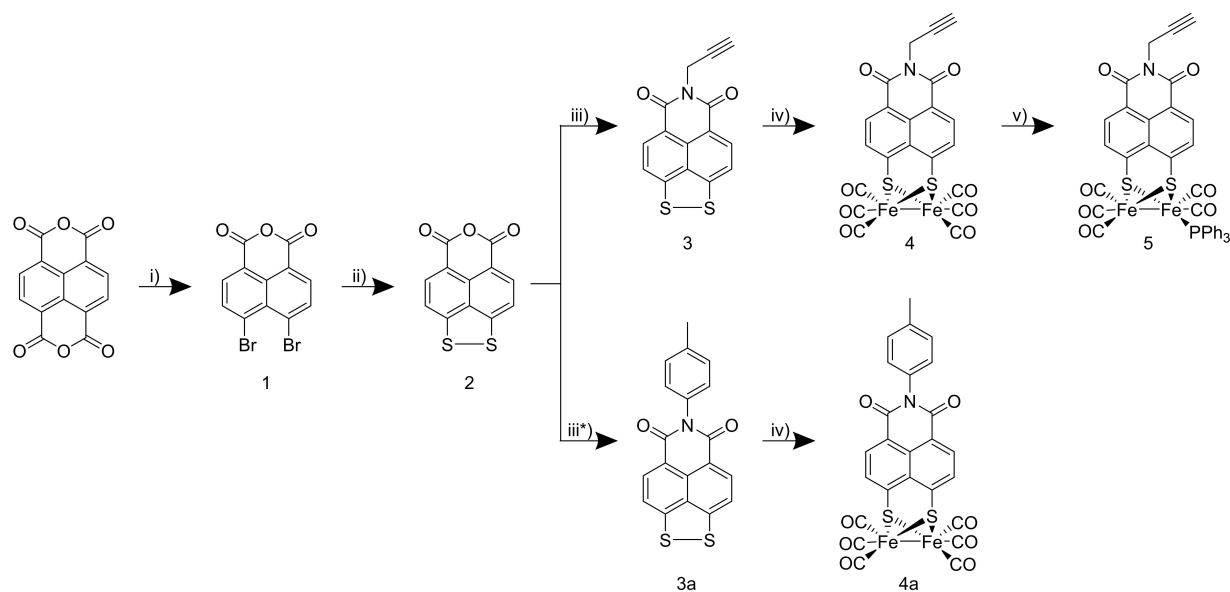
The precursor 3 (3a) was dissolved in NMP at 90 °C to get a clear solution. After dilution with toluene, triirondodecacarbonyl was added in one portion and the resulting solution was stirred for five minutes, until the dark green solution became dark red, affording target complex 4 (4a) as red solids in decent 42% (38%) yields after purification.<sup>[12]</sup> Compound 5 was synthesized by mixing compound 4 and trimethylamine *N*-oxide dihydrate in acetonitrile for 20 min, adding 1 eq. of triphenylphosphane and stirring for 1 h at RT. Target complex 5 was isolated as a brown solid in 59% yield (Scheme 1).

### Molecular structure

Figure 1 depicts the molecular structure of compound 4 with ellipsoids drawn at 50% probability level. The structure revealed the characteristic butterfly conformation of the  $[\text{Fe}_2\text{S}_2]$  cluster (Figure 1). The Fe–Fe (2.5017(8) Å) and average Fe–S (2.2545 Å) bond lengths of complex 4 are in good agreement with similar naphthalene containing hydrogenase mimics.<sup>[8c,11b,e,f]</sup> The coordination sphere in the vicinity of each Fe atom can be described as a distorted octahedron with three terminal CO ligands, two S atoms, each linked to both Fe centres. The FeFe axis is arranged almost orthogonal (91.87°) to the planar naphthalene moiety.

### Electrochemical investigation

Cyclic voltammetry (CV) was carried out to investigate the redox behaviour of compounds 4, 4a and 5. The already published compound 4a was synthesized in order to analyse the influence of the substituent at the imide N atom.<sup>[8c,11b]</sup> The CV of 4 (Figure 2) reveals two quasi-reversible reduction events at



**Scheme 1.** Synthesis route for hydrogenase model complexes 4, 4a<sup>[11b]</sup> and 5; i)  $\text{NaOH}_{\text{aq}}$ , AcOH,  $\text{Br}_2$ , 90 °C, 24 h; ii) Na, S<sub>8</sub>, DMF, 100 °C, 10 min, 140 °C, 15 min; iii) propargylamine, NMP, AcOH, 120 °C, 24 h; iii\*) p-toluidine, NMP, AcOH, 120 °C, 24 h; iv)  $\text{Fe}_3(\text{CO})_{12}$ , toluene, NMP, 90 °C, 5 min; v) trimethylamine *N*-oxide dihydrate,  $\text{PPh}_3$ , ACN, RT, 1 h.

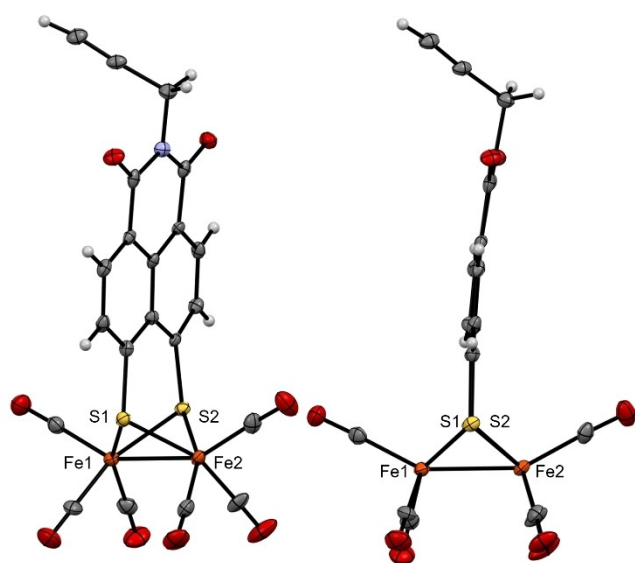


**Figure 1.** Molecular structure of complex **4** and its side view through S1–S2 axis (right). The ellipsoids represent a probability of 50%, H atoms are drawn with arbitrary radii.

$E_{1/2}^1 = -1.16$  V and  $E_{1/2}^2 = -1.52$  V, which shows an enhanced reversibility by reversing the forward scan after the second reduction (Figure S1A), and two irreversible reductions at  $E_{pc}^3 = -2.05$  V and  $E_{pc}^4 = -2.16$  V. At lower scan rates  $E_{pc}^4$  is incisive compared to higher scan rates (Figure 2).

Previous studies were exclusively focused on the first as well as on the second reduction event.<sup>[9,11b,e,f]</sup> The electrochemical data provided in the present contribution points to a more complicate electrochemistry for this kind of [FeFe] hydrogenase mimicking complexes.

To determine the number of electrons transferred in each step, the scan rate dependence of the current function for complex **4** was plotted (see Figure S2),<sup>[13]</sup> indicating a one-electron step without any chemical reactivity (EE mechanism, E=electron transfer) for the first two reduction steps, respectively. The third reduction event exhibits high  $i_{pc}/c \cdot \nu^{1/2}$  values for small scan rates ( $< 1$  Vs<sup>-1</sup>), which start to decrease significantly at faster scan rates ( $> 1$  Vs<sup>-1</sup>), suggesting consequently a rather slow electron transfer for the third reduction event (Figure S2). This scan rate dependence suggests that at slow scan rates (Figure 2A) the third and fourth reductions follow an ECE-type mechanism (E=electron transfer, C=chemical process). The electrochemical behaviour of **4a** (see Figure S1A) is very similar to that for **4**,  $E_{1/2}^1 = -1.13$  V,  $E_{1/2}^2 = -1.48$  V,  $E_{pc}^3 = -2.05$  V and  $E_{pc}^4 = -2.19$  V, indicating a minor influence of the toluene moiety.

Quantum chemical simulations performed at the density functional level of theory (DFT) allow to assess the species involved in the first and the second reduction events. In case of complex **4**, the first reduction step yields a singly reduced doublet species **4<sup>•-</sup>** predicting a redox potential of  $E_{1/2}^1 = -1.16$  V vs Fc/Fc<sup>+</sup> – in full agreement with the experimental data. This reduction was found to take place at the NMI ligand

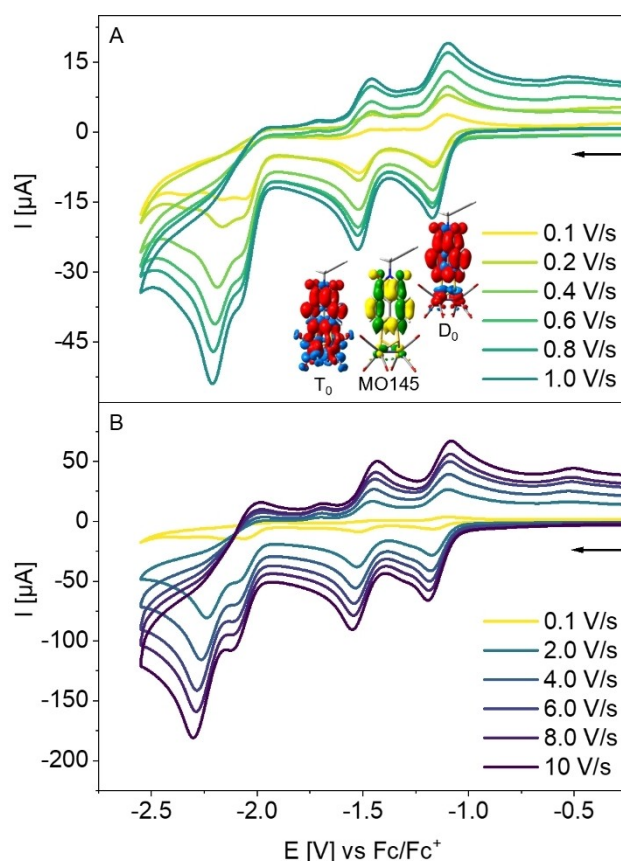


**Figure 2.** Cyclic voltammograms with different scan rates of compound **4** ( $c = 1$  mmol/L) in N<sub>2</sub>-purged ACN/[NBu<sub>4</sub>][BF<sub>4</sub>] (0.1 mol/L) at RT. Slower scan rates (0.1–1.0 V/s, A) and faster scan rates (2.0–10 V/s, B) were separated to illustrate the different development of third and fourth reduction. The arrow indicates the scan direction. The potential  $E$  is given in V and referenced to the Fc/Fc<sup>+</sup> couple. The localization of the first reduction event is indicated by the spin density of the singly reduced doublet ground state as well as for the second reduction by the highest occupied molecular orbital (HOMO) of the doubly reduced singlet and the spin density of doubly reduced triplet species, respectively, as predicted by density functional theory.

as shown by the spin density of the doublet ground state ( $D_0$ ) in Figure 2 and Table S6.

For the second reduction event, the formation either of the doubly reduced singlet species (closed shell) or of the doubly reduced triplet species (opened shell) are feasible, while the singlet species predicted at  $E_{1/2}^2 = -1.54$  V is associated to a second NMI-centred reduction. On the other hand, the doubly reduced triplet state features one accessory electron in the lowest  $\pi^*$  orbital of the NMI ligand and the second electron in the  $\sigma_{FeFe}^*$  orbital, thus formally yielding a FeFe<sup>0</sup> redox state at potential of  $E_{1/2}^2 = -1.44$  V. Therefore, the nature of the second reduction event cannot be elucidated exclusively based on the driving forces associated to the formation of the doubly reduced singlet vs the double reduced triplet species of **4**, as an energy gap of 0.1 eV is within the typical error range of DFT. In case of **4a**, very similar results are obtained, see Figure S1A and Tables S3, S4, S6 and S7 for more details.

The replacement of a terminal carbonyl ligand at the iron core by electron-donating ligands, like phosphanes, leads to

different electrochemical behaviours caused by increased electron density. In the case of compound **5**, the first quasi-reversible reduction event appears at  $E_{1/2}^1 = -1.30$  V and the second at  $E_{1/2}^2 = -1.71$  V (Figure S3), showing shifts to more negative potentials by  $\Delta E = 140$  mV and 190 mV, respectively, compared to those for **4**. A similar trend has been observed for  $[\mu-(4\text{-pyCH}_2\text{-NMI-S}_2)\text{Fe}_2(\text{CO})_4(\text{dppv})]$ .<sup>[9]</sup>

To illustrate these observations, we take a closer look at the cyclic voltammograms of naphthalene monoimides (NMI) to get a deeper insight into their redox behaviour. They tend to show a similar shape of CVs, compared to those for the first two quasi-reversible reduction steps in complexes **4** and **4a**.<sup>[14]</sup> The proposed mechanism of *Asir* et al. suggests the formation of a radical anion for the first reduction, located at the C=O bond of the imide moiety, resulting in a longer C=O bond.<sup>[14f,15]</sup> An additional disulfide group at the NMI results in a remarkable change in the electrochemical behaviour. The CVs of **3** and **3a** (Figure S1B) are showing strong reduction waves at  $E^1 = -1.28$  V and  $E^1 = -1.29$  V, respectively. The comparison between the NMI compounds and their [FeFe] complexes suggests that the first reduction event could be attributed to the NMI moiety. To clarify where the reduction steps take place, IR and

UV-Vis spectroelectrochemical and EPR measurements were performed.

### IR and UV-Vis spectroelectrochemical investigations

IR-absorption spectroelectrochemistry was carried out in an OTTLE (optically transparent thin layer electrochemical) cell ( $c(\text{complex } 4) = 2$  mmol/L, ACN,  $c(n\text{-Bu}_4\text{NBF}_4) = 0.1$  mol/L). The potential was increased in negative direction with slow scan rates (2 mV/s, Figure S9) to study structural changes during reduction of the complexes. Due to the use of different working and reference electrodes, the absolute potentials were shifted anodically by  $\Delta E = 600$  mV, compared to prior electrochemical experiments and UV-Vis spectroelectrochemical measurements.

The spectroscopic changes for the first reduction step of compound **4**, between  $E = -0.512$  V and  $E = -0.832$  V, are depicted in Figure 3A and Figure 3B, indicating bathochromic shifts by  $\Delta\nu(\text{CO}) = 26\text{--}29$   $\text{cm}^{-1}$  of the terminal carbonyl signals, due to the increased electron density at the iron cores and the resulting enhanced back donation to the anti-bonding  $\pi^*$  orbital of the carbonyl ligands. The shifts, predicted by DFT

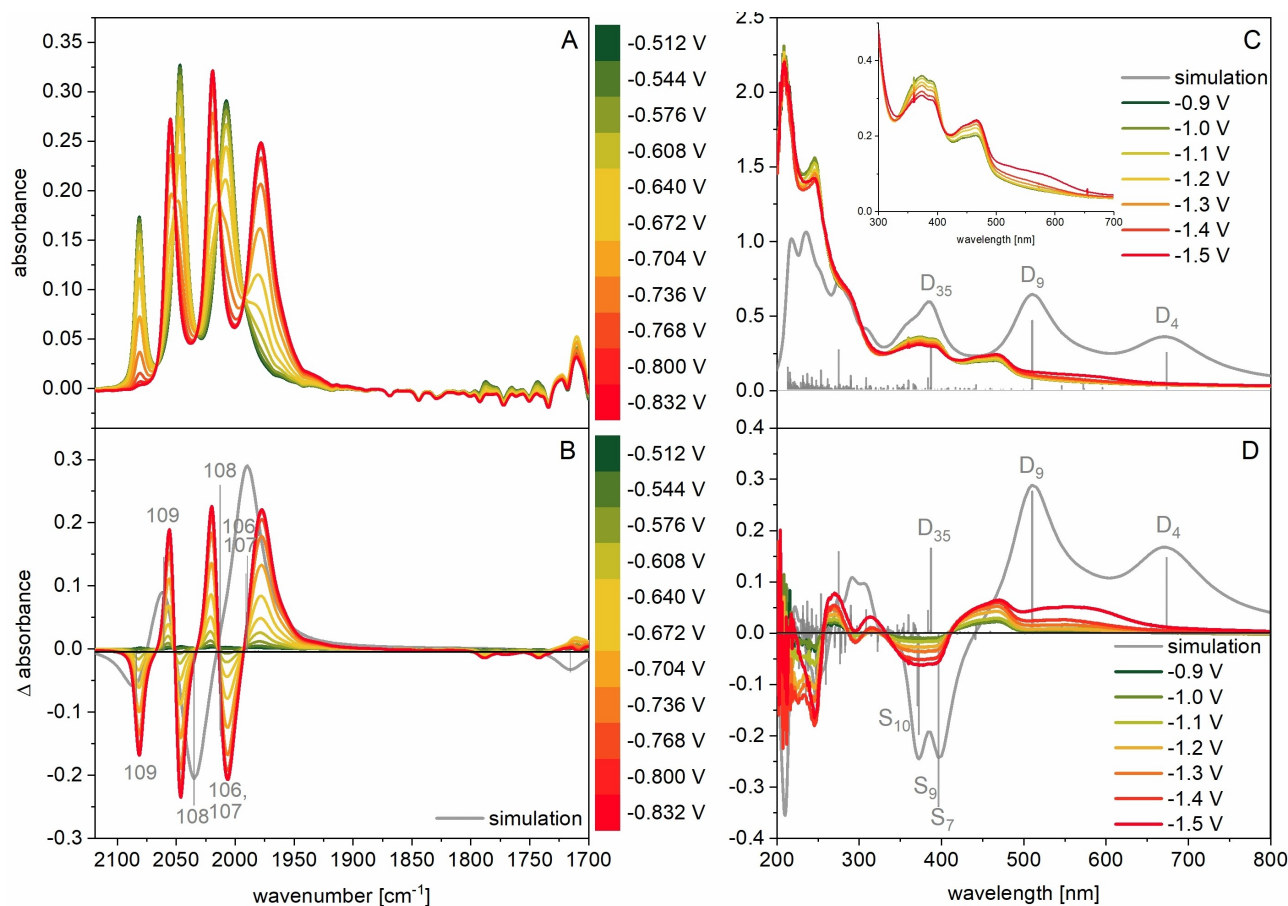


**Figure 3.** Comparison of IR (A) and UV-Vis (C) spectroelectrochemical measurements and their respective differential spectra (B, D), respectively, during the first reduction of complex **4** (IR: ACN,  $c = 2$  mmol/L, UV-Vis: ACN,  $c = 1 \times 10^{-5}$  M). The  $\Delta$  absorbance spectra were calculated by subtracting a spectrum recorded immediately before the reducing phase. Keep in mind that the difference in cathodic shift between IR and UV-Vis SEC comes from the use of different electrodes.



simulations, of  $\Delta\nu(\text{CO}) = 22\text{--}23\text{ cm}^{-1}$  for the singly reduced doublet state and the SEC experiments of Reek *et al.* support this result consistently (see Figure 3B, Table 1 and S9).<sup>[9]</sup> These shifts are significantly smaller than those expected for a one-electron reduction delocalized over the two iron centres ( $[\text{Fe}_2(\text{CO})_6(\mu\text{-naphdt})]$  (naphdt = naphthalene-1,8-dithiolate,  $\Delta\nu(\text{CO}) = 79\text{ cm}^{-1}$ ,<sup>[9]</sup>  $[\text{Fe}_2(\text{CO})_6(\mu\text{-SC}_3\text{H}_5\text{S})]$ ,  $\Delta\nu(\text{CO}) = 60\text{ cm}^{-1}$ , Figure S10), indicating that the accessory electron is located at the NMI moiety and not at the iron cores.<sup>[16]</sup> In full agreement, DFT localizes the first reduction event on the NMI moiety as evident from the spin density of the singly reduced doublet species ( $D_0$  inset in Figure 2A). This assumption is supported by a strong shift to lower wavenumbers of the NMI C=O signals by  $\Delta\nu(\text{CO}) = 70\text{ cm}^{-1}$  (Figure S11).<sup>[9]</sup> The shape of the spectra maintains the same and implies an intact coordination sphere for  $4^{\bullet-}$ .<sup>[17]</sup>

UV-Vis spectroelectrochemical measurements (UV-Vis SEC) complement the mid-IR absorption experiments and reveal changes in the naphthalene monoimide during reduction, which are further supported by simulations. Figure 3C and Figure 3D show the first reduction step from  $E = -0.9\text{ V}$  to  $E = -1.5\text{ V}$  of **4** to the anion radical and its respective differential spectrum. The spectra of **3** (Figure S12) and **4** clearly show the formation of a red-shifted absorption band from 500 nm to 650 nm during the first reduction. This band is assigned to the radical anion on the NMI moiety and is further supported by time-dependent DFT (TDDFT) simulations which predict an NMI-based intraligand excitation into the  $D_9$  state at 510 nm.<sup>[18]</sup>

The spectral changes during the second reduction, between  $E = -0.928\text{ V}$  and  $E = -1.216\text{ V}$ , are depicted in Figure 4A and Figure 4B. In the case of the second reduction, there are two possibilities, the formation of a doubly reduced singlet or a triplet species. For the singlet species, in which the second reduction is again localized on the NMI moiety, no pronounced structural rearrangement is predicted by DFT. However, in case of the triplet, the simulations reveal a pronounced rearrangement in the vicinity of the H cluster, as evident from the spin density ( $T_0$  inset in Figure 2A) visualizing the unpaired electrons to be delocalized on the NMI moiety and on the Fe–Fe bond ( $\sigma_{\text{FeFe}}^*$ ) (Table S8). The final spectrum of  $4^{2-}$  is characterized by four well-resolved absorption bands (1983, 1925, 1902, 1859  $\text{cm}^{-1}$ ), indicating bathochromic shifts,  $\Delta\nu(\text{CO}) = \approx 80\text{ cm}^{-1}$ , like expected for a one-electron reduction of  $\text{Fe}^{\text{I}}\text{Fe}^{\text{I}} \rightarrow \text{Fe}^{\text{0}}\text{Fe}^{\text{I}}$ ,<sup>[16a]</sup> that involve structural rearrangements in the inner coordination sphere of the H cluster. Hammarström *et al.* followed the iron-

centred one-electron reduction of the  $\text{Fe}_2(\text{bdt})(\text{CO})_6$  complex (bdt = 1,2-benzenedithiolate) by photogenerated  $[\text{Ru}(\text{dmb})_3]^+$  (dmb = 4,4'-dimethyl-2,2'-bipyridine) and received similar spectra.<sup>[17b]</sup>

Furthermore, Ott *et al.* observed a similar behaviour for the iron-centred one-electron reduction of a  $\text{Fe}_2(\text{bpdt})(\text{CO})_6$  (bpdt = biphenyl-2,2'-dithiolate) hydrogenase mimic, however, these redshifts were less intense ( $\Delta\nu(\text{CO}) = 53\text{--}106\text{ cm}^{-1}$ ). In addition, they assumed the dimerization of the mono-reduced species by the formation of a bridging CO, indicated by a less prominent band at  $\nu(\mu\text{-CO}) = 1727\text{ cm}^{-1}$ , likewise to the minor absorption band at  $\nu(\mu\text{-CO}) = 1738\text{ cm}^{-1}$  in complex **4** (Figure 4B).<sup>[19]</sup>

The UV-Vis SEC of the second reduction from  $E = -1.5\text{ V}$  to  $E = -1.9\text{ V}$  is depicted in Figure 4C and its respective differential spectrum in Figure 4D along the computational results obtained for the doubly reduced singlet and triplet species. During the second reduction event, the intraligand band formed previously upon single reduction decreases again. This behaviour is fully supported by TDDFT simulations on the slightly energetically more favourable doubly reduced triplet form (see Tables S3 and S6 for details). Analogous to the previously described  $D_9$  ( $f = 0.276$ ), a dipole-allowed electronic excitation of mixed intraligand and metal-centred nature,  $T_{15}$  ( $f = 0.172$ ), is predicted at 503 nm. However, its oscillator strength is considerably smaller than in case of  $D_9$ , thus explaining the decrease of absorbance. Additionally, a ligand-to-metal charge transfer (LMCT) transition (into  $T_8$ ) at 589 nm with low oscillator strength ( $f = 0.086$ ) is obtained. In contradiction with the experimental observations, a strongly dipole-allowed LMCT transition ( $S_5$  at 557 nm) from the doubly reduced NMI ligand to the FeFe bond's  $\sigma^*$  orbital is observed for the doubly reduced singlet species – analogous to the weakly absorbing excitation into  $T_8$  of the triplet species. Therefore, the joint spectroscopy-theoretical study allows to unambiguously assign the second reduction event to be localized on the [FeFe] cluster.

Further reduction steps led to more complex spectra (see Figure 5), subsequently evolving from the four absorption bands of product  $4^{2-}$  (1983, 1925, 1902, 1859  $\text{cm}^{-1}$ ), due to the increased charge and additional structural changes. The only well-defined absorption band appeared at  $\nu = 1745\text{ cm}^{-1}$ , that could be assigned to the formation of tetracarbonyl ferrate,  $[\text{Fe}(\text{CO})_4]^{2-}$ , which is attributed to be a degradation product during the reduction of iron carbonyl complexes.<sup>[20]</sup> This irreversible appearance and its corresponding spectral changes

**Table 1.** Listing of  $\nu(\text{CO})$  [ $\text{cm}^{-1}$ ] of complex **4** in ground and reduced states.

$\nu(\text{CO})$ <sup>[b]</sup>	$\nu(\text{CO})$ <sup>[b]</sup>	$\nu(\text{CO})$ <sup>[b]</sup>	$\Delta\nu(\text{CO})$ <sup>[b]</sup>	$\Delta\nu(\text{CO})$ <sup>[c]</sup>	$\Delta\nu(\text{CO})$ <sup>[b]</sup>	$\Delta\nu(\text{CO})$ <sup>[d]</sup>	$\Delta\nu(\text{CO})$ <sup>[e]</sup>	$\Delta\nu(\text{CO})$ <sup>[f]</sup>	$\Delta\nu(\text{CO})$ <sup>[g]</sup>
<b>4</b>	$4^{\bullet-}$	$4^{2-}$	<b>4-4<sup>1\bullet-</sup></b>	<b>4-4<sup>1\bullet-</sup></b>	<b>4<sup>1\bullet-</sup>-4<sup>2-</sup></b>	<b>4<sup>1\bullet-</sup>-4<sup>2-</sup></b>	<b>4<sup>1\bullet-</sup>-4<sup>2-</sup></b>	<b>bpdt-bpdt<sup>-</sup></b>	<b>bdt-bdt<sup>-</sup></b>
2081 (m)	2055 (s)	1983 (m)	26	23	72	28	56	53	45
2047 (s)	2019 (s)	1925 (s)	28	22	94	31	77	68	65
2007 (s)	1978 (m, br)	1902 (m, br)	29	22	76	29	68	55	50
		1859 (w, br)	29	23	119	30	69	106	115

[a] Terminal carbonyl ligands at the iron centres [b] Experimental data [c] Calculated data for singly reduced doublet state [d] Calculated data for doubly reduced singlet state [e] Calculated data for doubly reduced triplet state [f] Differential between absorption bands of  $\text{Fe}_2(\text{bpdt})(\text{CO})_6$  and  $\text{Fe}_2(\text{bdt})(\text{CO})_6^{-1[9]}$  [g] Differential between absorption bands of  $\text{Fe}_2(\text{bdt})(\text{CO})_6$  and  $\text{Fe}_2(\text{bdt})(\text{CO})_6^{-1[7b]}$

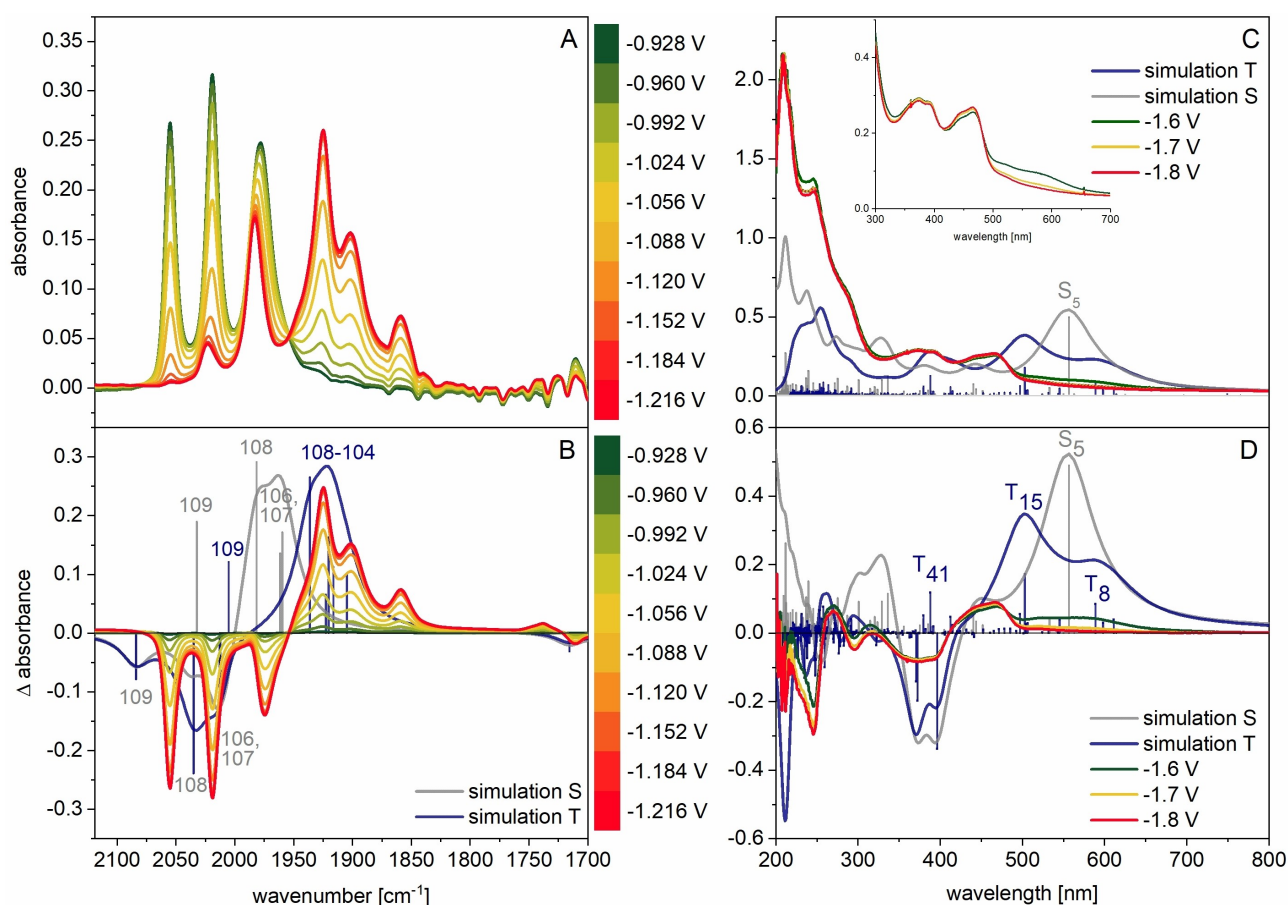


**Figure 4.** Comparison of IR (A) and UV-Vis (C) spectroelectrochemical measurements and their respective differential spectra (B, D), respectively, during the second reduction of complex **4** (IR: ACN,  $c = 2$  mmol/L, UV-Vis: ACN,  $c = 1 \times 10^{-5}$  M). The  $\Delta$  absorbance spectra were calculated by subtracting a spectrum recorded immediately before the reducing phase. Keep in mind that the difference in cathodic shift between IR and UV-Vis SEC comes from the use of different electrodes.

are consistent with the irreversible electrochemical behaviour (see Figure 2). Other reduced species could not be identified.

### Electron paramagnetic resonance spectroscopy

To further validate this assignment, EPR spectroscopy was performed to study **4** in its singly and doubly reduced state. Chemical reduction with one equivalent of  $\text{Cp}^*_2\text{Co}$  in acetonitrile revealed an organic radical with a  $g$ -value of 2.0028 at room temperature (Figure 6A). Two equivalents of  $\text{Cp}^*_2\text{Co}$  were used to carry out the second reduction – in consequence no signal could be detected any more. The IR SEC measurements indicate the formation of a dimeric structure after the second reduction, which according to literature, is not paramagnetic and, thus, cannot be detected by EPR spectroscopy.<sup>[19]</sup> Chemical reduction of **3** (Figure S13) with one equivalent  $\text{Cp}^*_2\text{Co}$  resulted in an organic radical with a  $g$ -value of 2.0019 which is closely related in value to **4**.

### Electrocatalysis

Due to the insights from the spectroelectrochemical, EPR and (TD)DFT investigations, we were interested, whether complexes **4** and **4a** are nevertheless capable to reduce protons to dihydrogen under electrocatalytic conditions. For this purpose, their electrocatalytic behaviour regarding hydrogen production were investigated by cyclic voltammetry in the presence of various amounts of acetic acid (AcOH) in acetonitrile (ACN) as solvent. The performances of the complexes **4** and **4a** are almost identical (Figure S1A). Therefore, CVs of complex **4** are illustrated in Figure 7. Addition of AcOH (Figure 7) induces no change for the first reduction wave, suggesting that AcOH ( $\text{p}K_a^{\text{ACN}} = 22.6$ )<sup>[22]</sup> is not strong enough to protonate the monoanionic complex  $\mathbf{4}^{\bullet-}$ , while the second reduction event exhibits a small shift ( $\approx 40$  mV) to less negative potential. This behaviour indicates the protonation of the dianionic species  $\mathbf{4}^{2-}$  to generate  $\mathbf{4H}^-$ .<sup>[23]</sup>

At more negative potentials, between  $E = -1.60$  V and  $E = -2.20$  V, the voltammograms exhibit catalytic activity through two processes: process I may be initiated by a new reduction event at  $E = -1.77$  V in the presence of AcOH yielding  $\mathbf{4H}^{2-}$ ,

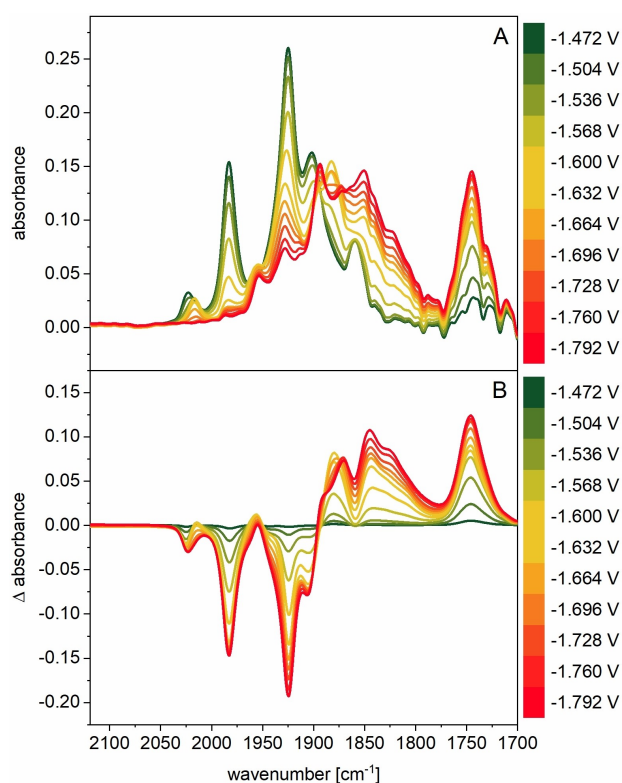


**Figure 5.** IR spectra (A) and differential IR spectra (B) of compound **4** (ACN,  $c = 2$  mmol/L) at different cathodic potentials ( $-1.472$  V to  $-1.792$  V), recorded within an OTTLE cell. The  $\Delta$  absorbance spectra were calculated by subtracting a spectrum recorded immediately before the reducing phase.

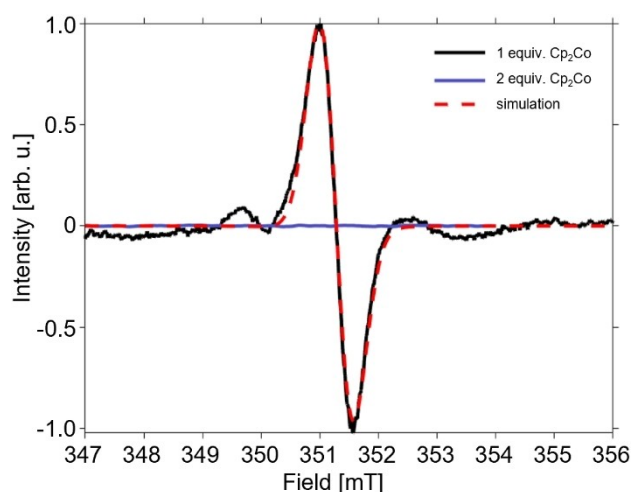


**Figure 6.** Chemical reduction of **4** ( $c = 1$  mM) with 1 (black line) and two (blue line) equivalents of  $\text{Cp}_2\text{Co}$ . Simulation (dashed red line) carried out with EasySpin<sup>[21]</sup> to study properties of paramagnetic compound.

followed by subsequent protonation to attain dihydrogen releasing species  $4\text{H}_2^{\bullet+}$ , according to Scheme 2. A supposable mechanism for the catalytic proton reduction via process II involves an additional electron uptake at  $E = -2.16$  V to reduce  $4\text{H}_2^{\bullet+}$  yielding  $4\text{H}_2^{2-}$ , which is also capable to generate

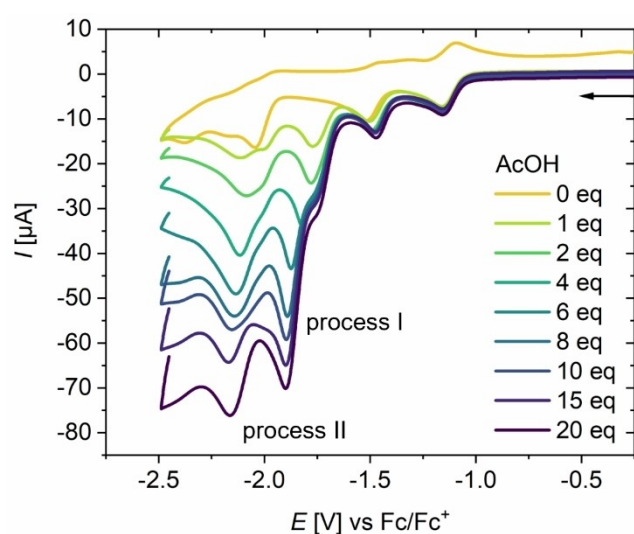
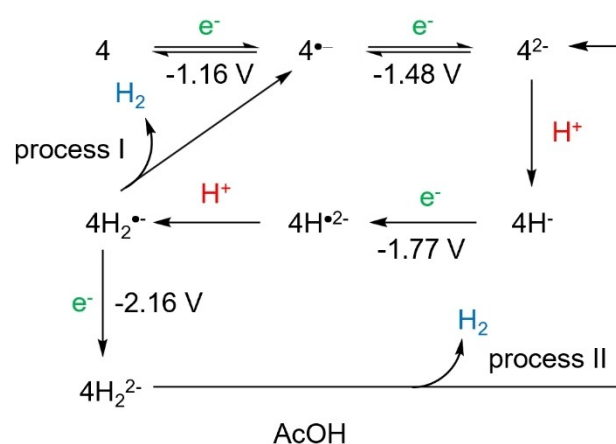


**Figure 7.** Cyclic voltammograms ( $v = 0.2$  V/s) of compound **4** ( $c = 1$  mmol/L) with various amounts of acetic acid in  $\text{N}_2$ -purged ACN/ $[\text{NBu}_4][\text{BF}_4]$  (0.1 mol/L) at RT. The arrow indicates the scan direction. The potential  $E$  is given in V and referenced to the  $\text{Fc}/\text{Fc}^+$  couple.



**Scheme 2.** Proposed mechanisms for the proton reduction cycle of complex **4** in the presence of AcOH.

dihydrogen and closing the circle to afford  $4^{2-}$ . The reduction of AcOH (4 mM) in ACN- $[\text{n-Bu}_4\text{N}][\text{BF}_4]$  without any catalyst occurs around  $E = -2.37$  V vs  $\text{Fc}/\text{Fc}^+$  (Figure S4), which specifies that the current increases with increasing concentration of AcOH belongs to process I and process II, as illustrated in Scheme 2 and Figure S5.

## Conclusion

This study elucidates the redox behaviour of naphthalene monoimide based  $[\text{FeFe}]$  hydrogenase model complexes with a substantial analysis of the new synthesized complex **4** by cyclic voltammetry, IR and UV-Vis spectroelectrochemistry, EPR spectroscopy and (TD)DFT calculations. Electrochemical measure-

ments for mimic **4** reveal two quasi-reversible well-separated one-electron processes with a linear scan rate dependence of the current function (EE mechanism) and two irreversible reduction events. The substitution of one carbonyl ligand with triphenylphosphane (**5**) shifts all reduction waves to more negative potentials, indicating the distribution of the additional electron density over the whole molecule. The results of our studies, especially the small shifts to smaller wavenumbers in IR SEC spectra, the EPR measurements and (TD)DFT calculations, revealing the non-innocent nature of NMI bridging ligands in [FeFe] hydrogenase mimicking complexes after the first reduction (**4<sup>•-</sup>**), are in good agreement with those reported by Reek *et al.*<sup>[9]</sup> Moreover, SEC and quantum chemistry indicate a doubly reduced complex in triplet state (**4<sup>2-</sup>**) for the second reduction, with a mono-reduced NMI moiety and the mono-reduced [FeFe<sup>0</sup>S<sub>2</sub>] subcluster, which was not described so far. The appearance of an absorption band at  $\nu(\mu\text{-CO}) = 1738\text{ cm}^{-1}$  suggests a bridging CO ligand and the formation of a dimer of the double reduced species.<sup>[19]</sup> Further reduction steps lead to decomposition reactions of complex **4**. After the reduction of the NMI moiety, the complex is still able to perform catalytic proton reduction in the presence of AcOH.

## Experimental Section

### $[\mu\text{-(HC}\equiv\text{CCH}_2\text{-NMI-S}_2\text{)}\text{Fe}_2(\text{CO})_6]$ (**4**)

In a Schlenk flask **3** (200 mg, 673  $\mu\text{mol}$ ) was suspended in anhydrous NMP (50 mL) under nitrogen atmosphere. After dissolving at 90 °C anhydrous toluene (35 mL) was added to get an orange, clear solution. Triirondodecarbonyl (508 mg, 1.01 mmol) was added, and the colour changed from dark green to dark brown within five minutes while a small amount of gas (CO) was developed. The reaction mixture was cooled down, poured into water (200 mL) and the orange toluene phase was separated. The aqueous phase was extracted with toluene (3  $\times$  25 mL). After drying the combined organic phase over Na<sub>2</sub>SO<sub>4</sub>, the toluene phase was put on a column packed with silica and *n*-hexane. After flushing the column with *n*-hexane to remove the toluene, the eluent was changed to *n*-hexane/DCM (4:1). The product was collected from the major red band to give a red, crystalline solid (161 mg, 278  $\mu\text{mol}$ , 42%).<sup>[12]</sup>

<sup>1</sup>H NMR (400 MHz, [D<sub>2</sub>]THF, 297 K, TMS)  $\delta$  (ppm) = 8.55–8.49 (d, <sup>3</sup>J<sub>H-H</sub> = 7.6 Hz, 2H; Ar-H), 8.43 (d, <sup>3</sup>J<sub>H-H</sub> = 7.6 Hz, 2H; Ar-H), 4.84 (d, <sup>4</sup>J<sub>H-H</sub> = 2.4 Hz, 2H; CH<sub>2</sub>), 2.54 (t, <sup>4</sup>J<sub>H-H</sub> = 2.4 Hz, 1H; CCH); <sup>13</sup>C{<sup>1</sup>H} NMR (101 MHz, [D<sub>2</sub>]THF, 297 K, TMS)  $\delta$  (ppm) = 208.3 (C≡O), 163.0 (C=O), 135.0 (Ar), 134.2 (Ar), 130.4 (Ar), 130.3 (Ar), 126.7 (Ar), 126.7 (Ar), 79.5 (CCH), 71.9 (CCH), 30.0 (CH<sub>2</sub>); MS (EI): m/z = 577[M]<sup>+</sup>; 549 [M-CO]<sup>+</sup>; 521 [M-(CO)<sub>2</sub>]<sup>+</sup>; 493 [M-(CO)<sub>3</sub>]<sup>+</sup>; 465 [M-(CO)<sub>4</sub>]<sup>+</sup>; 437 [M-(CO)<sub>5</sub>]<sup>+</sup>; 409 [M-(CO)<sub>6</sub>]<sup>+</sup>; 370 [M-(CO)<sub>6</sub>-C<sub>3</sub>H<sub>3</sub>]<sup>+</sup>; elemental analysis calcd. (%) for C<sub>21</sub>H<sub>7</sub>Fe<sub>2</sub>NO<sub>8</sub>S<sub>2</sub>: C 43.71, H 1.22, N 2.43, S 11.11; found: C 43.91, H 1.32, N 2.41, S 10.98.

### $[\mu\text{-(p-H}_3\text{C-C}_6\text{H}_4\text{-NMI-S}_2\text{)}\text{Fe}_2(\text{CO})_6]$ (**4a**)<sup>[11b]</sup>

In a Schlenk flask **3a** (200 mg, 572  $\mu\text{mol}$ ) was suspended in anhydrous NMP (20 mL) under nitrogen atmosphere. After dissolving at 90 °C anhydrous toluene (20 mL) was added to get an orange, clear solution. Triirondodecarbonyl (288 mg, 572  $\mu\text{mol}$ ) was added, and the colour changed from dark green to dark brown

within five minutes while a small amount of gas (CO) was developed. The reaction mixture was cooled down, poured into water (200 mL) and the orange toluene phase was separated. The aqueous phase was extracted with toluene (3  $\times$  25 mL). After drying the combined organic phase over Na<sub>2</sub>SO<sub>4</sub>, the toluene phase was put on a column packed with silica and *n*-hexane. After flushing the column with *n*-hexane to remove the toluene, the eluent was changed to *n*-hexane/DCM (4:1). The product was collected from the major red band to give a red, crystalline solid (138 mg, 220  $\mu\text{mol}$ , 38%). Compound **4a** was characterized by <sup>1</sup>H NMR spectroscopy and mass spectrometry. The results were fitting to the previously reported ones.<sup>[11b,12]</sup>

### $[\mu\text{-(HC}\equiv\text{CCH}_2\text{-NMI-S}_2\text{)}\text{Fe}_2(\text{CO})_5(\text{PPh}_3)]$ (**5**)

In a Schlenk flask **4** (50 mg, 87  $\mu\text{mol}$ ) and trimethylamine *N*-oxide dihydrate (10 mg, 87  $\mu\text{mol}$ ) were stirred in 10 mL anhydrous acetonitrile for 20 minutes. Triphenylphosphane (23 mg, 87  $\mu\text{mol}$ ) was added to the brown solution and the reaction mixture was stirred for another hour. The solvent was removed under reduced pressure and the crude product was purified by column chromatography (*n*-hexane/DCM 1:2) to get **5** as a brown, oxygen sensitive solid (41 mg, 51  $\mu\text{mol}$ , 59%).<sup>[24]</sup>

<sup>1</sup>H NMR (400 MHz, [D<sub>2</sub>]DCM, 297 K, TMS)  $\delta$  (ppm) = 8.07 (m, 4H; Ar-H), 7.24 (br s, 9H; PPh<sub>3</sub>), 7.03–7.19 (m, 6H; PPh<sub>3</sub>), 4.84 (br s, 2H, CH<sub>2</sub>), 2.16–2.30 (m, 1H, CCH); <sup>31</sup>P{<sup>1</sup>H} (162 MHz, [D<sub>2</sub>]DCM, 297 K)  $\delta$  (ppm) = 61.1; MS (ESI positive mode): m/z = 811.934 (M + H<sup>+</sup>, calcd. 811.935), 833.917 (M + Na<sup>+</sup>, calcd. 833.917); elemental analysis calcd (%) for C<sub>38</sub>H<sub>22</sub>Fe<sub>2</sub>NO<sub>7</sub>PS<sub>2</sub> 0.25 C<sub>6</sub>H<sub>14</sub>: C 56.96, H 3.09, N 1.68, S 7.70; found: C 57.21, H 2.72, N 1.79, S 7.34.

### 2091233 (for 2), 2091234 (for 3), 2091235 (for 4), and 2116327 (for 5)

Deposition Numbers 2091233 (for 2), 2091234 (for 3), 2091235 (for 4), and 2116327 (for 5) contain the supplementary crystallographic data for this paper. These data are provided free of charge by the joint Cambridge Crystallographic Data Centre and Fachinformationszentrum Karlsruhe Access Structures service www.ccdc.cam.ac.uk/structures.

## Acknowledgements

Financial support by the German Science Foundation (DFG) via the TRR234 Catalight is gratefully acknowledged (project number 364549901, projects A2, A3, C5, Z2). All calculations were performed at the Universitätsrechenzentrum of the Friedrich Schiller University of Jena. Dr. Akintola and Dr. Buchholz are thanked for their help with EPR measurements at low temperatures. We are grateful to Dr. Abul-Futouh for important discussions. Open Access funding enabled and organized by Projekt DEAL.

## Conflict of Interest

The authors declare no conflict of interest.



# European Journal of Inorganic Chemistry

Supporting Information

## Unravelling the Mystery: Enlightenment of the Uncommon Electrochemistry of Naphthalene Monoimide [FeFe] Hydrogenase Mimics

Stefan Benndorf, Elisabeth Hofmeister, Maria Wächtler, Helmar Görls, Phil Liebing,  
Kalina Peneva, Stefanie Gräfe, Stephan Kupfer,\* Benjamin Dietzek-Ivanšić,\* and  
Wolfgang Weigand\*

# Supporting Information

## Table of contents

- Materials and Methods
- Molecular structure
- Synthesis and characterization / NMR spectra
- Electrochemical measurements
- Spectroscopy - protonation study
- Spectroelectrochemical measurements IR and UV-Vis
- EPR measurements
- Electrocatalysis
- Quantum chemical simulations

## Materials and Methods

All solvents as well as commercially available compounds were purchased (Sigma-Aldrich, Acros, abcr, Alfa Aesar, TCI) and used as received without further purification. Toluene was dried and deoxygenated over Na metal. The NMR spectra were recorded with a Bruker Avance 400 MHz spectrometer. Chemical shifts are given in ppm relative to internal SiMe<sub>4</sub> or CHCl<sub>3</sub> (<sup>1</sup>H, <sup>13</sup>C{<sup>1</sup>H}), external H<sub>3</sub>PO<sub>4</sub> (<sup>31</sup>P{<sup>1</sup>H}). IR and IR-SEC spectra were measured with a Tensor 27 FT-IR spectrometer. A Biologic SP-50 potentiostat was used for spectro-electro chemical experiments. A specac OMNI OTTLE cell with Pt mesh working and counter electrode and a Ag wire reference electrode, was used for IR-SEC measurements. DIPEI mass spectrometry (70 eV) was performed with a Finnigan MAT SSQ 710. Elemental analysis was performed using a Euro Vector EA3000 element analyser.

UV Vis spectroelectrochemistry was carried out at a Specord S600 with a BioLogic SP-50 potentiostat. A 1 mm pathway cuvette was equipped with a glassy carbon working electrode, a platin wire counter electrode and a Ag wire reference electrode. TBA BF<sub>4</sub> was used as the supporting electrolyte in acetonitrile. The concentration of the solutions were ~1 x 10<sup>-5</sup> M to ensure an appropriate absorbance in the UV-Vis spectrum. Ligand **3** was measured in comparison to complex **4**.

EPR measurements were carried out at X-Band ELEXSYS E500 spectrometer from Bruker at room temperature in a SHQE resonator and at low temperatures with HE-flow cryostat equipped with a MD5 resonator at 5 K. Simulation of experimental data was carried out with EasySpin.<sup>[1]</sup> EPR was measured in a flat cell for room temperature measurements and in an EPR tube at low temperatures. Illumination was carried out in the resonator by LED (450 nm) when necessary. Chemical reduction was carried out at 1 x 10<sup>-3</sup> M for **3** and **4** and one or two equivalents of Cp\*<sub>2</sub>Co for the necessary chemical reduction. ACN was used as the solvent for chemical reduction. Photochemical reduction was carried out at a concentration of 1 x 10<sup>-3</sup> M for **4** and 1 x 10<sup>-2</sup> M for ascorbic acid. A solvent mixture of ACN and H<sub>2</sub>O was used for photochemical reduction.

Cyclic voltammetric data were obtained in a conventional three-electrode glass cell (10 ml of solution) under nitrogen atmosphere and ambient temperature, using a Reference 600 Potentiostat/Galvanostat/ZRA from Gamry Instruments. The measurements were performed with a glassy carbon working electrode, that was successively polished with aluminum oxide powder prior to any cyclic voltammetric experiment, a non-aqueous Ag/AgCl reference electrode, a silver wire in contact with 0.01 M AgNO<sub>3</sub> and 0.1 M [*n*-Bu<sub>4</sub>N][PF<sub>6</sub>] in CH<sub>3</sub>CN, and a platinum wire counter electrode. Acetonitrile (Aldrich, spectroscopy grade), used for electrochemical measurements, was freshly distilled from CaH<sub>2</sub> under nitrogen. All the potentials (text, tables, and figures) were quoted versus ferrocene(Fc)/ferrocenium(Fc<sup>+</sup>) couple; ferrocene was added as an internal standard at the end of the experiments.

Structure Determinations: The intensity data for the compounds were collected on a Nonius KappaCCD diffractometer using graphite-monochromated Mo-K<sub>α</sub> radiation. Data were corrected for Lorentz and polarization effects; absorption was taken into account on a semi-empirical basis using multiple-scans<sup>[2]</sup>.

The structures were solved by intrinsic phases (SHELXT<sup>[3]</sup>) and refined by full-matrix least squares techniques against  $F_o^2$  (SHELXL-2014<sup>[4]</sup>). The hydrogen atoms bonded to the ethyne carbon C15 of compound **3** and **4** and all hydrogen atoms of **2** were located by difference Fourier synthesis and refined isotropically. All other hydrogen atoms were included at calculated positions with fixed thermal parameters.

## Molecular structure

**Table S1.** Crystal data and refinement details for the X-ray structure determinations.

Compound	<b>2</b>	<b>3</b>	<b>4</b>	<b>5</b>
formula	C <sub>12</sub> H <sub>4</sub> O <sub>3</sub> S <sub>2</sub>	C <sub>15</sub> H <sub>7</sub> NO <sub>2</sub> S <sub>2</sub>	C <sub>21</sub> H <sub>7</sub> Fe <sub>2</sub> NO <sub>8</sub> S <sub>2</sub>	C <sub>38</sub> H <sub>22</sub> Fe <sub>2</sub> NO <sub>7</sub> PS <sub>2</sub>
fw (g·mol <sup>-1</sup> )	260.27	297.34	577.10	811.35
T/°C	-140(2)	-140(2)	-140(2)	-140(2)
crystal system	monoclinic	monoclinic	Triclinic	triclinic
space group	P 2 <sub>1</sub> /n	P c	P $\bar{1}$	P $\bar{1}$
a/Å	7.5811(3)	8.7371(8)	7.6465(2)	9.3005(8)
b/Å	7.3928(3)	9.4051(8)	15.3144(4)	10.3062(8)
c/Å	16.9425(7)	7.1879(6)	18.4678(5)	18.7552(15)
$\alpha$ /°	90	90	76.507(1)	79.333(2)
$\beta$ /°	98.577(2)	93.806(5)	86.178(1)	79.112(2)
$\gamma$ /°	90	90	89.273(1)	76.977(2)
V/Å <sup>3</sup>	938.93(7)	589.35(9)	2098.23(10)	1700.8(2)
Z	4	2	4	2
$\rho$ (g·cm <sup>-3</sup> )	1.841	1.676	1.827	1.584
$\mu$ (cm <sup>-1</sup> )	5.55	4.5	16.34	10.76
measured data	5716	5043	20234	25890
data with $I > 2\sigma(I)$	1833	1873	7521	8148
unique data ( $R_{int}$ )	2143/0.0426	2222/0.0444	9515/0.0425	10408/0.0538
$wR_2$ (all data, on $F^2$ ) <sup>a)</sup>	0.0971	0.1206	0.1166	0.1188
$R_1$ ( $I > 2\sigma(I)$ ) <sup>a)</sup>	0.0422	0.0577	0.0547	0.0445
$S$ <sup>b)</sup>	1.099	1.094	1.066	1.037
Res. dens./e·Å <sup>-3</sup>	0.490/-0.281	0.379/-0.470	0.904/-0.582	1.356/-1.143
Flack parameter	-	0.09(9)	-	-
absorpt method	multi-scan	multi-scan	multi-scan	multi-scan
absorpt corr $T_{min/max}$	0.6883/0.7456	0.5947/0.7456	0.6574/0.7456	0.5633/0.7456
CCDC No.	2091233	2091234	2091235	2116327

<sup>a)</sup> Definition of the  $R$  indices:  $R_1 = (\sum ||F_o| - F_c|) / \sum |F_o|$ ;

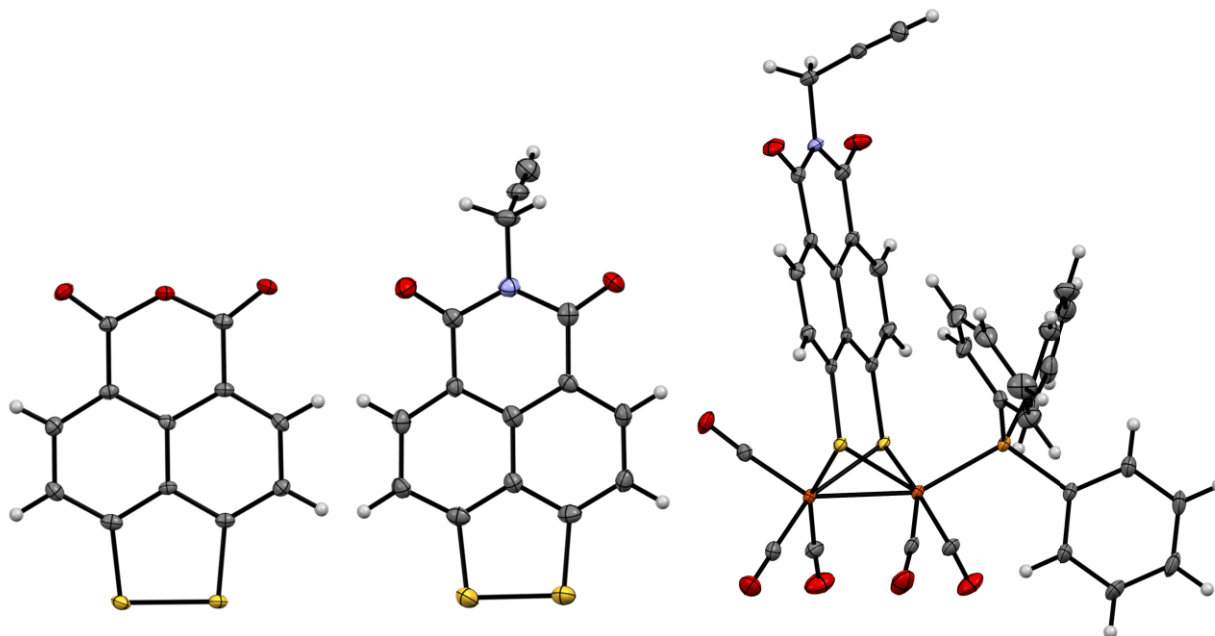
$wR_2 = \{\sum [w(F_o^2 - F_c^2)^2] / \sum [w(F_o^2)^2]\}^{1/2}$  with  $w^{-1} = \sigma^2(F_o^2) + (aP)^2 + bP$ ;  $P = [2F_c^2 + \text{Max}(F_o^2)]/3$ ;

<sup>b)</sup>  $s = \{\sum [w(F_o^2 - F_c^2)^2] / (N_o - N_p)\}^{1/2}$ .



Suitable single crystals for X-ray diffraction analysis were obtained by slow diffusion of *n*-hexane to a THF solution of compounds **4** and **5** at 4 °C. Single crystals of precursors **2** and **3** were gained by slow evaporation of THF solutions at RT, respectively. Crystallographic data as well as structure solution and refinement details are summarized in Table S1. MERCURY<sup>[5]</sup> was used for structure representations.

Crystallographic data (excluding structure factors) has been deposited with the Cambridge Crystallographic Data Centre as supplementary publication CCDC-2091233 for **2**, CCDC-2091234 for **3**, CCDC-2091235 for **4**, and CCDC-2116327 for **5**. Copies of the data can be obtained free of charge on application to CCDC, 12 Union Road, Cambridge CB2 1EZ, UK [E- mail: [deposit@ccdc.cam.ac.uk](mailto:deposit@ccdc.cam.ac.uk)].



Molecular structures of compound **2** (left), **3** (middle) and **5** (right). The ellipsoids represent a probability of 50 %, H atoms are drawn with arbitrary radii.

## Synthesis

The precursors **1**<sup>[6]</sup>, **2**<sup>[7]</sup> and **3a**<sup>[8]</sup> were prepared according to reported procedures.

### 4,5-Dithio-1,8-naphthalenedicarboxylic *N*-propargylmonoimide (**3**)

To a stirred suspension of **2** (200 mg, 786  $\mu$ mol) in NMP (4 mL) and glacial acetic acid (1.5 mL) was added propargylamine (54  $\mu$ L, 47 mg, 845  $\mu$ mol, 1.2 eq.) in one portion. The reaction was stirred for 24 h at 120 °C. The resulting orange, limpid reaction solution was poured into water (50 mL) and the precipitate was filtered off, washed with water, and dried at low pressure. The product was isolated as an orange solid (147 mg, 494  $\mu$ mol, 64 %).<sup>[9]</sup>

M.p. 320 °C (decomposition); <sup>1</sup>H NMR (400 MHz, CDCl<sub>3</sub>, 297 K, TMS):  $\delta$  (ppm) = 8.50 - 8.47 (d, <sup>3</sup>J<sub>H-H</sub> = 8.2 Hz, 2H; Ar-H), 7.52 - 7.49 (d, <sup>3</sup>J<sub>H-H</sub> = 8.2 Hz, 2H; Ar-H), 4.97 (d, <sup>4</sup>J<sub>H-H</sub> = 2.6 Hz, 2H, CH<sub>2</sub>), 2.18 (t, <sup>4</sup>J<sub>H-H</sub> = 2.6 Hz, 1H; CCH); MS (EI): *m/z* = 297[M]<sup>+</sup>; 268; 241; 214; 188 [M-C<sub>5</sub>H<sub>3</sub>O<sub>2</sub>]<sup>+</sup>; elemental analysis calcd (%) for C<sub>15</sub>H<sub>7</sub>NO<sub>2</sub>S<sub>2</sub>·0.2H<sub>2</sub>O: C 59.87, H 2.48, N 4.65, S 21.31; found: C 59.67, H 2.23, N 4.60, S 21.43.

## Characterization

### $[\mu\text{-(HC}\equiv\text{CCH}_2\text{-NMI-S}_2\text{)}\text{Fe}_2(\text{CO})_6]$ (**4**)

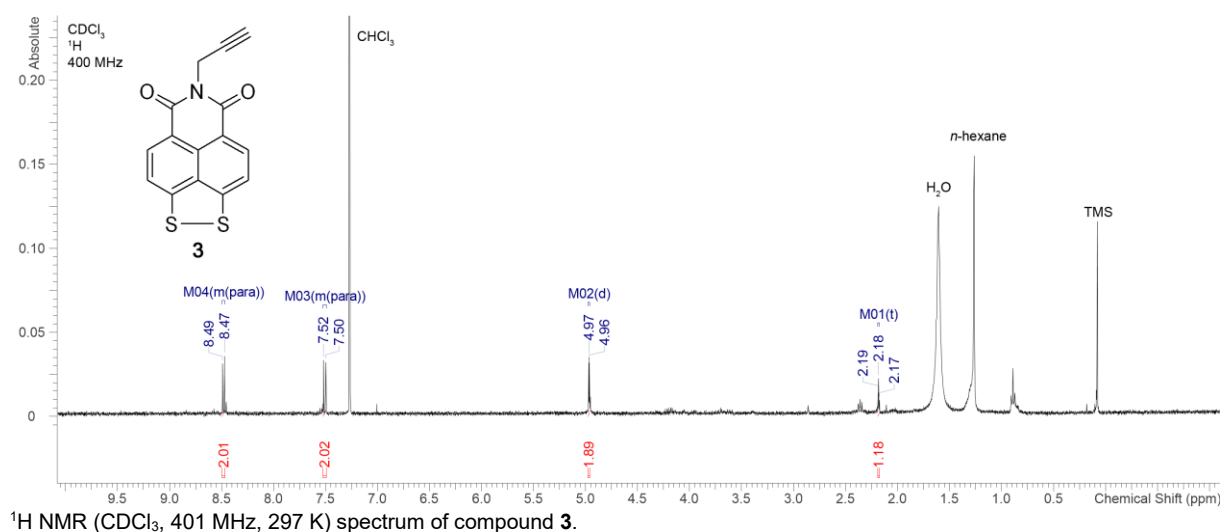
Compound **4** was characterized by  $^1\text{H}$  and  $^{13}\text{C}\{^1\text{H}\}$  NMR spectroscopy, FT IR spectroscopy, mass spectrometry, elemental analysis, and X-ray single crystal structure determination (Figure 1). Its  $^1\text{H}$  NMR spectrum (THF- $d_8$ , 400 MHz) shows two doublets at 8.53 and 8.43 ppm ( $^3J = 7.6$  Hz) for the aromatic protons, a doublet at 4.84 ppm ( $^4J = 2.4$  Hz) for the  $\text{CH}_2$  protons and a triplet at 2.54 ppm ( $^4J = 2.4$  Hz) for the terminal alkyne proton. The  $^{13}\text{C}\{^1\text{H}\}$  NMR spectrum exhibits only one signal at 208.3 ppm for the carbonyl ligands at room temperature as reported for similar hydrogenase mimicking complexes.<sup>[8,10]</sup> All assignments were confirmed by  $^1\text{H}, ^1\text{H}$ -COSY and  $^1\text{H}, ^{13}\text{C}\{^1\text{H}\}$ -HSQC NMR techniques. The IR spectrum of complex **4** exhibits three absorption bands for the terminal CO ligands at  $\nu(\text{C}\equiv\text{O}) = 2080$  (s), 2046 (s) and 2008 (s)  $\text{cm}^{-1}$  and two absorption bands for the imide moiety at  $\nu(\text{C}=\text{O}) = 1708$  (m), and 1667 (m)  $\text{cm}^{-1}$ . The mass spectrum (EI) shows the molecular ion and the peaks from the dissociation of the six CO ligands, successively.<sup>[11]</sup> The signals of the aromatic, imide and propargyl carbons were also detected (see Experimental section).

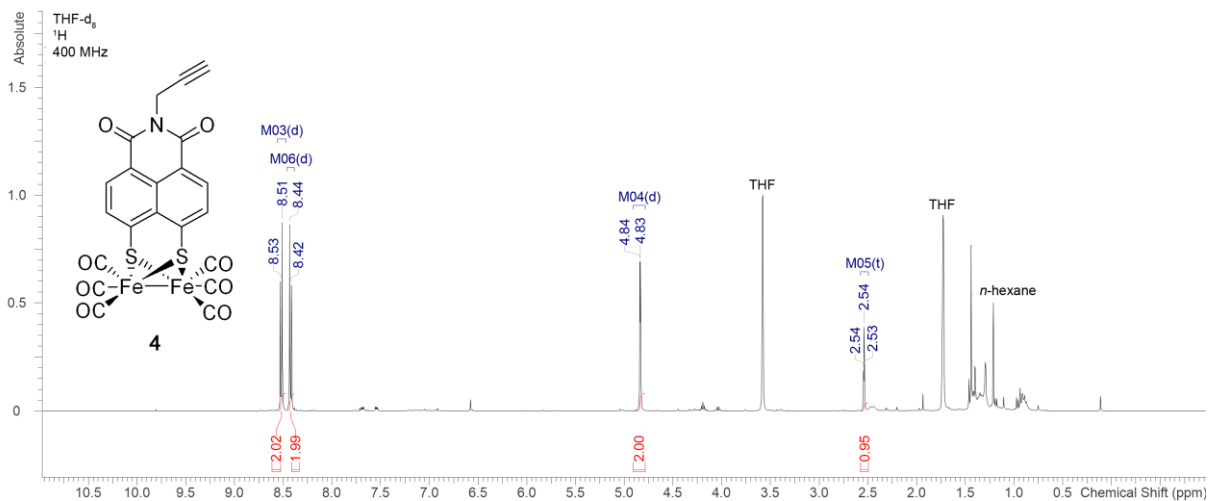
### $[\mu\text{-(HC}\equiv\text{CCH}_2\text{-NMI-S}_2\text{)}\text{Fe}_2(\text{CO})_5(\text{PPh}_3)]$ (**5**)

Compound **5** was analysed by  $^1\text{H}$  and  $^{31}\text{P}\{^1\text{H}\}$  NMR spectroscopy, Fourier Transformation IR spectroscopy, mass spectrometry and elemental analysis. Its  $^1\text{H}$  NMR spectrum (DCM- $d_2$ , 400 MHz) shows signals at 7.37-7.12 ppm assigned to the aryl protons of the triphenylphosphane ligand, additional to the signals observed for complex **4**. The  $^{31}\text{P}\{^1\text{H}\}$  NMR spectrum recorded at room temperature exhibits one singlet at 61.1 ppm from the triphenylphosphane ligand, as reported elsewhere for monosubstituted  $\text{PPh}_3$  containing hydrogenase mimics.<sup>[12]</sup>

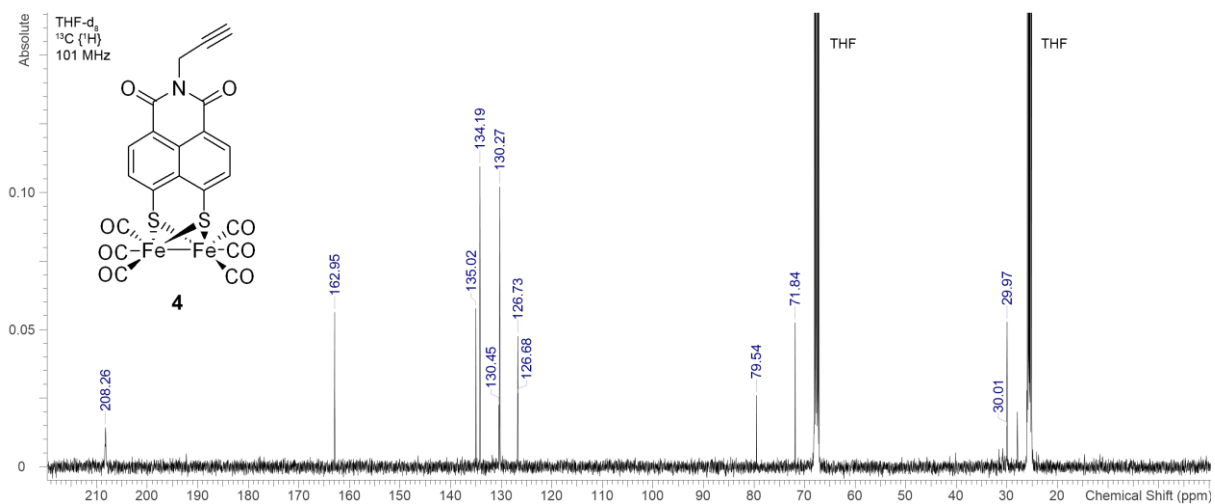
The IR spectrum of complex **5** includes three absorption bands for the terminal CO ligands at  $\nu(\text{C}\equiv\text{O}) = 2054$  (s), 1999 (s) and 1946 (s)  $\text{cm}^{-1}$  and two absorption bands for the imide moiety at  $\nu(\text{C}=\text{O}) = 1703$  (m), and 1662 (m)  $\text{cm}^{-1}$ . The lower CO frequencies of complex **5** compared with those in **4** are in good agreement with the data from the literature.<sup>[12,13]</sup> The small shift of the imide bands indicates an increase of electron density at the NMI moiety.<sup>[17]</sup> The mass spectrum (ESI) shows the protonated and the sodium adduct of the molecular ion.<sup>[8,14]</sup>

## NMR spectra

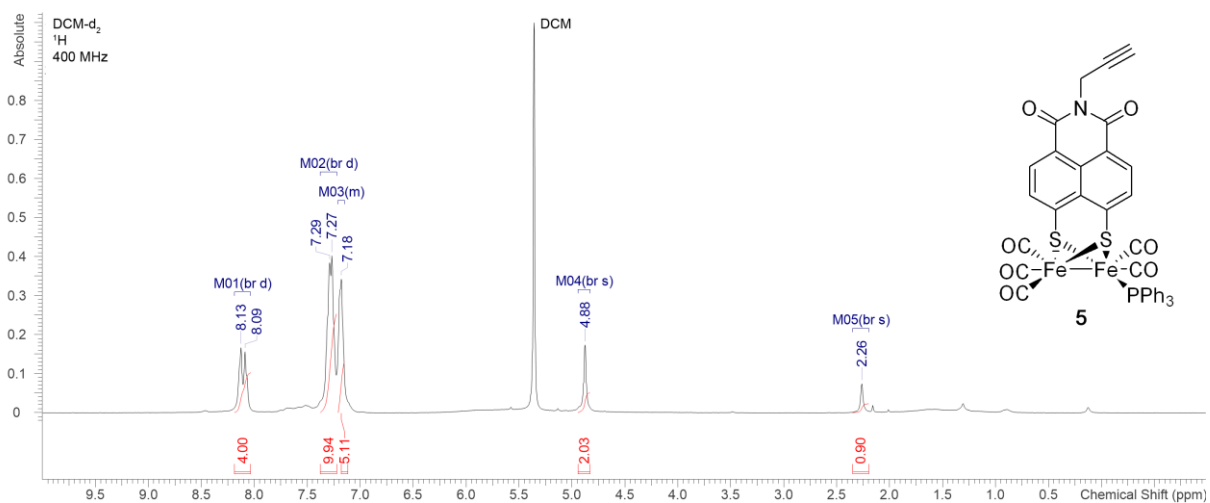




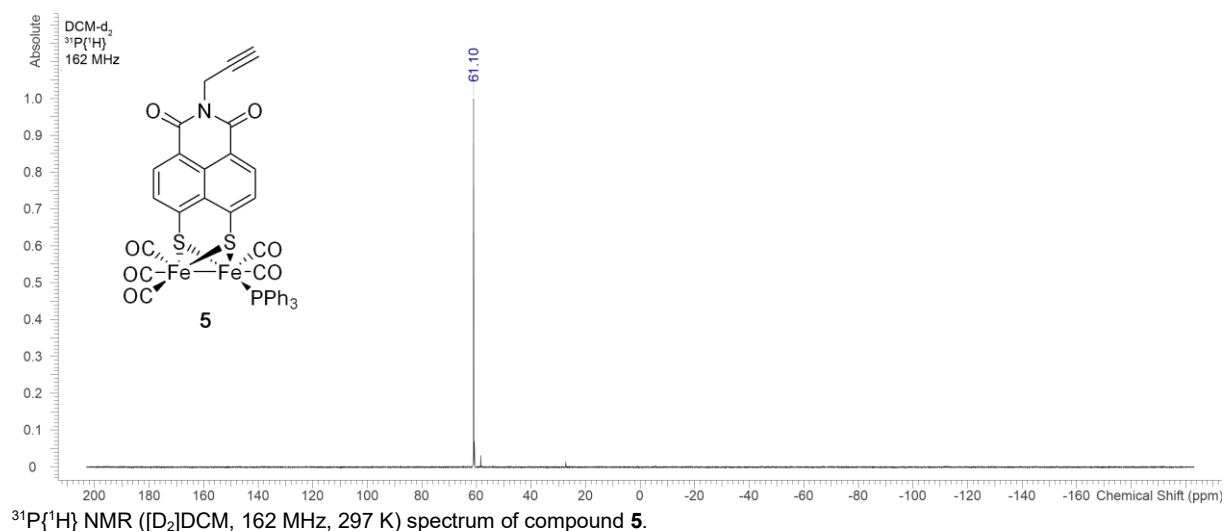
$^1\text{H}$  NMR ( $[\text{D}_8]\text{THF}$ , 400 MHz, 297 K) spectrum of compound **4**.



$^{13}\text{C}\{^1\text{H}\}$  NMR ( $[\text{D}_8]\text{THF}$ , 101 MHz, 297 K) spectrum of compound **4**.



$^1\text{H}$  NMR ( $[\text{D}_2]\text{DCM}$ , 400 MHz, 297 K) spectrum of compound **5**.



## Electrochemical measurements

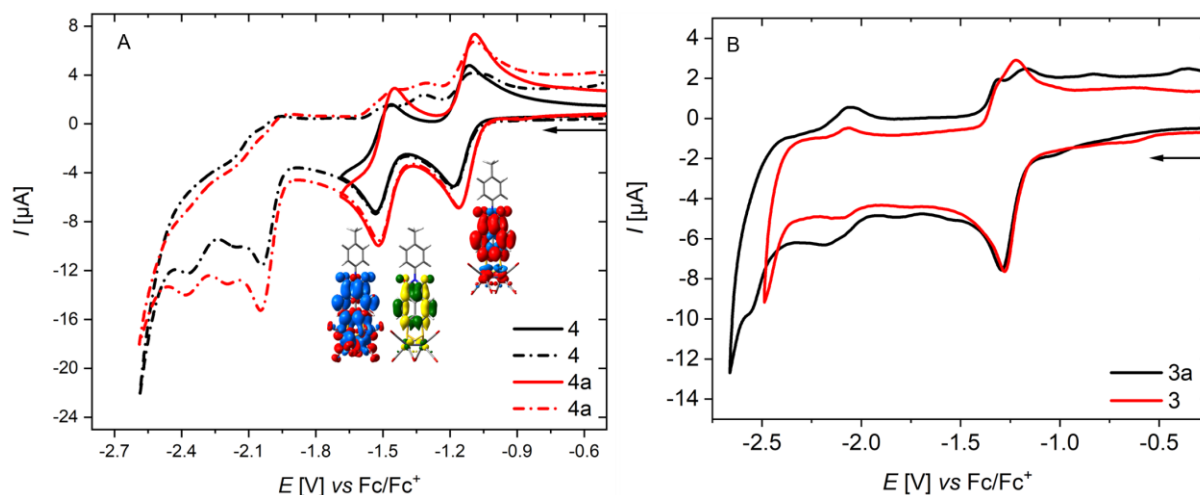


**Figure S1.** A) Cyclic voltammograms with different scan ranges of compound **4** and **4a** ( $c = 1$  mmol/L) in  $\text{N}_2$ -purged ACN/ $[\text{NBu}_4][\text{BF}_4]$  (0.1 mol/L) at RT. The arrow indicates the scan direction. The potential  $E$  is given in V and referenced to the  $\text{Fc}/\text{Fc}^+$  couple. For **4a**, the localization of the first reduction event is indicated by the spin density of the singly reduced doublet ground state as well as for the second reduction by the highest occupied molecular orbital (HOMO) of the doubly reduced singlet and the spin density of doubly reduced triplet species, respectively, as predicted by density functional theory. B) Cyclic voltammograms with different scan ranges of compound **3** and **3a** ( $c < 0.5$  mmol/L) in  $\text{N}_2$ -purged ACN/ $[\text{NBu}_4][\text{BF}_4]$  (0.1 mol/L) at RT. The arrow indicates the scan direction. The potential  $E$  is given in V and referenced to the  $\text{Fc}/\text{Fc}^+$  couple.

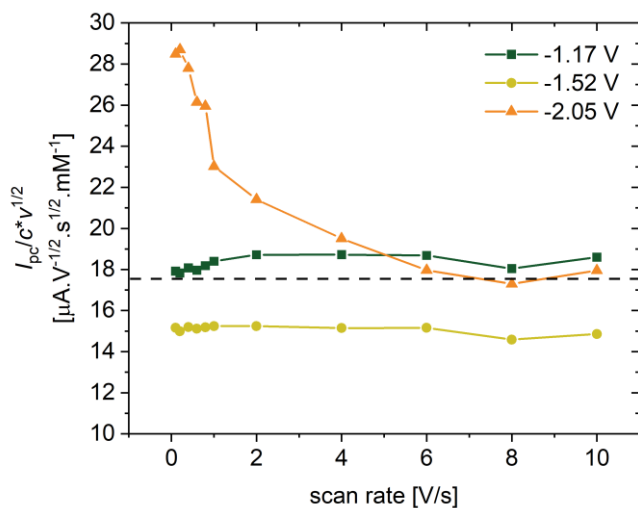


**Figure S2.** Current function of compound **4** at different cathodic potentials. Plotted for the reduction events at  $E = -1.17$  V,  $E = -1.52$  V and  $E = -2.05$  V. The dashed line indicates the expected value for a one electron process, calculated for various [FeFe] hydrogenase mimics ( $D \approx 9 \times 10^{-6} \text{ cm}^2 \text{ s}^{-1}$ ).<sup>[12b]</sup>

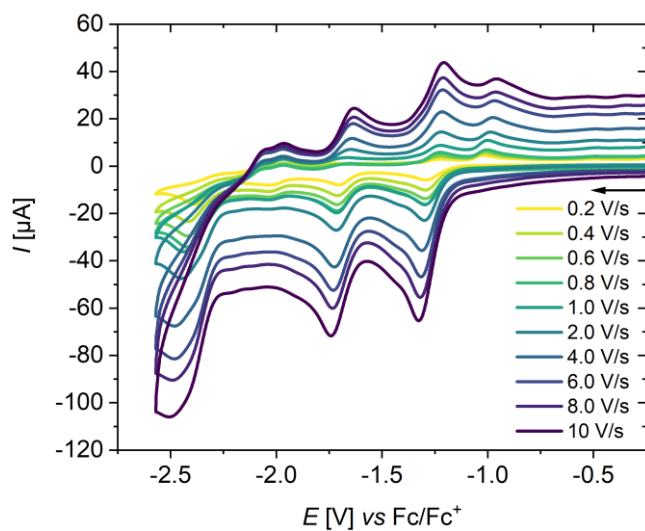


**Figure S3.** Cyclic voltammograms with different scan rates of compound **5** ( $c = 1$  mmol/L) in  $\text{N}_2$ -purged ACN/[NBu<sub>4</sub>][BF<sub>4</sub>] (0.1 mol/L) at RT. The arrow indicates the scan direction. The potential  $E$  is given in V and referenced to the Fc/Fc<sup>+</sup> couple.

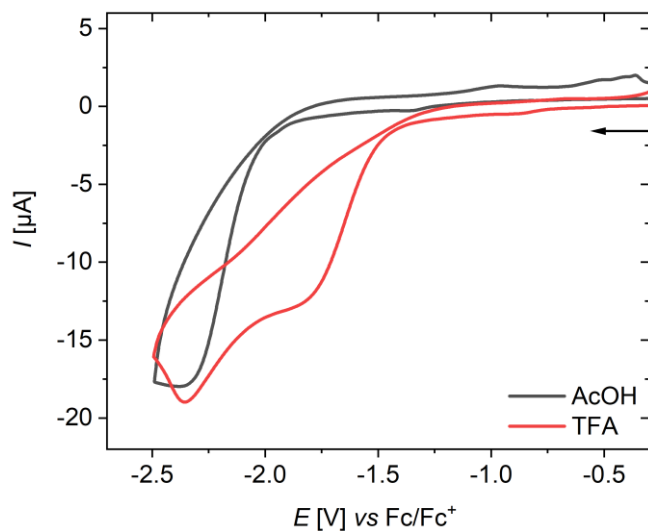


**Figure S4.** Cyclic voltammograms of AcOH and TFA in the absence of any catalyst. The arrow indicates the scan direction. The potential  $E$  is given in V and referenced to the  $\text{Fc}/\text{Fc}^+$  couple.

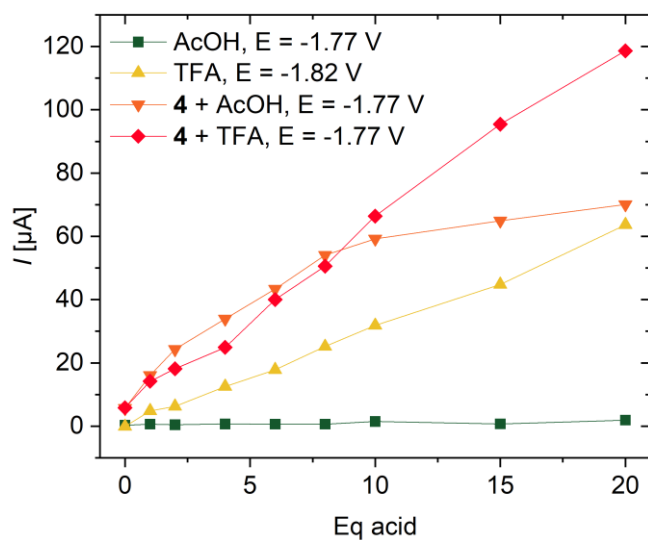


**Figure S5.** Dependence of the catalytic peak current for AcOH and TFA in the presence and absence of complex **4** ( $c = 1 \text{ mM}$ ).

## Spectroscopy - protonation study

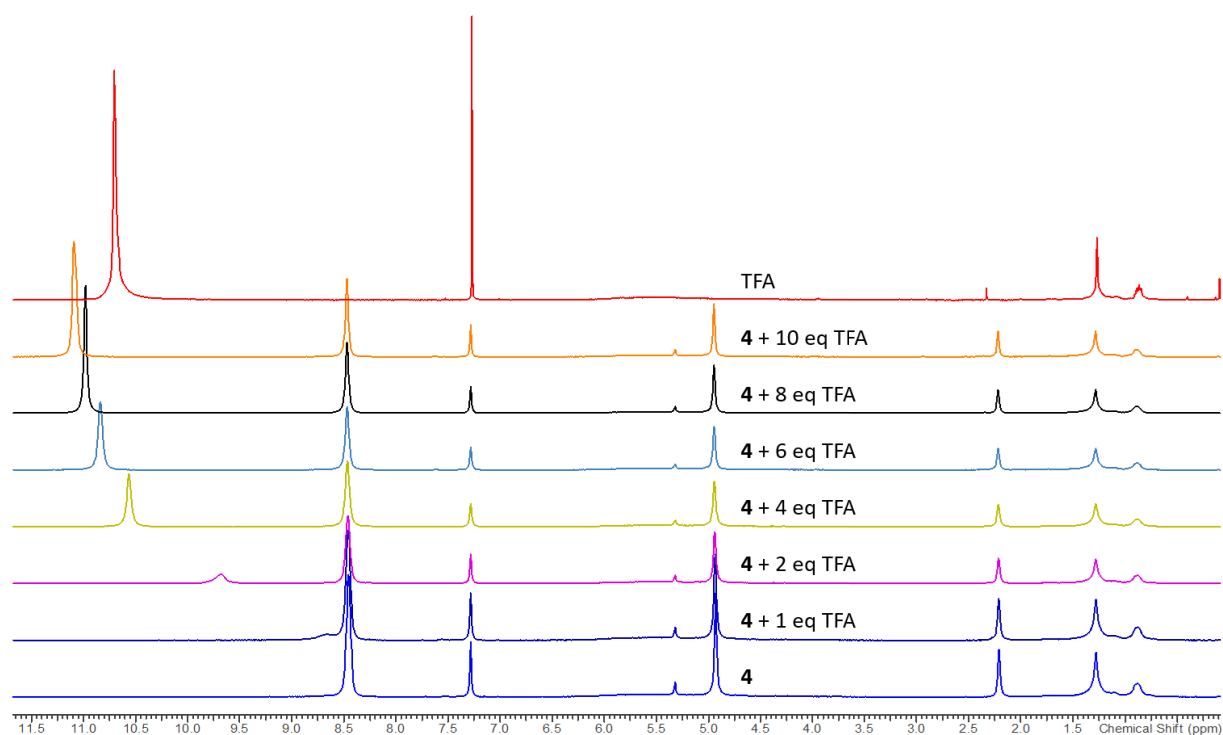


**Figure S6.** <sup>1</sup>H NMR (CDCl<sub>3</sub>, 401 MHz, 297 K) spectra of TFA (top) and compound **4** with various amounts of TFA.

The series spectra reveals interactions between complex **4** and TFA. With one equivalent of TFA a new signal appears at  $\delta = 8.7$  ppm, whose integral is growing, while downfield shifts are observed, when more TFA is added. This signal was assigned to the carboxylic proton of TFA. In comparison to the signal of TFA only at  $\delta = 10.7$  ppm, the new one is even further shifted downfield,  $\delta = 11.1$  ppm at ten equivalents. The carbonyl oxygen atoms at the imide moiety may be the predetermined vacancy where the protonation takes place.

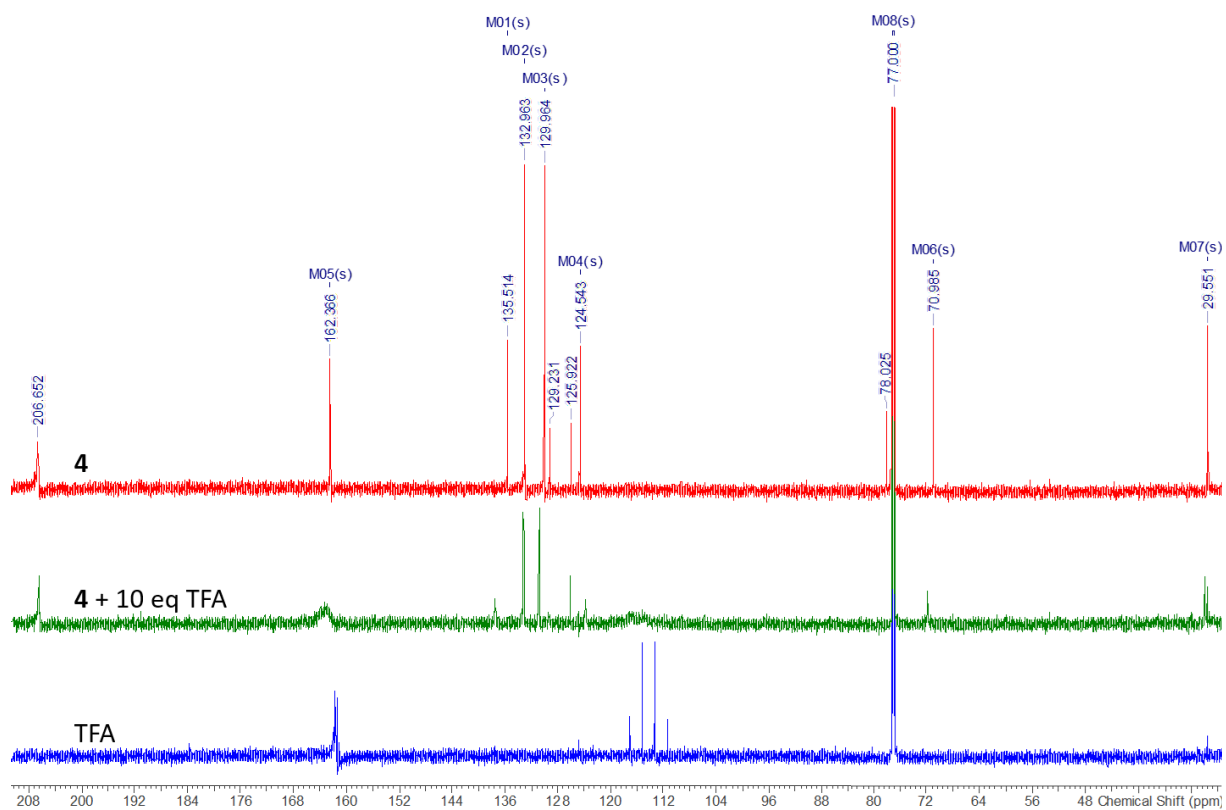


**Figure S7.**  $^{13}\text{C}$   $\{^1\text{H}\}$  NMR ( $\text{CDCl}_3$ , 151 MHz, 297 K) spectra of compound **4** (top), compound **4** with 10 eq TFA (centre) and TFA (bottom).

The signals, assigned to the imide carbonyl carbon atom at  $\delta = 162$  ppm as well as the carbon atom ( $\text{CF}_3$ ) at  $\delta = 114$  ppm are expanded from sharp signals to broad hills, which are slightly shifted downfield.

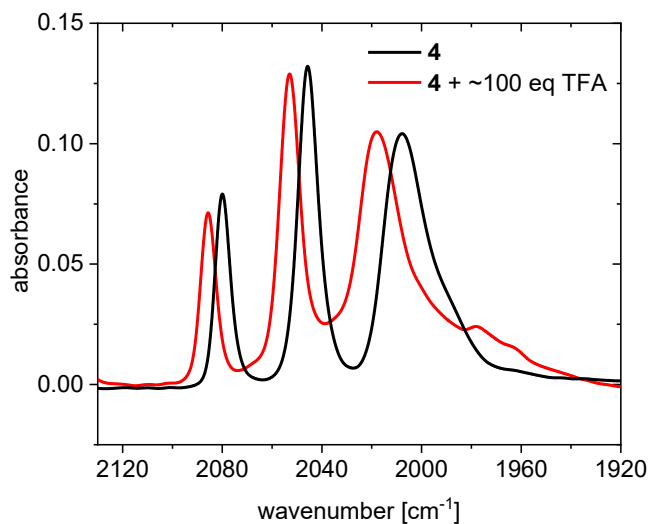


**Figure S8.** FT-IR spectra of complex **4** in the presence and absence of 100 eq TFA. The depicted wavenumber area shows the influence of added acid on the terminal CO ligands.



## IR spectroelectrochemical measurements

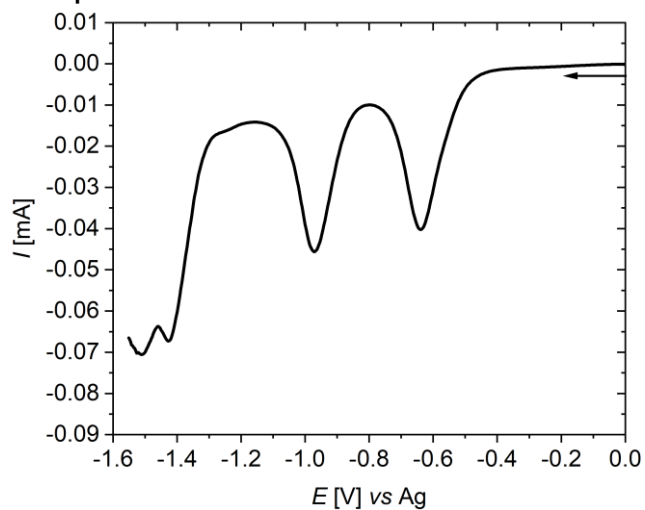


**Figure S9.** Voltammogram of compound **4** ( $c = 2$  mmol/L) during the SEC IR experiment with slow scan rate 2 mV/s. The arrow indicates the scan direction. The potential  $E$  is given in V and referenced to the Ag wire.

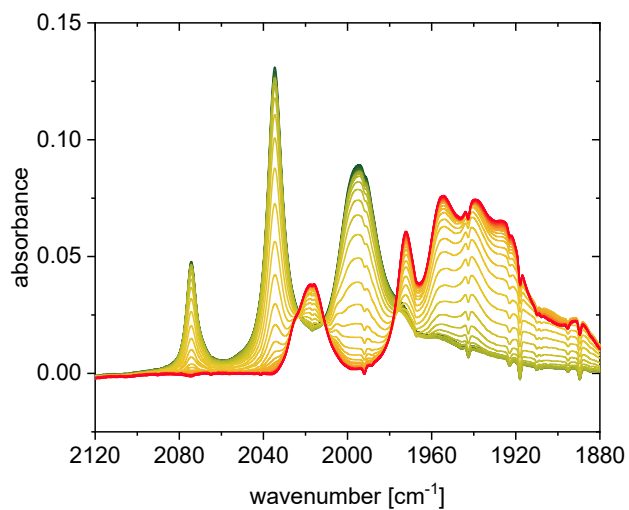


**Figure S10.** IR spectroelectrochemical measurements, during the first reduction of  $[\text{Fe}_2(\text{CO})_6(\mu\text{-SC}_3\text{H}_5\text{S})]$  (ACN,  $c = 2$  mmol/L).

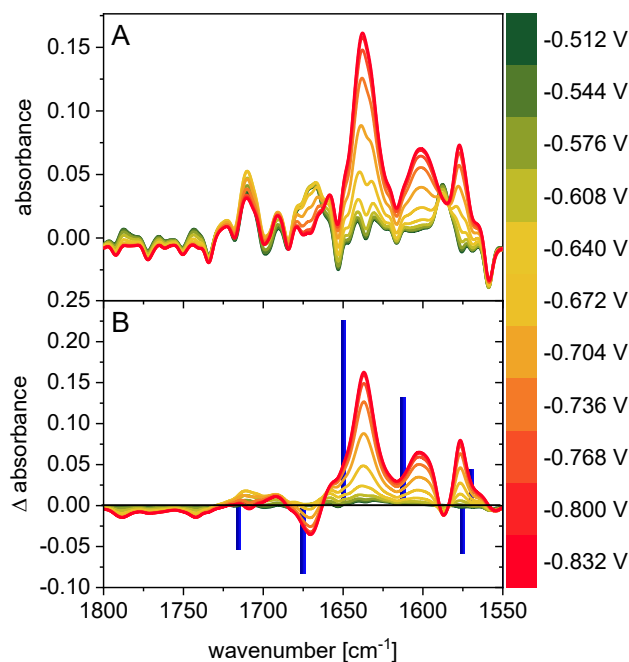


**Figure S11.** IR spectroelectrochemical measurements (A) and its differential spectra (B), during the first reduction of complex **4** (ACN,  $c = 2 \text{ mmol/L}$ ). The  $\Delta$  absorbance spectra were calculated by subtracting a spectrum recorded immediately before the reducing phase. The blue bars indicate the DFT calculated changes in the differential spectra.

## UV-Vis spectroelectrochemical measurements

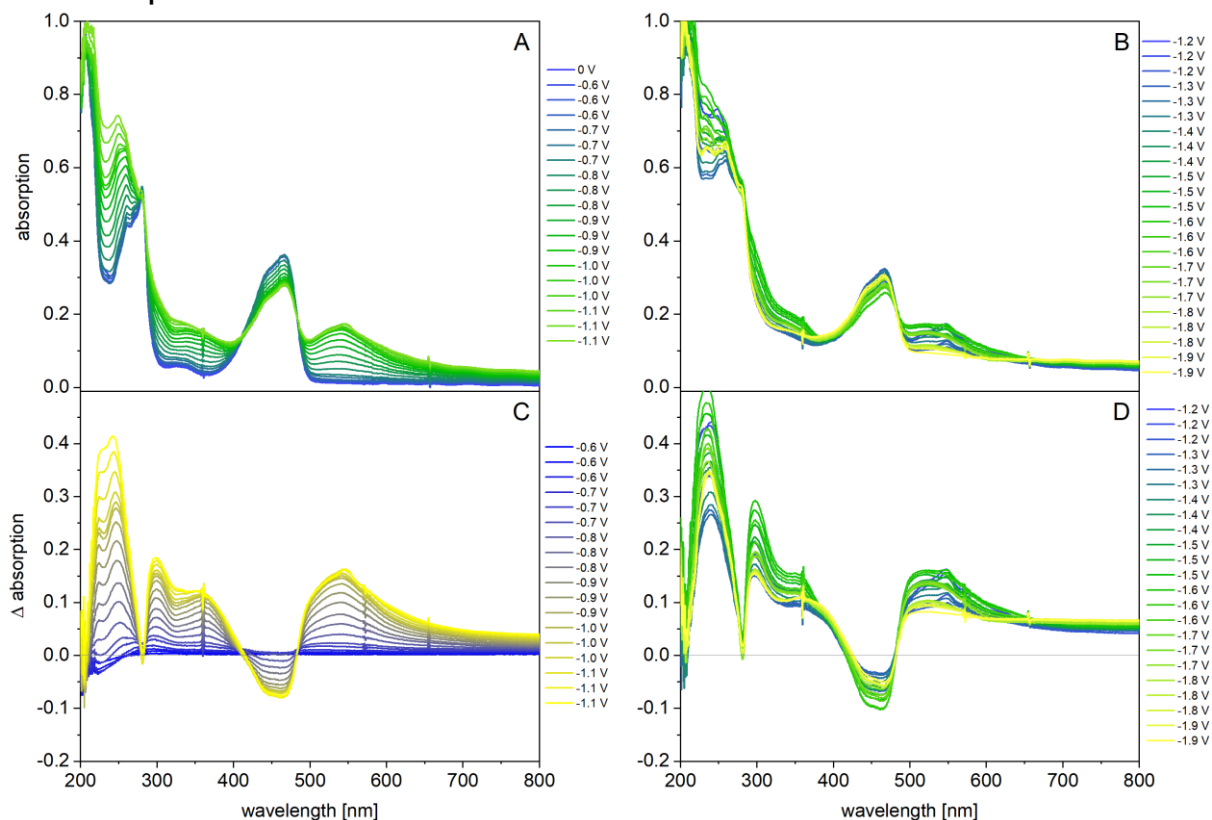


**Figure S12.** UV-Vis spectroelectrochemical measurements (A, B) and their differential spectra (C, D), respectively, during the first (A, C) and second (B, D) reduction of compound **3** (ACN,  $c = 1 \times 10^{-5} \text{ M}$ ). The  $\Delta$  absorbance spectra were calculated by subtracting a spectrum recorded immediately before the reducing phase.

## EPR measurements

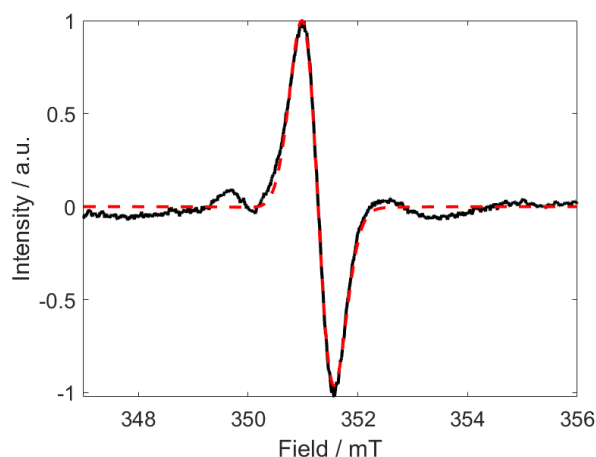


**Figure S13.** Chemical reduction of **3** ( $c = 1 \text{ mmol/L}$ ) with 1 (black line) equivalent of  $\text{Cp}^*_2\text{Co}$ . Simulation (dashed red line) carried out with EasySpin<sup>[1]</sup> to study properties of paramagnetic compound.

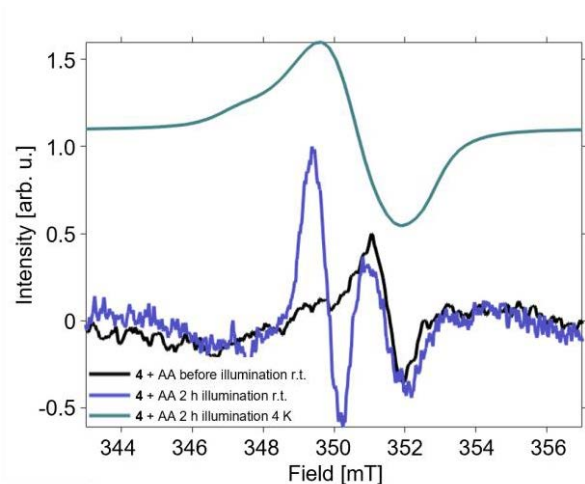


**Figure S14.** Photochemical reduction of **4** ( $c(\text{H cluster}) = 1 \times 10^{-3} \text{ M}$ ,  $c(\text{AA}) = 1 \times 10^{-2} \text{ M}$ ). Measurements before illumination at RT (black line), after 2 h illumination at RT (blue line) and after 2 h illumination at 4 K (turquoise line). Peak before illumination can be assigned to ascorbic acid. X-axis correction for measurement at low temperature carried out.

Photochemical reduction of **4** with ascorbic acid as the sacrificial electron donor (Figure S14) led to the detection of an organic radical ( $g = 2.0021$ ) as well as the ascorbic acid radical ( $g = 2.00$ ) at room temperature. Measurements at low temperature (4 K) resulted in the detection of an organic radical with a  $g$ -value of 2.0056. Thus, measurements under photocatalytic conditions at low temperatures do not indicate the formation of a catalytic active  $\text{Fe(I)-Fe(0)}$  species which would be EPR active.<sup>[15]</sup>

## Electrocatalysis

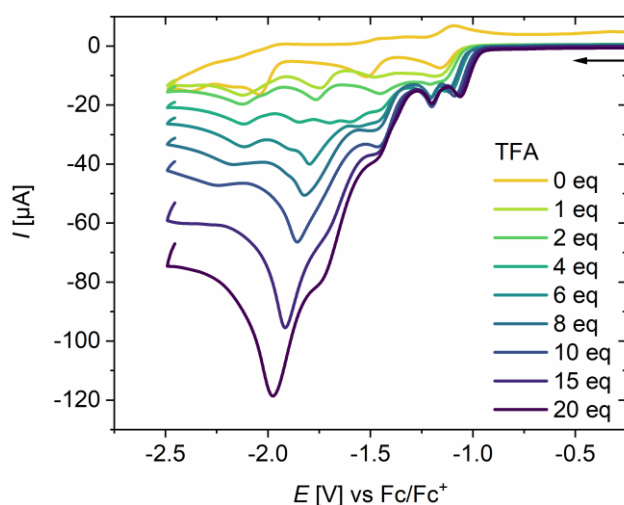


**Figure S15.** Cyclic voltammograms ( $v = 0.2$  V/s) of compound **4** ( $c = 1$  mmol/L) with various amounts of trifluoroacetic acid in  $\text{N}_2$ -purged  $\text{ACN}/[\text{NBu}_4][\text{BF}_4]$  (0.1 mol/L) at RT. The arrow indicates the scan direction. The potential  $E$  is given in V and referenced to the  $\text{Fc}/\text{Fc}^+$  couple.

Upon addition of TFA (Figure 7B, in particular if more than two equivalents are added) induces significant changes in the shape of the first reduction wave. Thus suggesting that TFA ( $\text{p}K_{\text{a}}^{\text{ACN}} = 12.7$ )<sup>[16]</sup> is strong enough to protonate the monoanionic complex **4**<sup>-</sup>, or even strong enough to protonate complex **4** in its non-reduced state.

To investigate this in more detail, protonation studies via  $^1\text{H}$  NMR,  $^{13}\text{C}\{^1\text{H}\}$  NMR and IR spectroscopy were performed. The series of  $^1\text{H}$  NMR spectra reveals interactions between complex **4** and TFA (Figure S6). A previous study shows strong hydrogen bond interactions between TFA and a  $\text{P}=\text{O}$  oxygen atom exhibiting a significant ion-pairing effect in  $[\text{Fe}_2(\text{CO})_6\{\mu\text{-S}(\text{CH}_2)_2(\text{R})\text{P}=\text{O}\}]$  ( $\text{R} = \text{Ph}, \text{Et}$ ) hydrogenase mimics.<sup>[17]</sup>

The  $^{13}\text{C}\{^1\text{H}\}$  NMR spectra (Figure S7) confirms this assumption. An additional support for the described effect of such hydrogen bonding is provided by IR spectroscopy, due to the highly sensitive technique and the high sensitivity of the terminal carbonyl wavenumbers to any alteration in the electron density of the majority of  $[\text{FeFe}]$  hydrogenase complexes.<sup>[17,18]</sup> In the presence of approximately 100 equivalents of TFA an average shift of  $\Delta\nu(\text{CO}) \approx 8$   $\text{cm}^{-1}$  to higher wavenumbers could be observed (Figure S8), indicating a slight decrease in electron density over the whole conjugated system. Based on these results, we assume a protonation at the imide oxygen atom.

The reduction of TFA (4 mM) in  $\text{ACN}-[n\text{-Bu}_4\text{N}][\text{BF}_4]$  without any catalyst takes place at around  $E = -1.82$  V vs  $\text{Fc}/\text{Fc}^+$  (Figure S4), which specifies that the increased current with increasing concentration of TFA is made up of a contribution of process II and the reduction of the free acid, as illustrated Figure S5.

## Quantum chemical simulations

All quantum chemical calculations determining structural and electronic properties of the free ligand **3** as well as of the [FeFe]-hydrogenase mimics **4** and **4a**, were performed using the Gaussian 16 program.<sup>[19]</sup> Fully relaxed equilibrium geometries of **3**, **4** and **4a** were obtained for the non-reduced singlet, the singly reduced doublet as well as for the doubly reduced species considering both singlet and triplet multiplicity at the density functional level of theory (DFT) by means of the B3LYP XC functional.<sup>[20]</sup> The def2-SVP basis set<sup>[21]</sup> was applied for all atoms. Subsequently, a vibrational analysis was carried out to verify that a minimum on the 3N-6 potential energy (hyper)surface (PES) was obtained for each redox species. To correct for the lack of anharmonicity and the approximate treatment of electron correlation, the harmonic frequencies were scaled by the factor 0.96.<sup>[22]</sup> Finally, the redox potentials were obtained based on the free energies of the redox species related to the first and second reduction events of **3**, **4** and **4a** with respect to the Fc/Fc<sup>+</sup> redox couple ( $\Delta E(\text{Fc}/\text{Fc}^+) = 4.75 \text{ eV}$ ,  $\Delta G(\text{Fc}/\text{Fc}^+) = 4.58 \text{ eV}$ ) – obtained at the same level of theory.<sup>[4]</sup>

Subsequently, excited state properties such as excitation energies, oscillator strengths and electronic characters for the lowest 150 excited states were calculated within the equilibrium structures of the respective redox state, *i.e.* non-reduced singlet, singly reduced doublet, doubly reduced singlet and doubly reduced triplet of **4** and **4a**, at the time-dependent DFT (TDDFT) level of theory. Therefore, the same XC functional and basis set were applied as for the preceding ground state calculations. Several computational as well as joint spectroscopic-theoretical studies on structurally related [FeFe]-hydrogenase mimics showed that this computational protocol enables an accurate prediction of ground and excited states properties with respect to experimental data, *e.g.* structural and electrochemical properties as well as with respect to UV-vis absorption.<sup>[23]</sup> In particular, a reliable description of the stability of various redox intermediates for hydrogenase mimics is of utmost importance to predict electrochemical processes, such as the localization of (multi-)redox events. State-of-the-art *ab initio* simulations, *e.g.* via CASPT2, RASPT2 and CCSD(T), show that B3LYP is able to predict such properties with reasonable accuracy for structurally related hydrogenase mimics,<sup>[24]</sup> while protonation of the active site may hamper an accurate description at the B3LYP level of theory.<sup>[25]</sup> Several theoretical studies addressing the photophysics of the active site of such [FeFe] hydrogenase models point to a dependency of the amount of exact exchange on the excited state properties of interest.<sup>[23e,26]</sup> However, in case of transition metal complexes, *e.g.* **4** and **4a**, a balanced description – as provided by the present computational setup – is essential that allows to investigate the excited state properties of the chromophore, of the catalytic center as well as the intramolecular interactions among both moieties.<sup>[27]</sup> The extraordinary rich photophysics and photochemistry of such transition metal complexes originates from the manifold of excited states involved, *i.e.*, metal-to-ligand charge transfer (MLCT), ligand-to-metal charge transfer (LMCT), ligand-to-ligand charge transfer (LLCT), intra-ligand charge transfer (ILCT), intra-ligand (IL) and metal-centered (MC) character. The present computational protocol, as provided by the present computational setup, is essential to assess the photophysics of transition metal complexes. Effects of interaction with a solvent (acetonitrile, THF:  $\epsilon = 35.688$ ,  $n = 1.3442$ ) were taken into account on the ground and excited states properties by the solute electron density (SMD) variant of the integral equation formalism of the polarizable continuum model.<sup>[28]</sup> All calculations were performed including D3 dispersion correction with Becke-Johnson damping.<sup>[29]</sup>

**Table S2.** Redox potentials ( $E_{\text{red1}}$  and  $E_{\text{red2}}$ ) associated to the first and second reduction (doubly reduced singlet vs. doubly reduced triplet) simulated at the B3LYP/def2-SVP level of theory for compound **3**. Redox potentials were obtained based on the driving forces of the reductive half-cell reaction ( $\Delta G$ ) against the Fc/Fc<sup>+</sup> redox couple ( $\Delta G = 4.58$  eV).

Non-reduced singlet ( $\Delta G = 0.00$ eV)	
Singly reduced doublet ( $\Delta G = -3.42$ eV, $E_{\text{red1}} = -1.72$ V)	
Doubly reduced singlet ( $\Delta G = -6.37$ eV, $E_{\text{red2}} = -1.40$ V)	
Doubly reduced triplet ( $\Delta G = -5.72$ eV, $E_{\text{red2}} = -1.72$ V)	

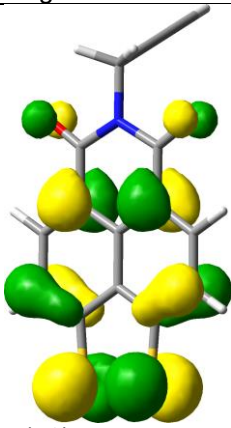
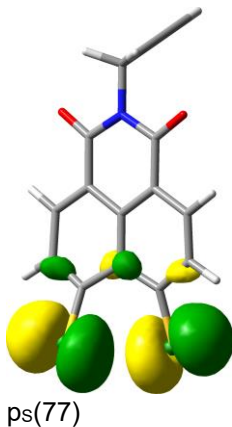
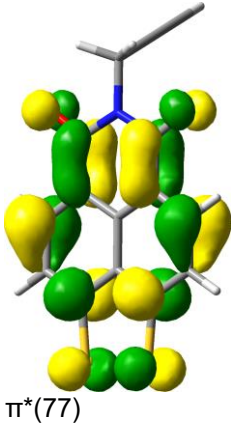
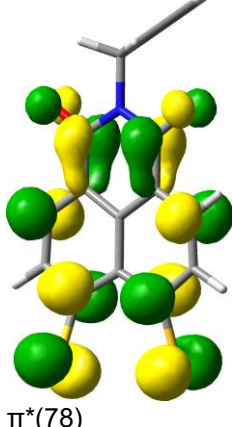
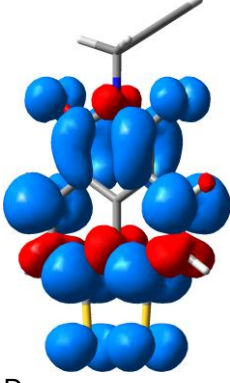
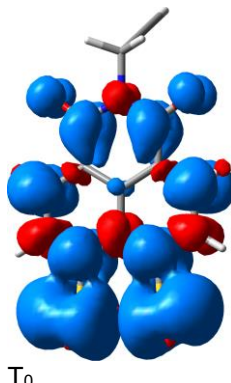
**Table S3.** Redox potentials ( $E_{\text{red1}}$  and  $E_{\text{red2}}$ ) associated to the first and second reduction (doubly reduced singlet vs. doubly reduced triplet) simulated at the B3LYP/def2-SVP level of theory for compound **4**. Redox potentials were obtained based on the driving forces of the reductive half-cell reaction ( $\Delta G$ ) against the Fc/Fc<sup>+</sup> redox couple ( $\Delta G = 4.58$  eV). Excited state properties such as electronic characters (MLCT: metal-to-ligand charge transfer, LMCT: ligand-to-metal charge transfer, MC: metal-centred, IL: intraligand), excitation energies ( $\Delta E$ ), excitation wavelengths ( $\lambda$ ), oscillator strengths ( $f$ ) and spin contamination are given for selected electronic excitations contributing to the electronic absorption spectrum of compound **4** in its non-reduced singlet, singly reduced doublet, doubly reduced singlet and doubly reduced triplet redox states.

Non-reduced singlet ( $\Delta G = 0.00$ eV)					
State	Character	$\Delta E / \text{eV}$	$\lambda / \text{nm}$	$f$	$\langle s^2 \rangle$
S <sub>1</sub>	MLCT	2.47	501	0.0005	0.00
S <sub>2</sub>	MC	2.81	441	0.0114	0.00
S <sub>7</sub>	IL/MLCT	3.13	396	0.3371	0.00
S <sub>9</sub>	IL/MLCT	3.33	372	0.1966	0.00
S <sub>10</sub>	MC	3.34	371	0.1406	0.00
S <sub>15</sub>	LMCT	3.54	350	0.0023	0.00
Singly reduced doublet ( $\Delta G = -3.26$ eV, $E_{\text{red1}} = -1.16$ V)					
State	Character	$\Delta E / \text{eV}$	$\lambda / \text{nm}$	$f$	$\langle s^2 \rangle$
D <sub>1</sub>	LMCT	0.78	1594	0.0014	0.78
D <sub>4</sub>	LMCT	1.84	674	0.1468	0.81
D <sub>9</sub>	IL	2.43	510	0.2763	0.88
D <sub>35</sub>	IL	3.20	387	0.1654	1.08
Doubly reduced singlet ( $\Delta G = -5.87$ eV, $E_{\text{red2}} = -1.54$ V)					
State	Character	$\Delta E / \text{eV}$	$\lambda / \text{nm}$	$f$	$\langle s^2 \rangle$
S <sub>1</sub>	LMCT	0.68	1833	0.0015	0.00
S <sub>5</sub>	LMCT	2.23	557	0.4897	0.00
S <sub>7</sub>	LMCT	2.33	533	0.0437	0.00
S <sub>13</sub>	MC	2.82	440	0.0650	0.00
Doubly reduced triplet ( $\Delta G = -5.99$ eV, $E_{\text{red2}} = -1.44$ V)					
State	Character	$\Delta E / \text{eV}$	$\lambda / \text{nm}$	$f$	$\langle s^2 \rangle$
T <sub>4</sub>	MLCT	1.78	696	0.0004	2.13
T <sub>8</sub>	LMCT	2.11	589	0.0859	2.12
T <sub>15</sub>	IL/MC	2.47	503	0.1718	2.51
T <sub>41</sub>	LMCT	3.19	388	0.1192	2.14

**Table S4.** Redox potentials ( $E_{\text{red1}}$  and  $E_{\text{red2}}$ ) associated to the first and second reduction (doubly reduced singlet vs. doubly reduced triplet) simulated at the B3LYP/def2-SVP level of theory for compound **4a**. Redox potentials were obtained based on the driving forces of the reductive half-cell reaction ( $\Delta G$ ) against the Fc/Fc<sup>+</sup> redox couple ( $\Delta G = 4.58$  eV). Excited state properties such as electronic characters (MLCT: metal-to-ligand charge transfer, LMCT: ligand-to-metal charge transfer, MC: metal-centred, IL: intraligand), excitation energies ( $\Delta E$ ), excitation wavelengths ( $\lambda$ ), oscillator strengths ( $f$ ) and spin contamination are given for selected electronic excitations contributing to the electronic absorption spectrum of compound **4a** in its non-reduced singlet, singly reduced doublet, doubly reduced singlet and doubly reduced triplet redox states.

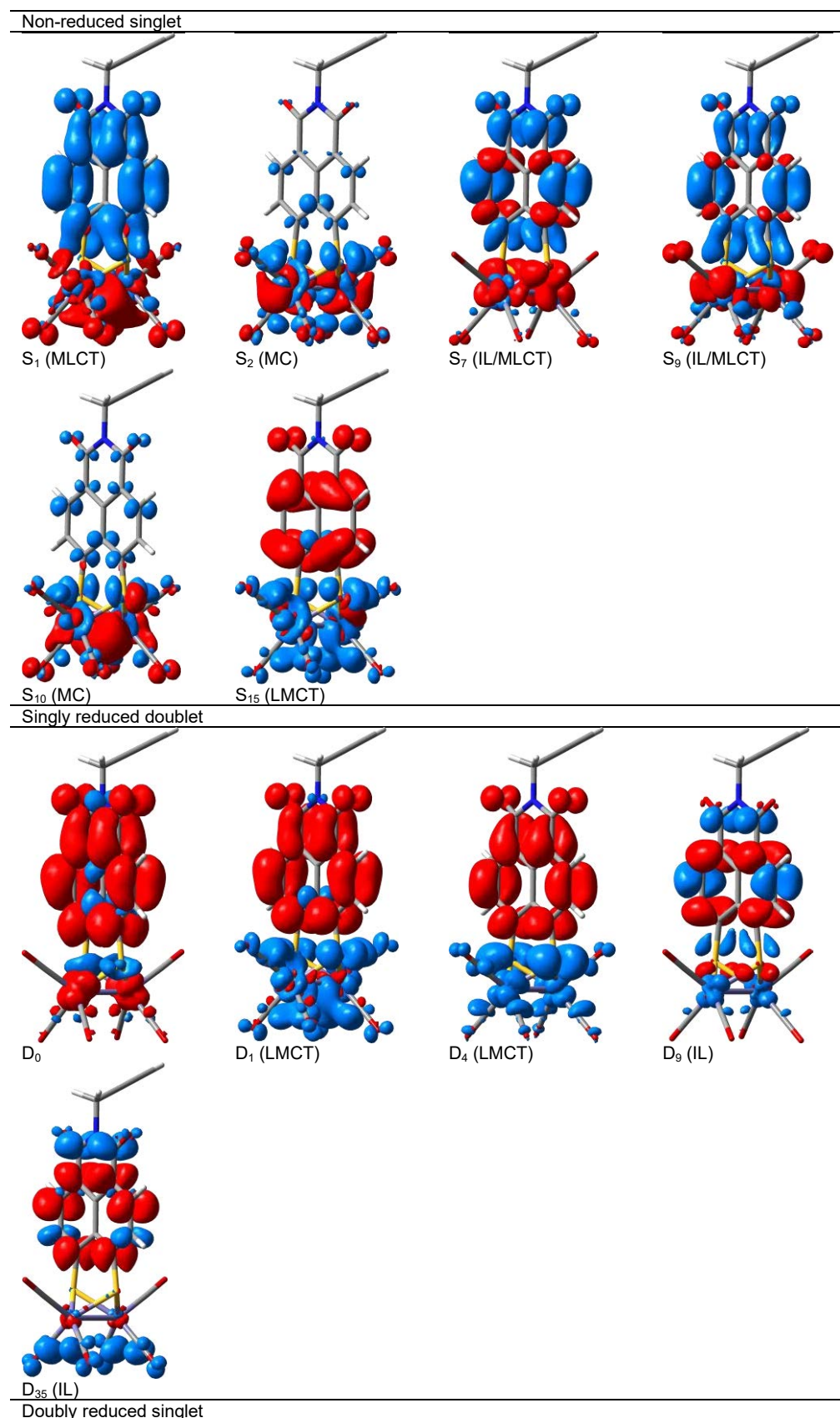
Non-reduced singlet ( $\Delta G = 0.00$ eV)					
State	Character	$\Delta E$ / eV	$\lambda$ / nm	$f$	$\langle S^2 \rangle$
S <sub>1</sub>	MLCT	2.50	496	0.0006	0.00
S <sub>2</sub>	MC	2.81	442	0.0112	0.00
S <sub>7</sub>	IL/MLCT	3.14	394	0.3887	0.00
S <sub>10</sub>	IL/MLCT	3.34	371	0.1884	0.00
S <sub>11</sub>	MC	3.35	370	0.1361	0.00
S <sub>16</sub>	LMCT	3.52	352	0.0027	0.00
Singly reduced doublet ( $\Delta G = -3.23$ eV, $E_{\text{red1}} = -1.25$ V)					
State	Character	$\Delta E$ / V	$\lambda$ / nm	$f$	$\langle S^2 \rangle$
D <sub>1</sub>	LMCT	0.75	1662	0.0013	0.78
D <sub>4</sub>	LMCT	1.82	682	0.1604	0.81
D <sub>9</sub>	IL	2.43	510	0.2963	0.88
D <sub>38</sub>	IL	3.21	386	0.1787	1.08
Doubly reduced singlet ( $\Delta G = -5.81$ eV, $E_{\text{red2}} = -1.63$ V)					
State	Character	$\Delta E$ / eV	$\lambda$ / nm	$f$	$\langle S^2 \rangle$
S <sub>1</sub>	LMCT	0.66	1890	0.0014	0.00
S <sub>5</sub>	LMCT	2.21	560	0.5177	0.00
S <sub>15</sub>	MC	2.81	441	0.0600	0.00
Doubly reduced triplet ( $\Delta G = -5.95$ eV, $E_{\text{red2}} = -1.54$ V)					
State	Character	$\Delta E$ / eV	$\lambda$ / nm	$f$	$\langle S^2 \rangle$
T <sub>8</sub>	LMCT	2.09	594	0.1012	2.12
T <sub>13</sub>	IL/MC	2.45	505	0.1418	2.42
T <sub>15</sub>	IL/MC	2.46	504	0.0847	2.67
T <sub>57</sub>	LMCT	3.43	362	0.0006	2.35

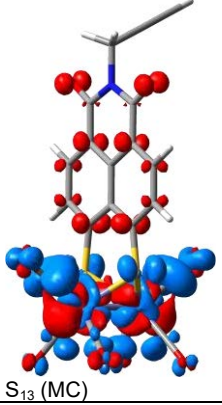
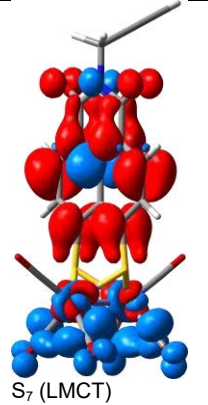
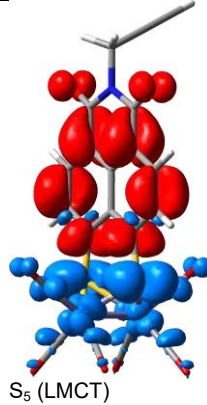
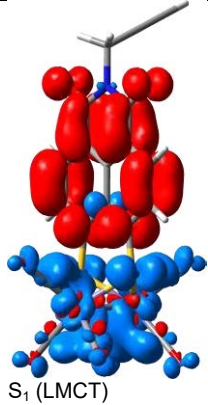
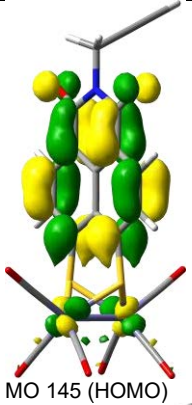
**Table S5.** Visualisation of reduction events based on frontier orbitals (HOMO: highest occupied molecular orbital; LUMO: lowest unoccupied molecular orbital) of closed-shell species, i.e. non-reduced singlet and doubly reduced singlet, as well as on spin densities of open-shell species, i.e. singly reduced doublet and doubly reduced triplet, of compound **3**.

	Redox state					
	Non-reduced singlet	Singly doublet	reduced	Doubly singlet	reduced	Doubly Triplet
HOMO	 $\pi(76)$	-		 $ps(77)$	-	
LUMO	 $\pi^*(77)$	-		 $\pi^*(78)$	-	
Spin density	-	 $D_0$	-	 $T_0$	-	



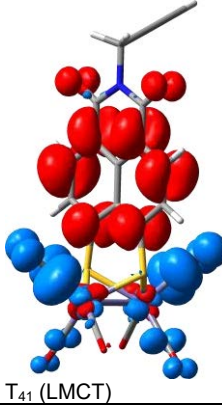
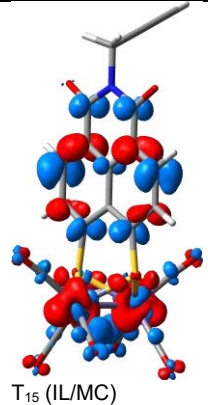
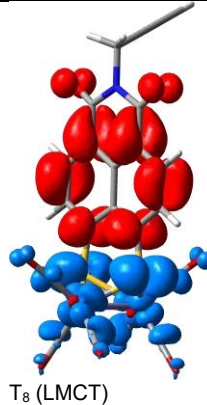
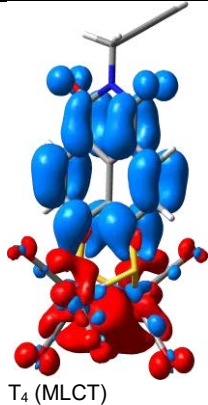
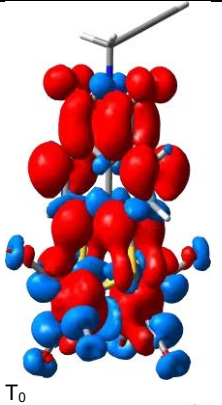
**Table S6.** Electronic characters (MLCT: metal-to-ligand charge transfer, LMCT: ligand-to-metal charge transfer, MC: metal-centred, IL: intraligand) of selected electronic excitations contributing to the electronic absorption spectrum of compound **4** in its non-reduced singlet, singly reduced doublet, doubly reduced singlet and doubly reduced triplet redox states visualised by charge density differences; charge transfer takes place from red to blue. Reduction sites are illustrated by frontier orbitals (doubly reduced singlet) or spin densities (doublet and triplet ground state,  $D_0$  and  $T_0$ ).



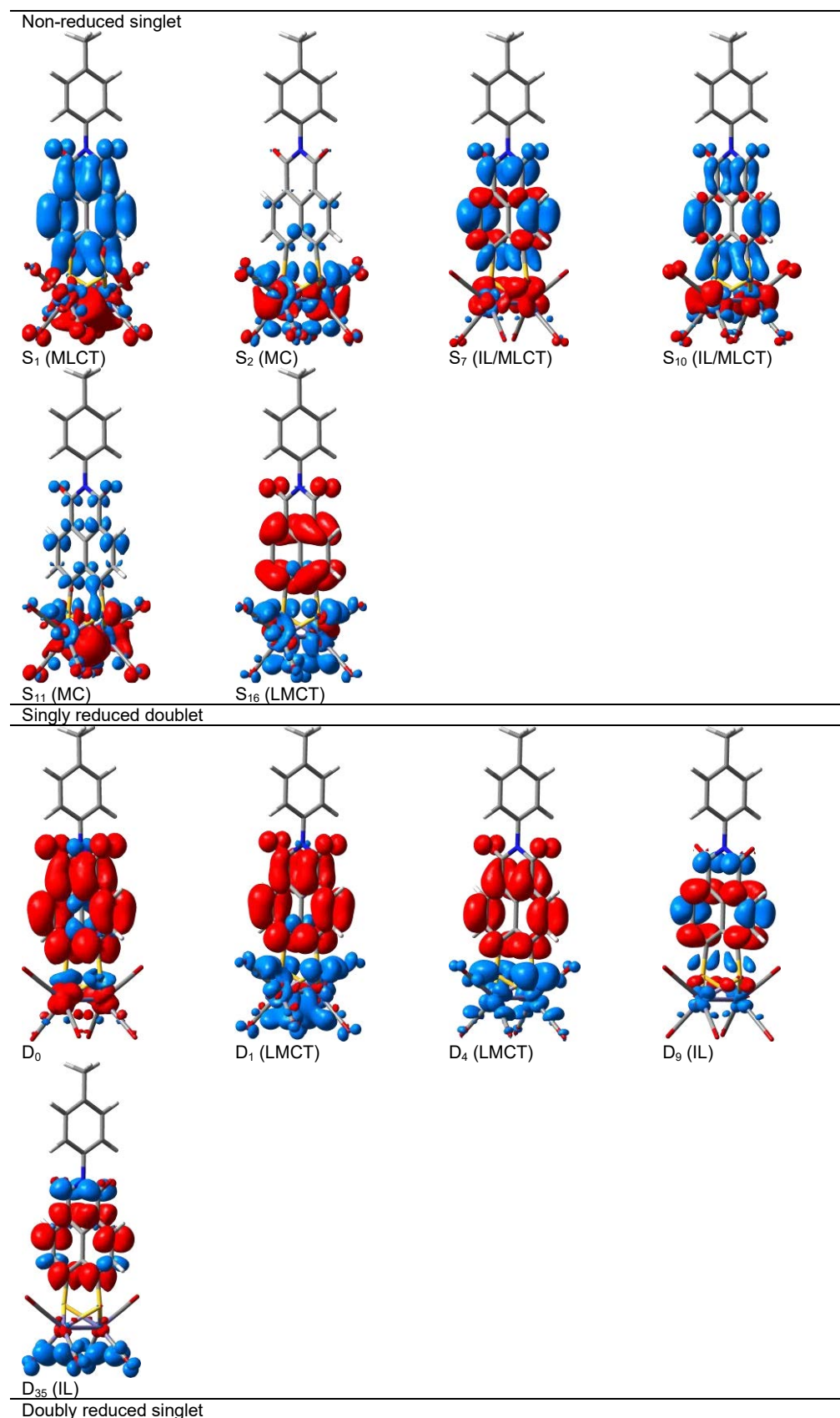


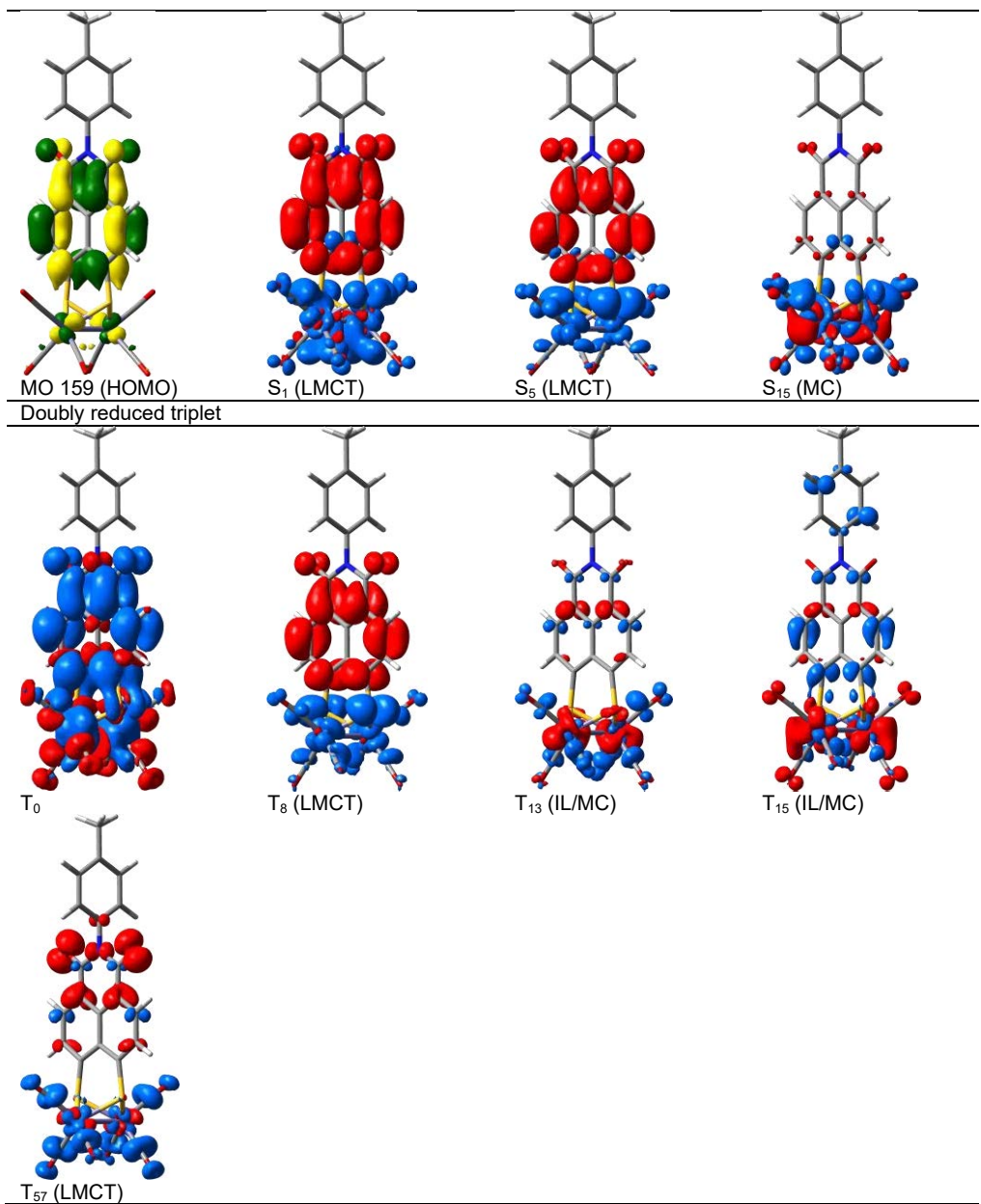
Doubly reduced triplet

---



**Table S7.** Electronic characters (MLCT: metal-to-ligand charge transfer, LMCT: ligand-to-metal charge transfer, MC: metal-centred, IL: intraligand) of selected electronic excitations contributing to the electronic absorption spectrum of compound **4a** in its non-reduced singlet, singly reduced doublet, doubly reduced singlet and doubly reduced triplet redox states visualised by charge density differences; charge transfer takes place from red to blue. Reduction sites are illustrated by frontier orbitals (doubly reduced singlet) or spin densities (doublet and triplet ground state,  $D_0$  and  $T_0$ ).

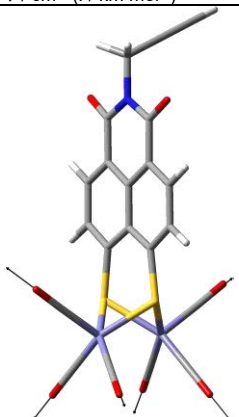
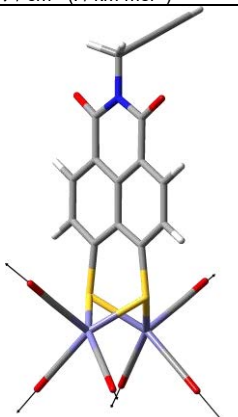
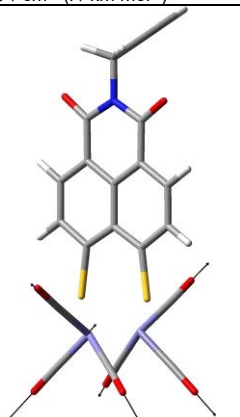
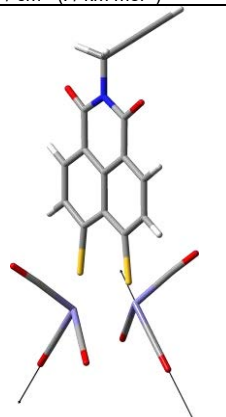
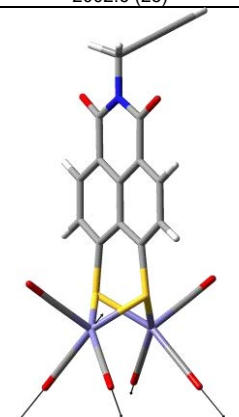
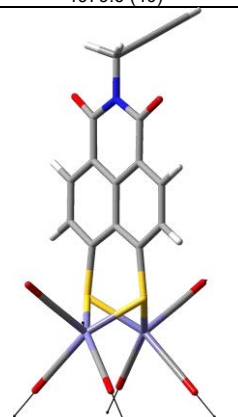
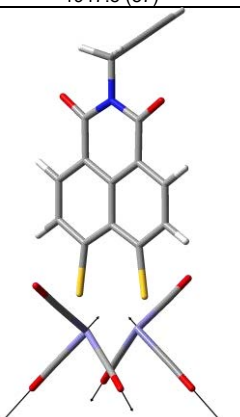
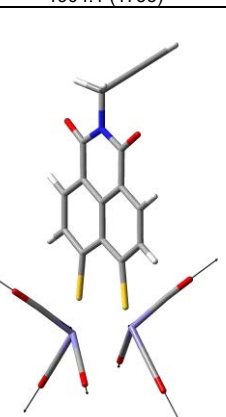
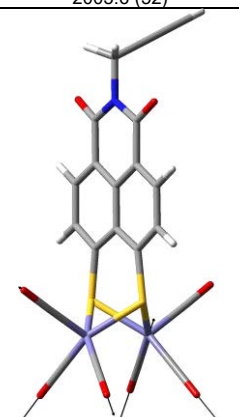
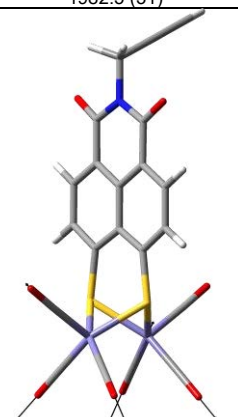
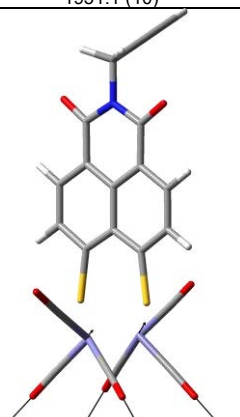
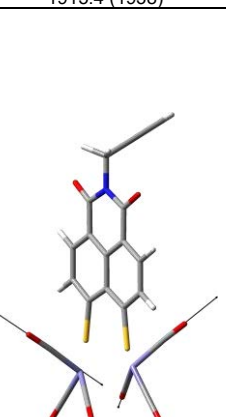




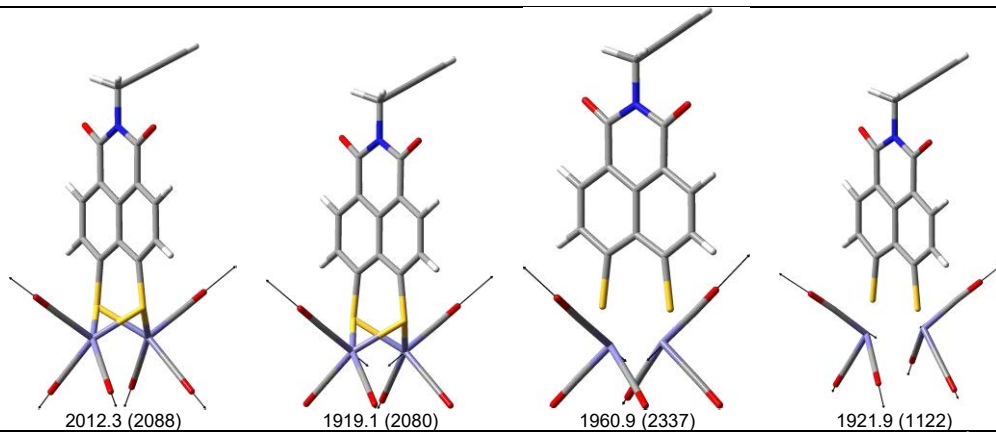
**Table S8.** Selected structural properties, such as Fe-Fe distance ( $d_{\text{FeFe}}$ ), Fe1-S1 and Fe2-S2 bond lengths ( $d_{\text{FeS}}$ ) and Fe-Fe-naphthalene dihedral angle ( $\delta$ ), as simulated for the non-reduced singlet, the singly reduced doublet and the doubly reduced singlet and triplet species of the hydrogenase mimics **4** and **4a**.

	Non-reduced singlet			Singly reduced doublet			Doubly reduced singlet			Doubly reduced triplet		
	$d_{\text{FeFe}} / \text{\AA}$	$d_{\text{FeS}} / \text{\AA}$	$\delta / ^\circ$	$d_{\text{FeFe}} / \text{\AA}$	$d_{\text{FeS}} / \text{\AA}$	$\delta / ^\circ$	$d_{\text{FeFe}} / \text{\AA}$	$d_{\text{FeS}} / \text{\AA}$	$\delta / ^\circ$	$d_{\text{FeFe}} / \text{\AA}$	$d_{\text{FeS}} / \text{\AA}$	$\delta / ^\circ$
<b>4</b>	2.4710	2.2895 2.2908	90.1	2.4816	2.2956 2.2959	90.1	2.4925	2.3100 2.3097	90.0	2.7176	2.3361 2.3360	90.0
<b>4a</b>	2.4762	2.2899 2.2889	90.0	2.4813	2.2965 2.2963	90.0	2.4927	2.3100 2.3098	90.0	2.7182	2.3360 2.3359	90.0

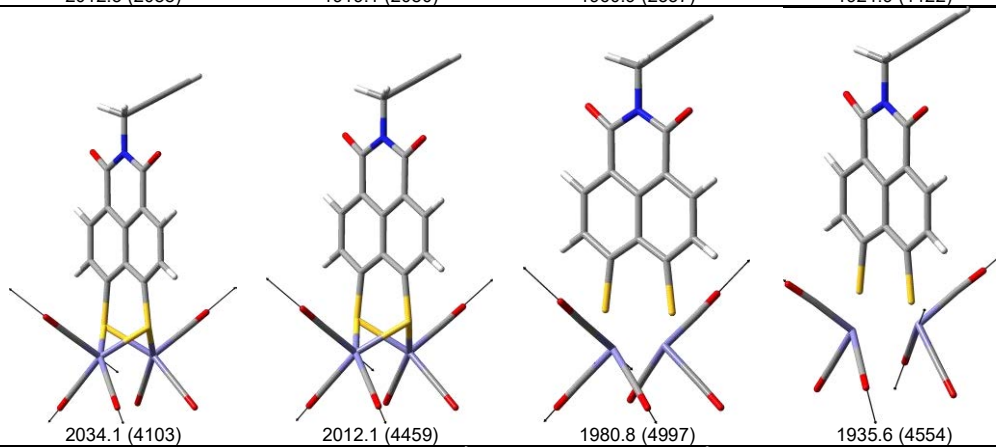
**Table S9.** Simulated infrared intensities of the six -CO vibrational normal modes of **4** within the non-reduced singlet, the singly reduced doublet and the doubly reduced singlet and triplet species. Wavenumbers are scaled by a factor of 0.96, infrared intensities are given in parenthesis. The respective normal modes are illustrated based on displacement vectors.

	<b>4</b>			
	Non-reduced singlet $\tilde{\nu} / \text{cm}^{-1}$ ( $I / \text{km}\cdot\text{mol}^{-1}$ )	Singly reduced doublet $\tilde{\nu} / \text{cm}^{-1}$ ( $I / \text{km}\cdot\text{mol}^{-1}$ )	Doubly reduced singlet $\tilde{\nu} / \text{cm}^{-1}$ ( $I / \text{km}\cdot\text{mol}^{-1}$ )	Doubly reduced triplet $\tilde{\nu} / \text{cm}^{-1}$ ( $I / \text{km}\cdot\text{mol}^{-1}$ )
Mode 104	 2002.6 (23)	 1979.6 (40)	 1947.8 (87)	 1904.1 (1733)
Mode 105	 2005.6 (52)	 1982.5 (31)	 1951.1 (10)	 1915.4 (1938)
Mode 106	 2011.6 (2252)	 1989.0 (2567)	 1958.9 (2943)	 1919.6 (2796)

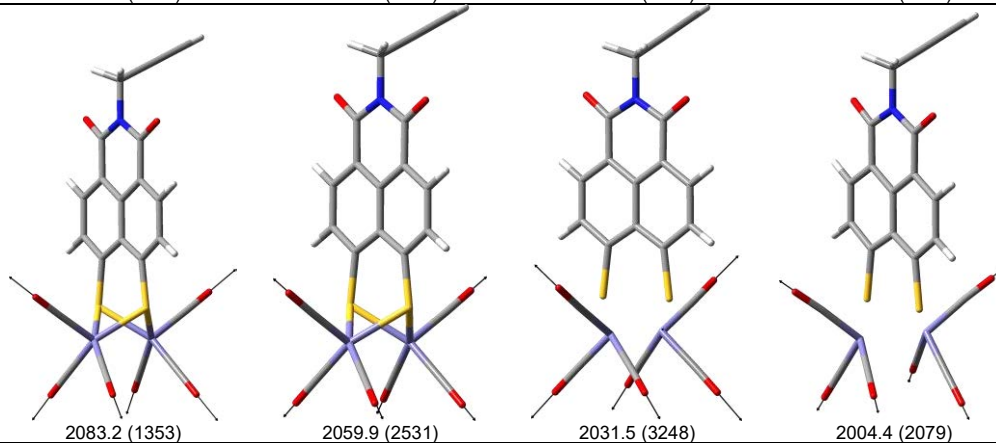
Mode 107



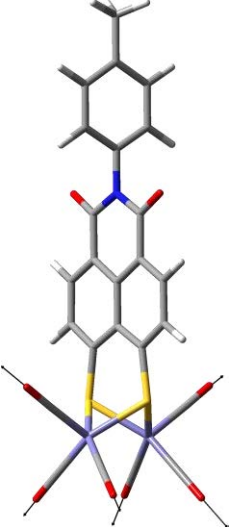
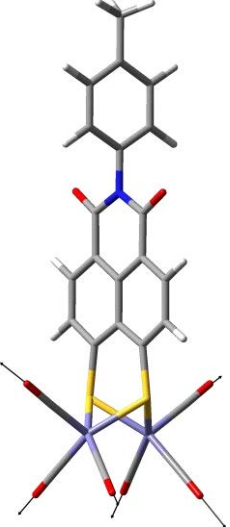
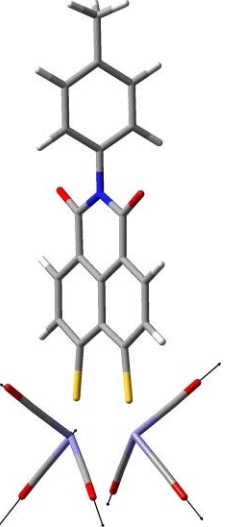
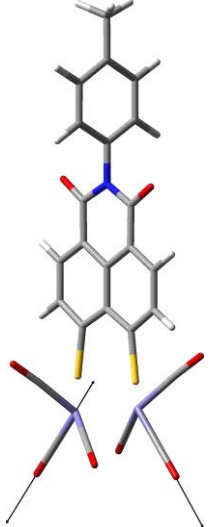
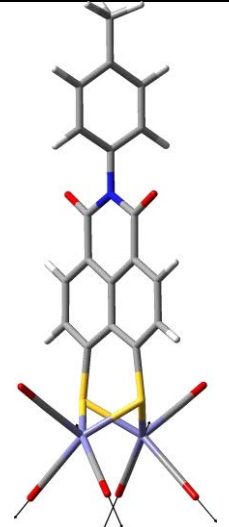
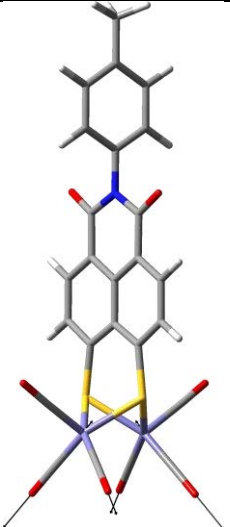
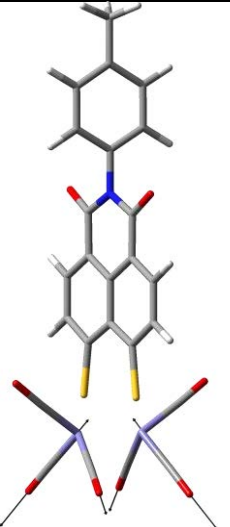
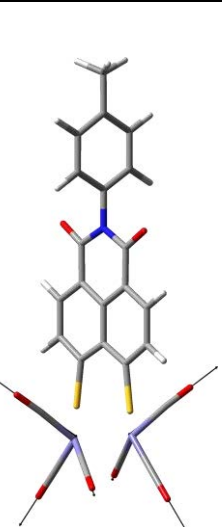
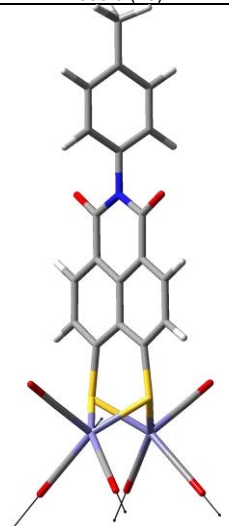
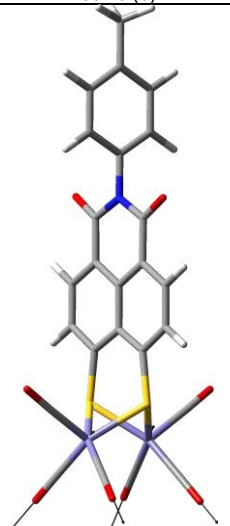
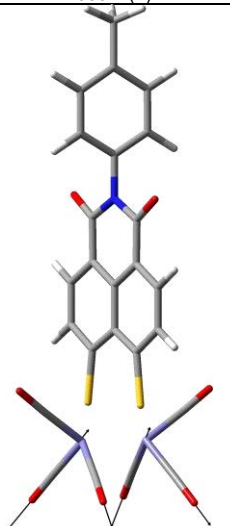
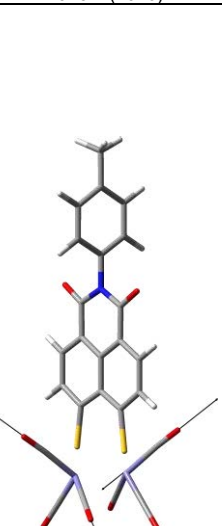
Mode 108



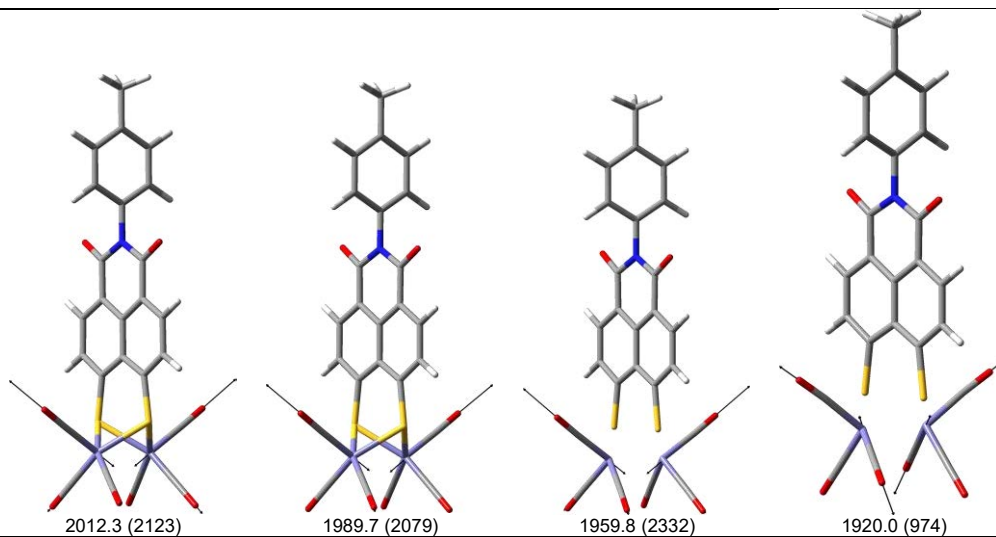
Mode 109



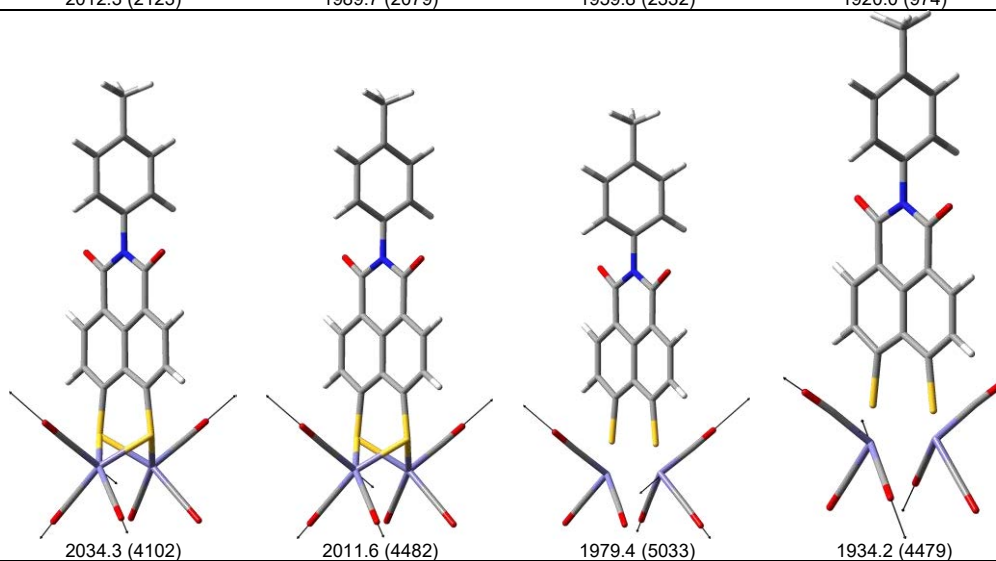
**Table S10.** Simulated infrared intensities of the six -CO vibrational normal modes of **4a** within the non-reduced singlet, the singly reduced doublet and the doubly reduced singlet and triplet species. Wavenumbers are scaled by a factor of 0.96, infrared intensities are given in parenthesis. The respective normal modes are illustrated based on displacement vectors.

<b>4a</b>				
	Non-reduced singlet $\tilde{\nu} / \text{cm}^{-1}$ (// km·mol <sup>-1</sup> )	Singly reduced doublet $\tilde{\nu} / \text{cm}^{-1}$ (// km·mol <sup>-1</sup> )	Doubly reduced singlet $\tilde{\nu} / \text{cm}^{-1}$ (// km·mol <sup>-1</sup> )	Doubly reduced triplet $\tilde{\nu} / \text{cm}^{-1}$ (// km·mol <sup>-1</sup> )
Mode 125	 2002.9 (9)	 1979.6 (9)	 1946.8 (81)	 1902.8 (1716)
Mode 126	 2006.3 (10)	 1982.6 (6)	 1950.2 (1)	 1913.4 (2046)
Mode 127	 2011.5 (2298)	 1988.8 (2615)	 1957.9 (2966)	 1917.3 (2903)

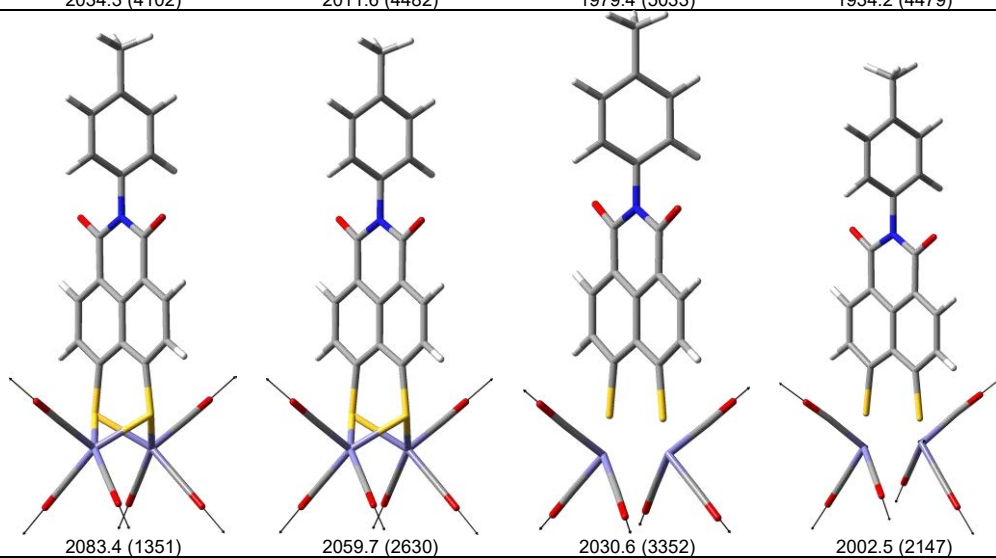
Mode 128



Mode 129



Mode 130





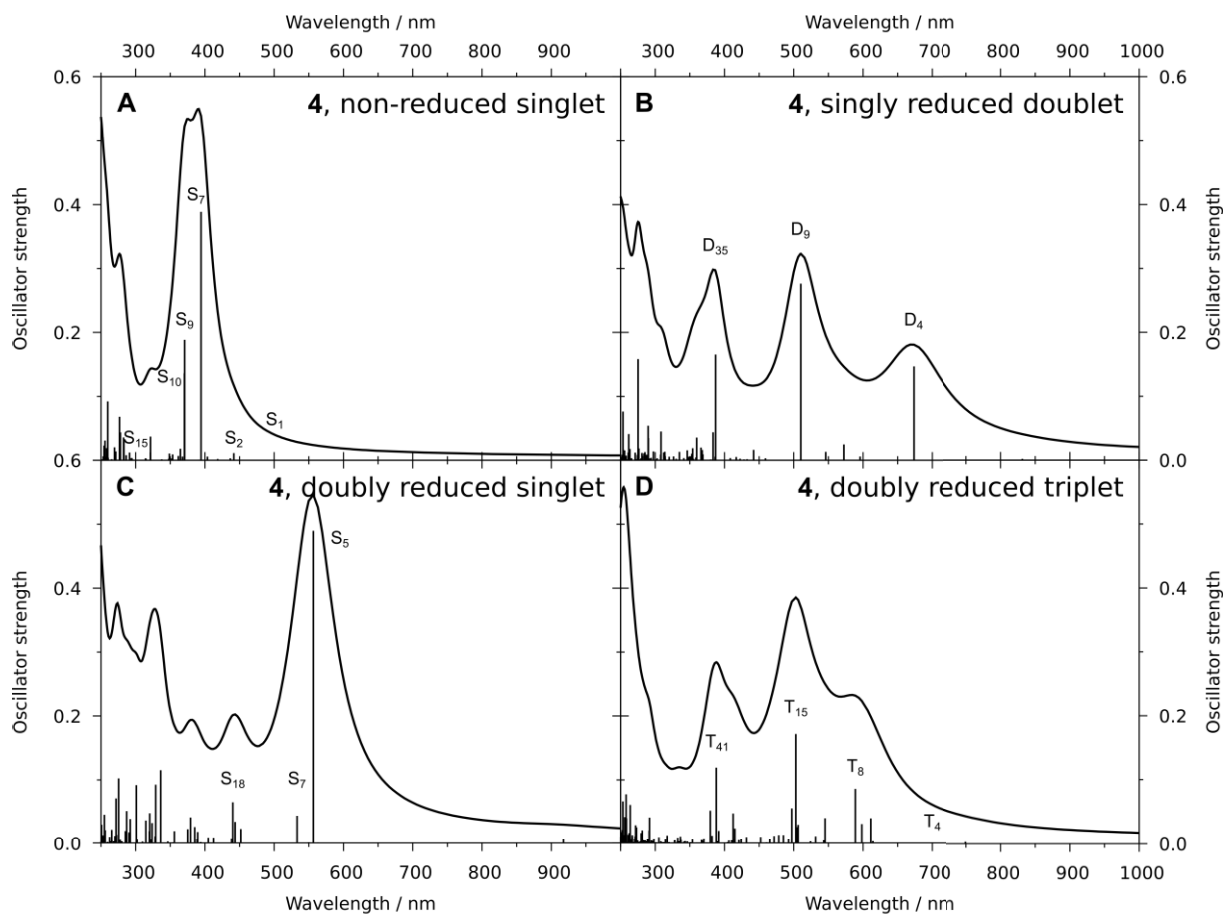


**Figure S16.** Simulated electronic absorption spectra of **4** (B3LYP/def2-SVP) in acetonitrile within the fully optimized equilibrium geometries of the non-reduced singlet (A), the singly reduced doublet (B), the doubly reduced singlet (C) and the doubly reduced triplet species (D).

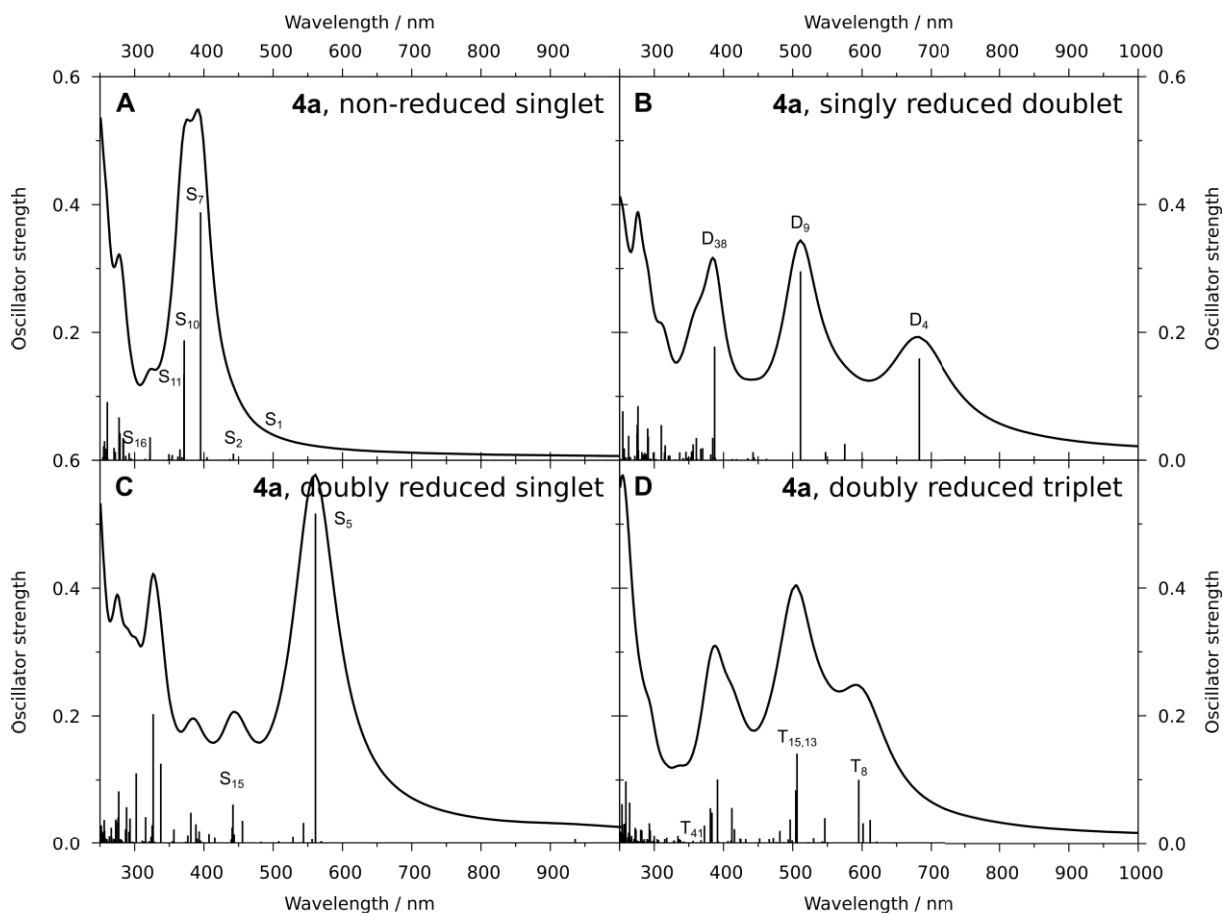


**Figure S17.** Simulated electronic absorption spectra of **4a** (B3LYP/def2-SVP) in acetonitrile within the fully optimized equilibrium geometries of the non-reduced singlet (A), the singly reduced doublet (B), the doubly reduced singlet (C) and the doubly reduced triplet species (D).

## References

- [1] S. Stoll, A. Schweiger, *J. Magn. Reson.* **2006**, *178*, 42–55.
- [2] a) COLLECT Data Collection Software, Nonius B.V, Netherlands, **1998**; b) Processing of X-Ray Diffraction Data Collected in Oscillation Mode: Otwinowski, Z, Minor, W. in Carter, C. W, Sweet, R. M. (eds.): *Methods in Enzymology, Vol. 276, Macromolecular Crystallography, Part A*, pp. 307–326, Academic Press, **1997**; c) SADABS 2.10: Bruker-AXS inc, Madison, WI, U.S.A., **2002**;
- [3] G. M. Sheldrick, *Acta Crystallogr. Sect. A: Found. Crystallogr.* **2015**, *71*, 3–8.
- [4] G. M. Sheldrick, *Acta Crystallogr. Sect. C: Struct Chem* **2015**, *71*, 3–8.
- [5] C. F. Macrae, P. R. Edgington, P. McCabe, E. Pidcock, G. P. Shields, R. Taylor, M. Towler, J. van de Streek, *J. Appl. Crystallogr.* **2006**, *39*, 453–457.
- [6] H. Wonneberger, H. Reichelt, Y. Zagranyski, C. Li, K. Müllen, L. Chen. Double Donor Functionalisation of the Peri-Positions of Perylene and Naphthalene Monoimide via versatile Building Blocks(WO 2014/033620 A 2).
- [7] M. Tesmer, H. Vahrenkamp, *Eur. J. Inorg. Chem.* **2001**, 1183–1188.
- [8] A. P. S. Samuel, D. T. Co, C. L. Stern, M. R. Wasielewski, *J. Am. Chem. Soc.* **2010**, *132*, 8813–8815.
- [9] S. Kaloyanova, Y. Zagranyski, S. Ritz, M. Hanulová, K. Koynov, A. Vonderheit, K. Müllen, K. Peneva, *J. Am. Chem. Soc.* **2016**, *138*, 2881–2884.
- [10] a) H. Abul-Futouh, A. Skabeev, D. Botteri, Y. Zagranyski, H. Görls, W. Weigand, K. Peneva, *Organometallics* **2018**, *37*, 3278–3285; b) H. Abul-Futouh, Y. Zagranyski, C. Müller, M. Schulz, S. Kupfer, H. Görls, M. El-khateeb, S. Gräfe, B. Dietzek, K. Peneva, W. Weigand, *Dalton Trans.* **2017**, *46*, 11180–11191; c) P. Li, S. Amirjalayer, F. Hartl, M. Lutz, B. de Bruin, R. Becker, S. Woutersen, J. N. H. Reek, *Inorg. Chem.* **2014**, *53*, 5373–5383;
- [11] a) T. Suzuki, Y. Maruyama, T. Akasaka, W. Ando, K. Kobayashi, S. Nagase, *J. Am. Chem. Soc.* **1994**, *116*, 1359–1363; b) R. Núñez, M. Tarrés, A. Ferrer-Ugalde, F. F. de Biani, F. Teixidor, *Chem. Rev.* **2016**, *116*, 14307–14378; c) M. D. Westmeyer, T. B. Rauchfuss, A. K. Verma, *Organometallics* **1993**, *12*, 4056–4060;
- [12] a) P. Li, M. Wang, C. He, G. Li, X. Liu, C. Chen, B. Åkermark, L. Sun, *Ber.* **2005**, *2005*, 2506–2513; b) H. Abul-Futouh, L. R. Almazahreh, S. J. Abaalkhail, H. Görls, S. T. Stripp, W. Weigand, *New J. Chem.* **2021**, *45*, 36–44;
- [13] P. C. Eilgen, J. N. Gerlach, *Inorg. Chem.* **1973**, *12*, 2526–2532.

- [14] a) Y. Na, P. Wei, L. Zhou, *Chem. Eur. J.* **2016**, *22*, 10365–10368; b) A. Q. Daraosheh, H. Abul-Futouh, R. A. Abdel-Rahem, H. Görls, H.-D. Stachel, W. Weigand, *Z. anorg. allg. Chem.* **2021**, *647*, 931–936;
- [15] P. S. Singh, H. C. Rudbeck, P. Huang, S. Ezzaher, L. Eriksson, M. Stein, S. Ott, R. Lomoth, *Inorg. Chem.* **2009**, *48*, 10883–10885.
- [16] K. Izutsu, *Acid-base dissociation constants in dipolar aprotic solvents*, Blackwell, Oxford, **1990**.
- [17] L. R. Almazahreh, F. Arrigoni, H. Abul-Futouh, M. El-khateeb, H. Görls, C. Elleouet, P. Schollhammer, L. Bertini, L. de Gioia, M. Rudolph, G. Zampella, W. Weigand, *ACS Catal.* **2021**, 7080–7098.
- [18] a) M. Mirmohades, S. Pullen, M. Stein, S. Maji, S. Ott, L. Hammarström, R. Lomoth, *J. Am. Chem. Soc.* **2014**, *136*, 17366–17369; b) M.-H. Chiang, Y.-C. Liu, S.-T. Yang, G.-H. Lee, *Inorg. Chem.* **2009**, *48*, 7604–7612; c) S. J. Borg, T. Behrsing, S. P. Best, M. Razavet, X. Liu, C. J. Pickett, *J. Am. Chem. Soc.* **2004**, *126*, 16988–16999; d) S. J. Borg, S. P. Best, *J. Electroanal. Chem.* **2002**, *535*, 57–64; e) A. Jablonskytė, J. A. Wright, S. A. Fairhurst, L. R. Webster, C. J. Pickett, *Angew. Chem. Int. Ed.* **2014**, *53*, 10143–10146; f) E. C. F. Schippers, S. S. Nurttila, J.-P. H. Oudsen, M. Tromp, W. I. Dzik, J. I. van der Vlugt, J. N. H. Reek, *Eur. J. Inorg. Chem.* **2019**, *2019*, 2510–2517; g) N. Chongdar, J. A. Birrell, K. Pawlak, C. Sommer, E. J. Reijerse, O. Rüdiger, W. Lubitz, H. Ogata, *J. Am. Chem. Soc.* **2018**, *140*, 1057–1068; h) J. Esselborn, C. Lambertz, A. Adamska-Venkates, T. Simmons, G. Berggren, J. Noth, J. Siebel, A. Hemschemeier, V. Artero, E. Reijerse, M. Fontecave, W. Lubitz, T. Happe, *Nat. Chem. Biol.* **2013**, *9*, 607–609; i) L. Kertess, F. Wittkamp, C. Sommer, J. Esselborn, O. Rüdiger, E. J. Reijerse, E. Hofmann, W. Lubitz, M. Winkler, T. Happe, U.-P. Apfel, *Dalton Trans.* **2017**, *46*, 16947–16958;
- [19] Gaussian 16 Rev. B.01: Frisch, M. J., Trucks, G. W., Schlegel, H. B., Scuseria, G. E., Robb, M. A., Cheeseman, J. R., Scalmani, G., Barone, V., Petersson, G. A., Nakatsuji, H., Li, X., Caricato, M., Marenich, A. V., Bloino, J., Janesko, B. G., Gomperts, R., Mennucci, B., Hratchian, H. P., Ortiz, J. V., Izmaylov, A. F., Sonnenberg, J. L., Williams, Ding, F., Lipparini, F., Egidi, F., Goings, J., Peng, B., Petrone, A., Henderson, T., Ranasinghe, D., Zakrzewski, V. G., Gao, J., Rega, N., Zheng, G., Liang, W., Hada, M., Ehara, M., Toyota, K., Fukuda, R., Hasegawa, J., Ishida, M., Nakajima, T., Honda, Y., Kitao, O., Nakai, H., Vreven, T., Throssell, K., Montgomery Jr, J. A., Peralta, J. E., Ogliaro, F., Bearpark, M. J., Heyd, J. J., Brothers, E. N., Kudin, K. N., Staroverov, V. N., Keith, T. A., Kobayashi, R., Normand, J., Raghavachari, K., Rendell, A. P., Burant, J. C., Iyengar, S. S., Tomasi, J., Cossi, M., Millam, J. M., Klene, M., Adamo, C., Cammi, R., Ochterski, J. W., Martin, R. L., Morokuma, K., Farkas, O., Foresman, J. B., Fox, D. J., Wallingford, CT, **2016**.
- [20] a) A. D. Becke, *J. Chem. Phys.* **1993**, *98*, 5648–5652; b) Lee, Yang, Parr, *Phys. Rev. B: Condens. Matter* **1988**, *37*, 785–789;
- [21] a) F. Weigend, *PCCP* **2006**, *8*, 1057–1065; b) F. Weigend, R. Ahlrichs, *PCCP* **2005**, *7*, 3297–3305;
- [22] J. P. Merrick, D. Moran, L. Radom, *J. Phys. Chem. A* **2007**, *111*, 11683–11700.
- [23] a) H. Abul-Futouh, Y. Zagranjarski, C. Müller, M. Schulz, S. Kupfer, H. Görls, M. El-khateeb, S. Gräfe, B. Dietzek, K. Peneva, W. Weigand, *Dalton Trans.* **2017**, *46*, 11180–11191; b) L. Bertini, C. Greco, L. de Gioia, P. Fantucci, *J. Phys. Chem. A* **2009**, *113*, 5657–5670; c) P. Buday, P. Seeber, C. Zens, H. Abul-Futouh, H. Görls, S. Gräfe, P. Matczak, S. Kupfer, W. Weigand, G. Mloston, *Chem. Eur. J.* **2020**, *26*, 11412–11416; d) R. Goy, L. Bertini, C. Elleouet, H. Görls, G. Zampella, J. Talarmin, L. de Gioia, P. Schollhammer, U.-P. Apfel, W. Weigand, *Dalton Trans.* **2015**, *44*, 1690–1699; e) P. E. M. Siegbahn, R.-Z. Liao, *J. Phys. Chem. A* **2020**, *124*, 10540–10549;
- [24] a) M. G. Delcey, K. Pierloot, Q. M. Phung, S. Vancoillie, R. Lindh, U. Ryde, *PCCP* **2014**, *16*, 7927–7938; b) P. E. M. Siegbahn, R.-Z. Liao, *ACS Catal.* **2020**, *10*, 5603–5613;
- [25] a) G. Dong, Q. M. Phung, S. D. Hallaert, K. Pierloot, U. Ryde, *PCCP* **2017**, *19*, 10590–10601; b) G. Dong, U. Ryde, *J Biol Inorg Chem* **2016**, *21*, 383–394; c) S. Qiu, Q. Li, Y. Xu, S. Shen, C. Sun, *WIREs Comput. Mol. Sci.* **2020**, *10*;
- [26] a) M. Sensi, C. Baffert, L. Fradale, C. Gauquelin, P. Soucaille, I. Meynial-Salles, H. Bottin, L. de Gioia, M. Bruschi, V. Fourmond, C. Léger, L. Bertini, *ACS Catal.* **2017**, *7*, 7378–7387; b) J. L. Bingaman, C. L. Kohnhorst, G. A. van Meter, B. A. McElroy, E. A. Rakowski, B. W. Caplins, T. A. Gutowski, C. J. Stromberg, C. E. Webster, E. J. Heilweil, *J. Phys. Chem. A* **2012**, *116*, 7261–7271;
- [27] a) L. Zedler, A. K. Mengele, K. M. Ziems, Y. Zhang, M. Wächtler, S. Gräfe, T. Pascher, S. Rau, S. Kupfer, B. Dietzek, *Angew. Chem. Int. Ed.* **2019**, *58*, 13140–13148; b) G. E. Shillito, T. B. J. Hall, D. Preston, P. Traber, L. Wu, K. E. A. Reynolds, R. Horvath, X. Z. Sun, N. T. Lucas, J. D. Crowley, M. W. George, S. Kupfer, K. C. Gordon, *J. Am. Chem. Soc.* **2018**, *140*, 4534–4542; c) C. Latouche, D. Skouteris, F. Palazzetti, V. Barone, *J. Chem. Theory Comput.* **2015**, *11*, 3281–3289; d) L. González, D. Escudero, L. Serrano-Andrés, *ChemPhysChem* **2012**, *13*, 28–51; e) D. Escudero in *Transition metals in coordination environments. Computational chemistry and catalysis viewpoints, Challenges and advances in computational chemistry and physics*; (Eds. E. Broclawik, T. Borowski, M. Radon), Springer, Cham Switzerland, **2019**, pp. 259–287;
- [28] a) B. Mennucci, C. Cappelli, C. A. Guido, R. Cammi, J. Tomasi, *J. Phys. Chem. A* **2009**, *113*, 3009–3020; b) A. V. Marenich, C. J. Cramer, D. G. Truhlar, *J. Phys. Chem. B* **2009**, *113*, 6378–6396;
- [29] S. Grimme, S. Ehrlich, L. Goerigk, *J. Comput. Chem.* **2011**, *32*, 1456–1465.

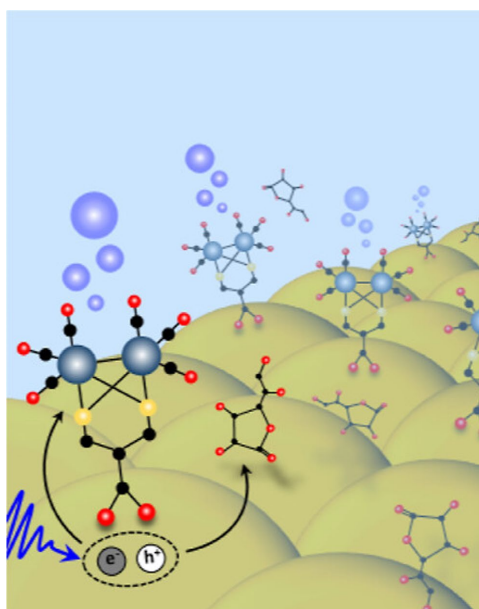
## 7.2 [SB-2]

### [SB-2] Covalent Functionalization of CdSe Quantum Dot Films with Molecular [FeFe] Hydrogenase Mimics for Light-Driven Hydrogen Evolution

Stefan Benndorf,<sup>‡</sup> Alexander Schleusener,<sup>‡</sup> Riccarda Müller, Mathias Micheel, Raktim Baruah, Jan Dellith, Andreas Undisz, Christof Neumann, Andrey Turchanin, Kerstin Leopold, Wolfgang Weigand and Maria Wächtler

<sup>‡</sup> These authors contributed equally.

*ACS Appl. Mater. Interfaces* **2023**, *15*, 18889–18897.



#### Covalent Functionalization of CdSe Quantum Dot Films with Molecular [FeFe] Hydrogenase Mimics for Light-Driven Hydrogen Evolution



Author: Stefan Benndorf, Alexander Schleusener, Riccarda Müller, et al

Publication: Applied Materials

Publisher: American Chemical Society

Date: Apr 1, 2023

Copyright © 2023, American Chemical Society

#### PERMISSION/LICENSE IS GRANTED FOR YOUR ORDER AT NO CHARGE

This type of permission/license, instead of the standard Terms and Conditions, is sent to you because no fee is being charged for your order. Please note the following:

- Permission is granted for your request in both print and electronic formats, and translations.
- If figures and/or tables were requested, they may be adapted or used in part.
- Please print this page for your records and send a copy of it to your publisher/graduate school.
- Appropriate credit for the requested material should be given as follows: "Reprinted (adapted) with permission from {COMPLETE REFERENCE CITATION}. Copyright (YEAR) American Chemical Society." Insert appropriate information in place of the capitalized words.
- One-time permission is granted only for the use specified in your RightsLink request. No additional uses are granted (such as derivative works or other editions). For any uses, please submit a new request.

<https://pubs.acs.org/doi/full/10.1021/acscami.3c00184>

# Covalent Functionalization of CdSe Quantum Dot Films with Molecular [FeFe] Hydrogenase Mimics for Light-Driven Hydrogen Evolution

Stefan Benndorf, Alexander Schleusener, Riccarda Müller, Mathias Micheel, Raktim Baruah, Jan Dellith, Andreas Undisz, Christof Neumann, Andrey Turchanin, Kerstin Leopold, Wolfgang Weigand,\* and Maria Wächtler\*



Cite This: *ACS Appl. Mater. Interfaces* 2023, 15, 18889–18897



Read Online

ACCESS |



Metrics & More



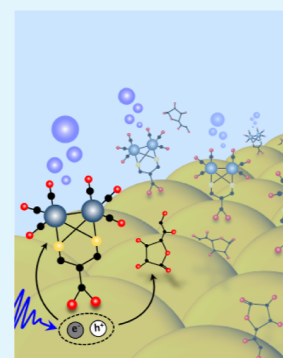
Article Recommendations



Supporting Information

**ABSTRACT:** CdSe quantum dots (QDs) combined with [FeFe] hydrogenase mimics as molecular catalytic reaction centers based on earth-abundant elements have demonstrated promising activity for photocatalytic hydrogen generation. Direct linking of the [FeFe] hydrogenase mimics to the QD surface is expected to establish a close contact between the [FeFe] hydrogenase mimics and the light-harvesting QDs, supporting the transfer and accumulation of several electrons needed to drive hydrogen evolution. In this work, we report on the functionalization of QDs immobilized in a thin-film architecture on a substrate with [FeFe] hydrogenase mimics by covalent linking via carboxylate groups as the anchoring functionality. The functionalization was monitored via UV/vis, photoluminescence, IR, and X-ray photoelectron spectroscopy and quantified via micro-X-ray fluorescence spectrometry. The activity of the functionalized thin film was demonstrated, and turnover numbers in the range of 360–580 (short linkers) and 130–160 (long linkers) were achieved. This work presents a proof-of-concept study, showing the potential of thin-film architectures of immobilized QDs as a platform for light-driven hydrogen evolution without the need for intricate surface modifications to ensure colloidal stability in aqueous environments.

**KEYWORDS:** semiconductor, nanoparticle, [FeFe] hydrogenase, photocatalysis, thin films



## 1. INTRODUCTION

Colloidal semiconductor nanoparticles are a prevalent material used in light-driven catalysis because of their size-tunable optoelectronic properties and their ability to efficiently generate multiple excitons.<sup>1</sup> In particular, CdSe quantum dots (QDs) are excellent photosensitizers for light-driven hydrogen evolution, which yields “green” hydrogen as a means of storing solar energy. To improve their photocatalytic activity, QDs are functionalized with suitable co-catalysts such as metal nanoparticles, inorganic semiconductors, or organometallic complexes.<sup>2–4</sup> The so-called hydrogenase mimics are designed to model the active center of naturally occurring [FeFe] or [NiFe] hydrogenase metalloenzymes and have received considerable attention as catalysts for hydrogen production.<sup>5–12</sup> They rely on earth-abundant elements and thus represent a sustainable alternative to noble-metal complexes or nanoparticles.

CdSe QDs functionalized with [FeFe] hydrogenase mimics have already shown their high catalytic proficiency with turnover numbers (TONs) in the order of up to  $10^4$  to  $10^5$  in the presence of sacrificial electron donors (SEDs).<sup>1,13–15</sup> In a QD–[FeFe] hydrogenase mimic complex, photoexcitation of the QD generates an exciton, i.e., a localized electron–hole pair, followed by electron transfer to the mimic, which reduces

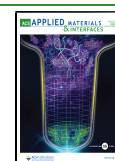
the  $[\text{Fe}^{\text{I}}\text{Fe}^{\text{I}}]$  center to an intermediate  $[\text{Fe}^{\text{I}}\text{Fe}^{\text{0}}]$  species. As described by Wu and co-workers,<sup>16</sup> this is followed by the addition of a proton, which yields  $[\text{Fe}^{\text{I}}\text{Fe}^{\text{II}}\text{H}]$ , and the subsequent uptake of an additional electron and a proton. The release of molecular hydrogen recovers the initial oxidized species.

In most cases, the photocatalytic reaction takes place in aqueous dispersion, i.e., water-dispersible photoexcited QDs and [FeFe] hydrogenase mimics form an encounter complex, where the catalyst is only loosely bound to the nanoparticle surface and in equilibrium with free molecules in solution. While even in such a weakly bound complex, the electron transfer is fast<sup>17</sup> and the catalytic activity high,<sup>18</sup> this approach suffers from two major drawbacks. First, water-dispersible CdSe QDs have to be surface-functionalized with hydrophilic molecules. The most commonly used surface ligands are mercaptocarboxylic acids, which bind to the surface via their

**Received:** January 5, 2023

**Accepted:** February 28, 2023

**Published:** April 4, 2023



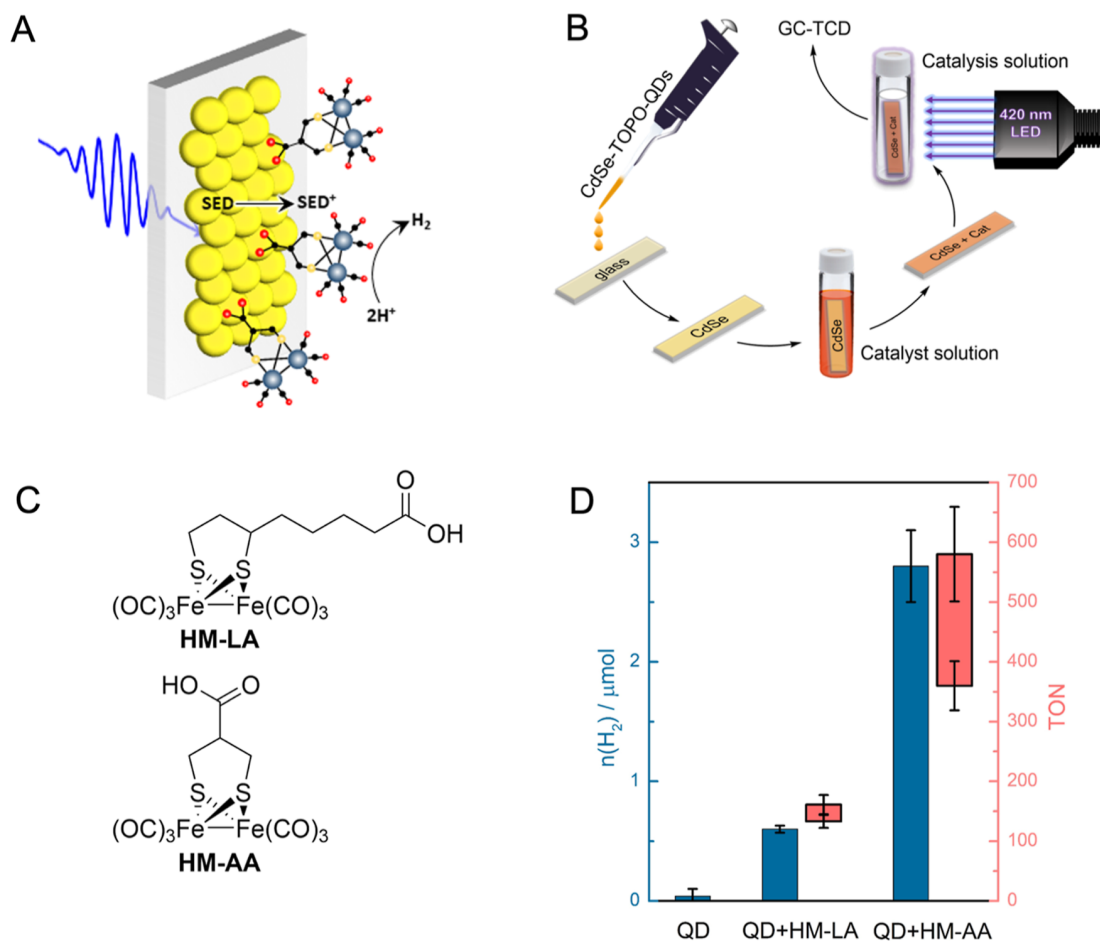


**Figure 1.** Summary of the work presented here. (A) Schematic illustration of QDs immobilized in a thin-film architecture on a substrate with [FeFe] hydrogenase mimics by covalent linking via carboxylate groups as the anchoring functionality to bind to the QD surface for light-driven hydrogen evolution in the presence of a SED. (B) Schematic overview of the functionalization procedure. First, CdSe QDs with their native TOPO and phosphonic acid ligands are dropcast on a substrate. The resulting film is placed in methanolic solutions of the molecular catalysts. Lastly, the functionalized films are irradiated, and the produced hydrogen is evaluated via GC analysis. (C) Molecular structures of the two [FeFe] hydrogenase mimics with varying linker lengths under investigation. (D) Hydrogen evolution performance of pristine and functionalized CdSe films upon 420 nm irradiation in ascorbic acid/ascorbate buffer (pH = 4.4). Error bars indicate a standard deviation of at least five separate measurements. The TONs (red) refer to catalytic activity per [FeFe] hydrogenase mimic calculated based on the amount of Fe determined by  $\mu$ XRF.

thiol(ate) moieties. However, the thiol's electron lone pairs act as hole traps,<sup>19</sup> and it has been shown that hole-trapping induced by thiol ligands can be detrimental to photocatalysis.<sup>20</sup> Additionally, [FeFe] hydrogenase mimics show higher activity at slightly acidic conditions (pH  $\sim$  4),<sup>5</sup> at which the ligands' carboxylic group is protonated, and the QDs lose their colloidal stability. Second, the catalyst has to accept two electrons for the reduction of protons to hydrogen. This becomes more likely the longer the mimic stays close to the surface. However, the bare catalytic center ( $(\mu\text{-S})_2\text{Fe}_2(\text{CO})_6$ ) only weakly adsorbs to the nanocrystal surface.<sup>21</sup> Thus, for efficient catalysis, the mimics need to be fixed in close proximity to the QDs. So far, most systems rely on indirect coupling via side-chain grafting onto hydrophilic polymers, followed by embedding CdSe QDs,<sup>22,23</sup> or electrostatic interactions with surface-grafted cyclodextrin.<sup>24,25</sup> Examples of coupling the catalyst to the QD surface via direct linking are rare, which might be caused by problems with colloidal stability upon covalent functionalization,<sup>21,26,27</sup> but directly coupled QD–[FeFe] hydrogenase mimic hybrid systems in

dispersion have shown photocatalytic TON in the order of 9000 (refers to the number of catalytic centers) in dispersion.<sup>27</sup>

To overcome the challenges of CdSe QDs' colloidal stability in water under varying pH conditions and upon linking of the catalyst to their surface, QDs with the original ligand system [trioctylphosphine oxide (TOPO), phosphonic acid] can be processed into thin films as they are synthesized without the need for intricate surface modification like exchange with hydrophilic ligands or embedding in water-soluble polymers. These films can then directly be functionalized with hydrogenase mimics with suitable anchoring groups without consideration for the final system's colloidal stability. This would in turn also allow the use of water insoluble catalysts for photocatalytic water splitting. Such immobilization of the QD–[FeFe] hydrogenase complex has the additional advantage that the photocatalytic system can be retrieved more easily from the reaction solution and put to recycling after use, which limits the ecotoxic potential of a cadmium-based system. To date, [FeFe] hydrogenase mimic-functionalized CdSe QD

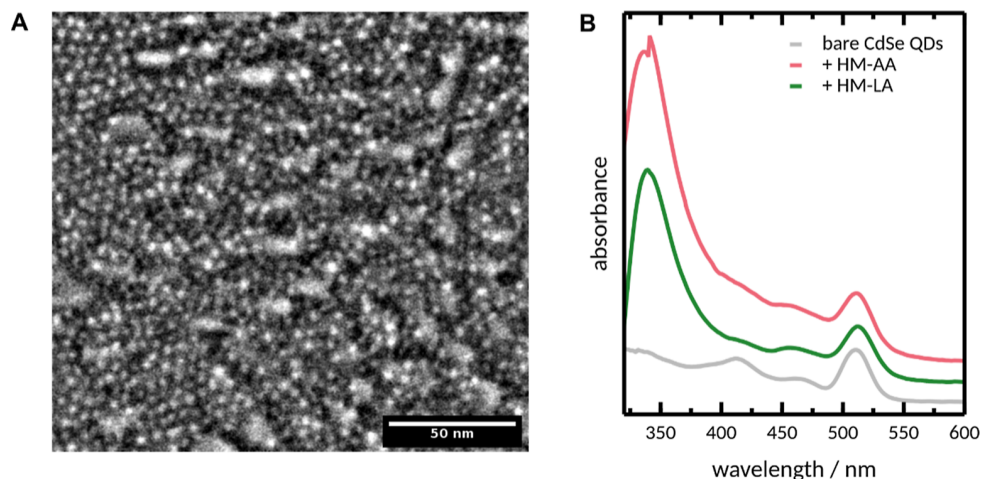


**Figure 2.** Characterization of CdSe QD films. (A) SEM image of an unfunctionalized dropcast film. (B) Absorption spectra of dropcast QD films before and after functionalization. Spectra of films have been corrected for a scattering background (see the Supporting Information), normalized to the first excitonic transition and offset for clarity.

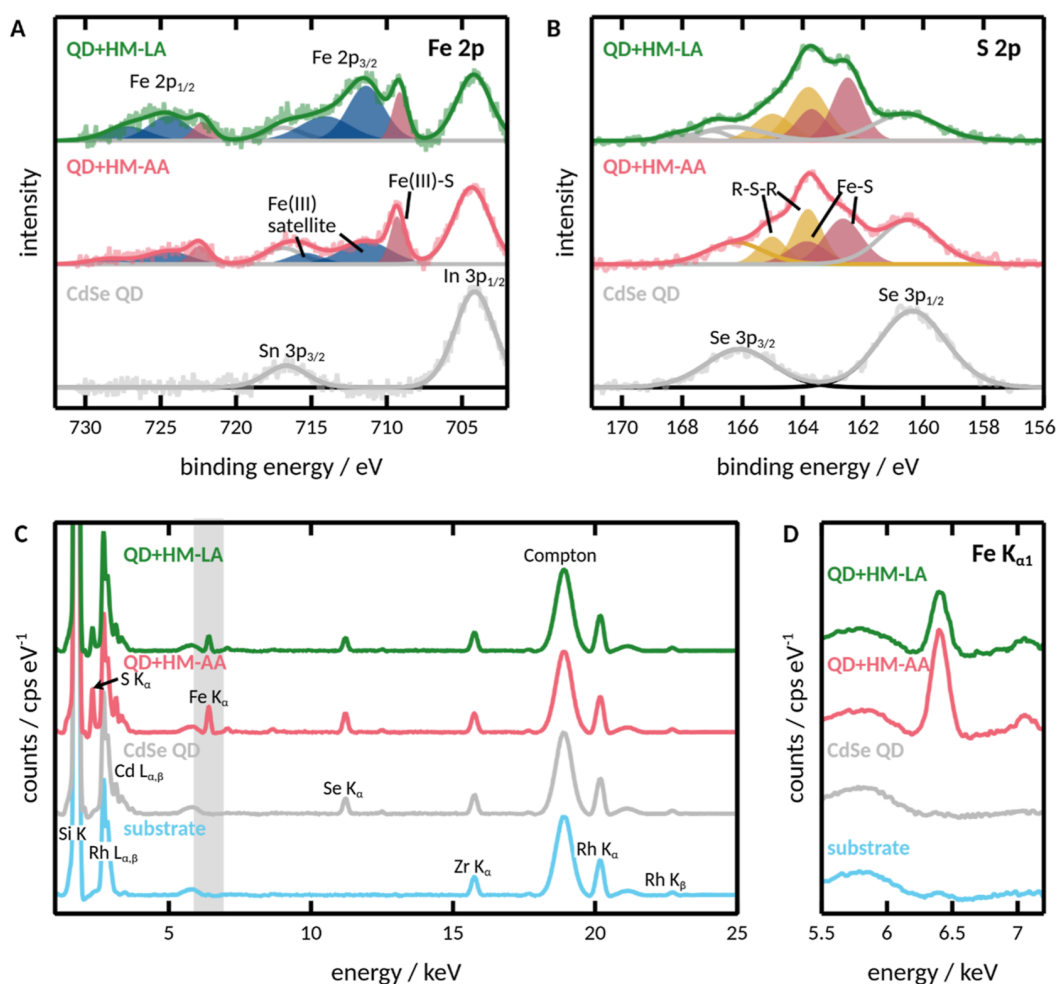


**Figure 3.** (A,B) High-resolution Fe 2p and S 2p XP spectra of functionalized and unfunctionalized QD films. Solid lines represent the results of a multi-Voigt peak fit. (C,D)  $\mu$ XRF sum spectra of a blank glass substrate, pristine QD films, and functionalized films. The highlighted region of interest refers to Fe  $K_{\alpha}$  lines ( $K_{\alpha 1}$ : 6.405 keV;  $K_{\alpha 2}$ : 6.392 keV) and has been magnified in (D). Other detected elements are S ( $K_{\alpha 1}$ : 2.307 keV;  $K_{\beta 1}$ : 2.467 keV) in [FeFe] hydrogenase mimics and Cd ( $L_{\alpha 1}$ : 3.133 keV;  $L_{\alpha 2}$ : 3.126 keV;  $L_{\beta 1}$ : 3.315 keV) and Se ( $K_{\alpha 1}$ : 11.224 keV;  $K_{\alpha 2}$ : 11.184 keV) in samples with QDs. Further elements result from the experimental setup, i.e., Si from the quartz glass substrate, Rh from the X-ray excitation source, and Zr from the detector aperture.

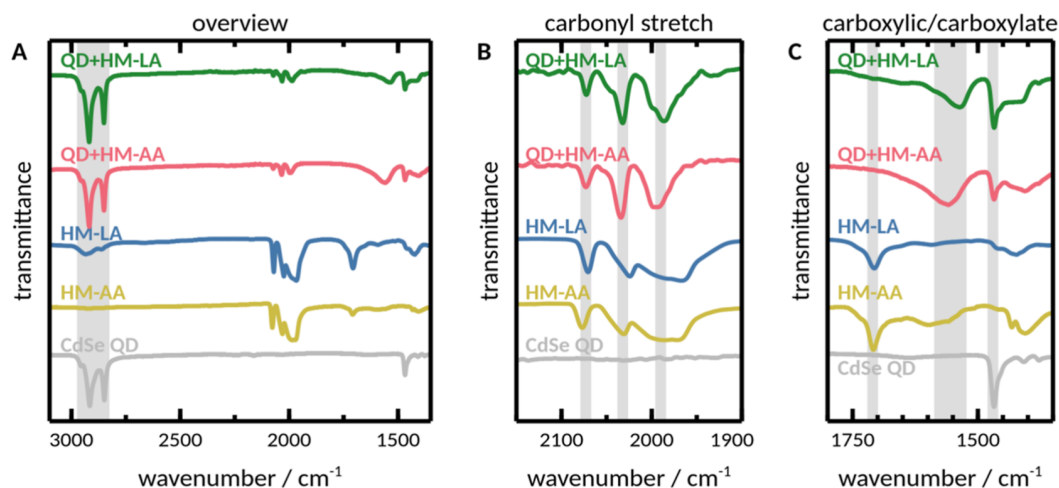


**Figure 4.** IR spectra of pristine QD films, pure [FeFe] hydrogenase mimics, and functionalized films. The highlighted regions of interest refer to (A) CdSe surface ligands ( $1470$  and  $2900$   $\text{cm}^{-1}$ ), (B) [FeFe] hydrogenase mimic carbonyl stretching modes ( $1900$ – $2100$   $\text{cm}^{-1}$ ), and (C) vibrations related to the catalysts' carboxylic and carboxylate groups ( $1550$  and  $1700$   $\text{cm}^{-1}$ ).

films have not been probed for their photocatalytic activity. With this motivation, in this work, we deposited CdSe QDs onto thin films, covalently functionalized them with molecular [FeFe] hydrogenase mimics, and evaluated their photocatalytic activity (Figure 1).

## 2. RESULTS AND DISCUSSION

We synthesized several batches of CdSe QDs (mean diameters in the order of  $2.4$ – $2.5$  nm, see the Supporting Information) via a hot-injection approach<sup>28</sup> and dropcasted them on transparent quartz substrates (Figure 1B) to form homogeneous thin films with an average thickness of  $17.0 \pm 1.2$  nm (Figures 2A and S4), i.e., on average, four QD layers including a roughly  $2.5$  nm organic surface ligand layer per particle.<sup>29</sup> [FeFe] Hydrogenase mimics containing a carboxylate group as an anchoring functionality to bind to the QD surface were synthesized by heating a mixture of lipoic acid for HM-LA or dihydroasparagusic acid for HM-AA (Figure 1C),  $\text{Fe}_3(\text{CO})_{12}$ , and *N*-methyl-2-pyrrolidone<sup>30</sup> as an additive (for details, see the Supporting Information). We chose this anchoring group over the more common thiol ligands for two reasons. First, because of the high affinity of iron to sulfur, thiol-substituted [FeFe] hydrogenase mimics are not readily available synthetically. Second, thiols (or thiolates) are much stronger hole quenchers than carboxylates,<sup>19</sup> which might impact the overall photocatalytic activity of the system.<sup>20</sup> For the functionalization, films were placed in a saturated solution of each mimic dissolved in methanol. The functionalization was monitored via UV/vis absorption, photoluminescence, and attenuated total reflectance Fourier transform infrared (ATR-FTIR) spectroscopy and confirmed by X-ray photoelectron spectroscopy (XPS) and micro-X-ray fluorescence spectrometry ( $\mu\text{XRF}$ ).

The absorption spectrum of QD films before functionalization shows the characteristic lowest excitonic transition at  $\sim 510$  nm and higher energy transitions at lower wavelengths (Figure 2B). Absorption spectra of QDs dispersed in toluene and dropcast into films are spectrally nearly identical. A small bathochromic shift in the absorption spectrum of films ( $\Delta E = 20$  meV at the lowest energy excitonic transition) is caused by a weak inter-particle electronic interaction in the film, as the average distance between QDs is in the order of  $1$ – $2$  nm due

to the original ligands covering the QD surfaces.<sup>31</sup> Absorption spectra of functionalized films show an additional, pronounced absorption peak at  $\sim 330$  nm, which is assigned to a metal-to-ligand charge-transfer state of the [FeFe] hydrogenase mimics (Figures 2B and S6).<sup>32</sup> Photoluminescence is completely quenched in the functionalized films (Figure S5B), which indicates an efficient electron transfer from photoexcited QDs to the surface-bound [FeFe] hydrogenase mimics.<sup>17</sup>

To confirm the presence of the [FeFe] hydrogenase mimics in the QD films, XPS was performed before and after functionalization (see Figures 3 and S9). In pure QD films, the binding energy region for the Fe 2p signal consists of two signals which originate from the substrate ITO, (Figure 3A), and the S 2p region is characterized by the Se 3p doublet only (Figure 3B). After catalyst functionalization, a Fe 2p doublet appears. According to the binding energy of the Fe  $2p_{3/2}$  main peak and the satellite peaks, this relates to Fe–S bonds<sup>33</sup> and confirms the presence of the [FeFe] hydrogenase mimics. Due to their similar binding energies, these peaks could also relate to Fe–O bonds.<sup>34</sup> In addition, a sulfur signature between both selenium peaks arises. The sulfur signal is separated from the selenium signal, as the spin–orbit splitting is different for both elements. The component at lower binding energy can be assigned to Fe–S bonds, whereas the second component at higher energies is typical for organic sulfur (R–S–R) bonds. These probably form during sample preparation or because of the X-ray irradiation during the measurement.<sup>33</sup> The attachment of the [FeFe] hydrogenase mimics was further confirmed in the C 1s region, which shows signatures of the organic backbone of the catalysts (see Supporting Information for further details).

Next, we quantified the [FeFe] hydrogenase mimic loadings of the films via  $\mu\text{XRF}$ . The films were scanned by an X-ray beam, and characteristic iron X-ray fluorescence was detected at  $6.4$  keV corresponding to  $K_{\alpha}$  lines (Figure 3C). To exclude considerable contamination of the substrates and films during sample preparation by ubiquitous iron, we also prepared two blank samples, a blank glass substrate and a pristine QD film. The investigation of these blanks confirmed the absence of iron contamination. To calibrate the measurement setup for iron quantification, we used synthetic quartz glass substrates loaded with known iron masses as external standards and



recorded a calibration curve (Figure S1). It is important to keep in mind that each catalyst contains two iron atoms. In the end, we determined loadings in the ranges of 3.8–6.1 nmol cm<sup>-2</sup> for HM-AA and 3.0–3.6 nmol cm<sup>-2</sup> for HM-LA. This difference in catalyst functionalization could be explained by the different dimensions of the [FeFe] hydrogenase mimics. The more compact HM-AA may show less interaction with surface ligands during the substitution process, whereas the “bulky” aliphatic chain of HM-LA could prevent the catalyst from getting close to the surface. In addition, both mimics show differences in the acidity of their carboxylic groups, i.e., pK<sub>a</sub> (asparagusic acid) = 4.0 (predicted)<sup>35</sup> and pK<sub>a</sub> (lipoic acid) = 4.7.<sup>36</sup> Therefore, HM-AA is more easily deprotonated than HM-LA during the functionalization process and might thus bind more strongly to the QD surface.

We used ATR-FTIR to gain a deeper understanding of the binding mode of the catalysts to the QD surface (Figure 4). ATR-FTIR spectra of pristine films and pure [FeFe] hydrogenase mimics are characterized by vibrations which relate to the native ligands (QDs) and carbonyl and carboxylic groups (mimics). We discuss the original IR spectra in detail in the Supporting Information. IR spectra of functionalized films are dominated in the fingerprint region (500–1300 cm<sup>-1</sup>) by vibrations related to the native CdSe surface ligands (Figure S8), which indicates the integrity of the original ligand sphere, whereas the higher-energy spectrum is mostly a superposition of vibrations of QD ligands and free [FeFe] hydrogenase mimics: it shows the aliphatic chain vibrations at 2900 and 1470 cm<sup>-1</sup> from the CdSe surface ligand and the characteristic carbonyl stretching modes between 1900 and 2100 cm<sup>-1</sup>. The spectral position of these bands remained unchanged after functionalization, which indicates that the linking of the mimics does not substantially affect the electronic structure of the catalytic center. However, the carbonyl vibrations are much narrower on the functionalized films. In particular, the lowest energy stretching mode is known to be sensitive to polar environments and becomes increasingly narrow with decreasing polarity.<sup>37</sup> The narrowing of the bands might thus indicate that the [FeFe] hydrogenase mimics are embedded in the nonpolar surface ligand sphere.

The most notable difference between the spectra before and after functionalization is the absence of the  $\nu(\text{CO})$  stretching vibration of the protonated carboxylic group at 1710 cm<sup>-1</sup>. Instead, broad bands between 1520–1550 cm<sup>-1</sup> appear in the functionalized system, which we assign to the antisymmetric stretching vibrations of the deprotonated carboxylate. In addition, broad bands related to the symmetric carboxylate stretching modes can be seen at  $\sim 1400$  cm<sup>-1</sup>. Thereby, we confirm that the [FeFe] hydrogenase mimics solely bind to the surface via their deprotonated carboxylate groups. Furthermore, the energetic distance  $\Delta\nu$  between the lower frequency symmetric and the higher frequency antisymmetric carboxylate stretching vibrations gives information about the bonding geometry of the catalysts to the surface.<sup>38</sup> A definite determination of  $\Delta\nu$  is complicated by the overlapping bands in this spectral area, but amounts to  $\sim 155$  cm<sup>-1</sup> for HM-AA and  $\sim 120$  cm<sup>-1</sup> for HM-LA. Thus, the carboxylate in HM-AA has a bridging configuration on the surface ( $\Delta\nu = 140$ – $190$  cm<sup>-1</sup>), whereas HM-LA is in between bridging and bidentate chelating ( $\Delta\nu < 100$  cm<sup>-1</sup>).<sup>38</sup>

Finally, we probed functionalized films for their photocatalytic activity in an aqueous solution (pH = 4.4; for information on optimization of pH, see Figure S11) with

ascorbic acid/ascorbate as SED under irradiation with an LED ( $\lambda = 420$  nm,  $P = 8.5$  mW cm<sup>-2</sup>) for 21 h (Figure 1D). The amount of produced hydrogen was determined using GC-TCD analysis by taking aliquots of the headspace. Unfunctionalized QD films already showed low photocatalytic activity under these conditions (42 nmol H<sub>2</sub>). However, hydrogenase mimic functionalization increased hydrogen production by up to 2 orders of magnitude under otherwise unchanged conditions (2.8  $\mu\text{mol}$  for HM-AA and 0.6  $\mu\text{mol}$  for HM-LA). We want to highlight that these photocatalytic systems can only be obtained via the immobilization–functionalization approach used since the QD–HM hybrid systems would normally not be water-dispersible due to the hydrophobic nature of the catalyst and the QDs. We then estimated TONs based on the number of hydrogenase mimics on the film, TON (HM-AA) = 361–579 and TON (HM-LA) = 133–161. Thus, the linker influences not only the overall loading of catalysts to the surface but also the catalytic efficiency. The Dukovic group previously found that the photocatalytic efficiency of a CdS nanorod–hydrogenase enzyme hybrid system decreased by 80% with the increase of the surface ligand length from 0.6 to 1 nm.<sup>39</sup> These lengths are comparable to HM-AA and HM-LA, and we see a similar decrease in catalytic activity of roughly 60%. This observation suggests that the ligand length introduces a barrier to charge transfer and controls the degree of electronic coupling, which impacts rates of charge transfer and the quantum efficiency of charge separation for both consecutive charge-transfer steps necessary for turn-over. With decreasing electron-transfer rates, the probability of recombination increases, reducing charge accumulation and catalytic activity of the system. The degree of difference in activity between HM-AA and HM-LA appears more pronounced at higher irradiation intensities (Figure S10). For both mimics, we observed a general increase in hydrogen evolution with increasing irradiation power, but only HM-LA plateaus at the highest irradiation powers applied. One reason could be that with increasing linker lengths, the necessary charge-transfer processes are less capable to compete with the second-order recombination processes at higher irradiation intensities, reducing the quantum efficiency of electron transfer.<sup>40</sup> Detailed spectroscopic studies are necessary to gain detailed insight into the linker length and intensity-dependent charge transfer in these systems, especially considering multi-charge carrier transfer events, which are beyond the scope of this proof-of-principle study.

In general, our photocatalytic semiconductor–molecule hybrid system performs comparable to non-covalent assemblies in aqueous solution, which reach TONs in the order of 10 to 100<sup>5,41,42</sup> but does not reach the high TON of supramolecular assemblies, which are in the order of 10<sup>4</sup> or higher.<sup>27,43</sup> We assign this to three factors. First, in our proof-of-concept study, we did not optimize experimental conditions, in particular with regard to hole quenching, which is known to be a limiting factor in semiconductor nanocrystal photocatalysis and is still diffusion limited in our system.<sup>44</sup> Additionally, experimental parameters such as different light sources, irradiation intensities and irradiation times, QD surface quality and ligand shell, and sample preparation vary across studies, which makes direct comparisons of TONs difficult. Second, our films show an extremely high catalyst-to-QD ratio. We estimated the number of CdSe QDs per film based on the Cd content on each glass slide via inductively coupled plasma–optical emission spectrometry (ICP–OES)

measurements (see Supporting Information), and estimate a QD film coverage of 0.2–0.3 nmol cm<sup>-2</sup> and catalyst loadings of 20 (HM-LA) to 40 (HM-AA) catalytic centers per QD. We know from the IR measurements that there are still residues of native ligands present in the system, which we attribute to layers deeper within the film. Thus, we assume that only the topmost QD layers are functionalized, and we estimate a complete surface ligand exchange of the topmost layer with [FeFe] hydrogenase mimics (see Supporting Information). From photocatalytic semiconductor–metal hybrid systems, we know that excessive catalyst loading is not necessarily beneficial to the hydrogen evolution rate, as recombination losses become dominant.<sup>45</sup> A similar observation has been made for ZnS QDs and hydrogenase mimics.<sup>46</sup> In contrast to our system, the loading in covalently connected QD–hydrogenase mimic systems, which showed high TONs, was in the order of 0.2 nm<sup>-2</sup> QD surface,<sup>21</sup> which is an order of magnitude less than the estimate for our system. Furthermore, excess catalyst naturally reduces the TON calculated. Thus, we assign the moderate TON to excessive catalyst loading to the surface. Lastly, by recording IR spectra after 24 h of photocatalysis (Figures S12 and S13), we found that the catalyst desorbs or degrades from the surface during photocatalysis.

### 3. CONCLUSIONS

In summary, we demonstrated an immobilized hybrid photocatalytic system generated by the successful covalent functionalization of thin CdSe QD films with molecular [FeFe] hydrogenase mimics. These functionalized films showed photocatalytic activities comparable to previously reported values in dispersion, avoiding the limitations in colloidal stability caused by ligand exchange via direct linking of the catalytic center to CdSe QD thin films with their native ligand shell.

### 4. EXPERIMENTAL SECTION

**4.1. Materials.** All solvents as well as commercially available compounds were purchased (Sigma-Aldrich, Acros, abcr, Alfa Aesar, TCI) and used as received without further purification. Toluene for synthesis was dried and deoxygenated over Na metal.

**4.2. Synthesis.** HM-LA was synthesized following an adapted<sup>30,47</sup> protocol developed by Jiang et al.<sup>48</sup> In a Schlenk flask, lipoic acid (100 mg, 485 μmol) was dissolved in anhydrous toluene (10 mL) and anhydrous NMP (1 mL) at 50 °C under a nitrogen atmosphere. Triirondodecarbonyl (244 mg, 485 μmol) was added, and the color changed from dark green to dark brown within 30 min, while a small amount of gas (CO) developed. The resulting crude product was purified by column chromatography (cyclo-hexane/THF 6:1). The product was collected from the major red band to give HM-LA as a red solid (210 mg, 432 μmol, 89%).

<sup>1</sup>H NMR (400 MHz, CDCl<sub>3</sub>, 297 K): δ (ppm) = 2.57 (br s, 1H), 2.39 (m, 2H), 2.11 (br s, 1H), 1.86 (br s, 2H), 1.64–1.44 (m, 6H), 1.29 (br s, 1H); IR (ATR) ν(C≡O) = 2073, 2032, 1992.

HM-AA was synthesized following an adapted<sup>30,49</sup> protocol developed by Thomas et al.<sup>50</sup> In a Schlenk flask, 2-carboxy-1,3-propanedithiol (100 mg, 657 μmol) was dissolved in anhydrous toluene (10 mL) and anhydrous NMP (1 mL) at 50 °C under a nitrogen atmosphere. Triirondodecarbonyl (331 mg, 657 μmol) was added, and the color changed from dark green to dark brown within 10 min, while a small amount of gas (CO) developed. The cold reaction mixture was treated with 1 M hydrochloric acid. The organic layer was extracted with 2 M KOH to transfer the complex in the aqueous phase. After acidifying with 1 M hydrochloric acid, the complex was extracted with toluene, (3 × 25 mL) and the organic layer was dried via Na<sub>2</sub>SO<sub>4</sub>. The resulting crude product was purified

by column chromatography (ethyl acetate/*n*-hexane 1:1). The product was collected from the major red band to give HM-AA as a red solid (115 mg, 267 μmol, 41%).

<sup>1</sup>H NMR (400 MHz, CDCl<sub>3</sub>, 297 K): δ (ppm) = 2.87 (dd, <sup>2</sup>J<sub>H-H</sub> = 13.6, <sup>3</sup>J<sub>H-H</sub> = 3.4 Hz, 1H), 2.17 (m, 1H), 1.76 (m, 2H); IR (ATR) ν(C≡O) = 2076, 2037, 1997.

CdSe QDs were synthesized by adopting a protocol published by Manna and co-authors.<sup>28</sup> 3.0 g of TOPO, 0.280 g of octadecylphosphonic acid (ODPA), and 60 mg of cadmium oxide (CdO) were mixed in a 25 mL three-neck flask, heated to 150 °C, and exposed to vacuum for 1 h. Then, under nitrogen, the solution was heated to 300 °C to dissolve CdO until it turns optically clear and colorless. At this point, 1.5 g of trioctylphosphine (TOP) was injected into the flask. The temperature is raised to 350 °C, a TOP/Se solution (0.058 g Se dissolved in 0.360 g TOP) is injected, and the reaction mixture is immediately cooled down by removing the heating mantle. After the synthesis, the nanocrystals were precipitated with methanol and were washed three times in total by redissolution in toluene and precipitation with the addition of methanol. Finally, the as-obtained QDs were dispersed in toluene and stored in a glovebox under a nitrogen atmosphere until further use.

QD films were prepared either via spin-coating or dropcasting. The deposition of the films was carried out either on quartz glass substrates for optical characterization and photocatalytic experiments, on indium tin oxide (ITO)-coated glass substrates for characterization via SEM and XPS, or on CaF<sub>2</sub> substrates for ATR-FTIR characterization. For the μXRF measurements, we used synthetic quartz (Suprasil, Microchemicals, Germany) substrates for their lower iron content. The substrates were cleaned for 20 min in an ultrasonic bath in methanol. Subsequently, the substrates were treated for 20 min in an ultrasonic bath in 2% aqueous Hellmanex solution. After washing twice with distilled water (each time for 20 min in the ultrasonic bath), the substrates were dried and stored in a glovebox under an inert atmosphere until further use. For spin-coating, the cleaned substrates were coated using a KLM SCC-200 spin coater under a normal atmosphere. For this purpose, 20 μL of a concentrated QD stock solution (0.3 mM) was added to a cleaned 10 mm × 10 mm substrate and coated for 60 s at 1200 rpm and 20 s at 1500 rpm. The QD films prepared with these parameters were macroscopically homogeneous and stored under a nitrogen atmosphere until further use. Spin-coating was used to prepare films to measure absorption and IR spectra. For all other characterization methods and catalysis, films were dropcast. For dropcast films, a dispersion of CdSe QDs in toluene (40 μL, 0.04 mM) was applied on substrates (25 mm × 5 mm for hydrogen evolution and μXRF measurements). The slides were covered with a Petri dish, and the solvent was allowed to evaporate for 1 h, followed by vacuum drying and storage under a nitrogen atmosphere.

The functionalization of the CdSe films was carried out under inert conditions inside a glovebox. Layers obtained via dropcasting were treated with [FeFe] hydrogenase mimics HM-LA or HM-AA (MeOH, saturated solution, ≈2 mM) for 21 h at RT and subsequently rinsed with 2 mL MeOH.

**4.3. Characterization Methods.** The <sup>1</sup>H NMR spectra were recorded with a Bruker Avance 400 MHz spectrometer. Chemical shifts are given in ppm relative to internal SiMe<sub>4</sub> or CHCl<sub>3</sub>.

Absorption spectra in dispersion were recorded in a quartz cell (*d* = 1 cm) using a JASCO V780 UV–visible/NIR spectrophotometer (JASCO GmbH, Pfungstadt, Germany). All measurements were performed in a wavelength range of 200 to 800 nm. A cuvette with a pure solvent was always measured as a reference. Absorption spectra of films were measured in the same spectrometer with a blank glass substrate as a reference. Photoluminescence spectra were recorded on an FLS980 photoluminescence spectrometer (Edinburgh Instruments Ltd., Livingston, UK) in 90° geometry. Spectra were obtained upon 400 nm excitation and recorded in a spectral region from 410–700 nm. For QD dispersions, QDs were dispersed in toluene in a quartz cuvette (*d* = 1 cm), and the optical density of the dispersion at the excitation wavelength was set to 0.05 to avoid inner filter effects and

reabsorption of photoluminescence. Films were placed in a sample holder provided by the manufacturer.

The FTIR spectra were acquired using a Tensor 27 spectrometer (Bruker) equipped with an ATR accessory (PLATINUM ATR, Bruker). Before each measurement, a background correction was performed by recording a spectrum against air. Subsequently, the IR spectrum of the dried films was recorded in the range of 600 and 4000  $\text{cm}^{-1}$ . Films were prepared either on 1 cm  $\times$  1 cm  $\text{CaF}_2$ , ITO, or glass substrates via spin coating or dropcasting and treated with [FeFe] hydrogenase mimics HM-LA or HM-AA (MeOH, saturated solution, 2 mM) for 21 h at RT. After rinsing with 2 mL MeOH, the samples were dried in vacuo. IR spectra of pure [FeFe] hydrogenase mimics were recorded as thin films formed by evaporation from saturated MeOH solutions.

Atomic force microscopy (AFM) images were collected by tapping mode in a Dimension Edge atomic force microscope (Bruker) with a large specimen stage.

Scanning electron microscopy (SEM) investigations of QD films on ITO-coated glass substrates were carried out using a dual-beam HELIOS NanoLab G3 UC scanning electron microscope.

Transmission electron microscopy (TEM) investigations were performed to confirm the size of the QDs. TEM images were recorded in bright field (BF) with high resolution (HR-TEM) and in scanning mode (STEM) using a JEM-ARM200F NEOARM (Jeol) operating at 80 kV, equipped with a spherical aberration corrector, BF, annular BF (ABF), and annular dark field (ADF) STEM detectors.

XPS was performed in an ultra-high-vacuum ( $<2 \times 10^{-10}$  mbar) multiprobe system (Scienta Omicron) using a monochromatized X-ray source (Al  $K_{\alpha}$ , 1486.7 eV) and an electron analyzer (Argus CU) with a spectral resolution of 0.6 eV. The spectra were calibrated using the In  $3d_{5/2}$  peak (444.6 eV, ITO) and fitted using Voigt functions (30:70) after background subtraction.

$\mu\text{XRF}$  were recorded using an M4 Tornado (Bruker Nano GmbH, Berlin, Germany). The instrument is equipped with a Rh X-ray tube, and the polychromatic beam is focused by polycapillary lenses to a spot of approximately 25  $\mu\text{m}$ . X-ray fluorescence is detected by an XFlash 430 PA detector with an active area of 30  $\text{mm}^2$  and a resolution of <145 eV at Mn  $K\alpha$ . An Rh X-ray tube was operated at maximum power (50 kV, 600  $\mu\text{A}$ ), and no filters were applied. Films for  $\mu\text{XRF}$  investigation were prepared on synthetic quartz glass substrates (Suprasil, Microchemicals, Germany) and scanned using a dwell time of 10 ms per pixel. For the iron quantification, sum spectra of external calibration standards were used. Suprasil glass substrates were prepared with drops of 10  $\mu\text{L}$  of iron standards, resulting in absolute iron masses of 200, 400, 600, 800, and 1000 ng on the substrates. Essential FTIR (v3.50.185) was used for the baseline correction and peak integration. The manual baseline correction was performed with the straight line baseline fit in an energy range from 6.19 to 6.58 keV. The confidence interval of the calibration function was calculated with  $N = 45$  and  $P = 95\%$ .

ICP-OES measurements (spectrometer 725ES (Fa. Agilent, Waldbronn) with a CCD detector) were performed to estimate the number of CdSe QDs by measuring the Cd content of each sample. Therefore, the slides were treated with aqua regia for 1 week at room temperature. After dilution with water to 10 mL total volume, the ICP-OES measurements were performed.

To test on hydrogen evolution, the slides were transferred into gas-tight glass vials (5 mL volume) with nitrogen-saturated (after bubbling) catalysis solution (3 mL;  $\text{H}_2\text{O}/\text{MeOH}$  3:1; 0.2 M ascorbic acid; 0.12 M NaOH, pH = 4.4) and irradiated with 420 nm LED (18  $\mu\text{W mm}^{-2}$ ) for 21 h at RT. A collimator was used to ensure a uniform light distribution over six samples irradiated simultaneously. A tenth part of the headspace volume (200  $\mu\text{L}$ ) was used for hydrogen quantification via GC-TCD.

## ■ ASSOCIATED CONTENT

### Data Availability Statement

The data underlying this study are openly available in Zenodo at <https://doi.org/10.5281/zenodo.7673863>.

### Supporting Information

The Supporting Information is available free of charge at <https://pubs.acs.org/doi/10.1021/acsami.3c00184>.

Materials; experimental details on synthesis and characterization methods; and TEM, AFM, absorption, IR, and XPS results (PDF)

## ■ AUTHOR INFORMATION

### Corresponding Authors

**Wolfgang Weigand** – Institute of Inorganic and Analytical Chemistry, Friedrich Schiller University Jena, 07743 Jena, Germany; [orcid.org/0000-0001-5177-1006](https://orcid.org/0000-0001-5177-1006); Email: [wolfgang.weigand@uni-jena.de](mailto:wolfgang.weigand@uni-jena.de)

**Maria Wächtler** – Institute of Physical Chemistry, Friedrich Schiller University Jena, 07743 Jena, Germany; Department: Functional Interface, Leibniz Institute of Photonic Technology, 07745 Jena, Germany; Present Address: RPTU Kaiserslautern-Landau, Chemistry Department and State Research Center Optimas, Erwin-Schrödinger-Strasse 52, 67663 Kaiserslautern, Germany.; [orcid.org/0000-0001-6073-1970](https://orcid.org/0000-0001-6073-1970); Email: [waechtler@chemie.uni-kl.de](mailto:waechtler@chemie.uni-kl.de)

### Authors

**Stefan Benndorf** – Institute of Inorganic and Analytical Chemistry, Friedrich Schiller University Jena, 07743 Jena, Germany

**Alexander Schleusener** – Institute of Physical Chemistry, Friedrich Schiller University Jena, 07743 Jena, Germany; Department: Functional Interface, Leibniz Institute of Photonic Technology, 07745 Jena, Germany; Present Address: Istituto Italiano di Tecnologia, Via Morego 30, 16163 Genova, Italy

**Riccarda Müller** – Institute of Analytical and Bioanalytical Chemistry, Ulm University, 89081 Ulm, Germany

**Mathias Micheel** – Department: Functional Interface, Leibniz Institute of Photonic Technology, 07745 Jena, Germany; [orcid.org/0000-0002-5017-3511](https://orcid.org/0000-0002-5017-3511)

**Raktim Baruah** – Institute of Physical Chemistry, Friedrich Schiller University Jena, 07743 Jena, Germany; Department: Functional Interface, Leibniz Institute of Photonic Technology, 07745 Jena, Germany

**Jan Dellith** – Department: Functional Interface, Leibniz Institute of Photonic Technology, 07745 Jena, Germany

**Andreas Undisz** – Institute of Materials Science and Engineering, Chemnitz University of Technology, 09125 Chemnitz, Germany; Otto Schott Institute of Materials Research, Friedrich Schiller University Jena, 07743 Jena, Germany

**Christof Neumann** – Institute of Physical Chemistry, Friedrich Schiller University Jena, 07743 Jena, Germany; [orcid.org/0000-0002-3598-7656](https://orcid.org/0000-0002-3598-7656)

**Andrey Turchanin** – Institute of Physical Chemistry, Friedrich Schiller University Jena, 07743 Jena, Germany; Abbe Center of Photonics (ACP), Friedrich Schiller University Jena, 07745 Jena, Germany; [orcid.org/0000-0003-2388-1042](https://orcid.org/0000-0003-2388-1042)

**Kerstin Leopold** – Institute of Analytical and Bioanalytical Chemistry, Ulm University, 89081 Ulm, Germany

Complete contact information is available at:

<https://pubs.acs.org/10.1021/acsami.3c00184>

### Author Contributions

S.B. and A.S. contributed equally. All authors have given approval to the final version of the manuscript. S.B.: conceptualization, data curation, formal analysis, investigation, methodology, validation, visualization, writing—review & editing. A.S.: conceptualization, data curation, formal analysis, investigation, methodology, validation, writing—original draft, review & editing. R.M.: data curation, formal analysis, investigation, methodology, validation, writing—review & editing. R.B.: formal analysis, investigation, validation, writing—review & editing. J.D.: investigation, resources. A.U.: investigation and resources. C. N.: formal analysis, investigation, writing—review & editing. M.M.: formal analysis, visualization, writing—original draft, review & editing. A.T.: funding acquisition, resources, supervision, writing—review & editing. K.L.: conceptualization, data curation, funding acquisition, resources, supervision, writing—review & editing. W.W.: conceptualization, data curation, funding acquisition, project administration, resources, supervision, writing—review & editing. M.W.: conceptualization, data curation, funding acquisition, project administration, resources, supervision, writing—review & editing.

### Notes

The authors declare no competing financial interest.

### ACKNOWLEDGMENTS

This research was funded by the German Research Foundation (DFG)—project numbers 364549901—TRR234 (CataLight, A2, B4, and Z2), 398816777—CRC1375 (NOA, C4), and the Fonds der Chemischen Industrie (FCI). Financial support by the German Research Foundation (DFG) within the infrastructure grants INST 275/357-1 FUGG (C.N. and A.T.) and 390918228—INST 275/391-1 (A.U.) is gratefully acknowledged. We are grateful to Dr. Merten and Kamp for performing ICP—OES measurements. We are thankful to Dr. Schulz and Rottluff for measuring hydrogen contents via GC—TCD.

### ABBREVIATIONS

QDs, quantum dots  
HM-AA, [FeFe] hydrogenase mimic based on 2-carboxy-1,3-propanedithiol  
HM-LA, [FeFe] hydrogenase mimic based on 6,8-dithiooctanoic acid  
ATR-FTIR, attenuated total reflection-Fourier transform infrared  
XPS, X-ray photoelectron spectroscopy  
 $\mu$ XRF, micro-X-ray fluorescence spectrometry  
SED, sacrificial electron donor

### REFERENCES

- (1) Li, X.-B.; Tung, C.-H.; Wu, L.-Z. Semiconducting Quantum Dots for Artificial Photosynthesis. *Nat. Rev. Chem.* **2018**, *2*, 160–173.
- (2) Moroz, P.; Boddy, A.; Zamkov, M. Challenges and Prospects of Photocatalytic Applications Utilizing Semiconductor Nanocrystals. *Front. Chem.* **2018**, *6*, 353.
- (3) Xu, Y.; Huang, Y.; Zhang, B. Rational Design of Semiconductor-Based Photocatalysts for Advanced Photocatalytic Hydrogen Production: The Case of Cadmium Chalcogenides. *Inorg. Chem. Front.* **2016**, *3*, 591–615.

- (4) Burke, R.; Bren, K. L.; Krauss, T. D. Semiconductor Nanocrystal Photocatalysis for the Production of Solar Fuels. *J. Chem. Phys.* **2021**, *154*, 030901.
- (5) Amaro-Gahete, J.; Pavliuk, M. V.; Tian, H.; Esquivel, D.; Romero-Salguero, F. J.; Ott, S. Catalytic Systems Mimicking the [FeFe]-Hydrogenase Active Site for Visible-Light-Driven Hydrogen Production. *Coord. Chem. Rev.* **2021**, *448*, 214172.
- (6) Weigand, W. [FeFe]-Hydrogenase Mimics: Bio-Inspired Hydrogen Production. *Phosphorus, Sulfur, Silicon Relat. Elem.* **2019**, *194*, 634–637.
- (7) Tard, C.; Pickett, C. J. Structural and Functional Analogues of the Active Sites of the [Fe]-, [NiFe]-, and [FeFe]-Hydrogenases. *Chem. Rev.* **2009**, *109*, 2245–2274.
- (8) Lubitz, W.; Ogata, H.; Rüdiger, O.; Reijerse, E. Hydrogenases. *Chem. Rev.* **2014**, *114*, 4081–4148.
- (9) Simmons, T. R.; Berggren, G.; Bacchi, M.; Fontecave, M.; Artero, V. Mimicking Hydrogenases: From Biomimetics to Artificial Enzymes. *Coord. Chem. Rev.* **2014**, *270–271*, 127–150.
- (10) Kleinhaus, J. T.; Wittkamp, F.; Yadav, S.; Siegmund, D.; Apfel, U.-P. [FeFe]-Hydrogenases: maturation and reactivity of enzymatic systems and overview of biomimetic models. *Chem. Soc. Rev.* **2021**, *50*, 1668–1784.
- (11) Wu, L.-Z.; Chen, B.; Li, Z.-J.; Tung, C.-H. Enhancement of the Efficiency of Photocatalytic Reduction of Protons to Hydrogen via Molecular Assembly. *Acc. Chem. Res.* **2014**, *47*, 2177–2185.
- (12) Yuan, Y.-J.; Yu, Z.-T.; Chen, D.-Q.; Zou, Z.-G. Metal-Complex Chromophores for Solar Hydrogen Generation. *Chem. Soc. Rev.* **2017**, *46*, 603–631.
- (13) Liu, J.; Ren, Y.-Y.; Wu, J.; Xia, W.; Deng, B.-Y.; Wang, F. Hybrid Artificial Photosynthetic Systems Constructed Using Quantum Dots and Molecular Catalysts for Solar Fuel Production: Development and Advances. *J. Mater. Chem. A* **2021**, *9*, 19346–19368.
- (14) Dalle, K. E.; Warnan, J.; Leung, J. J.; Reuillard, B.; Karmel, I. S.; Reisner, E. Electro- and Solar-Driven Fuel Synthesis with First Row Transition Metal Complexes. *Chem. Rev.* **2019**, *119*, 2752–2875.
- (15) Eckenhoff, W. T. Molecular catalysts of Co, Ni, Fe, and Mo for Hydrogen Generation in Artificial Photosynthetic Systems. *Coord. Chem. Rev.* **2018**, *373*, 295–316.
- (16) Jian, J.-X.; Ye, C.; Wang, X.-Z.; Wen, M.; Li, Z.-J.; Li, X.-B.; Chen, B.; Tung, C.-H.; Wu, L.-Z. Comparison of H<sub>2</sub> Photogeneration by [FeFe]-Hydrogenase Mimics with CdSe QDs and Ru(bpy)<sub>3</sub>Cl<sub>2</sub> in Aqueous Solution. *Energy Environ. Sci.* **2016**, *9*, 2083–2089.
- (17) Schleusener, A.; Micheel, M.; Benndorf, S.; Rettenmayr, M.; Weigand, W.; Wächtler, M. Ultrafast Electron Transfer from CdSe Quantum Dots to an [FeFe]-Hydrogenase Mimic. *J. Phys. Chem. Lett.* **2021**, *12*, 4385–4391.
- (18) Corredor, J.; Harankahage, D.; Gloaguen, F.; Rivero, M. J.; Zamkov, M.; Ortiz, I. Influence of QD Photosensitizers in the Photocatalytic Production of Hydrogen with Biomimetic [FeFe]-Hydrogenase. Comparative Performance of CdSe and CdTe. *Chemosphere* **2021**, *278*, 130485.
- (19) Peterson, M. D.; Cass, L. C.; Harris, R. D.; Edme, K.; Sung, K.; Weiss, E. A. The Role of Ligands in Determining the Exciton Relaxation Dynamics in Semiconductor Quantum Dots. *Annu. Rev. Phys. Chem.* **2014**, *65*, 317–339.
- (20) Abdellah, M.; Zhang, S.; Wang, M.; Hammarström, L. Competitive Hole Transfer from CdSe Quantum Dots to Thiol Ligands in CdSe-Cobaloxime Sensitized NiO Films Used as Photocathodes for H<sub>2</sub> Evolution. *ACS Energy Lett.* **2017**, *2*, 2576–2580.
- (21) Wen, F.; Wang, X.; Huang, L.; Ma, G.; Yang, J.; Li, C. A Hybrid Photocatalytic System Comprising ZnS as Light Harvester and an [Fe<sub>2</sub>S<sub>2</sub>] Hydrogenase Mimic as Hydrogen Evolution Catalyst. *ChemSusChem* **2012**, *5*, 849–853.
- (22) Wang, F.; Liang, W.-J.; Jian, J.-X.; Li, C.-B.; Chen, B.; Tung, C.-H.; Wu, L.-Z. Exceptional Poly(Acrylic Acid)-Based Artificial [FeFe]-Hydrogenases for Photocatalytic H<sub>2</sub> Production in Water. *Angew. Chem., Int. Ed.* **2013**, *52*, 8134–8138.

- (23) Wen, M.; Li, X.-B.; Jian, J.-X.; Wang, X.-Z.; Wu, H.-L.; Chen, B.; Tung, C.-H.; Wu, L.-Z. Secondary Coordination Sphere Accelerates Hole Transfer for Enhanced Hydrogen Photogeneration from [FeFe]-Hydrogenase Mimic and CdSe QDs in Water. *Sci. Rep.* **2016**, *6*, 29851.
- (24) Cheng, M.; Wang, M.; Zhang, S.; Liu, F.; Yang, Y.; Wan, B.; Sun, L. Photocatalytic H<sub>2</sub> Production Using a Hybrid Assembly of an [FeFe]-Hydrogenase Model and CdSe Quantum Dot Linked through a Thiolato-Functionalized Cyclodextrin. *Faraday Discuss.* **2017**, *198*, 197–209.
- (25) Li, X.-B.; Jian, J.-X.; Wang, X.-Z.; Wang, Y.; Xia, S.-G.; Tung, C.-H.; Wu, L.-Z. Per-6-Thiol-Cyclodextrin Engineered [FeFe]-Hydrogenase Mimic/CdSe Quantum Dot Assembly for Photocatalytic Hydrogen Production. *Sol. RRL* **2021**, *5*, 2000474.
- (26) Wen, M.; Wu, H.-L.; Jian, J.-X.; Wang, X.-Z.; Li, X.-B.; Chen, B.; Tung, C.-H.; Wu, L.-Z. Integrating CdSe Quantum Dots with a [FeFe]-Hydrogenase Mimic into a Photocathode for Hydrogen Evolution at a Low Bias Voltage. *ChemPhotoChem* **2017**, *1*, 260–264.
- (27) Li, C.-B.; Li, Z.-J.; Yu, S.; Wang, G.-X.; Wang, F.; Meng, Q.-Y.; Chen, B.; Feng, K.; Tung, C.-H.; Wu, L.-Z. Interface-Directed Assembly of a Simple Precursor of [FeFe]-H<sub>2</sub>ase Mimics on CdSe QDs for Photosynthetic Hydrogen Evolution in Water. *Energy Environ. Sci.* **2013**, *6*, 2597–2602.
- (28) Carbone, L.; Nobile, C.; De Giorgi, M.; Sala, F. D.; Morello, G.; Pompa, P.; Hytch, M.; Snoeck, E.; Fiore, A.; Franchini, I. R.; Nadasan, M.; Silvestre, A. F.; Chiodo, L.; Kudera, S.; Cingolani, R.; Krahn, R.; Manna, L. Synthesis and Micrometer-Scale Assembly of Colloidal CdSe/CdS Nanorods Prepared by a Seeded Growth Approach. *Nano Lett.* **2007**, *7*, 2942–2950.
- (29) Fisher, A. A. E.; Osborne, M. A.; Day, I. J.; Lucena Alcalde, G. Measurement of Ligand Coverage on Cadmium Selenide Nanocrystals and Its Influence on Dielectric Dependent Photoluminescence Intermittency. *Commun. Chem.* **2019**, *2*, 63.
- (30) Benndorf, S.; Hofmeister, E.; Wächter, M.; Görls, H.; Liebing, P.; Peneva, K.; Gräfe, S.; Kupfer, S.; Dietzek-Ivanšić, B.; Weigand, W. Unravelling the Mystery: Enlightenment of the Uncommon Electrochemistry of Naphthalene Monoimide [FeFe] Hydrogenase Mimics. *Eur. J. Inorg. Chem.* **2022**, *2022*, No. e202100959.
- (31) Murray, C. B.; Kagan, C. R.; Bawendi, M. G. Synthesis and Characterization of Monodisperse Nanocrystals and Close-Packed Nanocrystal Assemblies. *Annu. Rev. Mater. Sci.* **2000**, *30*, 545–610.
- (32) Bingaman, J. L.; Kohnhorst, C. L.; Van Meter, G. A.; McElroy, B. A.; Rakowski, E. A.; Caplins, B. W.; Gutowski, T. A.; Stromberg, C. J.; Webster, C. E.; Heilweil, E. J. Time-Resolved Vibrational Spectroscopy of [FeFe]-Hydrogenase Model Compounds. *J. Phys. Chem. A* **2012**, *116*, 7261–7271.
- (33) Knorr, G.; Costabel, D.; Skabeev, A.; Neumann, C.; Brossette, J.; Kupfer, S.; Turchanin, A.; Weigand, W.; Peneva, K. Towards Synthetic Unimolecular [Fe<sub>2</sub>S<sub>2</sub>]-Photocatalysts Sensitized by Perylene Dyes. *Dyes Pigments* **2022**, *198*, 109940.
- (34) Powell, C. NIST X-Ray Photoelectron Spectroscopy Database. *NIST Standard Reference Database 20*, version 4.1, 2000.
- (35) Marvin, 19.21.6; ChemAxon: Budapest, 2022.
- (36) Muhammad, M. T.; Khan, M. N. Kinetics, Mechanistic and Synergistic Studies of Alpha Lipoic Acid with Hydrogen Peroxide. *J. Saudi Chem. Soc.* **2017**, *21*, 123–131.
- (37) Caplins, B. W.; Lomont, J. P.; Nguyen, S. C.; Harris, C. B. Vibrational Cooling Dynamics of a [FeFe]-Hydrogenase Mimic Probed by Time-Resolved Infrared Spectroscopy. *J. Phys. Chem. A* **2014**, *118*, 11529–11540.
- (38) Kennehan, E. R.; Munson, K. T.; Doucette, G. S.; Marshall, A. R.; Beard, M. C.; Asbury, J. B. Dynamic Ligand Surface Chemistry of Excited PbS Quantum Dots. *J. Phys. Chem. Lett.* **2020**, *11*, 2291–2297.
- (39) Wilker, M. B.; Utterback, J. K.; Greene, S.; Brown, K. A.; Mulder, D. W.; King, P. W.; Dukovic, G. Role of Surface-Capping Ligands in Photoexcited Electron Transfer between CdS Nanorods and [FeFe] Hydrogenase and the Subsequent H<sub>2</sub> Generation. *J. Phys. Chem. C* **2018**, *122*, 741–750.
- (40) Hisatomi, T.; Takanabe, K.; Domen, K. Photocatalytic Water-Splitting Reaction from Catalytic and Kinetic Perspectives. *Catal. Lett.* **2015**, *145*, 95–108.
- (41) Troppmann, S.; König, B. Functionalized Vesicles with Co-Embedded CdSe Quantum Dots and [FeFe]-Hydrogenase Mimic for Light-Driven Hydrogen Production. *ChemistrySelect* **2016**, *1*, 1405–1409.
- (42) Wang, F.; Wang, W.-G.; Wang, X.-J.; Wang, H.-Y.; Tung, C.-H.; Wu, L.-Z. A Highly Efficient Photocatalytic System for Hydrogen Production by a Robust Hydrogenase Mimic in an Aqueous Solution. *Angew. Chem., Int. Ed.* **2011**, *50*, 3193–3197.
- (43) Liang, W.-J.; Wang, F.; Wen, M.; Jian, J.-X.; Wang, X.-Z.; Chen, B.; Tung, C.-H.; Wu, L.-Z. Branched Polyethylenimine Improves Hydrogen Photoproduction from a CdSe Quantum Dot/[FeFe]-Hydrogenase Mimic System in Neutral Aqueous Solutions. *Chem.–Eur. J.* **2015**, *21*, 3187–3192.
- (44) Wu, K.; Chen, Z.; Lv, H.; Zhu, H.; Hill, C. L.; Lian, T. Hole Removal Rate Limits Photodriven H<sub>2</sub> Generation Efficiency in CdS-Pt and CdSe/CdS-Pt Semiconductor Nanorod–Metal Tip Heterostructures. *J. Am. Chem. Soc.* **2014**, *136*, 7708–7716.
- (45) Simon, T.; Carlson, M. T.; Stolarczyk, J. K.; Feldmann, J. Electron Transfer Rate vs Recombination Losses in Photocatalytic H<sub>2</sub> Generation on Pt-Decorated CdS Nanorods. *ACS Energy Lett.* **2016**, *1*, 1137–1142.
- (46) Song, X.-W.; Wen, H.-M.; Ma, C.-B.; Hu, M.-Q.; Chen, H.; Cui, H.-H.; Chen, C.-N. Photocatalytic Hydrogen Evolution by Two Comparable [FeFe]-Hydrogenase Mimics Assembled to the Surface of ZnS. *Appl. Organomet. Chem.* **2014**, *28*, 267–273.
- (47) Shaver, A.; Lopez, O.; Harpp, D. N. The reactions of organosulfur transfer reagents with Fe<sub>2</sub>(CO)<sub>9</sub> and the synthesis of the Fe<sub>2</sub>(CO)<sub>6</sub> derivative of α-lipoic acid. *Inorganica Chimica Acta* **1986**, *119*, 13–18.
- (48) Jiang, X.; Long, L.; Wang, H.; Chen, L.; Liu, X. Diiron Hexacarbonyl Complexes as Potential CO-RMs: CO-Releasing Initiated by a Substitution Reaction with Cysteamine and Structural Correlation to the Bridging Linkage. *Dalton Trans.* **2014**, *43*, 9968–9975.
- (49) Volkers, P. I.; Rauchfuss, T. B.; Wilson, S. R. Coordination Chemistry of 3-Mercapto-2-(mercaptomethyl)propanoic Acid (Dihydroasparagusic Acid) with Iron and Nickel. *Eur. J. of Inorg. Chem.* **2006**, *23*, 4793–4799.
- (50) Thomas, C. M.; Rüdiger, O.; Liu, T.; Carson, C. E.; Hall, M. B.; Darensbourg, M. Y. Synthesis of Carboxylic Acid-Modified [FeFe]-Hydrogenase Model Complexes Amenable to Surface Immobilization. *Organometallics* **2007**, *26*, 3976–3984.

Supporting Information

# Covalent Functionalization of CdSe Quantum Dot Films with Molecular [FeFe] Hydrogenase Mimics for Light-Driven Hydrogen Evolution

*Stefan Benndorf<sup>1‡</sup>, Alexander Schleusener<sup>2,3‡#</sup>, Riccarda Müller<sup>4</sup>, Mathias Micheel<sup>3</sup>, Raktim Baruah<sup>2,3</sup>, Jan Dellith<sup>3</sup>, Andreas Undisz<sup>5,6</sup>, Christof Neumann<sup>2</sup>, Andrey Turchanin<sup>2,7</sup>, Kerstin Leopold<sup>4</sup>, Wolfgang Weigand<sup>1\*</sup>, Maria Wächtler<sup>2,3\*§</sup>*

<sup>1</sup> Institute of Inorganic and Analytical Chemistry, Friedrich Schiller University Jena,  
Humboldtstr. 8, 07743 Jena, Germany

<sup>2</sup> Institute of Physical Chemistry, Friedrich Schiller University Jena, Helmholtzweg 4, 07743,  
Jena, Germany

<sup>3</sup> Leibniz Institute of Photonic Technology, Department: Functional Interface, Albert-Einstein-  
Str. 9, 07745, Jena, Germany

<sup>4</sup> Institute of Analytical and Bioanalytical Chemistry, Ulm University, Albert-Einstein-Allee 11,  
89081 Ulm, Germany

<sup>5</sup> Institute of Materials Science and Engineering, Chemnitz University of Technology,  
Erfenschlager Str. 73, 09125 Chemnitz, Germany

<sup>6</sup>Otto Schott Institute of Materials Research, Friedrich Schiller University Jena, 07743 Jena,  
Germany

<sup>7</sup>Abbe Center of Photonics (ACP), Friedrich Schiller University Jena, Albert-Einstein-Straße 6,  
07745 Jena, Germany

‡these authors contributed equally

#### AUTHOR INFORMATION

##### **Corresponding Author**

\*Prof. Dr. Wolfgang Weigand, Institute of Inorganic and Analytical Chemistry, Friedrich Schiller University Jena, 07743 Jena, Germany, Email: [wolfgang.weigand@uni-jena.de](mailto:wolfgang.weigand@uni-jena.de)

\*Prof. Dr. Maria Wächtler, RPTU Kaiserslautern-Landau, Chemistry Department and State Research Center Optimas, 67663 Kaiserslautern, Germany; Email: [waechtler@chemie.uni-kl.de](mailto:waechtler@chemie.uni-kl.de)

##### **Present Addresses**

# Alexander Schleusener: Istituto Italiano di Tecnologia, Via Morego 30, 16163 Genova, Italy

§ Maria Wächtler: RPTU Kaiserslautern-Landau, Chemistry Department and State Research Center Optimas, Erwin-Schrödinger-Strasse 52, 67663 Kaiserslautern, Germany

### Calibration function micro X-ray fluorescence spectra ( $\mu$ XRF)

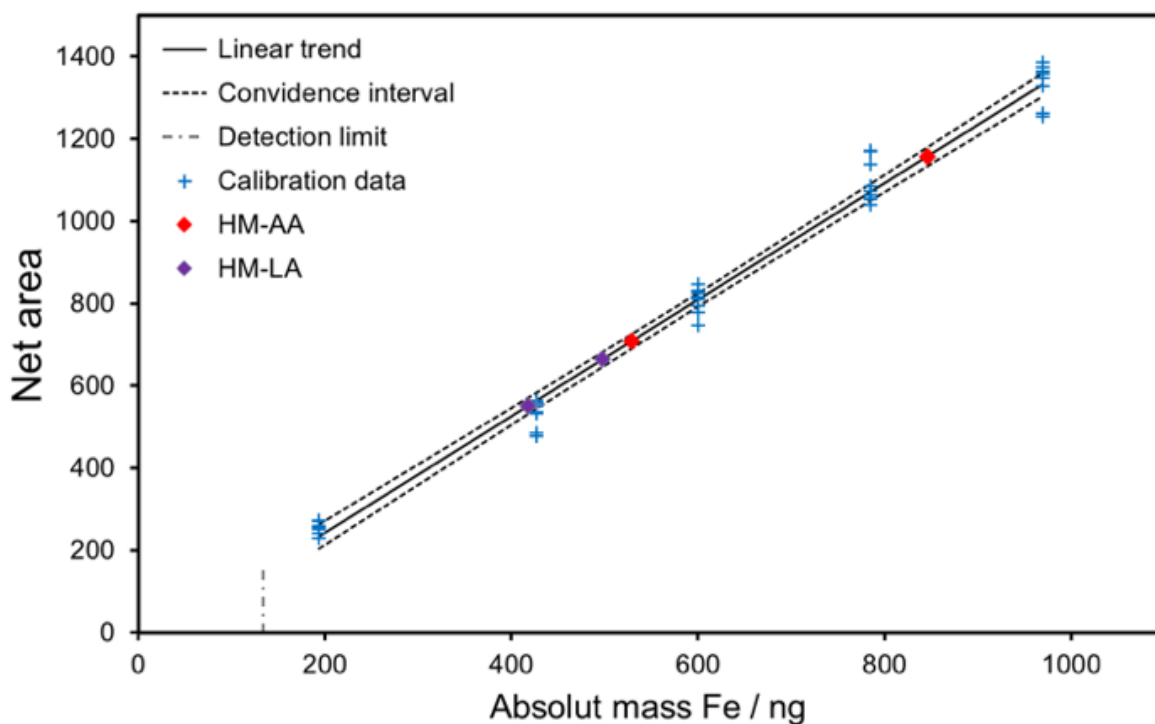


Figure S1: External calibration for Fe quantification by  $\mu$ XRF including measurement data for 2 parallel samples each, with HM-LA1:  $417 \pm 64$  ng; HM-LA2:  $498 \pm 65$  ng; HM-AA1:  $529 \pm 64$  ng; HM-AA2:  $846 \pm 65$  ng. With a substrate size of 25 mm x 5 mm, we determine the loading with catalyst to HM-LA1:  $3.0 \pm 0.5$  nmol  $\text{cm}^{-2}$ , HM-LA2:  $3.6 \pm 0.5$  nmol  $\text{cm}^{-2}$ ; HM-AA1:  $3.8 \pm 0.5$  nmol  $\text{cm}^{-2}$ ; HM-AA2:  $6.1 \pm 0.5$  nmol  $\text{cm}^{-2}$ .



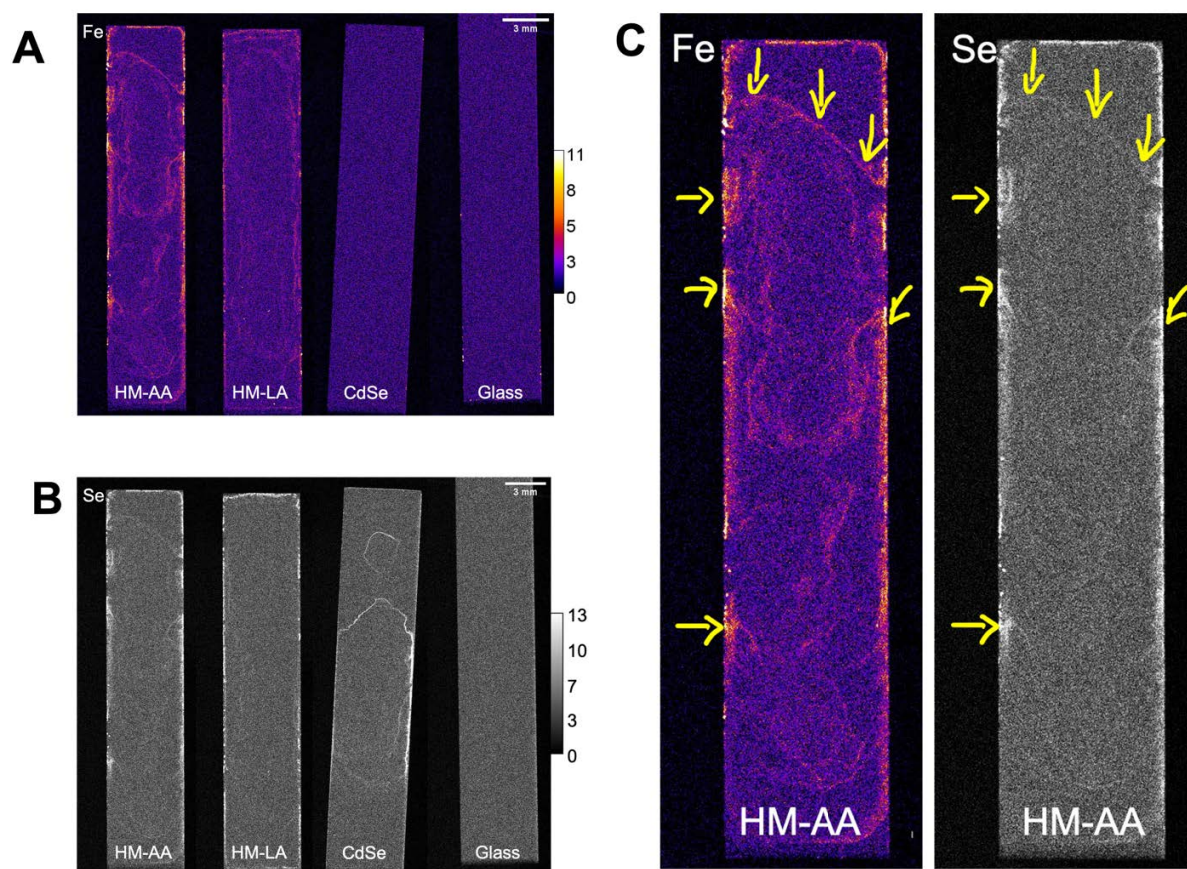


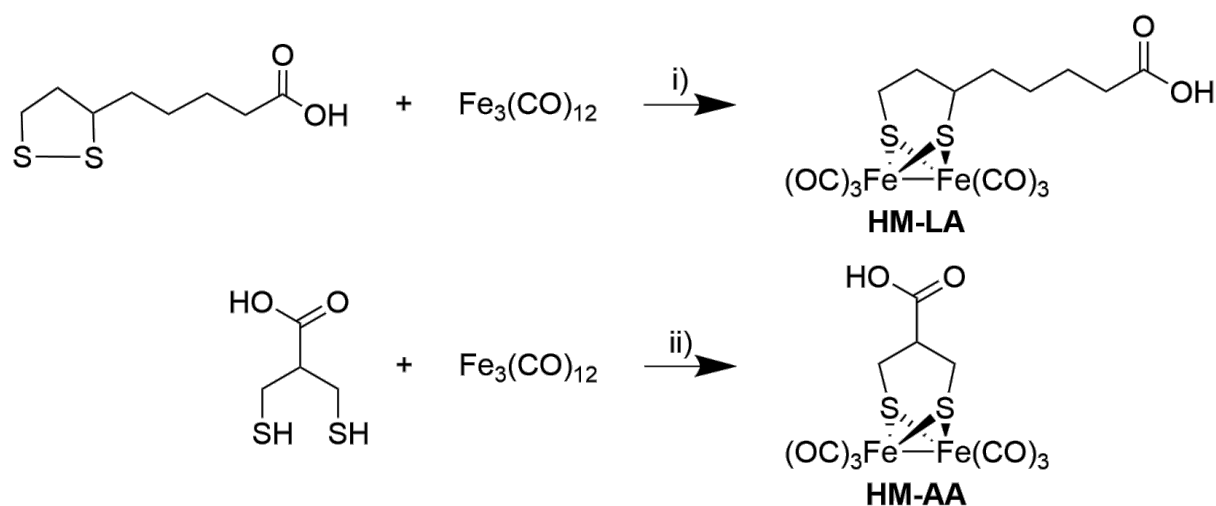
Figure S2: Element distribution of different films (HM-AA; HM-LA; CdSe) on quartz glass substrate and blank substrate (Glass) as measured by  $\mu$ XRF. (A) Iron (Fe) distribution; (B) Selenium (Se) distribution and (C) Fe and Se overlap on HM-AA (yellow arrows mark areas with higher element content). Fiji software (1.53f51) was used for visualization of Fe results in heat maps.<sup>1</sup> The preparation of the slides was confirmed to be reproducible with less than 16 % of relative standard deviation (Table S1).

Fe distribution in HM-AA and HM-LA films shows slight inhomogeneities (Fig. S2 A). Presumably, this results from minor variation in CdSe quantum dot films drop casted onto the substrate. This assumption was proved by investigation of Se distribution as shown in Fig. S2 B, while Cd signals are too low to make differences in the intensity clearly visible. However, Fe and

Se distribution show identical distribution pattern as illustrated in the overlaid element maps in Figure S2 C.

### Synthesis of [FeFe] hydrogenase mimics

The syntheses of complexes **HM-LA** and **HM-AA** were carried out by use of a recently developed synthetic pathway using NMP (N-Methyl-2-pyrrolidone) as an additive (see Scheme S1).<sup>2</sup>



Scheme S1: Synthesis route for hydrogenase model complexes **HM-LA** and **HM-AA**, i) toluene, NMP, 50 °C, 30 min; ii) toluene, NMP, 50 °C, 10 min.

### Size of CdSe quantum dots

The QD size was determined *via* their lowest energy absorption peak using a method by Yu *et al.*<sup>3</sup> In addition, we recorded TEM images (Figure S3).

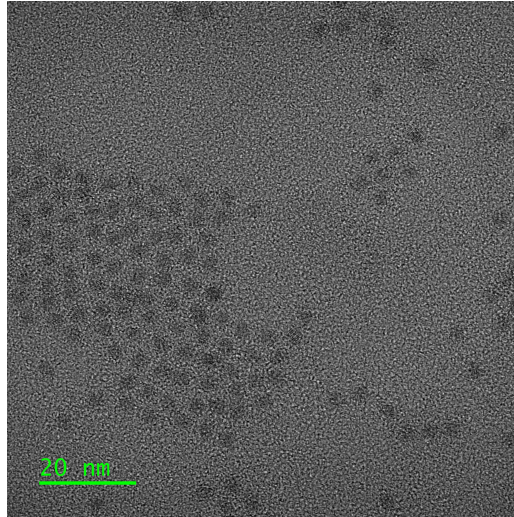


Figure S3: TEM image of one of the synthesized QD batches.

## Thickness of quantum dot films

The thickness of the drop casted films prepared for photocatalytic experiments was determined by atomic force microscopy. To this end, the films were scratched to partially remove the QD layer. Topographical maps of the scratched films were collected in tapping mode. The line profiles across the scratched region were linearly fitted to account for local inhomogeneities.

We performed this thickness analysis twice per film on different areas of the scratch and obtained an average thickness of  $17.0 \pm 1.2$  nm.

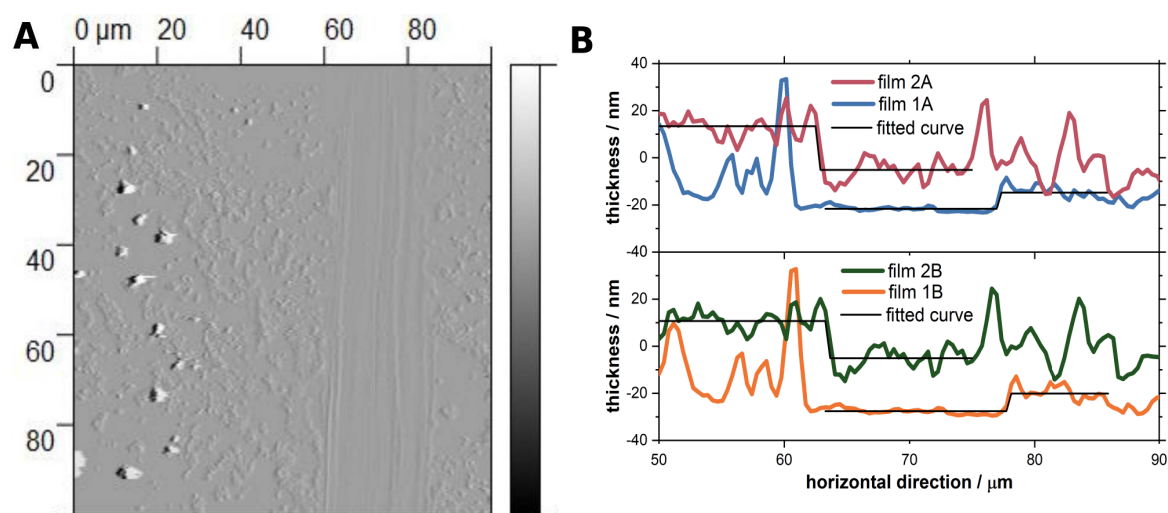


Figure S4. (A) AFM image of CdSe QD film on glass. (B) Thickness determination of QD films (film 1 & film 2) from two measurements A & B respectively.

## Correction of thin-film absorption spectra

To correct the absorption spectrum for the scattering contribution, a theoretical scattering curve  $S_\lambda$  in the wavelength range in which the quantum dots do not absorb (550 to 800 nm for quantum dots with a mean diameter of 2.4-2.5 nm) was fitted to the absorption spectrum according to

$$S_\lambda = m \cdot \lambda^n$$

With the wavelength  $\lambda$  in nm and the exponent  $n$  with values of -4 (Rayleigh scattering for spherical and small particles with a diameter  $d$ ) to -1 (for larger particles and/or non-spherical particles). The factor  $m$  serves to adapt the theoretical curve to the stray background in the absorption spectrum of the quantum dot film.<sup>4</sup>

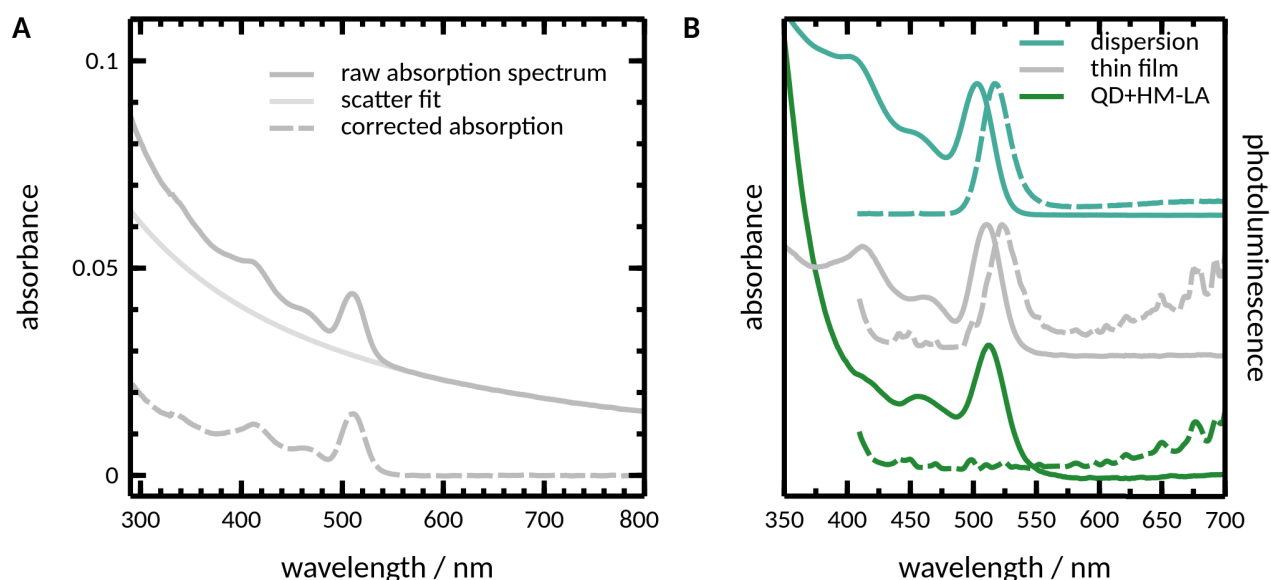


Figure S5. (A) As-recorded absorption spectrum, scattering correction, and scattering-corrected absorption spectrum for a quantum dot film. (B) Absorption (solid line) and photoluminescence (dashed line) spectra of quantum dots in toluene dispersion and in thin films. Absorption and photoluminescence spectra were normalized to their lowest and highest energy peak, respectively.

After fitting the theoretical curve to the absorption spectrum, the extrapolation to the entire measured wavelength range is performed. The resulting theoretical scattering curve is subtracted from the measured absorption spectrum and yields the corrected absorption spectrum of the QD layer. It should be noted that this procedure is subject to error due to extrapolation over the entire wavelength range. However, since the scattering is not identical for each sample due to fabrication inaccuracies, the spectra obtained by the described procedure provide a good basis to compare the functionalization of the QD thin films with **HM-LA** and **HM-AA**.

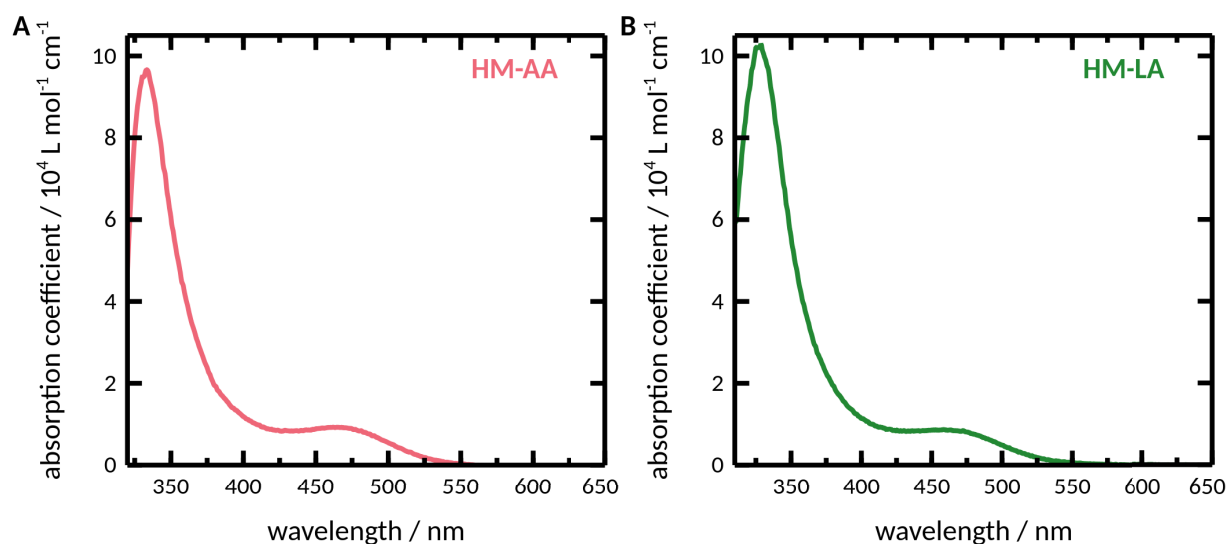


Figure S6: Absorption coefficients of the hydrogenase mimics in toluene: (A) HM-AA, (B) HM-LA.

## IR spectra

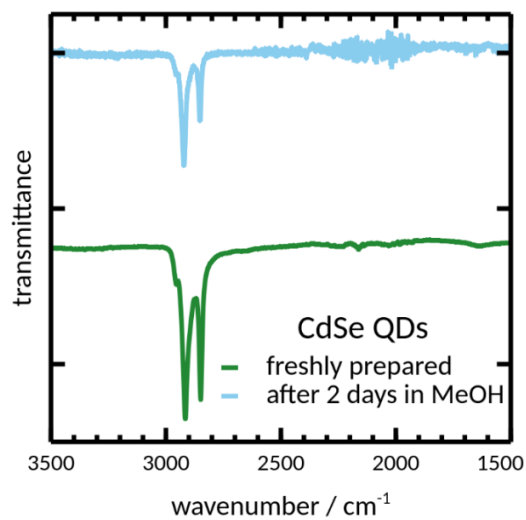


Figure S7: IR spectra of CdSe quantum dots (QDs) directly after dropcasting and after 2 days in methanol (MeOH).

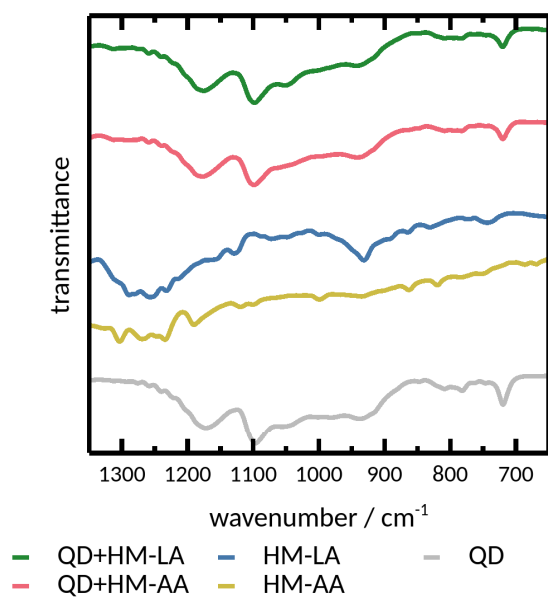


Figure S8. IR spectra of CdSe quantum dot films (QD), hydrogenase mimics and functionalized films in the fingerprint region.

IR spectra of pristine films in the region of interest (1200-3000  $\text{cm}^{-1}$ ) are mainly characterized by asymmetric (2920  $\text{cm}^{-1}$ ) and symmetric (2850  $\text{cm}^{-1}$ )  $-\text{CH}_3$  vibrations from the native alkyl phosphine oxide ligand sphere (Figure 2C).<sup>5</sup> IR spectra of quantum dot films placed in pure methanol are unchanged, further indicating that the quantum dots are inert under functionalization conditions (Figure S7). The hydrogenase mimics, deposited as thin films, show three prominent vibrations between 1900 and 2100  $\text{cm}^{-1}$  (Figure 2D), which are characteristics of the carbonyl ligand stretching modes in hydrogenase mimics,<sup>6</sup> and several vibrations related to the carboxylic group between 1400 and 1700  $\text{cm}^{-1}$  (Figure 2E). The band at 1710  $\text{cm}^{-1}$  relates to the  $\nu(\text{CO})$  stretching vibration of the protonated carboxylic group and a band at 1420  $\text{cm}^{-1}$  to the  $\nu(\text{C-OH})$  in-plane bend mode (Figure 2). Weak and broad bands between 1500 and 1600  $\text{cm}^{-1}$  might relate to deprotonated carboxylates which co-exist in the films. While both molecules exhibit very similar IR features, **HM-LA** shows  $-\text{CH}_2$  vibrations around 3000  $\text{cm}^{-1}$ , which **HM-AA** lacks. These can thus be attributed to the aliphatic linker chain. Last, CdSe quantum dots and **HM-LA** also show a vibration at  $\sim 1470 \text{ cm}^{-1}$ , which relates to the  $-\text{CH}_2-$  scissor vibration in the aliphatic backbone of the surface ligand or catalyst.<sup>5</sup>

The fingerprint region of pristine CdSe quantum dots is characterized by vibrations at 1172 ( $\text{P}=\text{O}$  stretch), 1096 ( $\text{CH}_2$  rock) and 718  $\text{cm}^{-1}$  (in phase rock  $-(\text{CH}_2)_n$  with  $n > 4$ ) of the long phosphonic acid and oxide surface ligands.<sup>7</sup> We observed characteristic C-O stretching vibration of carboxylic acids for both **HM-LA** and **HM-AA** and, in the case of **HM-LA**, a pronounced vibration at 930  $\text{cm}^{-1}$ , related to the long alkyl chain.<sup>5</sup> Functionalized films mostly resemble unfunctionalized CdSe QD films, which confirms the presence of the original surface ligands even after functionalization.



## XPS measurements

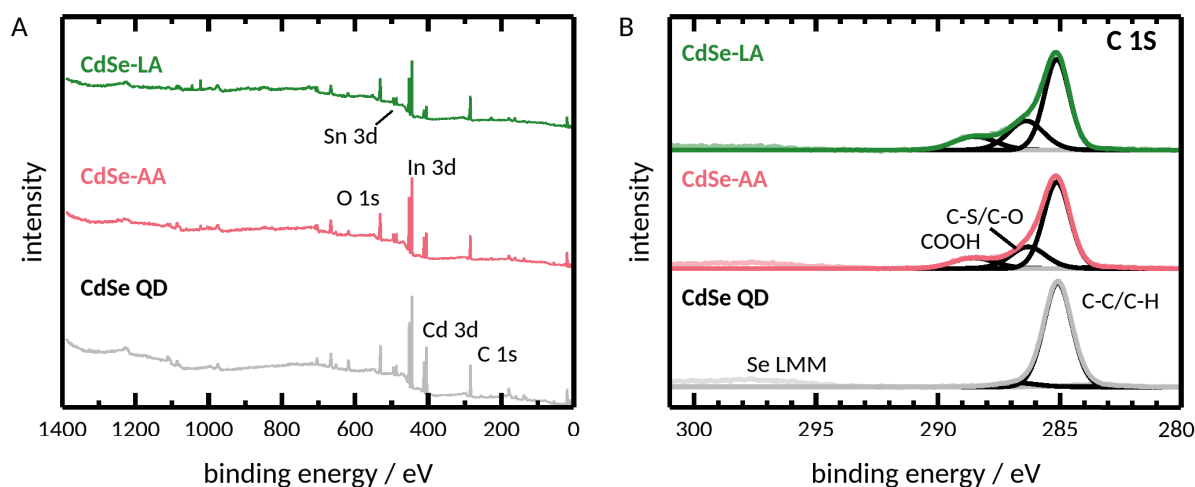


Figure S9: Overview (A) and high-resolution C 1s (C) X-ray photoelectron spectra of functionalized and unfunctionalized quantum dot films.

Figure S9 presents the overview XPS spectra of CdSe quantum dots before and after functionalization with **HM-LA** and **HM-AA**. All spectra show the signals of the substrate ITO and CdSe as well as the carbon signal from the surface ligand trioctylphosphinoxid (TOPO). The arising S and Fe signals after functionalization can be detected in the high-resolution Fe 2p S 2p (see main text Figure 2A and B) regions. The C 1s spectrum before functionalization shows a single carbon peak at  $\sim 285$  eV assigned to C-C bonds originating from the TOPO (Figure S9B). After functionalization, additional shoulders at 286.3 eV (C-S, C-O bonds) and  $\sim 288.4$  eV (COOH) indicate the presence of the hydrogenase mimics confirming the sulfur and iron spectra.

## Calculation of number of quantum dots

The number of CdSe quantum dots per layer was estimated using the calculated radius of one quantum dot ( $r = 1.25$  nm), the resulting volume ( $V_{\text{QD}} = 8.18$  nm<sup>3</sup>), the volume of the elementary cell from the Wurtzite type ( $V_{\text{W-EC}} = 0.112$  nm<sup>3</sup>)<sup>8</sup>, and the Cd content of the layers from ICP-OES measurements. By calculating the ratio of  $V_{\text{QD}}/V_{\text{W-EC}} = 292$  and dividing by 2 (number of CdSe units per elementary cell), we estimate 146 CdSe units per quantum dot. The preparation of the slides was confirmed to be reproducible with less than 16 % of relative standard deviation (Table S1).

**Table S1.** Number of quantum dots for several investigated films.

Samples	$\bar{n}_{\text{CdSeQDs}}$ [nmol]
CdSe QD	$0.383 \pm 0.028$
CdSe QD + HM-LA	$0.353 \pm 0.043$
CdSe QD + HM-AA	$0.283 \pm 0.048$

## Catalyst surface coverage

The mean diameter of the investigated QDs (2.4 – 2.5 nm) result in surface areas in the order of 20 nm<sup>2</sup>. From the XRF measurements, we obtain catalyst loadings of 20 (HM-LA) to 40 (HM-AA) catalytic centers per QD (see main text). With a film thickness of 4 QD layers and assuming that only the topmost layer is functionalized (and only the QD part which lies on the surface, which we approximate to be half the QD), we have to multiply the nominal loading by a factor of 8 to approximate the catalyst loading density of the topmost QD layer. This results in hydrogenase mimic loadings of 6 (HM-LA) to 12 (HM-AA) nm<sup>-2</sup>. Typical surface ligand coverages are in the order of 2-5 ligands nm<sup>-2</sup> QD surface,<sup>9-11</sup> which means we have a complete surface ligand exchange of the topmost QD layer.

## Dependence of activity on irradiation intensity

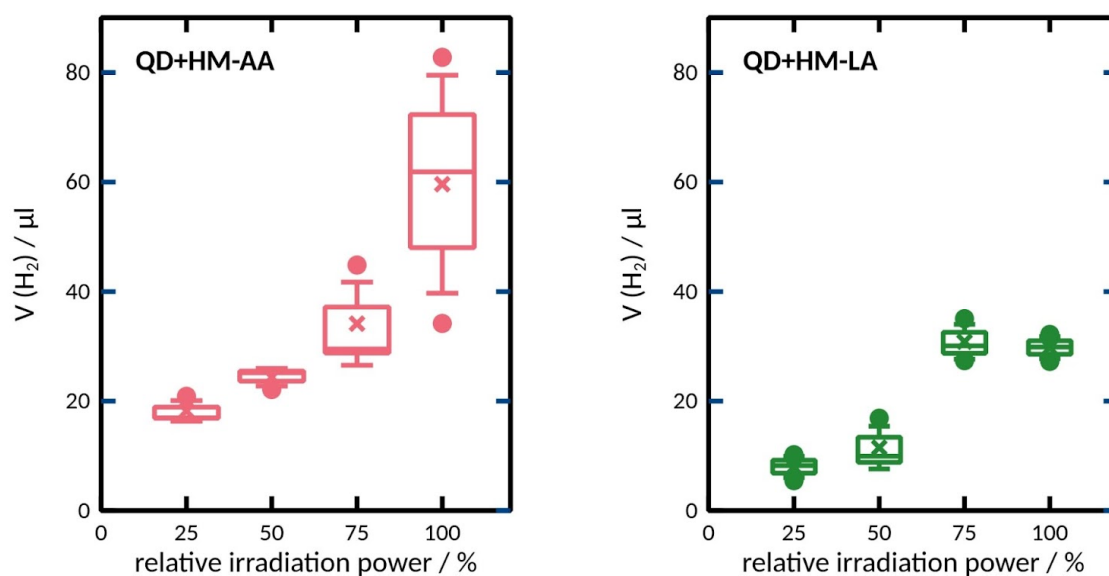


Figure S10: Irradiation power ( $\lambda = 420$  nm,  $P$  (100%) =  $8.5$  mW cm<sup>-2</sup>) dependent photocatalytic performance of hydrogenase mimic functionalized QD films ( $n = 6$  for 75 and 100% and  $n=3$  for 25 and 50 %).

For both catalysts we observed a general increase in efficiency with increasing irradiation power. HM-LA plateaus at the highest irradiation power applied (Figure S10). This effect could be caused by differences catalyst loadings. In films functionalized with HM-AA, even at the highest applied irradiation intensity sufficient acceptor centers are available, whereas for HM-LA, the lower surface coverage might lead at high irradiation intensities to situations where there is no suitable electron acceptor in proximity of a photoexcited QD, which then does not contribute to the catalytic activity of the system anymore.

## Dependence of activity on pH value

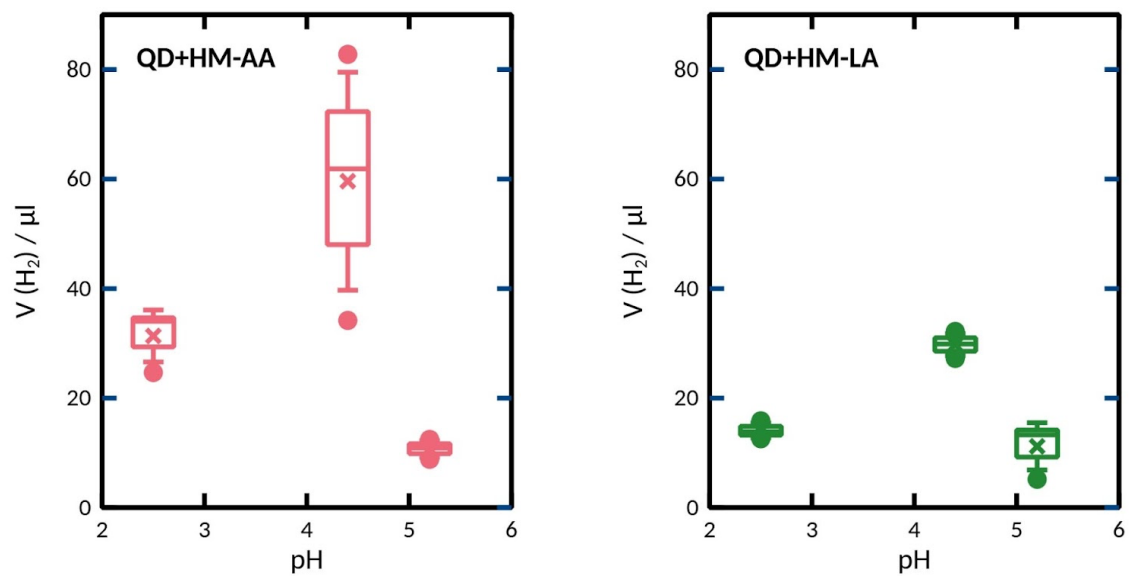


Figure S11: Photocatalytic experiments performed at different pH values.

## Evaluation of stability

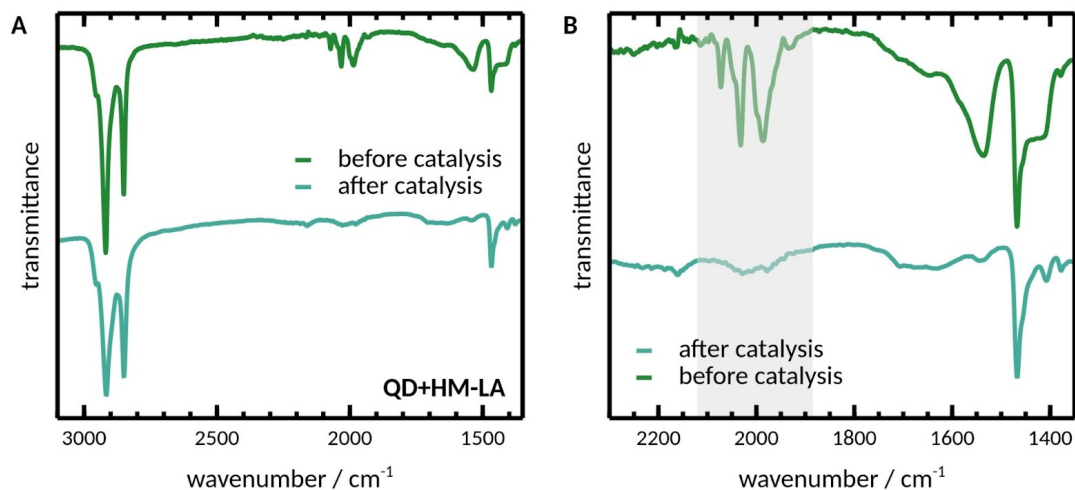


Figure S12: (A) IR spectra of HM-LA functionalized CdSe quantum dots (QDs) directly after drop casting and after 24 hours of photocatalysis. (B) Zoom-in into the CO vibration and vibrations related to the carboxylate of the hydrogenase mimic. After catalysis, these distinct signatures have near fully disappeared.

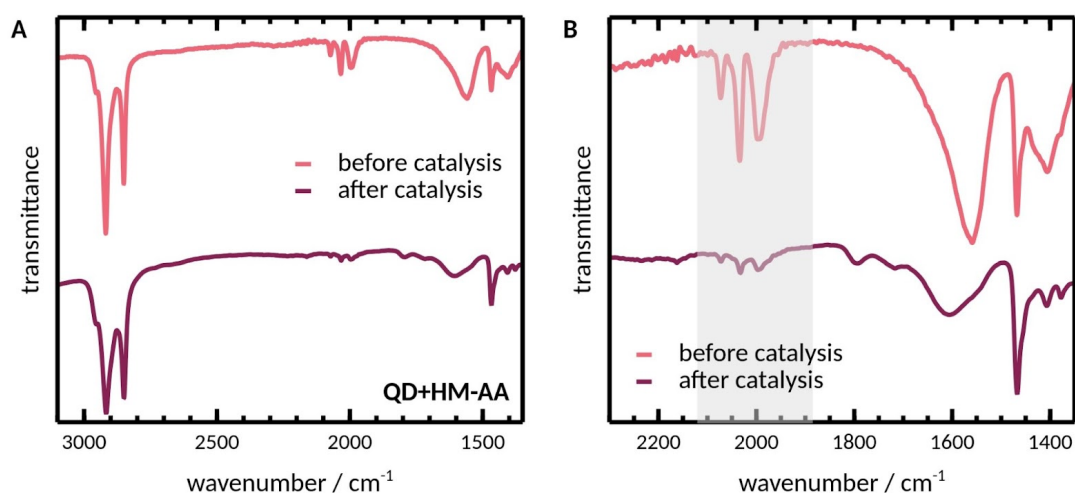


Figure S13: (A) IR spectra of HM-AA functionalized CdSe quantum dots (QDs) directly after drop casting and after 24 hours of photocatalysis. (B) Zoom-in into the CO vibration and vibrations related to the carboxylate of the hydrogenase mimic. After catalysis, these distinct signatures have near fully disappeared.

related to the carboxylate of the hydrogenase mimic. After catalysis, these distinct signatures have near fully disappeared.

## REFERENCES

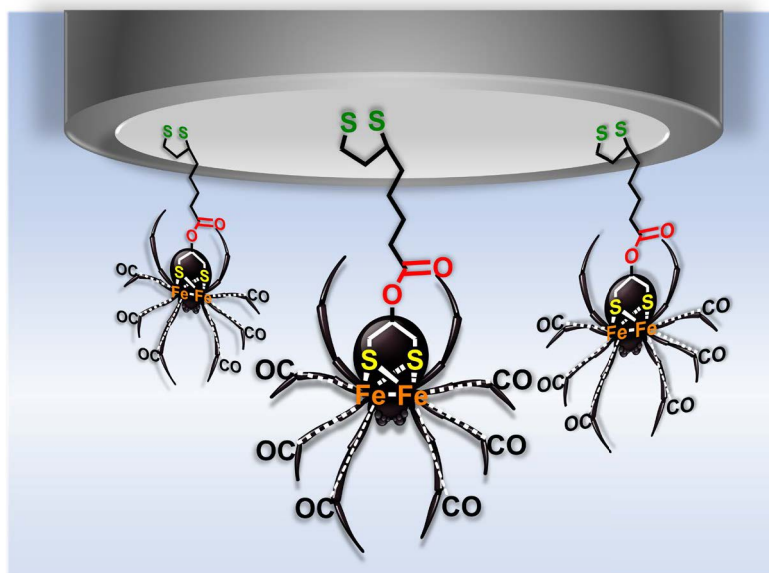
- (1) Schindelin, J.; Arganda-Carreras, I.; Frise, E.; Kaynig, V.; Longair, M.; Pietzsch, T.; Preibisch, S.; Rueden, C.; Saalfeld, S.; Schmid, B.; Tinevez, J.-Y.; White, D. J.; Hartenstein, V.; Eliceiri, K.; Tomancak, P.; Cardona, A. Fiji: An Open-Source Platform for Biological-Image Analysis. *Nat. Methods* **2012**, *9* (7), 676–682. <https://doi.org/10.1038/nmeth.2019>.
- (2) Benndorf, S.; Hofmeister, E.; Wächtler, M.; Görls, H.; Liebing, P.; Peneva, K.; Gräfe, S.; Kupfer, S.; Dietzek-Ivanšić, B.; Weigand, W. Unravelling the Mystery: Enlightenment of the Uncommon Electrochemistry of Naphthalene Monoimide [FeFe] Hydrogenase Mimics. *Eur. J. Inorg. Chem.* **2022**, *2022* (3), e202100959. <https://doi.org/10.1002/ejic.202100959>.
- (3) Yu, W. W.; Qu, L.; Guo, W.; Peng, X. Experimental Determination of the Extinction Coefficient of CdTe, CdSe, and CdS Nanocrystals. *Chem. Mater.* **2003**, *15* (14), 2854–2860. <https://doi.org/10.1021/cm034081k>.
- (4) Geißler, D.; Würth, C.; Wolter, C.; Weller, H.; Resch-Genger, U. Excitation Wavelength Dependence of the Photoluminescence Quantum Yield and Decay Behavior of CdSe/CdS Quantum Dot/Quantum Rods with Different Aspect Ratios. *Phys. Chem. Chem. Phys.* **2017**, *19* (19), 12509–12516. <https://doi.org/10.1039/C7CP02142A>.
- (5) Lin-Vien, D.; Colthup, N. B.; Fateley, W. G.; Grasselli, J. G. CHAPTER 2 - Alkanes. In *The Handbook of Infrared and Raman Characteristic Frequencies of Organic Molecules*; Lin-Vien, D., Colthup, N. B., Fateley, W. G., Grasselli, J. G., Eds.; Academic Press: San Diego, 1991; pp 9–28. <https://doi.org/10.1016/B978-0-08-057116-4.50008-0>.
- (6) Caplins, B. W.; Lomont, J. P.; Nguyen, S. C.; Harris, C. B. Vibrational Cooling Dynamics of a [FeFe]-Hydrogenase Mimic Probed by Time-Resolved Infrared Spectroscopy. *J. Phys. Chem. A* **2014**, *118* (49), 11529–11540. <https://doi.org/10.1021/jp510517z>.
- (7) Micheel, M.; Liu, B.; Wächtler, M. Influence of Surface Ligands on Charge-Carrier Trapping and Relaxation in Water-Soluble CdSe@CdS Nanorods. *Catalysts* **2020**, *10* (10), 1143. <https://doi.org/10.3390/catal10101143>.
- (8) Hotje, U.; Rose, C.; Binnewies, M. Lattice Constants and Molar Volume in the System ZnS, ZnSe, CdS, CdSe. *Solid State Sci.* **2003**, *5* (9), 1259–1262. [https://doi.org/10.1016/S1293-2558\(03\)00177-8](https://doi.org/10.1016/S1293-2558(03)00177-8).
- (9) Fisher, A. A. E.; Osborne, M. A.; Day, I. J.; Lucena Alcalde, G. Measurement of Ligand Coverage on Cadmium Selenide Nanocrystals and Its Influence on Dielectric Dependent Photoluminescence Intermittency. *Commun. Chem.* **2019**, *2* (1), 1–9. <https://doi.org/10.1038/s42004-019-0164-x>.
- (10) Fritzing, B.; Capek, R. K.; Lambert, K.; Martins, J. C.; Hens, Z. Utilizing Self-Exchange To Address the Binding of Carboxylic Acid Ligands to CdSe Quantum Dots. *J. Am. Chem. Soc.* **2010**, *132* (29), 10195–10201. <https://doi.org/10.1021/ja104351q>.
- (11) Hens, Z.; Martins, J. C. A Solution NMR Toolbox for Characterizing the Surface Chemistry of Colloidal Nanocrystals. *Chem. Mater.* **2013**, *25* (8), 1211–1221. <https://doi.org/10.1021/cm303361s>.

### 7.3 [SB-3]

#### [SB-3] Synthesis of [FeFe] Hydrogenase Mimics with Lipoic acid and its Selenium Analogue as Anchor Groups

Stefan Benndorf, Sihem Groni, Leanne M. Stafast, Helmar Görls, Claire Fave, Bernd Schöllhorn and Wolfgang Weigand

*Eur. J. Inorg. Chem.* **2023**, 26, e202200684.



© 2023 The Authors. European Journal of Inorganic Chemistry published by Wiley-VCH GmbH

This is an open-access article under the terms of the Creative Commons Attribution License, which permits use, distribution, and reproduction in any medium, provided the original work is properly cited.

<https://chemistry-europe.onlinelibrary.wiley.com/doi/10.1002/ejic.202200684>

# Synthesis of [FeFe] Hydrogenase Mimics with Lipoic acid and its Selenium Analogue as Anchor Groups

Stefan Benndorf,<sup>[a]</sup> Sihem Groni,<sup>[b]</sup> Leanne M. Stafast,<sup>[a]</sup> Helmar Görls,<sup>[a]</sup> Claire Fave,<sup>[b]</sup> Bernd Schöllhorn,<sup>\*[b]</sup> and Wolfgang Weigand<sup>\*[a, c]</sup>

[FeFe] hydrogenase (H<sub>2</sub>ase) mimicking complexes containing lipoic and selenolipoic acid moieties connected to 2-hydroxy-1,3-dithiopropane and 2-hydroxy-1,3-diselenopropane bridging ligands were synthesized and characterized using different spectroscopic methods. X-ray diffraction analysis was utilized to determine the molecular structure of a triphenylphosphane substituted analogue. Cyclic voltammetry (CV) investigations on the redox chemistry in presence and absence of acetic acid

(AcOH) revealed differing behaviours among the mimics. IR spectroelectrochemistry (IR SEC) enabled deeper insights of structural changes during electrochemical measurements. The elaboration of surface confined systems was studied in preliminary experiments. CV experiments showed that the lipoic acid derivatives of the [FeFe] H<sub>2</sub>ase mimics formed well-organized self-assembled monolayers (SAMs) on Pt electrodes, a promising result for future work.

## Introduction

Numerous mimics of the active site of natural [FeFe] H<sub>2</sub>ase enzymes were synthesized and analysed during the last decades, frequently accompanied by demonstrations of their catalytic activity regarding dihydrogen formation in electro and photochemical experiments.<sup>[1,2]</sup>

One significant issue in electrolysis and photocatalysis is the diffusion-limited transport of the catalytic centre to the electrode, that is necessary for an effective electron transfer.<sup>[3,4]</sup> Immobilizing [FeFe] H<sub>2</sub>ase enzymes or model complexes on the electrode surface to attain chemically modified electrodes were realized by electrostatic adsorption,<sup>[5]</sup> embedding in redox-active hydrogels or polymers,<sup>[6]</sup> absorption into mesoporous electrodes,<sup>[7]</sup> reduction of diazonium salt spacers on carbon electrodes,<sup>[8,9]</sup> by carboxylic acid group on fluorine-doped tin oxide (FTO) or nickel oxide electrodes,<sup>[10,11]</sup> and thiol spacer

groups on gold electrodes, with a functional moieties for further modification with the [FeFe] H<sub>2</sub>ase mimic or enzyme, amongst others.<sup>[4,12]</sup> However, [FeFe] H<sub>2</sub>ase mimics attached to electrodes lack consistency and high activity during the catalytic process, due to their sensitivity regarding high pH values or oxygen and irreversible electrocatalytic behaviour.<sup>[8,13]</sup> Additionally, Reek et al. surmised the depletion of the substrates was caused by hydrolysis of the carboxylate anchor groups from the FTO surface.<sup>[10]</sup>

Our approach is to use dithiolane or diselenolane anchoring groups with a great affinity to gold and platinum and the capability to form stable SAMs under electrochemical conditions.<sup>[3,14,15]</sup> Due to their adjustable reactivity, disulfide moieties gained great interest in the fields of biochemistry, organic synthesis, catalysis and coordination chemistry, amongst others.<sup>[16]</sup> Furthermore, they show versatile electrochemical behaviour, including the formation of a variety of lipoic acid S-oxides, the reduction to radical species, dimers and higher polymers to the point of dihydrolipoic acid.<sup>[17]</sup>

Lipoic and selenolipoic acid were connected to 2-hydroxy-1,3-propanedithiolate (pdt-2-OH)<sup>[18]</sup> or 2-hydroxypropanediselenolate (pds-2-OH)<sup>[19]</sup> [FeFe] H<sub>2</sub>ase mimics via esterification,<sup>[20]</sup> giving four complexes with the possible permutations distributing S and Se at the iron cluster along with the anchor group. They were analysed in terms of X-ray diffraction analysis, CV in the presence and absence of AcOH and IR SEC. In first experiments the H<sub>2</sub>ase mimics were immobilized as self-assembled monolayers on Au and Pt electrodes. The electrochemical properties and the stability of the formed SAMs was investigated by CV in order to evaluate their potential as surface confined electrocatalytical systems.

[a] S. Benndorf, L. M. Stafast, Dr. H. Görls, Prof. Dr. W. Weigand

Institute of Inorganic and Analytical Chemistry  
Friedrich Schiller University Jena

Humboldtstrasse 8, 07743 Jena (Germany)

E-mail: wolfgang.weigand@uni-jena.de

https://www.chemgeo.uni-jena.de/weigand

[b] Dr. S. Groni, Dr. C. Fave, Prof. Dr. B. Schöllhorn

Université Paris Cité

Laboratoire d'Electrochimie Moléculaire

F-75013 Paris (France)

E-mail: claire.fave@u-paris.fr

bernd.schollhorn@u-paris.fr

http://www.lemp7.cnrs.fr/directories/personal/B\_Schollhorn\_en.htm

[c] Prof. Dr. W. Weigand

Center for Energy and Environmental Chemistry Jena (CEEC Jena)

Jena Center of Soft Matter

Friedrich Schiller University Jena

Philosophenweg 7a, 07743 Jena (Germany)



Supporting information for this article is available on the WWW under  
https://doi.org/10.1002/ejic.202200684



© 2023 The Authors. European Journal of Inorganic Chemistry published by Wiley-VCH GmbH. This is an open access article under the terms of the Creative Commons Attribution License, which permits use, distribution and reproduction in any medium, provided the original work is properly cited.



## Results and Discussion

### Synthesis of [FeFe] H<sub>2</sub>ase model complexes 2, 3, 5, 6 and 7

The synthesis of complex 1 was carried out by use of a novel synthetic pathway developed recently in our group, to generate [FeFe] H<sub>2</sub>ase model complexes more efficiently, by using *N*-methyl-2-pyrrolidone (NMP) as an additive. The precursor 1,3-disulfanylpropane-2-ol was dissolved in NMP and toluene at 50 °C. Triirondodecacarbonyl (Fe<sub>3</sub>(CO)<sub>12</sub>) was added in one portion and the resulting solution was stirred for ten minutes, until the dark green solution became dark red, affording target complex 1 as a red solid after purification (Scheme 1).<sup>[21]</sup>

Complex 4 was synthesized by refluxing freshly prepared 1,3-bis(selenocyanato)propane-2-ol<sup>[22]</sup> and Fe<sub>3</sub>(CO)<sub>12</sub> in THF for 1 h, adapted from Harb et al.,<sup>[23,24]</sup> and obtained as a red solid after purification (Scheme 1).

The syntheses of complexes 2, 3, 5 and 6 were carried out by a modified Steglich esterification procedure of [FeFe] H<sub>2</sub>ase mimics 1 or 4 with lipoic acid or selenolipoic acid, respectively, in the presence of *N,N'*-dicyclohexylcarbodiimide (DCC) and 4-dimethylaminopyridine (DMAP).<sup>[20]</sup> The resulting compounds were isolated as red, high-viscous oils (Scheme 1). To analyze the influence of triphenylphosphane (PPh<sub>3</sub>) as a better σ donor concerning electrochemical behaviour, one CO-ligand was replaced by synthesis of complex 7. By mixing compound 2 and trimethylamine *N*-oxide dihydrate in dichloromethane (DCM) for 20 min, adding one equivalent of PPh<sub>3</sub> and stirring for 15 h

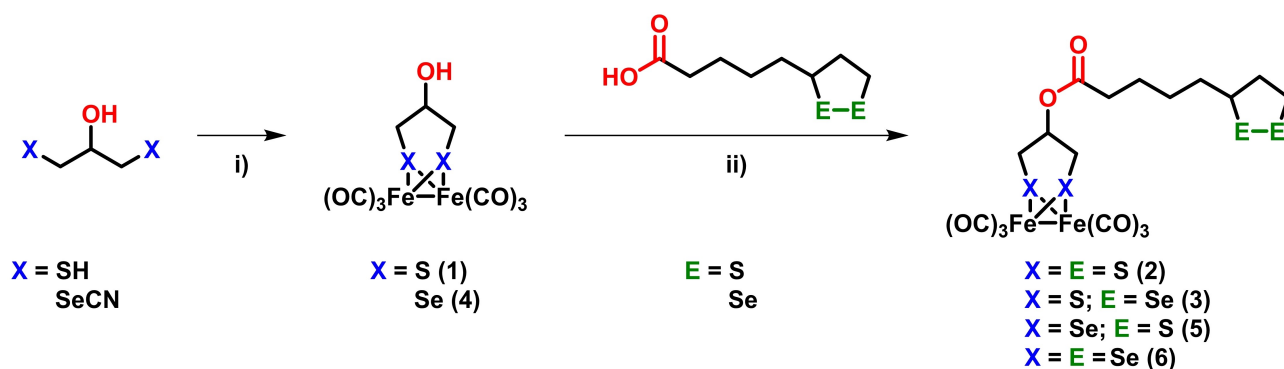
at room temperature (RT), target complex 7 was isolated as a brown solid (Scheme 2).<sup>[21]</sup>

### Molecular structure

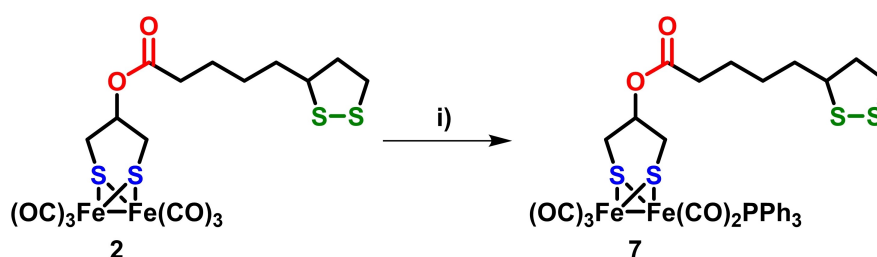
Exemplarily, Figure 1 shows one of the three conformers (Figure S1) of the molecular structure of compound 7. The structure revealed the characteristic butterfly conformation of the [Fe<sub>2</sub>S<sub>2</sub>] cluster. The coordination sphere in the vicinity of each Fe atom can be described as a distorted octahedron with two S atoms, each linked to both Fe centres, and three terminal CO ligands for Fe1 and two terminal CO ligands and a PPh<sub>3</sub> ligand for Fe2. Due to the electron density donating properties of PPh<sub>3</sub>, the Fe–Fe (2.5265(8) Å) bond length is elongated in comparison to the Fe–Fe (2.5039(6) Å) bond length of compound 1, published by our group,<sup>[18]</sup> however, in good agreement with the PPh<sub>3</sub> substituted derivative of complex 1, Fe–Fe (2.5255(8) Å), synthesized by Song and co-workers.<sup>[26]</sup> Furthermore, the lipoic acid moiety is arranged around the apical located PPh<sub>3</sub> ligand, indicating minor attractive interactions.

### Electrochemical Investigation

To study the influence of sulfur and selenium as well as the substituting of one CO ligand in complex 2 by PPh<sub>3</sub> toward electrochemical behaviour, CV was carried out on complexes 2, 3, 5, 6 and 7 in 0.1 M [*n*-Bu<sub>4</sub>N][BF<sub>4</sub>] acetonitrile (MeCN) solutions,



**Scheme 1.** Synthesis route for [FeFe] H<sub>2</sub>ase mimics 1–6; i) Fe<sub>3</sub>(CO)<sub>12</sub>, toluene, NMP, 50 °C, 10 min;<sup>[21]</sup> (1) Fe<sub>3</sub>(CO)<sub>12</sub>, THF, reflux, 1 h (4)<sup>[23]</sup>; ii) DCC, DMAP, DCM, RT, 14 h.<sup>[20]</sup>



**Scheme 2.** Synthesis route for [FeFe] H<sub>2</sub>ase mimics 7; i) trimethylamine *N*-oxide dihydrate, PPh<sub>3</sub>, DCM, RT, 15 h.<sup>[25]</sup>

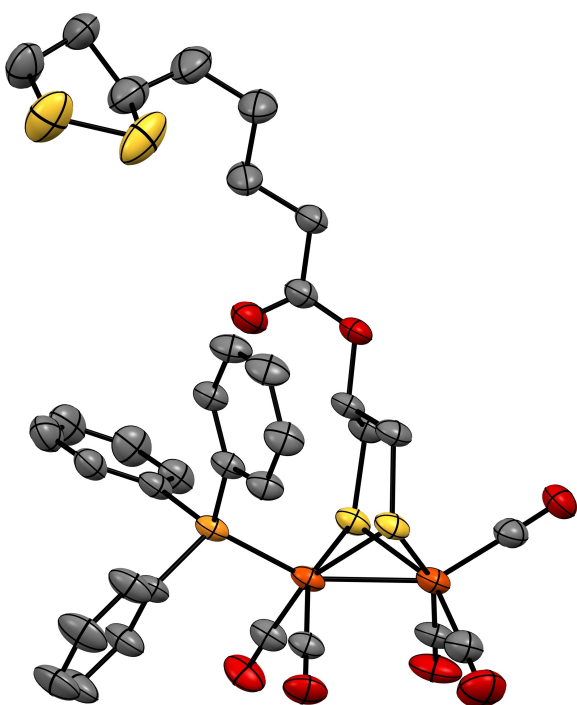


**Figure 1.** Molecular structure of complex 7. The ellipsoids represent a probability of 50%, (hydrogen atoms were omitted for clarity). Legend of the colour code: C (grey), O (red), S (yellow), Fe (orange), P (salmon).

as depicted in Figure 2 and S6. The CV of compound 2 (Figure 2, grey) reveals one partially reversible reduction at  $E_{pc}^1 = -1.57$  V, assigned to the one-electron-reduction of  $[Fe^I Fe^I]$  to  $[Fe^0 Fe^I]$  with a linear scan rate dependence of the current function (Figure S2), and two non-reversible reduction events at  $E_{pc}^2 = -1.75$  V and  $E_{pc}^3 = -2.28$  V (Figure 2). At higher scan rates,  $E_{pc}^2$  fades, and the reversibility of the first reduction process is enhanced (Figure S3), indicated by a rise of the anodic-to-

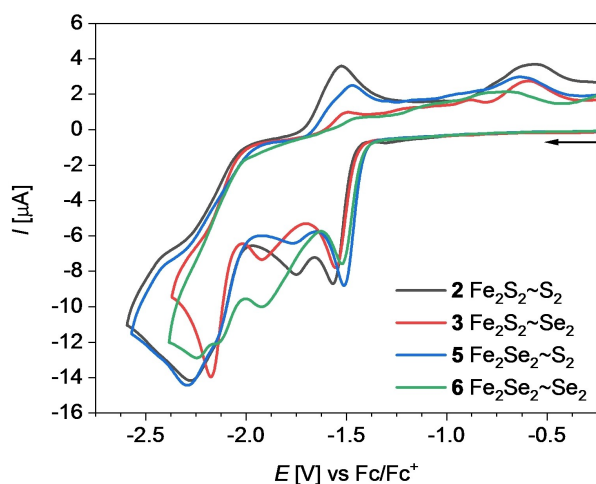


**Figure 2.** Cyclic voltammograms ( $\nu = 0.2$  V/s) of compounds 2, 3, 5 and 6 ( $c = 1$  mmol/L) in  $N_2$ -purged MeCN/ $[n-Bu_4N][BF_4]$  (0.1 mol/L) at RT. The arrow indicates the scan direction. The potential  $E$  is given in V and referenced to the  $Fc/Fc^+$  couple.

cathodic peak current ratio ( $I_{pa}/I_{pc}$ ). This behaviour implies an irreversible follow-up reaction appearing after the first reduction as described before.<sup>[27]</sup> The electrochemical analysis of compound 5 (blue) shows a similar behaviour for its reduction events. Both complexes are linked to lipoic acid, which might cause a follow-up reaction, forming side products, however, the reduction of lipoic acid occurs at more negative potentials (Figure S5).<sup>[14]</sup> The third reduction process at  $E_{pc}^4 = -2.28$  V and its shoulder signal at  $E_{pc}^3 = -2.13$  V are assigned to the second electron uptake of the iron center and the reduction of the sulfur-sulfur bond of the lipoic acid moiety, interfering with each other.<sup>[14,18,19,28]</sup> As a result, these overlapping reduction events show a broadened peak. Nevertheless, it should be noted, that the reduction of the dithiolane bridge is shifted by  $\Delta E_{pc}^{S-S} = 150$  mV at least to more positive values, compared to the pure lipoic acid (Figure S5). This occurrence might include an irreversible interaction between dithiolane sulfur atoms and the iron centre, which facilitates the electron uptake.

On the contrary, complexes 3 (red) and 6 (green) are showing their second reduction event at  $E_{pc}^2 = -1.92$  V, which can be assigned to the reduction of the diselenolane bridge, by comparison with the pure precursor selenolipoic acid (Figure S6). This reduction process remains at higher scan rates and the reversibility of the first reduction rises along with the other reduction waves (Figure S4). The second reduction of the iron centres is assigned to the third event at  $E_{pc}^3 = -2.18$  V, in good agreement with their precursor complexes 1 and 4, respectively.<sup>[18,19]</sup>

The potentials for the first reduction ( $[Fe^I Fe^I] \rightarrow [Fe^0 Fe^I]$ ) differ from  $\Delta E_{pc}^1 = 30$ –60 mV, among the sulfur and selenium containing iron centres, implying an influence on the electrochemical properties of the  $[FeFe]$   $H_2$ ase mimicking complexes, due to the weaker electron-donating properties of the Se-containing ligands (Figure 3; Table 1). This behaviour is also observed for other S- and Se-containing  $[FeFe]$   $H_2$ ase models.<sup>[23,27,29,30]</sup>

The substitution of one terminal carbonyl ligand at the iron core with electron-donating ligands, like  $PPh_3$ , induces a different electrochemical behaviour, caused by increased electron density at the iron center. The potential for the first reduction of compound 7 appears at  $E_{pc}^1 = -1.75$  V, exhibiting a shift to more negative potential by  $\Delta E_{pc}^1 = 180$  mV, compared to the first reduction event of 2 (Table 1), likewise to previously reported phosphane mono-substituted  $[FeFe]$   $H_2$ ase mimics.<sup>[25,31,32]</sup> Additionally, the second non-reversible reduction, as described for compound 2, vanishes or might be overlapped by the first electron uptake. However, the second occurring

**Table 1.** Summary of the reduction potentials of complexes 2, 3, 5, 6 and 7. Potentials  $E$  are given in V, referenced to the  $Fc/Fc^+$  couple.

complex	$E_{pc}^1$ [V]	$E_{pc}^2$ [V]	$E_{pc}^3$ [V]	$E_{pc}^4$ [V]
2	-1.57	-1.75	-2.13 <sup>[a]</sup>	-2.28
3	-1.55	-1.92	-2.18	
5	-1.51	-1.77	-2.13 <sup>[a]</sup>	-2.29
6	-1.52	-1.92	-2.13	-2.25
7	-1.75	-2.13 <sup>[a]</sup>	-2.30	

[a] This reduction event is appears as a weak shoulder.

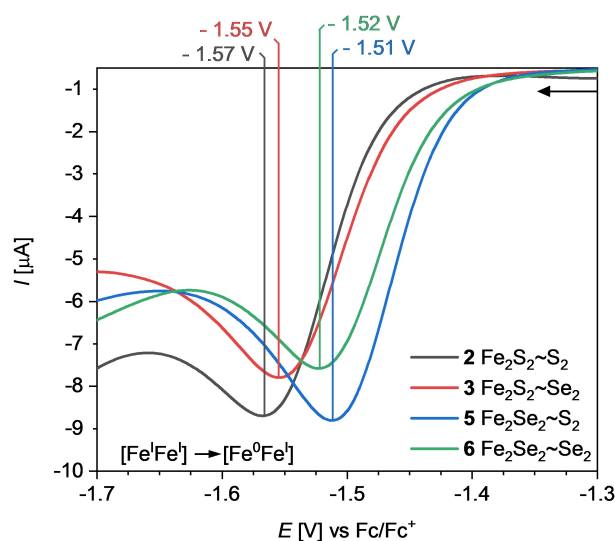


**Figure 3.** Cyclic voltammograms ( $\nu = 0.2$  V/s) of the first reduction of compounds **2**, **3**, **5** and **6** ( $c = 1$  mmol/L) in  $N_2$ -purged MeCN/[ $n$ -Bu $_4$ N][BF $_4$ ] (0.1 mol/L) at RT. The arrow indicates the scan direction. The potential  $E$  is given in V and referenced to the Fc/Fc $^+$  couple.

reduction event of compound **7** indicates no remarkable shift for the assigned second reduction of the iron centre (Figure S7).<sup>[32]</sup>

To support these assignments, we took a closer look where the reduction events take place and how many electrons were involved, therefore, IR SEC investigations were performed, due to the high sensitivity of the  $\tilde{\nu}(\text{CO})$  bands of metal carbonyls to the charge state and geometry of the complex.<sup>[33–35]</sup>

### IR SEC investigations

IR SEC was carried out in an OTTLE (optically transparent thin layer electrochemical) cell ( $c(\text{complex}) = 2$  mmol/L, MeCN,  $c(n\text{-Bu}_4\text{NBF}_4) = 0.1$  mol/L).<sup>[36]</sup> The potential was raised in negative direction at slow scan rates ( $\nu = 2$  mV/s, Figure S8) to study structural changes of the complexes during the electron uptake. Due to the use of different working (WE) and reference electrodes, the absolute potentials were shifted to less negative potentials, compared to prior electrochemical experiments.

Figures 4A and 4C show the spectroscopic changes for the first reduction step of compound **2**, between  $E = -1.022$  V and  $E = -1.190$  V. The observable bathochromic shift by  $\Delta\tilde{\nu}(\text{CO}) = 55\text{--}103$   $\text{cm}^{-1}$  of the terminal carbonyl signals (2078, 2039, 2000  $\text{cm}^{-1} \rightarrow 2023, 1957, 1897$   $\text{cm}^{-1}$ ), respectively, is caused by

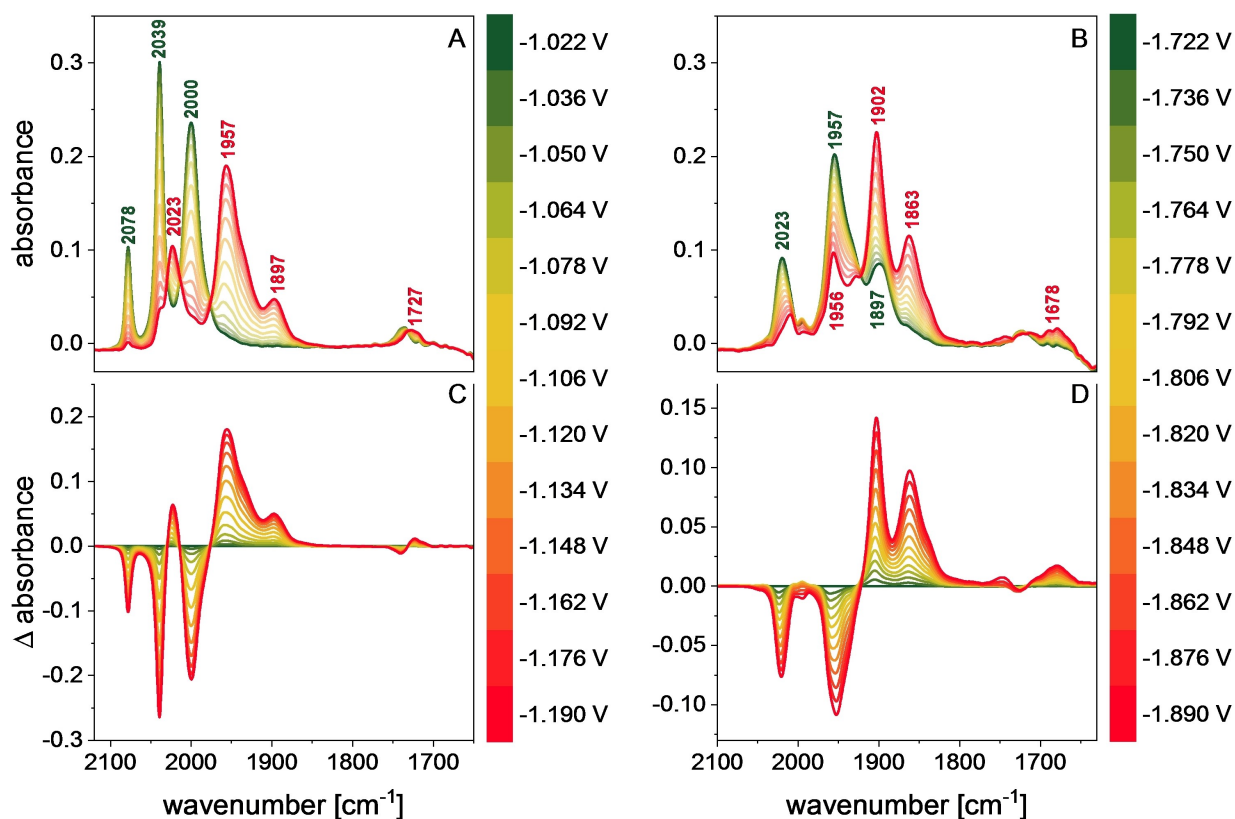


**Figure 4.** IR SEC measurements of the first (A) and second reduction (B) and their respective differential spectra (C, D) of compound **2** (MeCN,  $c = 2$  mmol/L). The  $\Delta$  absorbance spectra were calculated by subtracting a spectrum recorded immediately before the reducing phase. Keep in mind that there is a difference in cathodic shifts between the CV (glassy carbon WE, non-aqueous Ag/AgCl RE) and the IR SEC (Pt WE, Ag wire RE) experiments due to the use of different electrodes (for further details see SI).

the increased electron density at the iron cores and the subsequent enhanced back donation to the anti-bonding  $\pi^*$  orbital of the carbonyl ligands.<sup>[33,34,37]</sup> This change in the spectra is in good agreement with a one-electron reduction of  $[\text{Fe}^{\text{I}}\text{Fe}^{\text{I}}] \rightarrow [\text{Fe}^{\text{0}}\text{Fe}^{\text{I}}]$ , furthermore, the shape and ratio of the absorption bands is altering, indicating structural rearrangements after the electron uptake.<sup>[21,33,38,39,40]</sup> Additionally a new weak band occurs at  $\tilde{\nu}(\mu\text{-CO}) = 1727 \text{ cm}^{-1}$ , suggesting the formation of a bridging carbonyl.<sup>[33,41]</sup> However the CV of the SEC experiment show no peak between the first and second reduction of the iron centre (Figure S8), indicating that the second event  $E_{\text{pc}}^2$  is happening at the same time as the first reduction, due to the slow scan rate. The same experiment was performed with the precursor **1**, indicating differences in the spectroelectrochemical behaviour (see Figure S9). The spectra of complex **1** exhibit a pattern likewise to its  $\text{Fe}_2(\text{pdt})(\text{CO})_6^-$  (pdt = propanedithiolate) analogue, defined by the formation of four partially separated absorption bands of the terminal carbonyl ligands and one bridging carbonyl  $\tilde{\nu}(\mu\text{-CO}) = 1720 \text{ cm}^{-1}$ .<sup>[21,33]</sup> The substitution with lipoic acid leads to differing behaviour during the electrochemical treatment of the complexes.

The spectroscopic changes during the second reduction of complex **2** between  $E = -1.722 \text{ V}$  and  $E = -1.890 \text{ V}$  are depicted in Figure 4B and its respective differential spectra (Figure 4D). The terminal carbonyl signals were shifted by  $\Delta\tilde{\nu}(\text{CO}) = 33\text{--}66 \text{ cm}^{-1}$  (2023, 1957, 1897  $\text{cm}^{-1} \rightarrow$  1956, 1902, 1863  $\text{cm}^{-1}$ ), respectively. These values are indicating another one-electron reduction step, assigned to the reduction of  $[\text{Fe}^{\text{0}}\text{Fe}^{\text{I}}] \rightarrow [\text{Fe}^{\text{0}}\text{Fe}^{\text{0}}]$ . The band of the bridging carbonyl is also bathochromically shifted to  $\tilde{\nu}(\mu\text{-CO}) = 1678 \text{ cm}^{-1}$ , and reveals a absorption pattern, likewise to the  $\text{Fe}_2(\text{bdt})(\text{CO})_6^{2-}$  (bdt = benzenedithiolate) analogue, indicating structural rearrangements.<sup>[37,40]</sup>

Further reduction of compound **2** led to new absorption bands in the spectra (see Figure S10), subsequently evolving from product  $2^{2-}$ , due to the increased charge and additional structural changes. A well-defined absorption band appeared at  $\tilde{\nu} = 1745 \text{ cm}^{-1}$ , that could be ascribed to the formation of tetracarbonyl ferrate,  $[\text{Fe}(\text{CO})_4]^{2-}$ , which is assigned to be a degradation product during the excessive reduction of iron carbonyl complexes.<sup>[21,38,42,43]</sup> This appearance is consistent with the irreversible electrochemical behaviour (see Figure 2). At even more negative potential  $E > -2.128 \text{ V}$ , another explicit band evolves at  $\tilde{\nu} = 2118 \text{ cm}^{-1}$ , which might be assigned to the formation of an (iso)thiocyanate species arising at the edge of the potential window of MeCN and its reaction with the reduced dithiolane bridge (Figure S10). Unfortunately, no sample of this product could be isolated for further investigations.

During the SEC experiments complexes **3**, **5** and **6** show similar behaviour as compound **2** (see Figure S11, S12 and S13, respectively). The reduction of the diselenolane bridge of complexes **5** and **6** caused only minor changes in the spectra (Figure S14), even though they were observable in the respective CV during the SEC (Figure S15).

The IR SEC of compound **7** exhibits an interesting performance (Figure S16). The resulting IR spectrum after the first

reduction to  $7^-$  is almost identical to that of compound **2** in the mono-reduced state (Figure S17). The follow-up reduction of both compounds leads to almost very similar spectra as well, implying comparable complex geometry and electron density at the iron cores. These findings explain the same reduction potential ( $-2.13 \text{ V}$ ) and shape of the CV spectra for the second reduction event (Figure S7). Speculatively, one could assume that  $\text{PPh}_3$  dissociates from **7** after the first reduction step and that the same species is formed when **2** is reduced to  $2^-$ .

## Electrocatalysis

To examine the catalytic features of complexes **2**, **3**, **5** and **6** regarding hydrogen production, CV in the presence of various amounts of AcOH in 0.1 M  $[n\text{-Bu}_4\text{N}][\text{BF}_4]$  MeCN solutions was performed. The behaviour of complex **2** is illustrated in Figure 5, defined by three reduction events at  $E_{\text{pc}}^1 = -1.56 \text{ V}$ ,  $E_{\text{p}}^{\text{cat}2} = -1.84 \text{ V}$  and  $E_{\text{p}}^{\text{cat}3} = -2.17 \text{ V}$ . The addition of one equivalent of AcOH shifts the first reduction potential to more negative values by  $\Delta E_{\text{pc}}^1 = 50 \text{ mV}$ , compared to the pure complex. Additionally, the current is increased to the doubled value, indicating an additional electron uptake (Figure S18). Further addition of AcOH induces a potential shift to less negative potentials and the current increases, however, it levels off at four equivalents. This shift indicates a proton uptake, that is facilitated by raising amounts of AcOH. That supports the assumption that there is the uptake of two electrons while the mono-reduced species is usually not basic enough to be protonated by a weak acid such as AcOH.<sup>[44,45]</sup>

Another reduction appears at  $E_{\text{p}}^{\text{cat}2} = -1.84 \text{ V}$ , that shows catalytic increase of the current, implying subsequent protonation and the potential dihydrogen-release to close a catalytic cycle. Additional electron uptake at  $E_{\text{p}}^{\text{cat}3} = -2.16 \text{ V}$  enables the formation of another catalytic active species, that is capable to

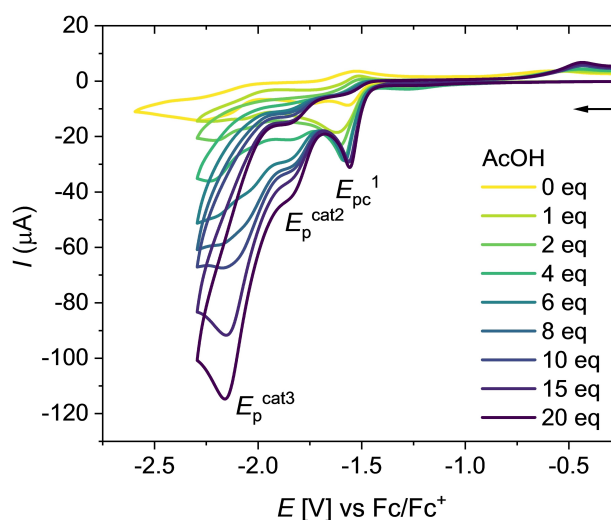


**Figure 5.** Cyclic voltammograms ( $\nu = 0.2 \text{ V/s}$ ) of compound **2** ( $c = 1 \text{ mmol/L}$ ) with various amounts of AcOH in  $\text{N}_2$ -purged MeCN/ $[n\text{-Bu}_4\text{N}][\text{BF}_4]$  (0.1 mol/L) at RT. The arrow indicates the scan direction. The potential  $E$  is given in V and referenced to the  $\text{Fc}/\text{Fc}^+$  couple.

discharge dihydrogen. Scheme S1 demonstrates a potential catalytic cycle for the two processes at  $E_p^{\text{cat}2}$  and  $E_p^{\text{cat}3}$ .

This catalytic behaviour is similar to previously reported hexacarbonyl [FeFe]  $H_2$ ase mimics in the literature, that show a two electron reduction during the first reduction step.<sup>[27,30,42,44,46]</sup>

Further increase of the reduction potential leads to another reduction event at  $E_p^4 = -2.50$  V, that is attributed to the reduction of AcOH (Figure S19). The comparison to the same experiment utilizing complex **1** exhibits a similar behaviour, except the first reduction event, that does not show such a strong increase of the current (Figure S20 and S21). This observation supports the notion, that there is an influence of the lipoic acid moiety on the catalytic cycle.

The CV experiment of complex **3** shows a slightly different performance, indicated by two reduction events (Figure S22). The addition of AcOH shifts the first reduction event at  $E_{pc}^1 = -1.55$  V to slightly more negative values by  $\Delta E_{pc}^1 = 20$  mV, however, the current and the potential of this process remains constant after the addition of four equivalents. The second reduction event occurs at  $E_p^{\text{cat}2} = -2.07$  V, showing no additional process at less negative potential, in comparison to complex **2**.

Figure S23 shows the differing behavior of complex **5**, regarding electrocatalysis in the presence of AcOH. After the addition of one equivalent, the current of the first reduction,  $E_{pc}^1 = -1.51$  V, is increased by 20% only, however, a new peak appears at  $E_{pc}^2 = -1.61$  V. Due to the less negative first reduction potential of complex **5** (Figure 3), the two reduction events are separated. Following steps in the catalytic process are similar to complex **3**.

The first reduction of complex **6** in the presence of AcOH exhibits no shift of the potential and remains at  $E_{pc}^1 = -1.52$  V (Figure S24), though, the current does not level off until fifteen equivalents. The catalytic process remains around  $E_p^{\text{cat}2} \approx -2.1$  V, analogous to complexes **2**, **3** and **5**, as well as several examples from the literature.<sup>[47]</sup>

In order to compare the catalytic performance towards proton reduction of these complexes, the turn-over frequency (TOF) and catalytic efficiency (C.E.) were calculated, utilizing equations 1 and 2, respectively.<sup>[2,47–49]</sup> Table 2 summarizes the obtained data.

$$\frac{i_{\text{cat}}}{I_p} = \frac{n}{0.4463} \sqrt{\frac{RT^* \text{TOF}_{\text{max}}}{F\nu}} \quad (1)$$

**Table 2.** Electrochemical data for the catalysis of complexes **2**, **3**, **5** and **6** ( $c = 1$  mmol/L) in the presence of AcOH ( $c = 20$  mmol/L). Potentials  $E$  are given in V, referenced to the Fc/Fc<sup>+</sup> couple.

complex	$E_{\text{cat}}$ [V]	$i_{\text{cat}}/I_p$	$k$ (TOF) [ $s^{-1}$ ] <sup>[a]</sup>	C.E. <sup>[b]</sup>
<b>2</b>	-2.16	13.18	67	0.66
<b>3</b>	-2.07	11.59	52	0.58
<b>5</b>	-2.11	9.45	35	0.47
<b>6</b>	-2.10	13.15	67	0.66

[a] Calculated by using equation 1 with  $\nu = 0.2$  V/s and  $n = 2$ .<sup>[2,48–50]</sup>,  
[b] Calculated by using equation 2.<sup>[2]</sup>

$$C.E. = \frac{i_{\text{cat}}/I_p}{[HA]_{\text{[catalyst]}}} \quad (2)$$

To determine the number of electrons necessary for the hydrogen evolution reaction (HER), plots of the catalytic current ( $i_{\text{cat}}$ ) and peak current ( $I_p$ ) ratio versus  $c$  (AcOH) were illustrated (Figure S25). The observed linear relationship of  $i_{\text{cat}}/I_p$  to  $c$  (AcOH) indicates a second-order dependence of the catalytic pathway.<sup>[48]</sup> Subsequent use of equation 1 ( $R$  – ideal gas constant,  $T$  – absolute temperature,  $F$  – Faraday's constant,  $\nu$  – scan rate) leads to TOF values, that are within one magnitude. Complex **2** and **6** exhibit the same TOF value  $67 s^{-1}$  at slightly different reduction potential, although their catalytic processes may vary in their sequence (see Figure 5 and S23). In comparison, the mixed sulfur and selenium complexes show significantly less activity. A similar outcome could be achieved from the C.E. calculation, which declares all complexes in the medium scope (0.25–0.75) of efficiency.<sup>[47]</sup>

#### Formation and electrochemical behaviour of SAMs on Au and Pt

Previously polished Au and Pt disc electrodes were exposed for 12 h to 1 mM solutions of compounds **2** or **6** in MeCN, and carefully rinsed before electrochemical characterization. CVs of the resulting modified electrodes were performed in an electrolyte solution of 0.1 M [*n*-Bu<sub>4</sub>N][PF<sub>6</sub>] in MeCN. On gold (**Au-SAM-2**) a small irreversible signal could be detected with a cathodic current peak potential  $E_{pc}^1 = -1.24$  V (Figure S26), a value close to the first reduction wave of compound **2** in solution (in MeCN:  $E_{pc}^1 = -1.22$  V vs. SCE). A less well-defined reduction wave at approximately  $E_{pc} = -1.25$  V vs. SCE was observed for **Au-SAM-6** (Figure S27). Both results are suggesting the presence of the redox active iron clusters on the electrode surface. However, the lack of reversibility and the shape of the CVs make analysis complicated.

Recently, we have reported the advantage of higher stability of dithiolane SAMs on platinum<sup>[51]</sup> over gold.<sup>[52]</sup> In the case of compound **2** the use of a platinum working electrode improved its chemisorption affording **Pt-SAM-2**. Several CVs were performed at a scan speed of  $\nu = 10$  V/s (Figure S28) yielding a quasi-reversible wave centered at the formal standard potential  $E^{\circ\prime}_1 = -1.52$  V (vs. SCE) (Figure 6A and S29). This signal was attributed to the first reduction [Fe<sup>II</sup>Fe]<sup>+</sup> → [Fe<sup>0</sup>Fe]<sup>0</sup> of the adsorbed clusters, the corresponding  $E_{pc}$  being shifted to a more negative value of compared to **Au-SAM-2**.

Analysis of the cathodic peak currents as a function of the scan rate displayed a linear dependence (Figure 6B and S30), characteristic of an electrode-surface confined electroactive species. As in solution no electro-catalytic HER could be observed on this first reduction wave. Unfortunately, the second reduction process could not be probed with a SAM modified electrode. The application of electrode potentials less negative

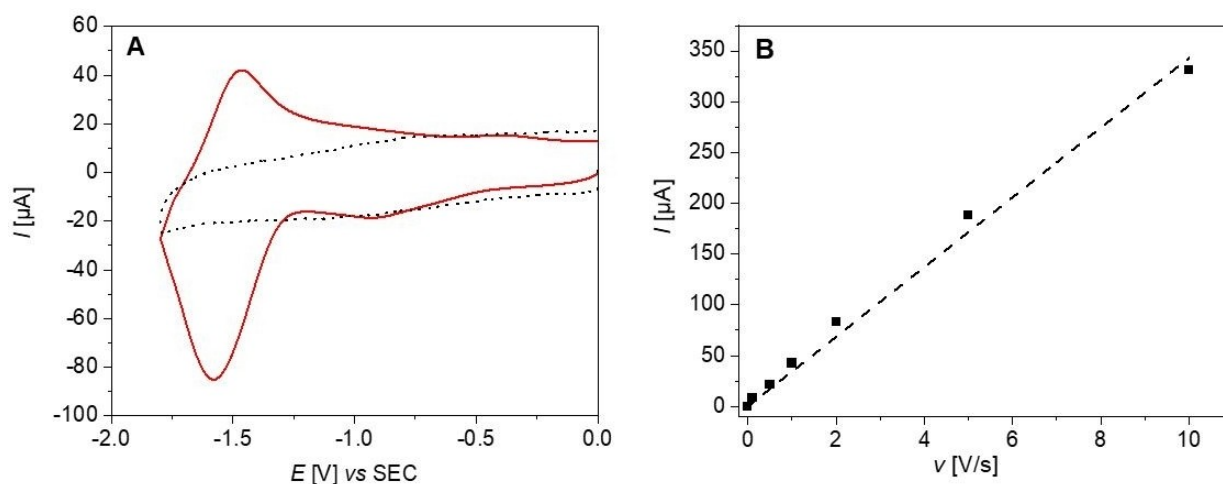


**Figure 6.** A) Cyclic voltammograms ( $\nu = 1$  V/s) of the bare (grey line) and the modified Pt electrode Pt-SAM-2 (red line) in 0.1 M  $[n\text{-Bu}_4\text{N}][\text{PF}_6]$  MeCN solution. WE diameter = 3 mm. B) Plot of the peak current vs. the scan speed of a modified platinum electrode Pt-SAM-2.

than  $E = -1.8$  V (vs. SCE) afforded the desorption of the SAM via reduction of the thioctic derivatives.

## Conclusions

This study focused on the synthesis and electrochemical investigation of lipoic acid ester-based [FeFe] H<sub>2</sub>ase model complexes and their formation of SAMs on Au and Pt electrodes. The substantial analysis of the new synthesized complexes **2**, **3**, **5**, and **6** by cyclic voltammetry in the presence and absence of the weak acid AcOH as well as IR SEC experiments revealed a strong influence of lipoic and selenolipoic acid moieties on the electrochemical properties of the [FeFe] H<sub>2</sub>ase mimics and their facility to perform catalytic proton reduction under electrocatalytic conditions. Complex **2** exposed a doubled increase in current by adding one equivalent of AcOH, indicating a change of the catalytic cycle in comparison to previously described precursor molecule **1**. A differing behavior was also observed by CV and IR SEC experiments in the absence of acid. However, [FeFe] H<sub>2</sub>ase mimics lacked in stability and reversibility.

The substitution of one CO ligand with PPh<sub>3</sub> led to complex **7**, that was further analyzed by X-ray crystallography. The CV exhibited an anticipated shift for the first reduction event by  $\Delta E_{pc}^1 = 180$  mV, compared to the first reduction event of **2**. The second reduction of both compounds exhibit similar reduction potentials and IR SEC data, that reveal comparable structures and electron densities at the iron cores of both complexes. Further DFT calculation supported investigation might expose the unidentified reduced species.

Furthermore, we were able to form intact SAMs of complexes **2** and **6** on Au and Pt electrodes, that were confirmed by CV experiments. Unfortunately, these SAMs were not able to perform HER in the given potential window terminated by the desorption of the complexes. However, the

approach of a catalyst transfer from homogeneous solution to a surface confined system was validated. Stronger covalent bonding of the catalysts to the electrode surface will be necessary for the development of a supported system. Reductive electrografting of diazonium salts onto the electrode may provide catalyst layers being stable within a larger potential range well adapted to the electrocatalytic process.

## Experimental Section

The formation of the known complexes **1** and **4** was carried out by other reaction pathways then described in the literature. Therefore, we included the new synthesis routes.

### H<sub>2</sub>ase mimic 1 – Fe<sub>2</sub>S<sub>2</sub>

In a Schlenk flask 1,3-disulfanylpropane-2-ol (100 mg, 0.8 mmol) was dissolved in anhydrous toluene (10 mL) and anhydrous NMP (1 mL) under nitrogen atmosphere. After raising the temperature to 50 °C, Fe<sub>3</sub>(CO)<sub>12</sub> (405 mg, 0.8 mmol) was added, and the colour changed from dark green to dark brown within ten minutes while a small amount of gas (CO) was developed. The reaction mixture was cooled down and was put on a column packed with silica and *n*-hexane. After flushing the column with *n*-hexane to remove the toluene and NMP, the eluent was changed to cyclo-hexane/THF (6:1). The product was collected from the major red band to give a red, crystalline solid (300 mg, 0.75 mmol, 93 %).<sup>[18,21]</sup>

<sup>1</sup>H NMR (400 MHz, CDCl<sub>3</sub>, 297 K, TMS)  $\delta$  (ppm) = 3.19–3.07 (m, 1H, CH(OH)), 2.81 (dd, <sup>3</sup>J<sub>H-H</sub> = 13.2, 4.1 Hz, 2H, CH<sub>2</sub>H<sub>b</sub>), 1.86 (d, <sup>3</sup>J<sub>H-H</sub> = 5.6 Hz, 1H, OH), 1.56–1.48 (m, 2H, CH<sub>2</sub>H<sub>b</sub>); {<sup>1</sup>H}<sup>13</sup>C NMR (101 MHz, CDCl<sub>3</sub>, 297 K, TMS)  $\delta$  (ppm) = 207.4, 72.9, 29.6.

### H<sub>2</sub>ase mimic 4 – Fe<sub>2</sub>Se<sub>2</sub>

In a Schlenk flask 1,3-bis(selenocyanato)propane-2-ol (500 mg, 1.87 mmol) and Fe<sub>3</sub>(CO)<sub>12</sub> (939 mg, 1.87 mmol) were dissolved in THF (60 mL) and the mixture was heated at reflux for 1 h. The solvent was evaporated to dryness under vacuum. The crude

product was purified by column chromatography (cyclo-hexane/THF 4:1) to get a red oil from the major red fraction. Recrystallization from DCM/*n*-pentane at 0 °C gave complex **4** as red crystalline product (402 mg, 0.81 mmol, 43 %).<sup>[19,23]</sup>

<sup>1</sup>H NMR (600 MHz, CD<sub>2</sub>Cl<sub>2</sub>, 297 K, TMS) δ (ppm) = 3.02–2.94 (m, 1H, CH(OH)), 2.85 (br dd, <sup>3</sup>J<sub>H-H</sub> = 11.6, 2.8 Hz, 2H, CH<sub>a</sub>H<sub>b</sub>), 2.05 (br d, <sup>3</sup>J<sub>H-H</sub> = 5.5 Hz, 1H, OH), 1.55 (br t, <sup>3</sup>J<sub>H-H</sub> = 11.3 Hz, 2H, CH<sub>d</sub>H<sub>e</sub>); {<sup>1</sup>H}<sup>13</sup>C NMR (151 MHz, CD<sub>2</sub>Cl<sub>2</sub>, 297 K, TMS) δ (ppm) = 209.4, 72.9, 19.7; {<sup>1</sup>H}<sup>77</sup>Se (76 MHz, CD<sub>2</sub>Cl<sub>2</sub>, 297 K) δ (ppm) = 202.04; elemental analysis calcd. (%) for C<sub>9</sub>H<sub>6</sub>Fe<sub>2</sub>O<sub>7</sub>Se<sub>2</sub>: C 21.80, H 1.22; found: C 22.09, H 1.12.

### General procedure: Steglich esterification

In a Schlenk flask complex **1** or **4** (0.2 mmol), 1,2-Dithiolane-3-pentanoic acid or 1,2-diselenolane-3-pentanoic acid (0.22 mmol, 1.1 eq) and DMAP (27 mg, 0.2 mmol) were stirred in 10 mL anhydrous DCM for 5 minutes. DCC (46 mg, 0.22 mmol) was dissolved in 2 mL anhydrous DCM and was added in one portion. The resulting mixture was stirred overnight. The desired complexes **2**, **3**, **5** and **6** could be isolated as red high-viscous oils after purification via column chromatography (*n*-hexane/DCM 1:1).<sup>[20]</sup>

### H<sub>2</sub>ase mimic 2 – Fe<sub>2</sub>S<sub>2</sub>~S<sub>2</sub>

Yield 102 mg, 87%; <sup>1</sup>H NMR (400 MHz, CDCl<sub>3</sub>, 297 K) δ (ppm) = 4.37–4.22 (m, 1H, CH(O)), 3.55 (quin, <sup>3</sup>J<sub>H-H</sub> = 6.8 Hz, 1H, CH(S)), 3.22–3.08 (m, 2H, CH<sub>2</sub>(S)), 2.75 (dd, <sup>3</sup>J<sub>H-H</sub> = 12.9, <sup>3</sup>J<sub>H-H</sub> = 4.1 Hz, 2H, CH<sub>a</sub>H<sub>b</sub>(CHO)), 2.46 (dq, <sup>3</sup>J<sub>H-H</sub> = 12.5, <sup>3</sup>J<sub>H-H</sub> = 6.3 Hz, 1H, CH<sub>a</sub>H<sub>b</sub>(CH<sub>2</sub>S)), 2.25 (t, <sup>3</sup>J<sub>H-H</sub> = 7.3 Hz, 2H, CH<sub>2</sub>(C=O)), 1.90 (dq, <sup>3</sup>J<sub>H-H</sub> = 13.0, <sup>3</sup>J<sub>H-H</sub> = 6.8 Hz, 1H, CH<sub>a</sub>H<sub>b</sub>(CH<sub>2</sub>S)), 1.71–1.53 (m, 6H, COCH<sub>2</sub>CH<sub>2</sub>CH<sub>2</sub>CH<sub>2</sub> + CH<sub>a</sub>H<sub>b</sub>(CHO)), 1.51–1.37 (m, 2H, CO(CH<sub>2</sub>)<sub>2</sub>CH<sub>2</sub>); {<sup>1</sup>H}<sup>13</sup>C NMR (101 MHz, CDCl<sub>3</sub>, 297 K) δ (ppm) = 207.2, 171.6, 73.4, 56.3, 40.2, 38.5, 34.5, 33.8, 28.6, 26.9, 24.5; MS (ESI positive mode): m/z = 612.8 (M + Na<sup>+</sup>, calcd. 612.8); IR (ATR, CHCl<sub>3</sub>, 297 K)  $\tilde{\nu}$  (cm<sup>-1</sup>) = 2077, 2036, 1993; elemental analysis calcd. (%) for C<sub>17</sub>H<sub>18</sub>Fe<sub>2</sub>O<sub>8</sub>S<sub>4</sub>: C 34.59, H 3.07, S 21.73; found: C 34.70, H 2.99, S 21.80.

### H<sub>2</sub>ase mimic 3 – Fe<sub>2</sub>S<sub>2</sub>~Se<sub>2</sub>

Yield 122 mg, 90%; <sup>1</sup>H NMR (400 MHz, CDCl<sub>3</sub>, 297 K) δ (ppm) = 4.31 (tt, <sup>3</sup>J<sub>H-H</sub> = 11.1, 4.3 Hz, 1H, CH(O)), 3.90 (ddt, <sup>3</sup>J<sub>H-H</sub> = 9.3, 7.5, 4.9 Hz, 1H, CH(Se)), 3.38–3.29 (m, 2H, CH<sub>2</sub>Se), 3.02–2.90 (m, 1H, CH<sub>a</sub>H<sub>b</sub>(CH<sub>2</sub>Se)), 2.77 (dd, <sup>3</sup>J<sub>H-H</sub> = 12.9, 4.4 Hz, 2H, CH<sub>a</sub>H<sub>b</sub>(CHO)), 2.58–2.47 (m, 1H, CH<sub>a</sub>H<sub>b</sub>(CH<sub>2</sub>Se)), 2.27 (t, <sup>3</sup>J<sub>H-H</sub> = 7.5 Hz, 2H, CH<sub>2</sub>(C=O)), 1.85–1.56 (m, 6H, COCH<sub>2</sub>CH<sub>2</sub>CH<sub>2</sub>CH<sub>2</sub> + CH<sub>a</sub>H<sub>b</sub>(CHO)), 1.49–1.38 (m, 2H, CO(CH<sub>2</sub>)<sub>2</sub>CH<sub>2</sub>); {<sup>1</sup>H}<sup>13</sup>C NMR (101 MHz, CDCl<sub>3</sub>, 297 K) δ (ppm) = 207.1, 171.6, 73.4, 52.5, 45.7, 35.3, 33.8, 29.6, 29.4, 26.9, 24.4; {<sup>1</sup>H}<sup>77</sup>Se (76 MHz, CDCl<sub>3</sub>, 297 K) δ (ppm) = 376.09, 299.67; MS (EI): m/z = 600 (M-3CO), 572 (M-4CO), 544 (M-5CO), 516 (M-6CO); IR (ATR, CHCl<sub>3</sub>, 297 K)  $\tilde{\nu}$  (cm<sup>-1</sup>) = 2077, 2037, 1995; elemental analysis calcd. (%) for C<sub>17</sub>H<sub>18</sub>Fe<sub>2</sub>O<sub>8</sub>S<sub>2</sub>Se<sub>2</sub>: C 30.41, H 2.79, S 9.28; found: C 30.38, H 2.71, S 8.97.

### H<sub>2</sub>ase mimic 5 – Fe<sub>2</sub>Se<sub>2</sub>~S<sub>2</sub>

Yield 92 mg, 67%; <sup>1</sup>H NMR (400 MHz, CDCl<sub>3</sub>, 297 K) δ (ppm) = 4.16 (br t, <sup>3</sup>J<sub>H-H</sub> = 11.0 Hz, 1H, CH(O)), 3.61–3.50 (m, 1H, CH(S)), 3.22–3.08 (m, 2H, CH<sub>2</sub>(S)), 2.80 (br d, <sup>3</sup>J<sub>H-H</sub> = 10.6 Hz, 2H, CH<sub>a</sub>H<sub>b</sub>(CHO)), 2.46 (br dd, <sup>3</sup>J<sub>H-H</sub> = 12.3, 6.2 Hz, 1H, CH<sub>a</sub>H<sub>b</sub>(CH<sub>2</sub>S)), 2.25 (t, <sup>3</sup>J<sub>H-H</sub> = 6.6 Hz, 2H, CH<sub>2</sub>(C=O)), 1.90 (br dd, <sup>3</sup>J<sub>H-H</sub> = 12.3, 7.0 Hz, 2H, CH<sub>a</sub>H<sub>b</sub>(CH<sub>2</sub>S)), 1.72–1.56 (m, 6H, COCH<sub>2</sub>CH<sub>2</sub>CH<sub>2</sub>CH<sub>2</sub> + CH<sub>a</sub>H<sub>b</sub>(CHO)), 1.49–1.38 (m, 2H, CO(CH<sub>2</sub>)<sub>2</sub>CH<sub>2</sub>); {<sup>1</sup>H}<sup>13</sup>C NMR (151 MHz, CDCl<sub>3</sub>, 297 K) δ (ppm) = 208.3, 171.5, 73.7, 56.3, 40.2, 38.5, 34.5, 33.8, 28.6, 24.4, 16.3; {<sup>1</sup>H}<sup>77</sup>Se

(76 MHz, CDCl<sub>3</sub>, 297 K) δ (ppm) = 205.4; MS (EI): m/z = 600 (M-3CO), 516 (M-6CO); IR (ATR, CHCl<sub>3</sub>, 297 K)  $\tilde{\nu}$  (cm<sup>-1</sup>) = 2070, 2031, 1992; elemental analysis calcd. (%) for C<sub>17</sub>H<sub>18</sub>Fe<sub>2</sub>O<sub>8</sub>S<sub>2</sub>Se<sub>2</sub>: C 30.68, H 2.87, S 9.28; found: C 30.66, H 2.77, S 8.98.

### H<sub>2</sub>ase mimic 6 – Fe<sub>2</sub>Se<sub>2</sub>~Se<sub>2</sub>

Yield 82 mg, 52%; <sup>1</sup>H NMR (400 MHz, CDCl<sub>3</sub>, 297 K) δ (ppm) = 4.16 (tt, <sup>3</sup>J<sub>H-H</sub> = 11.5, 3.5 Hz, 1H, CH(O)), 3.89 (ddt, <sup>3</sup>J<sub>H-H</sub> = 9.2, 7.6, 4.8 Hz, 1H, CH(Se)), 3.39–3.25 (m, 2H, CH<sub>2</sub>Se), 2.95 (dq, <sup>3</sup>J<sub>H-H</sub> = 13.6, 5.4 Hz, 1H, CH<sub>a</sub>H<sub>b</sub>(CH<sub>2</sub>Se)), 2.87–2.72 (m, 2H, CH<sub>a</sub>H<sub>b</sub>(CHO)), 2.57–2.46 (m, 1H, CH<sub>a</sub>H<sub>b</sub>(CH<sub>2</sub>Se)), 2.25 (t, <sup>3</sup>J<sub>H-H</sub> = 7.5 Hz, 2H, CH<sub>2</sub>(C=O)), 1.85–1.55 (m, 6H, COCH<sub>2</sub>CH<sub>2</sub>CH<sub>2</sub>CH<sub>2</sub> + CH<sub>a</sub>H<sub>b</sub>(CHO)), 1.49–1.36 (m, 2H, CO(CH<sub>2</sub>)<sub>2</sub>CH<sub>2</sub>); {<sup>1</sup>H}<sup>13</sup>C NMR (101 MHz, CDCl<sub>3</sub>, 297 K) δ (ppm) = 208.3, 208.3, 171.5, 73.7, 52.5, 45.7, 35.2, 33.8, 29.6, 29.3, 24.4, 16.3; {<sup>1</sup>H}<sup>77</sup>Se (76 MHz, CDCl<sub>3</sub>, 297 K) δ (ppm) = 376.27, 299.80, 205.46; MS (EI): m/z = 750 (M-CO), 696 (M-3CO), 640 (M-5CO), 612 (M-6CO); IR (ATR, CHCl<sub>3</sub>, 297 K)  $\tilde{\nu}$  (cm<sup>-1</sup>) = 2069, 2029, 1989; elemental analysis calcd. (%) for C<sub>17</sub>H<sub>18</sub>Fe<sub>2</sub>O<sub>8</sub>Se<sub>4</sub>: C 26.25, H 2.33; found: C 26.69, H 2.76.

### H<sub>2</sub>ase mimic 7 – Fe<sub>2</sub>S<sub>2</sub>PPh<sub>3</sub>~S<sub>2</sub>

In a Schlenk flask **2** (100 mg, 0.17 mmol) and trimethylamine *N*-oxide dihydrate (19 mg, 0.17 mmol) were stirred in 10 mL anhydrous MeCN for 10 minutes. PPh<sub>3</sub> (44 mg, 0.17 mmol) was added to the brown solution and the reaction mixture was stirred for another hour. The solvent was removed under reduced pressure and the crude product was purified by column chromatography (*n*-hexane/THF 2:1) to get **7** as a brown, oxygen sensitive solid (77 mg, 0.09 mmol, 55 %).<sup>[25]</sup>

<sup>1</sup>H NMR (400 MHz, CD<sub>2</sub>Cl<sub>2</sub>, 297 K) δ (ppm) = 7.73–7.59 (m, 6H, Ar-H), 7.51–7.39 (m, 9H, Ar-H), 3.59–3.44 (m, 2H, CH(O) + CH(S)), 3.21–3.06 (m, 2H, CH<sub>2</sub>(S)), 2.43 (m, 1H, CH<sub>a</sub>H<sub>b</sub>(CH<sub>2</sub>S)), 2.21 (m, 2H, CH<sub>a</sub>H<sub>b</sub>(CHO)), 2.01 (t, <sup>3</sup>J<sub>H-H</sub> = 7.3 Hz, 2H, CH<sub>2</sub>(C=O)), 1.88 (m, 1H, CH<sub>a</sub>H<sub>b</sub>(CH<sub>2</sub>S)), 1.73–1.50 (m, 4H, COCH<sub>2</sub>CH<sub>2</sub>CH<sub>2</sub>CH<sub>2</sub>), 1.48–1.37 (m, 4H, CH<sub>a</sub>H<sub>b</sub>(CHO) + CO(CH<sub>2</sub>)<sub>2</sub>CH<sub>2</sub>); {<sup>1</sup>H}<sup>13</sup>C NMR (101 MHz, CD<sub>2</sub>Cl<sub>2</sub>, 297 K) δ (ppm) = 214.6, 171.4, 136.1, 135.8, 134.0, 130.9, 129.0, 74.4, 56.9, 40.8, 39.1, 35.0, 34.3, 29.1, 27.3, 25.1; {<sup>1</sup>H}<sup>31</sup>P NMR (162 MHz, CD<sub>2</sub>Cl<sub>2</sub>, 297 K) δ (ppm) = 63.17; MS (ESI positive mode): m/z = 846.7 (M + Na<sup>+</sup>, calcd. 846.9); IR (ATR, CHCl<sub>3</sub>, 297 K)  $\tilde{\nu}$  (cm<sup>-1</sup>) = 2045, 1982, 1961, 1937; elemental analysis calcd. (%) for C<sub>34</sub>H<sub>33</sub>Fe<sub>2</sub>O<sub>7</sub>PS<sub>4</sub>: C 49.97, H 4.19, S 15.35; found: C 50.22, H 4.21, S 15.40.

Deposition Numbers 2209004 (for selenolipoic acid) and 2209005 (for **7**) contain the supplementary crystallographic data for this paper. These data are provided free of charge by the joint Cambridge Crystallographic Data Centre and Fachinformationszentrum Karlsruhe Access Structures service [www.ccdc.cam.ac.uk/structures](http://www.ccdc.cam.ac.uk/structures).

## Acknowledgements

Financial support by the German Science Foundation (DFG) via the TRR234 Catalight is gratefully acknowledged (project number 364549901, project A2), as well as the support from the French GDR 2088 BIOMIM . We are thankful to Dr. Kupfer and Dr. Abul-Futouh for important discussions. Open Access funding enabled and organized by Projekt DEAL.

## Conflict of Interest

The authors declare no conflict of interest.

## Data Availability Statement

The data that support the findings of this study are available from the corresponding author upon reasonable request.

**Keywords:** cyclic voltammetry · electrode modification · [FeFe] hydrogenase mimics · monolayers · spectroelectrochemistry

- [1] a) W. Weigand, *Phosphorus Sulfur Silicon Relat. Elem.* **2019**, *194*, 63 b) H.-L. Wu, X.-B. Li, C.-H. Tung, L.-Z. Wu, *Chem. Commun.* **2020**, *56*, 1549; c) L. Sun, C. Duboc, K. Shen, *ACS Catal.* **2022**, *12*, 9159; d) J. T. Kleinhaus, F. Wittkamp, S. Yadav, D. Siegmund, U.-P. Apfel, *Chem. Soc. Rev.* **2021**, *50*, 1668; e) Y. Li, T. B. Rauchfuss, *Chem. Rev.* **2016**, *116*, 704; f) S. Gao, W. Fan, Y. Liu, D. Jiang, Q. Duan, *Int. J. Hydrogen Energy* **2020**, *45*, 430; g) W. Lubitz, H. Ogata, O. Rüdiger, E. Reijerse, *Chem. Rev.* **2014**, *114*, 408; h) J. Noth, J. Esselborn, J. Güldenhaupt, A. Brünje, A. Sawyer, U.-P. Apfel, K. Gerwert, E. Hofmann, M. Winkler, T. Happe, *Angew. Chem. Int. Ed.* **2016**, *55*, 839; i) J.-F. Capon, F. Gloaguen, F. Y. Pétillon, P. Schollhammer, J. Talarmin, *Coord. Chem. Rev.* **2009**, *253*, 147; j) Y.-C. Liu, T.-H. Yen, K.-T. Chu, M.-H. Chiang, *Comments Inorg. Chem.* **2016**, *36*, 14; k) F. Wang, W.-G. Wang, H.-Y. Wang, G. Si, C.-H. Tung, L.-Z. Wu, *ACS Catal.* **2012**, *2*, 40; l) A. Zamader, B. Reuillard, J. Pécaut, L. Billon, A. Bousquet, G. Berggren, V. Artero, *Chem. Eur. J.* **2022**, *28*, e20220226.
- [2] S. Gao, Y. Liu, Y. Shao, D. Jiang, Q. Duan, *Coord. Chem. Rev.* **2020**, *402*, 213081.
- [3] M. B. Wilker, J. K. Utterback, S. Greene, K. A. Brown, D. W. Mulder, P. W. King, G. Dukovic, *J. Phys. Chem. C* **2018**, *122*, 741.
- [4] J. C. Ruth, A. M. Spormann, *ACS Catal.* **2021**, *11*, 5951.
- [5] R. E. Treviño, J. W. Slater, H. S. Shafaat, *ACS Appl. Energ. Mater.* **2020**, *3*, 11099.
- [6] a) J. C. Ruth, R. D. Milton, W. Gu, A. M. Spormann, *Chem. Eur. J.* **2020**, *26*, 7323; b) T. Yu, Y. Zeng, J. Chen, X. Zhang, G. Yang, Y. Li, *J. Mater. Chem. A* **2014**, *2*, 20500; c) S. K. Ibrahim, X. Liu, C. Tard, C. J. Pickett, *Chem. Commun.* **2007**, 1535; d) M. Karayilan, W. P. Brezinski, K. E. Clary, D. L. Lichtenberger, R. S. Glass, J. Pyun, *Angew. Chem. Int. Ed.* **2019**, *58*, 7537; e) D. Heine, C. Pietsch, U. S. Schubert, W. Weigand, *J. Polym. Sci. Part A* **2013**, *51*, 2171; f) L. Wang, Z. Xiao, X. Ru, X. Liu, *RSC Adv.* **2011**, *1*, 1211; g) E. Xu, Z. Xiao, H. Liu, L. Long, L. Li, X. Liu, *RSC Adv.* **2012**, *2*, 10171; h) D. Zhu, Z. Xiao, X. Liu, *Int. J. Hydrogen Energy* **2015**, *40*, 5081; i) X. Zhu, W. Zhong, X. Liu, *Int. J. Hydrogen Energy* **2016**, *41*, 14068.
- [7] K. Sakai, H. Xia, Y. Kitazumi, O. Shirai, K. Kano, *Electrochim. Acta* **2018**, *271*, 305.
- [8] V. Vijaiakanth, J.-F. Capon, F. Gloaguen, P. Schollhammer, J. Talarmin, *Electrochem. Commun.* **2005**, *7*, 427.
- [9] a) M. E. Ahmed, S. Dey, B. Mondal, A. Dey, *Chem. Commun.* **2017**, 53, 8188; b) A. Le Goff, V. Artero, R. Metayé, F. Moggia, B. Joussemme, M. Razavet, P. D. Tran, S. Palacin, M. Fontecave, *Int. J. Hydrogen Energy* **2010**, *35*, 10790.
- [10] R. Zaffaroni, R. J. Detz, J. I. van der Vlugt, J. N. H. Reek, *ChemSusChem* **2018**, *11*, 209.
- [11] M. Wen, H.-L. Wu, J.-X. Jian, X.-Z. Wang, X.-B. Li, B. Chen, C.-H. Tung, L.-Z. Wu, *ChemPhotoChem* **2017**, *1*, 260.
- [12] a) J. Sanabria-Chinchilla, A. Javier, D. Crouthers, J. H. Baricuatro, M. Y. Darensbourg, M. P. Soriaga, *Electrocatalysis* **2014**, *5*, 5; b) O. Rüdiger, C. Gutiérrez-Sánchez, D. Olea, I. A. C. Pereira, M. Vélez, V. M. Fernández, A. L. De Lacey, *Electroanalysis* **2010**, *22*, 776; c) X. Ru, X. Zeng, Z. Li, D. J. Evans, C. Zhan, Y. Tang, L. Wang, X. Liu, *J. Polym. Sci. Part A* **2010**, *48*, 2410; d) D. Millo, M.-E. Pandelia, T. Utesch, N. Wisitruangsakul, M. A. Mroginski, W. Lubitz, P. Hildebrandt, I. Zebger, *J. Phys. Chem. B* **2009**, *113*, 15344; e) C. Madden, M. D. Vaughn, I. Díez-Pérez, K. A. Brown, P. W. King, D. Gust, A. L. Moore, T. A. Moore, *J. Am. Chem. Soc.* **2012**, *134*, 1577; f) C. Gutiérrez-Sánchez, D. Olea, M. Marques, V. M. Fernández, I. A. C. Pereira, M. Vélez, A. L. De Lacey, *Langmuir* **2011**, *27*, 6449; g) B. Chmielowiec, F. H. Saadi, J. H. Baricuatro, A. Javier, Y.-G. Kim, G. Sun, M. Y. Darensbourg, M. P. Soriaga, *J. Electroanal. Chem.* **2014**, *716*, 63; h) A. Nayek, M. E. Ahmed, S. Samanta, S. Dinda, S. Patra, S. G. Dey, A. Dey, *J. Am. Chem. Soc.* **2022**, *144*, 8402; i) X. Zhang, L. Liu, W. Cao, D. Lv, *Catal. Lett.* **2020**, *150*, 3409; j) M. E. Ahmed, D. Saha, L. Wang, M. Gennari, S. Ghosh Dey, V. Artero, A. Dey, C. Duboc, *ChemElectroChem* **2021**, *8*, 1674; k) M. Watanabe, Y. Honda, H. Hagiwara, T. Ishihara, *J. Photochem. Photobiol. C* **2017**, *33*, 1; l) M. Cao, Z. Wang, J. Zhang, S. Xu, S. Zhang, X. Dai, X. Jiang, *Inorg. Chim. Acta* **2018**, *469*, 402.
- [13] a) P. D. Tran, V. Artero, M. Fontecave, *Energy Environ. Sci.* **2010**, *3*, 727; b) L. J. Antila, P. Ghamgosar, S. Maji, H. Tian, S. Ott, L. Hammarström, *ACS Energy Lett.* **2016**, *1*, 1106; c) C. M. Thomas, O. Rüdiger, T. Liu, C. E. Carson, M. B. Hall, M. Y. Darensbourg, *Organometallics* **2007**, *26*, 3976.
- [14] R. Sahli, C. Fave, N. Raouafi, K. Boujlel, B. Schöllhorn, B. Limoges, *Langmuir* **2013**, *29*, 5360.
- [15] a) K. M. Joly, G. Mirri, Y. Willener, S. L. Horswell, C. J. Moody, J. H. R. Tucker, *J. Org. Chem.* **2010**, *75*, 2395; b) A. G. Young, D. P. Green, A. J. McQuillan, *Langmuir* **2007**, *23*, 12923.
- [16] a) J. Hildebrandt, R. Trautwein, D. Kritsch, N. Häfner, H. Görls, M. Dürst, I. B. Runnebaum, W. Weigand, *Dalton Trans.* **2019**, *48*, 936; b) X. Liu, M.-C. Barth, K. Cseh, C. R. Kowol, M. A. Jakupec, B. K. Keppler, D. Gibson, W. Weigand, *Chem. Biodiversity* **2022**, *19*, e202200695.
- [17] a) C. V. Krishnan, M. Garnett, *Int. J. Electrochem. Sci.* **2011**, *6*, 3607; b) B. Ke, *Biochim. Biophys. Acta* **1957**, *25*, 650.
- [18] U.-P. Apfel, Y. Halpin, H. Görls, J. G. Vos, B. Schweizer, G. Linti, W. Weigand, *Chem. Biodiversity* **2007**, *4*, 2138.
- [19] L.-C. Song, W. Gao, C.-P. Feng, D.-F. Wang, Q.-M. Hu, *Organometallics* **2009**, *28*, 6121.
- [20] B. Neises, W. Steglich, *Angew. Chem. Int. Ed.* **1978**, *17*, 522.
- [21] S. Benndorf, E. Hofmeister, M. Wächtler, H. Görls, P. Liebing, K. Peneva, S. Gräfe, S. Kupfer, B. Dietzek-Ivanšić, W. Weigand, *Eur. J. Inorg. Chem.* **2022**, *3*, e202100959.
- [22] I. Cordova-Reyes, H. Hu, J.-H. Gu, E. Vandenhoven, A. Mohammed, S. Holdcroft, B. M. Pinto, *Can. J. Chem.* **1996**, *74*, 533.
- [23] M. K. Harb, U.-P. Apfel, H. Görls, G. A. N. Felton, T. Sakamoto, D. H. Evans, R. S. Glass, D. L. Lichtenberger, M. El-khateeb, W. Weigand, *Organometallics* **2009**, *28*, 6666.
- [24] M. K. Harb, H. Alshurafa, M. El-khateeb, A. Al-Zuheiri, H. Görls, H. Abul-Futouh, W. Weigand, *ChemistrySelect* **2018**, *3*, 8867.
- [25] H. Abul-Futouh, L. R. Almazahreh, S. J. Abaalkhail, H. Görls, S. T. Stripp, W. Weigand, *New J. Chem.* **2021**, *45*, 36.
- [26] L.-C. Song, X.-F. Liu, J.-B. Ming, J.-H. Ge, Z.-J. Xie, Q.-M. Hu, *Organometallics* **2010**, *29*, 610.
- [27] H. Abul-Futouh, M. El-khateeb, H. Görls, K. J. Asali, W. Weigand, *Dalton Trans.* **2017**, *46*, 2937.
- [28] U.-P. Apfel, Y. Halpin, H. Görls, J. G. Vos, B. Schweizer, G. Linti, W. Weigand, *Chem. Biodiversity* **2007**, *4*, 2138.
- [29] a) U.-P. Apfel, Y. Halpin, M. Gottschaldt, H. Görls, J. G. Vos, W. Weigand, *Eur. J. Inorg. Chem.* **2008**, *2008*, 5112; b) L.-C. Song, B. Gai, H.-T. Wang, Q.-M. Hu, *J. Inorg. Biochem.* **2009**, *103*, 805; c) R. Trautwein, L. R. Almazahreh, H. Görls, W. Weigand, *Z. Anorg. Allg. Chem.* **2013**, *639*, 1512; d) C. Figliola, L. Male, P. N. Horton, M. B. Pitak, S. J. Coles, S. L. Horswell, R. S. Grainger, *Organometallics* **2014**, *33*, 4449.
- [30] R. Trautwein, L. R. Almazahreh, H. Görls, W. Weigand, *Dalton Trans.* **2015**, *44*, 18780.
- [31] a) H. Abul-Futouh, S. J. Abaalkhail, M. K. Harb, H. Görls, W. Weigand, *Polyhedron* **2021**, *207*, 115382; b) F. Wang, M. Wang, X. Liu, K. Jin, W. Dong, L. Sun, *Dalton Trans.* **2007**, *34*, 3812; c) L.-C. Song, J.-H. Ge, X.-G. Zhang, Y. Liu, Q.-M. Hu, *Eur. J. Inorg. Chem.* **2006**, *2006*, 3204; d) G. Durgaprasad, R. Bolligarla, S. K. Das, *J. Organomet. Chem.* **2011**, *696*, 3097; e) C.-G. Li, Y. Zhu, X.-X. Jiao, X.-Q. Fu, *Polyhedron* **2014**, *67*, 416; f) P. Li, M. Wang, C. He, G. Li, X. Liu, C. Chen, B. Åkermark, L. Sun, *Eur. J. Inorg. Chem.* **2005**, 2506; g) M. L. Singleton, R. M. Jenkins, C. L. Klemashevich, M. Y. Darensbourg, *C. R. Chim.* **2008**, *11*, 861; h) W.-G. Wang, H.-Y. Wang, G. Si, C.-H. Tung, L.-Z. Wu, *Dalton Trans.* **2009**, 2712; i) Z. Wang, W. Jiang, J. Liu, W. Jiang, Y. Wang, B. Åkermark, L. Sun, *J. Organomet. Chem.* **2008**, *693*, 2828.
- [32] T. Liu, B. Li, M. L. Singleton, M. B. Hall, M. Y. Darensbourg, *J. Am. Chem. Soc.* **2009**, *131*, 8296.
- [33] S. J. Borg, T. Behing, S. P. Best, M. Razavet, X. Liu, C. J. Pickett, *J. Am. Chem. Soc.* **2004**, *126*, 16988.
- [34] K. Nakamoto, in *Infrared and Raman Spectra of Inorganic and Coordination Compounds, Part B: Applications in Coordination, Organometallic, and Bioinorganic Chemistry*, John Wiley & Sons, New York, **1997**.
- [35] S. P. Best, *Coord. Chem. Rev.* **2005**, *249*, 1536.



- [36] M. Krejčík, M. Daněk, F. Hartl, *J. Electroanal. Chem.* **1991**, *317*, 179.
- [37] J. P. H. Oudsen, B. Venderbosch, D. J. Martin, T. J. Korstanje, J. N. H. Reek, M. Tromp, *Phys. Chem. Chem. Phys.* **2019**, *21*, 14638.
- [38] S. J. Borg, J. W. Tye, M. B. Hall, S. P. Best, *Inorg. Chem.* **2007**, *46*, 384.
- [39] a) S. Wang, A. Aster, M. Mirmohades, R. Lomoth, L. Hammarström, *Inorg. Chem.* **2018**, *57*, 768; b) E. C. F. Schippers, S. S. Nurttala, J.-P. H. Oudsen, M. Tromp, W. I. Dzik, J. I. van der Vlugt, J. N. H. Reek, *Eur. J. Inorg. Chem.* **2019**, *2019*, 2510; c) D. Chong, I. P. Georgakaki, R. Mejia-Rodriguez, J. Sanabria-Chinchilla, M. P. Soriaga, M. Y. Darensbourg, *Dalton Trans.* **2003**, *21*, 4158.
- [40] M. Mirmohades, S. Pullen, M. Stein, S. Maji, S. Ott, L. Hammarström, R. Lomoth, *J. Am. Chem. Soc.* **2014**, *136*, 17366.
- [41] P. S. Singh, H. C. Rudbeck, P. Huang, S. Ezzaher, L. Eriksson, M. Stein, S. Ott, R. Lomoth, *Inorg. Chem.* **2009**, *48*, 10883.
- [42] S. J. Borg, S. K. Ibrahim, C. J. Pickett, S. P. Best, *C. R. Chim.* **2008**, *11*, 852.
- [43] D. J. Curran, P. B. Graham, M. D. Rausch, *Organometallics* **1993**, *12*, 2380.
- [44] G. A. N. Felton, A. K. Vannucci, J. Chen, L. T. Lockett, N. Okumura, B. J. Petro, U. I. Zakai, D. H. Evans, R. S. Glass, D. L. Lichtenberger, *J. Am. Chem. Soc.* **2007**, *129*, 12521.
- [45] a) J.-F. Capon, S. Ezzaher, F. Gloaguen, F. Y. Pétilion, P. Schollhammer, J. Talarmin, T. J. Davin, J. E. McGrady, K. W. Muir, *New J. Chem.* **2007**, *31*, 2052; b) S. Roy, T.-A. D. Nguyen, L. Gan, A. K. Jones, *Dalton Trans.* **2015**, *44*, 14865.
- [46] a) C. Greco, G. Zampella, L. Bertini, M. Bruschi, P. Fantucci, L. de Gioia, *Inorg. Chem.* **2007**, *46*, 108; b) J. Chen, A. K. Vannucci, C. A. Mebi, N. Okumura, S. C. Borowski, M. Swenson, L. T. Lockett, D. H. Evans, R. S. Glass, D. L. Lichtenberger, *Organometallics* **2010**, *29*, 5330; c) L. Schwartz, P. S. Singh, L. Eriksson, R. Lomoth, S. Ott, *C. R. Chim.* **2008**, *11*, 875; d) J.-F. Capon, F. Gloaguen, P. Schollhammer, J. Talarmin, *J. Electroanal. Chem.* **2006**, *595*, 47.
- [47] G. A. Felton, C. A. Mebi, B. J. Petro, A. K. Vannucci, D. H. Evans, R. S. Glass, D. L. Lichtenberger, *J. Organomet. Chem.* **2009**, *694*, 2681.
- [48] P.-H. Zhao, M.-Y. Hu, J.-R. Li, Z.-Y. Ma, Y.-Z. Wang, J. He, Y.-L. Li, X.-F. Liu, *Organometallics* **2019**, *38*, 385.
- [49] D. H. Pool, D. L. DuBois, *J. Organomet. Chem.* **2009**, *694*, 2858.
- [50] M. E. Ahmed, A. Dey, *Curr. Opin. Electrochem.* **2019**, *15*, 155.
- [51] H. Hijazi, E. Levillain, B. Schöllhorn, C. Fave, *ChemElectroChem* **2022**, *9*, e20220019.
- [52] H. Hijazi, A. Vacher, S. Groni, D. Lorcy, E. Levillain, C. Fave, B. Schöllhorn, *Chem. Commun.* **2019**, *55*, 1983.

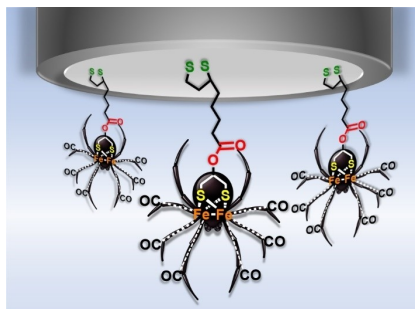
Manuscript received: November 4, 2022

Revised manuscript received: December 30, 2022

Accepted manuscript online: January 10, 2023

## RESEARCH ARTICLE

[FeFe] hydrogenase ( $H_2ase$ ) mimicking complexes containing lipoic and selenolipoic acid moieties connected to 2-hydroxy-1,3-dithio-propane and 2-hydroxy-1,3-diseleno-propane bridging ligands were synthesized and characterized. The elaboration of surface confined systems was studied in preliminary experiments. The [FeFe]  $H_2ase$  mimics formed well-organized self-assembled monolayers on Pt electrodes.



*S. Benndorf, Dr. S. Groni, L. M. Stafast, Dr. H. Görls, Dr. C. Fave, Prof. Dr. B. Schöllhorn\*, Prof. Dr. W. Weigand\**

1 – 11

**Synthesis of [FeFe] Hydrogenase Mimics with Lipoic acid and its Selenium Analogue as Anchor Groups**



# European Journal of Inorganic Chemistry

Supporting Information

## Synthesis of [FeFe] Hydrogenase Mimics with Lipoic acid and its Selenium Analogue as Anchor Groups

Stefan Benndorf, Sihem Groni, Leanne M. Stafast, Helmar Görls, Claire Fave,  
Bernd Schöllhorn,\* and Wolfgang Weigand\*

## Supporting Information

### Materials and Methods

All solvents as well as commercially available compounds were purchased (Sigma-Aldrich, Acros, abcr, Alfa Aesar, TCI) and used as received without further purification. Toluene was dried and deoxygenated over Na metal. The NMR spectra were recorded with a Bruker Avance 400 MHz spectrometer. Chemical shifts are given in ppm relative to internal SiMe<sub>4</sub> or CHCl<sub>3</sub> (<sup>1</sup>H, <sup>13</sup>C{<sup>1</sup>H}), external H<sub>3</sub>PO<sub>4</sub> (<sup>31</sup>P{<sup>1</sup>H}).

IR and IR-SEC spectra were measured with a Tensor 27 FT-IR spectrometer. A Biologic SP-50 potentiostat was used for spectroelectrochemical experiments. A specac OMNI OTTLE cell with Pt mesh working and counter electrode and a Ag wire reference electrode, was used for IR-SEC measurements. DIPEI mass spectrometry (70 eV) was performed with a Finnigan MAT SSQ 710. Elemental analysis was performed using a Euro Vector EA3000 element analyser.

Cyclic voltammetric (CV) data were obtained in a conventional three-electrode glass cell (10 ml of solution) under nitrogen atmosphere and ambient temperature, using a Reference 600 Potentiostat/Galvanostat/ZRA from Gamry Instruments. The measurements were performed with a glassy carbon working electrode (WE), that was successively polished with aluminum oxide powder prior to any cyclic voltammetric experiment, a non-aqueous Ag/AgCl reference electrode (RE), a silver wire in contact with 0.01 M AgNO<sub>3</sub> and 0.1 M [*n*-Bu<sub>4</sub>N][PF<sub>6</sub>] in MeCN, and a platinum wire counter electrode (CE). Acetonitrile (MeCN), used for electrochemical measurements, was freshly distilled from CaH<sub>2</sub> under nitrogen. All the potentials (text, tables, and figures) were quoted versus ferrocene(Fc)/ferrocenium(Fc<sup>+</sup>) couple; ferrocene was added as an internal standard at the end of the experiments.

Additional CV experiments were performed using a Potentiostat PGSTAT 128N equipped with a high speed module ADC10M (Metrohm Autolab) controlled by Nova 1.10.4 software. A conventional one-compartment three-electrode electrochemical cell was used. In experiments involving modified electrodes, the modified electrode (Au or Pt) was used as WE. In all experiments a platinum wire was employed as counter CE electrode and a salt bridge containing the electrolyte was used to connect the electrochemical cell with saturated calomel (SCE) RE. The electrolyte solution was purged with argon flow for few minutes prior to any electrochemical measurement. The absence of oxygen traces was confirmed by a background cyclic voltammetric measurement. The argon flux in the cell was maintained throughout the experiments. Unless otherwise stated, all measurements were performed at room temperature (ca. 20 °C). If not indicated otherwise the measurements were performed in a conventional one-compartment three-electrode cell containing 0.1 M solution of [NBu<sub>4</sub>][PF<sub>6</sub>] in anhydrous MeCN at 293 K.

All the electrodes that were destined to surface modification experiments were polished carefully prior to each immobilization experiment. Gold and platinum electrodes were mechanically polished with a slurry of graded alumina (from 1 to 0.3 μm), then ultra-sonicated in acetone, water, and absolute ethanol for 3 min each. The surfaces were further treated and were electrochemically restructured in 0.5 M aqueous H<sub>2</sub>SO<sub>4</sub> by applying consecutive cyclic voltammetric scans from -0.1 V to 1.5 V (vs. SCE) at a scan rate of 50 mV.s<sup>-1</sup>. The electrodes were finally rinsed with distilled milliQ water and pure electrolyte solvent before manipulation.

SAMs were prepared by simple immersion of clean, freshly polished and restructured electrodes in a solution of the adsorbate (1 mM) in acetonitrile for 12 hours. Consequently, electrodes were rinsed with pure acetonitrile prior to the electrochemical experiments.

Structure Determinations: The intensity data for the compounds were collected on a Nonius KappaCCD diffractometer using graphite-monochromated Mo-K<sub>α</sub> radiation. Data were corrected for Lorentz and polarization effects; absorption was taken into account on a semi-empirical basis using multiple-scans<sup>[1]</sup>. The structures were solved by intrinsic phases (SHELXT<sup>[2]</sup>) and refined by full-matrix least squares techniques against Fo<sup>2</sup> (SHELXL-2018<sup>[3]</sup>). The hydrogen atoms bonded to the hydroxyl-group O2 of **selenolipoic acid** (Figure S28) was located by difference Fourier synthesis and refined isotropically.

All hydrogen atoms were included at calculated positions with fixed thermal parameters. Disordered moieties of the lipoic acid and disordered dichloromethane (DCM) molecules of **7** were refined using bond lengths restraints and displacement parameter restraints. Some parts of the disorder DCM model were introduced by the program DSR.<sup>[4]</sup> MERCURY was used for structure representations.<sup>[5]</sup>

*Crystal Data for selenolipoic acid:* C<sub>8</sub>H<sub>14</sub>O<sub>2</sub>Se<sub>2</sub>, Mr = 300.11 gmol<sup>-1</sup>, yellow prism, size 0.066 x 0.064 x 0.062 mm<sup>3</sup>, triclinic, space group P  $\bar{1}$ , a = 6.7660(3), b = 8.0218(4), c = 10.8041(7) Å, α = 73.394(3), β = 75.051(3), γ = 67.723(3)°, V = 512.54(5) Å<sup>3</sup>, T = -140 °C, Z = 2, ρ<sub>calcd.</sub> = 1.945 gcm<sup>-3</sup>, μ (Mo-K<sub>α</sub>) = 71.74 cm<sup>-1</sup>, multi-scan, transmin: 0.6556, transmax: 0.7456, F(000) = 292, 5850 reflections in h(-8/8), k(-10/10), l(-14/13), measured in the range 3.083° ≤ Θ ≤ 27.475°, completeness Θ<sub>max</sub> = 99.4%, 2333 independent reflections, R<sub>int</sub> = 0.0290, 1956 reflections with F<sub>o</sub> > 4σ(F<sub>o</sub>), 113 parameters, 0 restraints, R<sub>1obs</sub> = 0.0367, wR<sub>2obs</sub><sup>2</sup> = 0.0731, R<sub>1all</sub> = 0.0485, wR<sub>2all</sub><sup>2</sup> = 0.0782, GOOF = 1.116, largest difference peak and hole: 0.718 / -0.513 e Å<sup>-3</sup>.

*Crystal Data for 7:* C<sub>34</sub>H<sub>33</sub>Fe<sub>2</sub>O<sub>7</sub>PS<sub>4</sub>, 0.5(CH<sub>2</sub>Cl<sub>2</sub>), Mr = 866.97 gmol<sup>-1</sup>, brown prism, size 0.092 x 0.090 x 0.068 mm<sup>3</sup>, triclinic, space group P  $\bar{1}$ , a = 10.4590(2), b = 14.4053(3), c = 15.0905(4) Å, α = 65.015(1), β = 73.673(1), γ = 87.116(1)°, V = 1971.61(8) Å<sup>3</sup>, T = -140 °C, Z = 2, ρ<sub>calcd.</sub> = 1.460 gcm<sup>-3</sup>, μ (Mo-K<sub>α</sub>) = 11 cm<sup>-1</sup>, multi-scan, transmin: 0.6609, transmax: 0.7456, F(000) = 895, 29266 reflections in h(-13/13), k(-18/18), l(-19/18), measured in the range 2.035° ≤ Θ ≤ 27.656°, completeness Θ<sub>max</sub> = 99.4%, 9014 independent reflections, R<sub>int</sub> = 0.0249, 7734 reflections with F<sub>o</sub> > 4σ(F<sub>o</sub>), 654 parameters, 909 restraints, R<sub>1obs</sub> = 0.0532, wR<sub>2obs</sub><sup>2</sup> = 0.1462, R<sub>1all</sub> = 0.0622, wR<sub>2all</sub><sup>2</sup> = 0.1544, GOOF = 1.018, largest difference peak and hole: 0.810 / -0.687 e Å<sup>-3</sup>.

**Supporting Information available:** Crystallographic data (excluding structure factors) has been deposited with the Cambridge Crystallographic Data Centre as supplementary publication CCDC- 2209004 for **selenolipoic acid**, and CCDC- 2209005 for **7**. Copies of the data can be obtained free of charge on application to CCDC, 12 Union Road, Cambridge CB2 1EZ, UK [E- mail: deposit@ccdc.cam.ac.uk].

## Additional figures and graphs

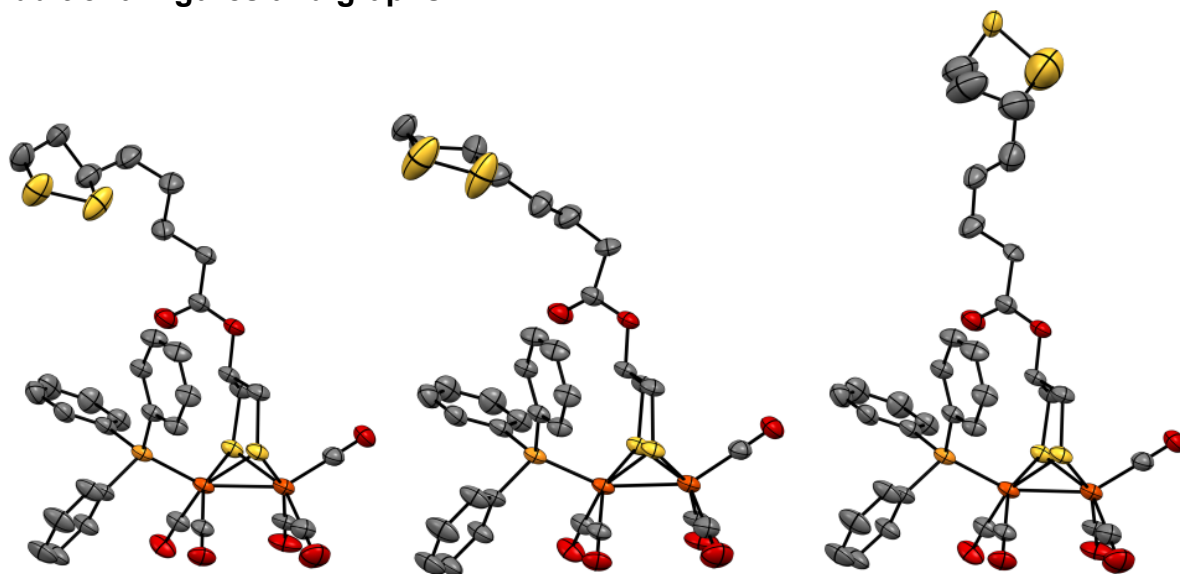


**Figure S1.** Molecular structures of three conformers of complex **7**. The ellipsoids represent a probability of 50 %, (hydrogen atoms were omitted for clarity). Legend of the colour code: C (grey), O (red), S (yellow), Fe (orange), P (salmon).

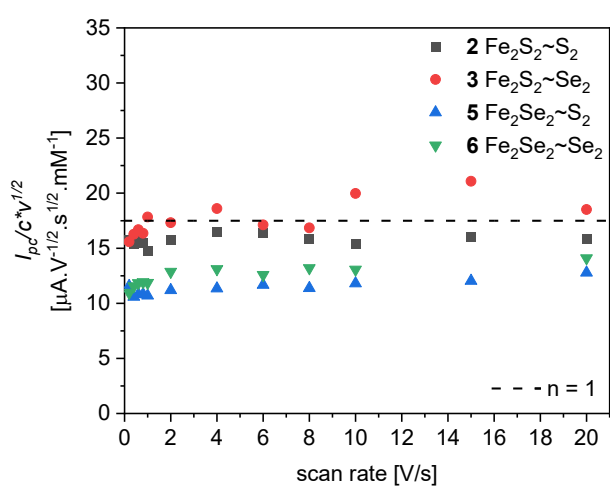


**Figure S2.** Scan-rate dependency of the Current function for the first reduction step of compounds **2**, **3**, **5** and **6**. The dashed line indicates the expected value for a one electron process, calculated for various [FeFe] hydrogenase mimics ( $D \approx 9 \times 10^{-6} \text{ cm}^2 \text{ s}^{-1}$ ).<sup>[6]</sup>

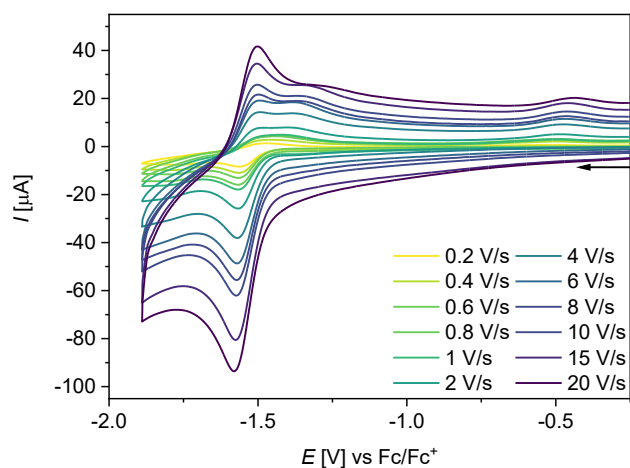


**Figure S3.** CV of compound **2** at different scan rates in  $N_2$ -purged MeCN/[NBu<sub>4</sub>][BF<sub>4</sub>] (0.1 mol/L) at RT. The arrow indicates the scan direction. The potential  $E$  is given in V and referenced to the Fc/Fc<sup>+</sup> couple.

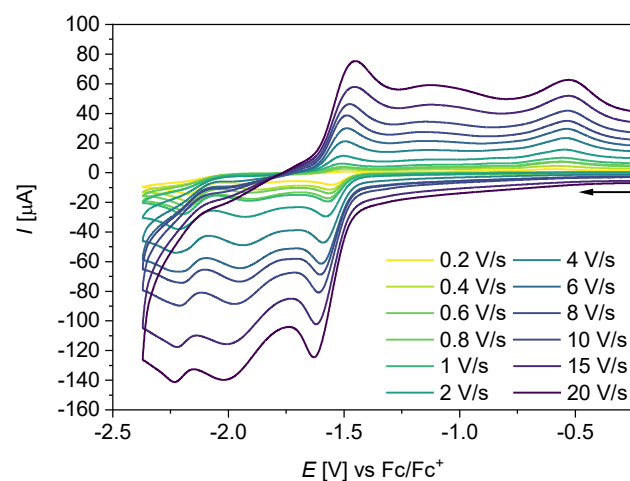


**Figure S4.** CV of compound **3** at different scan rates in  $N_2$ -purged MeCN/[NBu<sub>4</sub>][BF<sub>4</sub>] (0.1 mol/L) at RT. The arrow indicates the scan direction. The potential  $E$  is given in V and referenced to the Fc/Fc<sup>+</sup> couple.

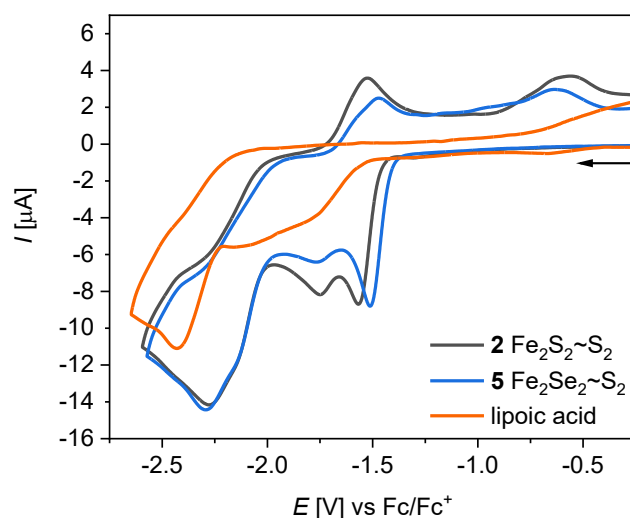


**Figure S5.** Cyclic voltammograms of complexes **2** and **5** with their precursor lipoic acid ( $c = 1$  mmol/L) in  $N_2$ -purged MeCN/[NBu<sub>4</sub>][BF<sub>4</sub>] (0.1 mol/L) at RT. The arrow indicates the scan direction. The potential  $E$  is given in V and referenced to the Fc/Fc<sup>+</sup> couple.

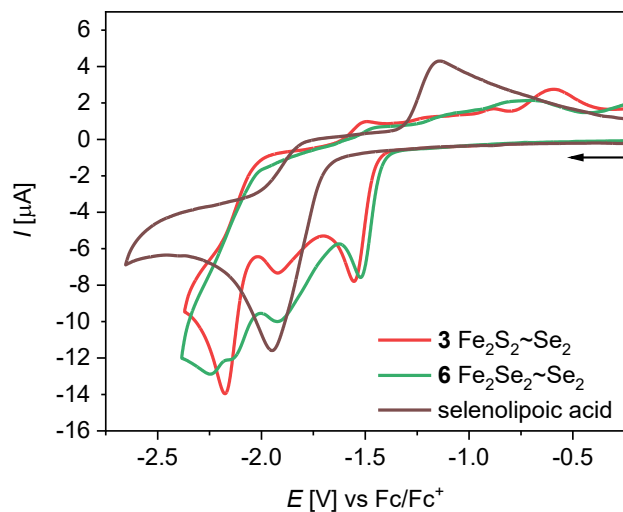


**Figure S6.** Cyclic voltammograms of complexes **3** and **6** with their precursor selenolipoic acid ( $c = 1$  mmol/L) in  $N_2$ -purged MeCN/[NBu<sub>4</sub>][BF<sub>4</sub>] (0.1 mol/L) at RT. The arrow indicates the scan direction. The potential  $E$  is given in V and referenced to the Fc/Fc<sup>+</sup> couple.

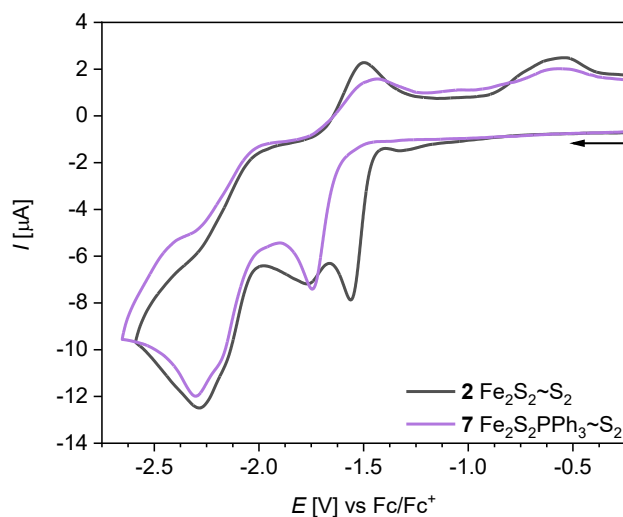


**Figure S7.** Cyclic voltammograms of complexes **2** and **7** ( $c = 1$  mmol/L) in  $N_2$ -purged MeCN/[NBu<sub>4</sub>][BF<sub>4</sub>] (0.1 mol/L) at RT. The arrow indicates the scan direction. The potential  $E$  is given in V and referenced to the Fc/Fc<sup>+</sup> couple.

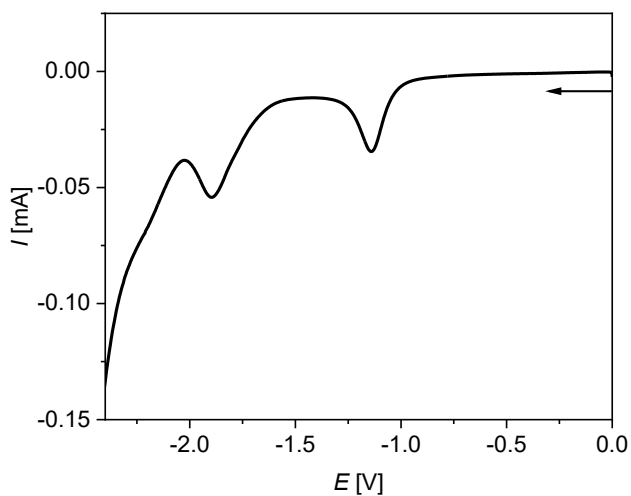


**Figure S8.** Voltammogram of compound **2** ( $c = 2$  mmol/L) during the SEC IR experiment with slow scan rate (2 mV/s). The arrow indicates the scan direction. The potential  $E$  is given in V and referenced to the Ag wire.



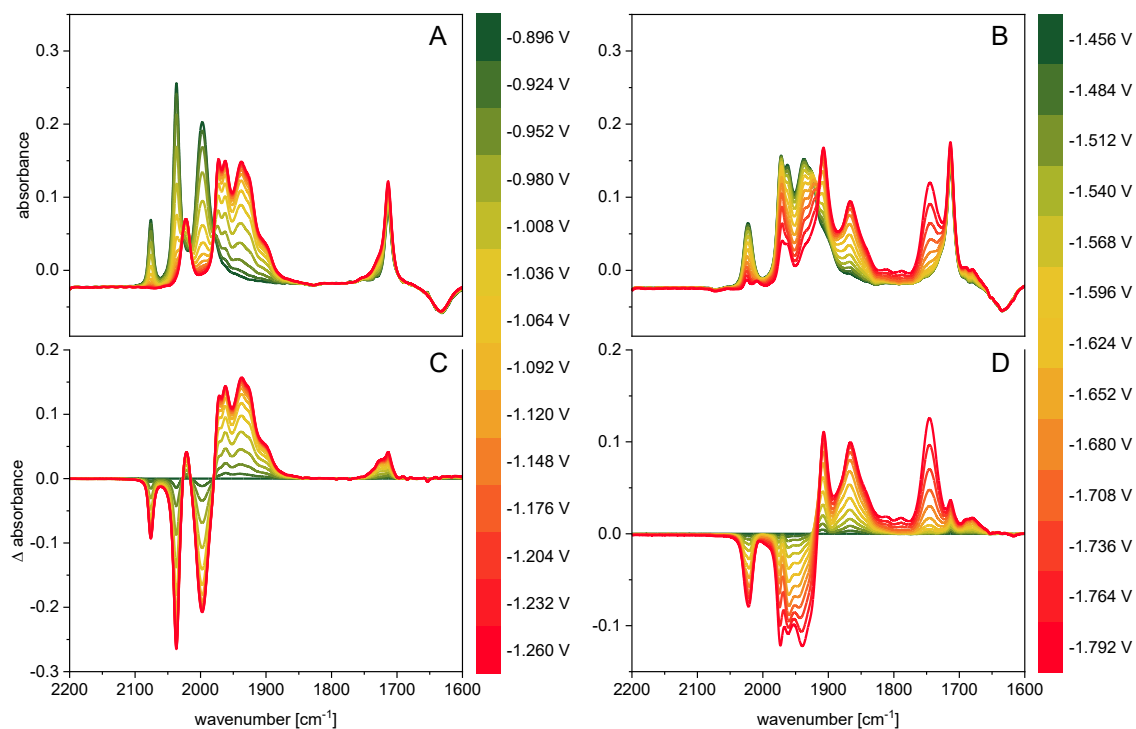


**Figure S9.** IR spectroelectrochemical measurements of the first (A) and second reduction (B) and their respective differential spectra (C, D) of compound **1** (MeCN,  $c = 2$  mmol/L). The  $\Delta$  absorbance spectra were calculated by subtracting a spectrum recorded immediately before the reducing phase. There is a cathodic shift between the CV and the IR SEC experiments due to the use of different electrodes.

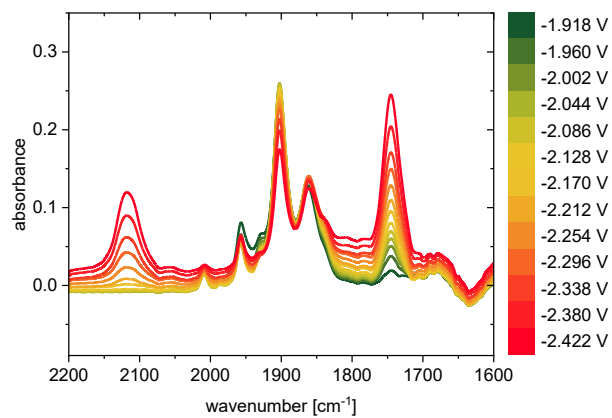


**Figure S10.** IR spectroelectrochemical measurements of further reduction steps of compound **2** (MeCN,  $c = 2$  mmol/L).

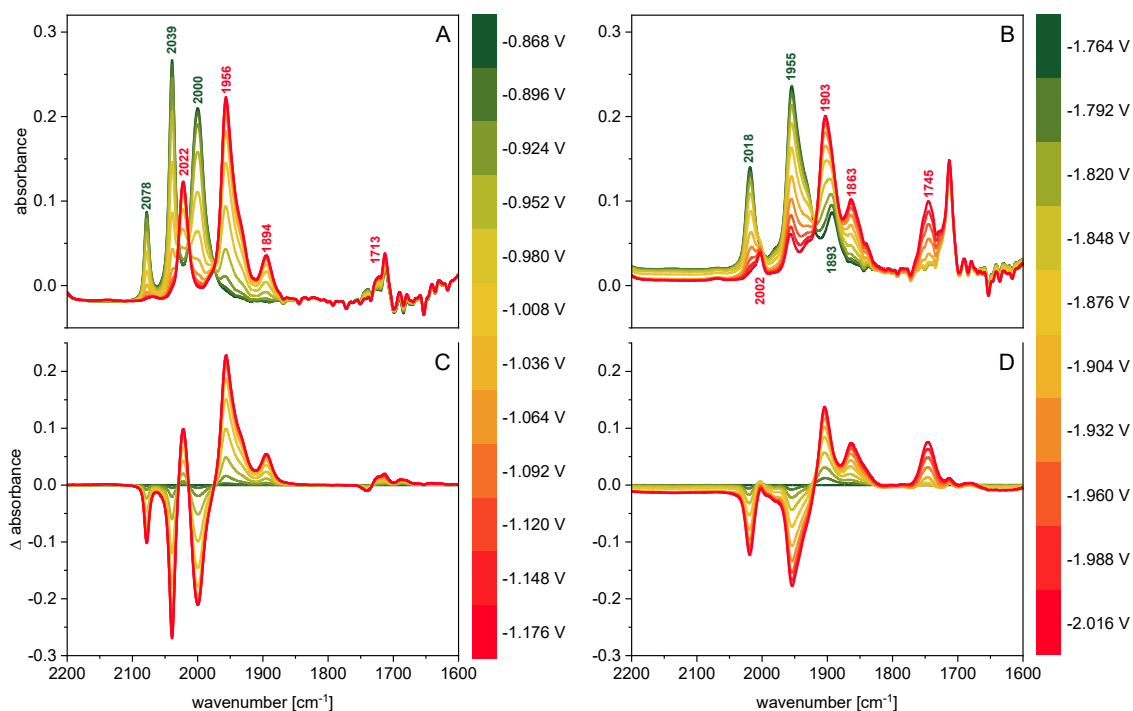


**Figure S11.** IR spectroelectrochemical measurements of the first (A) and second reduction (B) and their respective differential spectra (C, D) of compound **3** (MeCN,  $c = 2$  mmol/L). The  $\Delta$  absorbance spectra were calculated by subtracting a spectrum recorded immediately before the reducing phase. There is a cathodic shift between the CV and the IR SEC experiments due to the use of different electrodes.

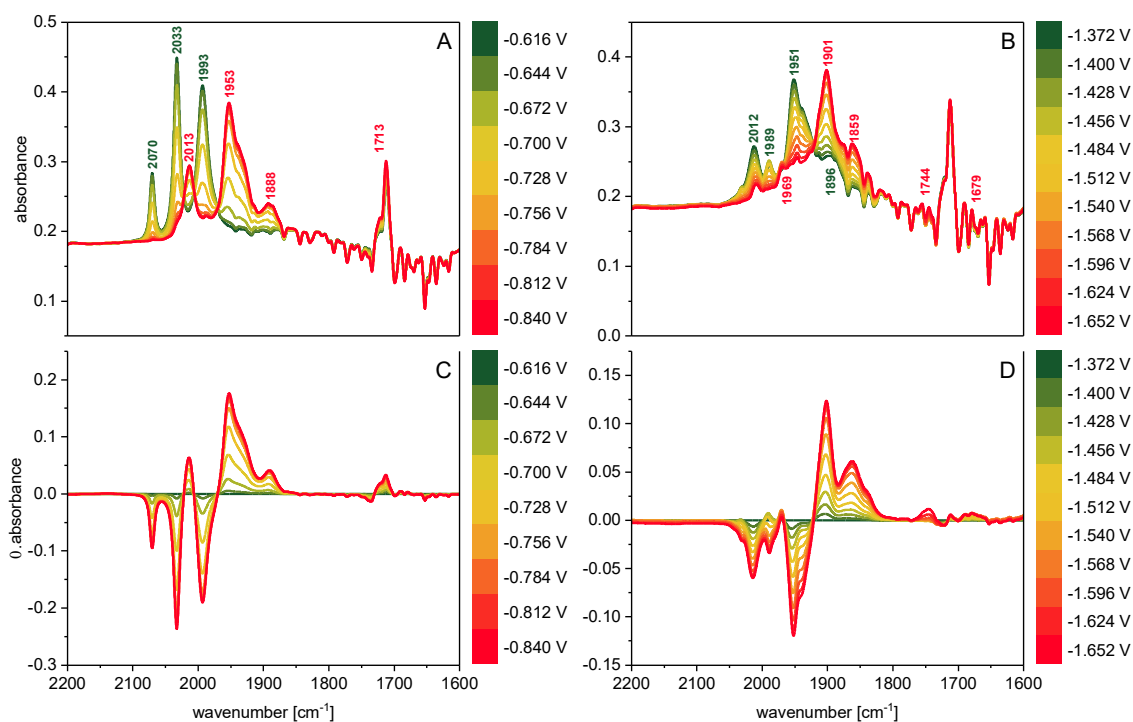


**Figure S12.** IR spectroelectrochemical measurements of the first (A) and second reduction (B) and their respective differential spectra (C, D) of compound **5** (MeCN,  $c = 2$  mmol/L). The  $\Delta$  absorbance spectra were calculated by subtracting a spectrum recorded immediately before the reducing phase. There is a cathodic shift between the CV and the IR SEC experiments due to the use of different electrodes.

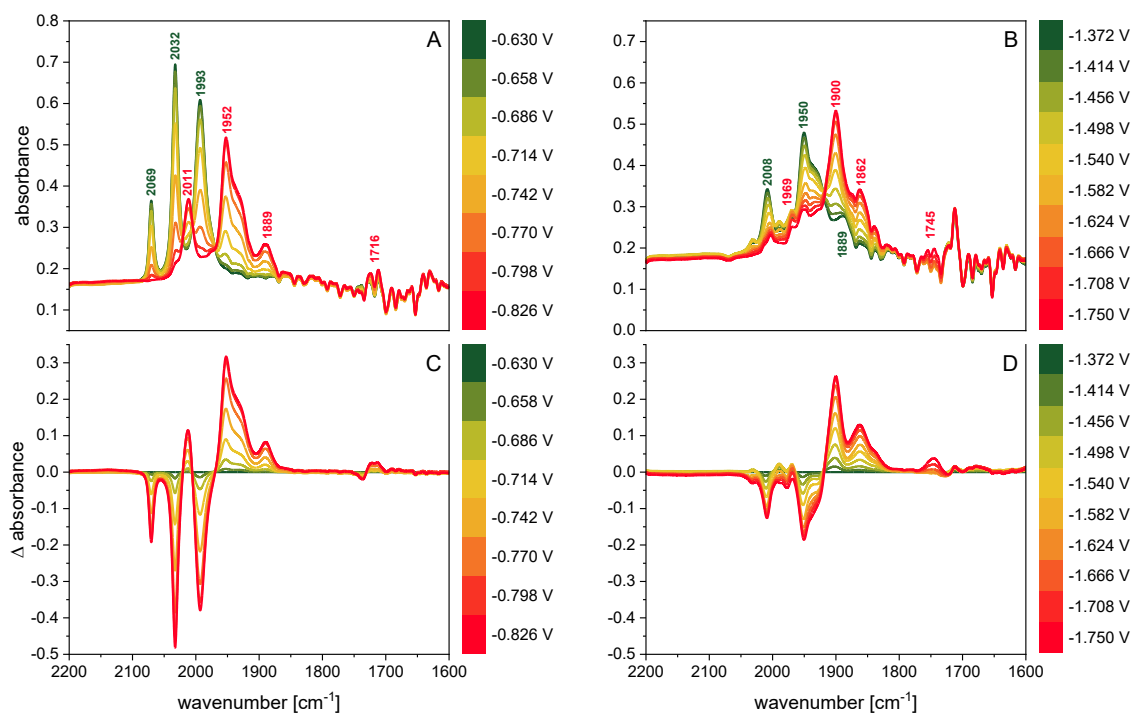


**Figure S13.** IR spectroelectrochemical measurements of the first (A) and second reduction (B) and their respective differential spectra (C, D) of compound **6** (MeCN,  $c = 2$  mmol/L). The  $\Delta$  absorbance spectra were calculated by subtracting a spectrum recorded immediately before the reducing phase. There is a cathodic shift between the CV and the IR SEC experiments due to the use of different electrodes.

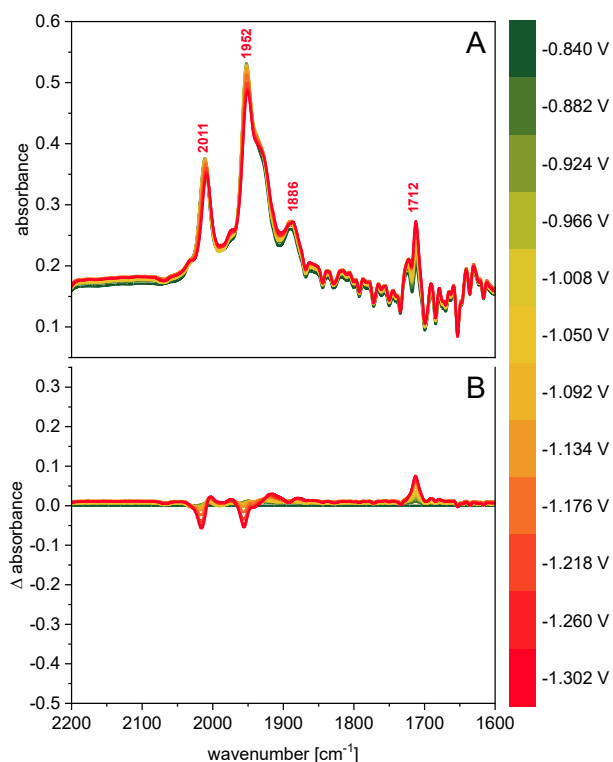


**Figure S14.** IR spectroelectrochemical measurements of the reduction of the diselenolane bridge (A) and the respective differential spectra (B) of compound **6** (MeCN,  $c = 2$  mmol/L). The  $\Delta$  absorbance spectra were calculated by subtracting a spectrum recorded immediately before the reducing phase. There is a cathodic shift between the CV and the IR SEC experiments due to the use of different electrodes.

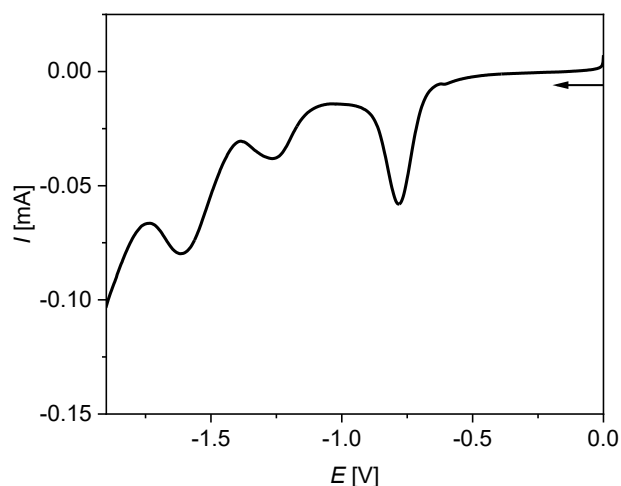


**Figure S15.** Voltammogram of compound **6** ( $c = 2$  mmol/L) during the SEC IR experiment with slow scan rate (2 mV/s). The arrow indicates the scan direction. The potential  $E$  is given in V and referenced to the Ag wire.

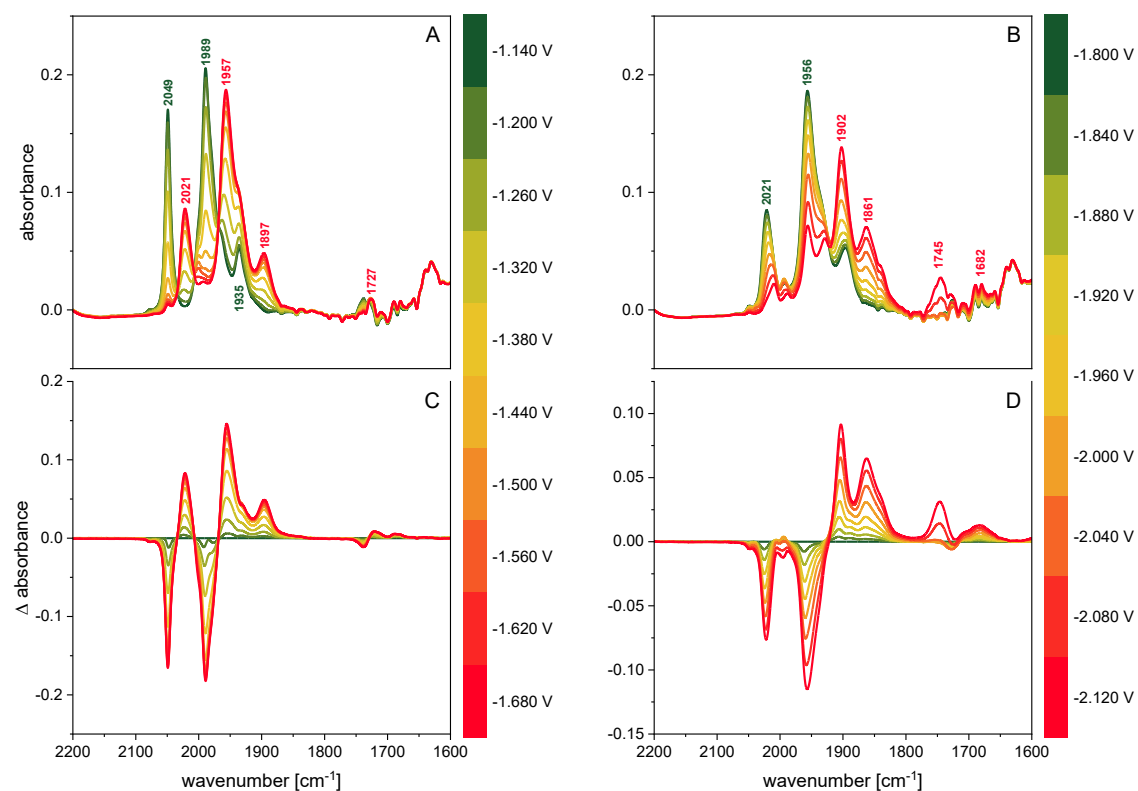


**Figure S16.** IR spectroelectrochemical measurements of the first (A) and second reduction (B) and their respective differential spectra (C, D) of compound **7** (MeCN,  $c = 2$  mmol/L). The  $\Delta$  absorbance spectra were calculated by subtracting a spectrum recorded immediately before the reducing phase. There is a cathodic shift between the CV and the IR SEC experiments due to the use of different electrodes.

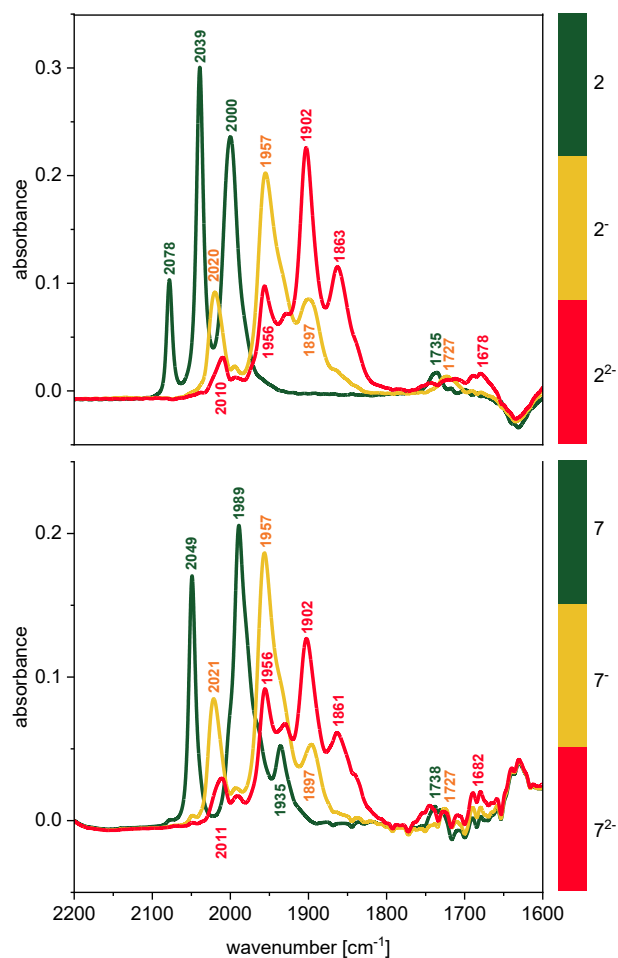


**Figure S17.** IR spectroelectrochemical measurements of the first and second reduction of compounds **2** (top) and **7** (bottom, MeCN,  $c = 2$  mmol/L).

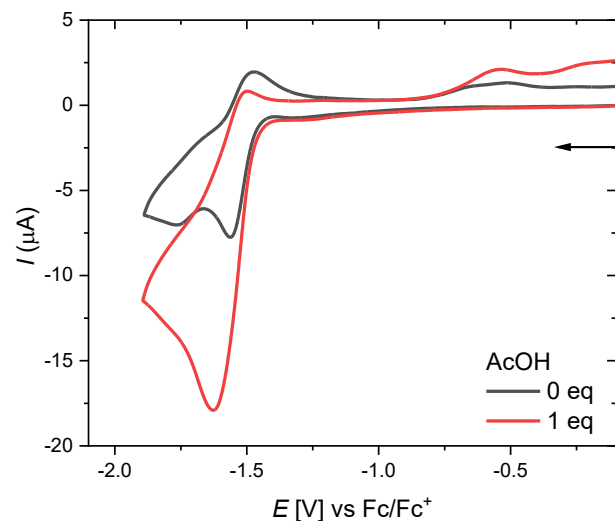


**Figure S18.** Cyclic voltammograms ( $v = 0.2$  V/s) of compound **2** ( $c = 1$  mmol/L) with and without one equivalent of AcOH in  $N_2$ -purged MeCN/[NBu<sub>4</sub>][BF<sub>4</sub>] (0.1 mol/L) at RT. The arrow indicates the scan direction. The potential  $E$  is given in V and referenced to the Fc/Fc<sup>+</sup> couple.

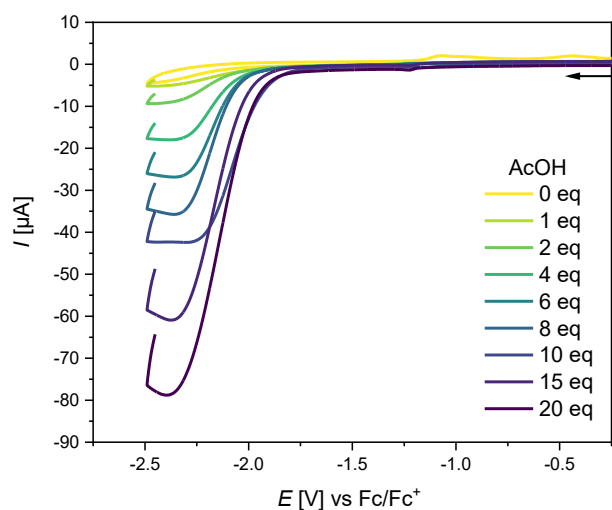


**Figure S19.** Cyclic voltammogram of various amounts of AcOH in the absence of any catalyst in  $N_2$ -purged MeCN/[NBu<sub>4</sub>][BF<sub>4</sub>] (0.1 mol/L) at RT. The arrow indicates the scan direction. The potential  $E$  is given in V and referenced to the Fc/Fc<sup>+</sup> couple.

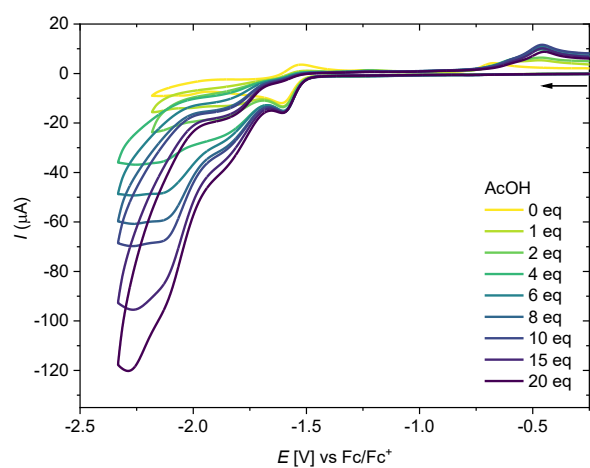


**Figure S20.** Cyclic voltammograms ( $v = 0.2$  V/s) of compound **1** ( $c = 1$  mmol/L) with various amounts of AcOH in  $N_2$ -purged MeCN/[NBu<sub>4</sub>][BF<sub>4</sub>] (0.1 mol/L) at RT. The arrow indicates the scan direction. The potential  $E$  is given in V and referenced to the Fc/Fc<sup>+</sup> couple.

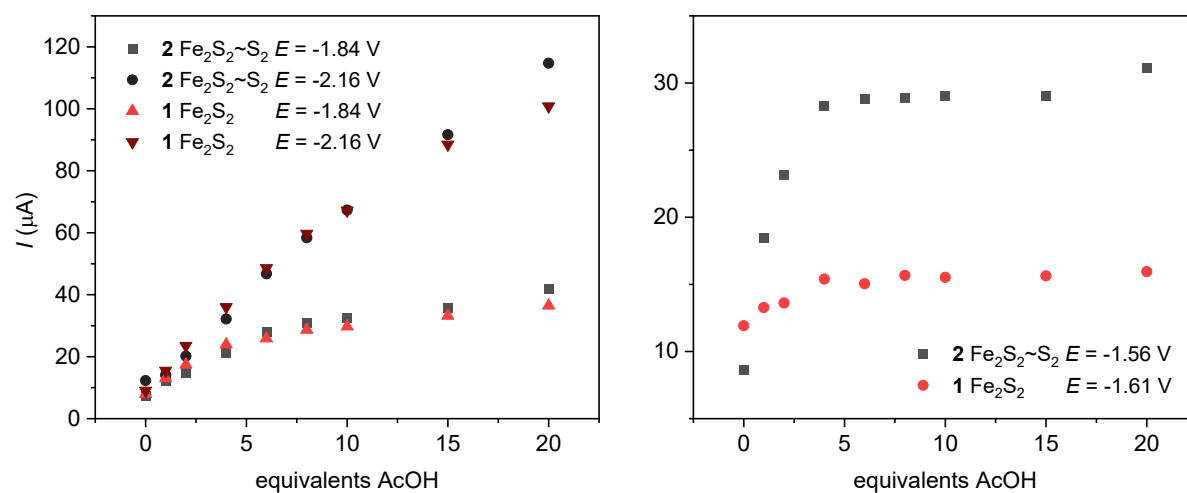


**Figure S21.** Comparison of the dependance of the catalytic current with various amounts of AcOH between complexes **1** and **2**.

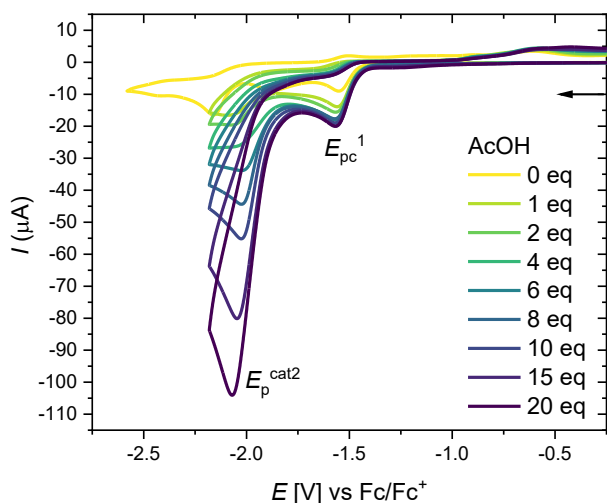


**Figure S22.** Cyclic voltammograms ( $v = 0.2$  V/s) of compound **3** ( $c = 1$  mmol/L) with various amounts of AcOH in N<sub>2</sub>-purged MeCN/[NBu<sub>4</sub>][BF<sub>4</sub>] (0.1 mol/L) at RT. The arrow indicates the scan direction. The potential  $E$  is given in V and referenced to the Fc/Fc<sup>+</sup> couple.

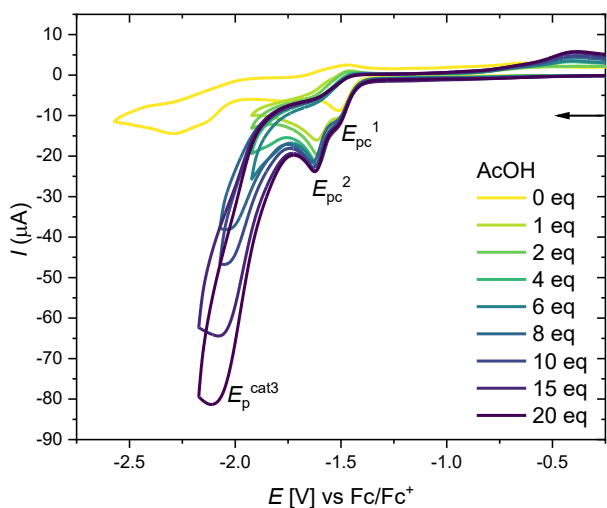


**Figure S23.** Cyclic voltammograms ( $v = 0.2$  V/s) of compound **5** ( $c = 1$  mmol/L) with various amounts of AcOH in N<sub>2</sub>-purged MeCN/[NBu<sub>4</sub>][BF<sub>4</sub>] (0.1 mol/L) at RT. The arrow indicates the scan direction. The potential  $E$  is given in V and referenced to the Fc/Fc<sup>+</sup> couple.

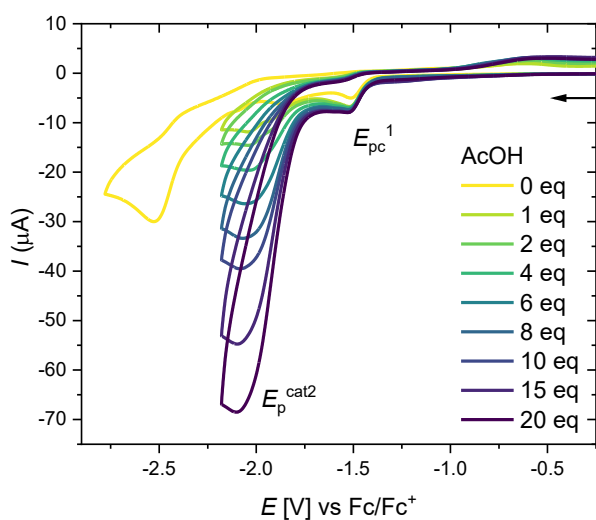
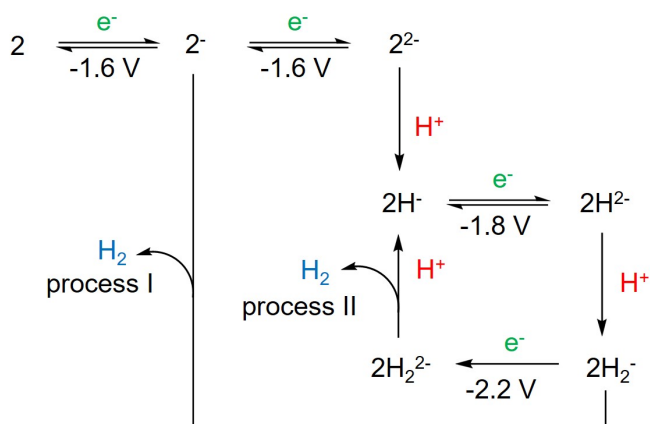


**Figure S24.** Cyclic voltammograms ( $v = 0.2$  V/s) of compound **6** ( $c = 1$  mmol/L) with various amounts of AcOH in N<sub>2</sub>-purged MeCN/[NBu<sub>4</sub>][BF<sub>4</sub>] (0.1 mol/L) at RT. The arrow indicates the scan direction. The potential  $E$  is given in V and referenced to the Fc/Fc<sup>+</sup> couple.



**Scheme S1.** Proposed mechanism for the proton reduction cycle of complex **2** in the presence of AcOH.

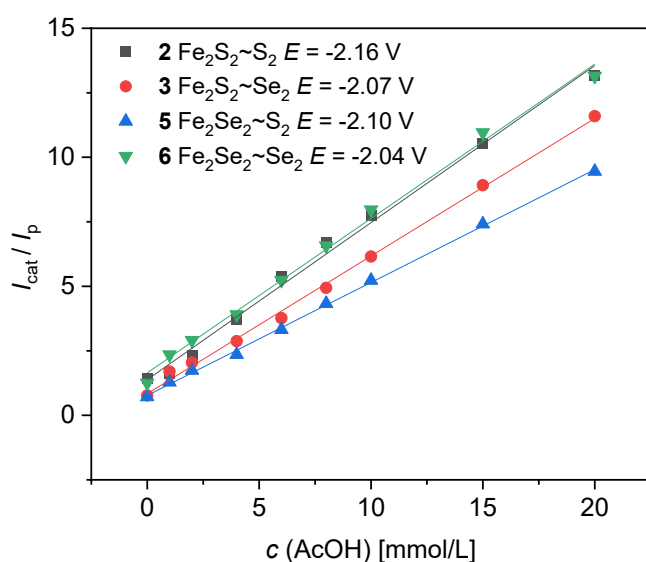


**Figure S25.** Plots of  $I_{\text{cat}}/I_p$  versus  $c(\text{AcOH})$  for complexes **2**, **3**, **5** and **6** ( $c = 1 \text{ mmol/L}$ ) in  $\text{N}_2$ -purged MeCN/[NBu<sub>4</sub>][BF<sub>4</sub>] (0.1 mol/L) at a scan rate of 0.2 V/s at RT. Lines are the best-linear fit to the data ( $R^2 = 0.9935$  (**2**),  $R^2 = 0.9972$  (**3**),  $R^2 = 0.9988$  (**5**),  $R^2 = 0.9943$  (**6**)).

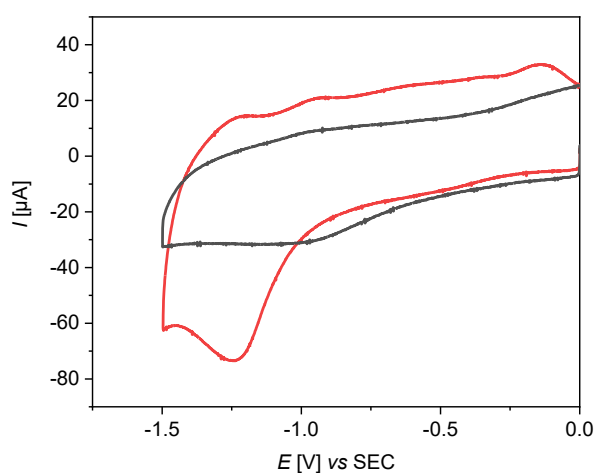


**Figure S26.** Cyclic voltammograms ( $\nu = 10 \text{ V/s}$ ) of the bare (grey line) and the modified platinum electrode **Au-SAM-2** (red line) in 0.1 M [NBu<sub>4</sub>][PF<sub>6</sub>] MeCN solution. Electrode diameter = 3 mm; saturated calomel reference electrode.



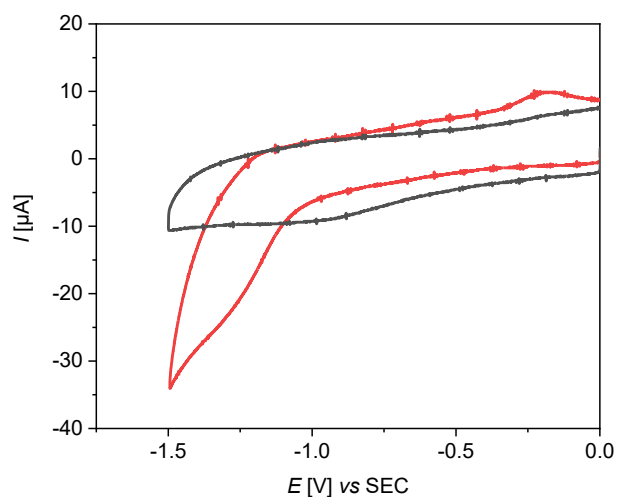


**Figure S27.** Cyclic voltammograms ( $\nu = 10$  V/s) of the bare (grey line) and the modified platinum electrode **Au-SAM-6** (red line) in 0.1 M  $[\text{NBu}_4][\text{PF}_6]$  MeCN solution. Electrode diameter = 3 mm; saturated calomel reference electrode.

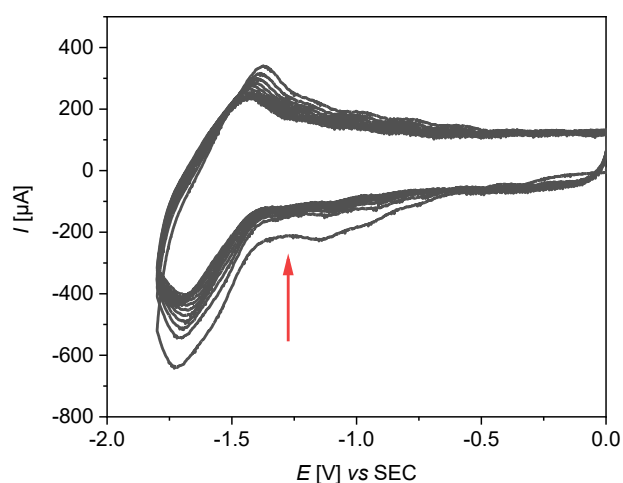


**Figure S28.** A series of 10 cyclic voltammograms ( $\nu = 10$  V/s) of a modified platinum electrode **Pt-SAM-2** in 0.1 M  $[\text{NBu}_4][\text{PF}_6]$  MeCN. Electrode diameter = 3 mm; saturated calomel reference electrode.

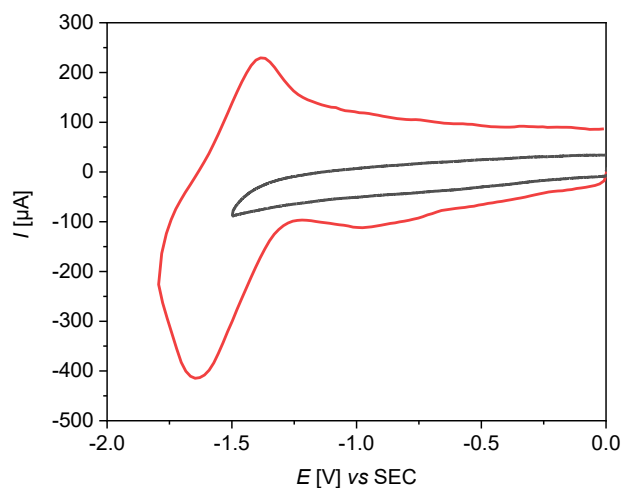


**Figure S29.** Cyclic voltammogram ( $\nu = 10$  V/s) of the bare (grey line) and the modified platinum electrode **Pt-SAM-2** (red line) in 0.1 M  $[\text{NBu}_4][\text{PF}_6]$  MeCN solution. Electrode diameter = 3 mm; saturated calomel reference electrode.

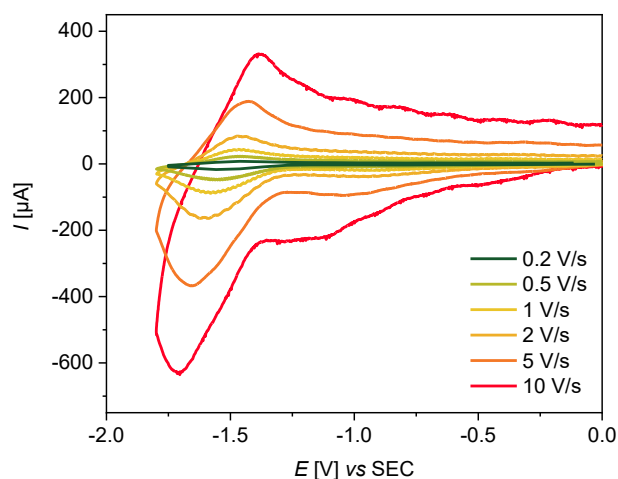


**Figure S30.** Cyclic voltammograms of a modified platinum electrode **Pt-SAM-2** in 0.1 M  $\text{NBu}_4\text{PF}_6$  acetonitrile at different scan speeds. Electrode diameter = 3 mm; saturated calomel reference electrode.

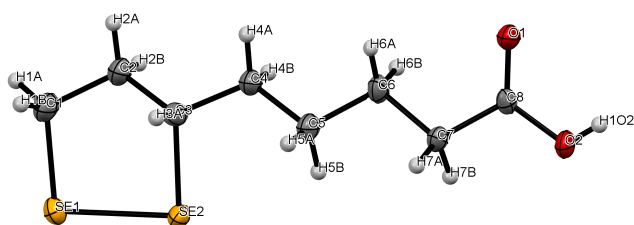


**Figure S31.** Molecular structure of **selenolipoic acid**. The ellipsoids represent a probability of 50 %, H atoms are drawn with arbitrary radii.

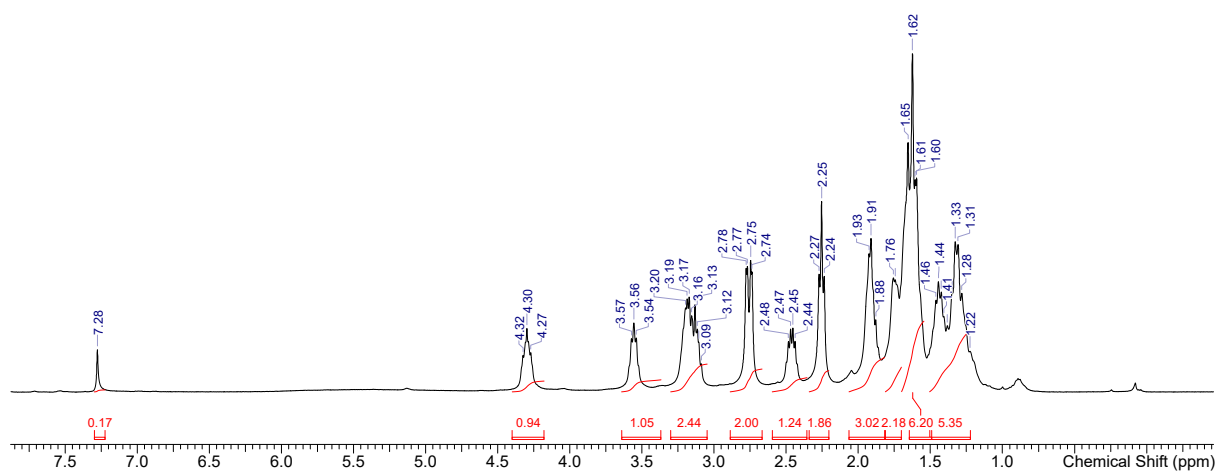


**Figure S32.**  $^1\text{H}$  NMR ( $\text{CDCl}_3$ , 297 K, 400 MHz) spectrum of compound **2**.

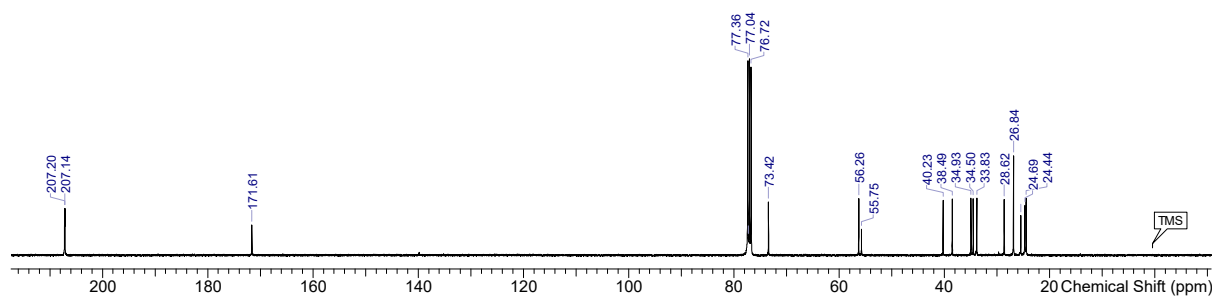


Figure S33.  $^{13}\text{C}$  NMR ( $\text{CDCl}_3$ , 297 K, 101 MHz) spectrum of compound **2**.

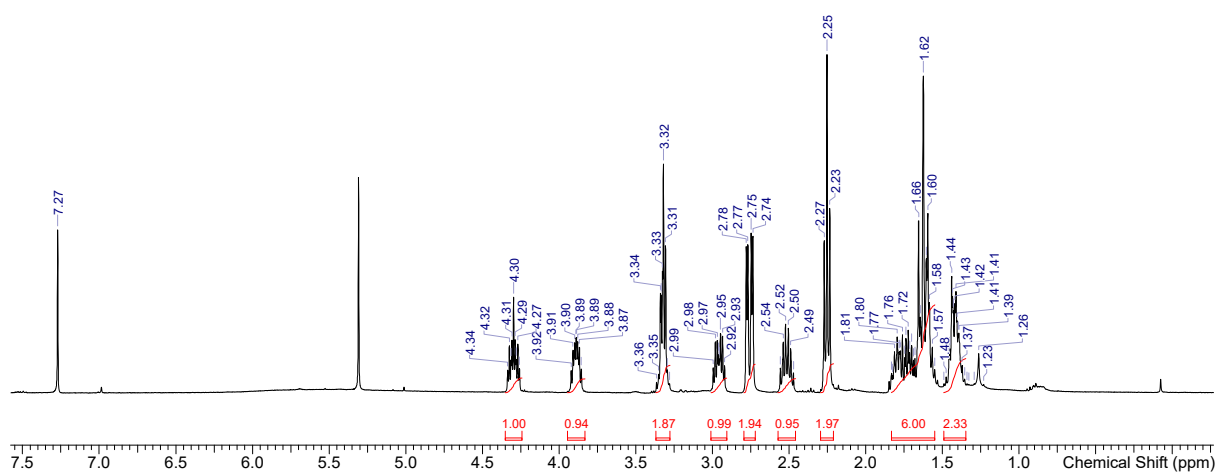


Figure S34.  $^1\text{H}$  NMR ( $\text{CDCl}_3$ , 297 K, 400 MHz) spectrum of compound **3**.

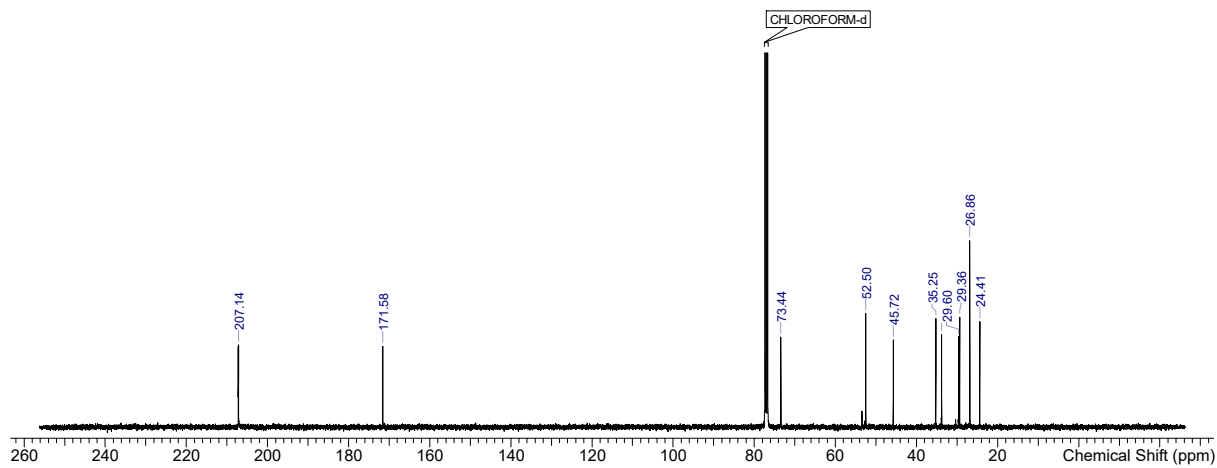
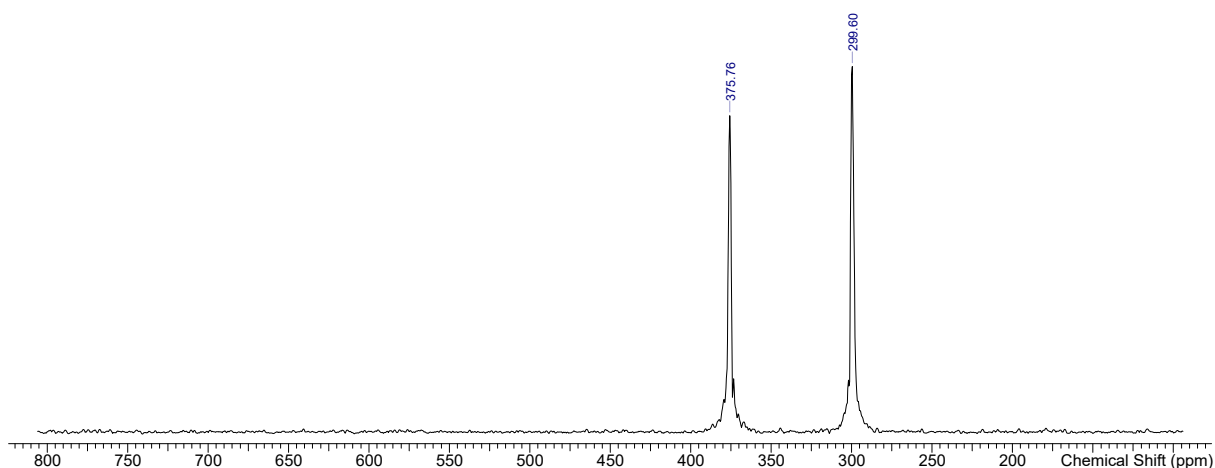
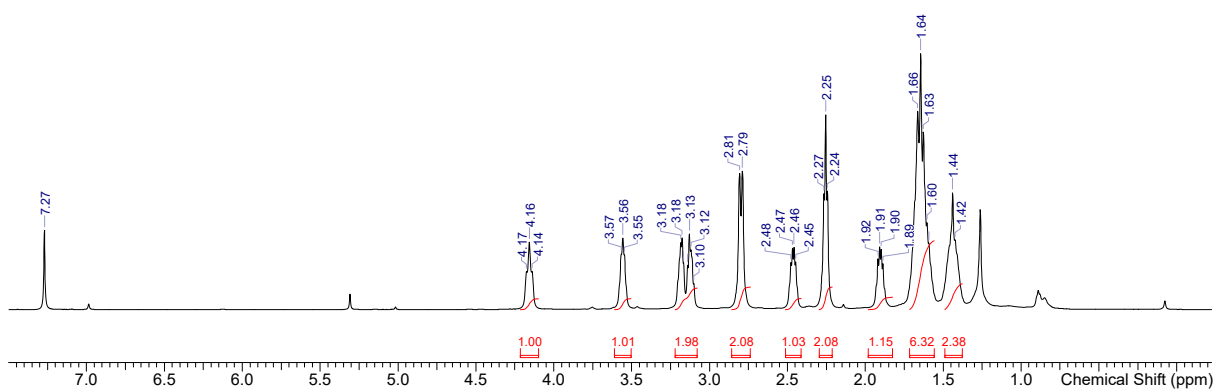


Figure S35.  $^{13}\text{C}$  NMR ( $\text{CDCl}_3$ , 297 K, 101 MHz) spectrum of compound **3**.



**Figure S36.** <sup>77</sup>Se NMR (CDCl<sub>3</sub>, 297 K, 76 MHz) spectrum of compound **3**.



**Figure S37.** <sup>1</sup>H NMR (CDCl<sub>3</sub>, 297 K, 600 MHz) spectrum of compound **5**.

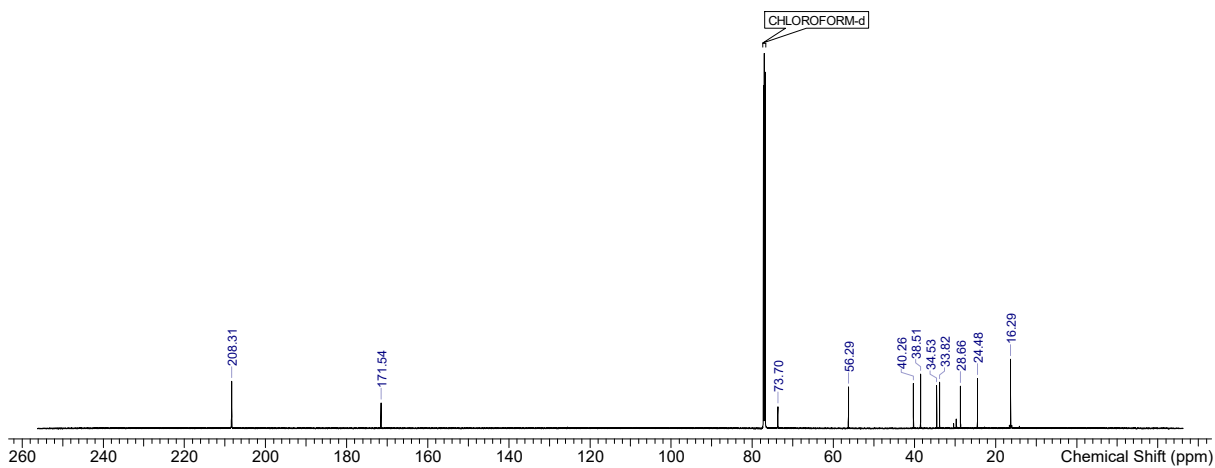


**Figure S38.** <sup>13</sup>C NMR (CDCl<sub>3</sub>, 297 K, 151 MHz) spectrum of compound **5**.

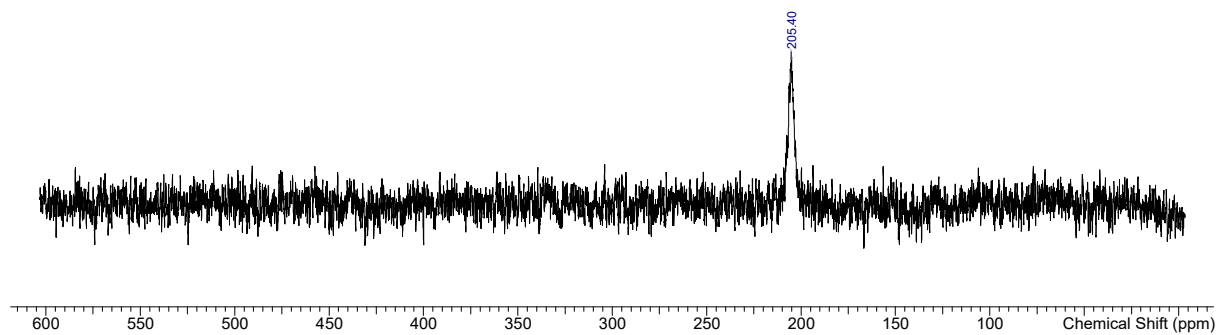


Figure S39. <sup>77</sup>Se NMR (CDCl<sub>3</sub>, 297 K, 76 MHz) spectrum of compound 5.

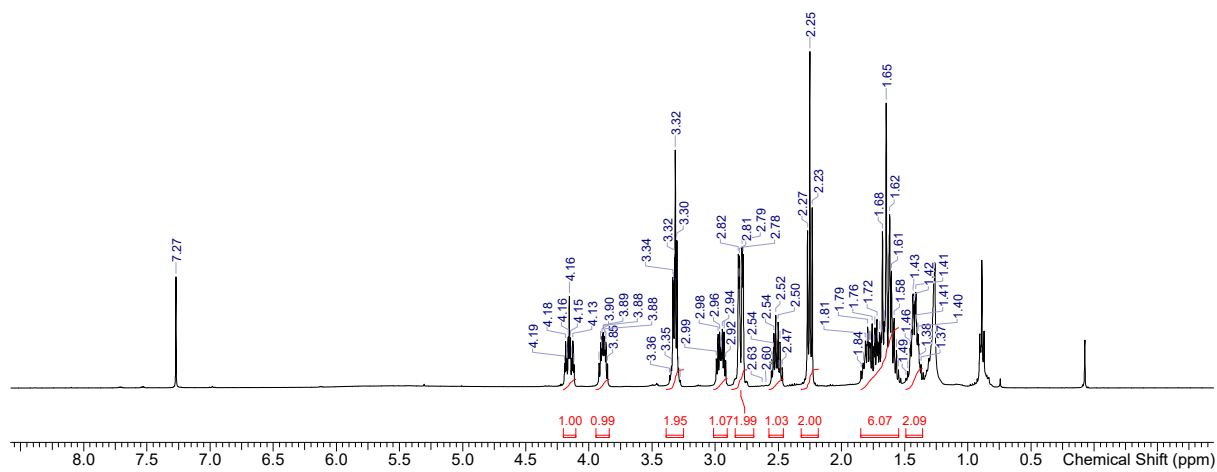


Figure S40. <sup>1</sup>H NMR (CDCl<sub>3</sub>, 297 K, 400 MHz) spectrum of compound 6.

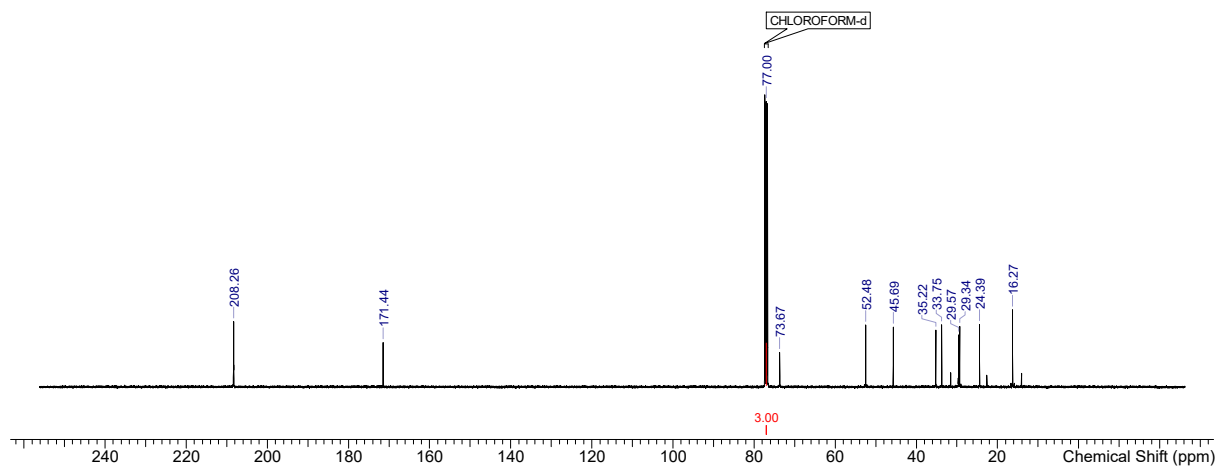


Figure S41. <sup>13</sup>C NMR (CDCl<sub>3</sub>, 297 K, 101 MHz) spectrum of compound 6.

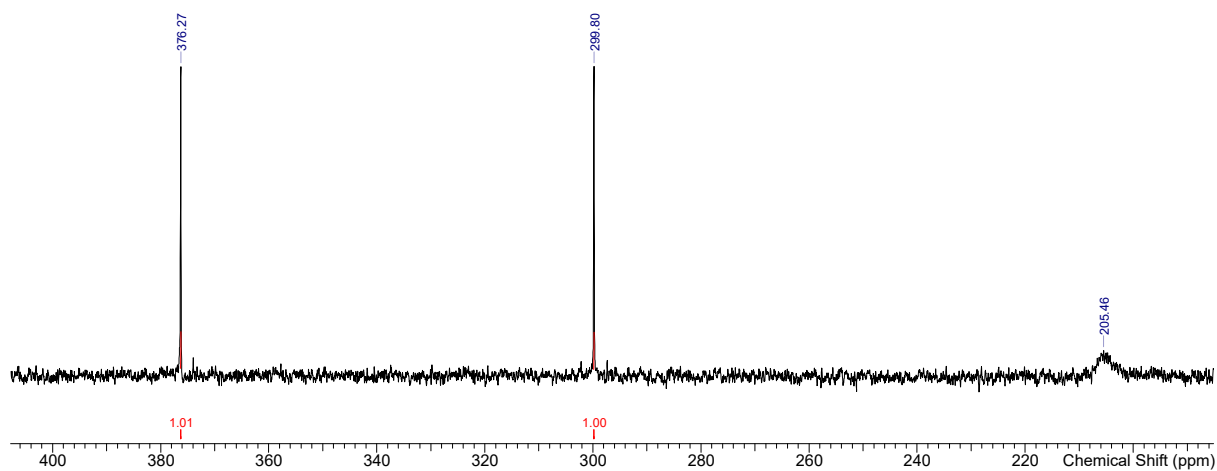


Figure S42. <sup>77</sup>Se NMR (CDCl<sub>3</sub>, 297 K, 76 MHz) spectrum of compound 6.

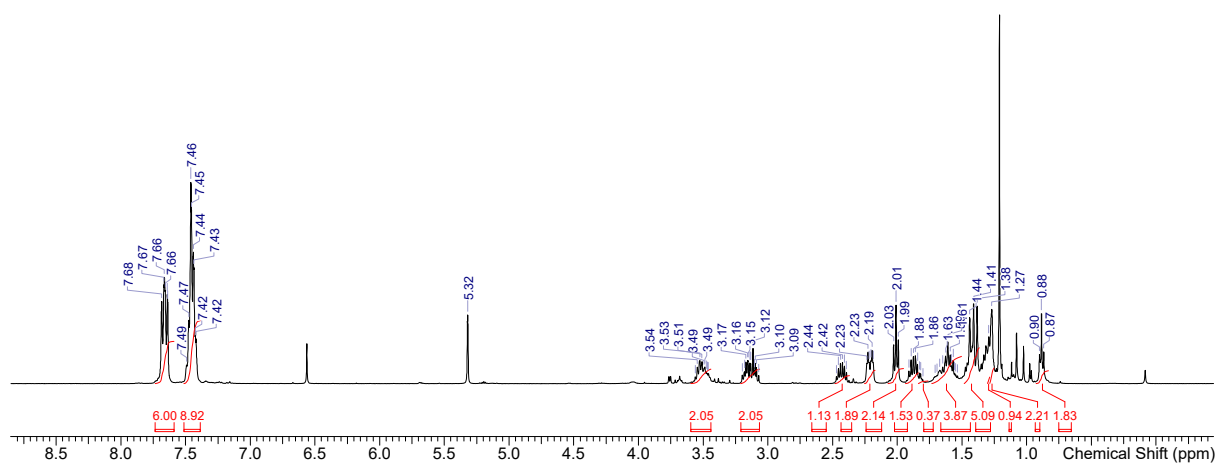


Figure S43. <sup>1</sup>H NMR (CD<sub>2</sub>Cl<sub>2</sub>, 297 K, 400 MHz) spectrum of compound 7.

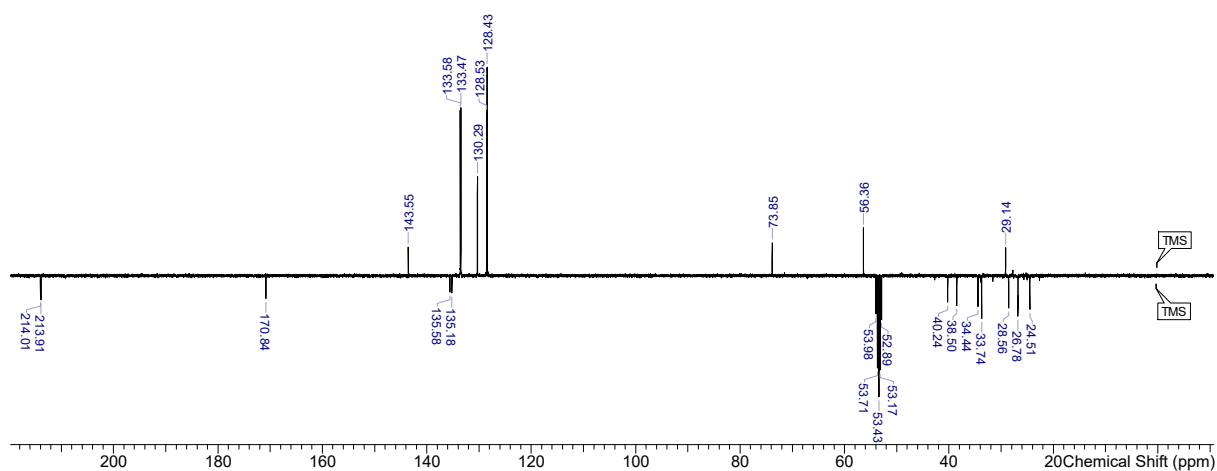
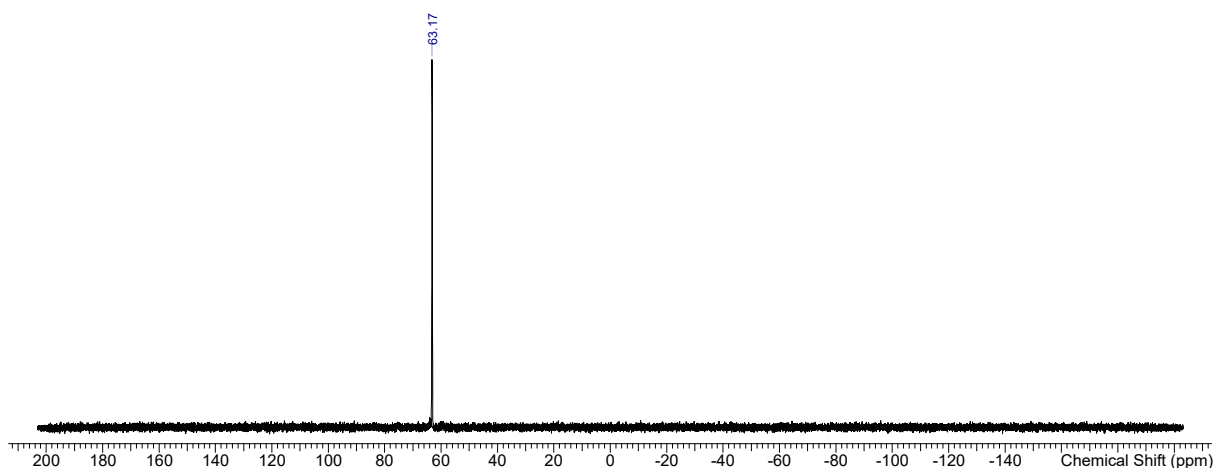


Figure S44. <sup>13</sup>C NMR (APT, CD<sub>2</sub>Cl<sub>2</sub>, 297 K, 101 MHz) spectrum of compound 7.



**Figure S45.**  $^{31}\text{P}$  NMR ( $\text{CD}_2\text{Cl}_2$ , 297 K, 162 MHz) spectrum of compound **7**.

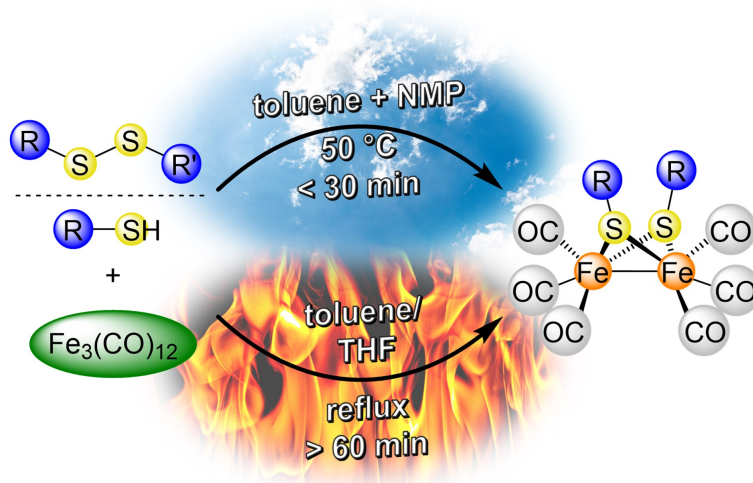
## References

- [1] a) COLLECT Data Collection Software, Nonius B.V., **1998**, Netherlands; b) Z. Otwinowski, Minor, W. in Carter, C. W., Sweet, R. M. (eds.), *Processing of X-Ray Diffraction Data Collected in Oscillation Mode. Methods in Enzymology, Vol. 276, Macromolecular Crystallography, Part A*, **1997**, Academic Press, pp. 307–326; c) Bruker-AXS inc., *SADABS 2.10*, **2002**, Madison, WI, U.S.A.
- [2] G. M. Sheldrick, *Acta Crystallogr., Sect. A: Found. Crystallogr.* **2015**, *71*, 3.
- [3] G. M. Sheldrick, *Acta Crystallogr. Sect. C: Struct Chem* **2015**, *71*, 3.
- [4] D. Kratzert, I. Krossing, *J Appl Crystallogr* **2018**, *51*, 928.
- [5] C. F. Macrae, P. R. Edgington, P. McCabe, E. Pidcock, G. P. Shields, R. Taylor, M. Towler, J. van de Streek, *J. Appl. Crystallogr.* **2006**, *39*, 453.
- [6] H. Abul-Futouh, L. R. Almazahreh, S. J. Abaalkhail, H. Görls, S. T. Stripp, W. Weigand, *New J. Chem.* **2021**, *45*, 36.


**[SB-4] NMP makes the Difference –****Facilitated Synthesis of [FeFe] Hydrogenase Mimics**

Stefan Benndorf, Philipp Buday, Benedikt Callies, Helmar Görls, Stephan Kupfer and Wolfgang Weigand

*Dalton Trans.* **2023**, 52, 7421.



**NMP makes the difference – facilitated synthesis of [FeFe] hydrogenase mimics**

S. Benndorf, P. Buday, B. Callies, H. Görls, S. Kupfer and W. Weigand, *Dalton Trans.*, 2023, **52**, 7421 DOI: 10.1039/D3DT00796K 

To request permission to reproduce material from this article, please go to the [Copyright Clearance Center request page](#).

If you are **an author contributing to an RSC publication**, you do not need to request permission provided correct acknowledgement is given.

If you are **the author of this article**, you do not need to request permission to reproduce figures and diagrams provided correct acknowledgement is given. If you want to reproduce the whole article in a third-party publication (excluding your thesis/dissertation for which permission is not required) please go to the [Copyright Clearance Center request page](#).

<https://pubs.rsc.org/en/content/articlelanding/2023/dt/d3dt00796k>



# Dalton Transactions

An international journal of inorganic chemistry

rsc.li/dalton

Volume 52  
Number 22  
14 June 2023  
Pages 7357-7756



ISSN 1477-9226



ROYAL SOCIETY  
OF CHEMISTRY

## PAPER

Wolfgang Weigand *et al.*

NMP makes the difference – facilitated synthesis of [FeFe]  
hydrogenase mimics

Cite this: *Dalton Trans.*, 2023, **52**, 7421

## NMP makes the difference – facilitated synthesis of [FeFe] hydrogenase mimics†

Stefan Benndorf,<sup>a</sup> Philipp Buday,<sup>a</sup> Benedikt Callies,<sup>a</sup> Helmar Görls,<sup>a</sup> Stephan Kupfer<sup>b</sup> and Wolfgang Weigand<sup>b,\*a,c</sup>

To overcome the limitations of high reaction temperatures and long reaction times of conventional synthesis routes towards [FeFe] hydrogenase (H<sub>2</sub>ase) mimicking complexes, we introduced a more efficient synthesis route in the presence of aprotic polar co-solvents such as *N*-methyl-2-pyrrolidone (NMP). Versatile (di)thiol or disulfide ligands as well as selenium and tellurium analogues were converted to their corresponding complexes. While both reaction times and temperatures were reduced significantly, yields could be increased. Intensive kinetic monitoring of the formation of two [FeFe] H<sub>2</sub>ase mimics *via* UV-vis spectroscopy was performed, revealing an increase of the rate constant by one order of magnitude compared to that obtained in the same reaction without NMP. IR spectroscopic examination of the formation of the 1,3-propanedithiole analogue (**2a**) revealed the appearance of a side product, analyzed by IR and UV-vis spectroscopy and mass spectrometry, which was proposed to be a NMP monosubstituted triiron-dodecacarbonyl (**Fe<sub>3</sub>(CO)<sub>11</sub>NMP**) cluster. Reacting triiron-dodecacarbonyl (**Fe<sub>3</sub>(CO)<sub>12</sub>**) with NMP in the absence of any additional ligand yielded this species as well. Quantum chemical simulations of **Fe<sub>3</sub>(CO)<sub>11</sub>NMP** indicated structural rearrangements including the omission of bridging carbonyls ( $\mu$ -CO). Similar observations were made on utilizing other aprotic polar co-solvents.

Received 16th March 2023,  
Accepted 4th April 2023

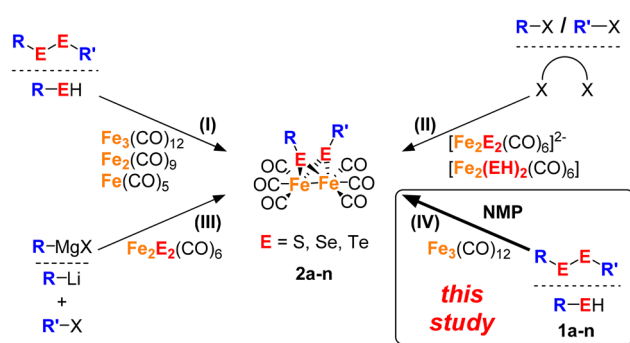
DOI: 10.1039/d3dt00796k

rsc.li/dalton

## Introduction

In times of ever-increasing fuel cost and the desire to reduce carbon emissions, the search for alternative clean energy sources has become essential. Hydrogen fits that role, if produced by sustainable means.<sup>1</sup> Moreover, it is already indispensable in a plethora of industrial applications today, *e.g.*, in the frame of the Haber–Bosch process, the Fischer–Tropsch synthesis, petroleum refinement, fat hardening, and as an energy carrier in fuel cells.<sup>2</sup> To meet the demand for hydrogen, natural gas is used for steam reforming, which generates massive amounts of CO<sub>2</sub> each year.<sup>3</sup> An alternative path towards sustainable formation could be the utilization of inexpensive base metal catalysts. A promising class of natural enzymes, found in bacteria like *Desulfovibrio desulfuricans* or algae, called [FeFe] H<sub>2</sub>ases, are known to be highly active cata-

lysts in either hydrogen oxidation or proton reduction with turnover frequencies (TOF) up to 10<sup>4</sup> s<sup>-1</sup>.<sup>4</sup> Their structure and the active center were first described by Peters *et al.* in 1998, exhibiting a similar structure to [FeFe] complexes first synthesized by Reihlen *et al.* in the late 1920s.<sup>5</sup> To date, numerous [FeFe] H<sub>2</sub>ase mimicking complexes with varying results in yield, accessibility, and catalytic activity have been developed, sharing the diiron dithiolate core of the active site and varying bridging ligands, *e.g.* aliphatic, olefinic or aromatic moieties with different functional groups.<sup>6,7</sup> Various reaction pathways were established (*e.g.* Scheme 1, I–III) to synthesize these com-



**Scheme 1** Well-established reaction pathways towards [FeFe] H<sub>2</sub>ase mimics (I–III) and the new approach (IV).

<sup>a</sup>Institute of Inorganic and Analytical Chemistry, Friedrich Schiller University Jena, Humboldtstrasse 8, 07743 Jena, Germany. E-mail: wolfgang.weigand@uni-jena.de

<sup>b</sup>Institute of Physical Chemistry, Friedrich Schiller University Jena, Helmholtzweg 4, 07743 Jena, Germany

<sup>c</sup>Center for Energy and Environmental Chemistry Jena (CEEC Jena), Jena Center of Soft Matter, Friedrich Schiller University Jena, Philosophenweg 7a, 07743 Jena, Germany

†Electronic supplementary information (ESI) available. CCDC 2205533. For ESI and crystallographic data in CIF or other electronic format see DOI: <https://doi.org/10.1039/d3dt00796k>

pounds, usually accompanied by harsh reaction conditions.<sup>8</sup> The use of  $\text{Fe}_3(\text{CO})_{12}$  requires high reaction temperatures up to 110 °C and long reaction times up to four hours, depending on the ligand. However, this procedure presents a versatile applicability with yields up to 90%.<sup>6</sup> The use of other neutral iron carbonyl complexes, iron pentacarbonyl and diiron nonacarbonyl requires even harsher reaction conditions due to the lower reactivity of the precursors.<sup>6,9</sup>

Since there are several  $[\text{FeFe}] \text{H}_2\text{ase}$  mimics that cannot be obtained by established methods, we aimed to optimize and to develop new synthetic pathways. The addition of polar aprotic co-solvents was chosen to stabilize charged intermediates that are obtained in the formation of  $[\text{FeFe}] \text{H}_2\text{ase}$  model complexes.<sup>6,10</sup> *N*-Methyl-2-pyrrolidone (NMP), dimethyl sulfoxide (DMSO), *N,N'*-tetraalkylureas, like dimethylpropyleneurea (DMPU), and 1,3-dimethyl-2-imidazolidinone (DMI) are excellent candidates to facilitate such kinds of (metal)organic reactions. Wang *et al.* improved their Fe–Cr metathesis reactions by adding selected amides (*e.g.* NMP or dimethylacetamide (DMA)).<sup>11</sup> Furthermore, Cahiez *et al.* reported an enhanced yield for catalyzed cross-coupling reactions by using NMP as a co-solvent.<sup>12</sup> Recently, Muñoz *et al.* studied the influence of NMP on the previously reported cross-coupling reaction, revealing the formation of a highly reactive  $[\text{Mg}(\text{NMP})_6][\text{FeMe}_3]_2$  species from  $\text{Fe}(\text{acac})_3$  and Grignard reagents, explaining the enhanced reactivity.<sup>13</sup>

However, to date, polar aprotic solvents or co-solvents such as NMP have not been used to synthesize  $[\text{FeFe}] \text{H}_2\text{ase}$  mimics. Herein, we report an improved method for preparing  $[\text{FeFe}] \text{H}_2\text{ase}$  mimicking complexes utilizing NMP as a co-solvent (Scheme 1, IV). Our approach allows the reduction of both reaction times and temperatures, while simultaneously increasing the product yields to new heights, thus, paving the way for large-scale application in the field of sustainable hydrogen evolution.

## Results and discussion

### Synthesis

All complexes were synthesized by an improved synthetic pathway developed recently by our group that utilizes NMP as an additive to generate  $[\text{FeFe}] \text{H}_2\text{ase}$  mimicking complexes more efficiently. The precursors were dissolved in a toluene/NMP (10:1) mixture at 50 °C.  $\text{Fe}_3(\text{CO})_{12}$  was added in one portion and the resulting solution was stirred until its dark green colour became dark red, giving the target complexes after purification. This method shows great advantages in comparison with known procedures, *e.g.*, short reaction times, mild reaction conditions and good yields. Fig. S3† illustrates the rate of the reaction of **1a** with  $\text{Fe}_3(\text{CO})_{12}$  and Table 1 summarizes detailed information about the performed reactions.

### UV-vis spectroscopic studies

UV-vis studies with varying reaction temperatures were performed to investigate the influence of NMP on the known reac-

tion of dithiols or disulfides with  $\text{Fe}_3(\text{CO})_{12}$  to give their respective hexacarbonyl diiron complexes (Scheme 1). The concentration of  $\text{Fe}_3(\text{CO})_{12}$  had to be very low ( $c = 2.2 \times 10^{-4} \text{ M}$ ), due to its strong UV-vis absorption. A traceable distinctive absorption band is observed at  $\lambda = 606 \text{ nm}$ , and is assigned to the ligand-field excitation of  $\text{Fe}_3(\text{CO})_{12}$ .<sup>26</sup> A rather slow conversion during the reaction was expected compared to the synthesis on a laboratory scale since the rate constant itself is concentration dependent. Therefore, the time scale for the kinetic experiments was expanded. For each experiment, a tempered glass cuvette was loaded with equimolar quantities of Ar-purged solutions of 1,3-propanedithiol (**1a**) and  $\text{Fe}_3(\text{CO})_{12}$  in a toluene/NMP mixture (10:1) to record UV-vis spectra in certain time periods and at varying temperatures.

Fig. 1 shows the perfect UV-vis absorption spectra over a reaction time of 300 seconds at 50.9 °C. Differential spectra were calculated to take a closer look at the changes during the reaction (Fig. S6†). Unfortunately, **1a** and **2a** showed no prominent distinctive absorption maxima in the visible region.

Therefore, the chromophore containing ligand **1n** was selected for further experiments (Scheme 2). **1n** ( $\lambda_{\text{max}} = 463 \text{ nm}$ ) and its respective  $[\text{FeFe}] \text{H}_2\text{ase}$  mimic **2n** ( $\lambda_{\text{max}} = 375 \text{ nm}$ ) exhibit absorption bands in the visible spectral region which show only minor interferences in the spectrum of the  $\text{Fe}_3(\text{CO})_{12}$  precursor (Fig. 2, top). The differential absorption spectra clearly display the progress of the reaction, the destruction of  $\text{Fe}_3(\text{CO})_{12}$  ( $\lambda_{\text{max}} = 606 \text{ nm}$ ) and **1n** and the rise of a signal stemming from **2n** (Fig. 2, bottom and Fig. S7†).

### Kinetic studies

To enable time- and temperature-dependent kinetics, the reactions were carried out with a ten-fold excess of ligand **1n** in the absence and presence of NMP in excess ( $\approx 5000$  equivalents). The limited solubility of **1n** excluded a higher ligand-to-iron cluster ratio. Plots of the natural logarithm of the relative  $\text{Fe}_3(\text{CO})_{12}$  concentration exhibit nearly linear gradients (Fig. S8†) and agree well with a pseudo first-order reaction kinetic. The determination of the rate constant was realized by applying eqn (1) (Table 2).

$$\ln c/c_0 = -k \times t \quad (1)$$

The most important outcome of these experiments is the increase of the reaction rate by approximately one magnitude in the presence of NMP and **1n** (Table 2).

The Arrhenius plots of the inverted absolute temperature and the natural logarithm of the rate constant (eqn (2)), followed by linear regression gave a good fitting slope (Fig. 3), revealing activation energies of  $E_A = 91.4 \text{ kJ mol}^{-1}$  and  $E_A = 99.5 \text{ kJ mol}^{-1}$  in the presence and absence of NMP, respectively.

$$\ln k = \ln A - E_A/R \times 1/T_{\text{abs}} \quad (2)$$

Following the destruction of **1n** and the formation of **2n**, the natural logarithm of their relative absorptions indicates a non-linear shape (Fig. S9†), revealing a more complex reaction kinetic.

Table 1 Synthesized [FeFe] H<sub>2</sub>ase mimics 2a–n, reaction conditions and isolated yields

Ligand index	Ligand	This study		Literature	
		Reaction conditions	Yield	Reaction conditions	Yield
1a		50 °C, 3 min	59%	66 °C, 120 min	63% <sup>14</sup>
1b		50 °C, 10 min	93%	111 °C, 120 min	63% <sup>15</sup>
1c		50 °C, 3 min	65% ( <i>anti</i> )	−78 °C → RT, 165 min	35% <sup>16</sup>
1d		50 °C, 15 min	70% ( <i>anti</i> )	−78 °C → RT, 165 min	35% <sup>16</sup>
1e		50 °C, 30 min	89%	66 °C, 120 min	62% <sup>14</sup>
1f		50 °C, 10 min	41%	66 °C, 145 min	43% <sup>17</sup>
1g		50 °C, 1 min	53%	111 °C, 90 min	57% <sup>18</sup>
1h		50 °C, 15 min	82%	66 °C, 240 min	76% <sup>19</sup>
1i		50 °C, 20 min	67%	80 °C, 60 min	65% <sup>20</sup>
1j		50 °C, 20 min	79% ( <i>anti</i> )	66 °C, 120 min	75% <sup>21</sup> ( <i>syn</i> + <i>anti</i> )
1k		50 °C, 10 min	90%	130 °C → 70 °C, 240 min	59% <sup>22</sup>
1l		50 °C, 35 min	30%	111 °C, 120 min	39% <sup>23</sup>
1m <sup>a</sup>		90 °C, 5 min	42%	90 °C, 5 min	42% <sup>24</sup>
1n <sup>a</sup>		90 °C, 5 min	38%	111 °C, 180 min	54% <sup>25</sup>

<sup>a</sup>The toluene/NMP ratio 1 : 1 was used for this reaction, due to poor solubility of the starting materials.

In addition, the thermal decomposition of  $\text{Fe}_3(\text{CO})_{12}$  in toluene was monitored in the absence of any additional reacting material to test its stability in hot solution (Table 2). As expected, the disappearance of the distinctive absorption band at  $\lambda_{\text{max}} = 606 \text{ nm}$  exhibited very slow conversion rates.

Furthermore, we strived to elucidate the impact of NMP on the reaction by comparison of the reaction of **1n** with  $\text{Fe}_3(\text{CO})_{12}$  in an equimolar ratio in the presence or absence of NMP at 75.1 °C (Fig. S10†). The differential spectra in the absence of NMP reveal less intense changes in the spectra, even though the reaction time is more than two-fold longer, implying a rather slow reaction (Fig. 4).

To analyze the influence of the NMP concentration towards the rate constant of the reaction of **1a** with  $\text{Fe}_3(\text{CO})_{12}$ , various toluene/NMP ratios were tested while the temperature ( $T = 50.9 \text{ °C}$ ) and concentration of the starting materials ( $c = 2.2 \times 10^{-4} \text{ M}$ ) were kept constant. These studies reveal a strong dependency of the rate constant (Fig. S11†). Addition of up to thousand equivalents of NMP affects the rates only in minor degrees, excluding a catalytic influence on the reaction. We suggest that the increase of polarity of the solvents might stabilize the charged intermediates that are supposed to be involved during the formation of the desired type of [FeFe] H<sub>2</sub>ase mimic.<sup>1–6</sup>

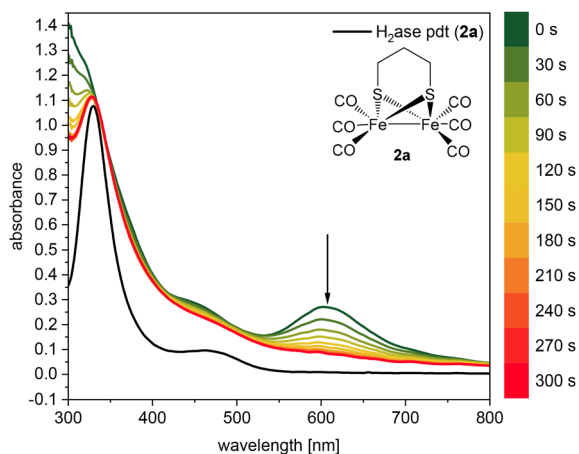
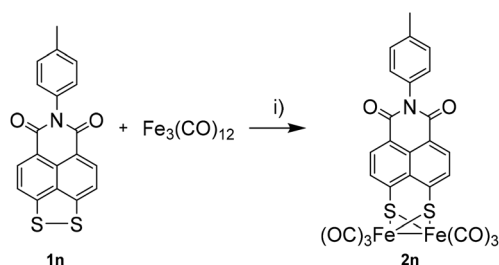


**Fig. 1** Time-resolved UV-vis spectra during the reaction of **1a** with equimolar amounts of  $\text{Fe}_3(\text{CO})_{12}$  (toluene/NMP (10 : 1),  $c = 2.2 \times 10^{-4}$  M) at 50.9 °C.



**Scheme 2** Synthesis of compound **2n** during the kinetic experiments, (i) toluene/NMP (10 : 1), at varying temperatures.

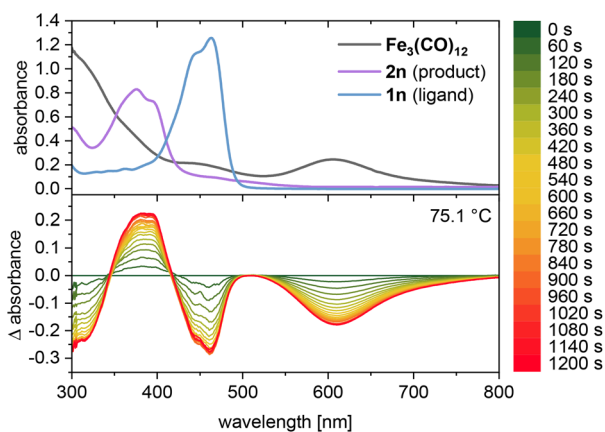


**Fig. 2** UV-vis spectra of the starting materials and the desired product (top); time-resolved differential UV-vis spectra during the reaction of **1n** with equimolar amounts of  $\text{Fe}_3(\text{CO})_{12}$  (toluene/NMP (10 : 1),  $c = 2.2 \times 10^{-4}$  M) at 75.1 °C (bottom). The  $\Delta$  absorbance spectra were calculated by subtracting the initial spectrum ( $t = 0$  s).

### IR spectroscopic studies

Subsequently, the conversion of  $\text{Fe}_3(\text{CO})_{12}$  with equimolar amounts of **1a** in the presence of NMP to complex **2a** was

**Table 2** Rate constants in toluene for the decline of  $\text{Fe}_3(\text{CO})_{12}$  (606 nm,  $c = 2.2 \times 10^{-4}$  M) during the reaction with ligand **1n** ( $\text{Fe}_3(\text{CO})_{12}/\mathbf{1n}$  (1 : 10)) and NMP ( $\text{Fe}_3(\text{CO})_{12}/\text{NMP}$  (1 : 4300)) without any ligand at varying temperatures

Ligand	$T$ [°C]	$T_{\text{abs}}$ [K]	$k_{\text{obs}}$ ( $\text{Fe}_3(\text{CO})_{12}$ ) [ $\text{s}^{-1}$ ]
<b>1n</b>	49.0	322.2	$1.2 \times 10^{-3}$
<b>1n</b>	57.0	330.2	$2.8 \times 10^{-3}$
<b>1n</b>	64.0	337.1	$5.4 \times 10^{-3}$
<b>1n</b>	72.0	345.1	$1.1 \times 10^{-2}$
<b>1n<sup>a</sup></b>	49.0	322.2	$1.6 \times 10^{-4}$
<b>1n<sup>a</sup></b>	57.0	330.2	$3.2 \times 10^{-4}$
<b>1n<sup>a</sup></b>	64.0	337.1	$7.5 \times 10^{-4}$
<b>1n<sup>a</sup></b>	72.0	345.1	$1.8 \times 10^{-3}$
<b>NMP<sup>b</sup></b>	45.0	318.15	$4.7 \times 10^{-3}$
<b>NMP<sup>b</sup></b>	53.2	326.35	$9.0 \times 10^{-3}$
<b>NMP<sup>b</sup></b>	60.4	333.55	$9.3 \times 10^{-3}$
<b>NMP<sup>b</sup></b>	68.9	342.05	$2.1 \times 10^{-2}$
<b>Fe<sub>3</sub>(CO)<sub>12</sub><sup>a,b</sup></b>	43.2	316.35	$3.7 \times 10^{-5}$
<b>Fe<sub>3</sub>(CO)<sub>12</sub><sup>a,b</sup></b>	53.2	326.35	$1.1 \times 10^{-4}$
<b>Fe<sub>3</sub>(CO)<sub>12</sub><sup>a,b</sup></b>	62.6	335.75	$1.1 \times 10^{-4}$
<b>Fe<sub>3</sub>(CO)<sub>12</sub><sup>a,b</sup></b>	71.1	344.25	$2.6 \times 10^{-4}$
<b>Fe<sub>3</sub>(CO)<sub>12</sub><sup>a,b</sup></b>	75.1	348.25	$3.2 \times 10^{-4}$

<sup>a</sup> Without NMP. <sup>b</sup> Without any ligand.

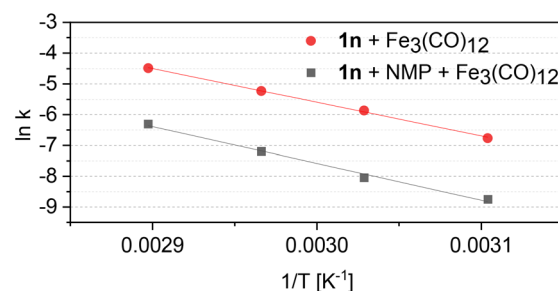


**Fig. 3** Arrhenius plot for the decline of  $\text{Fe}_3(\text{CO})_{12}$  ( $\lambda = 606$  nm) during the reaction with excess **1n** ( $R^2 = 0.99$ ) and excess **1n** + NMP ( $R^2 = 0.99$ ).

monitored by IR measurements in an OTTLE (optically transparent thin layer electrochemical) cell over a period of 4500 seconds at room temperature (RT) (toluene/NMP (10 : 1),  $c \approx 2.2 \times 10^{-3}$  M, RT)<sup>27</sup> (Fig. 5). The structural properties of the metal carbonyl complexes can be evaluated efficiently by means of IR analysis. In particular, the  $\nu(\text{CO})$  bands are highly sensitive with respect to the oxidation state and structural alterations, especially in the vicinity of the metal center.<sup>28</sup>

Slow appearance of three main bands associated with complex **2a** ( $\tilde{\nu} = 2072 \text{ cm}^{-1}$ ,  $2032 \text{ cm}^{-1}$  and  $1994 \text{ cm}^{-1}$ ), and the disappearance of the main band of  $\text{Fe}_3(\text{CO})_{12}$  could be observed. However, the ratio does not match to the spectrum of **2a**, implying the overlap with another absorption band around  $\tilde{\nu} = 1994 \text{ cm}^{-1}$ . The IR spectra (Fig. 5) revealed the formation of an additional compound which was identified as  $\text{Fe}_3(\text{CO})_{11}\text{NMP}$ , as described below.

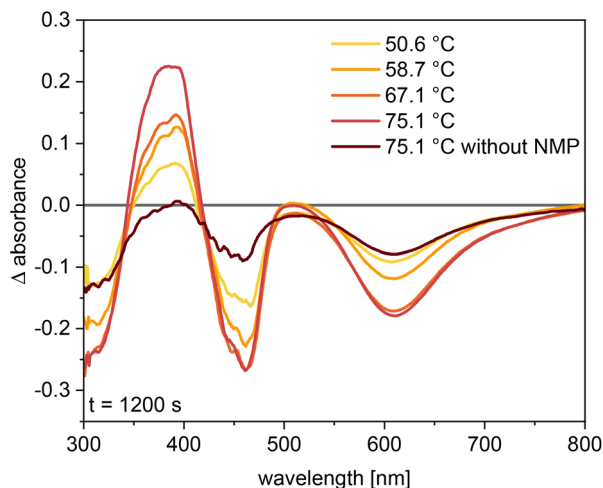


**Fig. 4** Differential UV-vis spectra during the reaction of **1n** with equimolar amounts of  $\text{Fe}_3(\text{CO})_{12}$  (toluene/NMP (10 : 1),  $c = 2.2 \times 10^{-4}$  M) at varying temperatures and without NMP after 1200 s. The  $\Delta$  absorbance spectra were calculated by subtracting the initial spectrum ( $t = 0$  s).

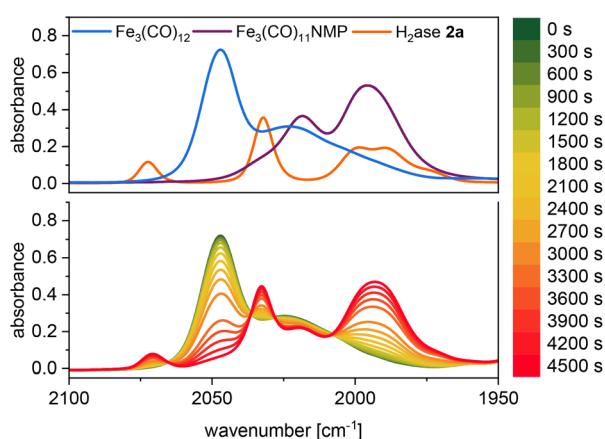


**Fig. 5** IR spectra of  $\text{Fe}_3(\text{CO})_{12}$ ,  $\text{Fe}_3(\text{CO})_{11}\text{NMP}$  and **2a** (top); time-resolved IR spectra during the reaction of **1a** with equimolar amounts of  $\text{Fe}_3(\text{CO})_{12}$  (toluene/NMP (10 : 1),  $c = 2.2 \times 10^{-3}$  M) at 24.3 °C (bottom).

### Reaction of $\text{Fe}_3(\text{CO})_{12}$ with NMP

For this reason, we investigated the reaction of  $\text{Fe}_3(\text{CO})_{12}$  with NMP in the absence of any additional ligand under inert conditions, subsequently obtaining an oxygen-sensitive, purple solid material, which was soluble in water and organic solvents. Mass spectrometric analysis revealed the species as  $\text{Fe}_3(\text{CO})_{11}\text{NMP}$ . This type of monosubstituted  $\text{Fe}_3(\text{CO})_{11}\text{L}$  cluster is already known with  $\text{L} =$  phosphines, phosphites, arsines, stibines, hydrides, cyanides and isocyanides, resulting in dark green, oxygen-sensitive complexes.<sup>29–34</sup> The fast formation of  $\text{Fe}_3(\text{CO})_{11}\text{NMP}$  was followed by UV-vis spectroscopy (toluene/NMP (10 : 1),  $c \approx 2.2 \times 10^{-3}$  M,  $T = 52$  °C), exhibiting a local maximum at  $\lambda = 543$  nm (Fig. 6 and S12<sup>†</sup>). The concentration was ten-fold increased for a better visualization of the new species, due to its low absorption coefficient.

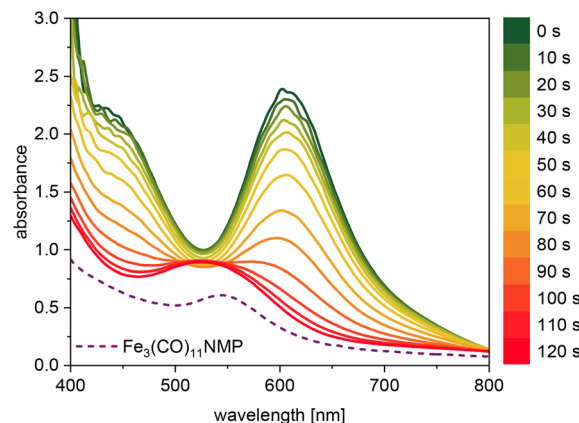


**Fig. 6** UV-vis spectra during the reaction of  $\text{Fe}_3(\text{CO})_{12}$  with NMP (toluene/NMP (10 : 1),  $c \approx 2.2 \times 10^{-3}$  M) at 52 °C.

In the first instance, the reaction of  $\text{Fe}_3(\text{CO})_{12}$  with NMP was monitored by IR spectroscopy in an OTTLE cell at RT (Fig. 7). Within 25 minutes, all detectable amount of  $\text{Fe}_3(\text{CO})_{12}$  ( $\tilde{\nu} = 2047$   $\text{cm}^{-1}$  and  $2023$   $\text{cm}^{-1}$ ) was consumed and two new absorption bands appeared at  $\tilde{\nu} = 2018$   $\text{cm}^{-1}$  and  $\tilde{\nu} = 1991$   $\text{cm}^{-1}$ , associated with the previously isolated  $\text{Fe}_3(\text{CO})_{11}\text{NMP}$  product. Additionally, the bands of bridging carbonyls ( $\tilde{\nu} \approx 1825$ – $1875$   $\text{cm}^{-1}$ ) disappeared, indicating structural rearrangements. Due to the high fluxionality of the carbonyl ligands in solution, the bands of bridging carbonyls are very weak.<sup>29,30,32,33,35</sup> To check if there are still bridging carbonyl ligands present in the substitution product, solid state IR ATR measurements were performed, resulting in a more complex spectrum (Fig. S13<sup>†</sup>).<sup>34</sup> In contrast to the described mono-substituted  $\text{Fe}_3(\text{CO})_{11}\text{L}$  derivatives, the isolated product showed no absorption band in the region of bridging carbonyls.<sup>32</sup>

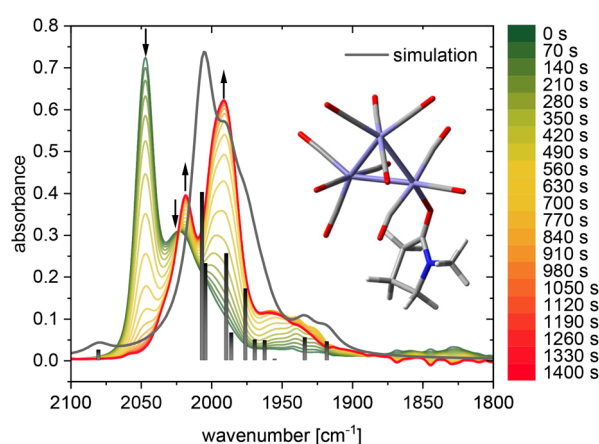


**Fig. 7** IR spectra during the reaction of  $\text{Fe}_3(\text{CO})_{12}$  with NMP (toluene/NMP (10 : 1),  $c \approx 2.5 \times 10^{-3}$  M) at RT and the simulated structure of  $\text{Fe}_3(\text{CO})_{11}\text{NMP}$  (isomer B) along with simulated IR absorption bands.

### Reactive Intermediate

To propose the chemical structure of  $\text{Fe}_3(\text{CO})_{11}\text{NMP}$ , we performed quantum chemical simulations at the density and time-dependent density functional level of theory for three selected coordination isomers (**A**, **B** and **C** in Fig. S14†). Isomers **A** and **C** feature two bridging CO ligands, while in **C** NMP is coordinated to Fe without  $\mu\text{-CO}$  coordination. In contrast, **B** features no  $\mu\text{-CO}$  ligands. Thermodynamically, **B** is  $\approx 15 \text{ kJ mol}^{-1}$  more favorable than **A** and **C** with two  $\mu\text{-CO}$  ligands. As the visible region of the predicted electronic absorption spectra of all three species is dominated by (weakly) dipole-allowed ligand field transitions (Fig. S17 as well as Tables S1 and S2†), assessing the structure of the byproduct by means of its UV-vis spectrum is rather challenging. However, based on the simulated IR spectra for the three isomers, such an assignment is possible based on the specific intensity pattern of the nine CO vibrational modes, respectively. Exclusively the CO signals obtained for **B** – the energetically most favorable isomer – match the experimental IR pattern (Fig. 7 and S18 and Tables S3 and S4†). This structure implies the rearrangement of bridging carbonyls to terminal ones, which supports the experimental observations that indicate no absorbance between  $1800$  and  $1900 \text{ cm}^{-1}$  in contrast to  $\text{Fe}_3(\text{CO})_{12}$  (Fig. S13†). The loss of this significant structural feature might enhance the sensitivity and reactivity towards oxygen which leads to the decomposition of the complex under a non-inert atmosphere.

To elucidate whether  $\text{Fe}_3(\text{CO})_{11}\text{NMP}$  is a side-product or an intermediate, we monitored its reaction with **1a**. Therefore, one equivalent of **1a** was added to freshly prepared  $\text{Fe}_3(\text{CO})_{11}\text{NMP}$  (for details check the Experimental section) and the mixture was stirred for ten minutes at  $50 \text{ }^\circ\text{C}$ . The reaction was monitored by TLC; however, there was no conversion to **2a**, even after the addition of another equivalent of **1a**.

Thus, the new species  $\text{Fe}_3(\text{CO})_{11}\text{NMP}$  could be described as a side product that does not interact with dithiols such as **1a**. This behaviour explains the formation of  $\text{Fe}_3(\text{CO})_{11}\text{NMP}$  during the IR experiments in the presence of **1a** (Fig. 5). The reactions of  $\text{Fe}_3(\text{CO})_{12}$  with NMP and **1a** compete if both components are in the reaction solution. Both products (**2a** and  $\text{Fe}_3(\text{CO})_{11}\text{NMP}$ ) are stable under the given conditions and no follow-up reaction occurs. While there is a large excess of NMP ( $>50 \text{ eq.}$ ) in the reaction, the formation of product **2a** is clearly favoured as indicated also by good yields of the other hexacarbonyl complexes **2b–n** (Table 1). Only a minor amount of  $\text{Fe}_3(\text{CO})_{11}\text{NMP}$  could be detected during the work-up of those reactions. The increased polarity of the solvents might stabilize the charged intermediates and favors the formation of the first intermediate on the reaction pathway to  $[\text{FeFe}] \text{H}_2\text{ase}$  mimics.

Furthermore, we were interested to know if other additives (besides NMP) would enhance the reactivity of  $\text{Fe}_3(\text{CO})_{12}$ . Here, dimethylacetamide (DMA), tetramethylurea (TMU) and  $\gamma$ -butyrolactone (GBL) were chosen and tested for their activating capabilities in the reaction course of  $\text{Fe}_3(\text{CO})_{12}$  with **1a**. UV-vis and IR spectroscopy were performed to examine the

reactivity and potential of substitution products with  $\text{Fe}_3(\text{CO})_{12}$ .

Reactions mediated by these candidates were similar to the NMP-mediated conversions. The formation of target complex **2a** occurred after 7 to 10 minutes (toluene/additive (10:1);  $c(\text{Fe}_3(\text{CO})_{12}) = 0.3 \text{ mM}$ ;  $c(\mathbf{1a}) = 0.9 \text{ mM}$ ;  $T = 51 \text{ }^\circ\text{C}$ ), depending on the additive. DMA turned out to be the best additive in terms of reaction time among the tested co-solvents, in contrast to GBL, which resulted in the highest duration. Fig. S15† shows the monitored performances of the four co-solvents, respectively.

The formation of the substitution products ( $\text{Fe}_3(\text{CO})_{11}\text{DMA}$ ,  $\text{Fe}_3(\text{CO})_{11}\text{TMU}$  and  $\text{Fe}_3(\text{CO})_{11}\text{GBL}$ ) was accomplished under similar conditions in the absence of any additional ligand. All substitution products were obtained as oxygen-sensitive, purple solid materials. Additionally, the IR spectra of these products exhibited similar absorption bands with minor differences, as illustrated in Fig. S16.†

Based on the color and the IR absorption spectra of these complexes, we assume that DMA, TMU and GBL follow the same coordination type *via* a carbonyl oxygen atom, as predicted for NMP and supported by DFT simulations.

## Conclusion

This study introduced a new method for an efficient synthesis of  $[\text{FeFe}] \text{H}_2\text{ase}$  mimicking complexes, reducing remarkably both reaction times and temperatures, in the presence of aprotic polar co-solvents such as NMP. IR spectroscopic measurements and analysis of UV-vis based kinetics at varying temperatures were performed to determine the rate constants and to monitor the reactions of  $\text{Fe}_3(\text{CO})_{12}$  with ligand **1n**. By means of UV-vis spectroscopy, we were able to follow the consumption of **1n** and the formation of **2n** in the presence and absence of NMP. The addition of NMP increased the rate constant approximately by one magnitude. Furthermore, the rate constant showed a strong dependency on the concentration of NMP, even though there was always an excess of the additive, excluding a catalytic effect of NMP. The synthesis of **2a** was tracked by IR spectroscopy in an OTTL cell at RT, revealing the formation of **2a** and the proposed  $\text{Fe}_3(\text{CO})_{11}\text{NMP}$  complex.

Upon utilizing other aprotic polar co-solvents such as DMA, TMU and GBL, comparable reaction times to those of NMP with respect to the formation of complex **2a** were observed. In addition, we proposed novel monosubstituted  $\text{Fe}_3(\text{CO})_{11}\text{solv}$  ( $\text{solv} = \text{NMP, DMA, TMU, GBL}$ ) clusters. DFT calculations were performed to identify the most likely constitution of the substitution product  $\text{Fe}_3(\text{CO})_{11}\text{NMP}$ , whose formation was observed *via* UV-vis and IR spectroscopy in the absence of any ligand. In good agreement with solid IR spectroscopic measurements, the generation of  $\text{Fe}_3(\text{CO})_{11}\text{NMP}$  was associated with the loss of any bridging carbonyl ligand that is the stabilizing motif in the precursor  $\text{Fe}_3(\text{CO})_{12}$ . Since  $\text{Fe}_3(\text{CO})_{11}\text{NMP}$  did not react with two equivalents of **1a**, it was excluded as an intermediate.

## Conflicts of interest

There are no conflicts to declare.

## Acknowledgements

Financial support from the German Science Foundation (DFG) via the TRR234 CataLight is gratefully acknowledged (project number 364549901, project A2 and A4). All calculations were performed at the Universitätsrechenzentrum of the Friedrich Schiller University of Jena. We are grateful to Dr Ueberschaar and Dr Sindlinger for their help with mass spectrometric methods as well as Mr Carstensen for his support with adjusting the temperature of the cuvette. We are thankful to Dr Micheel and Prof. Dr Vilotijevic for important discussions.

## References

- S. Singh, S. Jain, V. Ps, A. K. Tiwari, M. R. Nouni, J. K. Pandey and S. Goel, *Renewable Sustainable Energy Rev.*, 2015, **51**, 623.
- V. Dupont, *HELIA*, 2007, **30**, 103.
- B. Dou, H. Zhang, Y. Song, L. Zhao, B. Jiang, M. He, C. Ruan, H. Chen and Y. Xu, *Sustainable Energy Fuels*, 2019, **3**, 314.
- (a) J. A. Birrell, V. Pelmenchikov, N. Mishra, H. Wang, Y. Yoda, K. Tamasaku, T. B. Rauchfuss, S. P. Cramer, W. Lubitz and S. DeBeer, *J. Am. Chem. Soc.*, 2020, **142**, 222; (b) W. Lubitz, H. Ogata, O. Rüdiger and E. Reijerse, *Chem. Rev.*, 2014, **114**, 4081; (c) P. M. Vignais and B. Billoud, *Chem. Rev.*, 2007, **107**, 4206; (d) P. M. Vignais, B. Billoud and J. Meyer, *FEMS Microbiol. Rev.*, 2001, 455; (e) T. R. Cook, D. K. Dogutan, S. Y. Reece, Y. Surendranath, T. S. Teets and D. G. Nocera, *Chem. Rev.*, 2010, **110**, 6474; (f) C. Li, T. Gong, B. Bian and W. Liao, *Funct. Plant Biol.*, 2018, **45**, 783; (g) J. A. Birrell, P. Rodríguez-Maciá, E. J. Reijerse, M. A. Martini and W. Lubitz, *Coord. Chem. Rev.*, 2021, **449**, 214191.
- (a) H. Reihlen, A. Gruhl and G. V. Hessling, *Liebigs Ann. Chem.*, 1929, 268; (b) H. Reihlen, A. V. Friedolsheim and W. Oswald, *Liebigs Ann. Chem.*, 1928, 72; (c) J. W. Peters, W. N. Lanzilotta, B. J. Lemon and L. C. Seefeldt, *Science*, 1998, **282**, 1853.
- Y. Li and T. B. Rauchfuss, *Chem. Rev.*, 2016, **116**, 7043.
- (a) S. Gao, Y. Liu, Y. Shao, D. Jiang and Q. Duan, *Coord. Chem. Rev.*, 2020, **402**, 213081; (b) W. P. Brezinski, M. Karayilan, K. E. Clary, N. G. Pavlopoulos, S. Li, L. Fu, K. Matyjaszewski, D. H. Evans, R. S. Glass, D. L. Lichtenberger, *et al.*, *Angew. Chem., Int. Ed.*, 2018, **57**, 11898; (c) S. Gao, W. Fan, Y. Liu, D. Jiang and Q. Duan, *Int. J. Hydrogen Energy*, 2020, **45**, 4305; (d) J. T. Kleinhaus, F. Wittkamp, S. Yadav, D. Siegmund and U.-P. Apfel, *Chem. Soc. Rev.*, 2021, **50**, 1668; (e) W. Weigand, *Phosphorus, Sulfur Silicon Relat. Elem.*, 2019, **194**, 634; (f) H.-L. Wu, X.-B. Li, C.-H. Tung and L.-Z. Wu, *Chem. Commun.*, 2020, **56**, 15496; (g) L. Sun, C. Duboc and K. Shen, *ACS Catal.*, 2022, **12**, 9159; (h) J.-F. Capon, F. Gloaguen, F. Y. Pétilion, P. Schollhammer and J. Talarmin, *Coord. Chem. Rev.*, 2009, **253**, 1476; (i) Y.-C. Liu, T.-H. Yen, K.-T. Chu and M.-H. Chiang, *Comments Inorg. Chem.*, 2016, **36**, 141; (j) F. Wang, W.-G. Wang, H.-Y. Wang, G. Si, C.-H. Tung and L.-Z. Wu, *ACS Catal.*, 2012, **2**, 407.
- (a) J. A. Cabeza, M. A. Martínez-García, V. Riera, D. Ardura and S. García-Granda, *Organometallics*, 1998, **17**, 1471; (b) G. Durgaprasad, R. Bolligarla and S. K. Das, *J. Organomet. Chem.*, 2012, **706–707**, 37; (c) M. K. Harb, U.-P. Apfel, J. Kübel, H. Görls, G. A. N. Felton, T. Sakamoto, D. H. Evans, R. S. Glass, D. L. Lichtenberger, M. El-khateeb, *et al.*, *Organometallics*, 2009, **28**, 6666; (d) M. K. Harb, U.-P. Apfel, T. Sakamoto, M. El-khateeb and W. Weigand, *Eur. J. Inorg. Chem.*, 2011, **2011**, 986; (e) Y. Zhou, L. Li, X. Dong, Y. Zhang, D. Yang, Y. Liu and J. Qu, *Inorg. Chem. Commun.*, 2017, **80**, 10; (f) L.-C. Song, X.-F. Liu, J.-B. Ming, J.-H. Ge, Z.-J. Xie and Q.-M. Hu, *Organometallics*, 2010, **29**, 610.
- (a) M. M. van Dyk, P. H. van Rooyen and S. Lotz, *Inorg. Chim. Acta*, 1989, **163**, 167; (b) N. S. Nametkin, V. D. Tyurin and M. A. Kukina, *J. Organomet. Chem.*, 1978, **149**, 355.
- (a) A. Winter, L. Zsolnai and G. Huttner, *J. Organomet. Chem.*, 1983, **250**, 409; (b) J. A. de Beer and R. J. Haines, *J. Organomet. Chem.*, 1970, **24**, 757; (c) R. Bau, B. Don, R. Greatrex, R. J. Haines, R. A. Love and R. D. Wilson, *Inorg. Chem.*, 1975, **14**, 3021.
- J.-H. Wang, Y. Zhang, M. Li, S. Yan, D. Li and X.-M. Zhang, *Angew. Chem., Int. Ed.*, 2017, **56**, 6478.
- G. Cahiez and H. Avedissian, *Synthesis*, 1998, 1199.
- S. B. Muñoz, S. L. Daifuku, J. D. Sears, T. M. Baker, S. H. Carpenter, W. W. Brennessel and M. L. Neidig, *Angew. Chem., Int. Ed.*, 2018, **57**, 6496.
- X. Jiang, L. Long, H. Wang, L. Chen and X. Liu, *Dalton Trans.*, 2014, **43**, 9968.
- U.-P. Apfel, Y. Halpin, H. Görls, J. G. Vos, B. Schweizer, G. Linti and W. Weigand, *Chem. Biodiversity*, 2007, **4**, 2138.
- L. Song, Q. Hu, Q. Dong and J. Wang, *Chin. J. Inorg. Chem.*, 1990, **6**, 256.
- P. I. Volkers, T. B. Rauchfuss and S. R. Wilson, *Eur. J. Inorg. Chem.*, 2006, 4793.
- L. Schwartz, P. S. Singh, L. Eriksson, R. Lomoth and S. Ott, *C. R. Chim.*, 2008, **11**, 875.
- Y. Si, M. Hu and C. Chen, *C. R. Chim.*, 2008, **11**, 932.
- E. D. Schermer and W. H. Baddley, *J. Organomet. Chem.*, 1971, **30**, 67.
- S. Lü, S. Gong, G.-H. Xu, Y.-Y. Liu, L. Lü, C.-R. Qin and Q.-L. Li, *Inorg. Chim. Acta*, 2020, **511**, 119797.
- F. Wen, X. Wang, L. Huang, G. Ma, J. Yang and C. Li, *ChemSusChem*, 2012, **5**, 849.
- R. Goy, L. Bertini, H. Görls, L. de Gioia, J. Talarmin, G. Zampella, P. Schollhammer and W. Weigand, *Chem. – Eur. J.*, 2015, **21**, 5061.



- 24 S. Benndorf, E. Hofmeister, M. Wächtler, H. Görls, P. Liebing, K. Peneva, S. Gräfe, S. Kupfer, B. Dietzek-Ivanšić and W. Weigand, *Eur. J. Inorg. Chem.*, 2022, 3, e202100959.
- 25 A. P. S. Samuel, D. T. Co, C. L. Stern and M. R. Wasielewski, *J. Am. Chem. Soc.*, 2010, **132**, 8813.
- 26 D. R. Tyler, R. A. Levenson and H. B. Gray, *J. Am. Chem. Soc.*, 1978, **100**, 7888.
- 27 M. Krejčík, M. Daněk and F. Hartl, *J. Electroanal. Chem.*, 1991, **317**, 179.
- 28 (a) S. J. Borg, T. Behrsing, S. P. Best, M. Razavet, X. Liu and C. J. Pickett, *J. Am. Chem. Soc.*, 2004, **126**, 16988; (b) *Infrared and Raman Spectra of Inorganic and Coordination Compounds, Part B: Applications in Coordination, Organometallic, and Bioinorganic Chemistry*, ed. K. Nakamoto, John Wiley & Sons, New York, 1997; (c) S. P. Best, *Coord. Chem. Rev.*, 2005, **249**, 1536.
- 29 H. Adams, N. A. Bailey, G. W. Bentley and B. E. Mann, *J. Chem. Soc., Dalton Trans.*, 1989, 1831.
- 30 H. Adams, S. C. M. Agostinho, K. Chomka, B. E. Mann, B. E. S. Smith, C. Squires and S. E. Spey, *Can. J. Chem.*, 2001, **79**, 760.
- 31 (a) M. L. Bruce, D. C. Kehoe, J. G. Matison, B. K. Nicholson, P. H. Rieger and M. L. Williams, *J. Chem. Soc., Chem. Commun.*, 1982, 442; (b) C. F. Campana, I. A. Guzei, E. G. Mednikov and L. F. Dahl, *J. Cluster Sci.*, 2014, **25**, 205; (c) C. J. Cardin, D. J. Cardin, N. B. Kelly, G. A. Lawless and M. B. Power, *J. Organomet. Chem.*, 1988, **341**, 447; (d) D. J. Dahm and R. A. Jacobson, *Chem. Commun.*, 1966, 496; (e) D. J. Dahm and R. A. Jacobson, *J. Am. Chem. Soc.*, 1968, **90**, 5106; (f) F. Gärtner, A. Boddien, E. Barsch, K. Fumino, S. Losse, H. Junge, D. Hollmann, A. Brückner, R. Ludwig and M. Beller, *Chem. – Eur. J.*, 2011, **17**, 6425; (g) R. Kumar, *J. Organomet. Chem.*, 1977, **136**, 235; (h) R. J. Angelici and E. E. Siefert, *Inorg. Chem.*, 1966, **5**, 1457–1459.
- 32 S. M. Grant and A. R. Manning, *Inorg. Chim. Acta*, 1978, **31**, 41.
- 33 A. Shojaie and J. D. Atwood, *Organometallics*, 1985, **4**, 187.
- 34 J. Watt, G. C. Bleier, M. J. Austin, S. A. Ivanov and D. L. Huber, *Nanoscale*, 2017, **9**, 6632.
- 35 (a) K. Noack, *Helv. Chim. Acta.*, 1962, **45**, 1847; (b) J. Geng, H. Li, W. T. S. Huck and B. F. G. Johnson, *Chem. Commun.*, 2004, 2122.

Supporting Information

## **NMP makes the Difference – Facilitated Synthesis of [FeFe] Hydrogenase Mimics**

Stefan Benndorf<sup>[a]</sup>, Philipp Buday<sup>[a]</sup>, Benedikt Callies<sup>[a]</sup>, Helmar Görls<sup>[a]</sup>, Stephan Kupfer<sup>[b]</sup> and Wolfgang Weigand<sup>\*[a,c]</sup>

---

[a] S. Benndorf, P. Buday, B. Callies, Dr. H. Görls, Prof. Dr. W. Weigand  
Institute of Inorganic and Analytical Chemistry, Friedrich Schiller University Jena,  
Humboldtstrasse 8, 07743 Jena, Germany  
E-mail: wolfgang.weigand@uni-jena.de

[b] Dr. S. Kupfer  
Institute of Physical Chemistry, Friedrich Schiller University Jena  
Helmholtzweg 4, 07743 Jena, Germany

[c] Center for Energy and Environmental Chemistry Jena (CEEC Jena), Jena Center of Soft Matter, Friedrich Schiller University Jena,  
Philosophenweg 7a, 07743 Jena, Germany

## Materials and Methods

All solvents as well as commercially available compounds were purchased (Sigma-Aldrich, Acros, abcr, Alfa Aesar, TCI) and used as received without further purification. Toluene was dried and deoxygenated over Na metal. The NMR spectra were recorded with a Bruker Avance 400 MHz spectrometer. Chemical shifts are given in ppm relative to internal SiMe<sub>4</sub> or CHCl<sub>3</sub> (<sup>1</sup>H, <sup>13</sup>C{<sup>1</sup>H}, <sup>77</sup>Se{<sup>1</sup>H}, <sup>125</sup>Te{<sup>1</sup>H}). IR spectra were measured with a Tensor 27 FT-IR spectrometer. Additionally, a Specac OMNI OTTLE cell was used for IR measurements in solution. DIPEI mass spectrometry (70 eV) was performed with a Finnigan MAT SSQ 710. UV-Vis spectroscopy was carried out at a Specord S600 A with 4- or 10-mm pathway cuvette.

Structure Determinations: The intensity data for the compound **2c** was collected on a Nonius KappaCCD diffractometer using graphite-monochromated Mo-K<sub>α</sub> radiation. Data were corrected for Lorentz and polarization effects; absorption was taken into account on a semi-empirical basis using multiple-scans.<sup>1</sup> The structure was solved by intrinsic phases (SHELXT<sup>2</sup>) and refined by full-matrix least squares techniques against Fo<sup>2</sup> (SHELXL-2018<sup>3</sup>). All hydrogen atoms were included at calculated positions with fixed thermal parameters. MERCURY was used for structure representations.<sup>4</sup>

## Molecular structure

*Crystal Data for 2c:* C<sub>10</sub>H<sub>10</sub>Fe<sub>2</sub>O<sub>8</sub>S<sub>2</sub>, Mr = 434.00 gmol<sup>-1</sup>, red-brown prism, size 0.104 x 0.102 x 0.088 mm<sup>3</sup>, triclinic, space group P  $\bar{1}$ , a = 9.9054(2), b = 12.9304(3), c = 14.3840(3) Å, α = 67.548(1), β = 75.695(1), γ = 72.133(1)°, V = 1602.78(6) Å<sup>3</sup>, T = -140 °C, Z = 4, ρ<sub>calcd.</sub> = 1.799 gcm<sup>-3</sup>, μ (Mo-K<sub>α</sub>) = 21.03 cm<sup>-1</sup>, multi-scan, transmin: 0.6818, transmax: 0.7456, F(000) = 872, 23102 reflections in h(-12/12), k(-16/16), l(-18/18), measured in the range 1.754° ≤ Θ ≤ 27.484°, completeness Θ<sub>max</sub> = 99.6%, 7304 independent reflections, R<sub>int</sub> = 0.0373, 6376 reflections with F<sub>o</sub> > 4σ(F<sub>o</sub>), 413 parameters, 0 restraints, R<sub>1obs</sub> = 0.0358, wR<sup>2</sup><sub>obs</sub> = 0.0772, R<sub>1all</sub> = 0.0438, wR<sup>2</sup><sub>all</sub> = 0.0815, GOOF = 1.054, largest difference peak and hole: 0.638 / -0.406 e Å<sup>-3</sup>.

Exemplarily, Figure S1 and S2 show the molecular structure and atom numbering scheme of compound **2c**. The X-ray structure determination exhibits two symmetry-independent molecules A (Figure S1) and B (Figure S2). Both structures reveal the characteristic butterfly conformation of the [Fe<sub>2</sub>S<sub>2</sub>] cluster. The coordination sphere in the vicinity of each Fe atom can be described as a distorted octahedral with two *m*-bridging S atoms, and three terminal CO ligands. The Fe-Fe bond length of both structures (Fe<sub>1A</sub>-Fe<sub>2A</sub> 2.5332(5) Å, Fe<sub>1B</sub>-Fe<sub>2B</sub> 2.5184(5) Å) are in good agreement with comparable non-bridged dithiolato complexes.<sup>5,6</sup>

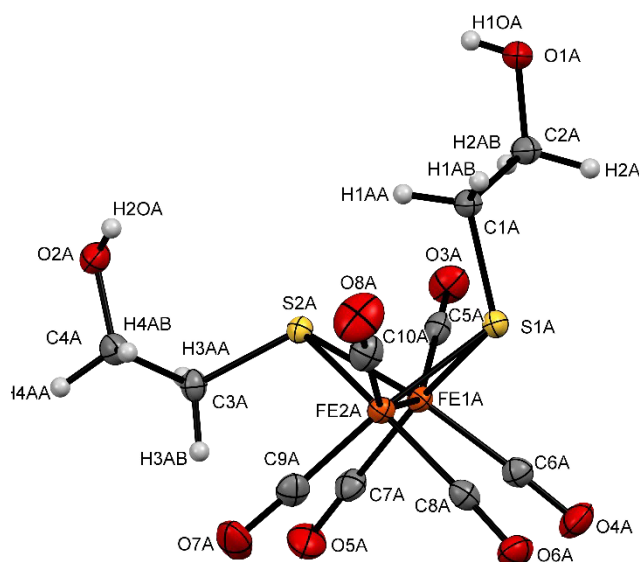


**Figure S1.** Molecular structure (A) and atom numbering of complex **2c**. The ellipsoids represent a probability of 50 %, H atoms are drawn with arbitrary radii.

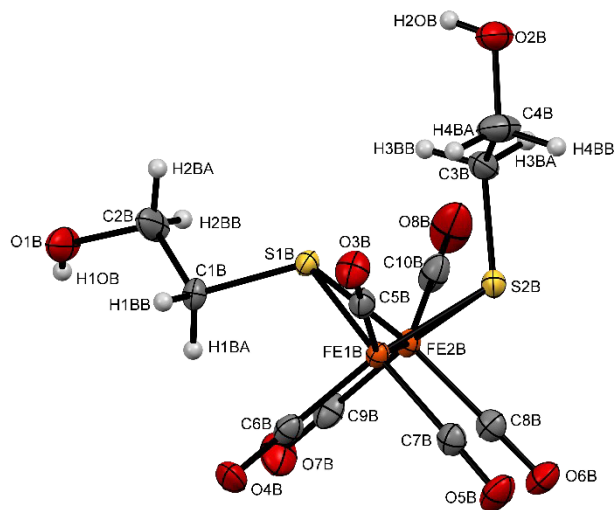


**Figure S2. Molecular structure (B) and atom numbering of complex 2c. The ellipsoids represent a probability of 50 %, H atoms are drawn with arbitrary radii.**

Crystallographic data (excluding structure factors) has been deposited with the Cambridge Crystallographic Data Centre as supplementary publication CCDC- 2205533 for **2c**. Copies of the data can be obtained free of charge on application to CCDC, 12 Union Road, Cambridge CB2 1EZ, UK [E- mail: [deposit@ccdc.cam.ac.uk](mailto:deposit@ccdc.cam.ac.uk)].

## Synthesis

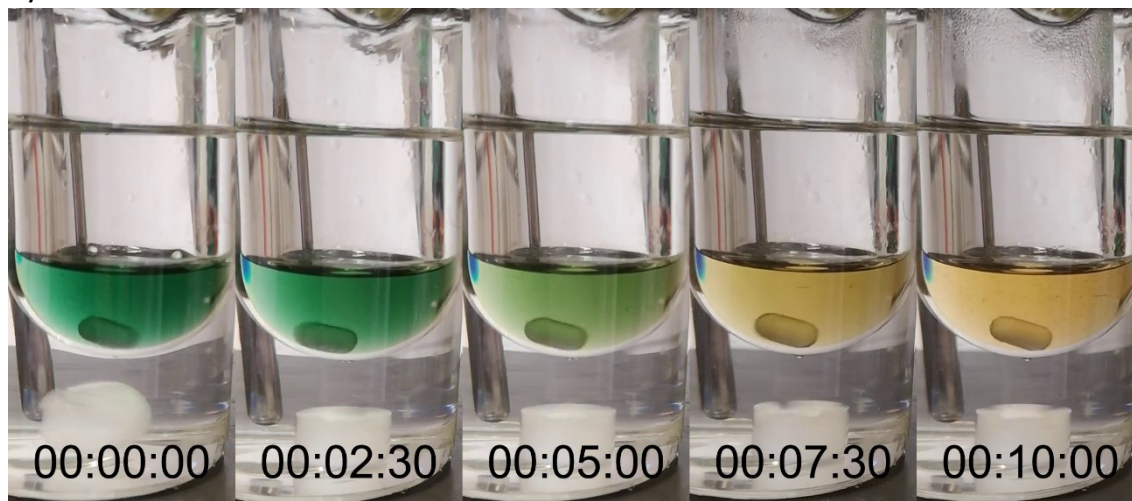


Figure S3. Photographs during the reaction of  $\text{Fe}_3(\text{CO})_{12}$  with equimolar amounts of **1a** (toluene/NMP (10:1),  $c \approx 2.2 \times 10^{-4}$  M) at 52 °C. Please keep in mind that the reaction time is extended in comparison to the experiment in Table 1, due to the less concentrated solution.

## Experimental

### Synthesis of diiron hexacarbonyl complexes **2a-n**

Precursors **1a-1n** (100 mg) were dissolved in toluene/NMP (10:1) mixture (11 mL) at 50 °C. After addition of  $\text{Fe}_3(\text{CO})_{12}$  (1 eq, 0.5 eq for **1c**) in one portion, the reaction was stirred until the dark green solution turned orange-red, monitored by TLC. Target compounds **2a-n** could be isolated as a red or brownish solids after purification via column chromatography (*n*-hexane/THF or *n*-hexane/ethyl acetate). All reaction times and isolated yields are depicted in Table 1. All complexes are known examples in the literature. Further characterization can be found in the cited original literature.

#### **H<sub>2</sub>ase mimics**

##### **2a<sup>7</sup>**

$^1\text{H}$  NMR (600 MHz,  $[\text{D}_2]$ DCM, 297 K, TMS)  $\delta$  (ppm) = 2.16 (br s, 4H,  $\text{CH}_2\text{S}$ ), 1.80 (br s, 2H,  $\text{CH}_2\text{CH}_2\text{CH}_2$ ); MS (EI):  $m/z$  = 386  $[\text{M}]^+$ , 358  $[\text{M}-\text{CO}]^+$ , 330  $[\text{M}-\text{CO}]_2^+$ , 302  $[\text{M}-\text{CO}]_3^+$ , 274  $[\text{M}-\text{CO}]_4^+$ , 246  $[\text{M}-\text{CO}]_5^+$ , 218  $[\text{M}-\text{CO}]_6^+$ ;  $\tilde{\nu}$  (CO)  $[\text{cm}^{-1}]$  = 2069, 2019, 1983, 1961, 1953; elemental analysis calcd. (%) for  $\text{C}_9\text{H}_6\text{Fe}_2\text{O}_6\text{S}_2$ : C 28.01, H 1.57, S 16.61; found: C 28.25, H 1.70, S 16.78.

##### **2b<sup>8</sup>**

$^1\text{H}$  NMR (400 MHz,  $\text{CDCl}_3$ , 297 K, TMS)  $\delta$  (ppm) = 3.19 – 3.07 (m, 1H,  $\text{CH}(\text{OH})$ ), 2.81 (dd,  $^3J_{\text{H-H}} = 13.2$ , 4.1 Hz, 2H,  $\text{CH}_2\text{H}_b$ ), 1.86 (d,  $^3J_{\text{H-H}} = 5.6$  Hz, 1H, OH), 1.56 – 1.48 (m, 2H,  $\text{CH}_2\text{H}_a$ );  $^{13}\text{C}\{^1\text{H}\}$  NMR (101 MHz,  $\text{CDCl}_3$ , 297 K, TMS)  $\delta$  (ppm) = 207.4, 72.9, 29.6; MS (EI):  $m/z$  = 374  $[\text{M}-\text{CO}]^+$ , 346  $[\text{M}-\text{CO}]_2^+$ , 318  $[\text{M}-\text{CO}]_3^+$ , 290  $[\text{M}-\text{CO}]_4^+$ , 262  $[\text{M}-\text{CO}]_5^+$ , 234  $[\text{M}-\text{CO}]_6^+$ ;  $\tilde{\nu}$  (CO)  $[\text{cm}^{-1}]$  = 2070, 2025, 1986, 1956; elemental analysis calcd. (%) for  $\text{C}_9\text{H}_6\text{Fe}_2\text{O}_7\text{S}_2$ : C 26.89, H 1.50, S 15.95; found: C 26.54, H 1.43, S 15.70.

##### **2c and 2d<sup>9</sup>**

$^1\text{H}$  NMR (600 MHz,  $\text{CDCl}_3$ , 297 K, TMS)  $\delta$  (ppm) = 4.18 – 3.53 (m, 4H,  $\text{CH}_2\text{S}$ ), 2.77 – 2.13 (m, 4H,  $\text{CH}_2\text{O}$ ), 2.01 – 1.73 (m, 2H, OH);  $^{13}\text{C}\{^1\text{H}\}$  NMR (151 MHz,  $\text{CDCl}_3$ , 297 K)  $\delta$  (ppm) = 209.25, 208.36, 63.00, 41.25, 40.10, 27.65; MS (ESI positive mode):  $m/z$  = 456.841 (M + Na<sup>+</sup>, calcd. 456.841);  $\tilde{\nu}$  (CO)  $[\text{cm}^{-1}]$  = 2070, 2027, 2008, 1988, 1975, 1956.

##### **2e<sup>7</sup>**

$^1\text{H}$  NMR (400 MHz,  $\text{CDCl}_3$ , 297 K, TMS)  $\delta$  (ppm) = 2.57 (br s, 1H), 2.39 (m, 2H), 2.11 (br s, 1H), 1.86 (br s, 2H), 1.64–1.44 (m, 6H), 1.29 (br s, 1H); MS (EI):  $m/z$  = 486  $[\text{M}]^+$ , 430  $[\text{M}-\text{CO}]_2^+$ , 402  $[\text{M}-\text{CO}]_3^+$ , 374  $[\text{M}-\text{CO}]_4^+$ , 346  $[\text{M}-\text{CO}]_5^+$ , 318  $[\text{M}-\text{CO}]_6^+$ ;  $\tilde{\nu}$  (CO)  $[\text{cm}^{-1}]$  = 2069, 2023, 1981, 1955.

##### **2f<sup>10</sup>**

$^1\text{H}$  NMR (400 MHz,  $\text{CDCl}_3$ , 297 K, TMS)  $\delta$  (ppm) = 2.87 (dd,  $^2J_{\text{H-H}} = 13.6$ ,  $^3J_{\text{H-H}} = 3.4$  Hz, 2H,  $\text{CH}_2\text{H}_b$ ), 2.17 (m, 1H, CH), 1.76 (t,  $J = 13.0$  Hz, 2H,  $\text{CH}_2\text{H}_a$ ); MS (EI):  $m/z$  = 402  $[\text{M}-\text{CO}]^+$ , 374  $[\text{M}-\text{CO}]_2^+$ , 346  $[\text{M}-\text{CO}]_3^+$ , 318  $[\text{M}-\text{CO}]_4^+$ , 290  $[\text{M}-\text{CO}]_5^+$ , 262  $[\text{M}-\text{CO}]_6^+$ ;  $\tilde{\nu}$  (CO)  $[\text{cm}^{-1}]$  = 2073, 2027, 1983, 1966.

### 2g<sup>11</sup>

<sup>1</sup>H NMR (400 MHz, CDCl<sub>3</sub>, 297 K, TMS)  $\delta$  (ppm) = 7.23 – 7.07 (m, 2H, Ar-H), 6.73 – 6.57 (m, 2H, Ar-H); MS (EI): m/z = 392 [M-(CO)]<sup>+</sup>, 364 [M-(CO)<sub>2</sub>]<sup>+</sup>, 336 [M-(CO)<sub>3</sub>]<sup>+</sup>, 308 [M-(CO)<sub>4</sub>]<sup>+</sup>, 280 [M-(CO)<sub>5</sub>]<sup>+</sup>, 252 [M-(CO)<sub>6</sub>]<sup>+</sup>;  $\tilde{\nu}$  (CO) [cm<sup>-1</sup>] = 2074, 2050, 2031, 2001, 1980, 1960.

### 2h<sup>5</sup>

<sup>1</sup>H NMR (400 MHz, CDCl<sub>3</sub>, 297 K, TMS)  $\delta$  (ppm) = 7.92 – 6.80 (m, 10H, Ar-H); MS (EI): m/z = 498 [M]<sup>+</sup>, 470 [M-(CO)]<sup>+</sup>, 442 [M-(CO)<sub>2</sub>]<sup>+</sup>, 358 [M-(CO)<sub>5</sub>]<sup>+</sup>, 330 [M-(CO)<sub>6</sub>]<sup>+</sup>;  $\tilde{\nu}$  (CO) [cm<sup>-1</sup>] = 2068, 2033, 1993, 1985, 1976.

### 2i<sup>12</sup>

<sup>1</sup>H NMR (400 MHz, [D<sub>2</sub>]DCM, 297 K, TMS)  $\delta$  (ppm) = 7.53 – 7.15 (m, 10H, Ar-H); <sup>77</sup>Se{<sup>1</sup>H} NMR (76 MHz, CDCl<sub>3</sub>, 297 K)  $\delta$  (ppm) = 321.66, 280.64, 226.17; MS (EI): m/z = 594 [M]<sup>+</sup>, 566 [M-(CO)]<sup>+</sup>, 538 [M-(CO)<sub>2</sub>]<sup>+</sup>, 510 [M-(CO)<sub>3</sub>]<sup>+</sup>, 482 [M-(CO)<sub>4</sub>]<sup>+</sup>, 454 [M-(CO)<sub>5</sub>]<sup>+</sup>, 426 [M-(CO)<sub>6</sub>]<sup>+</sup>;  $\tilde{\nu}$  (CO) [cm<sup>-1</sup>] = 2062, 2024, 1997, 1969; elemental analysis calcd. (%) for C<sub>18</sub>H<sub>10</sub>Fe<sub>2</sub>O<sub>6</sub>Se<sub>2</sub>: C 36.53, H 1.70; found: C 36.81, H 1.67.

### 2j<sup>13</sup>

<sup>1</sup>H NMR (400 MHz, [D<sub>2</sub>]DCM, 297 K, TMS)  $\delta$  (ppm) = 7.52 – 7.37 (m, 2H, Ar-H), 7.35 – 7.24 (m, 4H, Ar-H), 7.24 – 7.16 (m, 2H, Ar-H), 7.16 – 7.07 (m, 2H, Ar-H); <sup>125</sup>Te{<sup>1</sup>H} NMR (126 MHz, [D<sub>2</sub>]DCM, 297 K)  $\delta$  (ppm) = 485.10, 440.61; MS (EI): m/z = 689 [M]<sup>+</sup>, 661 [M-(CO)]<sup>+</sup>, 633 [M-(CO)<sub>2</sub>]<sup>+</sup>, 605 [M-(CO)<sub>3</sub>]<sup>+</sup>, 577 [M-(CO)<sub>4</sub>]<sup>+</sup>, 549 [M-(CO)<sub>5</sub>]<sup>+</sup>, 521 [M-(CO)<sub>6</sub>]<sup>+</sup>;  $\tilde{\nu}$  (CO) [cm<sup>-1</sup>] = 2050, 2009, 1993, 1970, 1941; elemental analysis calcd. (%) for C<sub>18</sub>H<sub>10</sub>Fe<sub>2</sub>O<sub>6</sub>Te<sub>2</sub>: C 31.37, H 1.46; found: C 31.52, H 1.38.

### 2k<sup>14</sup>

<sup>1</sup>H NMR (300 MHz, CDCl<sub>3</sub>, 297 K, TMS)  $\delta$  (ppm) = 7.06 (br s, 4H, Ar-H), 6.49 (br d, *J* = 6.9 Hz, 4H, Ar-H), 3.68 (br s, 4H, NH<sub>2</sub>); MS (EI): m/z = 528 [M]<sup>+</sup>, 499 [M-(CO)H]<sup>+</sup>, 471 [M-(CO)<sub>2</sub>H]<sup>+</sup>, 444 [M-(CO)<sub>3</sub>]<sup>+</sup>, 388 [M-(CO)<sub>5</sub>]<sup>+</sup>, 360 [M-(CO)<sub>6</sub>]<sup>+</sup>;  $\tilde{\nu}$  (CO) [cm<sup>-1</sup>] = 2070, 2064, 2026, 1992, 1982, 1973, 1961.

### 2l<sup>15</sup>

<sup>1</sup>H NMR (400 MHz, CDCl<sub>3</sub>, 297 K, TMS)  $\delta$  (ppm) = 7.87 (d, *J* = 7.0 Hz, 2H, Ar-H), 7.64 (d, *J* = 7.0 Hz, 2H, Ar-H), 7.36 (m, 4H, Ar-H), 2.76 (s, 4H, CH<sub>2</sub>); MS (EI): m/z = 536 [M]<sup>+</sup>, 508 [M-(CO)]<sup>+</sup>, 480 [M-(CO)<sub>2</sub>]<sup>+</sup>, 452 [M-(CO)<sub>3</sub>]<sup>+</sup>, 424 [M-(CO)<sub>4</sub>]<sup>+</sup>, 396 [M-(CO)<sub>5</sub>]<sup>+</sup>, 368 [M-(CO)<sub>6</sub>]<sup>+</sup>;  $\tilde{\nu}$  (CO) [cm<sup>-1</sup>] = 2068, 2019, 2003, 1962.

### 2m<sup>16</sup>

<sup>1</sup>H NMR (400 MHz, [D<sub>8</sub>]THF, 297 K, TMS)  $\delta$  (ppm) = 8.55 - 8.49 (d, <sup>3</sup>*J*<sub>H-H</sub> = 7.6 Hz, 2H; Ar-NMI), 8.43 (d, <sup>3</sup>*J*<sub>H-H</sub> = 7.6 Hz, 2H; Ar-NMI), 4.84 (d, <sup>4</sup>*J*<sub>H-H</sub> = 2.4 Hz, 2H; CH<sub>2</sub>), 2.54 (t, <sup>4</sup>*J*<sub>H-H</sub> = 2.4 Hz, 1H; CCH); MS (EI): m/z = 577 [M]<sup>+</sup>, 549 [M-(CO)]<sup>+</sup>, 521 [M-(CO)<sub>2</sub>]<sup>+</sup>, 493 [M-(CO)<sub>3</sub>]<sup>+</sup>, 465 [M-(CO)<sub>4</sub>]<sup>+</sup>, 437 [M-(CO)<sub>5</sub>]<sup>+</sup>, 409 [M-(CO)<sub>6</sub>]<sup>+</sup>;  $\tilde{\nu}$  (CO) [cm<sup>-1</sup>] = 2073, 2049, 2029, 2008, 1997, 1984, 1979, 1975; elemental analysis calcd. (%) for C<sub>21</sub>H<sub>7</sub>Fe<sub>2</sub>NO<sub>8</sub>S<sub>2</sub>: C 43.71, H 1.22, N 2.43, S 11.11; found: C 43.91, H 1.32, N 2.41, S 10.98.

### 2n<sup>17</sup>

<sup>1</sup>H NMR (400 MHz, CDCl<sub>3</sub>, 297 K, TMS)  $\delta$  (ppm) = 8.49 – 8.42 (m, 4H, Ar-Ph), 7.35 (d, <sup>3</sup>*J*<sub>H-H</sub> = 8.2 Hz, 2H, Ar-NMI), 7.17 (d, <sup>3</sup>*J*<sub>H-H</sub> = 8.2 Hz, 2H, Ar-NMI), 2.45 (s, 3H, CH<sub>3</sub>); MS (EI): m/z = 629 [M]<sup>+</sup>, 601 [M-(CO)]<sup>+</sup>, 573 [M-(CO)<sub>2</sub>]<sup>+</sup>, 516 [M-(CO)<sub>4</sub>H]<sup>+</sup>, 488 [M-(CO)<sub>5</sub>H]<sup>+</sup>;  $\tilde{\nu}$  (CO) [cm<sup>-1</sup>] = 2080, 2039, 2008, 1986, 1963.

### Fe<sub>3</sub>(CO)<sub>11</sub>NMP

In a Schlenk flask Fe<sub>3</sub>(CO)<sub>12</sub> (939 mg, 1.87 mmol) was dissolved in anhydrous, N<sub>2</sub>-saturated toluene/NMP mixture (10:1, 11 mL) and heated at 50 °C for 5 minutes, until the dark green solution turned purple, monitored by TLC. After complete consumption of the starting material, the solution was cooled down to RT. The target compound could be isolated as a purple, oxygen-sensitive solid after purification via column chromatography (*n*-hexane/acetone (1:0 -> 1:1)).

<sup>1</sup>H NMR (400 MHz, benzene-d<sub>6</sub>, 297 K, TMS)  $\delta$  (ppm) = 2.54 – 2.38 (m, 5H), 2.00 (br t, <sup>3</sup>*J*<sub>H-H</sub> = 8.2 Hz, 2H), 1.21 (quin, <sup>3</sup>*J*<sub>H-H</sub> = 7.6 Hz, 2H); <sup>13</sup>C{<sup>1</sup>H} NMR (101 MHz, benzene-d<sub>6</sub>, 297 K, TMS)  $\delta$  (ppm) = 174.76, 49.01, 30.89, 29.50, 17.77; MS (ESI negative mode): m/z = 573.7 [M-H]<sup>-</sup> (calc. 573.8), 545.7 [M-H(CO)]<sup>-</sup> (calc. 545.8), IR (toluene, 297 K)  $\tilde{\nu}$  (cm<sup>-1</sup>) = 2018, 1996.

### NMP

<sup>1</sup>H NMR (400 MHz, benzene-d<sub>6</sub>, 297 K, TMS)  $\delta$  (ppm) = 2.54 – 2.43 (m, 5H), 1.94 (t, *J* = 8.1 Hz, 2H), 1.32 – 1.10 (m, 2H); <sup>13</sup>C{<sup>1</sup>H} NMR (101 MHz, benzene-d<sub>6</sub>, 297 K, TMS)  $\delta$  (ppm) = 173.86, 48.76, 30.72, 29.41, 17.91.

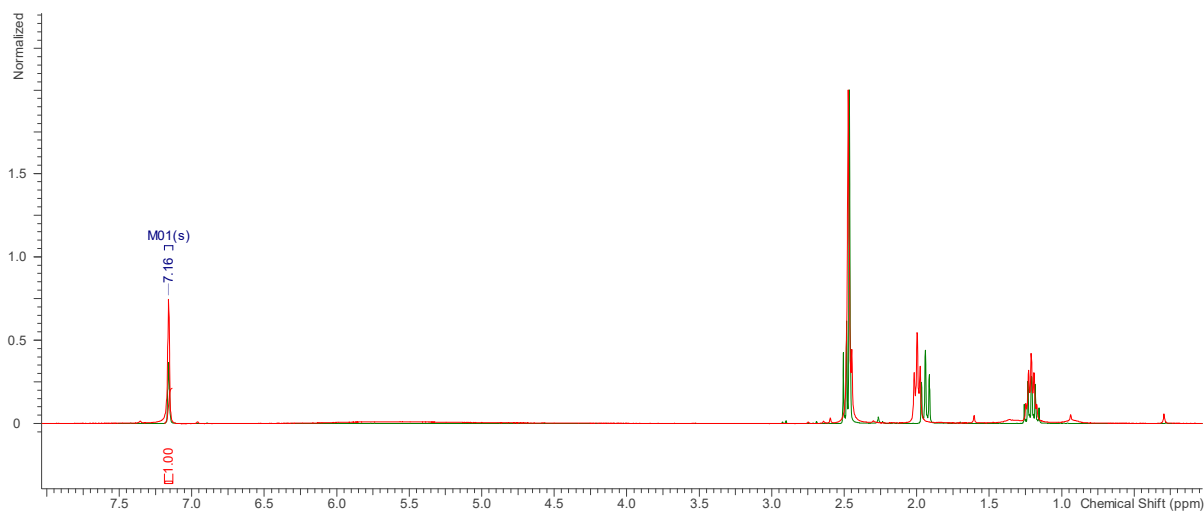


Figure S4.  $^1\text{H}$  NMR (benzene- $d_6$ , 400 MHz, 298 K) of  $\text{Fe}_3(\text{CO})_{11}\text{NMP}$  (red) and NMP (green)

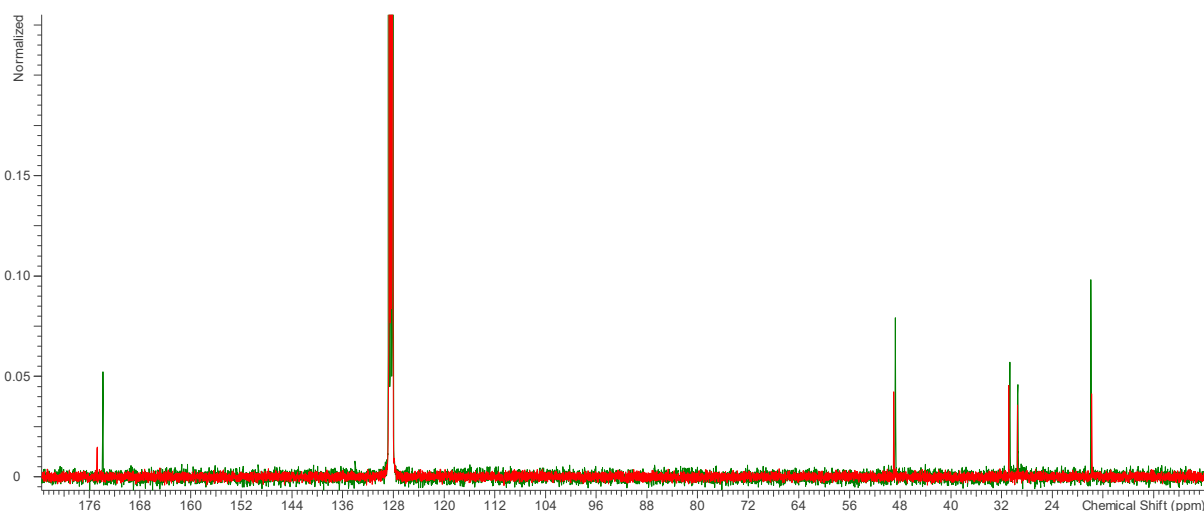


Figure S5.  $^{13}\text{C}\{^1\text{H}\}$  NMR (benzene- $d_6$ , 100 MHz, 298 K) of  $\text{Fe}_3(\text{CO})_{11}\text{NMP}$  (red) and NMP (green)

Proton NMR spectra (Figure S4) show small downfield shift around 2.0 ppm and 2.5 ppm, indicating the coordination of NMP to the triiron cluster with a small loss of electron density, as expected. A similar behavior was observed in the carbon NMR spectra, revealed by the small downfield shift of the carbonyl carbon of the NMP at 174 ppm.

## Quantum chemistry

Quantum chemical calculations determining structural and electronic properties of  $\text{Fe}_3(\text{CO})_{11}\text{NMP}$  were performed using Gaussian 16.<sup>18</sup> Fully relaxed singlet ground state equilibrium geometries were obtained for three preselected isomers of  $\text{Fe}_3(\text{CO})_{11}\text{NMP}$ , which are denoted **A**, **B** and **C** (see Figure S14). To this aim, density functional theory (DFT) was applied using the B3LYP XC functional,<sup>19</sup> while the def2-SVP basis set was applied for all atoms.<sup>20</sup> Subsequently, a vibrational analysis was carried out to verify that a minimum on the 3N-6 potential energy (hyper)surface (PES) was obtained for each redox species. To correct for the lack of anharmonicity and the approximate treatment of electron correlation, the harmonic frequencies were scaled by the factor 0.97.<sup>21</sup>

Furthermore, excited state properties such as excitation energies, oscillator strengths and electronic characters for the lowest 50 excited states were calculated within the equilibrium structures of the respective isomer, i.e. **A**, **B** and **C**, at the time-dependent DFT (TDDFT) level of theory. Therefore, the same computational protocol was applied as in case for the preceding DFT simulations. Several computational as well as joint spectroscopic-theoretical studies on structurally related [FeFe]  $\text{H}_2$ ase mimics showed that this computational protocol enables an accurate prediction of ground and excited states properties with respect to experimental data, e.g. structural and electrochemical properties as well as with respect to UV-Vis absorption.<sup>16,22</sup> Effects of interaction with a solvent (toluene:  $\epsilon = 2.3741$ ,  $n = 1.4969$ ) were taken into account on the ground and excited states properties by the solute electron density (SMD) variant of the integral equation formalism of the polarizable continuum model.<sup>23</sup> All calculations were performed including D3 dispersion correction with Becke-Johnson damping.<sup>24</sup>

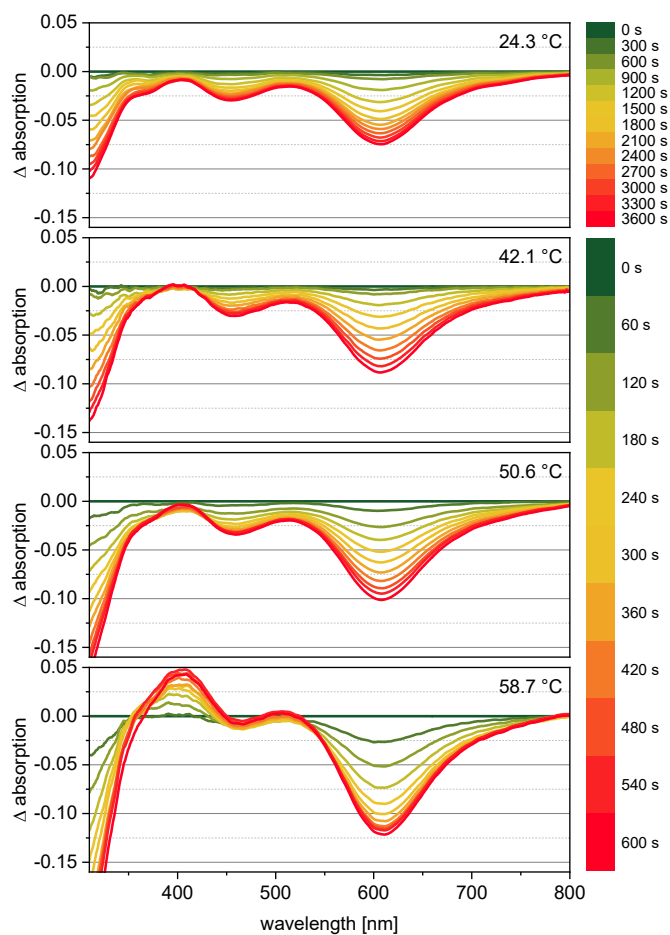


**Figure S6.** Differential UV-Vis spectra during the reaction of 1,3-propane-dithiol (1a) with equimolar amounts of  $\text{Fe}_3(\text{CO})_{12}$  (toluene/NMP (10:1),  $c = 2.2 \times 10^{-4}$  M) at varying temperatures. The  $\Delta$  absorbance spectra were calculated by subtracting the first spectrum (0 s).



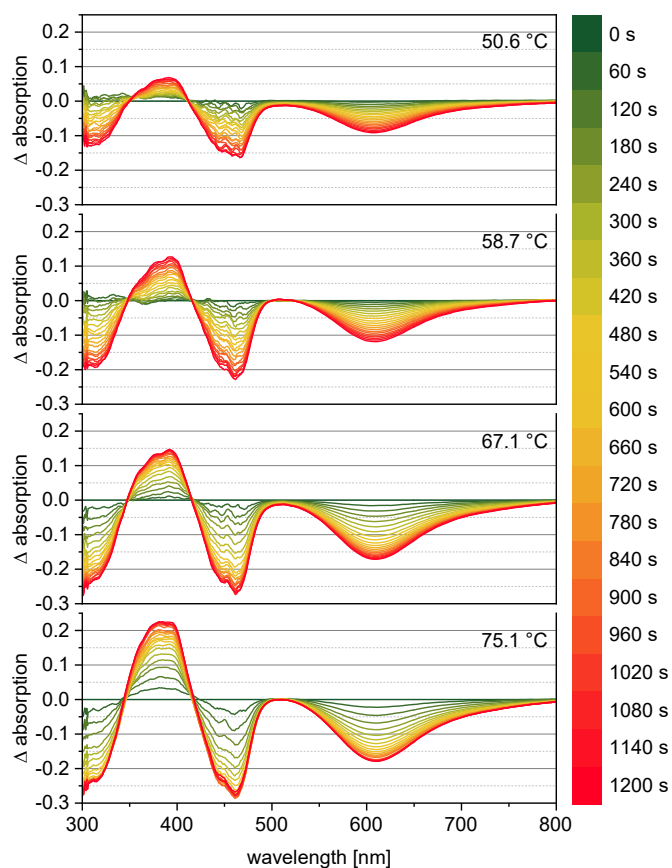


Figure S7. Differential UV-Vis spectra during the reaction of **1n** with equimolar amounts of  $\text{Fe}_3(\text{CO})_{12}$  (toluene/NMP (10:1),  $c = 2.2 \times 10^{-4}$  M) at varying temperatures. The  $\Delta$  absorbance spectra were calculated by subtracting the first spectrum (0 s).

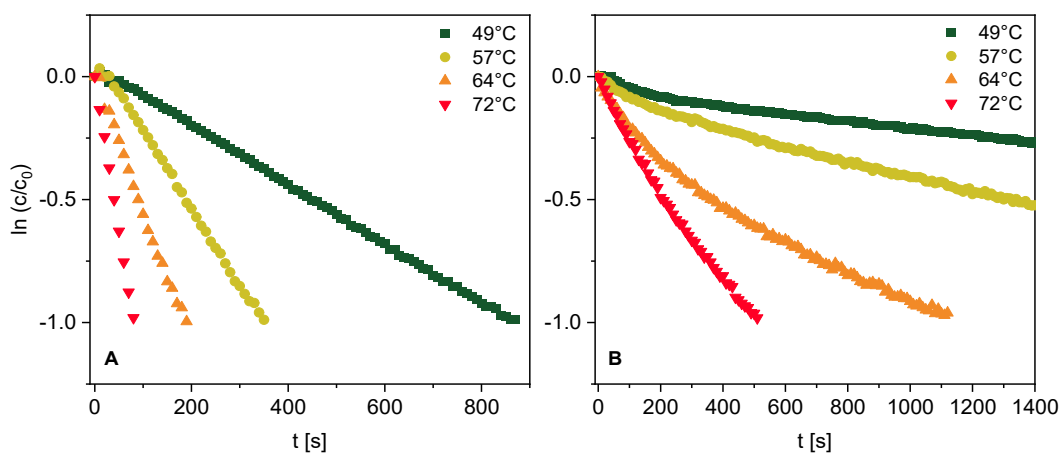


Figure S8. Plots of the natural logarithm of the relative concentration of  $\text{Fe}_3(\text{CO})_{12}$  versus time at varying temperatures during the reaction with excess amount of **1n** in presence (A) and absence (B) of NMP, respectively.

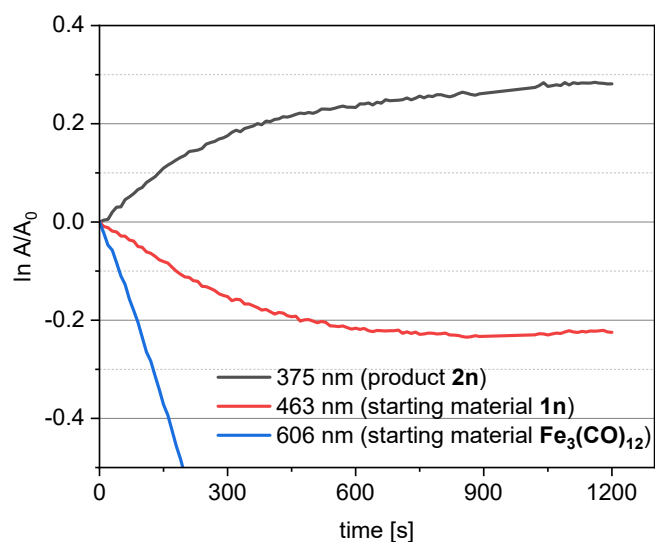


Figure S9. Plot of  $\ln A/A_0$  vs time during the reaction of 1n with equimolar amounts of  $\text{Fe}_3(\text{CO})_{12}$  ( $c = 2.2 \times 10^{-4}\text{ M}$ ) at  $75.1\text{ }^\circ\text{C}$ .

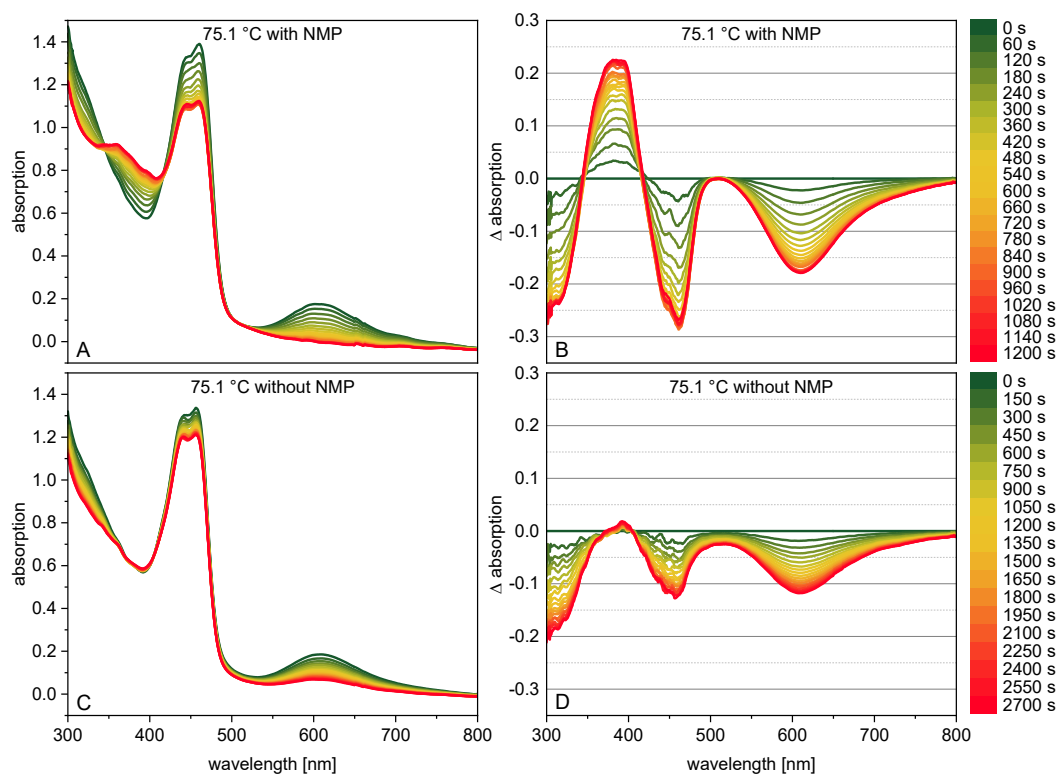


Figure S10. UV-Vis spectra (A, C) and differential UV-Vis spectra (B, D) during the reaction of 1n with equimolar amounts of  $\text{Fe}_3(\text{CO})_{12}$  ( $c = 2.2 \times 10^{-4}\text{ M}$ ) with and without NMP at  $75.1\text{ }^\circ\text{C}$ . The  $\Delta$  absorbance spectra were calculated by subtracting the first spectrum (0 s).

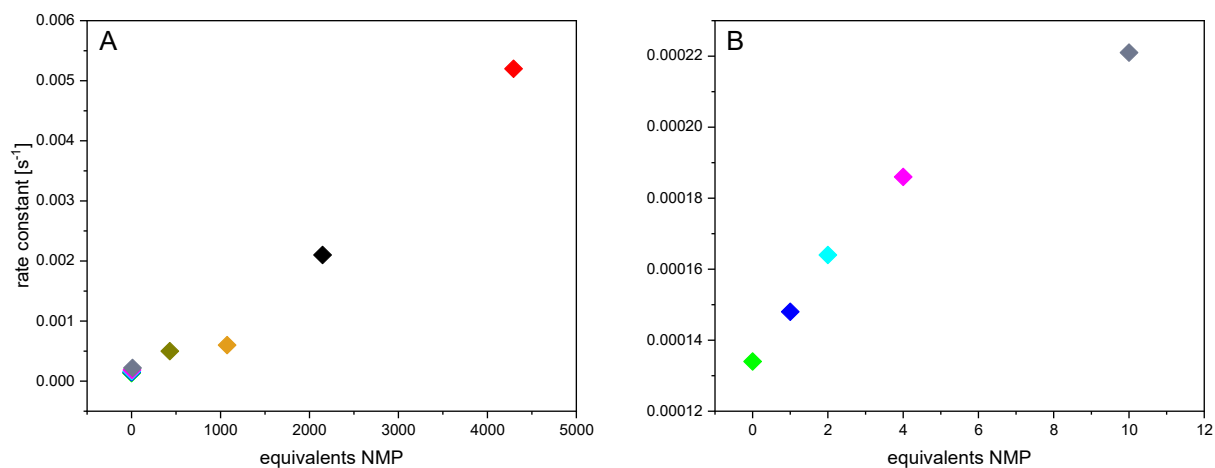


Figure S11. Rate constant dependency towards the concentration of added NMP for the reaction of 1a with equimolar amounts of  $\text{Fe}_3(\text{CO})_{12}$  (toluene,  $c = 2.2 \times 10^{-4} \text{ M}$ ) at 50.85 °C. Figure B shows the zoomed area of low equivalents.

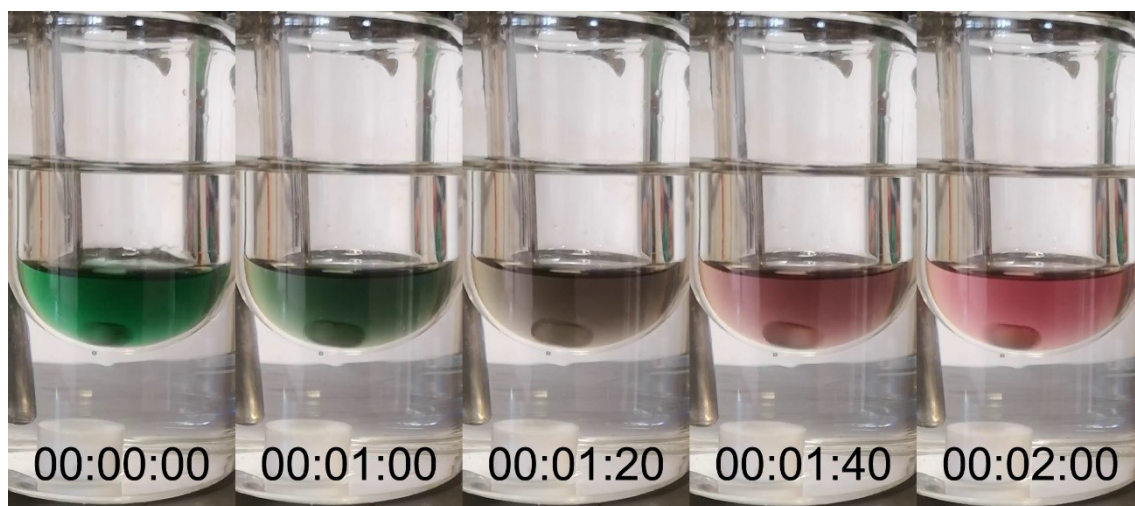


Figure S12. Photographs during the reaction of  $\text{Fe}_3(\text{CO})_{12}$  with NMP (toluene/NMP (10:1),  $c \approx 2.2 \times 10^{-3} \text{ M}$ ) at 52 °C.

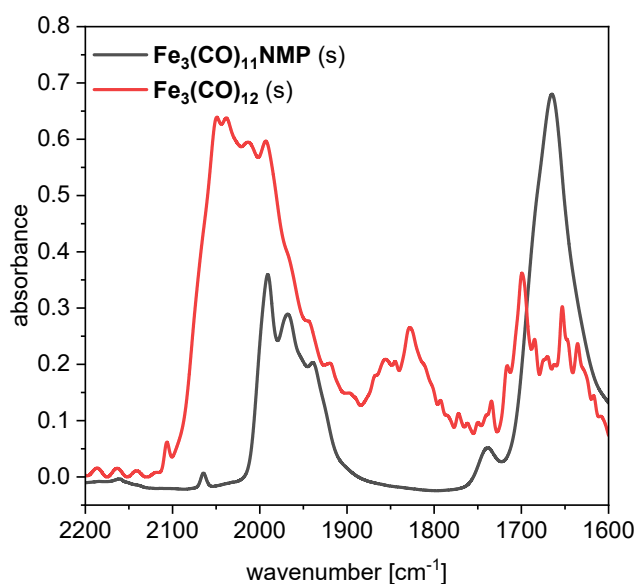


Figure S13. IR spectra of  $\text{Fe}_3(\text{CO})_{12}$  and its NMP-substituted analogue in solid state.

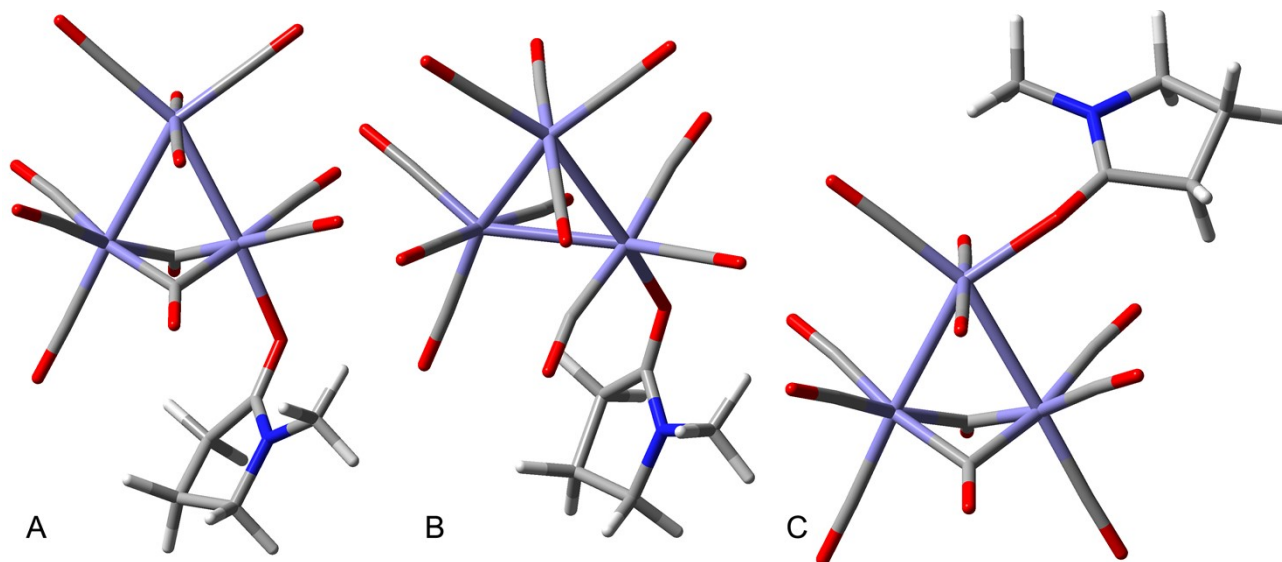


Figure S14. Simulated isomeric structures of  $\text{Fe}_3(\text{CO})_{11}\text{NMP}$ .

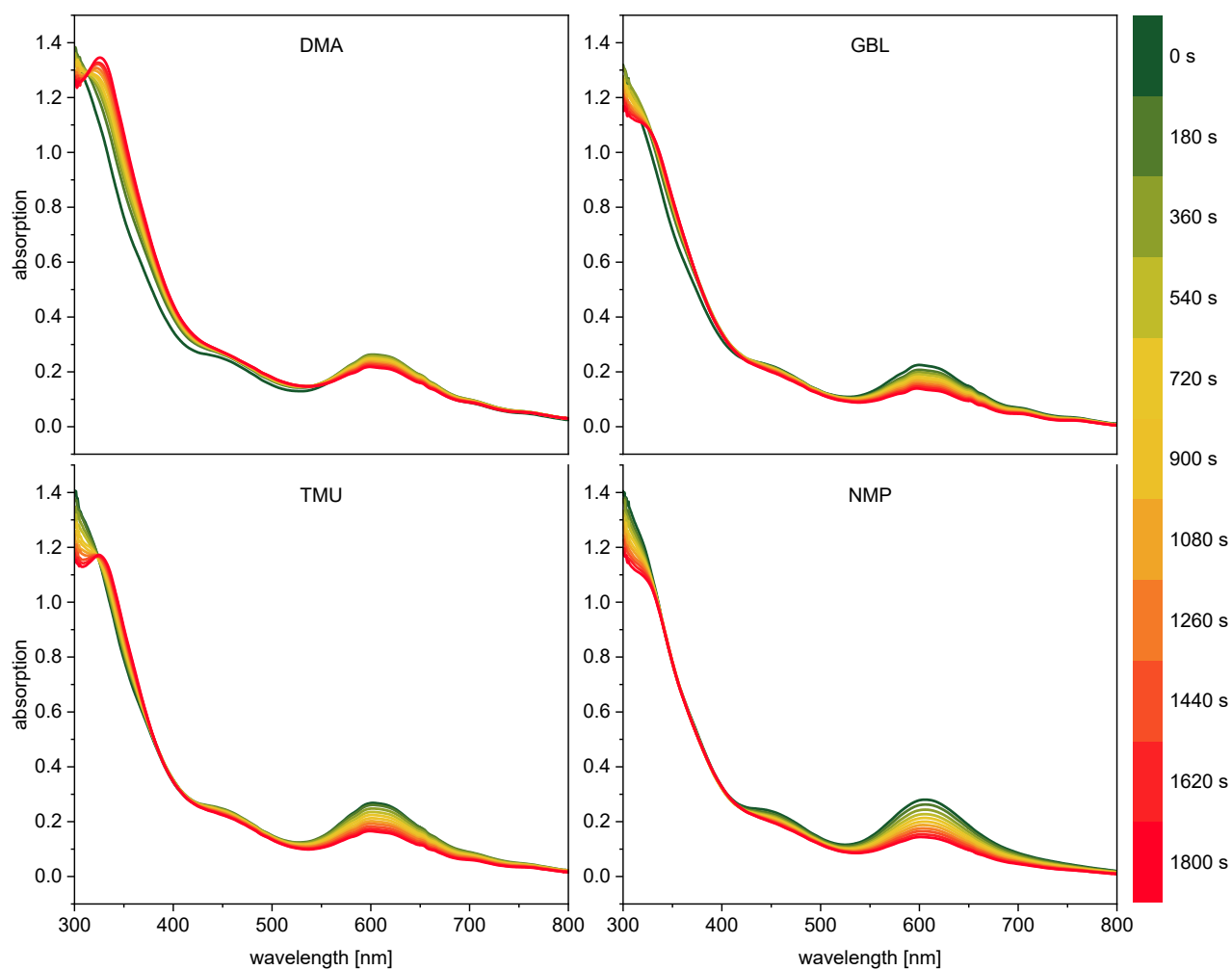


Figure S15. UV-Vis spectra during the reaction of 1a with  $\text{Fe}_3(\text{CO})_{12}$  (toluene/additive (10:1),  $c = 2.2 \times 10^{-4} \text{ M}$ ,  $T = 42 \text{ }^\circ\text{C}$ ) with varying additives.

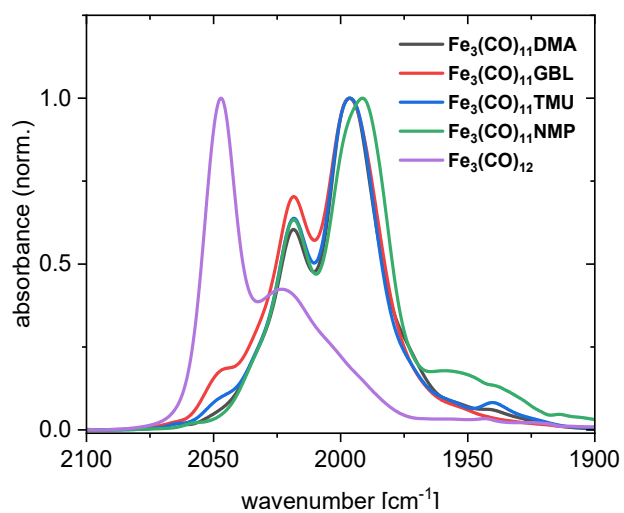
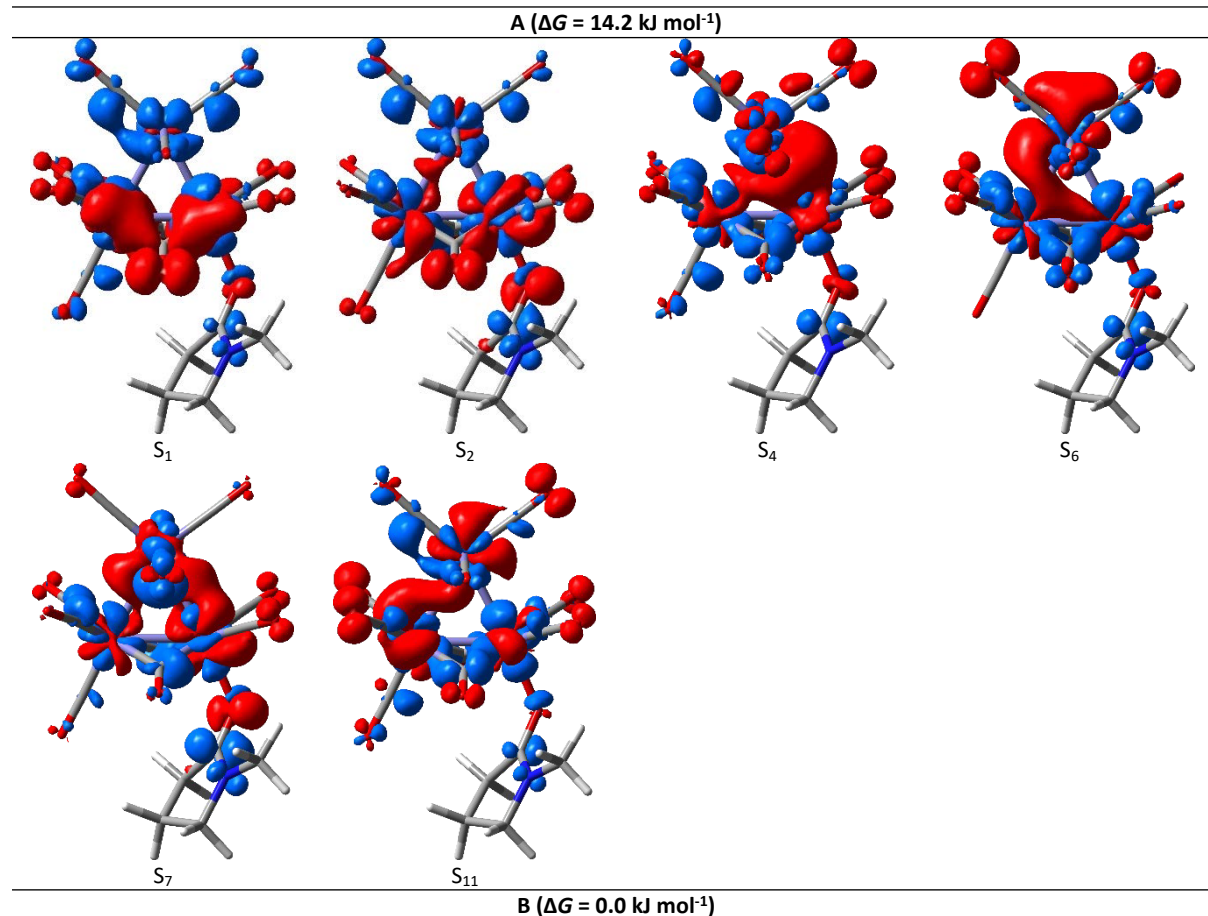


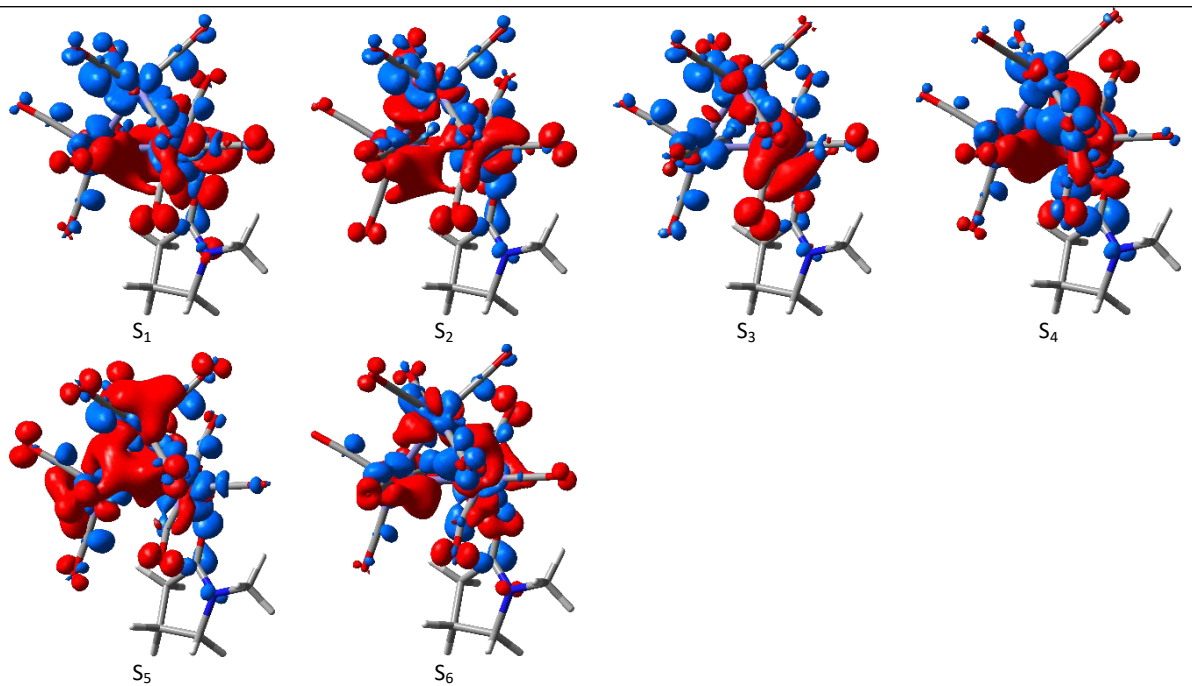
Figure S16. Normalized IR spectra of the substitution products of  $\text{Fe}_3(\text{CO})_{12}$  with dimethylacetamide (DMA),  $\gamma$ -butyrolactone (GBL), tetramethylurea (TMU) and *N*-methylpyrrolidone (NMP) as well as their starting material  $\text{Fe}_3(\text{CO})_{12}$ .

**Table S1:** Electronic properties, such as excitation energies ( $E$ ), wavelengths ( $\lambda$ ), oscillator strengths ( $f$ ) and electronic nature (ligand field, LF), of dipole-allowed transitions contributing to the UV-Vis absorption spectra of the three isomers of  $\text{Fe}_3(\text{CO})_{11}\text{NMP}$ .

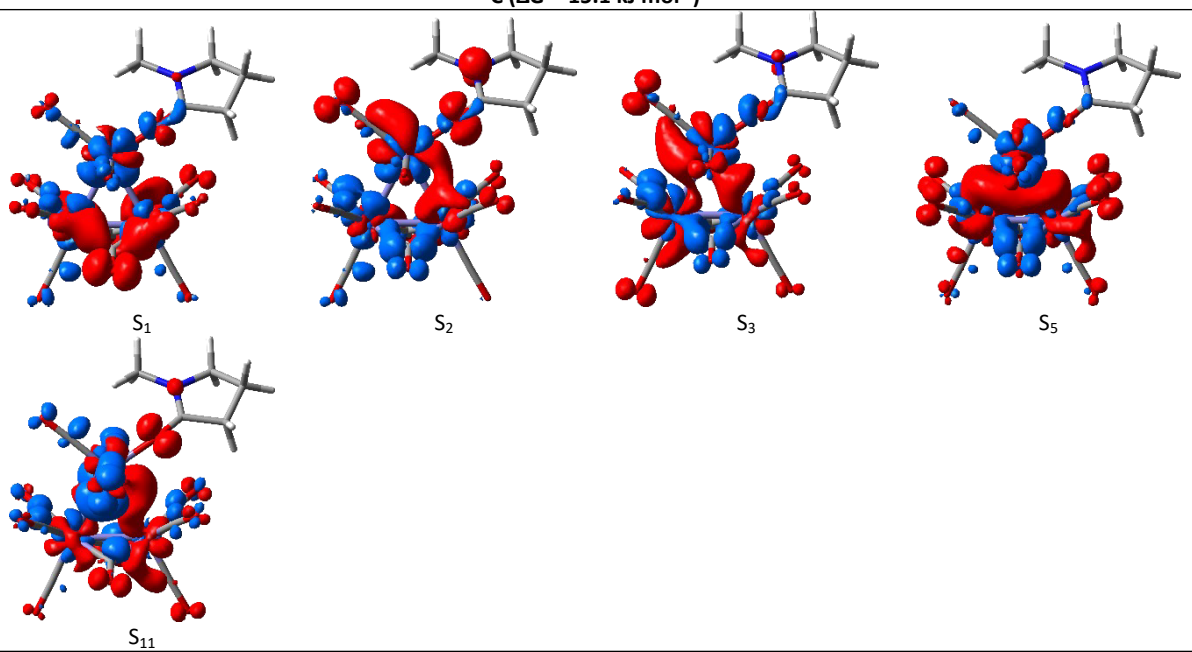
<b>A (<math>\Delta G = 14.2 \text{ kJ mol}^{-1}</math>)</b>				
State	Character	$E / \text{eV}$	$\lambda / \text{nm}$	$f$
$S_1$	LF	1.63	762	0.0031
$S_2$	LF	1.70	730	0.0117
$S_4$	LF	2.43	511	0.0239
$S_6$	LF	2.61	474	0.0317
$S_7$	LF	2.71	457	0.0207
$S_{11}$	LF	3.01	412	0.0204
<b>B (<math>\Delta G = 0.0 \text{ kJ mol}^{-1}</math>)</b>				
State	Character	$E / \text{eV}$	$\lambda / \text{nm}$	$f$
$S_1$	LF	1.64	755	0.0168
$S_2$	LF	1.88	659	0.0136
$S_3$	LF	2.08	596	0.0145
$S_4$	LF	2.38	522	0.0091
$S_5$	LF	2.47	501	0.0045
$S_6$	LF	2.57	483	0.0284
<b>C (<math>\Delta G = 15.1 \text{ kJ mol}^{-1}</math>)</b>				
State	Character	$E / \text{eV}$	$\lambda / \text{nm}$	$f$
$S_1$	LF	1.74	712	0.0062
$S_2$	LF	1.76	704	0.0136
$S_3$	LF	2.23	557	0.0525
$S_5$	LF	2.57	482	0.0187
$S_{11}$	LF	3.05	407	0.0169

**Table S2:** Electronic character of dipole-allowed transitions contributing to the UV-Vis absorption spectra of the three isomers of  $\text{Fe}_3(\text{CO})_{11}\text{NMP}$  as visualized by charge density differences; charge transfer occurs from red to blue.





C ( $\Delta G = 15.1 \text{ kJ mol}^{-1}$ )



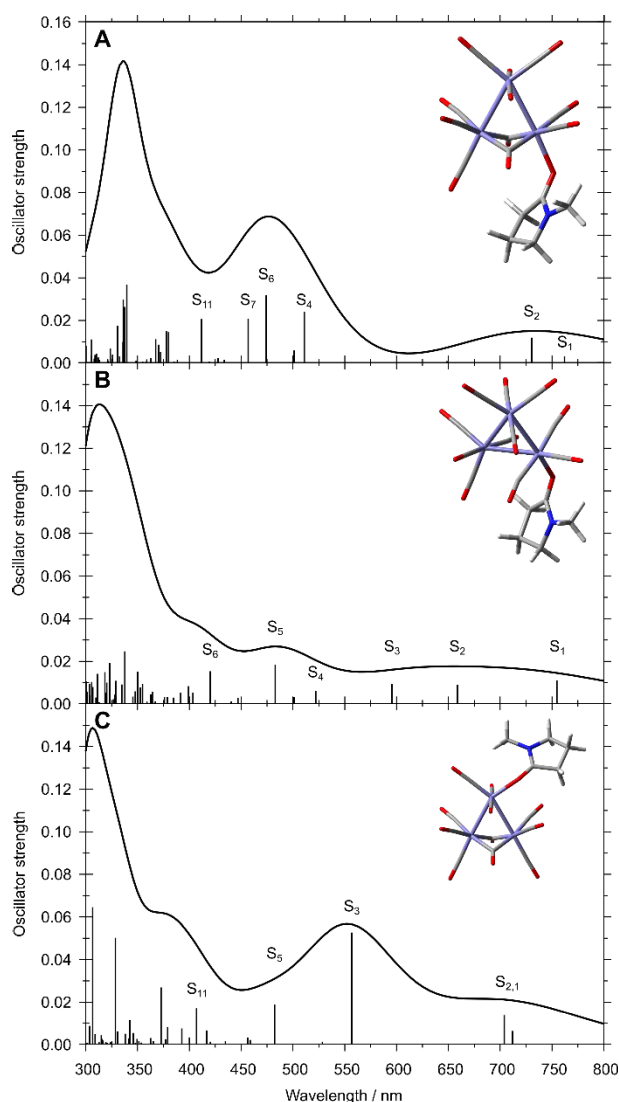


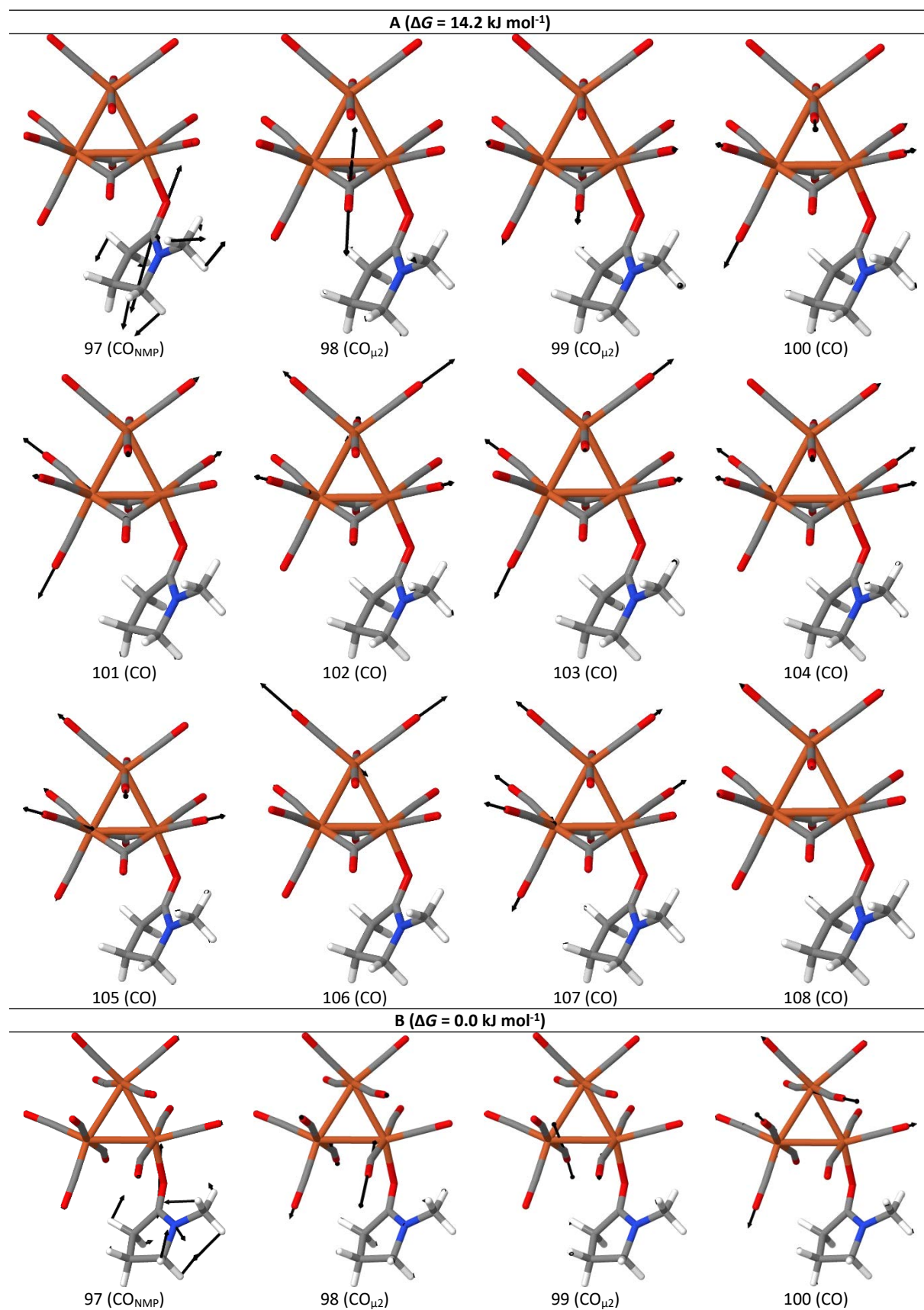
**Figure S17.** Simulated UV-Vis absorption spectra of the three isomers of  $\text{Fe}_3(\text{CO})_{11}\text{NMP}$ , i.e., A, B and C. Prominent electronic transitions are labeled.

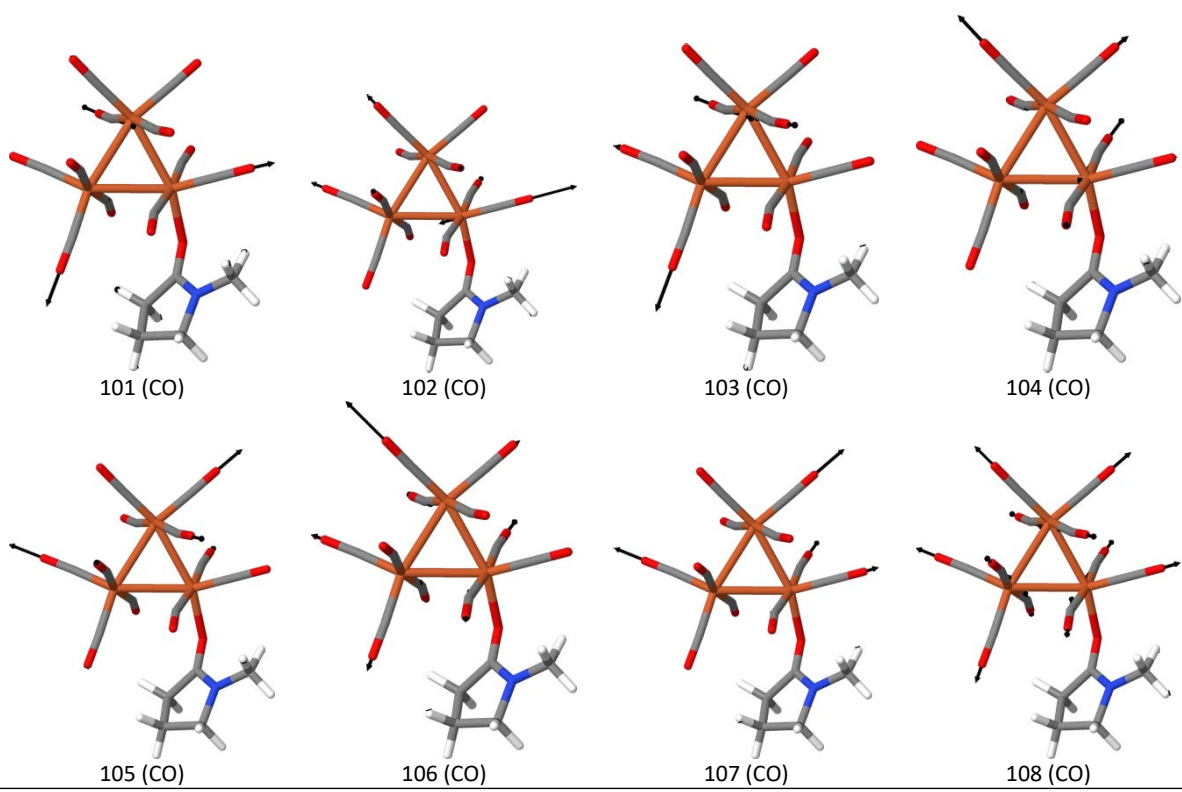
**Table S3:** Simulated vibrational normal modes of  $\text{Fe}_3(\text{CO})_{11}\text{NMP}$  associated to CO-stretching, i.e. to the carbonyl group of NMP (mode 97), to the bridging CO ligands (modes 98 and 99) and to the terminal CO ligands (modes 100-108). Predicted frequencies ( $\tilde{\nu}_{\text{CO}}$ ; unscaled and scaled by a factor of 0.97)<sup>21,25</sup> and IR intensities ( $I_{\text{IR}}$ ) are given for the three isomers, i.e., A, B and C.

Mode	A ( $\Delta G = 14.2 \text{ kJ mol}^{-1}$ )			B ( $\Delta G = 0.0 \text{ kJ mol}^{-1}$ )			C ( $\Delta G = 15.1 \text{ kJ mol}^{-1}$ )		
	$\tilde{\nu}_{\text{CO}} / \text{cm}^{-1}$	$\tilde{\nu}_{\text{CO}}^{\text{scaled}} / \text{cm}^{-1}$	$I_{\text{IR}} / \text{km mol}^{-1}$	$\tilde{\nu}_{\text{CO}} / \text{cm}^{-1}$	$\tilde{\nu}_{\text{CO}}^{\text{scaled}} / \text{cm}^{-1}$	$I_{\text{IR}} / \text{km mol}^{-1}$	$\tilde{\nu}_{\text{CO}} / \text{cm}^{-1}$	$\tilde{\nu}_{\text{CO}}^{\text{scaled}} / \text{cm}^{-1}$	$I_{\text{IR}} / \text{km mol}^{-1}$
97 (CO <sub>NMP</sub> )	1681	1631	1144	1680	1629	1206	1707	1656	1427
98 (CO <sub>μ2</sub> )	1868	1812	967	1978	1918	389	1894	1837	1054
99 (CO <sub>μ2</sub> )	1924	1867	656	1994	1934	476	1932	1874	532
100 (CO)	2030	1969	124	2016	1955	24	2010	1950	122
101 (CO)	2033	1972	514	2023	1962	414	2027	1966	679
102 (CO)	2042	1981	111	2030	1969	431	2035	1974	808
103 (CO)	2048	1987	688	2037	1976	1501	2041	1980	300
104 (CO)	2050	1988	141	2047	1986	575	2051	1989	205
105 (CO)	2061	2000	2673	2051	1990	2237	2058	1997	2367
106 (CO)	2064	2002	1854	2066	2004	2029	2070	2008	2649
107 (CO)	2074	2012	3592	2069	2007	3523	2077	2015	2785
108 (CO)	2147	2082	270	2145	2080	216	2145	2081	105

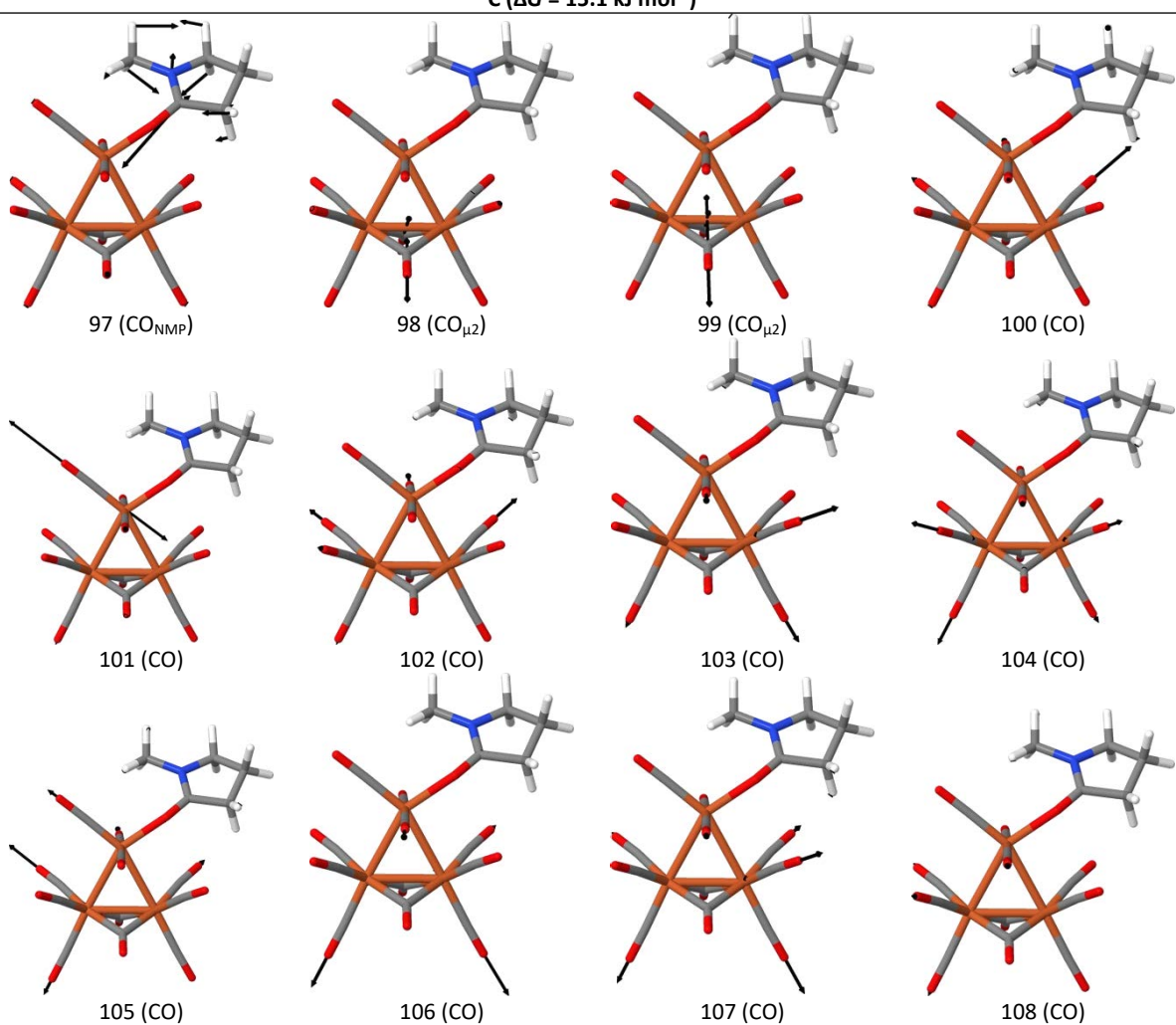


Table S4: Vibrational normal modes of three isomers of  $\text{Fe}_3(\text{CO})_{11}\text{NMP}$  associated to CO-stretching, i.e. to the carbonyl group of NMP (mode 97), to the bridging CO ligands (modes 98 and 99) and to the terminal CO ligands (modes 100-108) as visualized by displacement vectors.





**C ( $\Delta G = 15.1 \text{ kJ mol}^{-1}$ )**



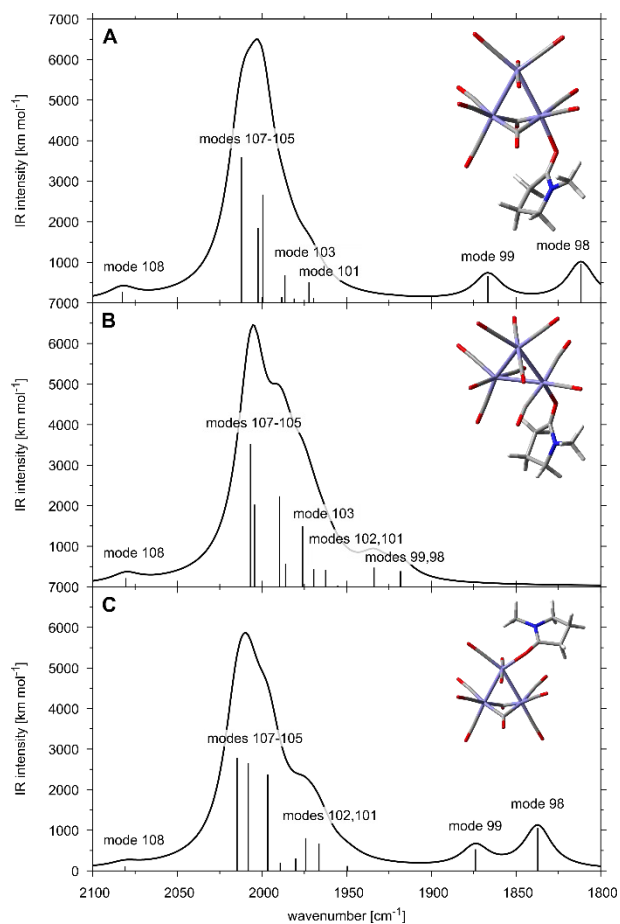


**Figure S18. Simulated IR spectra of the three isomers of  $\text{Fe}_3(\text{CO})_{11}\text{NMP}$ , i.e., A, B and C. Prominent vibrational modes are labeled.**

## References

- 1 a) COLLECT Data Collection Software and Nonius B.V., Netherlands, 1998; b) Z. Otwinowski, Minor, W. in Carter, C. W. and Sweet, R. M. (eds.), *Processing of X-Ray Diffraction Data Collected in Oscillation Mode. Methods in Enzymology, Vol. 276, Macromolecular Crystallography, Part A*, Academic Press, 1997, 307; c) Bruker-AXS inc., *SADABS 2.10*, Madison, WI, U.S.A, 2002;
- 2 G. M. Sheldrick, *Acta Crystallogr., Sect. A: Found. Crystallogr.*, 2015, **71**, 3.
- 3 G. M. Sheldrick, *Acta Crystallogr. Sect. C: Struct Chem*, 2015, **71**, 3.
- 4 C. F. Macrae, P. R. Edgington, P. McCabe, E. Pidcock, G. P. Shields, R. Taylor, M. Towler and J. van de Streek, *J. Appl. Crystallogr.*, 2006, **39**, 453.
- 5 Y. Si, M. Hu and C. Chen, *C.R. Chim.*, 2008, **11**, 932.
- 6 a) A. L. Haley, L. N. Broadbent, L. S. McDaniel, S. T. Heckman, C. H. Hinkle, N. N. Gerasimchuk, J. C. Hershberger and C. A. Mebi, *Polyhedron*, 2016, **114**, 218; b) H. T. Poh, B. T. Sim, T. S. Chwee, W. K. Leong and W. Y. Fan, *Organometallics*, 2014, **33**, 959;
- 7 X. Jiang, L. Long, H. Wang, L. Chen and X. Liu, *Dalton Trans.*, 2014, **43**, 9968.
- 8 U.-P. Apfel, Y. Halpin, H. Görls, J. G. Vos, B. Schweizer, G. Linti and W. Weigand, *C&B*, 2007, **4**, 2138.
- 9 L. Song, Q. Hu, Q. Dong and J. Wang, *Chin. J. Inorg. Chem.*, 1990, **6**, 256.
- 10 P. I. Volkers, T. B. Rauchfuss and S. R. Wilson, *Eur. J. Inorg. Chem.*, 2006, 4793.
- 11 L. Schwartz, P. S. Singh, L. Eriksson, R. Lomoth and S. Ott, *C.R. Chim.*, 2008, **11**, 875.
- 12 E. D. Schermer and W. H. Baddley, *J. Organomet. Chem.*, 1971, **30**, 67.
- 13 S. Lü, S. Gong, G.-H. Xu, Y.-Y. Liu, L. Lü, C.-R. Qin and Q.-L. Li, *Inorg. Chim. Acta*, 2020, **511**, 119797.
- 14 F. Wen, X. Wang, L. Huang, G. Ma, J. Yang and C. Li, *ChemSusChem*, 2012, **5**, 849.
- 15 R. Goy, L. Bertini, H. Görls, L. de Gioia, J. Talarmin, G. Zampella, P. Schollhammer and W. Weigand, *Chem. Eur. J.*, 2015, **21**, 5061.
- 16 S. Benndorf, E. Hofmeister, M. Wächtler, H. Görls, P. Liebing, K. Peneva, S. Gräfe, S. Kupfer, B. Dietzek-Ivanšić and W. Weigand, *Eur. J. Inorg. Chem.*, 2022, **3**, e202100959.
- 17 A. P. S. Samuel, D. T. Co, C. L. Stern and M. R. Wasielewski, *J. Am. Chem. Soc.*, 2010, **132**, 8813.
- 18 M. J. Frisch, G. W. Trucks, H. B. Schlegel, G. E. Scuseria, M. A. Robb, J. R. Cheeseman, G. Scalmani, V. Barone, G. A. Petersson, H. Nakatsuji, X. Li, M. Caricato, A. V. Marenich, J. Bloino, B. G. Janesko, R. Gomperts, B. Mennucci, H. P. Hratchian, J. V. Ortiz, A. F. Izmaylov, J. L. Sonnenberg, Williams, F. Ding, F. Lipparini, F. Egidi, J. Goings, B. Peng, A. Petrone, T. Henderson, D. Ranasinghe, V. G. Zakrzewski, J. Gao, N. Rega, G. Zheng, W. Liang, M. Hada, M. Ehara, K. Toyota, R. Fukuda, J. Hasegawa, M. Ishida, T. Nakajima, Y. Honda, O. Kitao, H. Nakai, T. Vreven, K. Throssell, J. A. Montgomery Jr., J. E. Peralta, F. Ogliaro, M. J. Bearpark, J. J. Heyd, E. N. Brothers, K. N. Kudin, V. N. Staroverov, T. A. Keith, R. Kobayashi, J. Normand, K. Raghavachari, A. P. Rendell, J. C. Burant, S. S. Iyengar, J. Tomasi, M. Cossi, J. M. Millam, M. Klene, C. Adamo, R. Cammi, J. W. Ochterski, R. L. Martin, K. Morokuma, O. Farkas, J. B. Foresman and D. J. Fox, *Gaussian 16 Rev. B.01*, Wallingford, CT, 2016.
- 19 a) A. D. Becke, *J. Chem. Phys.*, 1993, **98**, 5648; b) Lee, Yang and Parr, *Phys. Rev. B: Condens. Matter*, 1988, **37**, 785;
- 20 a) F. Weigend and R. Ahlrichs, *PCCP*, 2005, **7**, 3297; b) F. Weigend, *PCCP*, 2006, **8**, 1057;
- 21 J. P. Merrick, D. Moran and L. Radom, *J. Phys. Chem. A*, 2007, **111**, 11683.
- 22 a) P. Buday, C. Kasahara, E. Hofmeister, D. Kowalczyk, M. K. Farh, S. Riediger, M. Schulz, M. Wächtler, S. Furukawa, M. Saito, D. Ziegenbalg, S. Gräfe, P. Bäuerle, S. Kupfer, B. Dietzek-Ivanšić and W. Weigand, *Angew. Chem. Int. Ed.*, 2022, **61**, e202202079; b) H. Abul-Futouh, Y. Zagranjarski, C. Müller, M. Schulz, S. Kupfer, H. Görls, M. El-khateeb, S. Gräfe, B. Dietzek, K. Peneva and W. Weigand, *Dalton Trans.*, 2017, **46**, 11180; c) P. Buday, P. Seeber, C. Zens, H. Abul-

- Futouh, H. Görls, S. Gräfe, P. Matczak, S. Kupfer, W. Weigand and G. Mloston, *Chem. Eur. J.*, 2020, **26**, 11412; d) P. E. M. Siegbahn and R.-Z. Liao, *J. Phys. Chem. A*, 2020, **124**, 10540;
- 23 a) B. Mennucci, C. Cappelli, C. A. Guido, R. Cammi and J. Tomasi, *J. Phys. Chem. A*, 2009, **113**, 3009; b) A. V. Marenich, C. J. Cramer and D. G. Truhlar, *J. Phys. Chem. B*, 2009, **113**, 6378;
- 24 S. Grimme, S. Ehrlich and L. Goerigk, *J. Comput. Chem.*, 2011, **32**, 1456.
- 25 R. D. Johnson, *Computational Chemistry Comparison and Benchmark Database, NIST Standard Reference Database 101*, 2011.

7.5 [SB-5]

**[SB-5] Neue Synthesemethode zur Herstellung zweikerniger  
Eisenhexacarbonylkomplex mit schwefel-, selen- oder tellurhaltigen Liganden**

Stefan Benndorf<sup>1</sup> and Wolfgang Weigand<sup>2</sup>

*Offenlegungsschrift, DE 10 2021 001 823 A1, 06.10.2022.*

<https://worldwide.espacenet.com/patent/search/family/083282764/publication/DE102021001823A1?q=DE102021001823A1>



(12) **Offenlegungsschrift**

(21) Aktenzeichen: **10 2021 001 823.0**

(22) Anmeldetag: **01.04.2021**

(43) Offenlegungstag: **06.10.2022**

(51) Int Cl.: **C07F 15/02 (2006.01)**

<p>(71) Anmelder: <b>Friedrich-Schiller-Universität Jena, 07743 Jena, DE</b></p> <p>(72) Erfinder: <b>Benndorf, Stefan, 07743 Jena, DE; Weigand, Wolfgang, Prof. Dr., 80638 München, DE</b></p> <p>(56) Ermittelte Stand der Technik: <b>CAHIEZ, Gérard, AVEDISSIAN, Hovsep: Highly Stereo- and Chemoselective Alkenylation of</b></p>	<p><b>Organomagnesium Compounds. In: Synthesis 1998, 1199 - 1205.</b> <b>MUNOZ III, Salvador B. [et al.]: The N-Methylpyrrolidone (NMP) Effect in Iron-Catalyzed Cross-Coupling with Simple Ferric Salts and MeMgBr. In: Angew. Chem. 2018, Vol. 130, S. 6606 - 6610.</b> <b>WANG, Jun-Hao [et al.]: Solvent-Assisted Metal Metathesis: A Highly Efficient and Versatile Route towards Synthetically Demanding Chromium Metal–Organic Frameworks. In: Angew. Chem. Int. Ed. 2017, Vol. 56, S. 6478 - 6482.</b></p>
--	--

Rechercheantrag gemäß § 43 PatG ist gestellt.

**Die folgenden Angaben sind den vom Anmelder eingereichten Unterlagen entnommen.**

(54) Bezeichnung: **Neue Synthesemethode zur Herstellung zweikerniger Eisenhexacarbonylkomplexe mit schwefel-, selen- oder tellurhaltigen Liganden**

(57) Zusammenfassung: Neue energieeffiziente Synthese von zweikernigen Eisenhexacarbonylkomplexen mit schwefel-, selen- oder tellurhaltigen Liganden zur potenziellen Anwendung als Katalysator zur Wasserstoffherstellung oder als Kohlenmonoxid freisetzender pharmakologischer Wirkstoff (CO-releasing molecule CORM).

Aufgabe war es eine möglichst effiziente Methode zur Herstellung der Eisenhexacarbonylkomplexe zu finden, die unter möglichst milden Bedingungen und hohen Ausbeuten abläuft.

Dabei wurde überraschend festgestellt, dass N-Methyl-2-pyrrolidon (NMP) als Additiv in der Lage ist, diese Bedingungen zu erfüllen.

## Beschreibung

**[0001]** Die Erfindung betrifft eine neue Synthesemethode zur Herstellung spezieller zweikerniger Hexacarbonylverbindungen des Eisens mit schwefel-, selen- oder tellurhaltigen Liganden.

**[0002]** Molekularer Wasserstoff wird als nachhaltiger Energieträger der Zukunft angesehen (S. Singh; S. Jain; V. PS; A. K. Tiwari; M. R. Nouni; J. K. Pandey; S. Goel: Hydrogen: A sustainable fuel for future of the transport sector, Renewable and Sustainable Energy Reviews 2015, 51, 623-633).

**[0003]** In der Natur nutzen Eukaryoten und anaerobe Mikroorganismen wie Bakterien und Archaeen Wasserstoff als primären Energieträger (P. M. Vignais, B. Billoud, J. Meyer: Classification and phylogeny of hydrogenases, FEMS Microbiology Reviews, 2001, 455-501).

**[0004]** Die Organismen nutzen Hydrogenasen, eine spezielle Klasse von Metallenzymen, um die Reduktion von Protonen zu Wasserstoff, sowie die Rückreaktion, zu katalysieren (P. M. Vignais; B. Billoud: Occurrence, classification, and biological function of hydrogenases: an overview, Chemical reviews 2007, 107, 4206-4272).

**[0005]** Die Bestimmung der Struktur des aktiven Zentrums des Hydrogenaseenzym, der allgemeinen Form  $\text{Fe}_2(\mu\text{-SR})_2(\text{CN})_2(\text{CO})_3\text{L}_n$  (L =  $\text{H}_2\text{O}$  und ein cysteinerverknüpfter  $\text{Fe}_4\text{S}_4(\text{SR})_4$ -cluster), aus dem Bakterium *Desulfovibrio desulfuricans* (J. W. Peters; W. N. Lanzilotta; B. J. Lemon; L. C. Seefeldt: X-ray crystal structure of the Fe-only hydrogenase (Cpl) from *Clostridium pasteurianum* to 1.8 angstrom resolution, Science 1998, 282, 1853-1858) erfolgte 1998.

**[0006]** Die große Ähnlichkeit des aktiven Zentrums zu den bereits in den späten 1920er Jahren synthetisierten thiolatverbrückten Dieisenhexacarbonylkomplexen (H. Reihlen, A. Gruhl, G. v. Hessling: Über den photochemischen und oxydativen Abbau von Carbonylen, Justus Liebig's Annalen der Chemie 1929, 268-287; H. Reihlen, A. v. Friedolsheim, W. Oswald: Über Stickoxyd- und Kohlenoxydverbindungen des scheinbar einwertigen Eisens und Nickels. Zugleich Erwiderung an die Herren W. Manchot und W. Hieber, Justus Liebig's Annalen der Chemie 1928, 72-96) führte zur gezielten Erforschung der so genannten „Fe-only Hydrogenase“ der allgemeinen Formel (I).

**[0007]** Zahlreiche Synthesen von [FeFe]-Hydrogenasemodellkomplexen der allgemeinen Formel (I) folgten. Die organischen Reste R und R' können von aliphatischer, olefinischer oder aromatischer Natur sein. (Y. Li; T. B. Rauchfuss: Synthesis of Diiron(I) Dithiolato Carbonyl Complexes, Chemical reviews 2016, 116, 7043-7077; S. Gao; Y. Liu; Y. Shao; D. Jiang; Q. Duan: Iron carbonyl compounds with aromatic dithiolate bridges as organometallic mimics of [FeFe] hydrogenases, Coordination Chemistry Reviews 2020, 402, 213081; S. Gao; W. Fan; Y. Liu; D. Jiang; Q. Duan: Artificial water-soluble systems inspired by [FeFe]-hydrogenases for electro- and photocatalytic hydrogen production, International Journal of Hydrogen Energy 2020, 45, 4305-4327).

**[0008]** [FeFe]-Hydrogenasemodellkomplexe haben das Potential als Katalysatoren zur energieeffizienten Herstellung von elementarem Wasserstoff ( $\text{H}_2$ ) zu dienen. Zahlreiche Publikationen zeigen, dass diese Art von Katalysatoren in der Lage sind mithilfe eines angelegten Potentials (Elektrolyse) (M. Watanabe; K. Goto; T. Miyazaki; M. Shibahara; Y. J. Chang; T. J. Chow; T. Ishihara: Electrocatalytic hydrogen production using [FeFe]-hydrogenase mimics based on tetracene derivatives, New Journal of Chemistry 2019, 43, 13810-13815) oder durch Bestrahlung (Photokatalyse) (J.-X. Jian; Q. Liu; Z.-J. Li; F. Wang; X.-B. Li; C.-B. Li; B. Liu; Q.-Y. Meng; B. Chen; K. Feng; C.-H. Tung; L.-Z. Wu: Chitosan confinement enhances hydrogen photogeneration from a mimic of the diiron subsite of FeFe-hydrogenase, Nature communications 2013, 4, 2695; X.-B. Li; J.-X. Jian; X.-Z. Wang; Y. Wang; S.-G. Xia; C.-H. Tung; L.-Z. Wu: Per-6-Thiol-Cyclodextrin Engineered [FeFe]-Hydrogenase Mimic/CdSe Quantum Dot Assembly for Photocatalytic Hydrogen Production, Solar RRL 2020, 2000474) Wasserstoff herzustellen.

**[0009]** Dabei wurde die katalytische Aktivität des natürlichen Enzyms von 10 000 Molekülen  $\text{H}_2$  pro Sekunde (E. C. Hatchikian; N. Forget; V. M. Fernandez; R. Williams; R. Cammack: Further characterization of the Fe-hydrogenase from *Desulfovibrio desulfuricans* ATCC 7757, European Journal of Biochemistry 1992, 209, 357-365) bis heute nicht erreicht.

**[0010]** Nach der Entdeckung der Licht-induzierten, Enzym-katalysierten oder Ligandenaustauschinduzierten Kohlenmonoxid-Freisetzung von [FeFe]-Komplexen folgten zahlreiche Studien über den Einsatz als pharma-

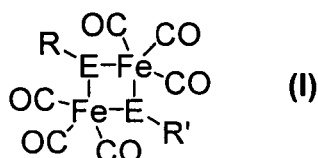


kologischer Wirkstoff (M. Faizan; N. Muhammad; K. U. K. Niazi; Y. Hu; Y. Wang; Y. Wu; H. Sun; R. Liu; W. Dong; W. Zhang; Z. Gao: CO-Releasing Materials: An Emphasis on Therapeutic Implications, as Release and Subsequent Cytotoxicity Are the Part of Therapy, Materials (Basel, Switzerland) 2019, 12, 1643; Z. Xiao; R. Jiang; J. Jin; X. Yang; B. Xu; X. Liu; Y. He; Y. He: Diiron(ii) pentacarbonyl complexes as CO-releasing molecules: their synthesis, characterization, CO-releasing behaviour and biocompatibility, Dalton Trans 2019, 48, 468-477; X. Jiang; Z. Xiao; W. Zhong; X. Liu: Brief survey of diiron and monoiron carbonyl complexes and their potentials as CO-releasing molecules (CORMs), Coordination Chemistry Reviews 2020, 213634).

**[0011]** Kohlenmonoxid (CO) kann aufgrund seiner vielfältigen physiologischen Eigenschaften als breit anwendbares Therapeutikum fungieren.

**[0012]** CO wirkt unter anderem gefäßerweiternd und antiinflammatorisch. Es kann die Abstoßung von transplantierten Organen unterdrücken und fördert den Schutz vor ischämischer Gewebeschädigung (K. Ling; F. Men; W.-C. Wang; Y.-Q. Zhou; H.-W. Zhang; D.-W. Ye: Carbon Monoxide and Its Controlled Release: Therapeutic Application, Detection, and Development of Carbon Monoxide Releasing Molecules (CORMs), Journal of medicinal chemistry 2018, 61, 2611-2635).

**[0013]** CO zählt neben Stickstoffmonoxid (NO) und Schwefelwasserstoff (H<sub>2</sub>S) zu den Gasotransmittern, einer Gruppe endogen gebildeter, gasförmiger Signalmoleküle (A. K. Mustafa; M. M. Gadalla; S. H. Snyder: Signaling by gasotransmitters, Science signaling 2009, 2, 1-17).



E = S, Se, Te

wobei R und R' gleiche oder unterschiedliche Substituenten der Klassifizierung: Alkyl-, Cycloalkyl-, Aryl- oder Heteroarylverbindungen, Heterozyklen, Alkohole, Mercaptane, Amine, Nitrile, Carbonsäuren, Amide, Imide, Hydroxamsäuren, Aminosäuren, Zucker, Ether, Thioether, Ketone, Thioketone, Aldehyde, Thioaldehyde, Ester, Imidine, Amidine, Carbonsäurechloride, Carbonsäureanhydride, Sulfonsäuren, Sulfoxide, Sulfonamide, Sulfone, Azide, Carbonsäureazide, Peptide, Lactone, Thiolactone sein können.

**[0014]** Nach heutigem Stand der Technik erfolgt die Synthese der Komplexe der allgemeinen Formel (I) vorwiegend über folgende Wege (Y. Li; T. B. Rauchfuss: Synthesis of Diiron(I) Dithiolato Carbonyl Complexes, Chemical reviews 2016, 116, 7043-7077):

Umsetzung des Liganden (REER', REH, RECN) mit Triisendodecacarbonyl in trockenem, siedendem Lösungsmittel (u.a. Toluol, Tetrahydrofuran, Dichlormethan) (II).

**[0015]** Diese Umsetzung zeichnet sich durch lange Reaktionszeiten, von 30 Minuten bis vier Stunden, bevorzugt ein bis zwei Stunden, und hohe Temperaturen, 40 - 110 °C, bevorzugt 66 °C (Tetrahydrofuran) oder 110 °C (Toluol) aus. Aufgrund der sehr guten Ausbeuten, welche bis über 90 % betragen können, (Y. Li; T. B. Rauchfuss: Synthesis of Diiron(I) Dithiolato Carbonyl Complexes, Chemical reviews 2016, 116, 7043-7077) ist diese Methode gebräuchlich.

**[0016]** Umsetzung des Liganden (REER', REH) mit Dieisennonacarbonyl in trockenem Lösungsmittel (u.a. Toluol, Tetrahydrofuran, Dichlormethan) (II).

**[0017]** Diese Umsetzung erfolgt unter milderen Reaktionstemperaturen, 25 - 65 °C, bevorzugt 25 °C, als die Umsetzung oben und langen Reaktionszeiten, von einer bis zu 24 Stunden, bevorzugt zwei bis 18 Stunden. Die Ausbeuten sind im Vergleich zur Umsetzung oben vermindert (Y. Li; T. B. Rauchfuss: Synthesis of Diiron (I) Dithiolato Carbonyl Complexes, Chemical reviews 2016, 116, 7043-7077).

**[0018]** Umsetzung des Liganden (REER', REH) mit Eisenpentacarbonyl in trockenem Lösungsmittel (u.a. Toluol, Tetrahydrofuran, Dichlormethan) mitunter unter Bestrahlung (II).

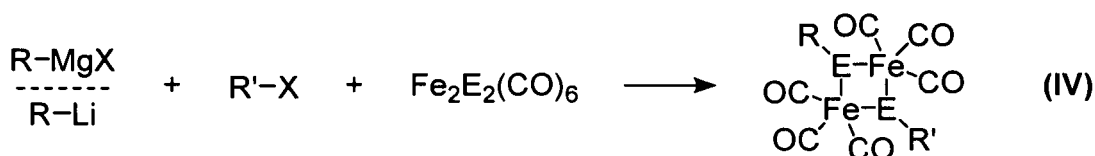
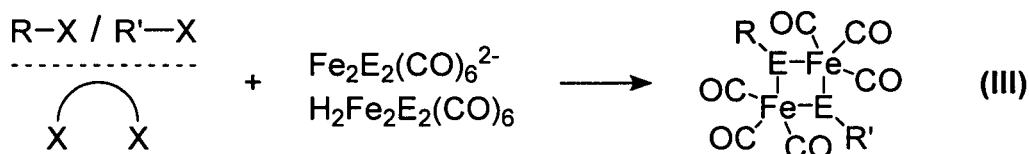
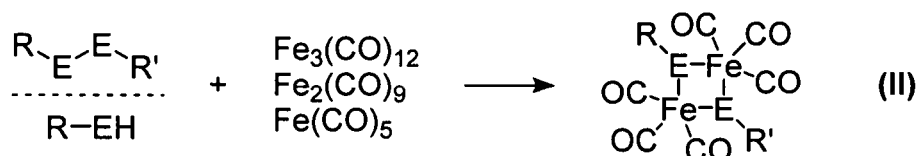
**[0019]** Diese Umsetzung erfolgt unter harschen Reaktionsbedingungen, 100 - 150 °C, bevorzugt 110 °C, und UV-Bestrahlung, und langen Reaktionszeiten, von bis zu 48 Stunden (J. Wang; T. Zhang; S. Jiang; X. Ma; X. Shao; Di Wang; X. Li; B. Li: Catalytic reduction of 1,4-benzoquinone to hydroquinone via [FeFe]-hydrogenase model complexes under mild conditions, Journal of Chemical Technology & Biotechnology 2020; M. M. van Dyk; P. H. van Rooyen; S. Lotz: Iron carbene complexes Part 4. Substitution reactions of diiron carbene complexes with P(OMe)<sub>3</sub>, PPh<sub>3</sub> and tBuNC ligands, Inorganica Chimica Acta 1989, 163, 167-172). Die Ausbeuten sind vermindert im Vergleich zur ersten Umsetzung oben. Dies ist auf die geringere Reaktivität des Eisenpentacarbonyl zurückzuführen. (N. S. Nametkin; v.d. Tyurin; M. A. Kukina: Synthesis and some properties of sulfur-containing iron tricarbonyl complexes, Journal of Organometallic Chemistry 1978, 149, 355-370).

**[0020]** Umsetzung eines Liganden mit entsprechender Abgangsgruppe (Cl, Br, I, Tos) und zweifach reduziertem (protoniertem) Hexacarbonyldieisendichalkogenid (III).

**[0021]** Diese Umsetzung erfolgt bei bei -78 °C und langen Reaktionszeiten, von einer bis zu 24 Stunden, bevorzugt 14 - 18 Stunden (Y. Tang; Z. Wei; W. Zhong; X. Liu: Diiron Complexes with Pendant Phenol Group (s) as Mimics of the Diiron Subunit of [FeFe]-Hydrogenase: Synthesis, Characterisation, and Electrochemical Investigation, European Journal of Inorganic Chemistry 2011, 2011, 1112-1120).

**[0022]** Umsetzung einer Grignard- oder Organolithium-Verbindung und einer organischen Halogenverbindung mit Hexacarbonyldieisendichalkogenid (IV).

**[0023]** Diese Umsetzung erfolgt bei -78 °C, mitunter in sehr guten Ausbeuten, welche über 90 % betragen können (D. Seyferth; R. S. Henderson; L.-C. Song; G. B. Womack: Chemistry of  $\mu$ -dithiobis(tricarbonyliron), an inorganic mimic of organic disulfides, Journal of Organometallic Chemistry 1985, 292, 9-17).

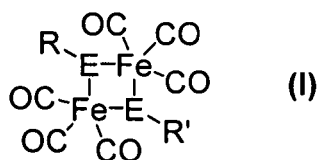


**[0024]** Zusammenfassend ist festzustellen, dass die Synthese von Eisenhexacarbonylkomplexen der allgemeinen Form  $[\text{Fe}_2(\mu\text{-ER})_2(\text{CO})_6]$  (E = S, Se, Te) bisher zeit- und energieaufwändig ist.

**[0025]** Aufgabe war es, eine möglichst effiziente Methode zur Herstellung der Eisenhexacarbonylkomplexe zu finden, die unter möglichst milden Bedingungen und hohen Ausbeuten abläuft.

**[0026]** Überraschend wurde festgestellt, dass N-Methyl-2-pyrrolidon (NMP) als Additiv in der Lage ist, diese Bedingungen zu erfüllen.

**[0027]** Erfindungsgemäß wird die Aufgabe durch ein Verfahren zur Herstellung von zweikernigen Eisenhexacarbonylkomplexen der Formel (I)



E = S, Se, Te

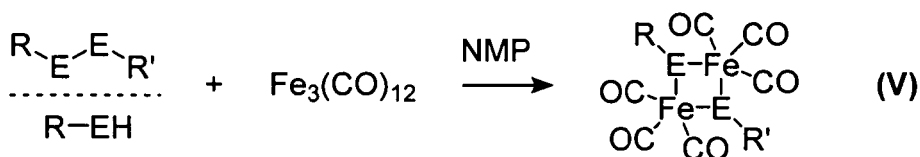
gelöst, wobei R und R' gleiche oder unterschiedliche Substituenten der Klassifizierung:

Alkyl-, Cycloalkyl-, Aryl- oder Heteroarylverbindungen, Heterozyklen, Alkohole, Mercaptane, Amine, Nitrile, Carbonsäuren, Amide, Imide, Hydroxamsäuren, Aminosäuren, Zucker, Ether, Thioether, Ketone, Thioketone, Aldehyde, Thioaldehyde, Ester, Imidine, Amidine, Carbonsäurechloride, Carbonsäureanhydride, Sulfonsäuren, Sulfoxide, Sulfonamide, Sulfone, Azide, Carbonsäureazide, Peptide, Lactone, Thiolactone,

bevorzugt Alkyl-, Cycloalkyl-, Aryl- oder Heteroarylverbindungen, Heterozyklen, Alkohole, Amine, Nitrile, Carbonsäuren, Amide, Imide, Hydroxamsäuren, Aminosäuren, Zucker, Ether, Ketone, Aldehyde, Ester, Imidine, Amidine, Sulfonsäuren, Sulfoxide, Sulfonamide, Sulfone, Azide, Peptide, Lactone sein können,

dadurch gekennzeichnet, dass eine Reaktion in Anwesenheit von N-Methyl-2-pyrrolidon (NMP) durchgeführt wird.

**[0028]** Die neue leistungsfähige Methode (V) zeichnet sich durch milde Reaktionsbedingungen, sehr kurze Reaktionszeiten, eine hohe Selektivität, breiter Anwendbarkeit und unkomplizierte Isolierung der Produkte aus.



**[0029]** Zudem ermöglicht sie die Synthese einiger neuer, auf herkömmliche Weise nicht herstellbarer, Komplexe (Vergleich Fallbeispiel XIV). Dies ist, unter anderem, auf die löslichkeitsvermittelnden Eigenschaften von NMP zurückzuführen.

**[0030]** NMP reagiert mit Trieisendodecacarbonyl bereits unter milden Bedingungen zu Sauerstoffempfindlichen Verbindungen.

**[0031]** Neben der Aktivierung des Trieisendodecacarbonyls, zeigt die Verwendung von NMP als Additiv weiterhin eine Verbesserung der Löslichkeit von schwerlöslichen Liganden (A. Jouyban; M. A. A. Fakhree; A. Shayanfar: Review of pharmaceutical applications of N-methyl-2-pyrrolidone, Journal of Pharmacy & Pharmaceutical Sciences 2010, 13, 524-535), was zu einer besseren Reaktivität führt (Vergleich Fallbeispiel VII).

**[0032]** Die Reaktion erfolgt in Toluol mit 3 - 60 Vol% NMP, bevorzugt 5 - 20 Vol%, besonders bevorzugt 9 - 10 Vol%, bei 25 °C bis 90 °C, bevorzugt bei 40 - 60 °C, besonders bevorzugt bei 50 °C. Die besonders bevorzugten Bedingungen erzielen hierbei Ausbeuten von 30 - 95 %. Abweichende Bedingungen erzielen hierbei Ausbeuten von 26 - 66 %. Dabei kann die sichtbare Reaktion, ein Farbumschlag von dunkelgrün nach dunkelrot, bereits nach 3 - 30 Minuten, bevorzugt 5 - 25 Minuten, besonders bevorzugt 10 - 15 Minuten, einsetzen. Die Ausbeuten sind zumeist größer oder vergleichbar zu literaturbekannten Methoden.

**[0033]** Die Erfindung soll nachstehend anhand von literaturbekannten Verbindungen Formel VI bis Formel XIII sowie von literaturunbekannten Verbindungen Formel XIV und Formel XVI näher erläutert werden. Die Synthese der Verbindung (VII) wurde bereits aus der Umsetzung von zweifach reduziertem Hexacarbonyldieisendisulfid mit Ethylenoxid (L. Song; Q. Hu; Q. Dong; J. Wang: Isolation and characterization of corresponding products of nucleophilic ring-opening of ethylene oxide and epichlorohydrin by  $(\mu\text{-RS})(\mu\text{-XMgS})\text{Fe}_2(\text{CO})_6$  or  $(\mu\text{-LiS})_2\text{Fe}_2(\text{CO})_6$ , Wuji Huaxue Xuebao 1990, 6, 256-260) beschrieben und erfolgte nun erstmalig über Syntheseroute (II).

**[0034]** Das Produkt (VII) kann aus 2-Mercaptoethanol und in gleicher Weise aus Bis-(2-hydroxyethyl)-disulfid dargestellt werden.

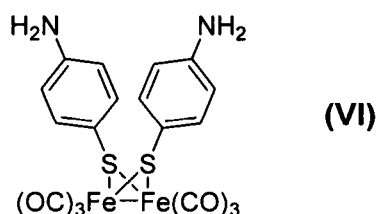
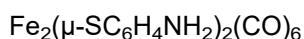
**[0035]** Aufgrund der geringeren Reaktivität von Bis-(2-hydroxyethyl)-disulfid (N. S. Nametkin; v.d. Tyurin; M. A. Kukina: Synthesis and some properties of sulfur-containing iron tricarbonyl complexes, Journal of Organometallic Chemistry 1978, 149, 355-370) ist die Reaktionszeit im 2. Versuch im Vergleich zum 1. Versuch bei der Synthese der Verbindung (VII) deutlich erhöht.

**[0036]** Bei der Synthese der Verbindung (XIII) wurde festgestellt, dass sich im Gegensatz zu bekannten Methoden nur das anti-Produkt gebildet hatte (S. Lü; S. Gong; G.-H. Xu; Y.-Y. Liu; L. Lü; C.-R. Qin; Q.-L. Li: Synthesis, characterization, and electrochemical properties of diiron bis(monotellurolate) carbonyls related to [FeFe]-hydrogenases, Inorganica Chimica Acta 2020, 511, 119797).

**[0037]** Alle Lösungsmittel wurden vor den Reaktionen nach bekannten Techniken getrocknet und entgast oder in entsprechender Qualität von Fischer, Sigma Aldrich oder TCI bezogen.

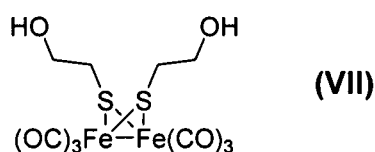
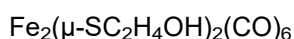
**[0038]** Literaturbekannte Verbindungen:

Bis( $\mu$ -4-aminophenylthiolato-S)-hexacarbonyldieisen(I)



In einem Schlenkgefäß wurde 4,4'-Dithiodianiline (100 mg, 403  $\mu\text{mol}$ ) vorgelegt und dreimal mit Stickstoff sekuriert. Nach Zugabe von 5 mL Toluol und 0,5 mL N-Methyl-2-pyrrolidon wurde auf 50 °C erhitzt. Zur entstandenen Lösung wurden Trieisendodecacarbonyl (203 mg, 403  $\mu\text{mol}$ ) in Substanz zugegeben und gerührt. Innerhalb von 10 min erfolgte ein Farbumschlag von dunkelgrün nach rot. Mittels Dünnschichtchromatographie konnte kein Trieisendodecacarbonyl mehr nachgewiesen werden und die Reaktion wurde beendet. Nach säulenchromatographischer Aufreinigung Cyclohexan/THF (4:1), konnte das Produkt als roter Feststoff (202 mg, 382  $\mu\text{mol}$ , 95 %) erhalten werden.

Bis( $\mu$ -2-hydroxyethylthiolato-S)-hexacarbonyldieisen(I)

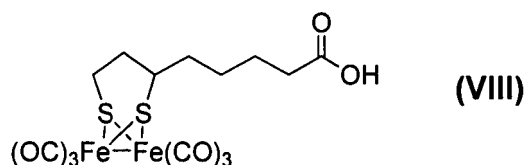
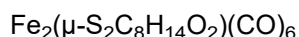


**[0039]** In einem dreimal mit Stickstoff sekuriertem Schlenkgefäß wurde 2-Mercaptoethanol (100 mg, 1,28 mmol) vorgelegt. Nach Zugabe von 10 mL Toluol und 1 mL N-Methyl-2-pyrrolidon wurde auf 50 °C erhitzt. Zur entstandenen Lösung wurden Trieisendodecacarbonyl (322 mg, 640  $\mu\text{mol}$ ) in Substanz zugegeben und gerührt. Innerhalb von 3 min erfolgte ein Farbumschlag von dunkelgrün nach rot. Mittels Dünnschichtchromatographie konnte kein Trieisendodecacarbonyl mehr nachgewiesen werden und die Reaktion wurde beendet. Nach säulenchromatographischer Aufreinigung Cyclohexan/THF (6:1), konnte das Produkt als roter Feststoff (182 mg, 419  $\mu\text{mol}$ , 65 %) erhalten werden.

**[0040]** In einem dreimal mit Stickstoff sekuriertem Schlenkgefäß wurde Bis-(2-hydroxyethyl)-disulfid (100 mg, 648  $\mu\text{mol}$ ) vorgelegt. Nach Zugabe von 10 mL Toluol und 1 mL N-Methyl-2-pyrrolidon wurde auf 50 °C erhitzt. Zur entstandenen Lösung wurden Trieisendodecacarbonyl (326 mg, 648  $\mu\text{mol}$ ) in Substanz zugegeben und gerührt. Innerhalb von 15 min erfolgte ein Farbumschlag von dunkelgrün nach rot. Mittels Dünnschichtchromatographie konnte kein Trieisendodecacarbonyl mehr nachgewiesen werden und die Reaktion

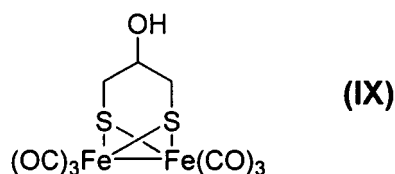
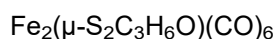
wurde beendet. Nach säulenchromatographischer Aufreinigung Cyclohexan/THF (6:1), konnte das Produkt als roter Feststoff (197 mg, 455  $\mu\text{mol}$ , 70 %) erhalten werden.

**[0041]** 5-(1,2-Dithiolan-3-yl)pentansäure-hexacarbonyldieisen(I)



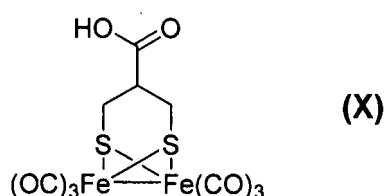
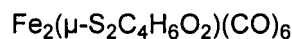
**[0042]** In einem Schlenkgefäß wurde 5-(1,2-Dithiolan-3-yl)pentansäure (100 mg, 485  $\mu\text{mol}$ ) vorgelegt und dreimal mit Stickstoff sekuriert. Nach Zugabe von 10 mL Toluol und 1 mL N-Methyl-2-pyrrolidon wurde auf 50 °C erhitzt. Zur entstandenen Lösung wurden Trieisendodecacarbonyl (244 mg, 485  $\mu\text{mol}$ ) in Substanz zugegeben und gerührt. Innerhalb von 30 min erfolgte ein Farbumschlag von dunkelgrün nach rot. Per Dünnschichtchromatographie konnte kein Trieisendodecacarbonyl mehr nachgewiesen werden und die Reaktion wurde beendet. Nach säulenchromatographischer Aufreinigung Cyclohexan/THF (6:1), konnte das Produkt als roter Feststoff (210 mg, 432  $\mu\text{mol}$ , 89 %) erhalten werden.

**[0043]** 1,3-dimercapto-2-hydroxypropan-hexacarbonyldieisen(I)



**[0044]** In einem Schlenkgefäß wurde 1,3-dimercapto-2-hydroxypropan-2-ol (100 mg, 805  $\mu\text{mol}$ ) vorgelegt und dreimal mit Stickstoff sekuriert. Nach Zugabe von 10 mL Toluol und 1 mL N-Methyl-2-pyrrolidon wurde auf 50 °C erhitzt. Zur entstandenen Lösung wurden Trieisendodecacarbonyl (405 mg, 805  $\mu\text{mol}$ ) in Substanz zugegeben und gerührt. Innerhalb von 10 min erfolgte ein Farbumschlag von dunkelgrün nach rot. Per Dünnschichtchromatographie konnte kein Trieisendodecacarbonyl mehr nachgewiesen werden und die Reaktion wurde beendet. Nach säulenchromatographischer Aufreinigung Cyclohexan/THF (6:1), konnte das Produkt als roter Feststoff (300 mg, 746  $\mu\text{mol}$ , 93 %) erhalten werden.

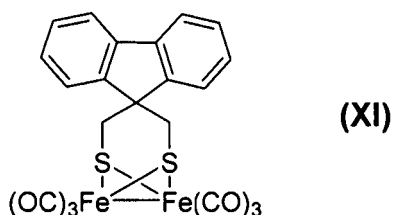
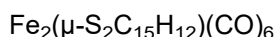
**[0045]** 3-Sulfanyl-2-(sulfanylmethyl)propansäure-hexacarbonyldieisen(I)



**[0046]** In einem Schlenkgefäß wurde 3-Sulfanyl-2-(sulfanylmethyl)propansäure (100 mg, 657  $\mu\text{mol}$ ) vorgelegt und dreimal mit Stickstoff sekuriert. Nach Zugabe von 10 mL Toluol und 1 mL N-Methyl-2-pyrrolidon wurde auf 50 °C erhitzt. Zur entstandenen Lösung wurden Trieisendodecacarbonyl (331 mg, 657  $\mu\text{mol}$ ) in Substanz zugegeben und gerührt. Innerhalb von 11 min erfolgte ein Farbumschlag von dunkelgrün nach rot. Per Dünnschichtchromatographie konnte kein Trieisendodecacarbonyl mehr nachgewiesen werden und die Reaktion wurde beendet. Die abgekühlte Reaktionslösung wurde mit 1 M Salzsäure gewaschen und die organische Phase mit 2 M Kaliumcarbonatlösung extrahiert. Nach Zugabe von 1 M Salzsäure bis zur sauren Reaktion wurde mit Toluol extrahiert (3 x 25 mL), die vereinigten organischen Phasen über Natriumsulfat

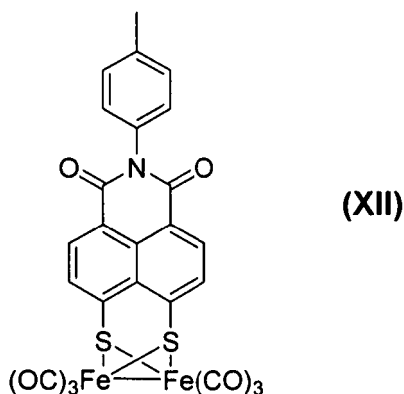
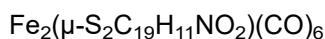
getrocknet und das Lösungsmittel im Vakuum entfernt. Das Produkt konnte als roter Feststoff (115 mg, 267  $\mu\text{mol}$ , 41 %) erhalten werden.

**[0047]** Spiro(fluoren-9,4'-[1,2]dithiolan)-hexacarbonyldieisen(I)



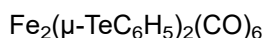
**[0048]** In einem Schlenkgefäß wurde Spiro(fluoren-9,4'-[1,2]dithiolan) (100 mg, 390  $\mu\text{mol}$ ) vorgelegt und dreimal mit Stickstoff sekuriert. Nach Zugabe von 10 mL Toluol und 1 mL N-Methyl-2-pyrrolidon wurde auf 50 °C erhitzt. Zur entstandenen Lösung wurden Trieisendodecacarbonyl (196 mg, 390  $\mu\text{mol}$ ) in Substanz zugegeben und gerührt. Innerhalb von 35 min erfolgte ein Farbumschlag von dunkelgrün nach rot. Per Dünnschichtchromatographie konnte kein Trieisendodecacarbonyl mehr nachgewiesen werden und die Reaktion wurde beendet. Nach säulenchromatographischer Aufreinigung Cyclohexan/THF (6:1), konnte das Produkt als roter Feststoff (62 mg, 116  $\mu\text{mol}$ , 30 %) erhalten werden.

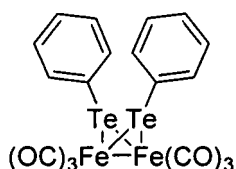
**[0049]** 6-(p-tolyl)-5H-[1,2]dithiolo[3',4',5':4,5]naphtho[1,8-cd]pyridin-5,7(6H)-dionhexacarbonyldieisen(I)



**[0050]** In einem Schlenkgefäß wurde 6-(p-tolyl)-5H-[1,2]dithiolo[3',4',5':4,5]naphtho[1,8-cd]pyridin-5,7(6H)-dion (200 mg, 572  $\mu\text{mol}$ ) vorgelegt und dreimal mit Stickstoff sekuriert. Nach Zugabe von 20 mL Toluol und 20 mL N-Methyl-2-pyrrolidon wurde auf 90 °C erhitzt. Zur entstandenen Lösung wurden Trieisendodecacarbonyl (288 mg, 572  $\mu\text{mol}$ ) in Substanz zugegeben und gerührt. Innerhalb von 1 min erfolgte ein Farbumschlag von dunkelgrün nach rot. Mittels Dünnschichtchromatographie konnte kein Trieisendodecacarbonyl mehr nachgewiesen werden und die Reaktion wurde beendet. Die abgekühlte Reaktionslösung wurde mit 200 mL Wasser gewaschen und die organische Phase abgetrennt. Nach Extraktion der wässrigen Phase mit Toluol (3 x 25 mL) wurde die kombinierte organische Phase über Natriumsulfat getrocknet und säulenchromatographisch Cyclohexan/Dichlormethan (6:1) aufgereinigt. Das Produkt wurde als roter Feststoff (138 mg, 220  $\mu\text{mol}$ , 38 %) erhalten.

**[0051]** Bis( $\mu$ -phenyltellurido-Te)-hexacarbonyldieisen(I)



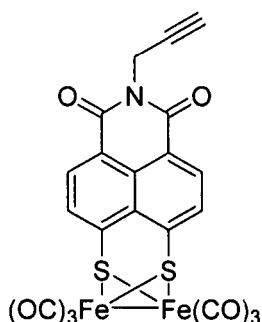
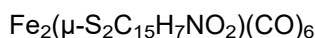


(XIII)

**[0052]** In einem Schlenkgefäß wurde Diphenylditellurid (120 mg, 293  $\mu\text{mol}$ ) vorgelegt und dreimal mit Stickstoff sekuriert. Nach Zugabe von 10 mL Toluol und 1 mL N-Methyl-2-pyrrolidon wurde auf 50 °C erhitzt. Zur entstandenen Lösung wurden Trieisendodecacarbonyl (148 mg, 293  $\mu\text{mol}$ ) in Substanz zugegeben und gerührt. Innerhalb von 20 min erfolgte ein Farbumschlag von dunkelgrün nach rot. Mittels Dünnschichtchromatographie konnte kein Trieisendodecacarbonyl mehr nachgewiesen werden und die Reaktion wurde beendet. Nach säulenchromatographischer Aufreinigung n-Hexan/Dichloromethan (10:1) konnte das Produkt als dunkelroter Feststoff (159 mg, 231  $\mu\text{mol}$ , 79 %) erhalten werden.

**[0053]** Literaturunbekannte Verbindungen:

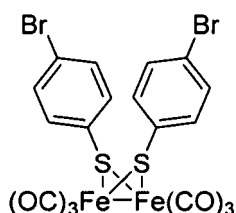
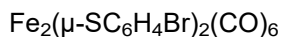
6-(prop-2-yn-1-yl)-5H-[1,2]dithiolo[3',4',5':4,5]naphtho[1,8-c]pyridin-5,7(6H)-dionhexacarbonyldieisen(I)



(XIV)

**[0054]** In einem Schlenkgefäß wurde 6-(prop-2-yn-1-yl)-5H-[1,2]dithiolo[3',4',5':4,5]naphtho- [1,8-cd]pyridin-5,7(6H)-dion (200 mg, 670  $\mu\text{mol}$ ) vorgelegt und dreimal mit Stickstoff sekuriert. Nach Zugabe von 35 mL Toluol und 50 mL N-Methyl-2-pyrrolidon wurde auf 90 °C erhitzt. Zur entstandenen Lösung wurden Trieisendodecacarbonyl (508 mg, 1,01 mmol) in Substanz zugegeben und gerührt. Innerhalb von 10 min erfolgte ein Farbumschlag von dunkelgrün nach rot. Mittels Dünnschichtchromatographie konnte kein Trieisendodecacarbonyl mehr nachgewiesen werden und die Reaktion wurde beendet. Die abgekühlte Reaktionslösung wurde mit 200 mL Wasser gewaschen und die organische Phase abgetrennt. Nach Extraktion der wässrigen Phase mit Toluol (3  $\times$  25 mL) wurde die kombinierte organische Phase über Natriumsulfat getrocknet und säulenchromatographisch Cyclohexan/Dichlormethan (4:1) aufgereinigt. Das Produkt wurde als roter Feststoff (161 mg, 278  $\mu\text{mol}$ , 42 %) erhalten.

**[0055]** Bis( $\mu$ -4-bromophenylthiolato-S)-hexacarbonyldieisen(I)

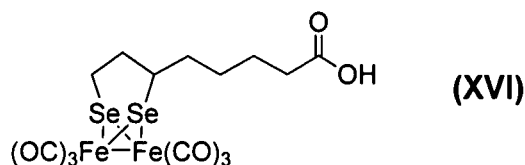
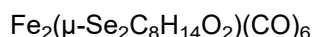


(XV)

**[0056]** In einem Schlenkgefäß wurde 4-Brom-thiophenol (100 mg, 529  $\mu\text{mol}$ ) vorgelegt und dreimal mit Stickstoff sekuriert. Nach Zugabe von 10 mL Toluol und 1 mL N-Methyl-2-pyrrolidon wurde auf 50 °C erhitzt. Zur entstandenen Lösung wurden Trieisendodecacarbonyl (133 mg, 264  $\mu\text{mol}$ ) in Substanz zugegeben und gerührt. Innerhalb von 10 min erfolgte ein Farbumschlag von dunkelgrün nach rot. Mittels Dünnschichtchromatographie konnte kein Trieisendodecacarbonyl mehr nachgewiesen werden und die Reaktion wurde been-

det. Nach säulenchromatographischer Aufreinigung Cyclohexan/THF (4:1), konnte das Produkt als roter Feststoff (136 mg, 208  $\mu$ mol, 78 %) erhalten werden.

**[0057]** 5-(1,2-Diselenolan-3-yl)pentansäure-hexacarbonyldleisen(I)



**[0058]** In einem Schlenkgefäß wurde 5-(1,2-Diselenolan-3-yl)pentansäure (100 mg, 333  $\mu$ mol) vorgelegt und dreimal mit Stickstoff sekuriert. Nach Zugabe von 10 mL Toluol und 1 mL N-Methyl-2-pyrrolidon wurde auf 50 °C erhitzt. Zur entstandenen Lösung wurden Triisendodecacarbonyl (168 mg, 333  $\mu$ mol) in Substanz zugegeben und gerührt. Innerhalb von 20 min erfolgte ein Farbumschlag von dunkelgrün nach rot. Per Dünnschichtchromatographie konnte kein Triisendodecacarbonyl mehr nachgewiesen werden und die Reaktion wurde beendet. Nach säulenchromatographischer Aufreinigung Cyclohexan/THF (4:1), konnte das Produkt als roter Feststoff (161 mg, 278  $\mu$ mol, 84 %) erhalten werden.

Zitierte Literatur

S. Singh; S. Jain; V. PS; A. K. Tiwari; M. R. Nouni; J. K. Pandey; S. Goel: Hydrogen: A sustainable fuel for future of the transport sector, *Renewable and Sustainable Energy Reviews* 2015, 51, 623-633.

P. M. Vignais, B. Billoud, J. Meyer: Classification and phylogeny of hydrogenases, *FEMS Microbiology Reviews*, 2001, 455-501.

P. M. Vignais; B. Billoud: Occurrence, classification, and biological function of hydrogenases: an overview, *Chemical reviews* 2007, 107, 4206-4272.

J. W. Peters; W. N. Lanzilotta; B. J. Lemon; L. C. Seefeldt: X-ray crystal structure of the Fe-only hydrogenase (Cpl) from *Clostridium pasteurianum* to 1.8 angstrom resolution, *Science* 1998, 282, 1853-1858.

H. Reihlen, A. Gruhl, G. v. Hessling: Über den photochemischen und oxydativen Abbau von Carbonylen, *Justus Liebig's Annalen der Chemie* 1929, 268-287.

H. Reihlen, A. v. Friedolsheim, W. Oswald: Über Stickoxyd- und Kohlenoxydverbindungen des scheinbar einwertigen Eisens und Nickels. Zugleich Erwiderung an die Herren W. Manchot und W. Hieber, *Justus Liebig's Annalen der Chemie* 1928, 72-96.

Y. Li; T. B. Rauchfuss: Synthesis of Diiron(I) Dithiolato Carbonyl Complexes, *Chemical reviews* 2016, 116, 7043-7077.

S. Gao; Y. Liu; Y. Shao; D. Jiang; Q. Duan: Iron carbonyl compounds with aromatic dithiolate bridges as organometallic mimics of [FeFe] hydrogenases, *Coordination Chemistry Reviews* 2020, 402, 213081.

S. Gao; W. Fan; Y. Liu; D. Jiang; Q. Duan: Artificial water-soluble systems inspired by [FeFe]-hydrogenases for electro- and photocatalytic hydrogen production, *International Journal of Hydrogen Energy* 2020, 45, 4305-4327.

M. Watanabe; K. Goto; T. Miyazaki; M. Shibahara; Y. J. Chang; T. J. Chow; T. Ishihara: Electrocatalytic hydrogen production using [FeFe]-hydrogenase mimics based on tetracene derivatives, *New Journal of Chemistry* 2019, 43, 13810-13815.

J.-X. Jian; Q. Liu; Z.-J. Li; F. Wang; X.-B. Li; C.-B. Li; B. Liu; Q.-Y. Meng; B. Chen; K. Feng; C.-H. Tung; L.-Z. Wu: Chitosan confinement enhances hydrogen photogeneration from a mimic of the diiron subsite of FeFe-hydrogenase, *Nature communications* 2013, 4, 2695.

X.-B. Li; J.-X. Jian; X.-Z. Wang; Y. Wang; S.-G. Xia; C.-H. Tung; L.-Z. Wu: Per-6-Thiol-Cyclodextrin Engineered [FeFe]-Hydrogenase Mimic/CdSe Quantum Dot Assembly for Photocatalytic Hydrogen Production, *Solar RRL* 2020, 2000474.



E. C. Hatchikian; N. Forget; V. M. Fernandez; R. Williams; R. Cammack: Further characterization of the Fe-hydrogenase from *Desulfovibrio desulfuricans* ATCC 7757, *European Journal of Biochemistry* 1992, 209, 357-365.

M. Faizan; N. Muhammad; K. U. K. Niazi; Y. Hu; Y. Wang; Y. Wu; H. Sun; R. Liu; W. Dong; W. Zhang; Z. Gao: CO-Releasing Materials: An Emphasis on Therapeutic Implications, as Release and Subsequent Cytotoxicity Are the Part of Therapy, *Materials (Basel, Switzerland)* 2019, 12, 1643.

Z. Xiao; R. Jiang; J. Jin; X. Yang; B. Xu; X. Liu; Y. He; Y. He: Diiron(ii) pentacarbonyl complexes as CO-releasing molecules: their synthesis, characterization, CO-releasing behaviour and biocompatibility, *Dalton Trans* 2019, 48, 468-477.

X. Jiang; Z. Xiao; W. Zhong; X. Liu: Brief survey of diiron and monoiron carbonyl complexes and their potentials as CO-releasing molecules (CORMs), *Coordination Chemistry Reviews* 2020, 213634.

K. Ling; F. Men; W.-C. Wang; Y.-Q. Zhou; H.-W. Zhang; D.-W. Ye: Carbon Monoxide and Its Controlled Release: Therapeutic Application, Detection, and Development of Carbon Monoxide Releasing Molecules (CORMs), *Journal of medicinal chemistry* 2018, 61, 2611-2635.

A. K. Mustafa; M. M. Gadalla; S. H. Snyder: Signaling by gasotransmitters, *Science signaling* 2009, 2, 1-17.

N. S. Nametkin; v.d. Tyurin; M. A. Kukina: Synthesis and some properties of sulfur-containing iron tricarbonyl complexes, *Journal of Organometallic Chemistry* 1978, 149, 355-370.

J. Wang; T. Zhang; S. Jiang; X. Ma; X. Shao; Di Wang; X. Li; B. Li: Catalytic reduction of 1,4-benzoquinone to hydroquinone via [FeFe]-hydrogenase model complexes under mild conditions, *Journal of Chemical Technology & Biotechnology* 2020.

M. M. van Dyk; P. H. van Rooyen; S. Lotz: Iron carbene complexes Part 4. Substitution reactions of diiron carbene complexes with P(OMe)<sub>3</sub>, PPh<sub>3</sub> and tBuNC ligands, *Inorganica Chimica Acta* 1989, 163, 167-172.

Y. Tang; Z. Wei; W. Zhong; X. Liu: Diiron Complexes with Pendant Phenol Group(s) as Mimics of the Diiron Subunit of [FeFe]-Hydrogenase: Synthesis, Characterisation, and Electrochemical Investigation, *European Journal of Inorganic Chemistry* 2011, 2011, 1112-1120.

D. Seyferth; R. S. Henderson; L.-C. Song; G. B. Womack: Chemistry of  $\mu$ dithiobis(tricarbonyliron), an inorganic mimic of organic disulfides, *Journal of Organometallic Chemistry* 1985, 292, 9-17.

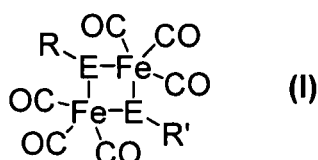
A. Jouyban; M. A. A. Fakhree; A. Shayanfar: Review of pharmaceutical applications of N-methyl-2-pyrrolidone, *Journal of Pharmacy & Pharmaceutical Sciences* 2010, 13, 524-535.

L. Song; Q. Hu; Q. Dong; J. Wang: Isolation and characterization of corresponding products of nucleophilic ring-opening of ethylene oxide and epichlorohydrin by  $(\mu\text{-RS})(\mu\text{-XMgS})\text{Fe}_2(\text{CO})_6$  or  $(\mu\text{-LiS})_2\text{Fe}_2(\text{CO})_6$ , *Wuji Huaxue Xuebao* 1990, 6, 256-260.

S. Lü; S. Gong; G.-H. Xu; Y.-Y. Liu; L. Lü; C.-R. Qin; Q.-L. Li: Synthesis, characterization, and electrochemical properties of diiron bis(monotellurolate) carbonyls related to [FeFe]-hydrogenases, *Inorganica Chimica Acta* 2020, 511, 119797.

### Patentansprüche

1. Verfahren zur Herstellung von zweikernigen Eisenhexacarbonylkomplexen der Formel (I)



E = S, Se, Te

wobei R und R' gleiche oder unterschiedliche Substituenten der Klassifizierung:

Alkyl-, Cycloalkyl-, Aryl- oder Heteroarylverbindungen, Heterozyklen, Alkohole, Mercaptane, Amine, Nitrile, Carbonsäuren, Amide, Imide, Hydroxamsäuren, Aminosäuren, Zucker, Ether, Thioether, Ketone, Thioketone,

Aldehyde, Thioaldehyde, Ester, Imidine, Amidine, Carbonsäurechloride, Carbonsäureanhydride, Sulfonsäuren, Sulfoxide, Sulfonamide, Sulfone, Azide, Carbonsäureazide, Peptide, Lactone, Thiolactone, bevorzugt Alkyl-, Cycloalkyl-, Aryl- oder Heteroarylverbindungen, Heterozyklen, Alkohole, Amine, Nitrile, Carbonsäuren, Amide, Imide, Hydroxamsäuren, Aminosäuren, Zucker, Ether, Ketone, Aldehyde, Ester, Imidine, Amidine, Sulfonsäuren, Sulfoxide, Sulfonamide, Sulfone, Azide, Peptide, Lactone sind, **dadurch gekennzeichnet**, dass eine Reaktion in Anwesenheit von N-Methyl-2-pyrrolidon (NMP) durchgeführt wird.

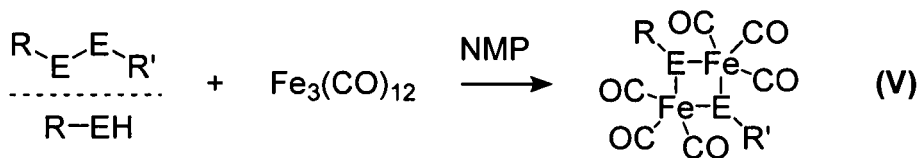
2. Verfahren nach Anspruch 1, **dadurch gekennzeichnet**, dass die Reaktion mit 3 - 60 Vol% NMP, bevorzugt 5 - 20 Vol%, besonders bevorzugt 9 - 10 Vol% erfolgt.

3. Verfahren nach Anspruch 1 oder 2, **dadurch gekennzeichnet**, dass die Reaktion bei 25 °C bis 90 °C, bevorzugt bei 40 - 60 °C, besonders bevorzugt bei 50 °C erfolgt.

4. Verfahren nach einem der Ansprüche 1 bis 3, **dadurch gekennzeichnet**, dass die Reaktion bei einer Reaktionszeit von 3 - 30 Minuten, bevorzugt 5 - 25 Minuten, besonders bevorzugt 10 - 15 Minuten, erfolgt.

5. Verfahren nach einem der Ansprüche 1 bis 4, **dadurch gekennzeichnet**, dass als Lösungsmittel ein aprotisches Lösungsmittel, bevorzugt Toluol, Tetrahydrofuran oder Dichlormethan, besonders bevorzugt Toluol, verwendet wird.

6. Verfahren nach einem der Ansprüche 1 bis 5, **dadurch gekennzeichnet**, dass die Reaktion gemäß Schema (V)



verläuft.

Es folgen keine Zeichnungen

## 8. Acknowledgments

Something that must not be missing is to acknowledge the support of all the people who contributed to this thesis.

First, I would like to acknowledge my supervisor, Prof. Wolfgang Weigand, who allowed me to continue working in his group and this fascinating field of research. He trusted me to complete this Ph.D. thesis and supported me on this journey. His enthusiasm for chemistry and his motivational guidance were infectious. He gave me room for my ideas and to follow my research strategies. Furthermore, he enabled my individual development and sent me to national and international conferences where I could present my research and socialize with chemists around the globe.

In this context, I have to thank the Erasmus+ student exchange program and the Gesellschaft Deutscher Chemiker (GDCh) for the financial support and guidance during my research stay at Saitama University, Japan, and Prof. Akihito Ishii for his permission and supervision in his group. It was the most exciting adventure of my life so far. Thank you to all the Japanese colleagues I met there, particularly Dr. Norio Nakata, Prof. Mao Minoura, Prof. Satoshi Ogawa, Koh, Nazuki, Yuki, Chihiru, Naoaki, and many more.

I am grateful for the excellent international colleagues of the Weigand group who helped me with discussions about chemistry, culture, and daily life. I always felt welcome and appreciated. Thank you, Sarah, Susi, Marie, Micheal, Ibrahim, Benedikt, Hassan, Anne, Xiao, Prathipa, Chizuru, Henning, Mario, Robert and Philipp. Moreover, I appreciate the work and help of the IAAC and IOMC Jena staff.

Additionally, I wanted to thank my co-authors, who invested their time and work and helped me many times with their experience and expertise to publish the results of our work in four nice papers. Thank you, Claire, Sihem, Prof. Bernd Schöllhorn, Prof. Maria Wächtler, Alex, Elisabeth, Mathias, Andreas, Raktim, Stephan, Philipp, Eric, Leanne, Benedikt, Martin, Prof. Benjamin Dietzek-Ivanšić, Prof. Kalina Peneva, Prof. Stefanie Gräfe, Riccarda, Prof. Kerstin Leopold, Christof, Prof. Andrey Turchanin, Jan, Yves, Dr. Helmar Görls, and Dr. Phil Liebing.

Additionally, I thank the DFG Catalight members for their support and fruitful collaborations.

I am grateful for all the students I could teach and guide through their first semesters in inorganic chemistry and Benedikt, Fabian, Julian, Leanne, and Toni, who performed their research internship under my supervision.

Special gratitude goes to Lizzy and Hassan for their patience and expertise while correcting this thesis with their helpful comments.

Finally, I would like to appreciate the support and love I get from my lovely wife Jeannine, my son Emil, my parents, my family, and my loyal friends. I would not have been able to go this way without you. Thank you!

## 9. Declaration of Authorship / Selbstständigkeitserklärung

Ich erkläre, dass ich die vorliegende Arbeit selbstständig und unter Verwendung der angegebenen Hilfsmittel, persönlichen Mitteilungen und Quellen angefertigt habe.

I certify that the here presented work is, to the best of my knowledge, original and the result of my investigations, except as knowledge, and has not been submitted, either in part or whole, for a degree at this or any other university.

---

Ort, Datum

---

Unterschrift (Stefan Benndorf)

## 10. References

- [001] E. Stephens, I. L. Ross, J. H. Mussgnug, L. D. Wagner, M. A. Borowitzka, C. Posten, O. Kruse, B. Hankamer, *Trends Plant Sci.* **2010**, *15*, 554.
- [002] D. I. Armstrong McKay, A. Staal, J. F. Abrams, R. Winkelmann, B. Sakschewski, S. Loriani, I. Fetzer, S. E. Cornell, J. Rockström, T. M. Lenton, *Science* **2022**, *377*, 1171.
- [003] *The limits to growth. A report for the Club of Rome's Project on the Predicament of Mankind*, Universe Books, New York, **1972**.
- [004] S. Dixson-Declève, O. Gaffney, J. Ghosh, J. Randers, J. Rockström, P. E. Stoknes, *Earth for all. A survival guide for humanity: a report to the Club of Rome (2022), fifty years after The Limits of Growth (1972)*, New Society Publishers, Gabriola Island, **2022**.
- [005] J. Randers, *2052. Der neue Bericht an den Club of Rome : eine globale Prognose für die nächsten 40 Jahre*, oekom verlag, München, **2014**.
- [006] F. R. Pazheri, M. F. Othman, N. H. Malik, *Renew. Sustain. Energy Rev.* **2014**, *31*, 835.
- [007] J. Knox-Hayes, M. A. Brown, B. K. Sovacool, Y. Wang, *Global Environ. Change* **2013**, *23*, 609.
- [008] A. Saavedra, N. A. Galvis, F. Mesa, E. Banguero, M. Castaneda, S. Zapata, A. J. Aristizabal, *IREA* **2021**, *9*, 115.
- [009] X.-C. Wang, J. J. Klemeš, X. Dong, W. Fan, Z. Xu, Y. Wang, P. S. Varbanov, *Renew. Sustain. Energy Rev.* **2019**, *105*, 71.
- [010] M. Lu, C. Zhou, C. Wang, R. B. Jackson, C. P. Kempes, *Worldwide scaling of waste generation in urban systems*, **2022**.
- [011] N. Nakicenovic, A. Grubler, *Int. J. Global Energy Issues* **2000**, *13(1-3)*, 4.
- [012] J. O. Abe, A. Popoola, E. Ajenifuja, O. M. Popoola, *Int. J. Hydrog. Energy* **2019**, *44*, 15072.
- [013] M. Mocker, J. Aigner, S. Kroop, R. Lohmeyer, M. Franke, *Chem. Ing. Tech.* **2015**, *87*, 439.
- [014] A. Midilli, M. Ay, I. Dincer, M. A. Rosen, *Renew. Sustain. Energy Rev.* **2005**, *9*, 255.
- [015] K. Riener, F. E. Kühn, *Chem. unserer Zeit* **2014**, *48*, 260.

- [016] R.-G. Cong, *Renew. Sustain. Energy Rev.* **2013**, *17*, 94.
- [017] J. L. Aleixandre-Tudó, L. Castelló-Cogollos, J. L. Aleixandre, R. Aleixandre-Benavent, *Renew. Energy* **2019**, *139*, 268.
- [018] R. Way, M. C. Ives, P. Mealy, J. D. Farmer, *Joule* **2022**, *6*, 2057.
- [019] T. M. Lenton, J. Rockström, O. Gaffney, S. Rahmstorf, K. Richardson, W. Steffen, H. J. Schellnhuber, *Nature* **2019**, *575*, 592.
- [020] G. Barnea, C. Hagemann, S. Wurster, *Energy Policy* **2022**, *168*, 113093.
- [021] M. P. Pablo-Romero, A. Sánchez-Braza, A. Galyan, *Renew. Sustain. Energy Rev.* **2021**, *138*, 110481.
- [022] C. Bohringer, *Oxford Rev. Econ. Policy* **2003**, *19*, 451.
- [023] B. C. O'Neill, M. Oppenheimer, *Science (New York, N.Y.)* **2002**, *296*, 1971.
- [024] K. Jagoda, R. Lonseth, A. Lonseth, T. Jackman, *Renew. Energy* **2011**, *36*, 1266.
- [025] T. J. Dijkman, R. Benders, *Renew. Sustain. Energy Rev.* **2010**, *14*, 3148.
- [026] K. Solaun, E. Cerdá, *Renew. Sustain. Energy Rev.* **2019**, *116*, 109415.
- [027] O. Ellabban, H. Abu-Rub, F. Blaabjerg, *Renew. Sustain. Energy Rev.* **2014**, *39*, 748.
- [028] C. Cormio, M. Dicorato, A. Minoia, M. Trovato, *Renew. Sustain. Energy Rev.* **2003**, *7*, 99.
- [029] R. Wüstenhagen, M. Wolsink, M. J. Bürer, *Energy Policy* **2007**, *35*, 2683.
- [030] S. Carley, *Energy Policy* **2009**, *37*, 3071.
- [031] I. Dincer, *Renew. Sustain. Energy Rev.* **2000**, *4*, 157.
- [032] L. Bird, M. Bolinger, T. Gagliano, R. Wiser, M. Brown, B. Parsons, *Energy Policy* **2005**, *33*, 1397.
- [033] F. Rizzi, N. J. van Eck, M. Frey, *Renew. Energy* **2014**, *62*, 657.
- [034] J. Cronin, G. Anandarajah, O. Dessens, *Clim. Change* **2018**, *151*, 79.
- [035] S. F. Ahmed, M. Mofijur, S. Nuzhat, N. Rafa, A. Musharrat, S. S. Lam, A. Boretti, *Int. J. Hydrog. Energy* **2022**, *47*, 37227.
- [036] P. V. Chombo, Y. Laonual, *J. Power Sources* **2020**, *478*, 228649.
- [037] L. Kong, C. Li, J. Jiang, M. Pecht, *Energies* **2018**, *11*, 2191.
- [038] K. Kubota, M. Dahbi, T. Hosaka, S. Kumakura, S. Komaba, *Chem. Rec.* **2018**, *18*, 459.

- [039] L. Xie, C. Tang, Z. Bi, M. Song, Y. Fan, C. Yan, X. Li, F. Su, Q. Zhang, C. Chen, *Adv. Energy Mater.* **2021**, *11*, 2101650.
- [040] R. B. Kaunda, *J. Energy Nat. Resour. Law* **2020**, *38*, 237.
- [041] S. Merazga, A. Cheriet, K. M'hammedi, A. Mefoued, N. Gabouze, *Int. J. Hydrog. Energy* **2019**, *44*, 9994.
- [042] S. Rana, J. P. Biswas, S. Paul, A. Paik, D. Maiti, *Chem. Soc. Rev.* **2021**, *50*, 243.
- [043] S. M. Kotay, D. Das, *Int. J. Hydrog. Energy* **2008**, *33*, 258.
- [044] P. R. Prabhukhot, M. M. Wagh, A. C. Gangal, *Adv. energy power* **2016**, *4*, 11.
- [045] S. Öberg, M. Odenberger, F. Johnsson, *Int. J. Hydrog. Energy* **2022**, *47*, 31684.
- [046] R. Juknelevičius, A. Rimkus, S. Pukalskas, J. Matijošius, *Int. J. Hydrog. Energy* **2019**, *44*, 10129.
- [047] W. L. Becker, M. Penev, R. J. Braun, *J. Energy Res. Technol.* **2019**, *141*.
- [048] R. Gao, C. Zhang, K.-W. Jun, S. K. Kim, H.-G. Park, T. Zhao, L. Wang, H. Wan, G. Guan, *Fuel* **2021**, *291*, 120111.
- [049] W. M. Verdegaal, S. Becker, C. von Olshausen, *Chem. Ing. Tech.* **2015**, *87*, 340.
- [050] A. M. Abdalla, S. Hossain, O. B. Nisfindy, A. T. Azad, M. Dawood, A. K. Azad, *Energy Convers. Manage.* **2018**, *165*, 602.
- [051] S. A. Grigoriev, V. N. Fateev, D. G. Bessarabov, P. Millet, *Int. J. Hydrog. Energy* **2020**, *45*, 26036.
- [052] S. Nižetić, F. Barbir, N. Djilali, *Int. J. Hydrog. Energy* **2019**, *44*, 9673.
- [053] B. Tanç, H. T. Arat, E. Baltacıoğlu, K. Aydın, *Int. J. Hydrog. Energy* **2019**, *44*, 10120.
- [054] M. Pagliaro, A. G. Konstandopoulos, R. Ciriminna, G. Palmisano, *Energy Environ. Sci.* **2010**, *3*, 279.
- [055] H. Singh, K. Paritosh, V. Vivekanand, N. Pareek, *Chem Eng & Technol* **2022**, ceat.202000561.
- [056] J. Andersson, S. Grönkvist, *Int. J. Hydrog. Energy* **2019**, *44*, 11901.
- [057] J. Ren, N. M. Musyoka, H. W. Langmi, M. Mathe, S. Liao, *Int. J. Hydrog. Energy* **2017**, *42*, 289.
- [058] M. R. Usman, *Renew. Sustain. Energy Rev.* **2022**, *167*, 112743.



- [059] J. Bellosta von Colbe, J.-R. Ares, J. Barale, M. Baricco, C. Buckley, G. Capurso, N. Gallandat, D. M. Grant, M. N. Guzik, I. Jacob, E. H. Jensen, T. Jensen, J. Jepsen, T. Klassen, M. V. Lototsky, K. Manickam, A. Montone, J. Puszkiel, S. Sartori, D. A. Sheppard, A. Stuart, G. Walker, C. J. Webb, H. Yang, V. Yartys, A. Züttel, M. Dornheim, *Int. J. Hydrog. Energy* **2019**, *44*, 7780.
- [060] A. M. Elberry, J. Thakur, A. Santasalo-Aarnio, M. Larmi, *Int. J. Hydrog. Energy* **2021**, *46*, 15671.
- [061] K. E. Lamb, M. D. Dolan, D. F. Kennedy, *Int. J. Hydrog. Energy* **2019**, *44*, 3580.
- [062] R. Pachaiappan, S. Rajendran, P. S. Kumar, D.-V. N. Vo, T. K. Hoang, L. Cornejo-Ponce, *Int. J. Hydrog. Energy* **2022**, *47*, 37490.
- [063] H. Ishaq, I. Dincer, C. Crawford, *Int. J. Hydrog. Energy* **2022**, *47*, 26238.
- [064] F. Dawood, M. Anda, G. M. Shafiullah, *Int. J. Hydrog. Energy* **2020**, *45*, 3847.
- [065] L. Cao, I. K. M. Yu, X. Xiong, D. C. W. Tsang, S. Zhang, J. H. Clark, C. Hu, Y. H. Ng, J. Shang, Y. S. Ok, *Environ. Res.* **2020**, *186*, 109547.
- [066] B. Dou, H. Zhang, Y. Song, L. Zhao, B. Jiang, M. He, C. Ruan, H. Chen, Y. Xu, *Sustain. Energy Fuels* **2019**, *3*, 314.
- [067] M. Wang, G. Wang, Z. Sun, Y. Zhang, D. Xu, *Global Energy Interconnect.* **2019**, *2*, 436.
- [068] P. Nikolaidis, A. Poullikkas, *Renew. Sustain. Energy Rev.* **2017**, *67*, 597.
- [069] O. Schmidt, A. Gambhir, I. Staffell, A. Hawkes, J. Nelson, S. Few, *Int. J. Hydrog. Energy* **2017**, *42*, 30470.
- [070] I. Dincer, C. Acar, *Int. J. Hydrog. Energy* **2015**, *40*, 11094.
- [071] S. Shiva Kumar, V. Himabindu, *Mater. Sci. Energy Technol.* **2019**, *2*, 442.
- [072] M. Carmo, D. L. Fritz, J. Mergel, D. Stolten, *Int. J. Hydrog. Energy* **2013**, *38*, 4901.
- [073] I. Dincer, *Int. J. Hydrog. Energy* **2012**, *37*, 1954.
- [074] H. Zhang, A. W. Maijenburg, X. Li, S. L. Schweizer, R. B. Wehrspohn, *Adv Funct Materials* **2020**, *30*, 2003261.
- [075] A. Kovač, D. Marciuš, L. Budin, *Int. J. Hydrog. Energy* **2019**, *44*, 9841.
- [076] J. Jia, L. C. Seitz, J. D. Benck, Y. Huo, Y. Chen, J. W. D. Ng, T. Bilir, J. S. Harris, T. F. Jaramillo, *Nat. Commun.* **2016**, *7*, 13237.

- [077] K. Scott (Ed.) *Energy and Environment Series, Vol. 25*, Royal Society of Chemistry, Cambridge, **2020**.
- [078] A. Fujishima, K. Honda, *Nature* **1972**, *238*, 37.
- [079] S. U. M. Khan, M. Al-Shahry, W. B. Ingler, *Science (New York, N.Y.)* **2002**, *297*, 2243.
- [080] Khaselev, Turner, *Science (New York, N.Y.)* **1998**, *280*, 425.
- [081] L. Amirav, A. P. Alivisatos, *J. Phys. Chem. Lett.* **2010**, *1*, 1051.
- [082] E. Aronovitch, P. Kalisman, L. Houben, L. Amirav, M. Bar-Sadan, *Chem. Mater.* **2016**, *28*, 1546.
- [083] P. Kalisman, L. Houben, E. Aronovitch, Y. Kauffmann, M. Bar-Sadan, L. Amirav, *J. Mater. Chem. A* **2015**, *3*, 19679.
- [084] P. Kalisman, Y. Kauffmann, L. Amirav, *J. Mater. Chem. A* **2015**, *3*, 3261.
- [085] P. Kalisman, Y. Nakibli, L. Amirav, *Nano Lett.* **2016**, *16*, 1776.
- [086] Y. Nakibli, L. Amirav, *Chem. Mater.* **2016**, *28*, 4524.
- [087] Y. Nakibli, P. Kalisman, L. Amirav, *J. Phys. Chem. Lett.* **2015**, *6*, 2265.
- [088] Y. Nakibli, Y. Mazal, Y. Dubi, M. Wächtler, L. Amirav, *Nano Lett.* **2018**, *18*, 357.
- [089] M. Wächtler, P. Kalisman, L. Amirav, *J. Phys. Chem. C* **2016**, *120*, 24491.
- [090] T. Simon, M. T. Carlson, J. K. Stolarczyk, J. Feldmann, *ACS Energy Lett.* **2016**, *1*, 1137.
- [091] K. Wu, Z. Chen, H. Lv, H. Zhu, C. L. Hill, T. Lian, *J. Am. Chem. Soc.* **2014**, *136*, 7708.
- [092] D. Schweitzer, A. Gredinger, M. Schmid, G. Waizmann, M. Beirow, R. Spörl, G. Scheffknecht, *Biomass Bioenergy* **2018**, *111*, 308.
- [093] S. Li, F. Li, X. Zhu, Q. Liao, J.-S. Chang, S.-H. Ho, *Chemosphere* **2022**, *291*, 132717.
- [094] D. Nagarajan, C.-D. Dong, C.-Y. Chen, D.-J. Lee, J.-S. Chang, *Biotechnol. J.* **2021**, *16*, e2000124.
- [095] M. Ni, D. Y. Leung, M. K. Leung, K. Sumathy, *Fuel Process. Technol.* **2006**, *87*, 461.
- [096] K. E. Redding, J. Appel, M. Boehm, W. Schuhmann, M. M. Nowaczyk, I. Yacoby, K. Gutekunst, *Trends Biotechnol.* **2022**, *40*, 1313.

- [097] R. L. Kerby, P. W. Ludden, G. P. Roberts, *J. Bacteriol.* **1995**, *177*, 2241.
- [098] G. Y. Jung, J. R. Kim, J.-Y. Park, S. Park, *Int. J. Hydrog. Energy* **2002**, *27*, 601.
- [099] A. M. Silva Benavides, M. C. Rudin, N. Villalobos, E. Touloupakis, G. Torzillo, *Int. J. Hydrog. Energy* **2019**, *44*, 9849.
- [100] K. L. Kovács, G. Maróti, G. Rákhely, *Int. J. Hydrog. Energy* **2006**, *31*, 1460.
- [101] P. Mishra, S. Krishnan, S. Rana, L. Singh, M. Sakinah, Z. Ab Wahid, *Energy Strategy Rev.* **2019**, *24*, 27.
- [102] Q. Zhang, H. Liu, X. Shui, Y. Li, Z. Zhang, *Bioresour. Technol.* **2022**, *362*, 127787.
- [103] H. Zheng, Y. Wang, X. Feng, S. Li, Y. K. Leong, J.-S. Chang, *Int. J. Hydrog. Energy* **2022**, *47*, 37359.
- [104] C. Greening, Z. F. Islam, S. K. Bay, *Trends Microbiol.* **2022**, *30*, 330.
- [105] W. Lubitz, W. Tumas, *Chem. Rev.* **2007**, *107*, 3900.
- [106] C. Lambertz, N. Leidel, K. G. V. Havelius, J. Noth, P. Chernev, M. Winkler, T. Happe, M. Haumann, *J. Biol. Chem.* **2011**, *286*, 40614.
- [107] H. Gaffron, *Nature* **1939**, *143*, 204.
- [108] M. L. Ghirardi, R. K. Togasaki, M. Seibert, *Appl Biochem Biotechnol* **1997**, *63-65*, 141.
- [109] W. Lubitz, H. Ogata, O. Rüdiger, E. Reijerse, *Chem. Rev.* **2014**, *114*, 4081.
- [110] M. Stephenson, L. H. Stickland, *Biochem. J* **1931**, *25*, 205.
- [111] J. W. Sidabras, S. T. Stripp, *J. Biol. Inorg. Chem.* **2023**, *28*, 355.
- [112] E. C. Hatchikian, N. Forget, V. M. Fernandez, R. Williams, R. Cammack, *Eur. J. Biochem.* **1992**, *209*, 357.
- [113] A. Melis, *Planta* **2007**, *226*, 1075.
- [114] A. Melis, T. Happe, *Plant Physiol.* **2001**, *127*, 740.
- [115] D. Das, T. Dutta, K. Nath, S. M. Kotay, A. K. Das, T. N. Veziroglu, *Curr. Sci.* **2006**, *90*, 1627.
- [116] P. M. Vignais, B. Billoud, J. Meyer, *FEMS Microbiol. Rev.* **2001**, 455.
- [117] S. Vogt, E. J. Lyon, S. Shima, R. K. Thauer, *J. Biol. Inorg. Chem.* **2008**, *13*, 97.
- [118] O. Pilak, B. Mamat, S. Vogt, C. H. Hagemeyer, R. K. Thauer, S. Shima, C. Vonrhein, E. Warkentin, U. Ermler, *J. Mol. Biol.* **2006**, *358*, 798.
- [119] S. Shima, U. Ermler, *Eur. J. Inorg. Chem.* **2011**, *2011*, 963.

- [120] E. J. Lyon, S. Shima, R. Boecher, R. K. Thauer, F.-W. Grevels, E. Bill, W. Roseboom, S. P. J. Albracht, *J. Am. Chem. Soc.* **2004**, *126*, 14239.
- [121] T. Fujishiro, K. Ataka, U. Ermler, S. Shima, *FEBS J.* **2015**, *282*, 3412.
- [122] K. Procko, S. Bakheet, J. T. Beckham, M. A. Franzen, H. Jakubowski, W. R. P. Novak, *J. Vis. Exp.* **2021**, *178*, e63170.
- [123] P. M. Vignais, B. Billoud, *Chem. Rev.* **2007**, *107*, 4206.
- [124] A. Volbeda, M. H. Charon, C. Piras, E. C. Hatchikian, M. Frey, J. C. Fontecilla-Camps, *Nature* **1995**, *373*, 580.
- [125] F. M. A. Valente, A. S. F. Oliveira, N. Gnad, I. Pacheco, A. V. Coelho, A. V. Xavier, M. Teixeira, C. M. Soares, I. A. C. Pereira, *J. Biol. Inorg. Chem.* **2005**, *10*, 667.
- [126] A. Volbeda, E. Garcin, C. Piras, A. L. de Lacey, V. M. Fernandez, E. C. Hatchikian, M. Frey, J. C. Fontecilla-Camps, *J. Am. Chem. Soc.* **1996**, *118*, 12989.
- [127] J. Fritsch, P. Scheerer, S. Frielingsdorf, S. Kroschinsky, B. Friedrich, O. Lenz, C. M. T. Spahn, *Nature* **2011**, *479*, 249.
- [128] A. Pardo, A. L. de Lacey, V. M. Fernández, H.-J. Fan, Y. Fan, M. B. Hall, *J. Biol. Inorg. Chem.* **2006**, *11*, 286.
- [129] J. W. Peters, W. N. Lanzilotta, B. J. Lemon, L. C. Seefeldt, *Science* **1998**, *282*, 1853.
- [130] Y. Nicolet, C. Piras, P. Legrand, C. E. Hatchikian, J. C. Fontecilla-Camps, *Structure* **1999**, *7*, 13.
- [131] J. T. Kleinhaus, F. Wittkamp, S. Yadav, D. Siegmund, U.-P. Apfel, *Chem. Soc. Rev.* **2021**, *50*, 1668.
- [132] B. J. Lemon, J. W. Peters, *Biochemistry* **1999**, *38*, 12969.
- [133] J. A. Birrell, P. Rodríguez-Maciá, E. J. Reijerse, M. A. Martini, W. Lubitz, *Coord. Chem. Rev.* **2021**, *449*, 214191.
- [134] H. Land, M. Senger, G. Berggren, S. T. Stripp, *ACS Catal.* **2020**, 7069.
- [135] O. Lampret, J. Duan, E. Hofmann, M. Winkler, F. A. Armstrong, T. Happe, *PNAS* **2020**, *117*, 20520.
- [136] P. Knörzer, A. Silakov, C. E. Foster, F. A. Armstrong, W. Lubitz, T. Happe, *J. Biol. Chem.* **2012**, *287*, 1489.

- [137] C. Wang, Z. Lai, G. Huang, H.-J. Pan, *Chem. Eur. J.* **2022**, *28*, e202201499.
- [138] G. Caserta, S. Hartmann, C. van Stappen, C. Karafoulidi-Retsou, C. Lorent, S. Yelin, M. Keck, J. Schoknecht, I. Sergueev, Y. Yoda, P. Hildebrandt, C. Limberg, S. DeBeer, I. Zebger, S. Frielingsdorf, O. Lenz, *Nat Chem Biol* **2023**, *19*, 498.
- [139] G. Berggren, A. Adamska, C. Lambertz, T. R. Simmons, J. Esselborn, M. Atta, S. Gambarelli, J. M. Mouesca, E. Reijerse, W. Lubitz, T. Happe, V. Artero, M. Fontecave, *Nature* **2013**, *499*, 66.
- [140] D. W. Mulder, E. S. Boyd, R. Sarma, R. K. Lange, J. A. Endrizzi, J. B. Broderick, J. W. Peters, *Nature* **2010**, *465*, 248.
- [141] M. C. Posewitz, P. W. King, S. L. Smolinski, L. Zhang, M. Seibert, M. L. Ghirardi, *J. Biol. Chem.* **2004**, *279*, 25711.
- [142] R. C. Driesener, M. R. Challand, S. E. McGlynn, E. M. Shepard, E. S. Boyd, J. B. Broderick, J. W. Peters, P. L. Roach, *Angew. Chem. Int. Ed.* **2010**, *49*, 1687.
- [143] P. Dinis, B. M. Wieckowski, P. L. Roach, *Curr. Opin. Struct. Biol.* **2016**, *41*, 90.
- [144] R. D. Britt, L. Tao, G. Rao, N. Chen, L.-P. Wang, *ACS Bio & Med Chem Au* **2022**, *2*, 11.
- [145] S. J. King, A. Jerkovic, L. J. Brown, K. Petroll, R. D. Willows, *Microb. Biotechnol.* **2022**, *15*, 1946.
- [146] A. Pagnier, B. Balci, E. M. Shepard, W. E. Broderick, J. B. Broderick, *Angew. Chem. Int. Ed.* **2022**, e202212074.
- [147] R. D. Britt, G. Rao, L. Tao, *Nat Rev Chem* **2020**, *4*, 542.
- [148] G. Rao, L. Tao, R. D. Britt, *Chem. Sci.* **2020**, *11*, 1241.
- [149] G. Caserta, L. Pecqueur, A. Adamska-Venkatesh, C. Papini, S. Roy, V. Artero, M. Atta, E. Reijerse, W. Lubitz, M. Fontecave, *Nat Chem Biol* **2017**, *13*, 779.
- [150] J. A. Birrell, O. Rüdiger, E. J. Reijerse, W. Lubitz, *Joule* **2017**, *1*, 61.
- [151] F. Wittkamp, M. Senger, S. T. Stripp, U.-P. Apfel, *Chem. Commun.* **2018**, *54*, 5934.
- [152] G. Berggren, A. Adamska, C. Lambertz, T. R. Simmons, J. Esselborn, M. Atta, S. Gambarelli, J. M. Mouesca, E. Reijerse, W. Lubitz, T. Happe, V. Artero, M. Fontecave, *Nature* **2013**, *499*, 66.

- [153] C. Sommer, C. P. Richers, W. Lubitz, T. B. Rauchfuss, E. J. Reijerse, *Angew. Chem. Int. Ed.* **2018**, *57*, 5429.
- [154] J. F. Siebel, A. Adamska-Venkatesh, K. Weber, S. Rumpel, E. Reijerse, W. Lubitz, *Biochemistry* **2015**, *54*, 1474.
- [155] J. Esselborn, C. Lambertz, A. Adamska-Venkatesh, T. Simmons, G. Berggren, J. Noth, J. Siebel, A. Hemschemeier, V. Artero, E. Reijerse, M. Fontecave, W. Lubitz, T. Happe, *Nat. Chem. Biol.* **2013**, *9*, 607.
- [156] J. Esselborn, N. Muraki, K. Klein, V. Engelbrecht, N. Metzler-Nolte, U.-P. Apfel, E. Hofmann, G. Kurisu, T. Happe, *Chem. Sci.* **2016**, *7*, 959.
- [157] Y. Li, T. B. Rauchfuss, *Chem. Rev.* **2016**, *116*, 7043.
- [158] C. Tard, C. J. Pickett, *Chem. Rev.* **2009**, *109*, 2245.
- [159] U.-P. Apfel, W. Weigand, *ChemBioChem* **2013**, *14*, 2237.
- [160] C. Sommer, A. Adamska-Venkatesh, K. Pawlak, J. A. Birrell, O. Rüdiger, E. J. Reijerse, W. Lubitz, *J. Am. Chem. Soc.* **2017**, *139*, 1440.
- [161] E. J. Reijerse, C. C. Pham, V. Pelmeshnikov, R. Gilbert-Wilson, A. Adamska-Venkatesh, J. F. Siebel, L. B. Gee, Y. Yoda, K. Tamasaku, W. Lubitz, T. B. Rauchfuss, S. P. Cramer, *J. Am. Chem. Soc.* **2017**, *139*, 4306.
- [162] A. Silakov, E. J. Reijerse, S. P. J. Albracht, E. C. Hatchikian, W. Lubitz, *J. Am. Chem. Soc.* **2007**, *129*, 11447.
- [163] A. L. de Lacey, V. M. Fernandez, M. Rousset, R. Cammack, *Chem. Rev.* **2007**, *107*, 4304.
- [164] A. Adamska, A. Silakov, C. Lambertz, O. Rüdiger, T. Happe, E. Reijerse, W. Lubitz, *Angew. Chem. Int. Ed.* **2012**, *51*, 11458.
- [165] A. Adamska-Venkatesh, D. Krawietz, J. Siebel, K. Weber, T. Happe, E. Reijerse, W. Lubitz, *J. Am. Chem. Soc.* **2014**, *136*, 11339.
- [166] M. Haumann, S. T. Stripp, *Acc. Chem. Res.* **2018**, *51*, 1755.
- [167] M. L. K. Sanchez, C. Sommer, E. Reijerse, J. A. Birrell, W. Lubitz, R. B. Dyer, *J. Am. Chem. Soc.* **2019**, *141*, 16064.
- [168] L. S. Mészáros, P. Ceccaldi, M. Lorenzi, H. J. Redman, E. Pfitzner, J. Heberle, M. Senger, S. T. Stripp, G. Berggren, *Chem. Sci.* **2020**, *11*, 4608.

- [169] J. A. Birrell, V. Pelmeshnikov, N. Mishra, H. Wang, Y. Yoda, K. Tamasaku, T. B. Rauchfuss, S. P. Cramer, W. Lubitz, S. DeBeer, *J. Am. Chem. Soc.* **2020**, *142*, 222.
- [170] S. Y. Reece, J. M. Hodgkiss, J. Stubbe, D. G. Nocera, *Philos. Trans. R. Soc. London, Ser. B* **2006**, *361*, 1351.
- [171] M. Senger, K. Laun, F. Wittkamp, J. Duan, M. Haumann, T. Happe, M. Winkler, U.-P. Apfel, S. T. Stripp, *Angew. Chem. Int. Ed.* **2017**, *56*, 16503.
- [172] M. E. Carroll, B. E. Barton, T. B. Rauchfuss, P. J. Carroll, *J. Am. Chem. Soc.* **2012**, *134*, 18843.
- [173] H. Reihlen, A. Gruhl, G. v. Hessling, *Liebigs Ann. Chem.* **1929**, 268.
- [174] H. Reihlen, A. v. Friedolsheim, W. Oswald, *Liebigs Ann. Chem.* **1928**, 72.
- [175] W. Hieber, P. Spacu, *ZAAC* **1937**, 233, 353.
- [176] W. Hieber, J. Gruber, *ZAAC* **1958**, 296, 91.
- [177] A. Winter, L. Zsolnai, G. Huttner, *Zeitschrift für Naturforschung* **1982**, 1430.
- [178] D. Seyferth, R. S. Henderson, L.-C. Song, *J. Organomet. Chem.* **1980**, *192*, C1-C5.
- [179] L. F. Dahl, C.-H. Wei, *Inorg. Chem.* **1963**, *2*, 328.
- [180] R. B. King, *J. Am. Chem. Soc.* **1962**, *84*, 2460.
- [181] W. Lubitz, H. Ogata, O. Rüdiger, E. Reijerse, *Chem. Rev.* **2014**, *114*, 4081.
- [182] S. Gao, Y. Liu, Y. Shao, D. Jiang, Q. Duan, *Coord. Chem. Rev.* **2020**, *402*, 213081.
- [183] J. Amaro-Gahete, M. V. Pavliuk, H. Tian, D. Esquivel, F. J. Romero-Salguero, S. Ott, *Coord. Chem. Rev.* **2021**, *448*, 214172.
- [184] S. Gao, W. Fan, Y. Liu, D. Jiang, Q. Duan, *Int. J. Hydrog. Energy* **2020**, *45*, 4305.
- [185] W. Weigand, *Phosphorus, Sulfur Silicon Relat. Elem.* **2019**, *194*, 634.
- [186] Y. Nicolet, J. C. Fontecilla-Camps, *J. Biol. Chem.* **2012**, *287*, 13532.
- [187] J. Noth, J. Esselborn, J. Güldenhaupt, A. Brünje, A. Sawyer, U.-P. Apfel, K. Gerwert, E. Hofmann, M. Winkler, T. Happe, *Angew. Chem. Int. Ed.* **2016**, *55*, 8396.
- [188] G. A. Felton, C. A. Mebi, B. J. Petro, A. K. Vannucci, D. H. Evans, R. S. Glass, D. L. Lichtenberger, *J. Organomet. Chem.* **2009**, *694*, 2681.

- [189] L. Kertess, F. Wittkamp, C. Sommer, J. Esselborn, O. Rüdiger, E. J. Reijerse, E. Hofmann, W. Lubitz, M. Winkler, T. Happe, U.-P. Apfel, *Dalton Trans.* **2017**, 46, 16947.
- [190] J. L. Stanley, T. B. Rauchfuss, S. R. Wilson, *Organometallics* **2007**, 26, 1907.
- [191] L.-C. Song, F.-X. Luo, H. Tan, X.-J. Sun, Z.-J. Xie, H.-B. Song, *Eur. J. Inorg. Chem.* **2013**, 2013, 2549.
- [192] L.-C. Song, C.-G. Li, J. Gao, B.-S. Yin, X. Luo, X.-G. Zhang, H.-L. Bao, Q.-M. Hu, *Inorg. Chem.* **2008**, 47, 4545.
- [193] C. Zhan, X. Wang, Z. Wei, D. J. Evans, X. Ru, X. Zeng, X. Liu, *Dalton Trans.* **2010**, 39, 11255.
- [194] X. Zhu, W. Zhong, X. Liu, *Int. J. Hydrogen Energy* **2016**, 41, 14068.
- [195] G. Si, W.-G. Wang, H.-Y. Wang, C.-H. Tung, L.-Z. Wu, *Inorg. Chem.* **2008**, 47, 8101.
- [196] S. Ott, M. Kritikos, B. Akermark, L. Sun, *Angew. Chem. Int. Ed.* **2003**, 42, 3285.
- [197] S. Ott, M. Borgström, M. Kritikos, R. Lomoth, J. Bergquist, B. Akermark, L. Hammarström, L. Sun, *Inorg. Chem.* **2004**, 43, 4683.
- [198] G. Qian, H. Wang, W. Zhong, X. Liu, *Electrochim. Acta* **2015**, 163, 190.
- [199] B. Chmielowiec, F. H. Saadi, J. H. Baricuatro, A. Javier, Y.-G. Kim, G. Sun, M. Y. Darensbourg, M. P. Soriaga, *J. Electroanal. Chem.* **2014**, 716, 63.
- [200] X.-W. Song, H.-M. Wen, C.-B. Ma, M.-Q. Hu, H. Chen, H.-H. Cui, C.-N. Chen, *Appl. Organomet. Chem.* **2014**, 28, 267.
- [201] L.-C. Song, M.-Y. Tang, S.-Z. Mei, J.-H. Huang, Q.-M. Hu, *Organometallics* **2007**, 26, 1575.
- [202] F. Gloaguen, J. D. Lawrence, T. B. Rauchfuss, *J. Am. Chem. Soc.* **2001**, 123, 9476.
- [203] R. Cammack, M. Frey, R. Robson, *Hydrogen as a fuel. Learning from nature*, Taylor & Francis, London, New York, **2001**.
- [204] T. R. Cook, D. K. Dogutan, S. Y. Reece, Y. Surendranath, T. S. Teets, D. G. Nocera, *Chem. Rev.* **2010**, 110, 6474.
- [205] C. Li, T. Gong, B. Bian, W. Liao, *Funct. Plant Biol.* **2018**, 45, 783.
- [206] W. Hieber, C. Scharfenberg, *Ber. dtsh. Chem. Ges. A/B* **1940**, 73, 1012.



- [207] N. S. Nametkin, v.d. Tyurin, M. A. Kukina, *J. Organomet. Chem.* **1978**, *149*, 355.
- [208] W. F. Liaw, C. Kim, M. Y. Darensbourg, A. L. Rheingold, *J. Am. Chem. Soc.* **1989**, *111*, 3591.
- [209] Maurizio Peruzzini, Isaac De Los Rios, Antonio Romerosa in *Progress in Inorganic Chemistry 2001*, pp. 169–453.
- [210] J. A. de Beer, R. J. Haines, *J. Organomet. Chem.* **1970**, *24*, 757.
- [211] R. Bau, B. Don, R. Greatrex, R. J. Haines, r. A. Love, R. D. Wilson, *Inorg. Chem.* **1975**, *14*, 3021.
- [212] A. Winter, L. Zsolnai, G. Huttner, *J. Organomet. Chem.* **1983**, *250*, 409.
- [213] U.-P. Apfel, Y. Halpin, M. Gottschaldt, H. Görls, J. G. Vos, W. Weigand, *Chem. Ber.* **2008**, *2008*, 5112.
- [214] U.-P. Apfel, M. Rudolph, C. Apfel, C. Robl, D. Langenegger, D. Hoyer, B. Jaun, M.-O. Ebert, T. Alpermann, D. Seebach, W. Weigand, *Dalton Trans.* **2010**, *39*, 3065.
- [215] K. Charreteur, M. Kdider, J.-F. Capon, F. Gloaguen, F. Y. Pétillon, P. Schollhammer, J. Talarmin, *Inorg. Chem.* **2010**, *49*, 2496.
- [216] M. T. Ashby, *Inorg. Chem.* **1995**, *34*, 5429.
- [217] C. A. Mebi, D. S. Karr, R. Gao, *J. Coord. Chem.* **2011**, *64*, 4397.
- [218] U.-P. Apfel, D. Troegel, Y. Halpin, S. Tschierlei, U. Uhlemann, H. Görls, M. Schmitt, J. Popp, P. Dunne, M. Venkatesan, M. Coey, M. Rudolph, J. G. Vos, R. Tacke, W. Weigand, *Inorg. Chem.* **2010**, *49*, 10117.
- [219] U.-P. Apfel, C. R. Kowol, F. Kloss, H. Görls, B. K. Keppler, W. Weigand, *J. Organomet. Chem.* **2011**, *696*, 1084.
- [220] M. Razavet, S. C. Davies, D. L. Hughes, C. J. Pickett, *Chem. Commun.* **2001**, 847.
- [221] P. I. Volkers, T. B. Rauchfuss, S. R. Wilson, *Eur. J. Inorg. Chem.* **2006**, *2006*, 4793.
- [222] A. K. Jones, B. R. Lichtenstein, A. Dutta, G. Gordon, P. L. Dutton, *J. Am. Chem. Soc.* **2007**, *129*, 14844.
- [223] G. Knorr, D. Costabel, A. Skabeev, C. Neumann, J. Brossette, S. Kupfer, A. Turchanin, W. Weigand, K. Peneva, *Dyes Pigm.* **2021**, 109940.

- [224] R. J. Day, A. J. Gross, E. S. Donovan, K. D. Fillo, G. S. Nichol, G. A. Felton, *Polyhedron* **2021**, *197*, 115043.
- [225] P. Buday, C. Kasahara, E. Hofmeister, D. Kowalczyk, M. K. Farh, S. Riediger, M. Schulz, M. Wächtler, S. Furukawa, M. Saito, D. Ziegenbalg, S. Gräfe, P. Bäuerle, S. Kupfer, B. Dietzek-Ivanšić, W. Weigand, *Angew. Chem. Int. Ed.* **2022**, *61*, e202202079.
- [226] H. Abul-Futouh, A. Skabeev, D. Botteri, Y. Zagranyarski, H. Görls, W. Weigand, K. Peneva, *Organometallics* **2018**, *37*, 3278.
- [227] H. Abul-Futouh, Y. Zagranyarski, C. Müller, M. Schulz, S. Kupfer, H. Görls, M. El-khateeb, S. Gräfe, B. Dietzek, K. Peneva, W. Weigand, *Dalton Trans.* **2017**, *46*, 11180.
- [228] W. Hieber, C. Scharfenberg, *Ber. dtsch. Chem. Ges. A/B* **1940**, *73*, 1012.
- [229] Z. Yu, M. Wang, P. Li, W. Dong, F. Wang, L. Sun, *Dalton Trans.* **2008**, 2400.
- [230] A. Shaver, O. Lopez, D. N. Harpp, *Inorg. Chim. Acta* **1986**, *119*, 13.
- [231] H. Abul-Futouh, Y. Zagranyarski, C. Müller, M. Schulz, S. Kupfer, H. Görls, M. El-khateeb, S. Gräfe, B. Dietzek, K. Peneva, W. Weigand, *Dalton Trans.* **2017**, *46*, 11180.
- [232] H. Abul-Futouh, A. Skabeev, D. Botteri, Y. Zagranyarski, H. Görls, W. Weigand, K. Peneva, *Organometallics* **2018**, *37*, 3278.
- [233] A. P. S. Samuel, D. T. Co, C. L. Stern, M. R. Wasielewski, *J. Am. Chem. Soc.* **2010**, *132*, 8813.
- [234] P. Li, M. Wang, J. Pan, L. Chen, N. Wang, L. Sun, *J. Inorg. Biochem.* **2008**, *102*, 952.
- [235] P. Kilian, F. R. Knight, J. D. Woollins, *Coord. Chem. Rev.* **2011**, *255*, 1387.
- [236] A. Q. Daraosheh, H. Abul-Futouh, R. A. Abdel-Rahem, H. Görls, H.-D. Stachel, W. Weigand, *ZAAC* **2021**, *647*, 931.
- [237] R. B. King, M. B. Bisnette, *Inorg. Chem.* **1965**, *4*, 1663.
- [238] A. Shaver, P. J. Fitzpatrick, K. Steliou, I. S. Butler, *J. Am. Chem. Soc.* **1979**, *101*, 1313.
- [239] A. Shaver, P. J. Fitzpatrick, K. Steliou, I. S. Butler, *J. Organomet. Chem.* **1979**, *172*, C59-C62.
- [240] D. Seyferth, B. W. Hames, *Inorg. Chim. Acta* **1983**, *77*, L1-L2.

- [241] A. Q. Daraosheh, H. Görls, M. El-khateeb, G. Mloston, W. Weigand, *Eur. J. Inorg. Chem.* **2011**, 2011, 349.
- [242] A. Q. Daraosheh, U.-P. Apfel, H. Görls, C. Friebe, U. S. Schubert, M. El-khateeb, G. Mloston, W. Weigand, *Eur. J. Inorg. Chem.* **2012**, 2012, 318.
- [243] A. Q. Daraosheh, H. Abul-Futouh, N. Murakami, K. M. Ziems, H. Görls, S. Kupfer, S. Gräfe, A. Ishii, M. Celeda, G. Mlostoń, W. Weigand, *Materials* **2022**, 15, 2867.
- [244] P. Buday, P. Seeber, C. Zens, H. Abul-Futouh, H. Görls, S. Gräfe, P. Matczak, S. Kupfer, W. Weigand, G. Mloston, *Chem. Eur. J.* **2020**, 26, 11412.
- [245] P. Buday, M. Celeda, H. Goerls, G. Mloston, W. Weigand, *Eur. J. Inorg. Chem.* **2022**, ejic.202200520.
- [246] M. K. Harb, U.-P. Apfel, J. Kübel, H. Görls, G. A. N. Felton, T. Sakamoto, D. H. Evans, R. S. Glass, D. L. Lichtenberger, M. El-khateeb, W. Weigand, *Organometallics* **2009**, 28, 6666.
- [247] M. K. Harb, H. Alshurafa, M. El-khateeb, A. Al-Zuheiri, H. Görls, H. Abul-Futouh, W. Weigand, *ChemistrySelect* **2018**, 3, 8867.
- [248] U.-P. Apfel, H. Görls, G. A. N. Felton, D. H. Evans, R. S. Glass, D. L. Lichtenberger, W. Weigand, *Helv. Chim. Acta* **2012**, 95, 2168.
- [249] R. Trautwein, L. R. Almazahreh, H. Görls, W. Weigand, *ZAAC* **2013**, 639, 1512.
- [250] R. Trautwein, L. R. Almazahreh, H. Görls, W. Weigand, *Dalton Trans.* **2015**, 44, 18780.
- [251] H. Abul-Futouh, M. El-khateeb, H. Görls, K. J. Asali, W. Weigand, *Dalton Trans.* **2017**, 46, 2937.
- [252] R. Trautwein, H. Abul-Futouh, H. Görls, W. Imhof, L. R. Almazahreh, W. Weigand, *New J. Chem.* **2019**, 43, 12580.
- [253] H. Abul-Futouh, M. El-khateeb, H. Görls, W. Weigand, *Heteroat. Chem* **2018**, 29, e21446.
- [254] U.-P. Apfel, Y. Halpin, H. Görls, J. G. Vos, B. Schweizer, G. Linti, W. Weigand, *Chem. Biodivers.* **2007**, 4, 2138.
- [255] Y. Zhang, Y. T. Si, M. Q. Hu, C. N. Chen, Q. T. Liu, *Acta Crystallogr., Sect. C: Cryst. Struct. Commun.* **2007**, 63, m499-500.

- [256] D. Seyferth, R. S. Henderson, L.-C. Song, G. B. Womack, *J. Organomet. Chem.* **1985**, *292*, 9.
- [257] D. Seyferth, R. S. Henderson, *J. Am. Chem. Soc.* **1979**, *101*, 508.
- [258] W. Gao, L.-C. Song, B.-S. Yin, H.-N. Zan, D.-F. Wang, H.-B. Song, *Organometallics* **2011**, *30*, 4097.
- [259] L.-C. Song, L.-X. Wang, B.-S. Yin, Y.-L. Li, X.-G. Zhang, Y.-W. Zhang, X. Luo, Q.-M. Hu, *Eur. J. Inorg. Chem.* **2008**, *2008*, 291.
- [260] L. R. Almazahreh, F. Arrigoni, H. Abul-Futouh, M. El-khateeb, H. Görls, C. Elleouet, P. Schollhammer, L. Bertini, L. de Gioia, M. Rudolph, G. Zampella, W. Weigand, *ACS Catal.* **2021**, 7080.
- [261] L. R. Almazahreh, U.-P. Apfel, W. Imhof, M. Rudolph, H. Görls, J. Talarmin, P. Schollhammer, M. El-khateeb, W. Weigand, *Organometallics* **2013**, *32*, 4523.
- [262] R. Goy, L. Bertini, H. Görls, L. de Gioia, J. Talarmin, G. Zampella, P. Schollhammer, W. Weigand, *Chem. Eur. J.* **2015**, *21*, 5061.
- [263] R. Goy, L. Bertini, T. Rudolph, S. Lin, M. Schulz, G. Zampella, B. Dietzek, F. H. Schacher, L. de Gioia, K. Sakai, W. Weigand, *Chem. Eur. J.* **2017**, *23*, 334.
- [264] R. Goy, U.-P. Apfel, C. Elleouet, D. Escudero, M. Elstner, H. Görls, J. Talarmin, P. Schollhammer, L. González, W. Weigand, *Eur. J. Inorg. Chem.* **2013**, *2013*, 4466.
- [265] R. Goy, L. Bertini, C. Elleouet, H. Görls, G. Zampella, J. Talarmin, L. de Gioia, P. Schollhammer, U.-P. Apfel, W. Weigand, *Dalton Trans.* **2015**, *44*, 1690.
- [266] H. Abul-Futouh, L. R. Almazahreh, T. Sakamoto, N. Y. T. Stessman, D. L. Lichtenberger, R. S. Glass, H. Görls, M. El-khateeb, P. Schollhammer, G. Mloston, W. Weigand, *Chem. Eur. J.* **2017**, *23*, 346.
- [267] H. Abul-Futouh, W. Imhof, W. Weigand, L. R. Almazahreh, *Inorganics* **2019**, *7*, 50.
- [268] D. Seyferth, G. B. Womack, R. S. Henderson, M. Cowie, B. W. Hames, *Organometallics* **1986**, *5*, 1568.
- [269] L.-C. Song, J.-S. Chen, G.-J. Jia, Y.-Z. Wang, Z.-L. Tan, Y.-X. Wang, *Organometallics* **2019**, *38*, 1567.
- [270] D. Seyferth, G. B. Womack, *Organometallics* **1986**, *5*, 2360.
- [271] M. D. Westmeyer, T. B. Rauchfuss, A. K. Verma, *Inorg. Chem.* **1996**, *35*, 7140.

- [272] A. Kramer, R. Lingnau, I.-P. Lorenz, H. A. Mayer, *Chem. Ber.* **1990**, *123*, 1821.
- [273] A. Kramer, I.-P. Lorenz, *J. Organomet. Chem.* **1990**, *388*, 187.
- [274] G. B. Hall, J. Chen, C. A. Mebi, N. Okumura, M. T. Swenson, S. E. Ossowski, U. I. Zakai, G. S. Nichol, D. L. Lichtenberger, D. H. Evans, R. S. Glass, *Organometallics* **2013**, *32*, 6605.
- [275] D. Seyferth, R. S. Henderson, L.-C. Song, G. B. Womack, *J. Organomet. Chem.* **1985**, *292*, 9.
- [276] D. Seyferth, L.-C. Song, R. S. Henderson, *J. Am. Chem. Soc.* **1981**, *103*, 5103.
- [277] L.-C. Song, M. Kadiata, J.-T. Wang, R.-J. Wang, H.-G. Wang, *J. Organomet. Chem.* **1990**, *391*, 387.
- [278] D. Seyferth, A. Kiwan, *J. Organomet. Chem.* **1985**, *286*, 219.
- [279] M. Cowie, R. L. DeKock, T. R. Wagenmaker, D. Seyferth, R. S. Henderson, M. K. Gallagher, *Organometallics* **1989**, *8*, 119.
- [280] N. Elgrishi, K. J. Rountree, B. D. McCarthy, E. S. Rountree, T. T. Eisenhart, J. L. Dempsey, *J. Chem. Educ.* **2018**, *95*, 197.
- [281] S. P. Best, *Coord. Chem. Rev.* **2005**, *249*, 1536.
- [282] S. P. Best, S. J. Borg, J. M. White, M. Razavet, C. J. Pickett, *Chem. Commun.* **2007**, 4348.
- [283] S. J. Borg, T. Behrsing, S. P. Best, M. Razavet, X. Liu, C. J. Pickett, *J. Am. Chem. Soc.* **2004**, *126*, 16988.
- [284] N. Chongdar, J. A. Birrell, K. Pawlak, C. Sommer, E. J. Reijerse, O. Rüdiger, W. Lubitz, H. Ogata, *J. Am. Chem. Soc.* **2018**, *140*, 1057.
- [285] S. J. George, Z. Cui, M. Razavet, C. J. Pickett, *Chem. Eur. J.* **2002**, *8*, 4037.
- [286] P. Li, S. Amirjalayer, F. Hartl, M. Lutz, B. de Bruin, R. Becker, S. Woutersen, J. N. H. Reek, *Inorg. Chem.* **2014**, *53*, 5373.
- [287] E. J. Lyon, I. P. Georgakaki, J. H. Reibenspies, M. Y. Darensbourg, *J. Am. Chem. Soc.* **2001**, *123*, 3268.
- [288] J. P. H. Oudsen, B. Venderbosch, D. J. Martin, T. J. Korstanje, J. N. H. Reek, M. Tromp, *PCCP* **2019**, *21*, 14638.
- [289] S. J. Borg, J. W. Tye, M. B. Hall, S. P. Best, *Inorg. Chem.* **2007**, *46*, 384.
- [290] M. H. Cheah, C. Tard, S. J. Borg, X. Liu, S. K. Ibrahim, C. J. Pickett, S. P. Best, *J. Am. Chem. Soc.* **2007**, *129*, 11085.

- [291] D. J. Curran, P. B. Graham, M. D. Rausch, *Organometallics* **1993**, *12*, 2380.
- [292] G. B. Hall, J. Chen, C. A. Mebi, N. Okumura, M. T. Swenson, S. E. Ossowski, U. I. Zakai, G. S. Nichol, D. L. Lichtenberger, D. H. Evans, R. S. Glass, *Organometallics* **2013**, *32*, 6605.
- [293] E. C. F. Schippers, S. S. Nurttilla, J.-P. H. Oudsen, M. Tromp, W. I. Dzik, J. I. van der Vlugt, J. N. H. Reek, *Eur. J. Inorg. Chem.* **2019**, *2019*, 2510.
- [294] F. Gloaguen, D. Morvan, J.-F. Capon, P. Schollhammer, J. Talarmin, *J. Electroanal. Chem.* **2007**, *603*, 15.
- [295] C. Greco, G. Zampella, L. Bertini, M. Bruschi, P. Fantucci, L. de Gioia, *Inorg. Chem.* **2007**, *46*, 108.
- [296] S. J. Borg, M. I. Bondin, S. P. Best, M. Razavet, X. Liu, C. J. Pickett, *Biochem. Soc. Trans.* **2005**, *33*, 3.
- [297] R. J. Wright, C. Lim, T. D. Tilley, *Chem. Eur. J.* **2009**, *15*, 8518.
- [298] G. Eilers, L. Schwartz, M. Stein, G. Zampella, L. de Gioia, S. Ott, R. Lomoth, *Chem. Eur. J.* **2007**, *13*, 7075.
- [299] B. E. Barton, T. B. Rauchfuss, *Inorg. Chem.* **2008**, *47*, 2261.
- [300] F. Wang, M. Wang, X. Liu, K. Jin, W. Dong, L. Sun, *Dalton Trans.* **2007**, *34*, 3812.
- [301] S.-F. Bai, J.-W. Ma, Y.-N. Guo, X.-M. Du, Y.-L. Wang, Q.-L. Li, S. Lü, *J. Mol. Struct.* **2023**, *1283*, 135287.
- [302] J.-F. Capon, F. Gloaguen, P. Schollhammer, J. Talarmin, *J. Electroanal. Chem.* **2004**, *566*, 241.
- [303] J.-F. Capon, F. Gloaguen, P. Schollhammer, J. Talarmin, *J. Electroanal. Chem.* **2006**, *595*, 47.
- [304] G. A. N. Felton, A. K. Vannucci, J. Chen, L. T. Lockett, N. Okumura, B. J. Petro, U. I. Zakai, D. H. Evans, R. S. Glass, D. L. Lichtenberger, *J. Am. Chem. Soc.* **2007**, *129*, 12521.
- [305] F. Gloaguen, *Inorg. Chem.* **2016**, *55*, 390.
- [306] M. B. Wilker, J. K. Utterback, S. Greene, K. A. Brown, D. W. Mulder, P. W. King, G. Dukovic, *J. Phys. Chem. C* **2018**, *122*, 741.
- [307] J. C. Ruth, A. M. Spormann, *ACS Catal.* **2021**, *11*, 5951.

- [308] R. E. Treviño, J. W. Slater, H. S. Shafaat, *ACS Appl. Energy Mater.* **2020**, *3*, 11099.
- [309] J. C. Ruth, R. D. Milton, W. Gu, A. M. Spormann, *Chem. Eur. J.* **2020**, *26*, 7323.
- [310] T. Yu, Y. Zeng, J. Chen, X. Zhang, G. Yang, Y. Li, *J. Mater. Chem. A* **2014**, *2*, 20500.
- [311] S. K. Ibrahim, X. Liu, C. Tard, C. J. Pickett, *Chem. Commun.* **2007**, *15*, 1535.
- [312] M. Karayilan, W. P. Brezinski, K. E. Clary, D. L. Lichtenberger, R. S. Glass, J. Pyun, *Angew. Chem. Int. Ed.* **2019**, *58*, 7537.
- [313] D. Heine, C. Pietsch, U. S. Schubert, W. Weigand, *J. Polym. Sci., Part A: Polym. Chem.* **2013**, *51*, 2171.
- [314] L. Wang, Z. Xiao, X. Ru, X. Liu, *RSC Adv.* **2011**, *1*, 1211.
- [315] E. Xu, Z. Xiao, H. Liu, L. Long, L. Li, X. Liu, *RSC Adv.* **2012**, *2*, 10171.
- [316] D. Zhu, Z. Xiao, X. Liu, *Int. J. Hydrogen Energy* **2015**, *40*, 5081.
- [317] V. Vijaikanth, J.-F. Capon, F. Gloaguen, P. Schollhammer, J. Talarmin, *Electrochem. Commun.* **2005**, *7*, 427.
- [318] M. E. Ahmed, S. Dey, B. Mondal, A. Dey, *Chem. Commun.* **2017**, *53*, 8188.
- [319] A. Le Goff, V. Artero, R. Metayé, F. Moggia, B. Jousset, M. Razavet, P. D. Tran, S. Palacin, M. Fontecave, *Int. J. Hydrog. Energy* **2010**, *35*, 10790.
- [320] R. Zaffaroni, R. J. Detz, J. I. van der Vlugt, J. N. H. Reek, *ChemSusChem* **2018**, *11*, 209.
- [321] M. Wen, H.-L. Wu, J.-X. Jian, X.-Z. Wang, X.-B. Li, B. Chen, C.-H. Tung, L.-Z. Wu, *ChemPhotoChem* **2017**, *1*, 260.
- [322] J. Sanabria-Chinchilla, A. Javier, D. Crouthers, J. H. Baricuatro, M. Y. Darensbourg, M. P. Soriaga, *Electrocatalysis* **2014**, *5*, 5.
- [323] O. Rüdiger, C. Gutiérrez-Sánchez, D. Olea, I. A. C. Pereira, M. Vélez, V. M. Fernández, A. L. De Lacey, *Electroanalysis* **2010**, *22*, 776.
- [324] X. Ru, X. Zeng, Z. Li, D. J. Evans, C. Zhan, Y. Tang, L. Wang, X. Liu, *J. Polym. Sci., Part A: Polym. Chem.* **2010**, *48*, 2410.
- [325] D. Millo, M.-E. Pandelia, T. Utesch, N. Wisitruangsakul, M. A. Mroginski, W. Lubitz, P. Hildebrandt, I. Zebger, *J. Phys. Chem. B* **2009**, *113*, 15344.
- [326] C. Madden, M. D. Vaughn, I. Díez-Pérez, K. A. Brown, P. W. King, D. Gust, A. L. Moore, T. A. Moore, *J. Am. Chem. Soc.* **2012**, *134*, 1577.

- [327] C. Gutiérrez-Sánchez, D. Olea, M. Marques, V. M. Fernández, I. A. C. Pereira, M. Vélez, A. L. de Lacey, *Langmuir* **2011**, *27*, 6449.
- [328] B. Chmielowiec, F. H. Saadi, J. H. Baricuatro, A. Javier, Y.-G. Kim, G. Sun, M. Y. Darensbourg, M. P. Soriaga, *J. Electroanal. Chem.* **2014**, *716*, 63.
- [329] A. Nayek, M. E. Ahmed, S. Samanta, S. Dinda, S. Patra, S. G. Dey, A. Dey, *J. Am. Chem. Soc.* **2022**, *144*, 8402.
- [330] X. Zhang, L. Liu, W. Cao, D. Lv, *Catal Lett* **2020**, *150*, 3409.
- [331] M. E. Ahmed, D. Saha, L. Wang, M. Gennari, S. Ghosh Dey, V. Artero, A. Dey, C. Duboc, *ChemElectroChem* **2021**, *8*, 1674.
- [332] M. Watanabe, Y. Honda, H. Hagiwara, T. Ishihara, *J. Photochem. Photobiol., C* **2017**, *33*, 1.
- [333] M. Cao, Z. Wang, J. Zhang, S. Xu, S. Zhang, X. Dai, X. Jiang, *Inorg. Chim. Acta* **2018**, *469*, 402.
- [334] P. D. Tran, V. Artero, M. Fontecave, *Energy Environ. Sci.* **2010**, *3*, 727.
- [335] L. J. Antila, P. Ghamgosar, S. Maji, H. Tian, S. Ott, L. Hammarström, *ACS Energy Lett.* **2016**, *1*, 1106.
- [336] C. M. Thomas, O. Rüdiger, T. Liu, C. E. Carson, M. B. Hall, M. Y. Darensbourg, *Organometallics* **2007**, *26*, 3976.
- [337] W. T. Eckenhoff, *Coordination Chemistry Reviews* **2018**, *373*, 295.
- [338] X. Li, M. Wang, S. Zhang, J. Pan, Y. Na, J. Liu, B. Akermark, L. Sun, *J. Phys. Chem. B* **2008**, *112*, 8198.
- [339] L.-C. Song, L.-X. Wang, M.-Y. Tang, C.-G. Li, H.-B. Song, Q.-M. Hu, *Organometallics* **2009**, *28*, 3834.
- [340] W.-G. Wang, F. Wang, H.-Y. Wang, G. Si, C.-H. Tung, L.-Z. Wu, *Chem. Asian J.* **2010**, *5*, 1796.
- [341] J. Liu, W. Jiang, *Dalton Trans.* **2012**, *41*, 9700.
- [342] S. Gao, W.-Y. Zhang, Q. Duan, Q. Liang, D. Jiang, J.-X. Zhao, J.-H. Hou, *Chem. Pap.* **2017**, *71*, 617.
- [343] A. M. Kluwer, R. Kapre, F. Hartl, M. Lutz, A. L. Spek, A. M. Brouwer, P. W. N. M. van Leeuwen, J. N. H. Reek, *PNAS* **2009**, *106*, 10460.
- [344] N. B. Williams, A. Nash, N. Yamamoto, M. Patrick, I. C. Tran, J. Gu, *Adv. Mater. Interfaces* **2021**, *8*, 2001961.



- [345] J. L. Bingaman, C. L. Kohnhorst, G. A. van Meter, B. A. McElroy, E. A. Rakowski, B. W. Caplins, T. A. Gutowski, C. J. Stromberg, C. E. Webster, E. J. Heilweil, *J. Phys. Chem. A* **2012**, *116*, 7261.
- [346] J. Ekström, M. Abrahamsson, C. Olson, J. Bergquist, F. B. Kaynak, L. Eriksson, L. Sun, H.-C. Becker, B. Åkermark, L. Hammarström, S. Ott, *Dalton Trans.* **2006**, 4599.
- [347] W. Gao, J. Liu, W. Jiang, M. Wang, L. Weng, B. Åkermark, L. Sun, *C.R. Chim.* **2008**, *11*, 915.
- [348] H.-H. Cui, M.-Q. Hu, H.-M. Wen, G. Chai, C.-B. Ma, H. Chen, C.-N. Chen, *Dalton Trans.* **2012**, *41*, 13899.
- [349] H.-Y. Wang, G. Si, W.-N. Cao, W.-G. Wang, Z.-J. Li, F. Wang, C.-H. Tung, L.-Z. Wu, *Chem. Commun.* **2011**, *47*, 8406.
- [350] F. Wang, W.-G. Wang, H.-Y. Wang, G. Si, C.-H. Tung, L.-Z. Wu, *ACS Catal.* **2012**, *2*, 407.
- [351] J.-X. Jian, Q. Liu, Z.-J. Li, F. Wang, X.-B. Li, C.-B. Li, B. Liu, Q.-Y. Meng, B. Chen, K. Feng, C.-H. Tung, L.-Z. Wu, *Nat. Commun.* **2013**, *4*, 2695.
- [352] M. Cheng, M. Wang, S. Zhang, F. Liu, Y. Yang, B. Wan, L. Sun, *Faraday Discuss.* **2017**, *198*, 197.
- [353] F. Wang, W.-J. Liang, J.-X. Jian, C.-B. Li, B. Chen, C.-H. Tung, L.-Z. Wu, *Angew. Chem. Int. Ed.* **2013**, *52*, 8134.
- [354] W.-J. Liang, F. Wang, M. Wen, J.-X. Jian, X.-Z. Wang, B. Chen, C.-H. Tung, L.-Z. Wu, *Chem. Eur. J.* **2015**, *21*, 3187.
- [355] M. Wen, X.-B. Li, J.-X. Jian, X.-Z. Wang, H.-L. Wu, B. Chen, C.-H. Tung, L.-Z. Wu, *Sci. Rep.* **2016**, *6*, 29851.
- [356] T. Yu, Y. Zeng, J. Chen, Y.-Y. Li, G. Yang, Y. Li, *Angew. Chem. Int. Ed.* **2013**, *52*, 5631.
- [357] D. Ziegenbalg, A. Pannwitz, S. Rau, B. Dietzek-Ivanšić, C. Streb, *Angew. Chem. Int. Ed.* **2022**, *61*, e202114106.
- [358] C. Figliola, L. Male, P. N. Horton, M. B. Pitak, S. J. Coles, S. L. Horswell, R. S. Grainger, *Organometallics* **2014**, *33*, 4449.
- [359] A. P. S. Samuel, D. T. Co, C. L. Stern, M. R. Wasielewski, *J. Am. Chem. Soc.* **2010**, *132*, 8813.

- [360] S. Asir, A. S. Demir, H. Icil, *Dyes Pigm.* **2010**, *84*, 1.
- [361] S. Benndorf, E. Hofmeister, M. Wächtler, H. Görls, P. Liebing, K. Peneva, S. Gräfe, S. Kupfer, B. Dietzek-Ivanšić, W. Weigand, *Eur. J. Inorg. Chem.* **2022**, *3*, e202100959.
- [362] S. Wang, A. Aster, M. Mirmohades, R. Lomoth, L. Hammarström, *Inorg. Chem.* **2018**, *57*, 768.
- [363] P. S. Singh, H. C. Rudbeck, P. Huang, S. Ezzaher, L. Eriksson, M. Stein, S. Ott, R. Lomoth, *Inorg. Chem.* **2009**, *48*, 10883.
- [364] S. J. Borg, S. K. Ibrahim, C. J. Pickett, S. P. Best, *C.R. Chim.* **2008**, *11*, 852.
- [365] M. Wang, K. Han, S. Zhang, L. Sun, *Coord. Chem. Rev.* **2015**, *287*, 1.
- [366] Q. Wang, K. Domen, *Chem. Rev.* **2020**, *120*, 919.
- [367] Y. Xu, Y. Huang, B. Zhang, *Inorg. Chem. Front.* **2016**, *3*, 591.
- [368] S. Troppmann, B. König, *ChemistrySelect* **2016**, *1*, 1405.
- [369] X.-B. Li, C.-H. Tung, L.-Z. Wu, *Nat Rev Chem* **2018**, *2*, 160.
- [370] A. Schleusener, M. Micheel, S. Benndorf, M. Rettenmayr, W. Weigand, M. Wächtler, *J. Phys. Chem. Lett.* **2021**, *12*, 4385.
- [371] R. Abe, *J. Photochem. Photobiol., C* **2010**, *11*, 179.
- [372] S. Benndorf, P. Buday, B. Callies, H. Görls, S. Kupfer, W. Weigand, *Dalton Trans.* **2023**, *52*, 7421.
- [373] X. Jiang, L. Long, H. Wang, L. Chen, X. Liu, *Dalton Trans.* **2014**, *43*, 9968.
- [374] M. Abdellah, S. Zhang, M. Wang, L. Hammarström, *ACS Energy Lett.* **2017**, *2*, 2576.
- [375] M. D. Peterson, L. C. Cass, R. D. Harris, K. Edme, K. Sung, E. A. Weiss, *Annu. Rev. Phys. Chem.* **2014**, *65*, 317.
- [376] S. Benndorf, A. Schleusener, R. Müller, M. Micheel, R. Baruah, J. Dellith, A. Undisz, C. Neumann, A. Turchanin, K. Leopold, W. Weigand, M. Wächtler, *ACS Appl. Mater. Interfaces* **2023**, *15*, 18889.
- [377] X.-B. Li, J.-X. Jian, X.-Z. Wang, Y. Wang, S.-G. Xia, C.-H. Tung, L.-Z. Wu, *Sol. RRL* **2021**, *5*, 2000474.
- [378] F. Wen, X. Wang, L. Huang, G. Ma, J. Yang, C. Li, *ChemSusChem* **2012**, *5*, 849.
- [379] A. Kaliyaraj Selva Kumar, Y. Zhang, D. Li, R. G. Compton, *Electrochem. Commun.* **2020**, *121*, 106867.

- [380] Y. N. Xu, W. Y. Ching, *Phys. Rev. B: Condens. Matter* **1993**, *48*, 4335.
- [381] R. Sahli, C. Fave, N. Raouafi, K. Boujlel, B. Schöllhorn, B. Limoges, *Langmuir* **2013**, *29*, 5360.
- [382] H. Hijazi, E. Levillain, B. Schöllhorn, C. Fave, *ChemElectroChem* **2022**, *9*, e20220019.
- [383] H. Hijazi, A. Vacher, S. Groni, D. Lorcy, E. Levillain, C. Fave, B. Schöllhorn, *Chem. Commun.* **2019**, *55*, 1983.
- [384] D. Captao, R. Sahli, N. Raouafi, B. Limoges, C. Fave, B. Schöllhorn, *ChemElectroChem* **2016**, *3*, 1422.
- [385] B. Neises, W. Steglich, *Angew. Chem. Int. Ed.* **1978**, *17*, 522.
- [386] S. Benndorf, S. Groni, L. M. Stafast, H. Görls, C. Fave, B. Schöllhorn, W. Weigand, *Eur. J. Inorg. Chem.* **2023**, e202200684.
- [387] C. V. Krishnan, M. Garnett, *Int. J. Electrochem. Sci.* **2011**, *6*, 3607.
- [388] L.-C. Song, W. Gao, C.-P. Feng, D.-F. Wang, Q.-M. Hu, *Organometallics* **2009**, *28*, 6121.
- [389] M. Mirmohades, S. Pullen, M. Stein, S. Maji, S. Ott, L. Hammarström, R. Lomoth, *J. Am. Chem. Soc.* **2014**, *136*, 17366.
- [390] H. Abul-Futouh, L. R. Almazahreh, S. J. Abaalkhail, H. Görls, S. T. Stripp, W. Weigand, *New J. Chem.* **2021**, *45*, 36.
- [391] T. Liu, B. Li, M. L. Singleton, M. B. Hall, M. Y. Darensbourg, *J. Am. Chem. Soc.* **2009**, *131*, 8296.
- [392] W.-G. Wang, H.-Y. Wang, G. Si, C.-H. Tung, L.-Z. Wu, *Dalton Trans.* **2009**, *15*, 2712.
- [393] G. Zampella, M. Bruschi, P. Fantucci, M. Razavet, C. J. Pickett, L. de Gioia, *Chem. Eur. J.* **2005**, *11*, 509.
- [394] D. R. Tyler, R. A. Levenson, H. B. Gray, *J. Am. Chem. Soc.* **1978**, *100*, 7888.